An International Forum For The AE Science and Technology

JOURNAL OF ACOUSTIC EMISSION

Vol.24/January-December 2006

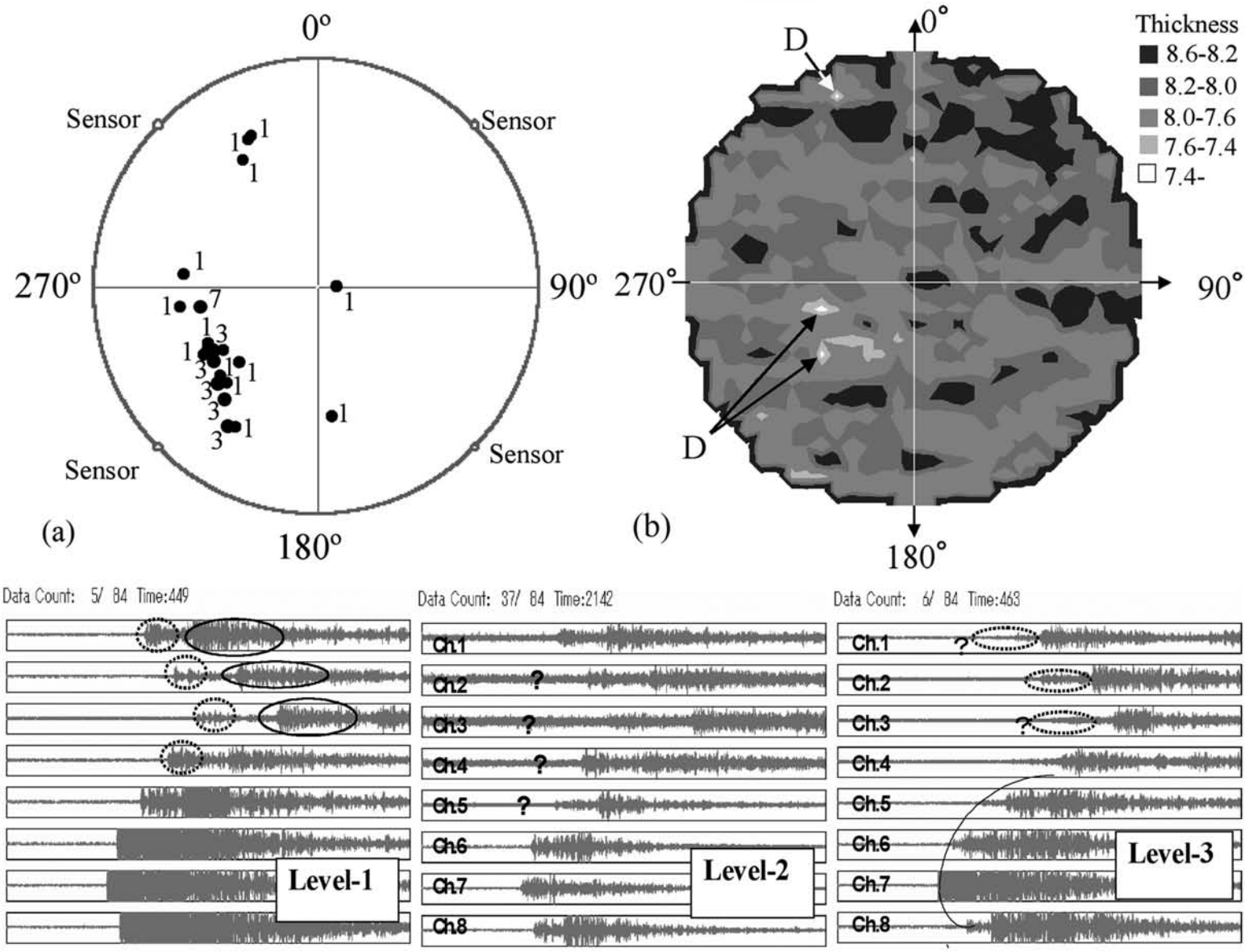

Aoyama Gakuin Univ (AGU) Tank Bottom Inspection with Lamb Waves

Endorsed by AEWG and EWGAE

Published by Acoustic Emission Group Encino, CA USA

JOURNAL OF ACOUSTIC EMISSION VOLUME 24, 2006

VIEWING AN ARTICLE

You need a software that can read a pdf-file. Two folders are provided for Windows 95/98/ME/2000/XP and for Macintosh. Each contains Adobe Acrobat Reader® Installer for respective OS. Install one first before going further. You can also download the latest version from www.adobe.com. Use of Adobe Acrobat ® (not provided) allows one to utilize the Search function. This gives the power to search for a name or a word in the entire volume and is highly recommended.

PDF Files: Contents are listed below**.** Individual papers have file names of **24-xxx.pdf**, with xxx as their first page number.

ISSN 0730-0050 Coden JACEDO

CONTENTS

24-001 A VARIABLE VELOCITY APPROACH TO LOCATE FATIGUE-INDUCED MICROCRACKS OCCURRED IN STRUCTURES WITH MULTIPLE MATERIAL LAYERS
JIHUI LI and GANG QI 1

24-012 LAMB-WAVE ACOUSTIC EMISSION FOR CONDITION MONITORING OF TANK BOTTOM PLATES
MIKIO TAKEMOTO, HIDEO CHO and HIROAKI SUZUKI 12

24-022 WAVELET TRANSFORM ANALYSIS OF EXPERIMENTAL AE WAVEFORMS ON STEEL PRESSURE VESSEL
MULU BAYRAY and FRANZ RAUSCHER 22

24-044 ACOUSTIC EMISSION PATTERN RECOGNITION ANALYSIS APPLIED TO THE OVER-STRAINED PIPES IN A POLYETHYLENE REACTOR
IRENEUSZ BARAN, MAREK NOWAK and KANJI ONO 44

24-052 ACOUSTIC EMISSION EVALUATION SYSTEMS OF TOOL LIFE FORSHEARING OF PIANO AND STAINLESS STEEL WIRES
MASANORI TAKUMA, NOBORU SHINKE, TAKAKO NISHIURA and KENSUKE AKAMATU 52

24-067 OPTICAL FIBER SYSTEM FOR AE MONITORING OF HIGH TEMPERATURE DAMAGE OF STAINLESS STEEL TUBING
TOMOHARU HAYANO, TAKUMA MATSUO, HIDEO CHO and MIKIO TAKEMOTO 67

24-076 DEVELOPMENT OF MEASUREMENT SYSTEM USING OPTICAL FIBER AE SENSORS FOR ACTUAL PIPING
SATOSHI NISHINOIRI, PORNTHEP CHIVAVIBUL, HIROYUKI FUKUTOMI and TAKASHI OGATA *76*

24-084 UTILIZATION OF CASCADE OPTICAL FIBER AE SYSTEM FOR SOURCE LOCATION OF LAMB WAVES THROUGH A CROSS-PLY CFRP PLATE
TAKUMA MATSUO, HIDEO CHO and MIKIO TAKEMOTO *84*

24-097 ELASTIC WAVES FROM FAST HEAVY-ION IRRADIATION ON SOLIDS
TADASHI KAMBARA, YASUYUKI KANAI, TAKAO M. KOJIMA, YOICHI NAKAI, AKIRA YONEDA, YASUNORI YAMAZAKI and KENSUKE KAGEYAMA 97

24-104 ACOUSTIC EMISSION RATE BEHAVIOR OF LAMINATED WOOD SPECIMENS UNDER TENSILE LOADING
ANDREAS J. BRUNNER, MARTIN T. HOWALD and PETER NIEMZ *104*

24-111 AE MEASUREMENTS FOR SUPERCONDUCTING DEVICES
KAZUAKI ARAI, KATSUYUKI KAIHO, HIROSHI YAMAGUCHI, HIROFUMI YAMASAKI, AKIRA NINOMIYA, TAKESHI ISHIGOHKA, KATSUTOSHI TAKANO, HIDEO NAKAJIMA and KIYOSHI OKUNO *111*

24-119 ACOUSTIC EMISSION OF SENSITIZED 304 STAINLESS STEEL WITH SIMULTANEOUS HYDROGEN CHARGING
S. H. CARPENTER, KANJI ONO and D. ARMENTROUT *119*

24-127 AE AND CORROSION POTENTIAL FLUCTUATION (CPF) FOR ENVIRONMENTAL ASSISTED FRACTURE
KOJI KAGAYAMA, TAKESHI OGAWA, AKIO YONEZU, HIDEO CHO and MIKIO TAKEMOTO *127*

24-139 DAMAGE EVALUATION BY FREQUENCY ANALYSIS OF CONTINUOUS RECORDED AE WAVEFORM
KAITA ITO and MANABU ENOKI *139*

24-145 FREQUENCY FILTERING ALGORITHMS OF PLATE WAVE AE FOR SOURCE LOCATION
YU KUROKAWA, YOSHIHIRO MIZUTANI and MASAMI MAYUZUMI *145*

24-153 EVALUATION OF TWO TYPES OF MARTENSITIC TRANSFORMATION IN Cu-Al-Ni SHAPE MEMORY ALLOY SINGLE CRYSTAL BY ACOUSTIC EMISSION WAVEFORM ANALYSIS
TAKESHI YASUDA, DAIKI TANI, HIDEO NISHINO and KENICHI YOSHIDA *153*

24-161 FATIGUE FRACTURE DYNAMICS OF HIGH STRENGTH STEEL STUDIED BY ACOUSTIC EMISSION TECHNIQUE
AKIO YONEZU, TAKESHI OGAWA and MIKIO TAKEMOTO *161*

24-173 QUANTITATIVE DETECTION OF MICROCRACKS IN BIOCERAMICS BY ACOUSTIC EMISSION SOURCE CHARACTERIZATION
SHUICHI WAKAYAMA, TAKEHIKO JIBIKI and JUNJI IKEDA *173*

24-179 DETERMINATION OF WAVE ATTENUATION IN ROCK SALT IN THE FREQUENCY RANGE 1 - 100 kHz USING LOCATED ACOUSTIC EMISSION EVENTS
GERD MANTHEI, JÜRGEN EISENBLÄTTER AND THOMAS SPIES *179*

24-187 ACOUSTIC EMISSION BEHAVIOR OF PRESTRESSED CONCRETE GIRDER DURING PROOF LOADING
LESZEK GOŁASKI, GRZEGORZ SWIT, MAŁGORZATA KALICKA and KANJI ONO *187*

24-196 MULTIPLET ANALYSIS FOR ESTIMATION OF STRUCTURES INSIDE AN AE CLOUD ASSOCIATED WITH A COMPRESSION TEST OF A SALT ROCK SPECIMEN
HIROKAZU MORIYA, GERD MANTHEI, HIROAKI NIITSUMA and JÜRGEN EISENBLÄTTER *196*

24-205 DAMAGE DIAGNOSIS OF RAILWAY CONCRETE STRUCTURES BY MEANS OF ONE-DIMENSIONAL AE SOURCES
TOMOKI SHIOTANI, XIU LUO and HIROSHI HAYA *205*

24-215 CHARACTARISTICS OF DAMAGE AND FRACTURE PROCESS OF SOLID OXIDE FUEL CELLS UNDER SIMULATED OPERATING CONDITIONS BY USING AE METHOD
KAZUHISA SATO, TOSHIYUKI HASHIDA, HIROO YUGAMI, KEIJI YASHIRO, TATSUYA KAWADA and JUNICHIRO MIZUSAKI *215*

24-222 ACOUSTIC EMISSION DETECTION OF DAMAGE EVOLUTION IN SHORT-FIBER COMPOSITES
JERZY SCHMIDT, IRENEUSZ BARAN, MAREK NOWAK and KANJI ONO *222*

24-228 AE MONITORING OF MICRODAMAGE DURING PROOF TEST OF BIOCERAMICS FOR ARTIFICIAL JOINTS
SHUICHI WAKAYAMA, CHIKAKO IKEDA and JUNJI IKEDA *228*

24-234 SMALL DIAMETER WAVEGUIDE FOR WIDEBAND ACOUSTIC EMISSION
M. A. HAMSTAD *234*

Contents24.pdf Contents of Volume 24 (2006) I-1, -2, -3
AUindex24.pdf Authors Index of Volume 24 I-4, -5
AusNotes.pdf Policy/Author's Notes/Meeting Calendar/Subscription Information I-6 - I-8

JAE Index Folder* Cumulative Indices of J. of Acoustic Emission, 1982 - 2006

* indicates the availability in CD-ROM only.

Volume 24 (2006) AUTHORS INDEX

KENSUKE AKAMATU	24-052
KAZUAKI ARAI	24-111
D. ARMENTROUT	24-119
IRENEUSZ BARAN	24-044, 24-222
MULU BAYRAY	24-022
ANDREAS J. BRUNNER	24-104
S. H. CARPENTER	24-119
PORNTHEP CHIVAVIBUL	24-076,
HIDEO CHO	24-012, 24-067, 24-084, 24-127, 24-161
JÜRGEN EISENBLÄTTER	24-179, 24-196
MANABU ENOKI	24-139
HIROYUKI FUKUTOMI	24-076
LESZEK GOŁASKI	24-187
M. A. HAMSTAD	24-234
TOSHIYUKI HASHIDA	24-215
HIROSHI HAYA	24-205
TOMOHARU HAYANO	24-067
MARTIN T. HOWALD	24-104
CHIKAKO IKEDA	24-228
JUNJI IKEDA	24-173, 24-228
TAKESHI ISHIGOHKA	24-111
KAITA ITO	24-139
TAKEHIKO JIBIKI	24-173
KOJI KAGAYAMA	24-127
KENSUKE KAGEYAMA	24-097
KATSUYUKI KAIHO	24-111
MAŁGORZATA KALICKA	24-187
TADASHI KAMBARA	24-097
YASUYUKI KANAI	24-097
TATSUYA KAWADA	24-215
TAKAO M. KOJIMA	24-097
YU KUROKAWA	24-145
JIHUI LI	24-001
XIU LUO	24-205
GERD MANTHEI	24-179, 24-196
TAKUMA MATSUO	24-067, 24-084
MASAMI MAYUZUMI	24-145
JUNICHIRO MIZUSAKI	24-215
YOSHIHIRO MIZUTANI	24-145
HIROKAZU MORIYA	24-196

YOICHI NAKAI	24-097
HIDEO NAKAJIMA	24-111
PETER NIEMZ	24-104
HIROAKI NIITSUMA	24-196
AKIRA NINOMIYA	24-111
HIDEO NISHINO	24-153
SATOSHI NISHINOIRI	24-076
TAKAKO NISHIURA	24-052
MAREK NOWAK	24-044, 24-222
TAKASHI OGATA	24-076
TAKESHI OGAWA	24-127, 24-161
KIYOSHI OKUNO	24-111
KANJI ONO	24-044, 24-119, 24-187, 24-222
GANG QI	24-001
FRANZ RAUSCHER	24-022
KAZUHISA SATO	24-215
JERZY SCHMIDT	24-222
NOBORU SHINKE	24-052
TOMOKI SHIOTANI	24-205
THOMAS SPIES	24-179
HIROAKI SUZUKI	24-012
GRZEGORZ SWIT	24-187
KATSUTOSHI TAKANO	24-111
MIKIO TAKEMOTO	24-012, 24-067, 24-084, 24-127, 24-161
MASANORI TAKUMA	24-052
DAIKI TANI	24-153
SHUICHI WAKAYAMA	24-173, 24-228
HIROSHI YAMAGUCHI	24-111
HIROFUMI YAMASAKI	24-111
YASUNORI YAMAZAKI	24-097
KEIJI YASHIRO	24-215
TAKESHI YASUDA	24-153
AKIRA YONEDA	24-097
AKIO YONEZU	24-127, 24-161
KENICHI YOSHIDA	24-153
HIROO YUGAMI	24-215

JOURNAL OF ACOUSTIC EMISSION

1. Aims and Scope of the Journal

Journal of Acoustic Emission is an international journal designed to be of broad interest and use to both researcher and practitioner of acoustic emission. It will publish original contributions of all aspects of research and significant engineering advances in the sciences and applications of acoustic emission. The journal will also publish reviews, the abstracts of papers presented at meetings, technical notes, communications and sum-maries of reports. Current news of interest to the acoustic emis-sion communities, announcements of future conferences and working group meetings and new products will also be included.

Journal of Acoustic Emission includes the following classes of subject matters;

A. Research Articles: Manuscripts should represent completed original work embodying the results of extensive investigation. These will be judged for scientific and technical merit.

B. Applications: Articles must present significant advances in the engineering applications of acoustic emission. Material will be subject to reviews for adequate description of procedures, substantial database and objective interpretation.

C. Technical Notes and Communications: These allow publications of short items of current interest, new or improved experimental techniques and procedures, discussion of published articles and relevant applications.

D. AE Literature section will collect the titles and abstracts of papers published elsewhere and those presented at meetings and conferences. Reports and programs of conferences and symposia will also be presented.

E. AE Program and Data Files: Original program files and data files that can be read by others and analyzed will be distributed in CD-ROM.

Reviews, Tutorial Articles and Special Contributions will address the subjects of general interest. Nontechnical part will cover book reviews, significant personal and technical accomplishments, current news and new products.

2. Endorsement

Acoustic Emission Working Group (AEWG), European Working Group on Acoustic Emission (EWGAE), Committee on Acoustic Emission from Reinforced Composites (CARP), and Acoustic Emission Working Group of India have endorsed the publication of Journal of Acoustic Emission.

3. Governing Body

The Editor and Associate Editors will implement the editorial policies described above. The Editorial Board will advise the edi tors on any major change. The Editor, Professor Kanji Ono, has the general responsibility for all the matters. Associate Editors assist the review processes as lead reviewers. Mr. Thomas F. Drouillard is responsible for the AE Literature section. The members of the Editorial Board are selected for their knowledge and experience on AE and will advise and assist the editors on the publication policies and other aspects. The Board presently includes the following members:

4. Publication

Journal of Acoustic Emission is published annually in CD-ROM by Acoustic Emission Group, PMB 409, 4924 Balboa Blvd, Encino, CA 91316. It may also be reached at 6531 Boelter Hall, University of California, Los Angeles, California 90095-1595 (USA). tel. 310-825-5233. FAX 818-990-1686. e-mail: kanjiono@gmail.com

5. Subscription

Subscription should be sent to Acoustic Emission Group. Annual rate for 2007 is US $111.00 including CD-ROM delivery, by priority mail in the U.S. and by air for Canada and elsewhere. For additional print copy, add $40. Overseas orders must be paid in US currencies with a check drawn on a US bank. Inquire for individual (with institutional order) and bookseller discounts.

6. Advertisement

No advertisement will be accepted, but announcements for books, training courses and future meetings on AE will be included without charge.

Notes for Contributors

1. General

The Journal will publish contributions from all parts of the world and manuscripts for publication should be submitted to the Editor. Send to:

Professor Kanji Ono, Editor - JAE
6531 Boelter Hall, MSE Dept.
University of California
Los Angeles, California 90095-1595 USA
FAX (1) 818-990-1686
e-mail: ono@ucla.edu

Authors of any AE related publications are encouraged to send a copy for inclusion in the AE Literature section to:

Mr. T.F. Drouillard, Associate Editor - JAE
11791 Spruce Canyon Circle
Golden, Colorado 80403 USA

Only papers not previously published will be accepted. Authors must agree to transfer the copyright to the Journal and not to publish elsewhere, the same paper submitted to and accepted by the Journal. A paper is acceptable if it is a revision of a governmental or organizational report, or if it is based on a paper published with limited distribution.

Compilation of annotated data files will be accepted for inclusion in CD-ROM distribution, so that others can share in their analysis for research as well as training. ASCII or widely accepted data formats will be required.

The language of the Journal is English. All papers should be written concisely and clearly.

2. Page Charges

No page charge is levied. One copy of CD-ROM will be supplied to the authors free of charge.

3. Manuscript for Review

Manuscripts for review need only to be typed legibly; preferably, double-spaced on only one side of the page with wide margins. The title should be brief. An abstract of 100-200 words is needed for Research and Applications articles. Except for short communications, descriptive heading should be used to divide the paper into its component parts. Use the International System of Units (SI).

References to published literature should be quoted in the text citing authors and the year of publication. These are to be grouped together at the end of the paper in alphabetical and chronological order. Journal references should be arranged as below. Titles for journal or book articles are helpful for readers, but may be omitted.

H.L. Dunegan, D.O. Harris and C.A. Tatro (1968), Eng. Fract. Mech., 1, 105-122.

Y. Krampfner, A. Kawamoto, K. Ono and A.T. Green (1975), "Acoustic Emission Characteristics of Cu Alloys under Low-Cycle Fatigue Conditions," NASA CR-134766, University of California, Los Angeles and Acoustic Emission Tech. Corp., Sacramento, April.

A.E. Lord, Jr. (1975), Physical Acoustics: Principles and Methods, vol. 11, eds. W. P. Mason and R. N. Thurston, Academic Press, New York, pp. 289-353.

Abbreviations of journal titles should follow those used in the ASM Metals Abstracts. In every case, authors' initials, appropriate volume and page numbers should be included. The title of the cited journal reference is optional.

Illustrations and tables should be planned to fit a single page width (6.5"). For the reviewing processes, these need not be of high quality, but submit glossy prints or equivalent electronic files with the final manuscript. Lines and letters should be legible.

4. Review

All manuscripts will be judged by qualified reviewer(s). Each paper is reviewed by one of the editors and may be sent for review by members of the Editorial Board. The Board member may seek another independent review. In case of disputes, the author may request other reviewers.

5. Electronic Media

This Journal will be primarily distributed electronically by CD-ROM. In order to expedite processing and minimize errors, the authors are requested to submit electronic files or floppy disk copy of the paper. We can read Macintosh and IBM PC formats. On the INTERNET, you can send an MS Word file to "ono@ucla.edu".

6. Color Illustration

We can process color illustration needed to enhance the technical content of an article. With the new format, authors are encouraged to use them.

MEETING CALENDAR:

The Fifth International Conference on Acoustic Emission/50th AEWG Meeting

The 5th ICAE and the 40th Anniversary meeting of AEWG will be at Lake Tahoe Nevada on Oct. 29-Nov. 2, 2007, organized by Mr. Allen Green. See http://www.aewg.org/index.html. Registration form, as well as hotel information regarding this conference, can be found there. Abstracts are due June 1, 2007.

5th Meeting of Latin American Group on Acoustic Emission, E-GLEA 5

In conjunction with the GLEA 10 years life celebration, E-GLEA5 will be held from August 29 to September 1, 2007, at the Engineering Faculty of the National University of Misiones (UNaM), Oberá city, Misiones province, Argentina. For more information, see:
http://e-glea5.demet.ufrgs.br; http://www.cnea.gov.ar/cac/endye/glea/default.htm

International Conference NDE for Safety

European NDT Days in Prague 07 is planned for November 5-9, 2007 at Prague, Czech Republic. Abstract deadline is May 31, 2007. Topics include power plants, transport, safety, standardization etc. This is organized by Czech NDT Society with European Federation of NDT. For details, see
http://cndt.cz/endtd07/content/index.php

IAES19, The 19th International AE Symposium

The IAES-19 is planned in Osaka area in the fall of 2008. It is sponsored by Japan Society for Non-Destructive Inspection. Details to be announced.

EWGAE2008

28th European Conference on Acoustic Emission Testing will be held at Krakow, Poland in the fall of 2008. It is organized by Dr. Jerzy Schmidt of Foundry Research Institute, Krakow. Meeting details to be announced.

2007 SUBSCRIPTION RATES

Base rate (CD-ROM) for one year	$111.00
CD-ROM + printed copy, US priority mail: add	$ 40.00
CD-ROM + printed copy, non-US priority mail: add	$ 45.00
Print copy only with priority shipping (US)	$140.00
Print copy only with priority/air shipping (non-US)	$145.00
For countries without Global Priority Service,	$160.00

Payment must be in U.S. dollars drawn on a U.S. bank. Bank transfer accepted at
California Bank and Trust, San Fernando Valley Office (Account No. 080-03416470)
16140 Ventura Blvd, Encino, CA 91436 USA (Swift code: CALBUS66)

Back issues available; Inquiry and all orders should be sent to (or Fax 1-818-990-1686):
Acoustic Emission Group
PMB 409, 4924 Balboa Blvd. Encino, CA 91316 USA

For inquiry through Internet, use the following address: kanjiono@gmail.com
Editor-Publisher Kanji Ono Tel. (818) 430-5152
Publication Date of This Issue (Volume 24): 9 April 2007.

A VARIABLE VELOCITY APPROACH TO LOCATE FATIGUE-INDUCED MICROCRACKS OCCURRED IN STRUCTURES WITH MULTIPLE MATERIAL LAYERS †

JIHUI LI and GANG QI*

Medical Acoustic Research Laboratory, Department of Biomedical Engineering, Joint program of The University of Memphis and University of Tennessee, * Department of Mechanical Engineering, The University of Memphis, TN 38152-6576, USA.

Abstract

In most AE source location applications, a constant signal velocity (or global velocity) is assumed in the Geiger's algorithm, which uses derivative information to represent the propagation of acoustic emission (AE) signals and is widely used to locate crack sources. However, the actual signal velocities vary notably from the constant velocity when the testing structures are composed of multiple material layers. This velocity variation is known to induce substantial location error and divergence in the computation. The present work proposed a variable velocity approach, which assigns a specific bulk velocity to the AE signal waves received at each sensor. In this approach, first an initial signal velocity is assumed for each sensor based on its relative location to a guessed microcrack; this initial velocity is then adjusted in the following computation according to the residual of arrival time. The performance of variable velocity approach in terms of convergence in computation was discussed. Using this approach, we studied fatigue-induced microcracks cumulated in a cemented total hip arthroplasty (THA) specimen. It was found that the static location error was reduced from 7.1 mm to 4.7 mm in pencil-lead break (PLB) tests. In the fatigue experiments performed on the specimen, we found this approach reduced computational divergence with respect to using the constant velocity approach, and achieved higher accuracy in microcrack source locations. The results indicated that the proposed variable velocity approach has significant advantages over the constant velocity approach when a specimen is composed of multiple material layers.

1. Introduction

Total hip arthroplasty (THA) has been successfully used for decades to replace the malfunctioned joints caused by severe osteoarthritis, rheumatoid arthritis and trauma. THA (Fig. 1) is composed of acetabular shell, polyethylene liner, femoral head, and hip implant (stem). Cement layer, as an option to anchor the implant into the femur, is mainly used in elderly patients or patients, who have poor potential of bone in-growth. Previous retrieval studies found that fatigue induced aseptic loosening is one of the leading causes of THA failure, and the loosening is correlated to the accumulation of microcracks in cement mantle, and the interfaces between cement/femur and cement/stem [1-3]. As a result, monitoring and investigating the microcrack performances become a main concern of researchers to better understand the fatigue mechanism of THA. Although various physical models has been developed to count and locate the microcracks occurred on certain cross sections after particular loading cycles [4-6], they all suffered some main drawbacks: failed to locate microcracks in three dimensional settings, failed to reveal the occurrence time, and lacked the capability of real time monitoring.

† A Student Award winner at the 48th Acoustic Emission Working Group Meeting, May 2005.

Recently we applied AE to study the THA fatigue mechanism [7-9] because of its high sensitivity and real-time monitoring capability [10-12]. In our research, THA integrity was evaluated by microcrack occurrence time, number and energy level and microcrack locations were computed based on the arrival time, signal velocity and coordinates of each receiving sensor. The testing results indicated that AE can effectively monitor the specimen integrity, but the current algorithm suffered serious divergence and significant location errors. In most AE applications, signals received by all channels were assigned a constant velocity, which was defined as Geiger's method, widely used in the studies of locating the microcracks. The constant velocity in Geiger's method can be used for specimens composed of single material. For specimens composed of multiple materials such as a THA that has four material layers, due to the refraction and reflection of AE signals at material interfaces, the actual signal velocity to a sensor is affected by material property and actual travel path. Because of the existence of these parameters, each sensor will receive an AE signal at a distinct velocity. In order to count for the signal velocity variation, we adapted a method that assigns each sensor a specific signal velocity to construct a specific velocity model. Although this method was widely used in seismology to determine the signal velocity of each sensor station [13, 14], it is unrealistic in the present study owing to the high sampling rate (>2 MHz) and the requirement of real-time monitoring.

The purpose of this work is to locate the fatigue-induced microcracks that occurred in THA specimens. We will accomplish this work by developing a variable velocity model using Geiger's method. We will first use static pencil-lead break (PLB) tests to verify the trustfulness of the velocity model. After the static validation, we will verify the variable velocity model in real fatigue tests.

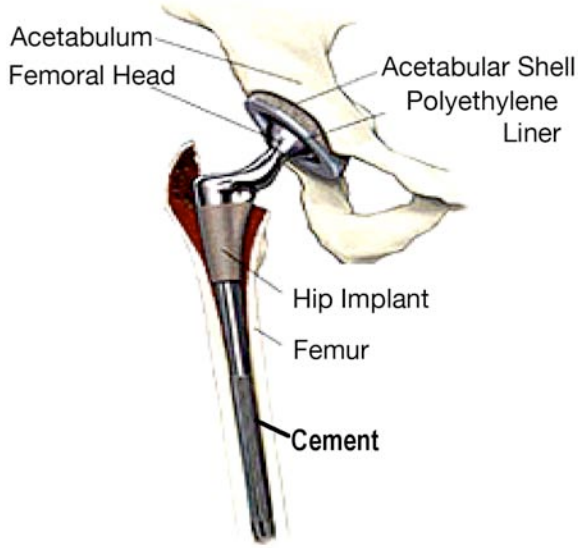

Fig. 1 Components of a total hip arthroplasty (THA). The thickness of the cement layer is between 3 to 10 mm.

2. Materials and Methods

Specimen Preparation

Standard THA specimens were prepared using Spectron hip stem (Smith & Nephew, Memphis, TN), Palacos R bone cement (Smith & Nephew, Australia) and synthetic Sawbone femur (Pacific Research Laboratory, Vashon, WA) (Fig. 2a). Each specimen had four layers of materials from outside to inside: glass fiber (representing femoral cortical bone), polyurethane foam

(representing cancellous bone), PMMA bone cement and CoCr stem (Fig. 2b). The average velocities of AE signal propagating in these materials were found to be 3.90, 3.00, 3.10 and 5.50 mm/μs, respectively, in experiments. A specimen without any radiographic defects was selected for this study. The specimen was potted distally into a steel cylindrical fixture using Fast cast (Goldenwest Mfg., Cedar Ridge, CA). The effective loading length of the specimen (from the loading point on the ball joint to the top surface of the cylinder) was 254 mm. A coordinate system was established at the center of the top surface of the cylinder (Fig. 2a).

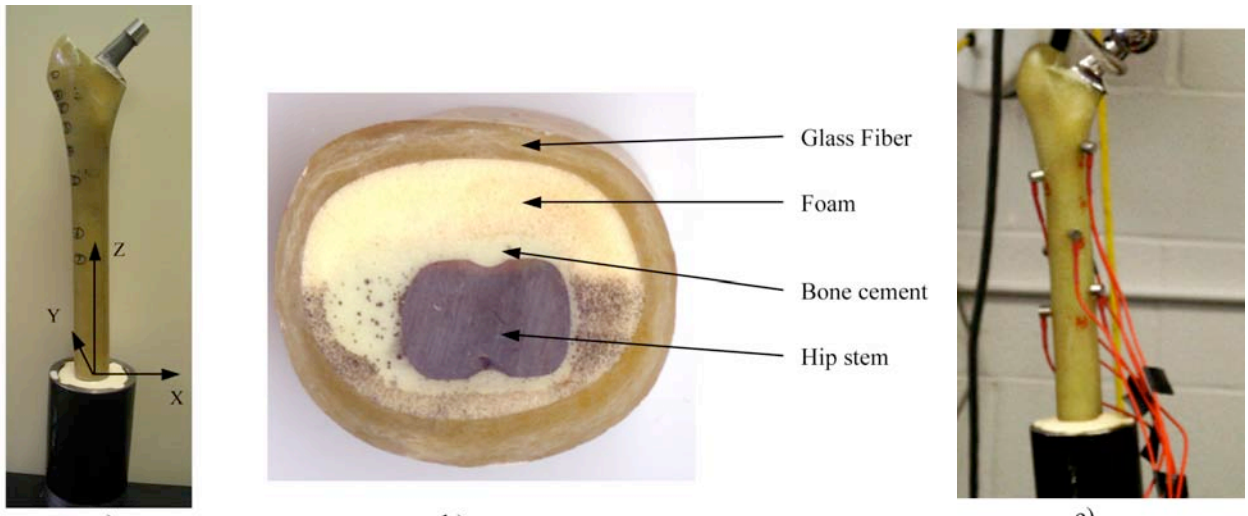

a) b) c)

Fig. 2(a) THA specimen and the coordinate system established on the top surface of the steel fixture. (b) Transverse section of the THA specimen. Four material layers are shown. (c) AE sensor placement.

AE Instruments

Eight AE sensors (Nano 30, Physical Acoustics Corp., Princeton, NJ) were attached on the specimen surface with silicon grease applied between the specimen and sensors (Fig. 2c). The sensors resonant frequency and operating frequency were 140 kHz and 125 - 750 kHz, respectively. The coordinates of sensors and randomly selected points for PLB tests were measured using machine lathe. The distances from break points to each sensor were calculated. The AE signals were conditioned by preamplifier (AEP4, Vallen Systeme, Icking, Germany) and then sent to an AE acquisition system (ASMY-5, Vallen Systeme) for data preprocessing.

Geiger's Source Location Method

Currently there are various microcrack location algorithms available. Ge [15-17] summarized these methods and demonstrated that iterative methods are more flexible and reliable. Geiger's method has been widely used in commercial AE software. This method simplifies the nonlinear system equations into first-order Taylor series and solves the linearized system using the least-square solution. The four unknowns in a source location problem are: the source location, S (x_s, y_s, z_s), and the origin time, t_s. The distance from the microcrack to sensor j is defined as [8, 16]:

$$L_j = v_j \times \tau_j = \sqrt{(X_j - x_s)^2 + (Y_j - y_s)^2 + (Z_j - z_s)^2} \quad (1)$$

where τ_j is the signal travel time (difference between detected arrival time T_j and t_s) from the microcrack to the sensor; (X_j, Y_j, Z_j) is the sensor coordinates; v_j is the actual signal velocity, which is usually replaced by an assumed value. For an AE signal received by n sensors, n equations establish the relationship among the unknowns and known parameters such as (X_j, Y_j, Z_j) and v_j.

Because there are four unknowns in the mathematical system, at least four picking sensors are needed to ensure the microcrack locatable. The solution of the problem is usually started from a guessed value $(x_s^0, y_s^0, z_s^0, t_s^0)$. Then, the residual of the arrival time of sensor *j* after the 1st iteration, r_{j1} is:

$$r_{j1} = T_j - [t_s^0 + \tau_j(x_s^0, y_s^0, z_s^0)] \tag{2}$$

r_{j1} can be expanded into the first-order Taylor series about (x_s^0, y_s^0, z_s^0):

$$r_{j1} \approx d\tau + \frac{\partial \tau_j}{\partial x}dx + \frac{\partial \tau_j}{\partial y}dy + \frac{\partial \tau_j}{\partial z}dz \qquad j = 1, 2, \ldots, \text{n} \tag{3}$$

where $d\tau = t_s^1 - t_s^0$, $dx = x_s^1 - x_s^0$, $dy = y_s^1 - y_s^0$, $dz = z_s^1 - z_s^0$, and *n* is the number of sensors. The event residual *RES* is [15],

$$RES = \sqrt{\frac{\sum r_{j1}^2}{n-m}} \qquad j = 1, 2, \ldots, \text{n} \tag{4}$$

where *m* is the degree of freedom; in this research, it is 4 because there are 4 unknowns. *RES* is often used as the stop criteria of the iteration process; more iteration is needed until a predefined tolerance is satisfied. If the process converges after the ith iteration, the residual of sensor *j*, r_{ji} is

$$r_{ji} = T_j - [t_s^{i-1} + \tau_j(x_s^{i-1}, y_s^{i-1}, z_s^{i-1})] \tag{5}$$

and the final results are:

$$t_s = t_s^i = d\tau + t_s^{i-1};\ x_s = x_s^i = dx + x_s^{i-1};\ y_s = y_s^i = dy + y_s^{i-1};\ z_s = z_s^i = dz + z_s^{i-1} \tag{6}$$

If no convergence is reached after certain number of iterations, the results of the last iteration are usually regarded as the final results, but its reliability is low compared to those that converged quickly.

Technical Difficulties in Specimens Composed of Multiple Material Layers

When a constant velocity is used in Geiger's method, divergence and location inaccuracy are likely to be the major technical problems encountered, especially if a specimen is composed of multiple material layers. Theoretically, four factors may contribute to these problems:

1) improper distribution of sensor array,
2) quality of arrival time,
3) accuracy of the assumed velocities and
4) truncation error of the first-order Taylor series.

Representing the nonlinear equations with first-order Taylor series can induce some truncation errors, but usually insignificant. The stability of the source location system is not a major concern in this study because the specimen is well covered by the sensor array. Two issues may cause the errors on arrival time: threshold setting and abnormal data sets. The floating threshold can effectively reduce error level on arrival time. The abnormal data received by some sensors in certain events is due to either environmental noise or one event is extremely close the other. Those data is few in this study and usually disregarded. Actual signal velocities may vary from the assumed value when the specimen is composed of multiple material layers. Due to the refraction and reflection of AE signals at material interfaces, signals can reach a sensor through multiple paths. The signal velocity of each path is the function of several factors including the signal travel length in each material, material properties and attenuation. The actual signal velocity determined by the first picking path is difficult to be anticipated.

To evaluate the actual signal velocities in a single microcrack event and to estimate the error level induced by the constant velocity, a theoretical study was performed to simulate the signal

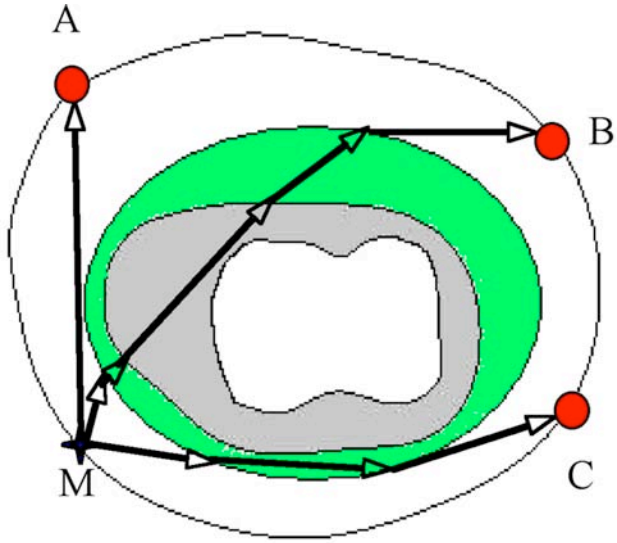

Fig. 3 Illustration of the travel paths of AE signals. M is a hypothetical microcrack location; A, B, and C are AE sensors. From this illustration, A is the closest sensor to M and the signal velocity of MA is the highest. B, involved most interfaces and materials, has the lowest signal velocity.

propagation from a microcrack (M) to three sensors (A, B, C) (Fig, 3). The possible first picking paths were designated and the travel length in each passing layer (L_i) was measured. The signal velocity of the path was:

$$v = \frac{L}{\tau} = \frac{L}{t_s - T} = \frac{L}{\sum_{i=1}^{n} \frac{L_i}{v_i}} \tag{7}$$

where L was the absolute distance from M to each sensor; τ was the total travel time, which was determined by L_i and corresponding theoretical velocity v_i. The estimated signal velocities of the three paths were 3.90, 2.75 and 3.20 mm/µs, respectively, indicating the variance on actual velocities was remarkable among sensors. Since no single value was close to all of these velocities, assuming a constant signal velocity to all sensors will induce velocity errors on certain sensors and further cause divergence and inaccurate location.

Variable velocity approach

It is common sense that those sensors close to a microcrack receive signals at higher velocity because of shorter travel path and few material interfaces. Therefore we can estimate the actual velocity of the signals according to the sensors relative location to the microcrack.

The first step of the variable velocity approach was to assign the signal an initial value at each sensor. For a certain event, we divided the specimen surface into four fields according to a guessed solution (x_s^0, y_s^0, z_s^0); and sensors in certain field were given the same initial signal velocity. We named this velocity as field velocity hereafter. The field velocity is the average signal velocity of all sensors in a given field. It is estimated through a series of PLB tests performed at different coordinates. Figure 4 showed an example of field partition. For example, a hypothetical microcrack was assumed at point P; the specimen surface (represented as a cylinder shell) was partitioned into four fields accordingly.

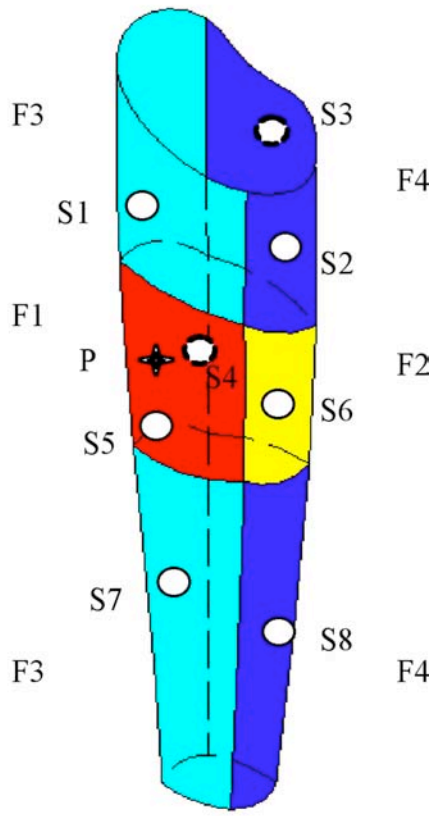

Fig. 4 The field partition in source location computation. The specimen surface is divided into 4 fields regarding to the guessed microcrack (P). Sensor 4 (S4) and S5 belonged to Field 1 (F1, in red color); S6 belonged to F2 (yellow); S1 and S7 belonged to F3 (cyan); and S2, S3 and S8 belonged to F4 (blue).

The second step is to adjust the initial velocity. The adjustment is performed according to the magnitude of the residual, r_{ji}:

$$r_{ji} = T_j - [t_s^{i-1} + \tau_j(x_s^{i-1}, y_s^{i-1}, z_s^{i-1}) = (T_j - t_s^i) - \tau(x_s^i, y_s^i, z_s^i) = \frac{L_j^i}{v_j^i} - \tau(x_s^i, y_s^i, z_s^i) \quad (8)$$

Where L_j^i is the distance between the computed microcrack (x_s^i, y_s^i, z_s^i) and sensor j; τ is the computed travel time; and v_j^i is v_j in the ith iteration. When a limit criterion ε is set, the adjustment will follow:

$$v_j^i = v_j^i \pm \Delta v; \qquad |r_{ji}| > \varepsilon \quad (9\text{-}1)$$

$$v_j^i = v_j^i; \qquad |r_{ji}| < \varepsilon \quad (9\text{-}2)$$

where Δv is the adjustment on v_j^i. "+" is used when r_{ji} is positive; otherwise using "–". The adjustment procedure will stop when Equation 9-2 is satisfied in all sensors or unsatisfied after certain number of iterations. In both case, the signal velocity of each sensor is regarded as the optimal velocity and sent to Geiger's method to finally compute the optimal location of the microcrack. The procedures of the variable velocity approach were presented as flowchart in Fig. 5. The approach was realized as a customized software, 3DMem, using Matlab (Mathworks, Natick, MA).

Static Location Error

The PLB tests were used to validate the variable velocity approach through static location errors. Two groups of PLB tests were performed on the specimen surface. The first group was used to determine the field velocities. Pencil leads were broken at four randomly selected locations. In each break, the specimen surface was partitioned into four fields according to the coordinates of the break point, and sensors were sorted into certain field. A reference sensor was attached next to the break point to monitor the signal's origin time t_s. The actual signal velocity of sensor j was:

$$v_j = \frac{L_j}{\tau_j} = \frac{L_j}{T_j - t_s} \tag{10}$$

where L_j was the distance from the PLB point to sensor j; and τ_j was travel time. As the field velocity was an estimated average signal velocity of all sensors sorted to the field, sensors from four PLB tests were considered together and the average signal velocity of all sensors belonged to each field was the corresponding field velocity.

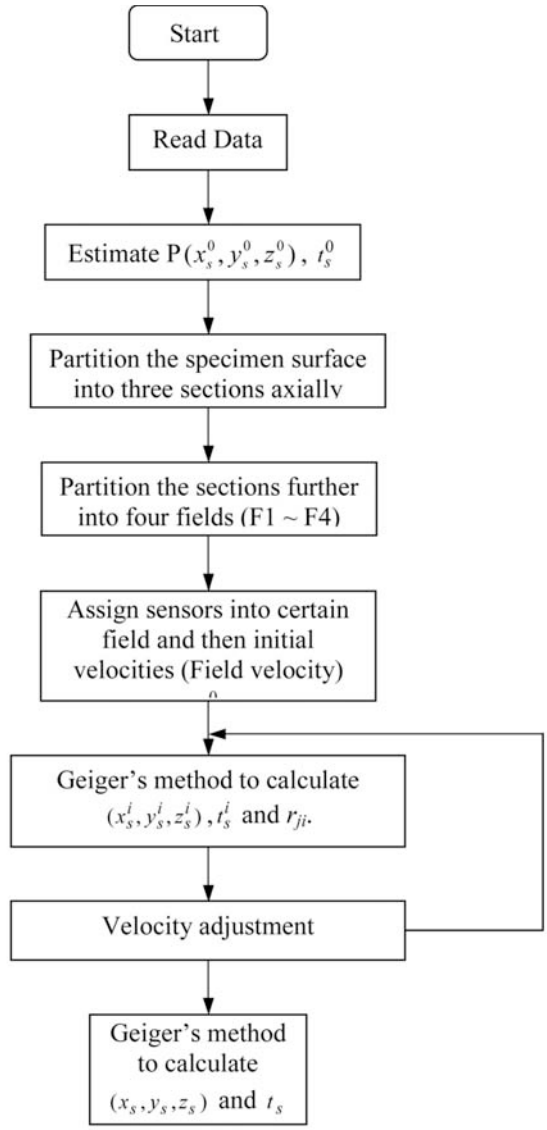

Fig. 5 Flowchart of the variable velocity approach.

The second group of PLB test was used to evaluate the location errors in static condition. Nine PLB tests were performed at three points on the specimen surface, three breaks at each point. The locations of break points were first computed using Geiger's method at a constant signal velocity of 3.20 mm/µs, and then 3D-Mem. The tolerance of *RES* was 5 µs, and the maximum iteration number was 50. The final *RES* and iteration number of each event were recorded and compared after computation. The differences between the computed and actual locations of break points were the static location errors. A reference sensor was attached next to break points and actual signal velocities were calculated using Equation 10. The specific velocities achieved by 3DMem and constant velocity were compared to actual velocities to indicate which velocity model was more accurate.

Dynamic Location Error

The THA specimen was hinge-hinge constrained at both ends onto a testing machine (HT 500, MTS Systems Corporation, Eden Prairie, MN). A sinusoidal compressive fatigue loading of 267/2670 N at 2 Hz was applied on the specimen for 5 million cycles. The locations of fatigue-induced microcracks were computed first using Geiger's method with a constant velocity of 3.20 mm/µs, and then 3DMem. The iteration number to convergence and corresponding *RES* of each microcrack were monitored in both algorithms. The tolerance of *RES* was set as 1 µs, and the

maximum iteration number was 50. After the fatigue experiment, the specimen was transversely sectioned at six levels using a low-speed diamond saw (Isomet 1000, Buehler Ltd., Lake Bluff, IL), from the stem collar with 15 mm interval (Fig. 6b). Section surfaces were polished and inspected using an environmental scanning electronic microscope (SEM, Model XL30; Philips, Achtsewed, Netherlands) operated at an accelerating voltage of 1 kV. Cracks on each section were identified and measured; their locations were compared to the computed microcracks to assess the dynamic location error. Because the observable cracks were limited only on the surface of those sections, the error level in Z direction was unavailable. The dynamic error in XY plane was:

$$e_{XY} = \sqrt{e_X^2 + e_Y^2} \tag{11}$$

where e_X was the measured location error in X direction, and e_Y was the error in Y direction.

3. Results

In the PLB tests used to determine the field velocities, there were totally 28 sensors received the PLB signals (each PLB signal was received by 7 sensors). After the field partition, 11 sensors were sorted into Field 1; 6, 9 and 2 sensors were sorted into Field 2 to 4, respectively. The average signal velocity of sensors in Field 1 was 3.59 ± 0.37 mm/μs, those of Field 2 to 4 were 2.67 ± 0.19, 3.44 ± 0.17 and 3.38 ± 0.03 mm/μs, respectively, which were assigned to be the corresponding field velocities.

Table 1. Computed static location error on the three PLB points using global velocity approach and variable velocity approach.

PLB	PLB coordinates (mm)			Errors of GV				Errors of VV			
				Relative (%)			Abs.	Relative (%)			Abs.
	X	Y	Z	X	Y	Z	(mm)	X	Y	Z	(mm)
B1	-9.6	15.4	276.0	45.8	42.3	0.5	8.0	34.7	30.8	0.1	5.8
B2	-6.2	-13.3	243.0	70.6	42.6	0.1	7.2	47.4	19.3	0.0	4.0
B3	11.1	-7.2	211.0	27.2	74.3	0.5	6.2	5.1	56.9	0.1	4.2
Avg.							7.1				4.7
S.D.							0.9				1.0

Note: GV: global velocity approach; VV: variable velocity approach; Abs.: absolute errors, which are obtained by: $\sqrt{(\Delta x)^2 + (\Delta y)^2 + (\Delta z)^2}$

In the second group of PLB test, the constant velocity approach generated an average static location error of 7.1 mm on the three points (B1 to B3), whereas 3DMem generated an average error of 4.7 mm (Table 1). Sensors had various signal velocities after the function of variable velocity approach. For example, in B2, the initial signal velocities of sensors 1 to 7 were set as 2.67, 3.59, 3.59, 2.67, 3.44, 3.44, and 3.44 mm/μs; they became 2.51, 3.76, 3.69, 2.62, 3.44, 3.21, and 3.13 mm/μs after velocity adjustment. The actual signal velocities calculated through Equation 10 were 2.58, 3.61, 3.54, 2.78, 3.59, 3.20 and 3.03 mm/μs. Comparing to the constant velocity (3.20 mm/μs), the specific velocities achieved in the variable velocity approach were closer to actual signal velocities ($p = 0.012$). Under the same convergence criterion ($RES < 5$ μs), only the three breaks at B1 can reach convergence at 49 times of iteration when constant velocity approach was used, the average *RES* of B1 to B3 were 4.7, 5.4 and 8 μs; On the other hand, all breaks at the three points converge after 1 time of iteration when the variable velocity approach was used, and *RES* were 0.5, 0.58 and 0.7 μs, respectively.

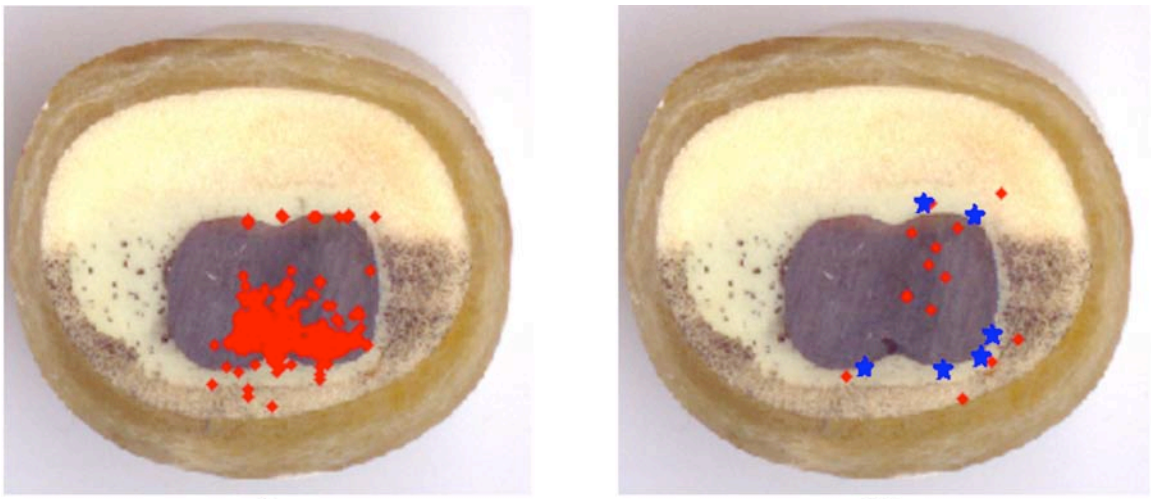

a) b)

Fig. 7 Computed microcracks (red dots) superimposed onto the picture of Section #2. a) Geiger's method. b) 3DMem. Cracks observed by SEM are presented by blue stars.

There were 5655 microcracks occurred in the fatigue test. When plotted onto the X-ray image (YZ plane), the computed microcracks using constant velocity approach scattered mainly in the proximal side of the specimen (Fig. 6a). A large percentage of microcracks were outside of the boundary of the specimen, indicating constant velocity approach generated a large-scale error in Z-axis. Most microcracks located by variable velocity approach were congregated in a small area in the proximal side (Fig. 6b). When plotted onto the picture of transverse section #2 (XY plane), the computed microcracks using constant velocity approach scattered mainly in the stem (Fig. 7a); whereas microcracks computed with 3DMem accumulated into 13 clusters distributing in the stem and along the stem/cement interface (Fig. 7b). The microcracks were so concentrated that they were likely to be thought as only 13 microcracks. This phenomenon occurred in other studies as well, but microcracks were more scattered in most cases. The computation were unable to converge after 50 iterations in all microcracks when constant velocity approach was used, and the average *RES* was 470 ms. On the other hand, there were only 84 microcracks diverged using variable velocity approach. All other data converged after 1 to 3 times of iterations, and the average *RES* was 0.77 μs. SEM inspection did not find cracks on the transverse sections except Section #2, the one cumulated most microcracks computed by variable velocity approach. On the section, 6 cracks were identified along stem/cement interface (Fig. 7b). When matching the computed microcracks to the observed cracks, the average error using 3DMem was 3.3 mm in X direction and 1.7 mm in Y direction. The total dynamic location error in XY plane was 3.7 mm (Eq. 11). Error level on microcracks computed by constant velocity approach was unavailable because they were scattered and difficult to be matched to certain observed cracks. But it could be seen that constant velocity approach generated larger errors on microcrack locations.

The results of both PLB tests and fatigue tests indicated that the variable velocity approach significantly reduced system divergence encountered in the constant velocity approach. The algorithm of the variable velocity model could be worded into a theorem under a weak condition in the following statement: if a system of equations of a source location problem is convergent using the approach of constant velocity, this system will not diverge using the approach of variable velocity in Geiger's algorithm[1].

[1] See note after References section.

4. Conclusions

In this work, AE technique was used to locate the fatigue-induced microcracks occurred in a cemented femur stem construct of a THA specimen composed of multiple material layers. To reduce the divergence and location error level caused by the constant velocity, a variable velocity approach was developed to assign each sensor a specific signal velocity. The results of pencil-lead break tests indicated that in comparison with the constant velocity approach, the specific signal velocities determined by the variable velocity approach were closer to the actual signal velocities; the source location error levels were decreased (from 7.1 mm to 4.7 mm) and the convergence of computational algorithm was increased. In THA fatigue tests, microcracks location accuracy and convergence was significantly improved as well. The output of this research suggests that the variable velocity approach could function better than the constant velocity approach in cases where multiple material layers were involved.

Acknowledgements

The project was supported in part by the Whitaker Foundation, RG-01-048. The hip implants and bone cement were donated by Smith & Nephew, Inc. The authors would like to thank Mr. Andy Whitten and Dr. Abraham Salehi for test preparation.

References

[1] N. Verdonschot and R. Huiskes "Cement debonding process of total hip arthroplasty stems". Clinical Orthopaedics and Related Research **336**: 297-307, 1997.
[2] A. Race, MA. Miller, DC. Ayers, KA. Mann. "Early cement damage around a femoral stem is concentrated at the cement/bone interface". Journal of Biomechanics. **36** (4): 489-96; 2003
[3] H. Malchau, P. Herberts, 1998. "Prognosis of total hip replacement. revision and re-revision rate in THR: a revision-risk study of 148,359 primary operations". *Scientific Exhibition Presented at the 65th Annual Meeting of the AAOS.*
[4] J. Stolk, N. Verdonschot, K.A. Mann, R. Huiskes. "Prevention of mesh-dependent damage growth in finite element simulations of crack formation in acrylic bone cement" Journal of Biomechanics **36**: 861-871, 2003.
[5] B. McCormack, C. Walsh, P. Prendergast. "An analysis of crack propagation paths at implant/bone-cement interfaces", Journal of Biomechanical Engineering. **118**(4): 579-85, 1996.
[6] B. McCormack, P. Prendergast, D. Gallagher. "An experimental study of damage accumulation in cemented hip prostheses". Clinical Biomechanics, **11**: 214–219. 1996.
[7] G. Qi, J. Li, W. Mouchon and G. Lewis, "Defect-Induced Fatigue Microcrack Formation in Cement Mantle". Journal of Biomedical Materials Research, **75** (2): 414-24, 2005.
[8] G. Qi, J. Li, K. Mann, A. Whitten, M. Hamstad, A. Salehi, "3D Real Time Methodology to Monitor Cement Failure in Femoral Component of Total Hip Arthroplasty". Journal of Biomedical Materials Research, **71** (3): 391-402, 2004.
[9] J. Li, G. Qi, and W. Mouchon, "Noninvasive Investigation of early Microcrack development in cemented Femur stem models". Transactions of Orthopedic Research Society, **31**: 0681, 2006.
[10] M. Hamstad, K. Downs. "On characterization and location of acoustic emission sources in real size composite structures: a waveform study". Journal of Acoustic Emission, **13**: 31–41, 1995.
[11] H. Fuchs, and R. Riehle; "Ten years of experience with leak detection by acoustic signal analysis", Applied acoustics, England, 1990.

[12] Y. Tian, P. Lewin, A. Davies, Z. Richardson, "Acoustic emission detection of partial discharges in polymeric insulation", *High Voltage Engineering Symposium*, 22–27 Aug. 1999, Conference Publication No. 467, IEE.
[13] L. Geiger "Probability method for the determination of earthquake epicenters from the arrival time only", *Bulletin of St. Louis University*. **8**, 60-71.
[14] C. Thurber "Nonlinear earthquake location: theory and examples", Bulletin of Seismological Society of America. **75**, 779-790
[15] M. Ge, " Analysis of Source Location Algorithms Part I: Overview and Non-iterative Methods", Journal of Acoustic Emission, **21**, 14-28, 2004.
[16] M. Ge, "Analysis of Source Location Algorithms Part II: Iterative Methods", Journal of Acoustic Emission, **21**, 29-51, 2004.
[17] M. Ge, "Analysis of AE Data from a Rocket Motor Case: Key Questions in AE Source Location". *40th Meeting of Acoustic Emission Working Group*, Chicago, 1997
[18] M. Ge, "Interpretation of Physical Status of Arrival Picks for Microseismic Source Location", Bulletin of Seismological Society of America. **80**, 1643-1660
[19] J. Li, Dissertation: "Investigation of the Performances of Fatigue-induced Microcracks Occurred in the Cemented Total Hip Arthroplasty", 2006. The Universiy of Memphis and University of Tennessee Health Science Center, Memphis, TN.

Note: Due to the complexity of the theoretical deduction, we have illustrated this theorem by using a simplified model in 2D hyperbolae. For a microcrack signal received by three or more sensors, a hyperbola can be defined by two sensors based on the signal travel times and velocities [18]. The ideal source location should be the intersection point of all ideal hyperbolae (defined by correct travel times and signal velocities). Due to the inaccuracy of the assumed constant velocity, the actual hyperbolae are often likely not to intersect at a point. The difference between the intersecting points forms an area, whereas the maximum difference is the actual error that produced in source location computation. The size of this area is affected strongly by the selection of proper velocity. When using the variable velocities, since the assumed velocities are closer to the actual signal velocities, all hyperbolae are closer to the ideal ones. This area is reduced and as a result, computed microcrack location will be much closer to the real one. The 3D case is similar to the 2D model, the ideal location should be the intersection of a series of hyperboloids; and the volume (instead of area in 2D) defined by the variable velocity approach is closer to the ideal location. For detail information regarding this theorem, please refer to [19].

LAMB-WAVE ACOUSTIC EMISSION FOR CONDITION MONITORING OF TANK BOTTOM PLATES

MIKIO TAKEMOTO, HIDEO CHO and HIROAKI SUZUKI*
Faculty of Science and Engineering, Aoyama Gakuin University,
5-10-1, Fuchinobe, Sagamihara, Kanagawa, 229-8558, Japan.
*Chiyoda Advanced Solutions Co., 1-1-25, Urashima, Kanagawa, Kanagawa 221-0031, Japan.

Abstract

Corrosion of the bottom plates of a 10,000-kl cylindrical tank was studied twice by monitoring the Lamb-wave acoustic emission (AE) signals. AE signals from rust fractures were detected by resonant sensors with center frequency of 50 or 30 kHz, mounted on the terrace of annular plates. Purpose of AE monitoring from the tank is the accurate location of corrosion zone, and not the estimation of corrosion rate from AE hits. The first AE monitoring of an open tank was performed in 2003 before the tank maintenance, and revealed that the located zones of AE signals agreed well with the zones of wall reduction detected by ultrasonic test. The second AE monitoring was done in 2005 for the same tank with naphtha, at one year and two months after the maintenance. AE signals were located in both the zones of inspection in 2003 and other zones nearby. This paper discusses the discrimination of signals from noise, arrival time determination of Lamb waves and location accuracy.

Keywords: Corrosion, rust fracture, source location, Lamb wave, wall reduction, location accuracy

Introduction

Condition monitoring of aged storage tanks is becoming an important issue in Japan. Japanese regulation by the Fire and Disaster Management Agency (FDMA) requires an open inspection of wall reduction (allowable wall reduction is 20 % of the design thickness) at 7 to 12 years. Tank owners have to inspect the corrosion damages by themselves utilizing adequate method. Principe of the condition monitoring by acoustic emission (AE) methods is that hard rusts produce AE signals when they crack [1, 2]. Since short-time AE monitoring cannot estimate the wall reduction or the corrosion rate, AE should be used as a screening method of tank integrity. Our purpose of AE inspection is to locate the corrosion zones in the floor plates correctly and to save the cost of open inspection. Accurate location of AE sources can contribute to minimize missing of deepest local corrosion by focusing the UT inspection in the estimated corrosion zones.

It should be noted that AE hits do not necessarily monitor the fracture of rusts produced by active corrosion during AE monitoring. For instance, the rust produced by the active corrosion a couple of years ago can emit AE signals even if the active corrosion under the rust stopped by the time of monitoring. This suggests that what we can estimate from AE data is not the direct information on the corrosion rate at the monitoring time, but the estimation of some of zones corroded or under corrosion. We cannot possibly detect the AE signals from all corroded zones if the rusts are not active [3].

For the accurate source location of AE signals, we monitored AE signals using AE sensors mounted on the terrace of annular plate, because our previous research revealed some difficulties in the source

location of AE signals monitored by sensors mounted on the sidewall (sidewall sensors, hereafter) [4, 5]. Difficulties arise from the fact that the AE sensors do not monitor the direct liquid-born P-waves, but various AE signals propagated via another paths. As the Lamb waves possess dispersive nature, we need an advanced source location method [6].

With the cooperation of Japanese Federation of Petroleum and tank owners, we performed AE inspections of storage tanks. First inspection was done for an open tank of 10,000 kl in 2003 [7], and the second inspection for the same tank containing naphtha in 2005. We report the source location results of AE signals from rust fractures on the floor plates. Accuracy of source locations was studied by correlating with the wall reduction data supplied by tank owner.

AE Monitoring Method

Tank Inspected

The storage tank inspected is a cylindrical tank of 10,000 kl capacity with a floating roof, and has been used for 40 years in the coastal area. Inner diameter and height of the tank are 32.93 m and 13.76 m, respectively. Thicknesses of the annular and floor plates at the time of construction were recorded as 10 mm and 9 mm, respectively. This tank was inspected twice, i.e., November 5th and 6th, 2003 and February 8th and 9th, 2005. We used different sensors and sensor combinations in the two inspections, and the methods are discussed separately below.

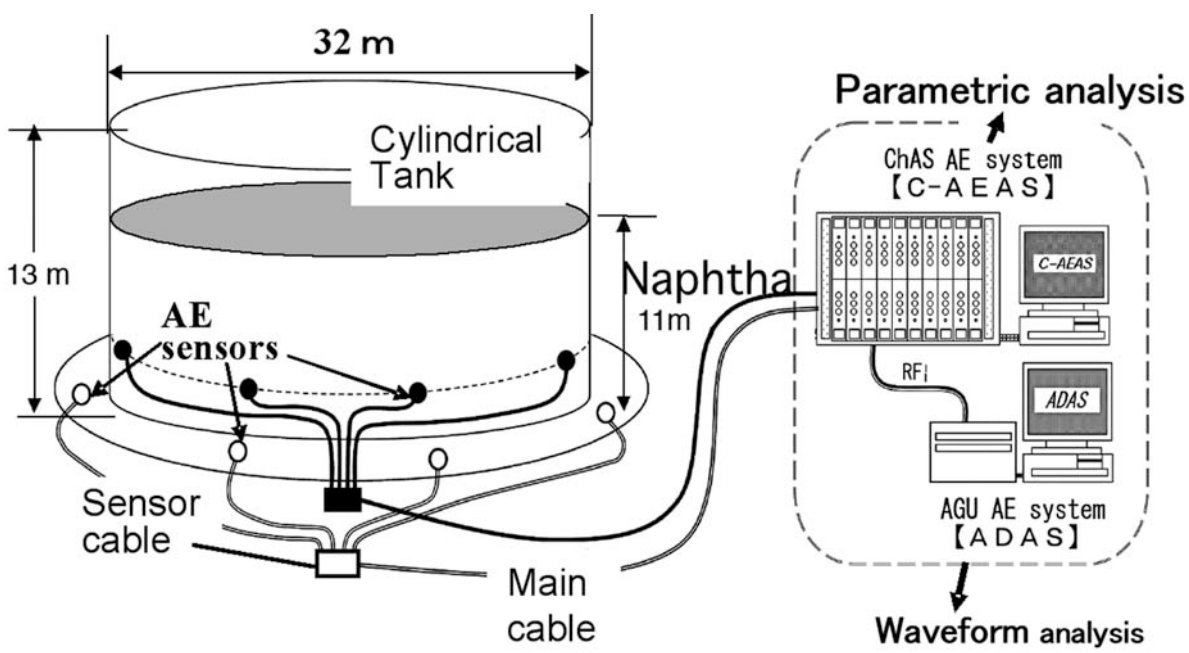

Fig. 1 AE monitoring method from corrosion of floor plate of opened and naphtha tank in November 2003 and February 2005.

Monitoring Method in 2003

This insepction was our first field experience. The tank was open for maintenance operation. We monitored AE signals using 8 sensors with center frequency of 50 kHz, mounted on the terrace of annular plates (abbreviated as annular 50-kHz sensors), and analyzed the monitored AE events using two

systems, as shown in Fig. 1. One is the system developed in our laboratory, named as ADAS (AE Data Acquisition and Analyzing System), and another a commercial system (C-AEAS, developed at Chiyoda Adv. Solutions) with 16 channels. The C-AEAS does not analyze waveforms in detail, but can perform real-time source location and parametric analyses. Source location of AE signals by the C-AEAS is estimated from the arrival times of waves crossing the threshold level using all sensors outputs. The ADAS stores all digital waveform data using the RF outputs of the C-AEAS, and performs signal/noise separation based on the detail waveform analysis and the source location. We changed the methods for arrival time determination, depending on the waveforms of Lamb wave.

AE signals were monitored twice on Nov. 6, 2003. The first monitoring was from 12:00 to 13:00 and the second monitoring from 14:00 to 15:00. Weather condition was cold and gusty with occasional heavy showers. Wind velocity and temperature were 3-8 m/s and 11-12˚C, respectively. In spite of strong wind, the monitoring was not interrupted to study how the wind-induced noise disturbs the detection of AE signals.

Monitoring Method in 2005

The C-AEAS system of 16 channels was utilized and the ADAS were utilized. Two set of eight resonant sensors with center frequencies of 30 or 50 kHz were mounted on the annular terrace or the side wall. Outputs of the C-AEAS were digitized and transferred to the ADAS system and analyzed in the laboratory after the test. Monitoring was done on Feb. 8 and 9, 2005. Both days were warm with weak wind of less than 2.5 m/s, but we had heavy shower at midnight of Feb. 8.

Results and Discussion

Source location was done for the AE signals according to the following steps.

1) classification of signals and noise,
2) best selection of sensor combinations and
3) determination of arrival times of selected mode waves at selected frequencies,
4) two dimensional source location,
5) accuracy examination of located zones.

Steps 1) to 3) are important operations for accurate source locations of AE signals. But the most important step is the last step. This is possible only by correlating the wall reduction data measured by ultrasonic testing (UT). Thus, we scheduled the AE monitoring just before or after the open inspection.

Source Locations of Signals Detected in November, 2003

Signals were selected from noise by careful visual inspection. Here, the “signals" was defined as the waves with sufficient S/N ratio and reasonable time sequence among the sensors, as shown in Fig. 2. We detected Ao-mode Lamb waves in this inspection and then determined the arrival times of first components of Ao-waves by visual inspection. As shown in the figure, arrival times of eight signals must be on a smooth curve. As the output of the sensor at 90˚ is weak, we located the sources using two sets (A and B) of four sensors. Sensor combinations were changed optionally depending on the waveforms detected. It is noted that the selection of odd and even sensors is not necessarily the best selection.

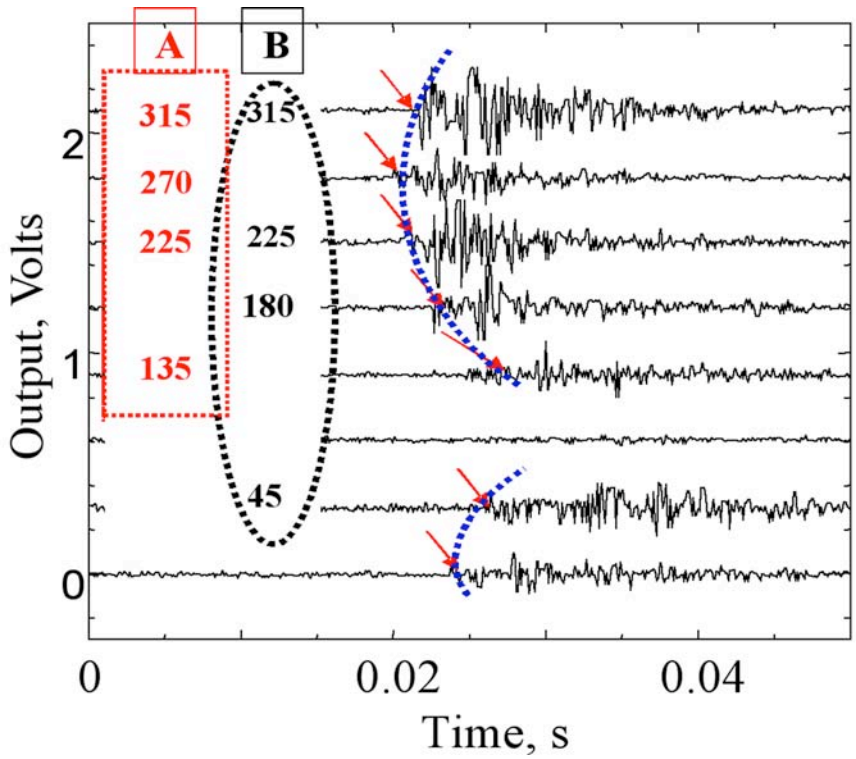

Fig. 2 Examples of signals for source location monitored by annular sensors on an open tank with sensor combinations A and B.

Figure 3 shows the change of cumulative signal counts with monitoring time on Nov. 6. It is noted that the total signal counts during one-hour monitoring are less than 85 or 4.5% of total AE events. AE generation rate changes within one hour, i.e., high for the last 40 minutes in Fig. 3(a) and for the first 20 minutes in Fig. 3(b). This strongly indicates that we cannot estimate the corrosion rate from hit counts detected by short-time monitoring. Continuous or periodic monitoring using an inexpensive cascade sensing system [3] is absolutely needed for damage progression estimation of high-risk tanks.

Figure 4 shows the location results of AE signals detected by the first and second one-hour monitoring. Here, the symbols, ○ and **x**, designate the source locations estimated by different sensor combinations. AE sources were located in limited zones in the third quadrant of the floor plates. It is noted that the source locations of AE signals during first and second one-hour monitoring are almost in the identical zone, indicating that the rust in these zones were active during the monitoring periods.

Figure 5(a) shows the location results estimated by the threshold-crossing time method with the C-AEAS. Numbers near the symbol designates the signal counts located. AE sources are located in the same zone of Fig. 4. This is because we detected the Lamb wave AE signals with strong Ao-modes, from which the arrival times were correctly determined by either of the threshold crossing method (C-AEAS) and our first arrival time method (ADAS). Figure 5(b) shows the contour maps of wall thickness, measured by the tank owner. Residual wall thickness less than 7.4 mm are indicated by D. The zone D in the third quadrant agrees well with the AE sources of Figs. 4 and 5(a). However, the zone D in the second quadrant was not detected. This implies that the rust in the zone D of the second quadrant was inactive during AE monitoring. Missing of corrosion zone cannot be avoided for short-time AE monitoring.

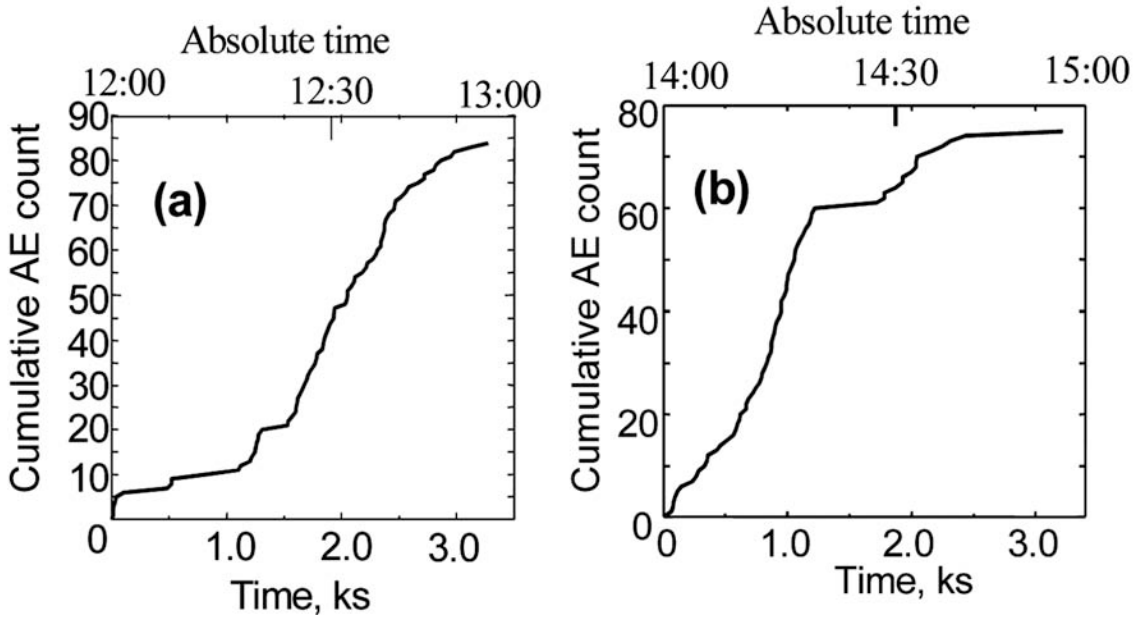

Fig. 3 Cumulative signal counts detected by first (a) and second (b) monitoring used for open tank in the Nov. 2003.

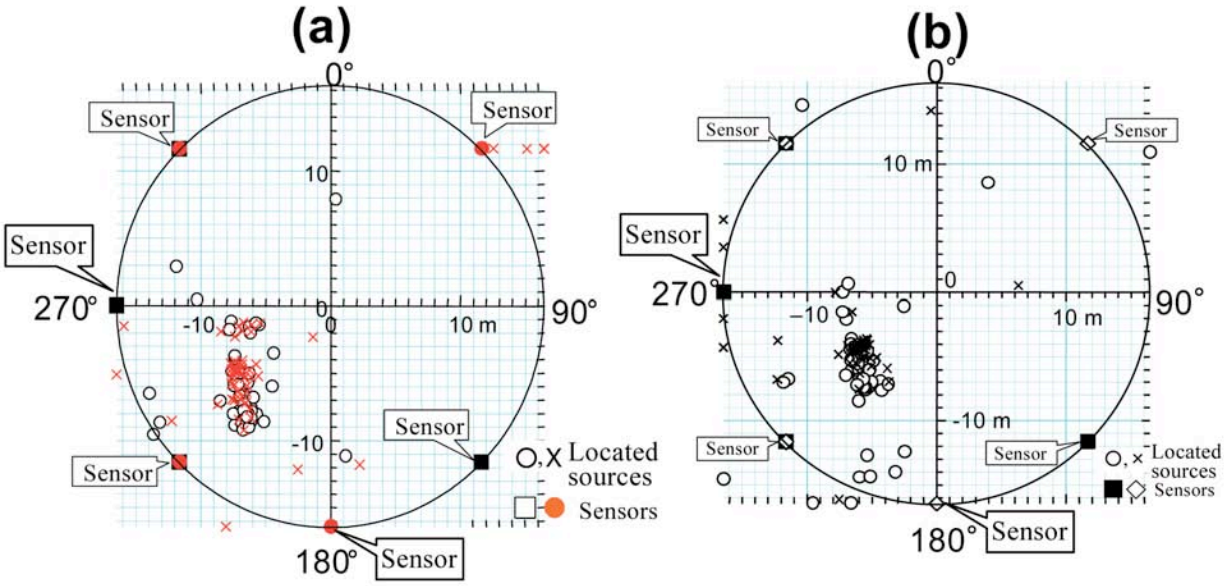

Fig. 4 Location results of Lamb-wave AE signals monitored by first (a) and second (b) one-hour inspection utilizing annular sensors in Nov. 2003. Location by arrival time differences of first Ao-mode wave method.

Source Locations of AE Signals Monitored in February 2005

Table 1 shows the weather condition, data number and events counts of noise and signals. We monitored AE signals for a total of 7 hours over two days; three hours on Feb. 9 and four hours on Feb. 10. We monitored AE signals using eight 30- or 50-kHz sensors mounted on the terrace of annular plate (suffix A) and on the sidewall (suffix S). Here, the data number 3-30A, for instance, designates monitoring No. 3 using 30-kHz sensors mounted on the annular plate. Gray columns mean the AE

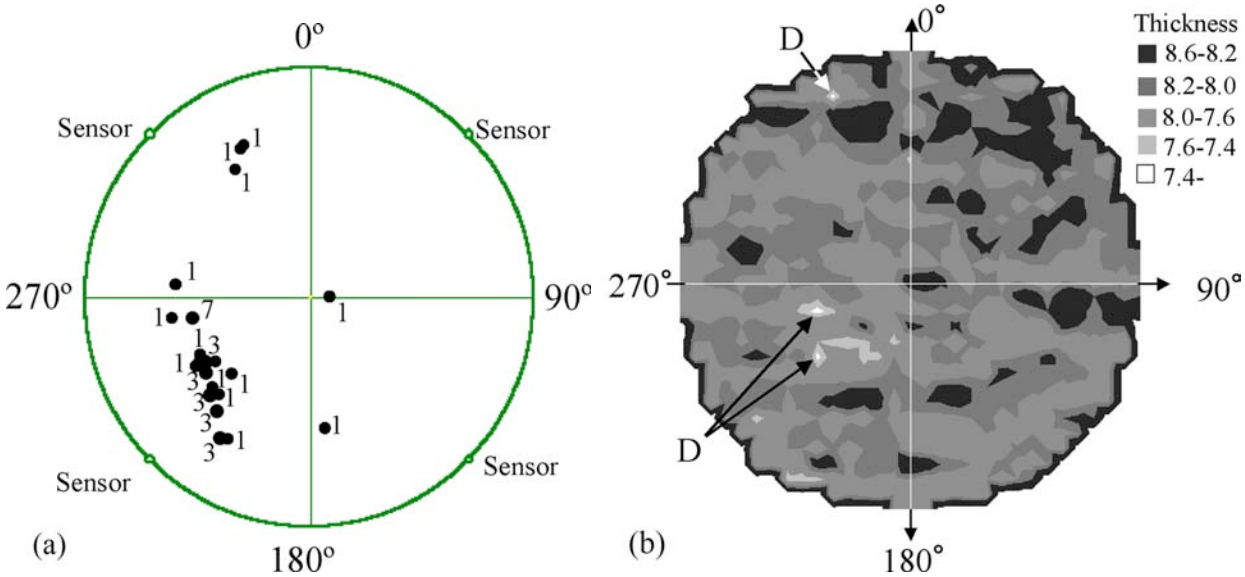

Fig. 5(a) Location results of Lamb-wave AE signals by threshold crossing arrival time difference method. AE data obtained utilizing annular sensors on Nov. 6, 2003. (b) Contour map of residual wall thickness of tank floor plates inspected by UT in Oct. 2003.

Table 1 Weather condition, data number, monitoring method and signal and noise counts.

Date	Feb, 9, 2005				Feb. 10, 2005			
Weahter	Temp. :12°C, humidity: 63%, Wind:2m/s				Temp. : 15°C, Humidity: 46%, Wind: 2.5m/s			
Monitoring No.	No.1		No.2		No.3		No.4	
Data Number	1-30A	1-50S	2-30A	2-50S	3-30A	3-50A	4-30S	4-50A
Sensor Type	30kHz	50kHz	30kHz	50 kHz	30kHz	50kHz	30kHz	50kHz
Sensor Location	Annular	Side wall	Annular	Side wall	Annular	Annular	Side wall	Annular
Start Time	13:30		14:31		8:57		11:28	
Finish Time	14:30		16:31		10:57		13:28	
Monitoring hour	1 hour		2 hour		2 hour		2 hour	
Total Events	530	65	1100	95	1800	220	1100	190
Total Noises	483	60	1077	89	1722	195	1058	179
Total Signals	46	5	23	9	84	25	42	11
% of signals to total events	8.70%	7.70%	2.10%	9.50%	4.70%	11.40%	3.80%	5.70%

monitoring using the annular sensors. It is noted that the signal counts are as low as 11%. Data numbers: 2, 3 and 4 are the data from 2-hour monitoring. Total signal counts by the 30-kHz annular sensors are higher than those by the 50-kHz sidewall sensors, but less than 84 counts (No. 3-30A) during 2-hour monitoring. Extremely low signal count percentages are due to noise from frequent steam hammers from steam pipeline. Obstacles in AE monitoring in winter season are strong north wind and steam hammer. As the AE system monitors the strong noise rather the weak AE signals, signal percentage to total events becomes low.

In the source location analysis of the second monitoring data, we ranked AE signals into three levels (Level-1, -2 and -3) based on the waveforms shown in Fig. 6. Three levels are defined below. It is noted that the source locations were estimated by using the four outputs of odd and even sensors for these data.

Level-1: Four odd and even sensors detected the signals with sufficient S/N ratios and the expected location reliability is high. (Level-1 waveforms in Fig. 6).

Level-2: Three sensors detected the signals with sufficient S/N ratios, and the expected location reliability is medium (Level-2 waveforms in Fig. 6).

Level-3: Arrival times of three sensors can hardly be determined, and the location reliability is low.

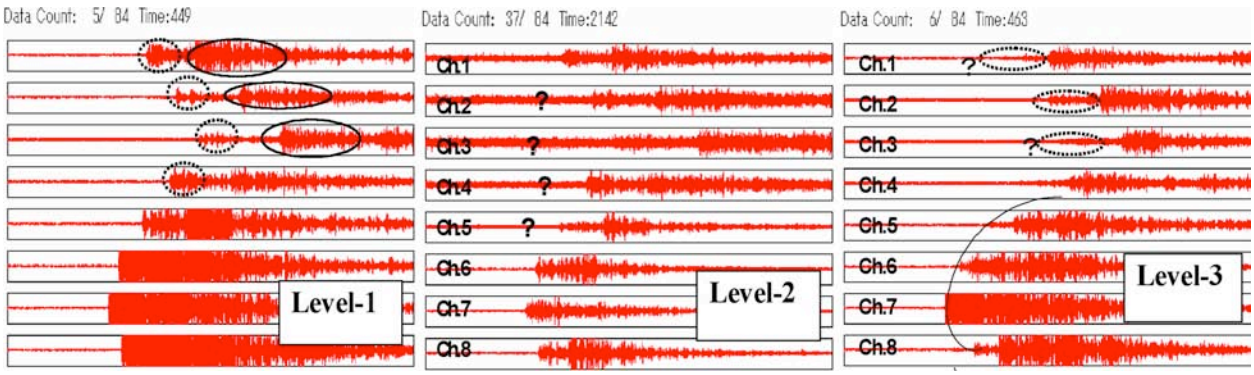

Fig. 6 Typical waveform examples of Level-1, -2 and-3 Lamb-wave signals detected by annular sensors.

Table 2 Signal counts of level-1, -2 and -3.

Monitoring No.	No.1		No.2		No.3		No.4	
Data number	1-30A	1-50S	2-30A	2-50S	3-30A	3-50A	4-30S	4-50A
Total signals	46	5	23	9	84	25	42	11
Located signals	31	3	19	8	50	7	10	9
Level-1signals	3	3	10	6	33	7	10	1
Level-2 signals	10	0	6	2	16	16	15	8
Level-3 signals	18	0	3	0	1	0	1	0

Table 2 shows the ranking results. Among the data of 7 hours of monitoring, only the data: 3-30A by the annular 30 kHz sensors counted 33 signals of level-1 and 16 signals of level-2 signals. Figure 7 shows the change of cumulative events and signal counts of data No.3-30A. Signals increased linearly during two hours, but counted only 4.7% of total events. As strong So-mode waves were detected in the second monitoring, we estimated the source locations from first arrival times of So-packet and the sheet velocity of 5400 m/s. This method is the most reliable method, and results in accurate source locations.

Location results of Data 3-30A are shown in Fig. 8. Further, we studied the location reliability by examining the distance error of the locations estimated by odd and even sensors outputs. Here, the reliable source clusters are indicated by dotted ellipses on the contour map of wall thickness data of Oct. 2003. The ellipses indicate that the distance error between the source location by odd (○) and even (●) sensors was less than 2 m. Five ellipses (a - e) are the signal clusters of Data No. 3-30A. Source locations of a total of 72 AE signals at Level-1 and -2 of both Data No. 3-30A and 3-50A are shown in

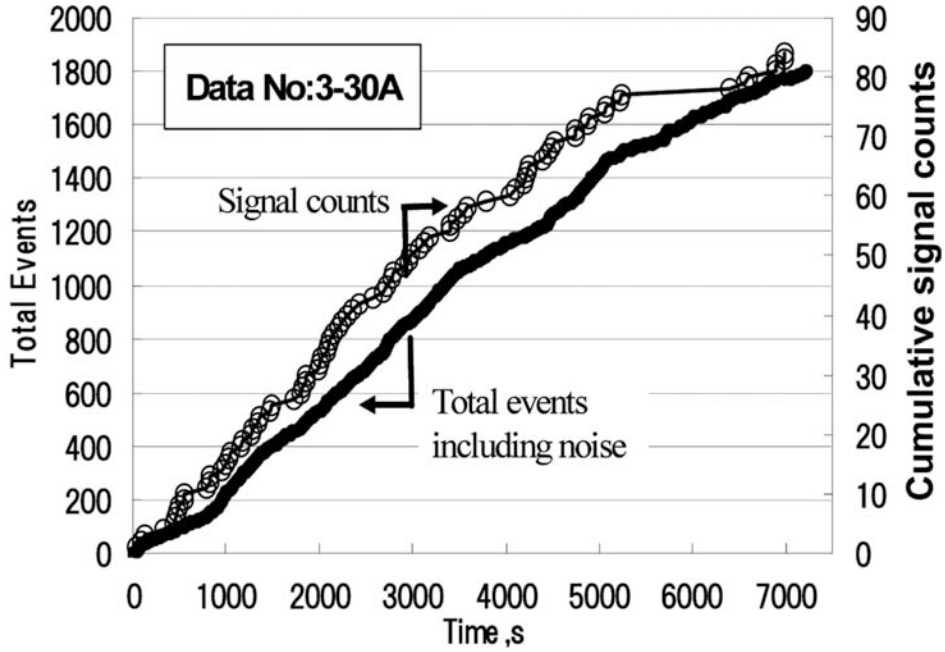

Fig. 7 Changes of cumulative events and signal counts during 2-hour monitoring (Data No. 3-30A) by 30-kHz annular sensors.

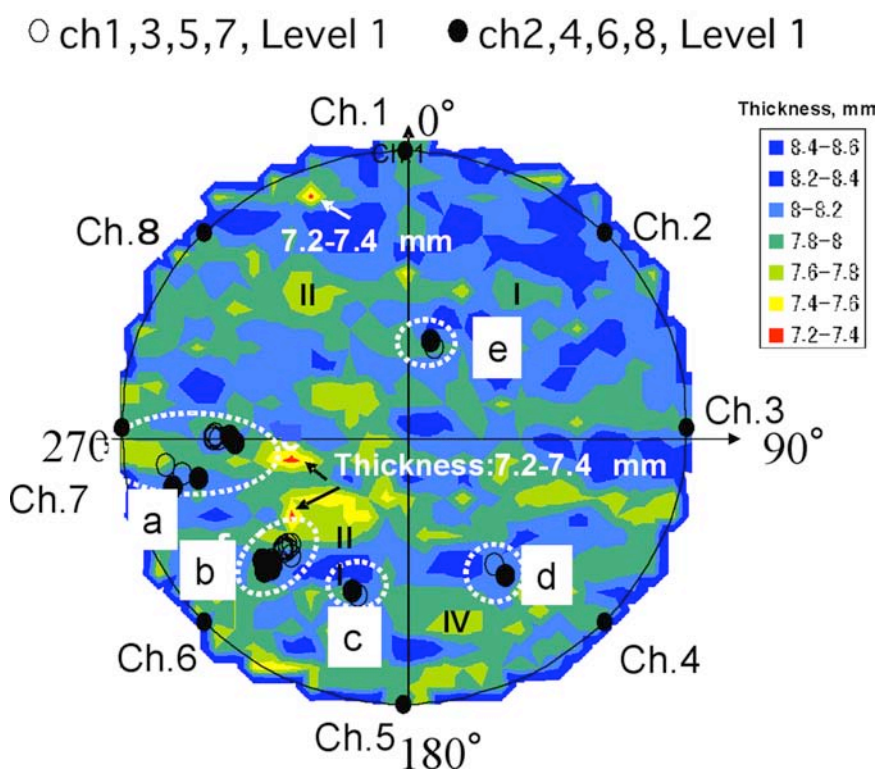

Fig. 8 Overlapping of source clusters of data 2-30A on wall thickness data measured in Oct. 2003.

Fig. 9. Summarizing the location results shown in Figs. 8 and 9, corrosion zones appear to be expanding from the limited zone in the third quadrant of Fig. 5, but mostly still in the third quadrant. Figure 10 shows the energy distribution of AE signals monitored by the C-AEAS system. It shows high energy signals in the third quadrant, supporting the locations in Figs. 9 and 10.

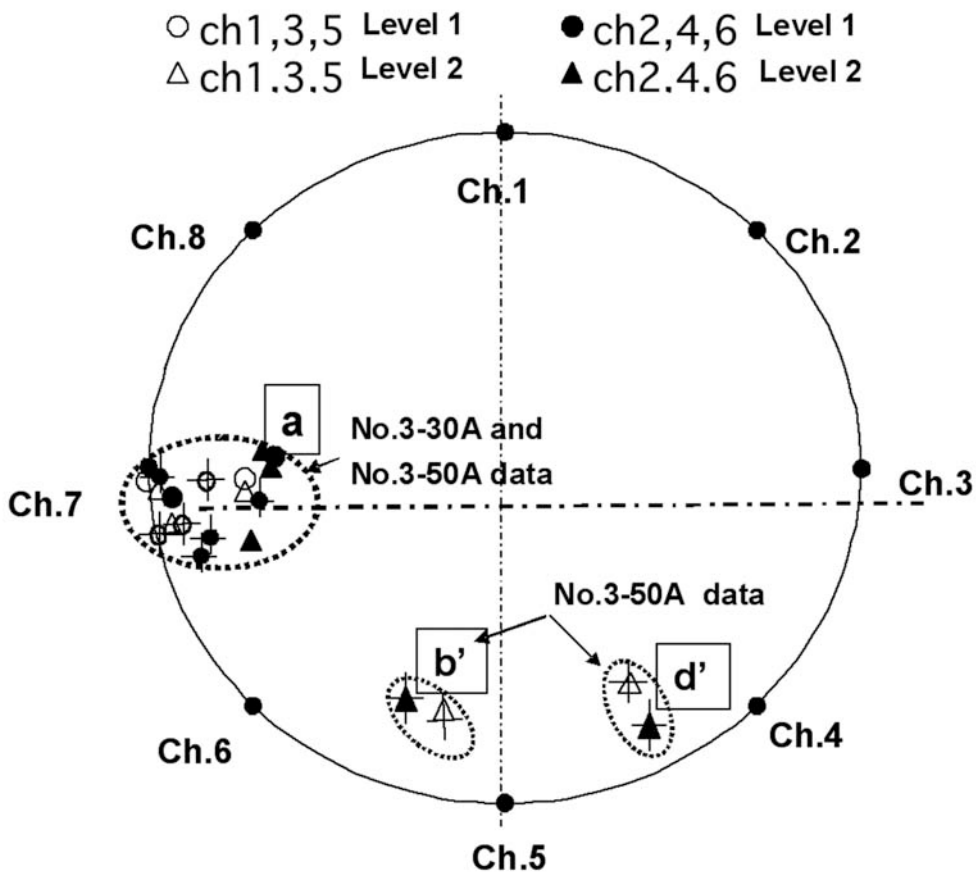

Fig. 9 Source clusters of Data No. 2-30A and 2-50A.

Conclusions

We monitored AE signals from rust fractures on the floor plates of 10,000 kL open and naphtha tank using the AE sensors mounted on the terrace of annular plates in 2003 and 2005, respectively, and estimated the source locations of AE signals. Results are summarized below.

1) Source locations of AE signals are the most important information, which we can supply the tank owners. The location of a corrosion zone contributes to reduce the cost of detailed inspection of residual wall thickness by UT.
2) Source locations must be performed for the signals separated from noise by waveform inspection. Wind-induced noise and steam hammer were serious obstacles to AE monitoring in winter season. Signal percentages to total events were less than 10% in our field inspections.
3) Source locations of Lamb-wave signals detected for an open tank in 2003 were found in the limited zones of the third quadrant of the tank bottom. This zones agreed well with the zones with large wall thickness reduction. However, another zone with a large wall reduction could not be detected due to the acoustic inactivity of the zone.
4) For the AE data monitored for the naphtha tank in 2005, we carefully separated the signals from noise and estimated the location accuracy by evaluating the signal levels of four odd and even sensors. Source locations of Lamb-wave signals were estimated in and around the limited zone of the third quadrant estimated in 2003, indicating an expanding of corrosion.

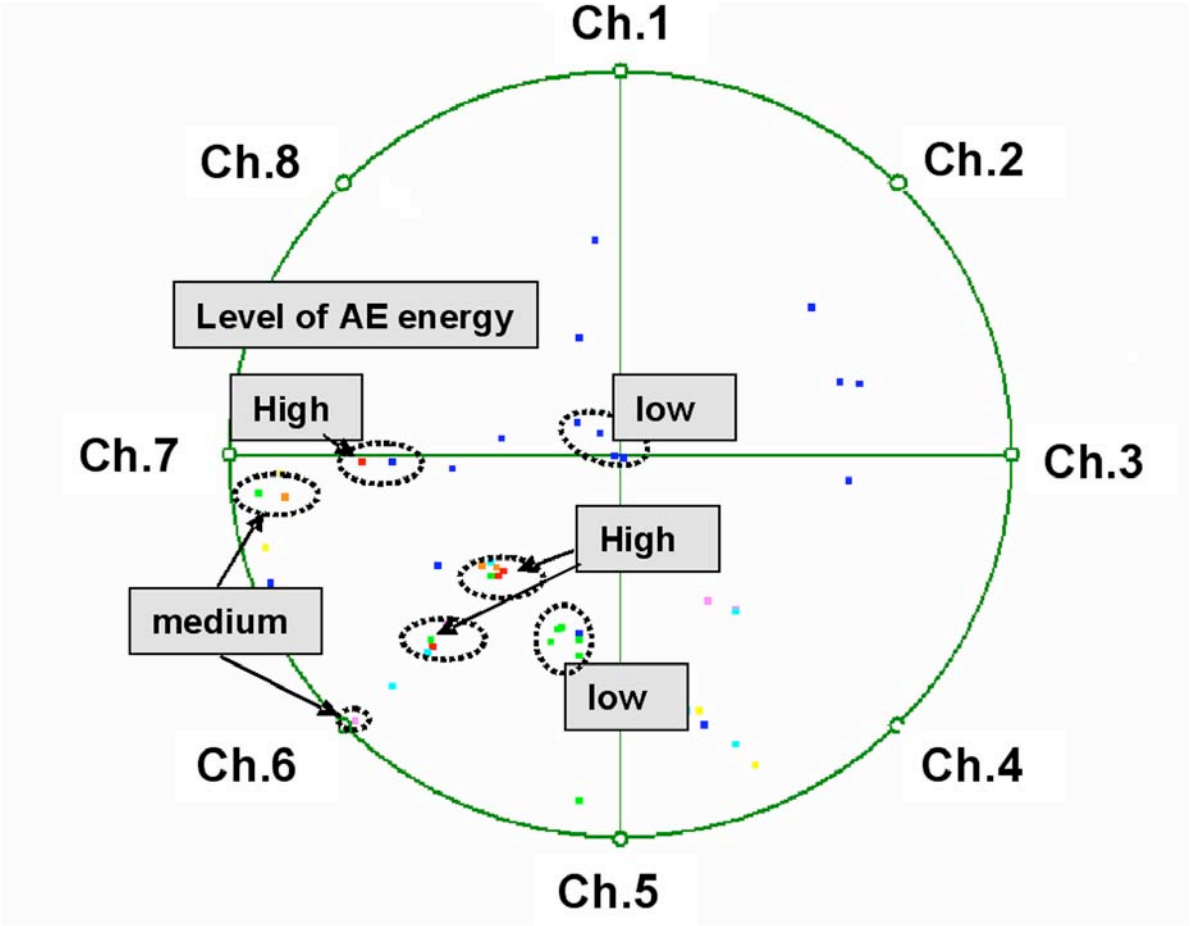

Fig. 10 Source locations of AE signals (Data No. 3-30A) estimated by the threshold-crossing time method and the level of AE energy.

References

[1] M. Takemoto, T. Sogabe, K. Matsuura and K. Ono; Acoustic Emission from Atmospheric Rust Fracture, Progress in Acoustic Emission XI, JSNDI, (2002), pp. 45-52.
[2] M. Takemoto, T. Sogabe, K. Matsuura and K. Ono, Acoustic Emission from the Fracture of Atmospheric Rust, J. Acoustic Emission, **21** (2003), 120-130.
[3] T. Matsuo, H. Cho and M. Takemoto, Source Location of Floor Plate Corrosion of Model Tank Using Multi-sensing Optical Fiber System, Prog. In AE XIII, JSNDI, 2006, pp. 327-333.
[4] M. Takemoto, Propagation Behavior and Source Location of AEs in Liquid Loading Tank, J. JHPI (in Japanese), **40**-4, (2002), 22-30.
[5] T. Sogabe and M. Takemoto, Sensing and Sugnal Processing Method to Improve the location Accuracy of AE Sources on the Bottom Plate of a Liquid Storage Cylindrical Tank, J. JSNDI (in Japanese), **53**-1, (2004) 29-34
[6] H. Cho, M. Takemoto, A. Yonezu, R. Ikeda, H. Suzuki and M. Nakano, Location of Corrosion Damage on the Floor Plate of A Cylindrical Storage Tank by Lamb Wave Acoustic Emission. J. JSNDI (in Japanese) **54**-5, (2005) 259-264.
[7] H. Cho, M. Takemoto, A. Yonezu, R. Ikeda, H. Suzuki and M. Nakano, Detection and Source Location of Lamb Wave AEs from Floor Plate Corrosion of An oil Storage Tank, Correspondence with Wall Reduction by Ultrasonic Test, J. JSNDI (in Japanese) **54**-6, (2005) 318-323.

WAVELET TRANSFORM ANALYSIS OF EXPERIMENTAL AE WAVE-FORMS ON STEEL PRESSURE VESSEL

MULU BAYRAY and FRANZ RAUSCHER*
Department of Mechanical Engineering, Mekelle University, Mekelle, Ethiopia.
*Vienna University of Technology, Vienna A-1040, Austria.

Abstract

Recent literature on wavelet transform (WT) discusses the use of the method in identification of wave modes in an acoustic emission (AE) signal. Theoretical models and results of experiments on test specimen are discussed. These models and experimental results are mostly for thin plates. This paper considers an experimental work carried out on a steel pressure vessel with a thickness of 15 mm. One of the aims of the experiment was to study the WT method on AE signals in identifying wave modes in the signals. The paper discusses the theoretical dispersion of waves for the thickness of 15 mm and steel material as a background. Mathematically calculated signals based on the dispersion curves are first analyzed using the WT method. AE signals, acquired using pencil lead break as source, are then analyzed. Finally, AE signals acquired during pressure tests are analyzed. The paper presents the details of the experimental set up, test procedures, and detailed WT analysis of selected AE signals. In most of the AE signals acquired during the pressure tests the WT method failed to identify the wave modes. The paper describes the problems associated with mode identification employing resonant sensors.

Introduction

In previous research studies reported in [Bayray, 2002a, 2002b] short-time Fourier transform (STFT) and wavelet transform (WT) were employed to analyze acoustic emission (AE) signals from simulated sources and due to crack growth in pressure vessels. The thickness of the vessels and the frequency range of the AE sensors resulted in the consideration of the principal plate wave modes S_0 and A_0. The STFT and the WT were utilized to identify the arrival of the two modes and to find out their relative intensity in the AE signal. The relative amplitude was then used to identify the type of the AE source. A series of studies made on database of wideband AE modeled signals, created by use of finite element code are reported by Hamstad and coworkers [Hamstad, 2002a; 2002b; 2003; Downs et al., 2003]. The signals were obtained through the finite element code on aluminum plates with thickness of 4.7 mm for different kinds of sources. The papers discuss on the use of WT in source identification and source location. The plate wave modes considered were the S_0 and A_0 modes.

Most of the above papers discuss thin plates and the assumption that only the two principal modes exist in the AE signal. In the case of relatively thick plates there will be the possibility of exciting higher modes and acquired in the AE signal. In this current paper, AE signals obtained from experiment carried out on 15 mm thick steel vessel will be considered. The effect of higher mode (especially A_1) on the AE signal and the problems associated will be discussed. The WT method will be employed to identify the plate modes based on the plate wave dispersion.

Theoretical back ground

Mathematical Signal Based on Dispersion

Considering the dispersion curve of plate waves for the frequency range 100 – 300 kHz and a plate thickness of 15 mm, the following characteristics of the AE signal is expected. The dispersion curve for steel material is shown in Fig. 1 for reference.

- In this range the four modes S_0, S_1, A_1 and A_0 are possibly excited.
- At around 250 kHz frequency the S_1 mode will arrive first with group velocity of 4600 m/s and at around 100 kHz the S_0 mode will arrive at group velocity of 4500 m/s. The S_1 mode at about 250 kHz will trigger the acquisition of the signal but only if the AE event has high frequency content. Otherwise, the S_0 mode with 100 kHz will trigger the acquisition if the AE event has no significant high frequency content.
- Next to arrive will be the A_1 mode with frequency of around 180 kHz followed by A_0. The A_1 mode arrives with group velocity of 3650 m/s, while the A_0 mode arrives almost un-dispersed in this range having a group velocity of 3100 m/s.

In the experimental work, sensors with resonance frequency at around 150 kHz were employed. The sensor effective sensitivity is within the range 100 – 180 kHz, though it has a second peak at about 250 kHz. For this reason the discussion below will exclude the S_1 mode and consider the remaining three modes only.

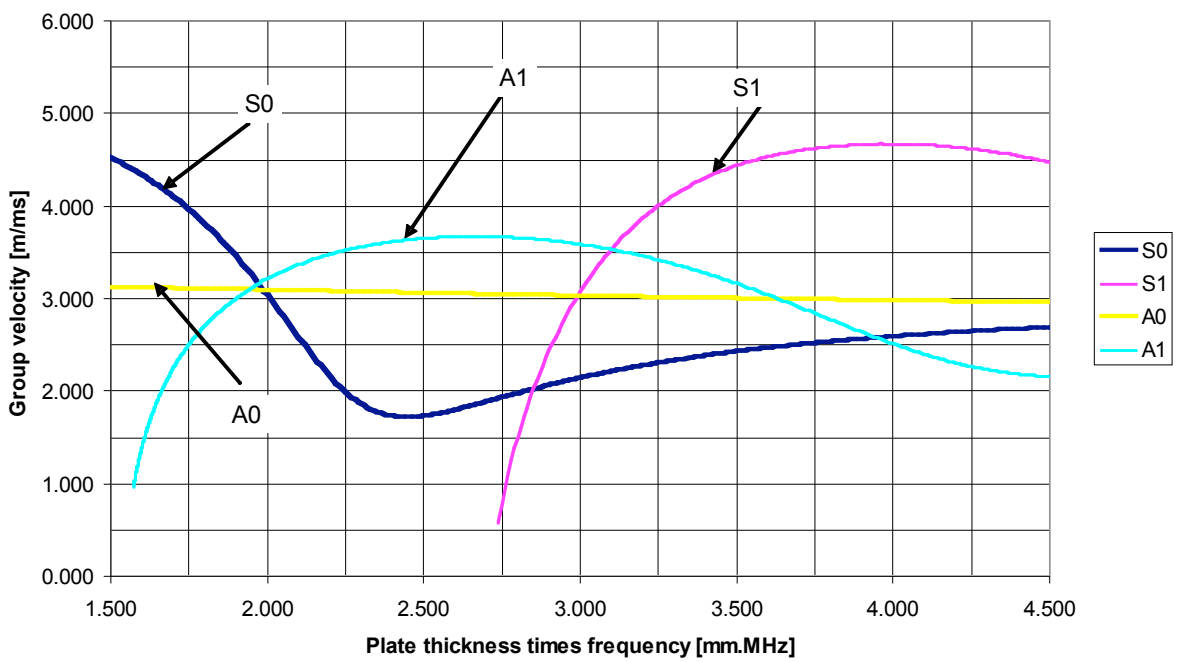

Fig. 1 Dispersion curves for steel material.

In order to look at signals having the above characteristics mathematically calculated waveforms were first analyzed. These signals provide an insight on how the three modes are superposed to form a signal. The mathematical calculation employs the theoretical dispersion curve for a plate with a thickness 15 mm to a delta-impulse and the result was filtered with a Gaussian window with mean frequency of 150 kHz and standard deviation of 50 kHz. The resulting signals of each wave mode were scaled to the same amplitude. The range of frequency selected is in the range of experimental AE signals obtained utilizing a resonant sensor with 150 kHz. Figures 2 and 3 are plots of such waveforms where the three modes are shown separately and superposed

with each other. Table 1 below shows the delay in the arrival times of the peak of the packet of the three modes on the distances shown, as extracted from Figs. 2 and 3.

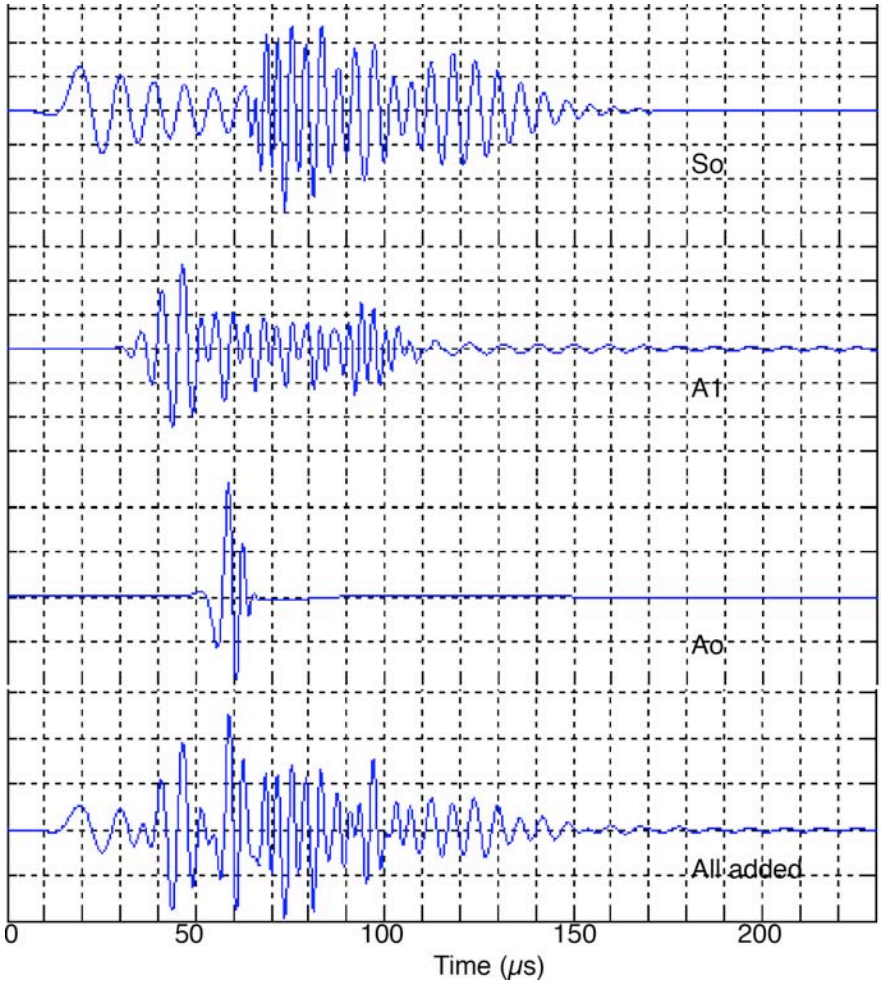

Fig. 2 Scaled signals for (top to bottom) S_0, A_1, A_0 and the superposition of the three modes at distance of 30 cm. (Amplitude: arbitrary scale)

Table 1 Delays in μs of the peak of the packet for the modes with respect to a trigger by S_0 mode with 100 kHz frequency.

Distance (cm)	S_0 (100-130 kHz)	A_1 (130-180 kHz)	A_0 (100-180 kHz)	S_0 (160-180 kHz)
30	20	45	60	120
36	20	50	65	140

The S_0 mode at 100 kHz arrives first, being the base of the delays given in Table 1. In Table 1, delays for the maximum amplitude of the packets of the respective mode are given for the three modes and on the respective sensors, positioned at the distances shown (Fig. 2 distance of 30 cm and Fig. 3 distance of 36 cm). The S_0 mode is separated into two parts, one at low frequency coming early at the beginning and one at higher frequencies coming later at the end of the signal. The part coming at the end of the signal arrives behind the wave-packets of the A_0 and A_1 modes because the group velocity for the S_0 at a frequency of 170 kHz decreases to 1780 m/s.

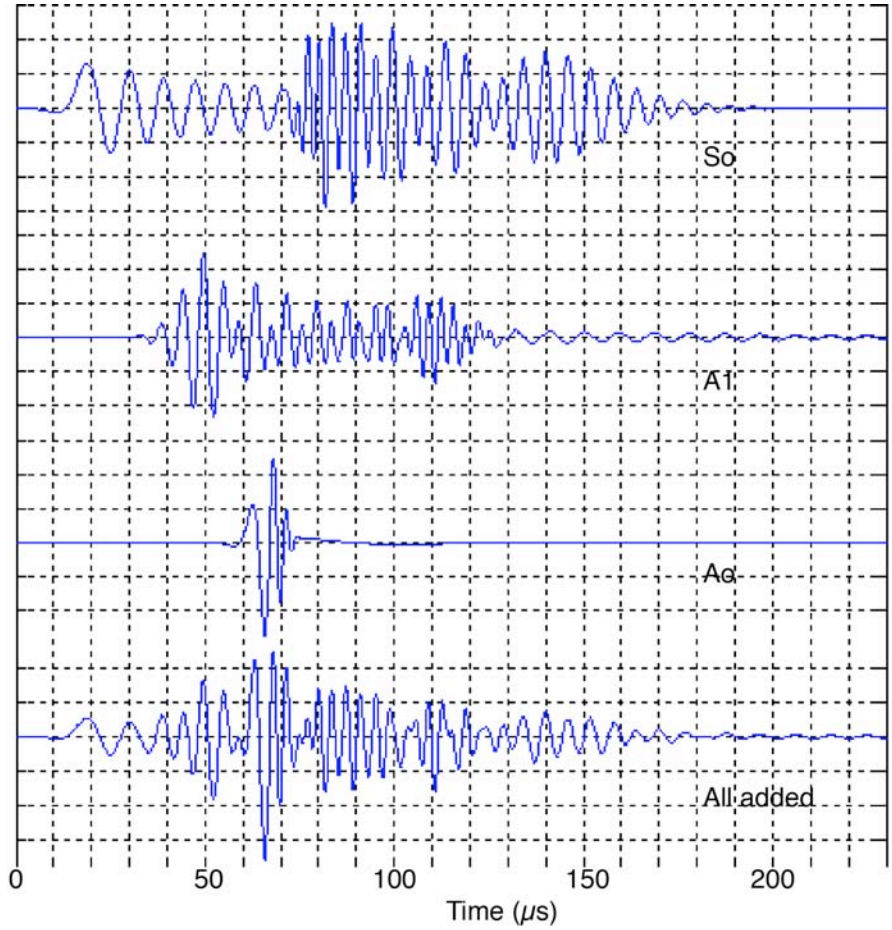

Fig. 3 Scaled signals for (top to bottom) S_0, A_1, A_0 and the superposition of the three modes at distance of 36 cm. (Amplitude: arbitrary scale).

To identify the modes on an AE signal the frequency at about 100 kHz and the frequency around 170 kHz were found to be important because:

- At about 100 kHz the only two modes S_0 and A_0 exist. Since the difference in their group velocity is significant both could be identified from the delay in arrival time as shown in Table 1 above.
- At around 160-180 kHz all the three modes exist. Again, due to differences in group velocity, the three modes may be identified from the delay in arrival time.

The wavelet transform method that is discussed below will concentrate on the 100 kHz and 170 kHz frequencies.

Wavelet Transform of the Mathematical Signal

Wavelet transform of the theoretical signals was carried out employing the software AGU-Vallen, the details of which may be found in [Vallen, 2005]. The software carries out WT of the signal and produces color plots of the WT coefficient against the Frequency and Time. The result of the wavelet transform can also be exported to a worksheet for further analysis on a frequency of interest. The wavelet set up employed in all our discussions here were: Maximum frequency 500 kHz, Frequency resolution 2 kHz, Wavelet size (samples) 200, Number of samples 1024, offset samples 0 and scale factor 100. The results of the WT at the frequencies of interest 100 kHz and 170 kHz were extracted and the plate modes were identified.

Figure 4 shows the signal, the color plot of the WT and the plot of the WT coefficients at 100 kHz and 170 kHz. The dispersion curve is also shown superposed on the color plot. Investigating the wavelet coefficients at 100 kHz frequency, the plot shows two peaks at around 60 µs and around 95 µs. These peaks approximate the significant arrival of S_0 and A_0 modes, respectively. The theoretical dispersion curve intersection at 100 kHz shows relatively earlier time, at around 58 µs and 88 µs for the S_0 and A_0 modes, respectively.

Similarly, observing the wavelet coefficients at 170 kHz frequency, the plot shows two distinct peaks that can be associated with the modes. The first peak at around 76 µs is clearly due to the A_1 mode. The second peak around 150 µs is associated with late arriving part of the S_0 mode. The A_0 mode, which is expected to arrive at about 90 µs, did not show an identifiable peak.

AE Events due to Pencil Lead Break (PLB)

Test Arrangement

In this section waveform of events due to pencil lead breaks (PLB) on the test vessel will be analyzed. The PLB test was carried out after the vessel failed by leakage on the weld defect. The failure area was cut out for fracture samples for the microscopic investigation. It was then possible to make in-plane type source on the edge of the shell. Two sensors (channel 1 and 2) were positioned in similar distances and orientation to that of sensors 3 and 5 during the pressure tests, as shown in Fig. 5. The distance from the PLB at the edge to sensor 1 was about 29 cm and positioned at perpendicular line to the edge of the vessel. This was similar to the sensor 3 during pressure tests with distance of 30 cm and perpendicular to the longitudinal weld line. The distance from the PLB at the edge to sensor 2 was about 35 cm at an angle of about 35º from the perpendicular line. This was also a similar position to the sensor 5 during the pressure tests.

The sketch in Fig. 5 shows the arrangement of the sensors in the PLB tests. The tests were carried out on the edge of the vessel:

i) at mid plane of the shell (7.5 mm from outer surface),
ii) at about 4 mm below the outer surface and
iii) out-of-plane (OOP) on the surface of the shell.

Wavelet Transform of AE Events

Among the events recorded the following discussion will deal with a few representative events. Wavelet transform of the AE signals was carried out in a similar way as discussed in the previous section. The results of the WT at the frequencies of interest 100 kHz and 170 kHz were extracted and the plate modes were identified.

Figures 6, 7 and 8 show the time signal, the color plot of the WT and the plot of the WT coefficients at 100 kHz and 170 kHz of in-plane and out-of-plane PLB sources. In the plots of the WT results on the 100 kHz and 170 kHz, the modes S_0, A_0 and A_1 are identified from their respective arrival time. The peaks on the WT coefficients are an indication of the arrival of the intensity of the respective modes. The respective delay times from the signal trigger until the arrival of peak WT coefficient are extracted for each event as shown in Table 2.

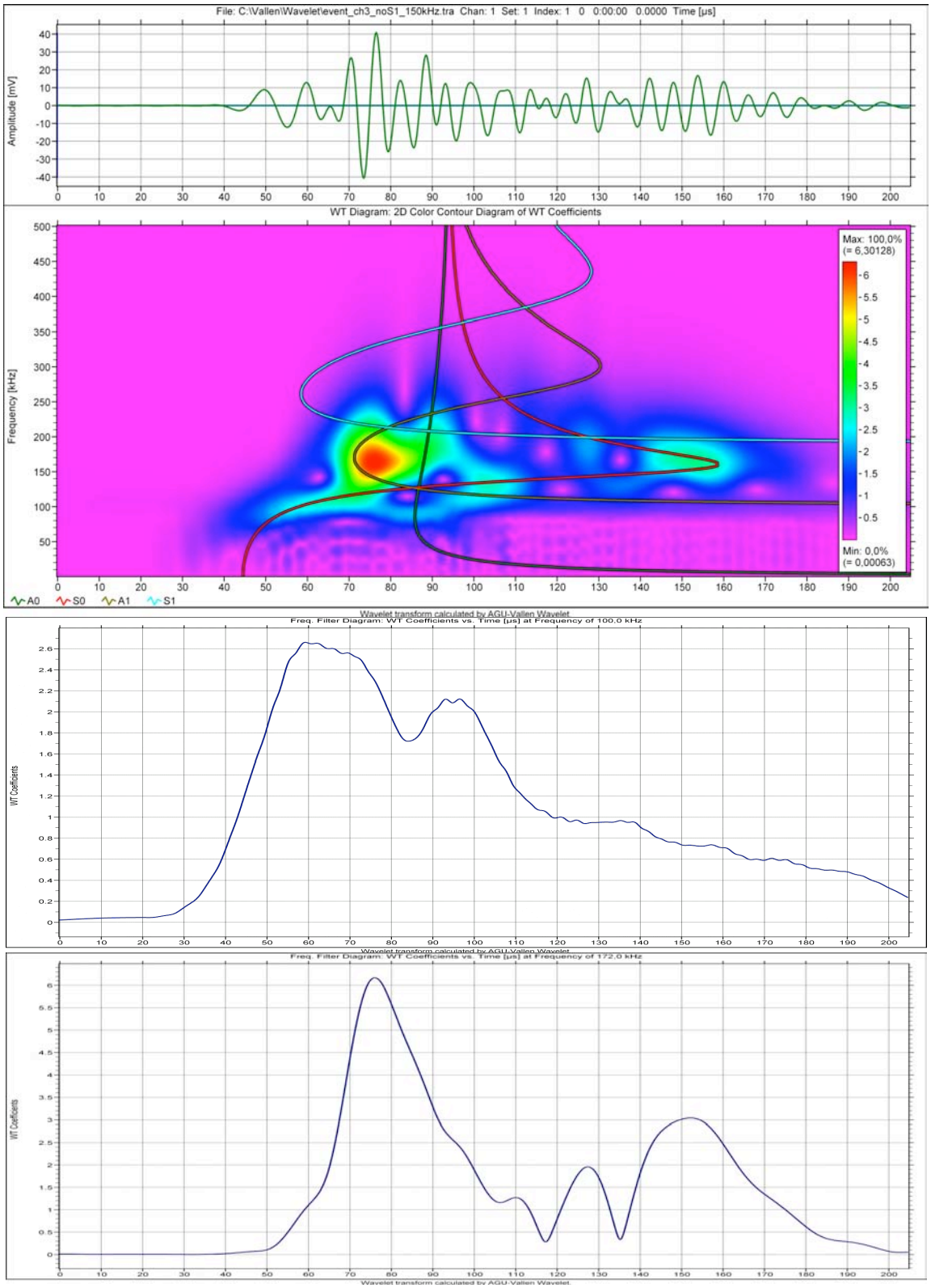

Fig. 4 Wavelet transform of a theoretical signal shown in Fig. 2. Top to bottom, time signal, color plot of wavelet transform coefficients, wavelet coefficients at 100 kHz and wavelet coefficients at 170 kHz.

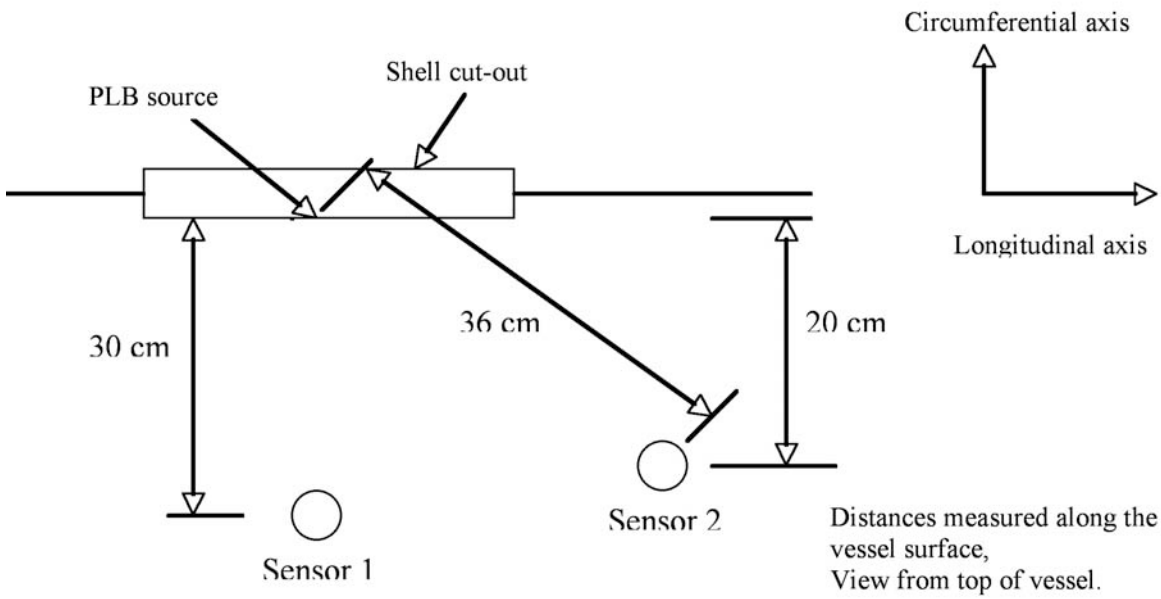

Fig. 5 Arrangement of sensors with respect to PLB source at the edge of the shell cut-out.

Table 2 Arrival time and the respective values of the WT coefficient for the modes.

Source	TRI	S_0 (100 kHz)		A_0 (100 kHz)		A_1 (170 kHz)		A_0 (170 kHz)		S_0 (170 kHz)	
		Time µs	WTC	Time µs	WTC	Time µs	WTC	Time µs	WTC	Time µs	WTC
IP Mid plane	**683**	35	0.82	NRP		12	0.6	32	0.48	60	1.42
	684	35	0.26	NRP		NRP		25	0.08	68	0.54
	709	35	0.7	NRP		NRP		NRP		60	1.2
	710	35	0.28	NRP		NRP		NRP		75	0.5
IP 4 mm below surface	**729**	NRP		62	1.8	25	0.35	70	1.08	118	0.88
	730	30	0.2	68	1.08	28	0.15	60	1.38	100	0.7
	754	NRP		62	1.4	25	0.32	52	0.78	85	0.93
	755	32	0.26	65	0.85	28	0.2	58	1.1	132	0.6
OOP On the surface	**765**	NRP		60	0.72	22	0.12	48	0.58	125	1.26
	766	30	0.2	68	1.08	28	0.15	60	1.38	100	0.7
	782	NRP		55	0.75	25	0.22	50	0.68	125	1.35
	783	NRP		60	1.2	25	0.18	52	0.7	135	0.54

Note: TRI = Transient Record Index, WTC = Wavelet Transform Coefficient,
NRP = No Recognizable Peak

Remarks:

On the 100 kHz, as expected from IP type of source, low or no peak WT coefficient was observed for the A_0 mode. Similarly, as expected from OOP type of source, low or no peak WT coefficient was observed for the S_0 mode. But on the 170 kHz significant peak values of the WT coefficient are observed around the arrival time of the S_0 mode that is not expected from the OOP type of source. On the IP type source on channel 2 (i.e. TRI 684 and 710) significant peak WT coefficient was observed for the A_1 mode at high frequency range 250-400 kHz. Figure 9 shows the signal and WT color plot of the TRI 684 signal.

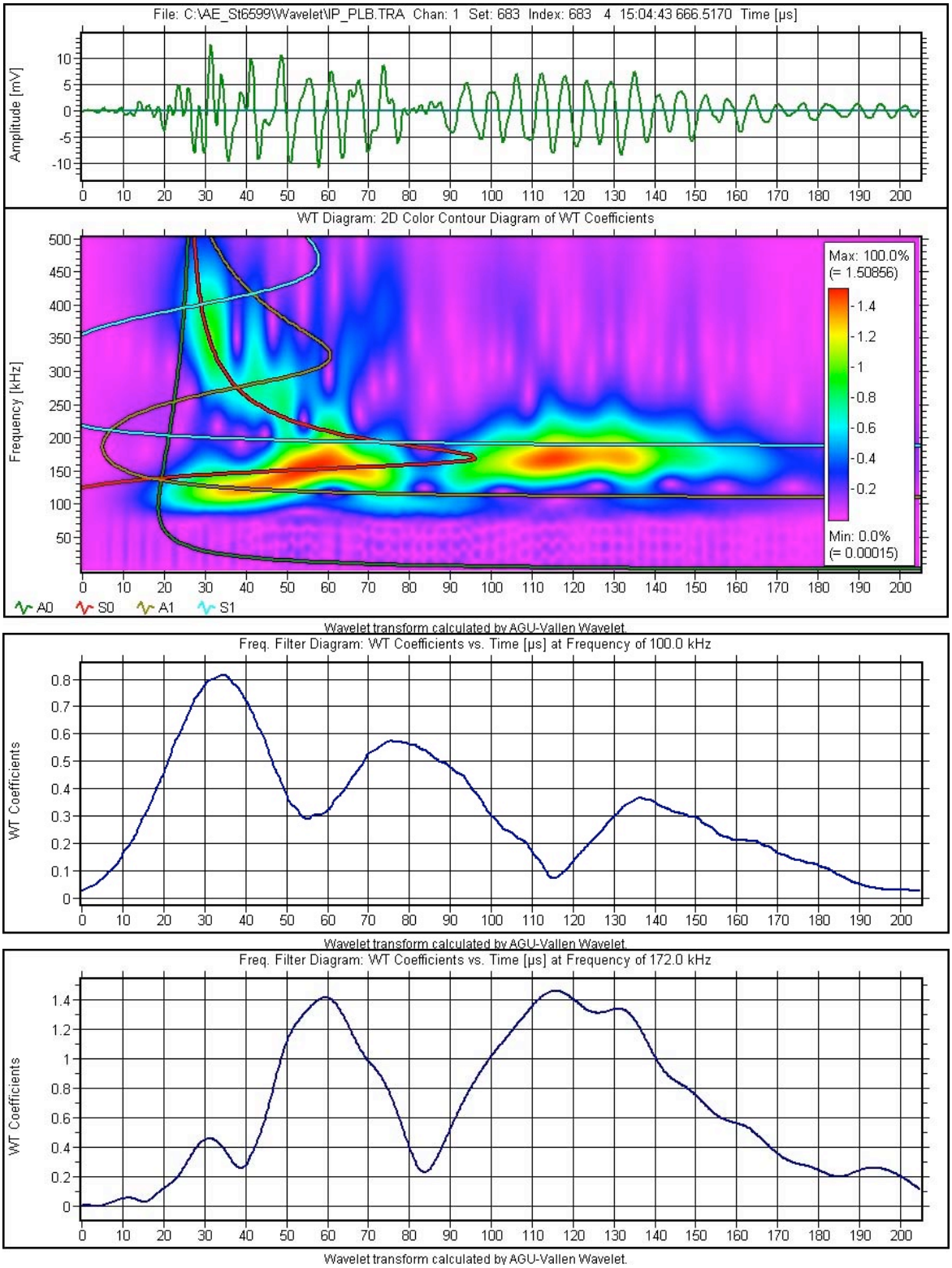

Fig. 6 Top to bottom: AE signal, Color plot of the WT, wavelet coefficients at 100 kHz and wavelet coefficients at 170 kHz. IP at mid plane type source, channel 1 at 30 cm from source.

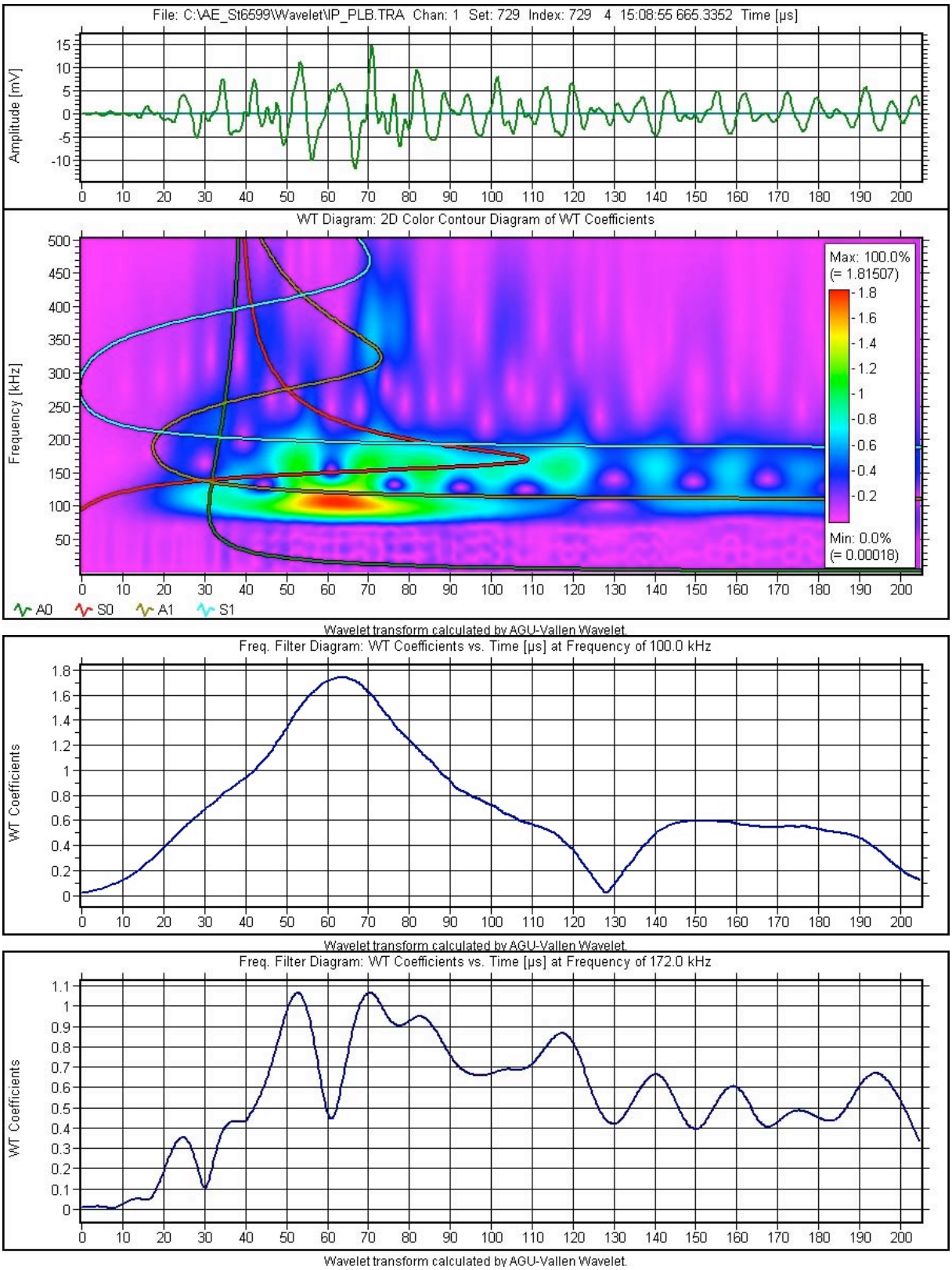

Fig. 7 Top to bottom: AE signal, Color plot of the WT, wavelet coefficients at 100 kHz and wavelet coefficients at 170 kHz. IP at 4 mm from surface, channel 1 at 30 cm from source.

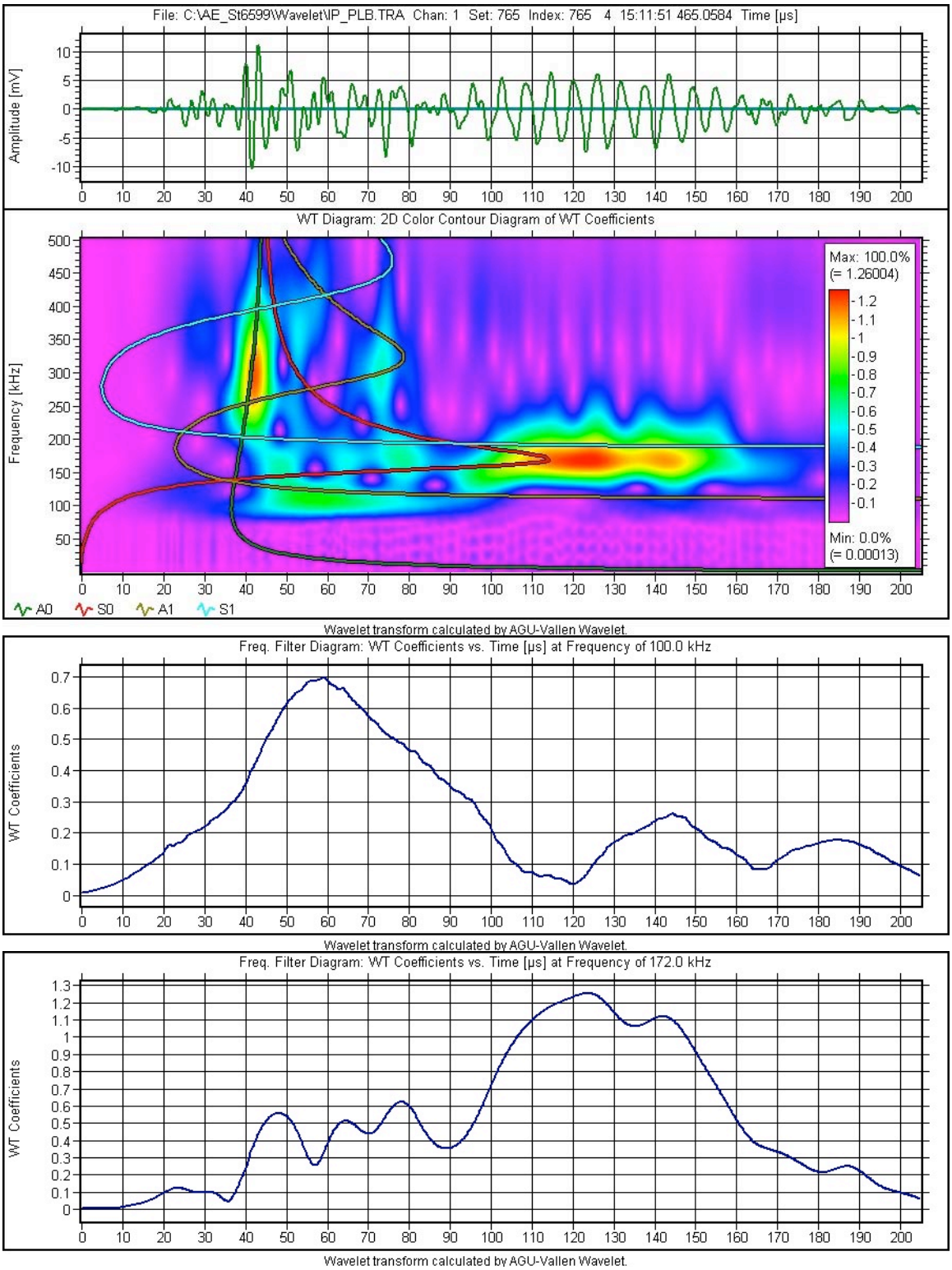

Fig. 8 Top to bottom: AE signal, Color plot of the WT, wavelet coefficients at 100 kHz and wavelet coefficients at 170 kHz. OOP type source, channel 1 at 30 cm from source.

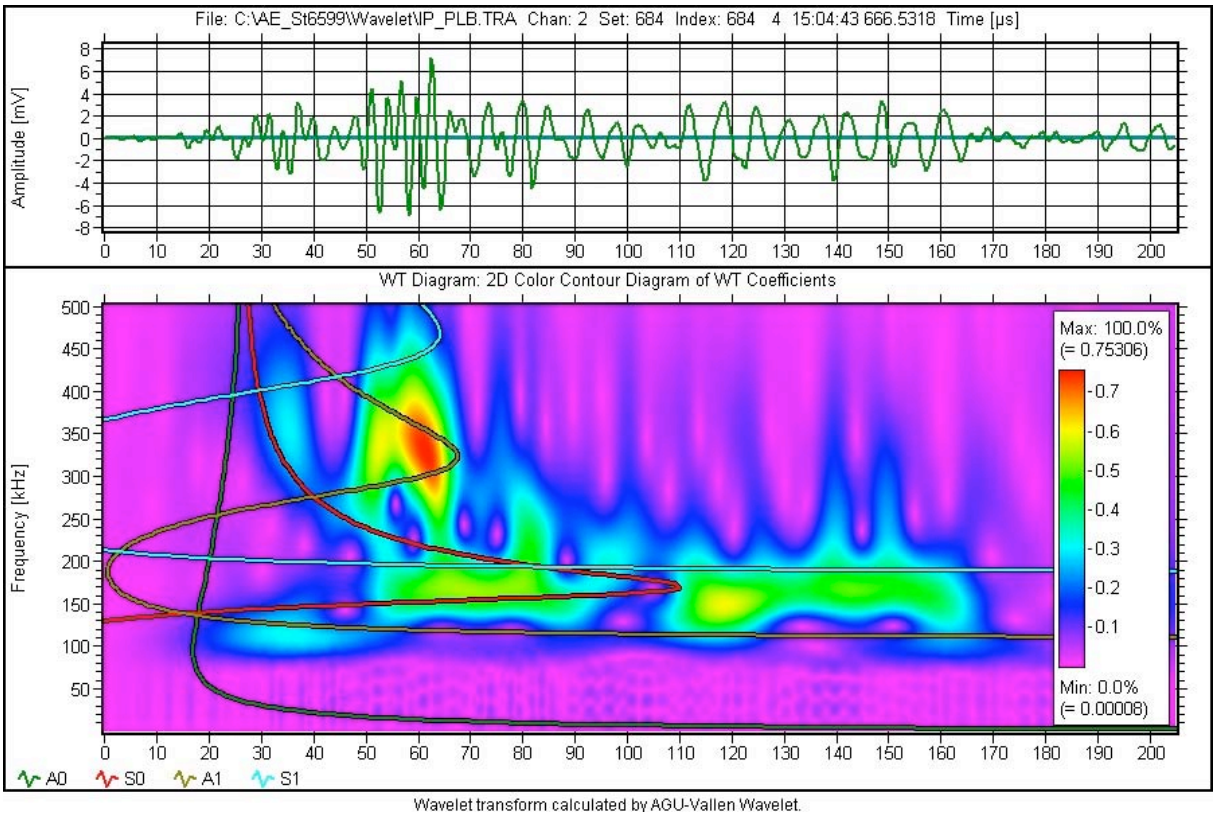

Fig. 9 Top to bottom: AE signal and Color plot of the WT. IP at mid plane type source, channel 2 at 36 cm from source. This figure shows significant A1 mode around 250-400 kHz.

AE Events from Pressure Tests

Experimental investigation to study AE characteristics generated due to weld defects was carried out at the Institute of Pressure Vessels and Plant Technology. The complete information on experimental set up, test procedure, microscopic investigation of fracture surface and crack tip and general AE data analysis is reported in [Rauscher, 2005]. However, some of the sections that describe the experiment and AE events are briefly discussed here.

Description of the test vessel

The vessel is made of a cylindrical shell and two hemi-spherical ends (material: steel St41KT ÖNORM M3121 from Dec. 1955). The material corresponds to EN 10028-3 P265GH, has an actual ladle carbon content of 0.17%C, 0.007%P, 0.018%S and actual yield strength of 322 MPa. The overall dimensions of the vessel are: outer diameter 800 mm, thickness 15.5 mm, overall length of 2400 mm and the capacity of the vessel 1100 l. The picture in Fig. 10 shows the test vessel after doing the welding but before setting up the instrumentation. The sketch shows some dimensions of the vessel, the positions of the investigated regions, the position of the strain gauges, and the AE sensors.

Pressure Test Specification

As a reference, the maximum allowable pressure P_S was specified with 32 bar. The pressure test at the beginning of the experiment and pressure tests to be conducted intermittently after fatigue cycling were carried out as follows:

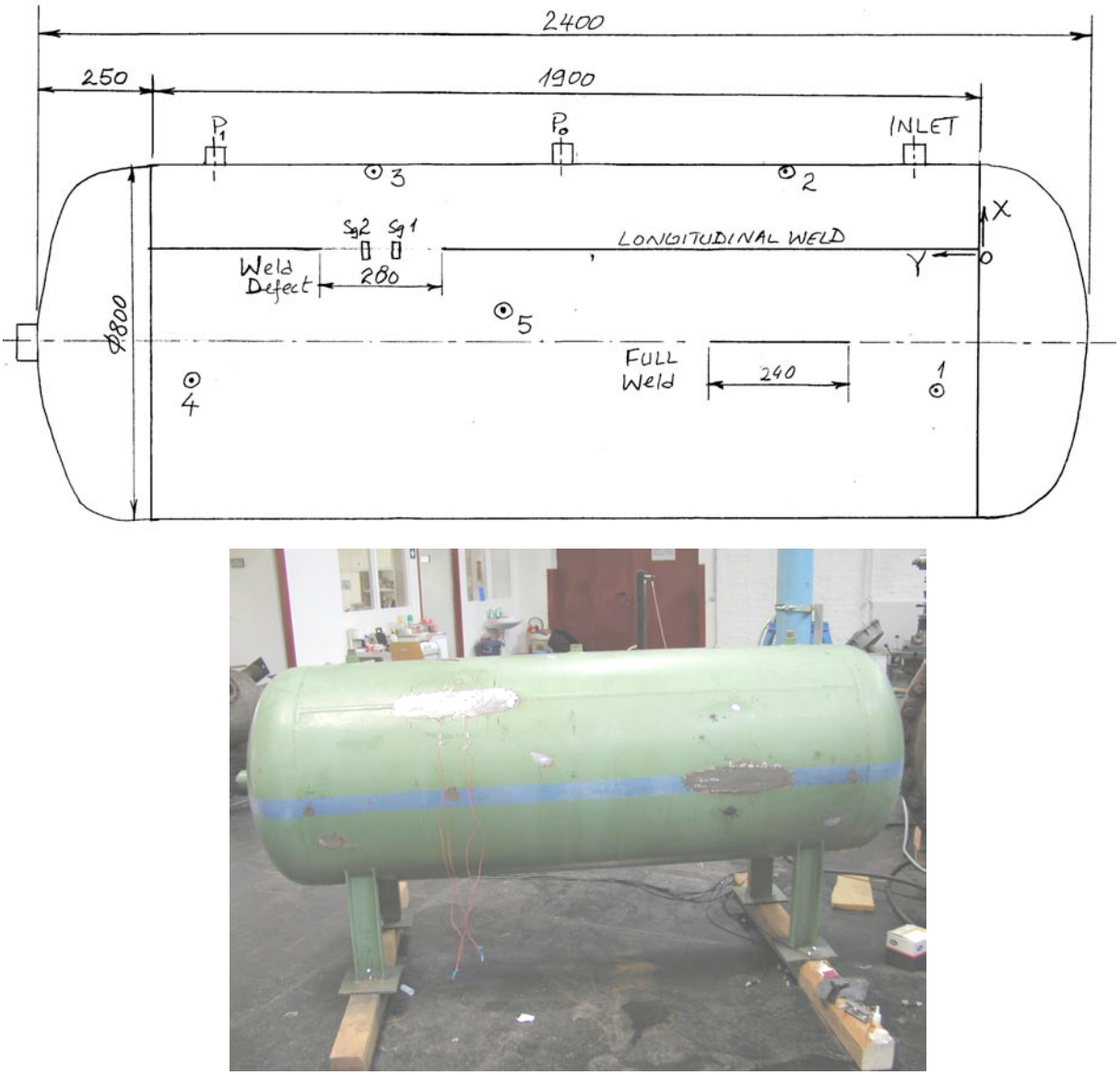

Fig. 10 Tested vessel.

- Every pressure test consisted of three cycles. The first cycle had holds at 80%, 100%, 120% and 143.5% of P_s, where P_s is the specified maximum allowable pressure. The specified pressure curve for the pressure test is shown in Fig. 11.
- The two subsequent pressure test cycles had only holds at 120% and 143% P_s as shown in Fig. 12.

The specification of the duration for the hold and the rate of pressure increase during the different phases and the rate of decrease in pressure at the end of the cycles are described in Figs. 11 and 12.

Fatigue Cyclic Pressurization

After conducting the first pressure test, the vessel was cyclically pressurized with a minimum of 2 bar and maximum of 30 bar (this is 2 bar below the specified maximum admissible pressure P_S of the vessel). The pressure was varied in a sinusoidal form with a frequency of 0.1 Hz.

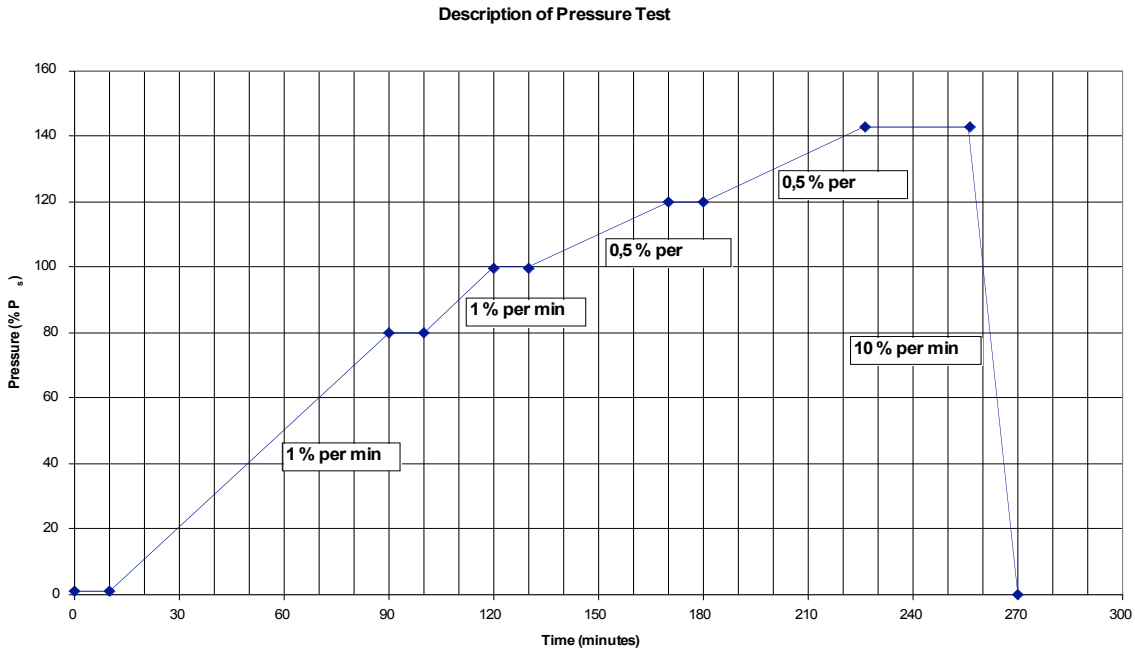

Fig. 11 Specification of pressure test, first cycle.

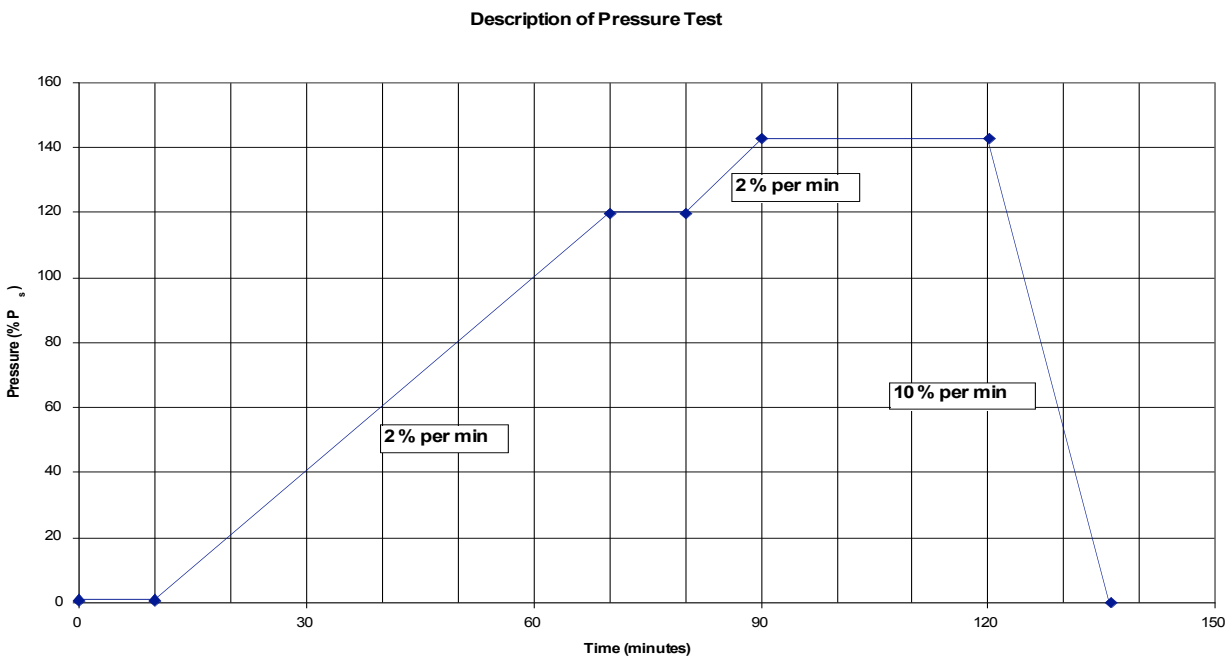

Fig. 12 Specification of the pressure test, second and third cycles.

Cyclic pressurization was done until crack propagation was clearly indicated. The experiment was continued with cyclic pressurization and intermediate pressure tests. The vessel eventually failed by leakage at the sixth pressure test.

The number of AE events recorded during the pressure tests located around the longitudinal weld defect are summarised in the following table.

Table 3 AE events during pressure tests.

Pressure Test	Number of AE events on the longitudinal weld defect		
	>= 80 dB, located	>= 60 dB, located	>= 40 dB, according to channel sequence
1	2	160	12300
2	0	2	47
3	0	0	22
4	1	1	16
5	0	0	30
6	0	1	39

Figure 13 shows the fracture surface around the failure indicating the six pressure tests and fatigue crack growth. Figure 14 shows the microscopic investigation of the crack tip cross section of a sample taken from the area of the weld defect. It can be seen that the crack was opened due to the pressure tests and steps in the crack surface, which were generated by the last two pressure tests, 5th and 6th pressure tests, can be clearly seen.

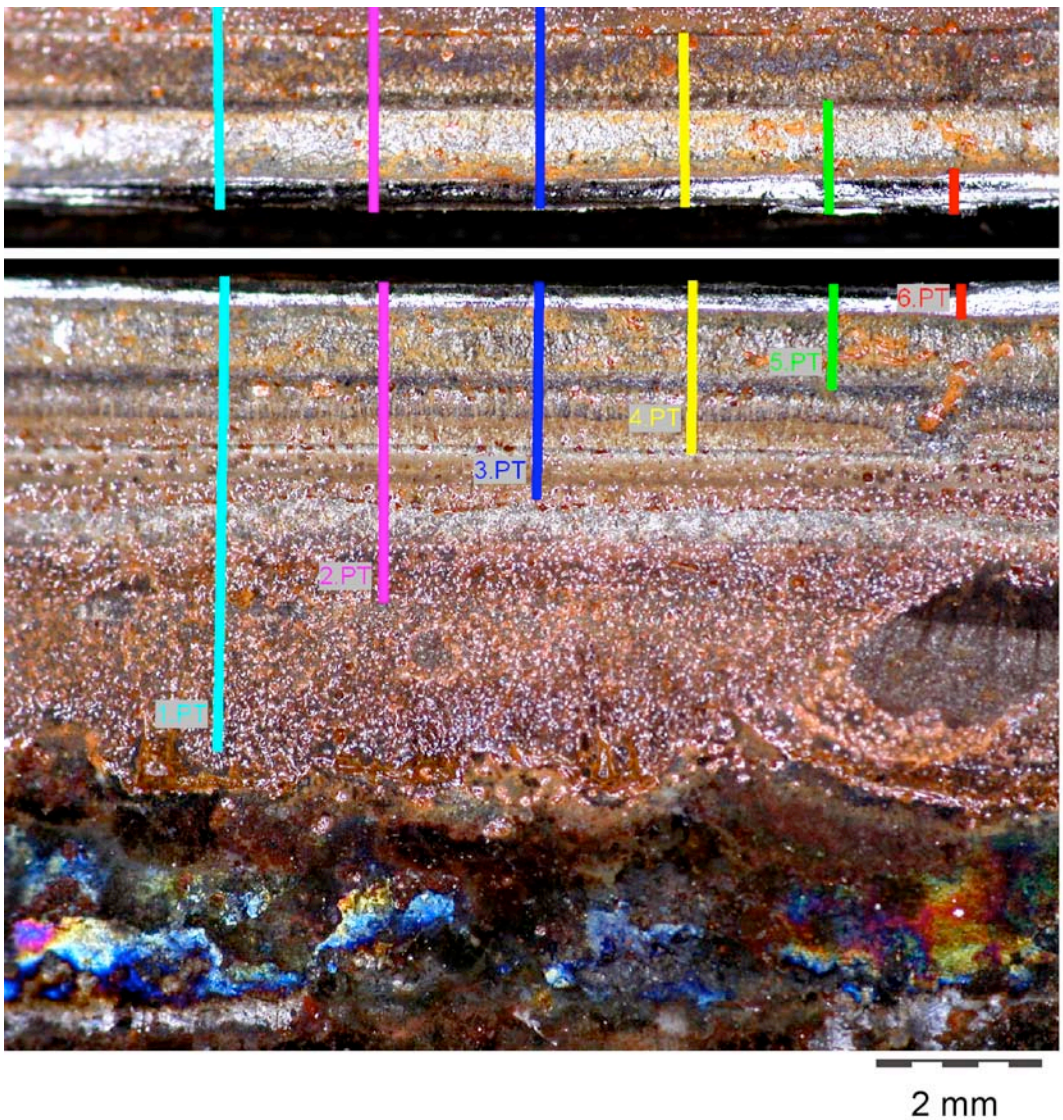

Fig. 13 Fracture surface in the failing area (leakage) of the longitudinal weld defect.

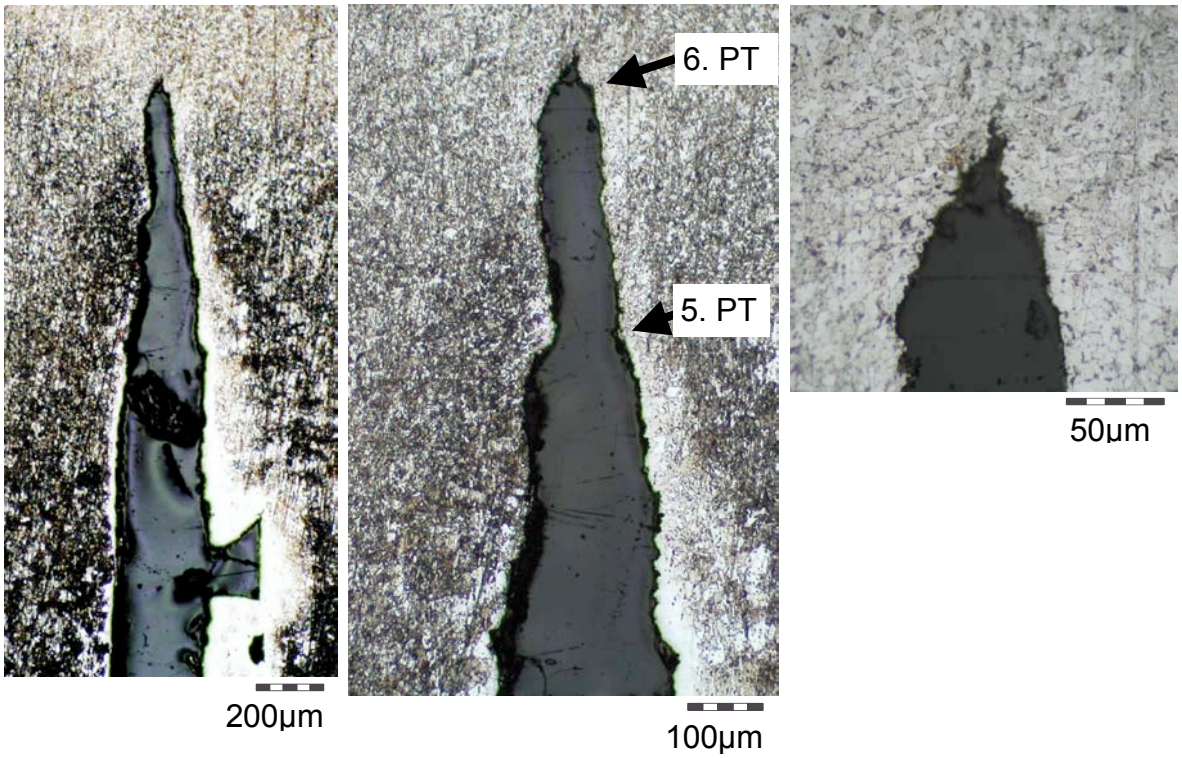

Fig. 14 Microscopic investigation of the crack tip.

Discussion of AE Events Recorded during Pressure Tests

The overall summary of the AE events recorded during the pressure test was given previously in Table 3. Out of the events outlined in the table the following events were selected:

i) From the First and Second Pressure Tests, four events each with the highest amplitudes,
ii) From the Third until the Sixth Pressure Tests, two events each with the highest amplitudes.

Table 4 below shows the summary of the event characteristics. The table shows the pressure at which the event occurred in the test, the transient recorder index, the first and second hit channels, the amplitude of the hits and the FFT frequency content (maximum peak FFT and second peak). The frequency content of the AE signals, as observed from the table, is limited around the peak resonant frequency (150 kHz) of the sensor. Even though the sensor has also a second peak around 250 kHz no significant content was observed above 180 kHz in most of the events. It can be noted from the table that on most of the events the maximum peak frequency occurred around 100-130 kHz and the second peak occurred around 170-180 kHz. Exceptions are event numbers 5, 6, 9 and 16 that had high frequency content observed on the FFT. In these four cases higher frequency content at about 400 kHz was observed.

The figures of some of the events showing the waveform and the respective FFT plot are included here for discussion. Among the signal waveforms there were hits where the expected wave modes can be clearly identified by inspection. The following are the respective channels with clearly identified S_0 (100 kHz), A_1, A_0 and S_0 (170 kHz) modes.

i) Fig. 15 channel 3, TRAI 9241,
ii) Fig. 16 channel 3, TRAI 724,
iii) Fig. 17 channel 3, TRAI 500.

The wave modes as identified by inspecting the signal are indicated in the respective figures. Figures 15 and 16 show significant intensity on the S_0 mode having frequency 170 kHz. This is an indication that the AE source was an in-plane type source.

The WT analysis of the three signals listed above are shown in Figs. 18, 19 and 20. In the figures the dispersion curve was superposed on to the signal WT by sliding a best fit between the signal and what is expected on the WT color plot. However, the color plot and the WT coefficients plot at 100 kHz and 170 kHz did not show the expected peaks that identify the wave modes.

Table 4 Selected events on Pressure Tests and their frequency content.

No.	Event at Pressure (bar)		TRAI	Channel	Amplitude (dB)	FFT Frequency (kHz) at	
						Max. Peak	Second Peak
1	First Pressure Test	23	9240 9241	5 3	85.9	135 170	170 100
2		32	10606 10607	3 5	78.9 72.1	110 100	180 170
3		33	10809 10810	5 3	78.9 75.1	110 100	100 180
4		45 pressure hold	12023 12024	5 3	81.2 73.1	120 110	170 175
5	Second Pressure Test	8.5	153 154	5 3	73.3 72.0	100 100	170* 170
6		8.5	157 158	5 3	71.5 69.2	110 110	400* 400
7		40	188 189	5 3	59.8 49.8	170 160	140 110
8		45 pressure hold	200 NA	3 5	60.5 49.1	140 NA	110 NA
9	Third Pressure	8	410 411	3 5	61.6 51.9	100 100	310* 120
10		40	556 557	5 3	62.4 56.9	170 130	110 100
11	Fourth Pressure	45 pressure hold	689 690	3 5	65.1 36.4	170 100	100 170
12		45 pressure hold	724 725	3 5	89.8 84.5	170 100	110 120
13	Fifth Pressure	44	500 501	3 5	53.8 48.3	160 110	130 170
14		44	506 507	5 3	51.3 49.8	160 100	110 170
15	Sixth Pressure	40	544 545	5 3	61.6 63.1	100 170	160 130
16		40	507 508	3 5	52.7 44.6	180 110	130* 130

* Significant high frequency intensity at about 400 kHz; NA = Not Available

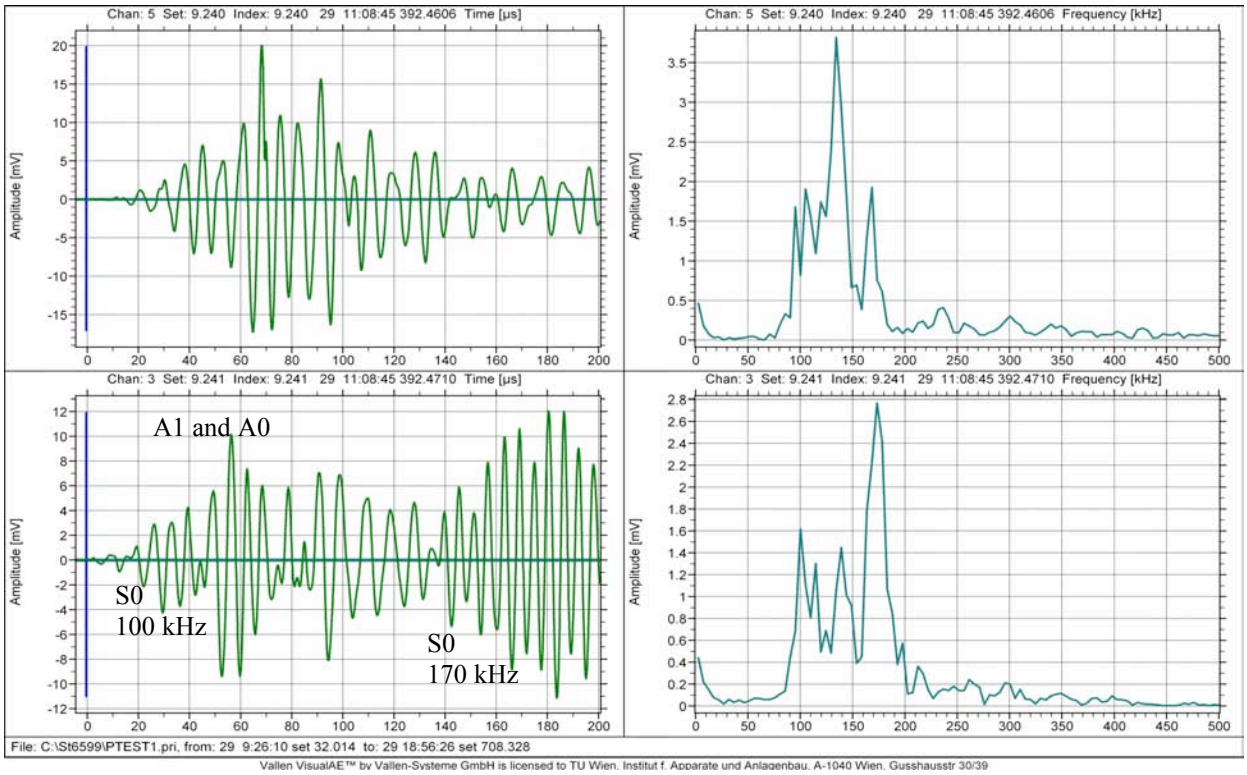

Fig. 15 Signals and the respective FFT diagram, First pressure test at 23 bar, first hit Channel 5 and second hit Channel 3, located around the weld defect.

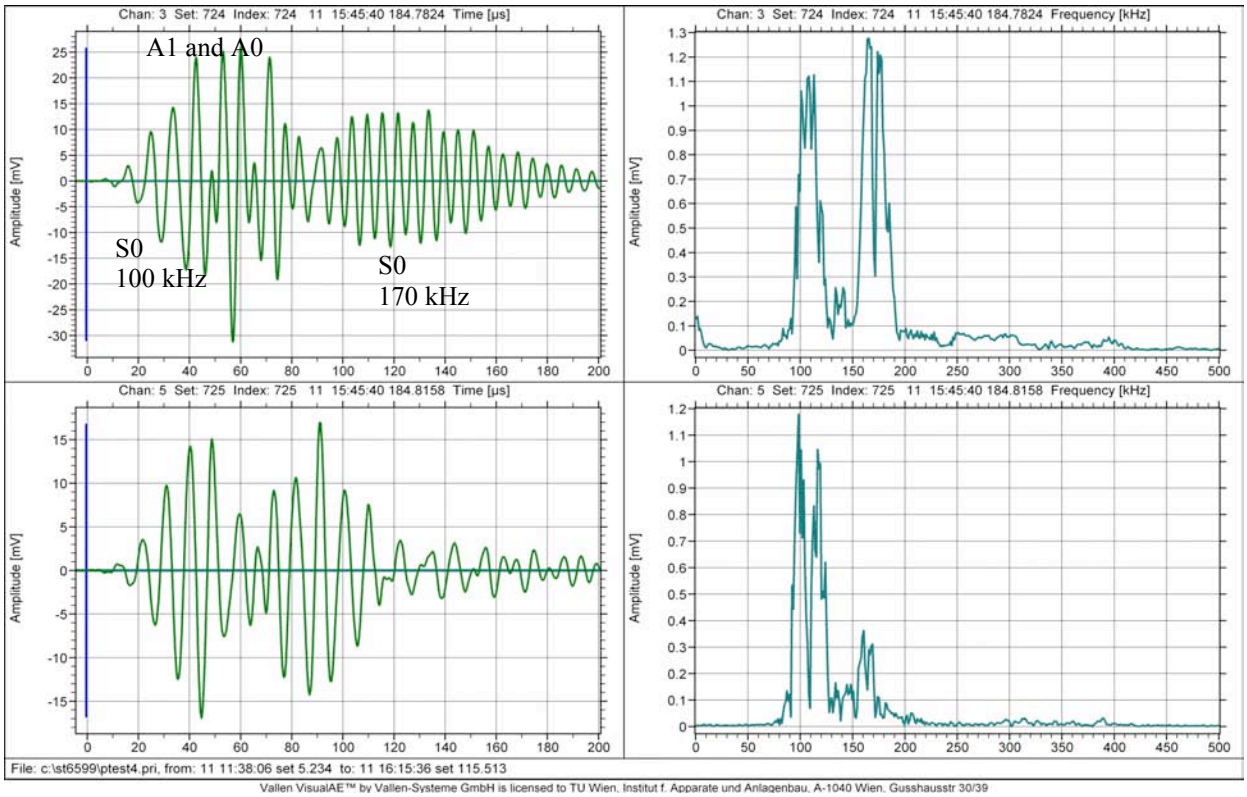

Fig. 16 Signals and the respective FFT diagram, Fourth pressure test at 45 bar maximum pressure hold, first hit Channel 3 and second hit Channel 5, located around the weld defect.

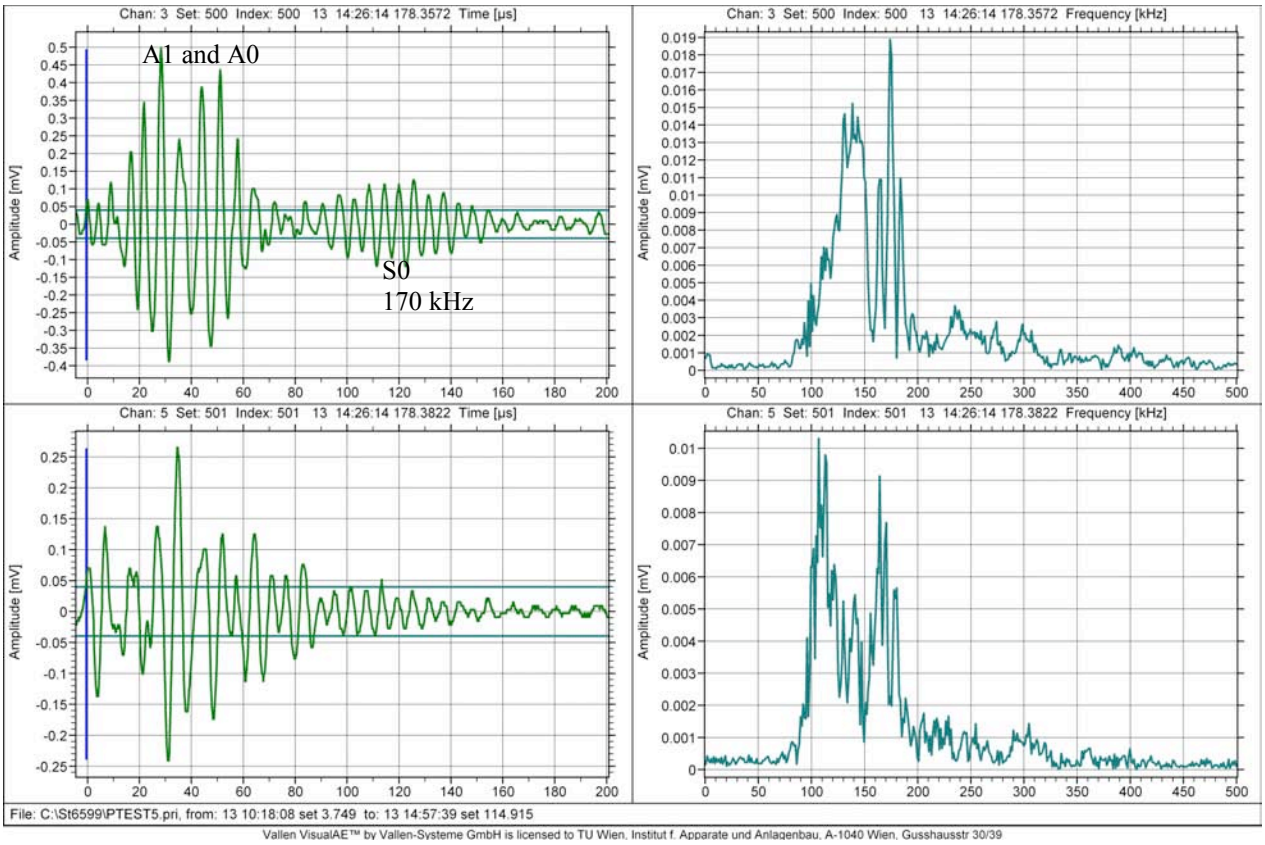

Fig. 17 Signals and the respective FFT diagram, Fifth pressure test at 44 bar maximum pressure hold, first hit Channel 3 and second hit Channel 5, located around the weld defect.

Conclusion

The analysis of the mathematical signals derived from dispersion curve has shown that the wave modes S_0 and A_0 can be identified using the WT method. Analyzing the wavelet coefficients at 100 kHz frequency, the plot shows two peaks at around 60 µs and around 95 µs. These peaks approximate the significant arrival of S_0 and A_0 modes respectively. At 170 kHz three peaks are expected from the dispersion. But, observing the wavelet coefficients at 170 kHz frequency, the plot shows only two distinct peaks that can be associated with the modes. Hence, the three modes (S_0, A_0 and A_1) were not clearly identified from the WT coefficient plot.

The analysis of the PLB AE signals and AE signals from the pressure tests have shown the difficulty to identify the wave modes. The main problem associated with failure of the WT in identifying the modes were:

i) mode identification using resonant sensors is difficult,
ii) the signals are affected due to reflections from edges, nozzles, etc.,
iii) due to the dispersion characteristics the delay in the arrival of the wave modes was not significant to clearly separate one mode from the other.

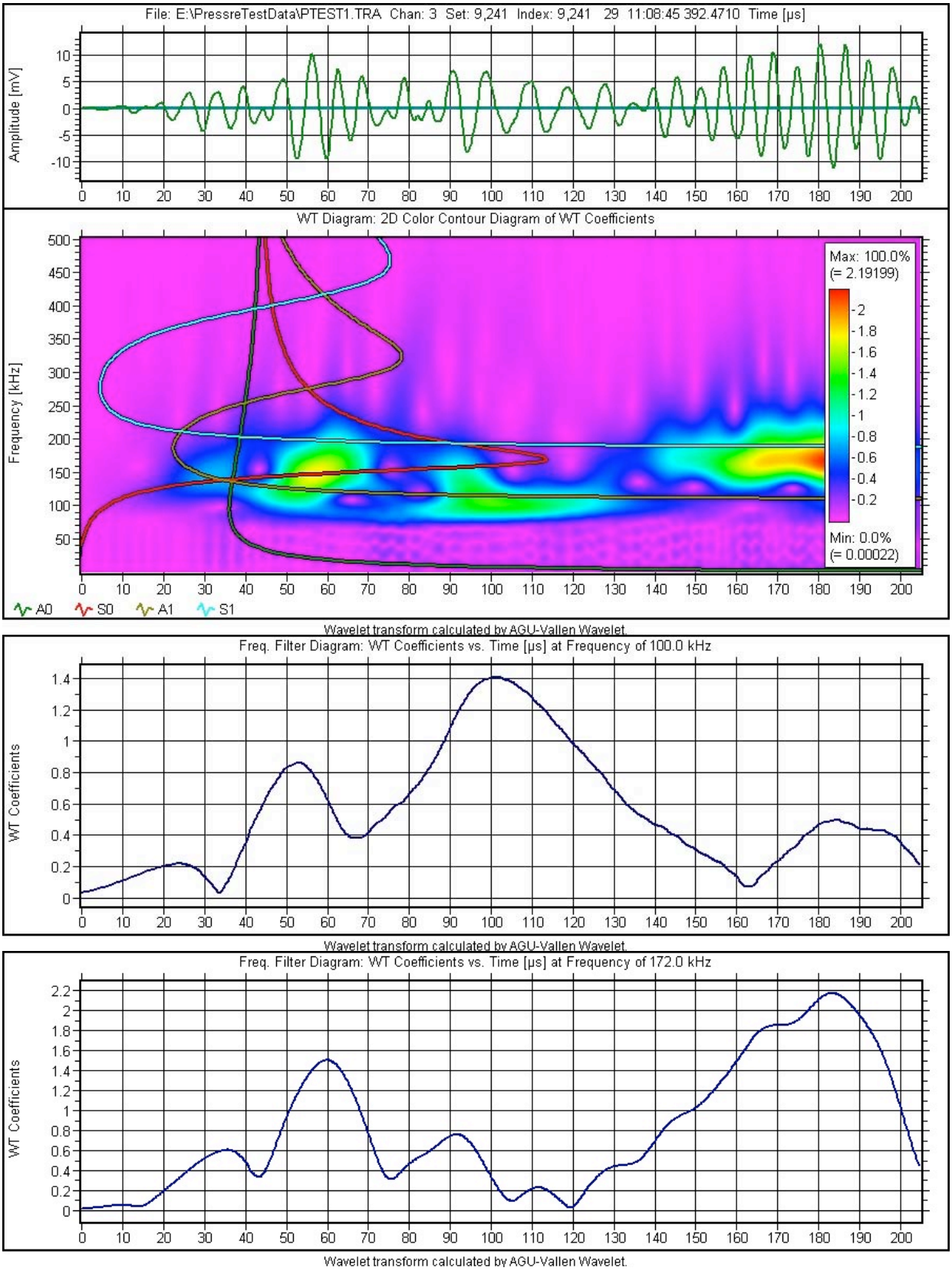

Fig. 18 Top to bottom: AE signal, Color plot of the WT, wavelet coefficients at 100 kHz and wavelet coefficients at 170 kHz, Event no 1, TRAI 9241.

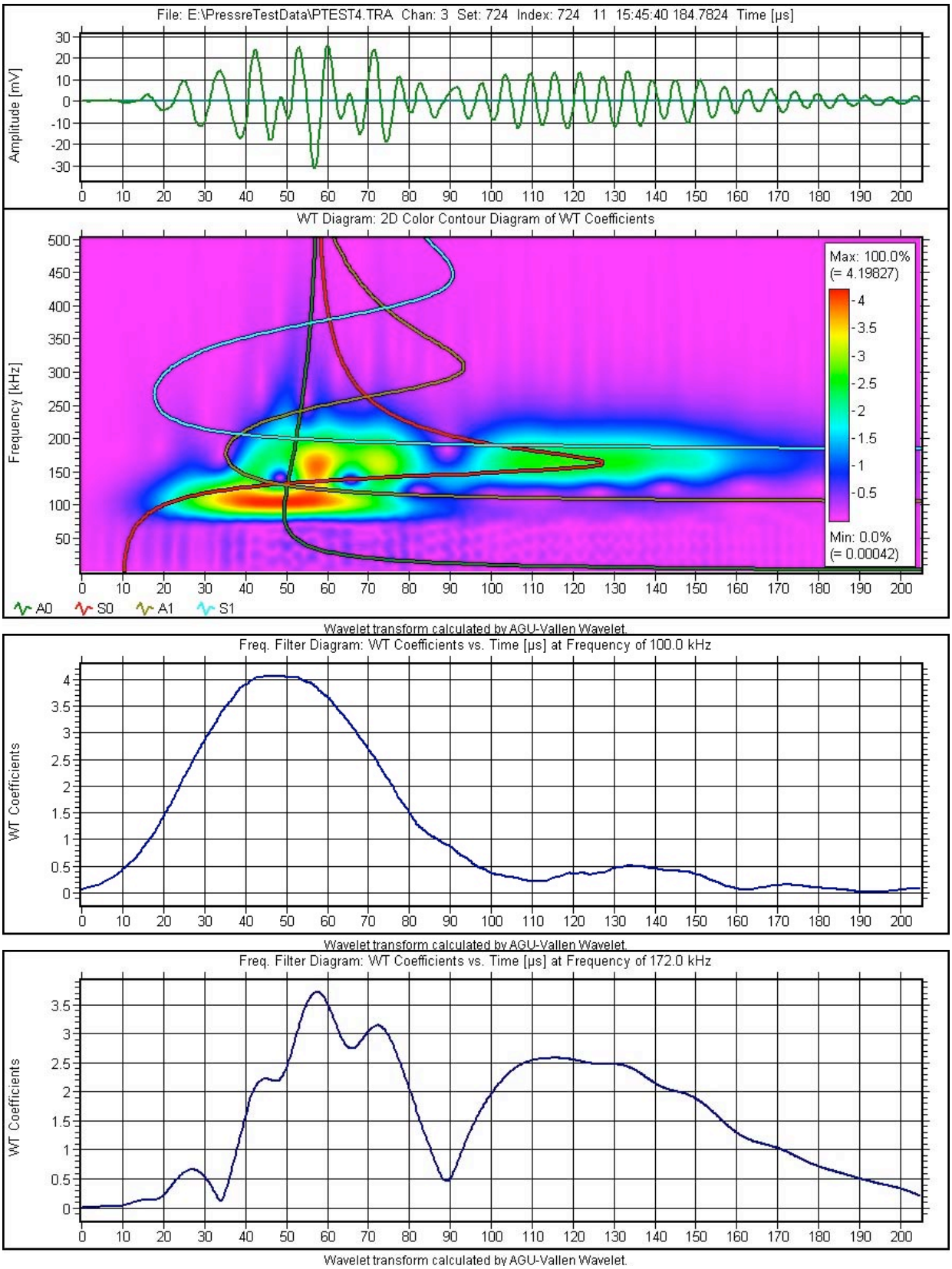

Fig. 19 Top to bottom: AE signal, Color plot of the WT, wavelet coefficients at 100 kHz and wavelet coefficients at 170 kHz, Event no 12, TRAI 724.

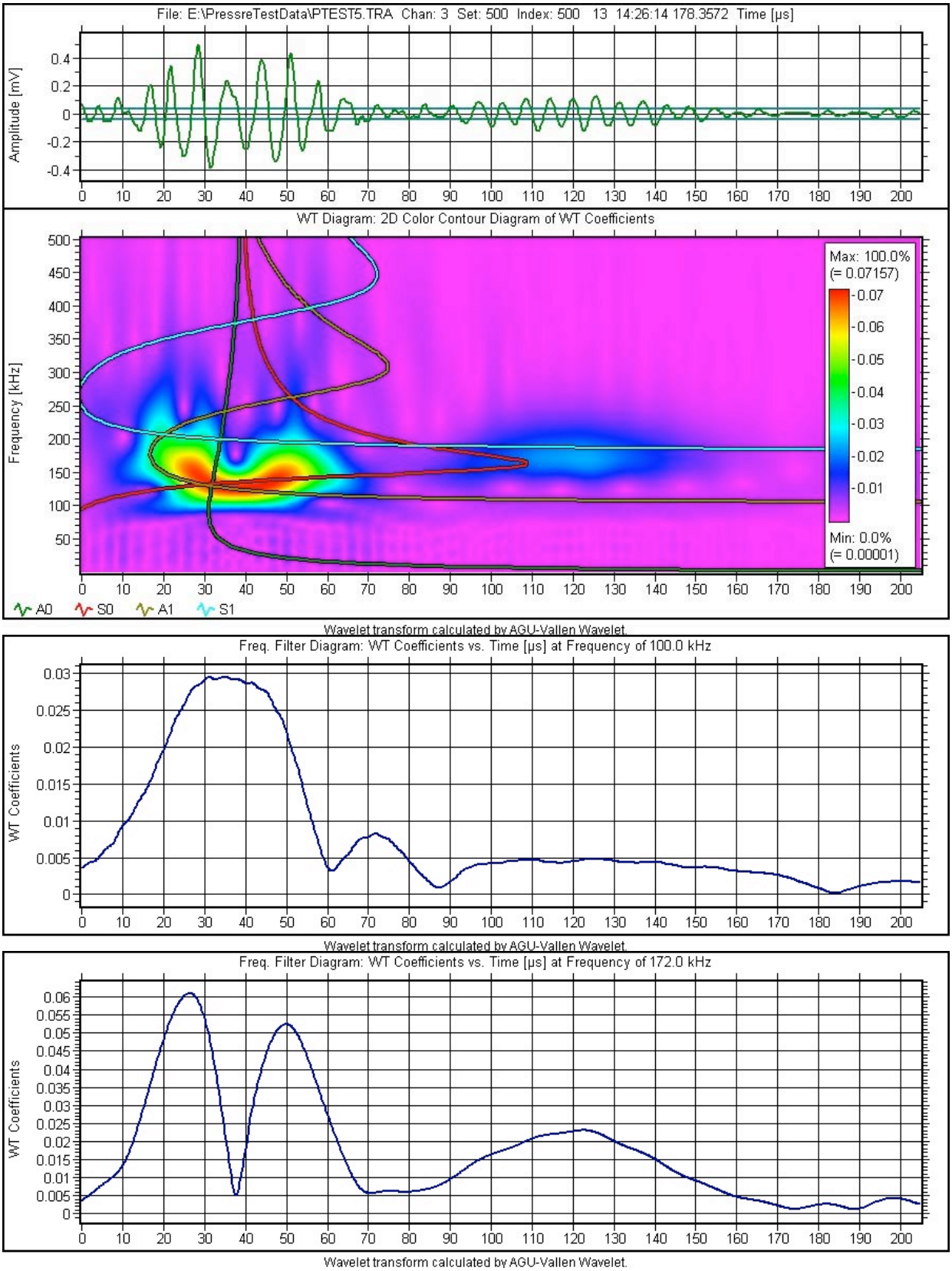

Fig. 20 Top to bottom: AE signal, Color plot of the WT, wavelet coefficients at 100 kHz and wavelet coefficients at 170 kHz, Event no 13, TRAI 500.

References

Bayray, M. (2002a), “Crack growth investigations in pressure vessels using acoustic emission technique,” Institute of Pressure Vessels and Plant Technology, Vienna University of Technology, Dissertation.

Bayray, M., Rauscher, F. (2002b), "Window Fourier Transform and Wavelet Transform in Acoustic Emission Signal Analysis," Proceedings of the EWGAE 2002 conference, Vol. I, Prague, Czech Republic, Sept. 11-13, pp. I/37-44.

Downs, K.S., Hamstad, M.A., and O’Gallagher, A. (2003), “Wavelet transform signal processing to distinguish different acoustic emission sources,” Journal of Acoustic Emission, **21**, 52 – 69.

Hamstad, M.A., O’Gallagher, A. and Gary, J. (2002a), “A wavelet transform applied to acoustic emission signals: Part 1: Source identification,” Journal of Acoustic Emission, **20**, 39 – 61.

Hamstad, M.A., O’Gallagher, A. and Gary, J. (2002b), “A wavelet transform applied to acoustic emission signals: Part 2: Source location,” Journal of Acoustic Emission, **20**, 62 – 82.

Hamstad, M.A., Downs, K.S., and O’Gallagher, A. (2003), “Practical aspects of acoustic emission source location by wavelet transform,” Journal of Acoustic Emission, **21**, 70 – 94.

Rauscher, F., Bayray, M. (2005), “Weld defect in a pressure vessel: Investigation of acoustic emission during pressure tests and pressure cycling,” Institute of Pressure Vessels and Plant Technology, Vienna University of Technology, Report 26.

Vallen-Systeme GmbH, Munich, Germany, http://www.vallen.de, October, 2005.

ACOUSTIC EMISSION PATTERN RECOGNITION ANALYSIS APPLIED TO THE OVER-STRAINED PIPES IN A POLYETHYLENE REACTOR

IRENEUSZ BARAN, MAREK NOWAK and KANJI ONO*
Laboratory of Applied Research, Foundry Research Institute, Krakow, Poland.
* Materials Science and Engr. Department, University of California, Los Angeles, CA USA.

Abstract

Techniques of acoustic emission (AE) were used during the over-straining applied on straight pipes and elbows of a polyethylene reactor operating in a factory. This reactor has several dozen pipes, straight and bent, of 10-m length. Over-straining is done before the pipes were put in operation and also periodically during service. AE enables us to monitor the stability of the deformation process and indicates the zones, which will require further detailed examinations by other NDT techniques; it should also improve safety during this process through early detection of critical damage. After a few series of tests and using evaluation criteria with AE parameters, we examined next 45 pipes with recorded waveforms for additional analysis. Vallen VisualClass pattern recognition analysis program enabled us to separate the signals due to the plastic deformation of materials during over-straining process from the signals generated by cracking damage. The presence of damages in three groups of over-strained pipes was identified and confirmed by other NDT techniques.

Keywords: Polyethylene reactor, overstraining, pattern recognition analysis

Introduction

The strength and life of heavy-wall pipes operating in installations of petrochemical industry can improve by the process of their over-straining. Due to plastic deformation, over-straining produces desirable residual stresses in the internal layer of the pipes. However, it is necessary to carefully control the value of these stresses and to ensure their uniform distribution. When the pipes are in use, the residual stresses introduced previously undergo relaxation, and the process of over-straining has to be repeated periodically.

The use of Pattern Recognition (PR) analysis techniques has expanded in the field of acoustic emission [1-3]. For example, wind turbine blades have been examined using AE and PR methods [3]. See a recent general review of this analysis technique [4]. However, more experience is needed to expand the use of PR methods in practical applications of AE monitoring of industrial structures. It is here where we must discriminate various spurious signals from the AE from critical flaws.

This paper describes the application of PR techniques in the examination and evaluation of over-strained pipes operating in a polyethylene reactor. The process of over-straining was carried out according to a scheme of loading with internal pressure, developed and adopted to the pipe material and pipe configuration. The evaluation mainly consisted of the analysis of AE signals recorded during the over-straining process. The first series of tests (33 straight and bent pipes) with a PAC Mistras 2001 system evaluated signal parameters and quantitative criteria were developed with the results of laboratory tests [5]. In the final series, a new analysis approach was

used in examining 29 10-m long straight pipes (and 16 elbows not included here). It differs from the standard AE testing, and uses the criteria developed from an analysis of the AE signals recorded during laboratory research and in-field tests [5]. Parts of the initial work will be introduced here for completeness. The AE signals emitted during over-straining process were recorded on Vallen AMSY-4 and AMSY-5 AE systems. Vallen VisualClass software, based on the frequency characteristics of the recorded signals, was used in the PR analysis. The results of AE PR analysis techniques are presented utilizing the already accumulated database on AE signal characteristics and criteria, based on 78 pipes tested and evaluated.

Description of the Problem

The strength and performance life of heavy-wall pipes operating in petrochemical installations are improved by the application of over-straining process. The over-straining produces plastic deformation and hardening of the processed material, resulting in the formation of a thin, hardened layer in the internal pipe wall with desirable residual stresses. However, the rate and distribution of this deformation and hardening should be carefully controlled, as it may cause damages to the pipe due to the induced stresses, consequently leading to flaws, and in some extreme cases even to failure of the whole reactor.

Generally speaking, the process of over-straining is made on pipes both new as well as operating for some years. In pipes, which have already been in operation for some time, the process of over-straining should be repeated, since the stresses and the hardening introduced by over-straining will undergo relaxation during pipe operation.

This article describes the results of analysis made on 10-m long straight pipes with outer/inner diameter of 100 and 46 mm, respectively. The pipes were operating in a polyethylene reactor (two types of pipes are, as a rule, operating in reactors of this type, viz. straight pipes and elbows). The pipes are expected to operate under a pressure of 250 MPa and at a temperature of up to 290°C. Pipes were made from the material designated by ASTM as 4333M4 and 4333M6. The pipe ended in special assembly joints, used for service assembly and on a high-pressure stand for over-straining. During over-straining, the internal pressure of 600 MPa was applied to the pipes, inducing the plastic deformation in the internal part of their walls. The over-straining was carried out according to a special program with a few cycles of loading, which ensured a uniform deformation in the inside wall. AE testing used six VS150RIC resonance sensors. The sensors were positioned considering the signal attenuation factor of the pipe material. Actually, the number of sensors could be less than used strictly from attenuation, but it was needed to obtain a high sensitivity on the entire pipe length. The process of pipe over-straining was examined and evaluated using Vallen VisualClass software for the PR analysis of AE signals.

Pipes described in this article have already been operating for several years or more, and therefore, they needed to be over-strained again. AE signals were recorded during this operation. Pipe dimensions and lay out of AE sensors are schematically shown in Fig. 1.

Evaluation Criteria

To obtain criteria of pipe evaluation some laboratory tests and examinations were done. The uniaxial tensile tests were conducted on material samples taken from the pipes withdrawn from operation. The stress-strain characteristics are necessary for further determination by finite ele-

ment method (FEM), so that we can determine the stress/strain values and distribution in pipe-wall during over-straining, and for calculation of the residual stresses.

We also wanted to determine the characteristic of acoustic emission generated in the uniaxial tensile test and during crack onset and propagation in the internal volume of pipe material. The mode of pipe loading was consistent with the adopted scheme of over-straining pressure and allowed for the values of residual stresses estimated by FEM. The specimens were loaded with and without a crack of radial orientation. The C type specimens used for this purpose were made from a half section of the pipe out of service. The geometry of the specimens is shown in Fig. 2.

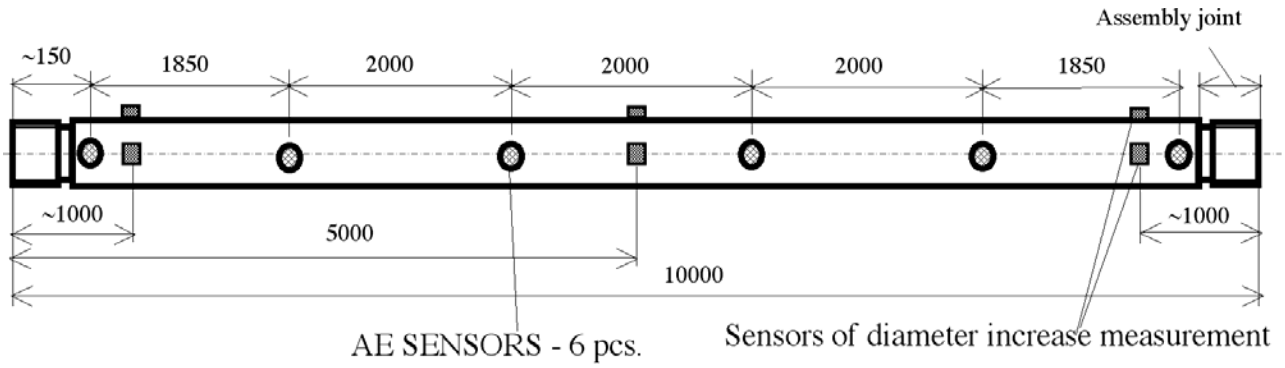

Fig. 1 Layout of AE sensors on the length of a straight pipe.

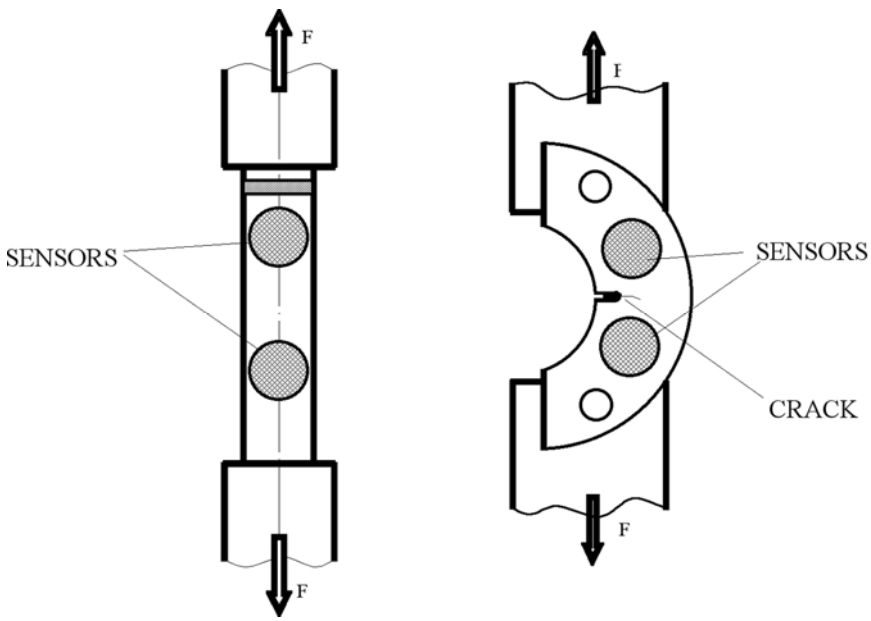

Fig. 2 Examples of specimen geometry and mode of loading.

For the scheme of over-straining, utilizing own experience and the results of laboratory tests, the following evaluation criteria of the located events were adopted:

A. Amplitude criterion for load application and load hold,
B. AE activity criterion for load application,
C. AE activity criterion for load hold,
D. AE activity criterion for load release.

For each of the adopted evaluation criteria the corresponding values were determined. In initial laboratory tests and during over-straining of the first 33 straight and bent pipes, a PAC Mistras 2001 AE system was used along with the resonance sensors of 150-kHz frequency.

Background

At the beginning, the following general assumptions were made:

- All pipes are subjected to the process of over-straining performed under the same conditions and in the same mode of application.
- The method of taking measurements and the system of AE recording during over-straining are identical for all pipes.
- Practically all effects related with the over-straining process (regarded as noise by AE) are similar for each over-strained pipe
- Each pipe is of different „age" and has remained in operation for a different period of time.
- The examined pipes have been operating under variable conditions of temperature and pressure within the standard regime of pipe operation in a reactor.
- The structural hardening and the changed state of stresses introduced by over-straining conducted previously will certainly undergo some relaxation, different in each pipe and depending on the above mentioned variable conditions
- Final thickness of the layer hardened by plastic deformation should be the same in all the properly over-strained pipes.

From the above it follows that since the recorded AE signals originated from the same source, resulting from the plastic deformation and hardening of pipe material, these signals should be of a similar nature, though varying in intensity depending on the degree of relaxation in the internal layer of each pipe during its operation. Figure 3 shows example of different AE activity obtained for two bent pipes. Finally, it can be assumed that all the anomalies taking place in the process of plastic deformation and hardening, e.g. the crack formation process, will be captured and recognized.

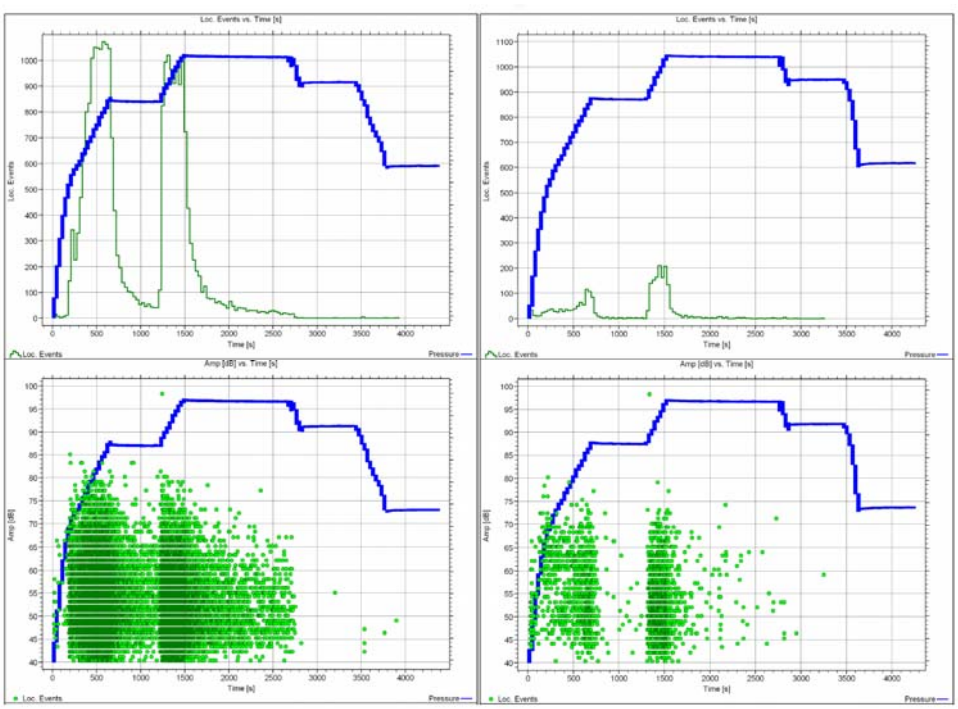

Fig. 3 AE activity and amplitude distribution in two pipes: (a: left) bent pipe failing in 3 criteria (A, B and C), (b; right) bent pipe satisfying all criteria.

From the data analysis of the first series and on evaluation of the results of AE measurements during over-straining, 14 pipes were indicated to fail in one of the above-mentioned criteria. Additionally, two bent pipes (numbers 32 and 33) were indicated to fail in three of the above-mentioned AE criteria. The pipes failing AE criteria were examined by eddy current and ultrasonic tests and correlation was used to correct and adjust the values selected for the adopted AE criteria. In the next batch of pipes examined, the effectiveness of the over-straining process was checked and evaluated by Mistras 2001 and AMSY-4 systems used simultaneously. Sensor signals were split into the two systems. This test was to establish evaluation criteria for both systems. Having examined 26 pipes, we found 2 straight pipes failed in three of the adopted criteria. Checking the located AE sources by means of ultrasonic flaw detection, damages were revealed in the internal layer of pipe material. Using this revised criteria, we evaluated overstraining of 20 additional pipes with recording of the AE made on AMSY-5 system. In one of the straight pipes the tests detected an AE source exceeding the allowable limits in 3 criteria. The presence of this source was confirmed by other NDT methods as a defect in the microstructure of pipe material.

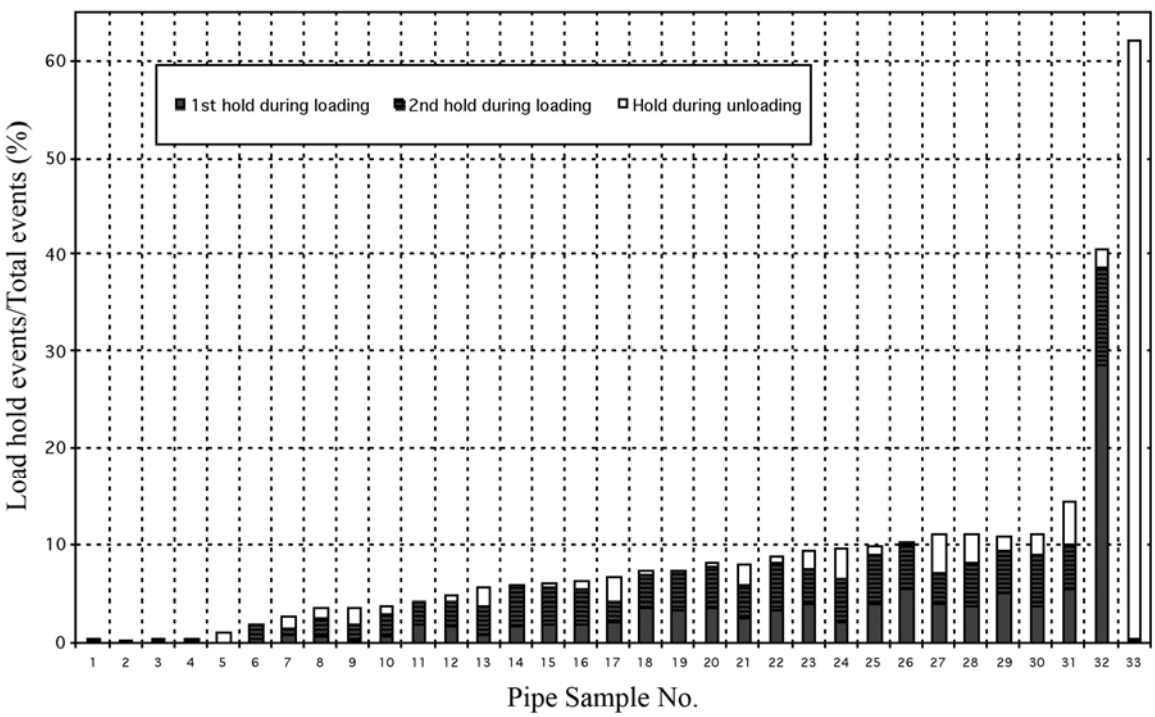

Fig. 4 Percentage share of events for every pipe during holds relative to the sum of total events.

Analysis

For the numerical analysis performed using VisualClass software, 29 pieces of the straight pipes were selected for the final series. The first stage of the analysis consisted in separating for each pipe the data obtained from AE measurements recorded within the range of pressures corresponding to the yield strength of material exceeded in the zone of the internal pipe wall. Next, among the obtained data, only the AE signals located along pipe length were accepted.

The measured dataset was used for a comparative analysis of AE signals emitted from the individual pipes. For this purpose, we used supervised learning available in the VisualClass software. An output of this operation was grouping of pipes with similar features of the recorded AE signals. A step-by-step description of the analysis is shown in Fig. 5. From this analysis, Group **I** contained 17 pipes; Groups **II** and **III**, 6 and 3 pipes, respectively. The remaining 3 pipes formed

Group **IV**; they differed within their own group and with respect to the other three. Figure 6a shows the output of analysis made for several pipes with similar characteristics of the recorded AE signals (each color represents one pipe), where the separation was not possible. Figure 6b shows the output of analysis made for several pipes whose features differed enough and the separation was possible.

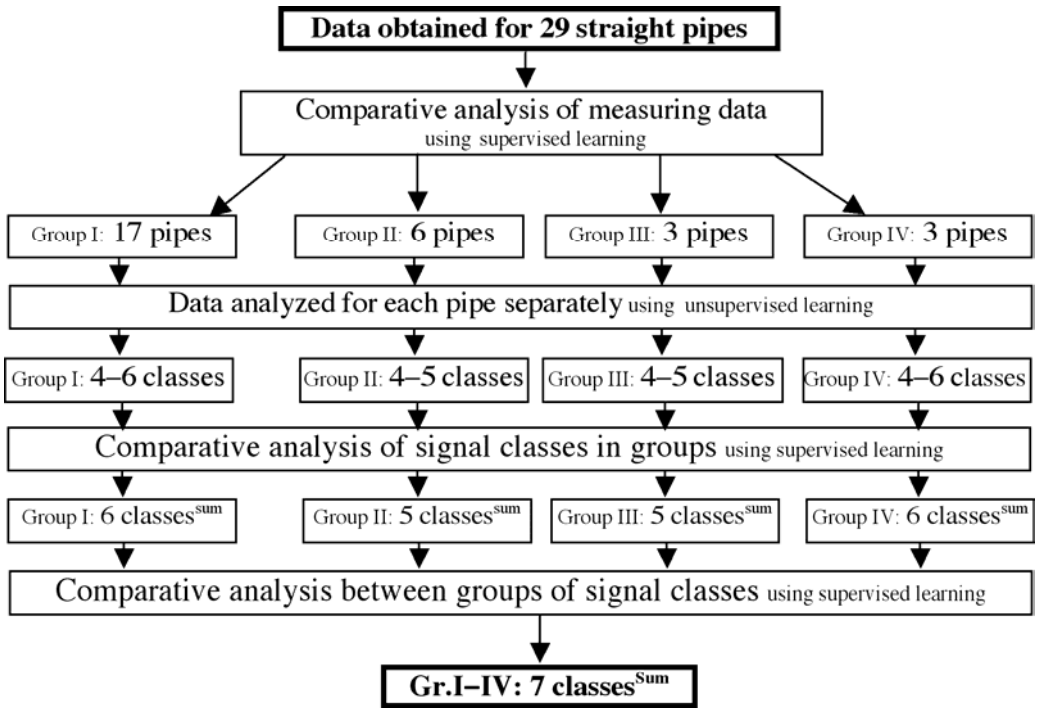

Fig. 5 Successive steps in the analysis of AE data measured on straight pipes.

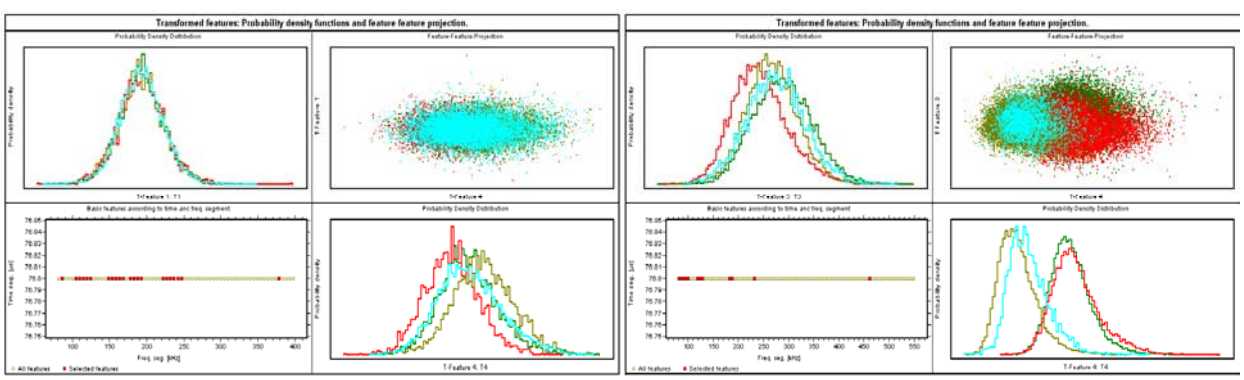

Fig. 6 Separation of features for pipes with AE signals similar (a: left) and different (b: right).

At the next stage, unsupervised PR analysis was made separately for each pipe, isolating the classes of AE signals, for which the separation was possible. The assignment of signals to a given class was at a level of at least 75% of the population. Finally, 4 to 6 classes of AE signals were obtained, depending on the pipe.

The next step using supervised learning was to compare in groups the classes of the obtained signals. This produced for Group **I** - 6 classes of signals, for Group **II** - 5 classes, and for Group **III** - 5 classes. In Group **IV** pipes with no features in common, 6 classes of signals were obtained. These classes resulted from the summation of individual pipe data, so it has "class^{Sum}" designation. The last stage of the analysis (using supervised learning) compared the groups of the

signal classes. As an output, seven classes^{Sum} of signals were obtained, with the assignment of signals to a given class kept at a level of at least 80% of the population.

Results

Based on the obtained seven classes^{Sum} of signals, a classifier was designed. Its task was to enable classification of the individual data measured for each pipe separately. The percent share of signals in each of the classes^{Sum} was obtained for each pipe separately. Using these data, Table 1 comprising the results of classification was drawn. Figure 7 shows graphical representation of the results.

For pipes qualified as sound, based on the AE criteria developed previously and verified by other NDT methods, Classes^{Sum} 5 and 7 with occasional deviations were predominant. Pipes found as failing to satisfy the established AE criteria [5] (including pipes with damages detected by other NDT methods) were characterized by the predominance of Classes^{Sum} 2, 3 and 4. Classes^{Sum} 6 showed relatively little change between sound and potentially damaged pipes.

Table 1 Results of classification, showing the number of signals assigned to each class.

Pipe no	Class no							Group no
	1	**2**	**3**	**4**	**5**	**6**	**7**	
1	0	14	11	44	0	29	2	**II**
2	0	8	7	23	8	30	25	**III**
3	0	12	9	40	0	34	5	**II**
4	0	21	16	36	0	25	3	**III**
5	0	21	14	42	0	22	1	**II**
6	0	15	13	45	0	25	2	**II**
7	0	23	17	34	0	22	3	**III**
8	0	19	14	45	0	22	1	**II**
9	0	13	11	45	0	27	4	**II**
10	1	1	2	8	36	20	32	**I**
11	0	11	12	48	3	19	6	**IV**
12	7	2	3	8	30	18	32	**IV**
13	0	1	2	7	43	17	31	**I**
14	0	1	2	6	50	13	28	**I**
15	0	3	4	11	19	29	34	**I**
16	0	2	2	9	30	21	37	**I**
17	1	2	4	15	23	28	27	**I**
18	1	1	3	10	30	20	35	**I**
19	0	4	4	14	20	27	30	**I**
20	0	4	3	11	23	23	37	**I**
21	1	4	3	10	28	20	36	**I**
22	0	24	22	43	0	12	0	**IV**
23	1	3	4	9	32	19	34	**I**
24	0	3	4	11	19	25	39	**I**
25	1	4	5	11	26	22	32	**I**
26	0	4	5	12	23	23	34	**I**
27	1	2	3	11	27	22	34	**I**
28	6	2	3	7	41	16	26	**I**
29	0	2	3	11	28	23	33	**I**

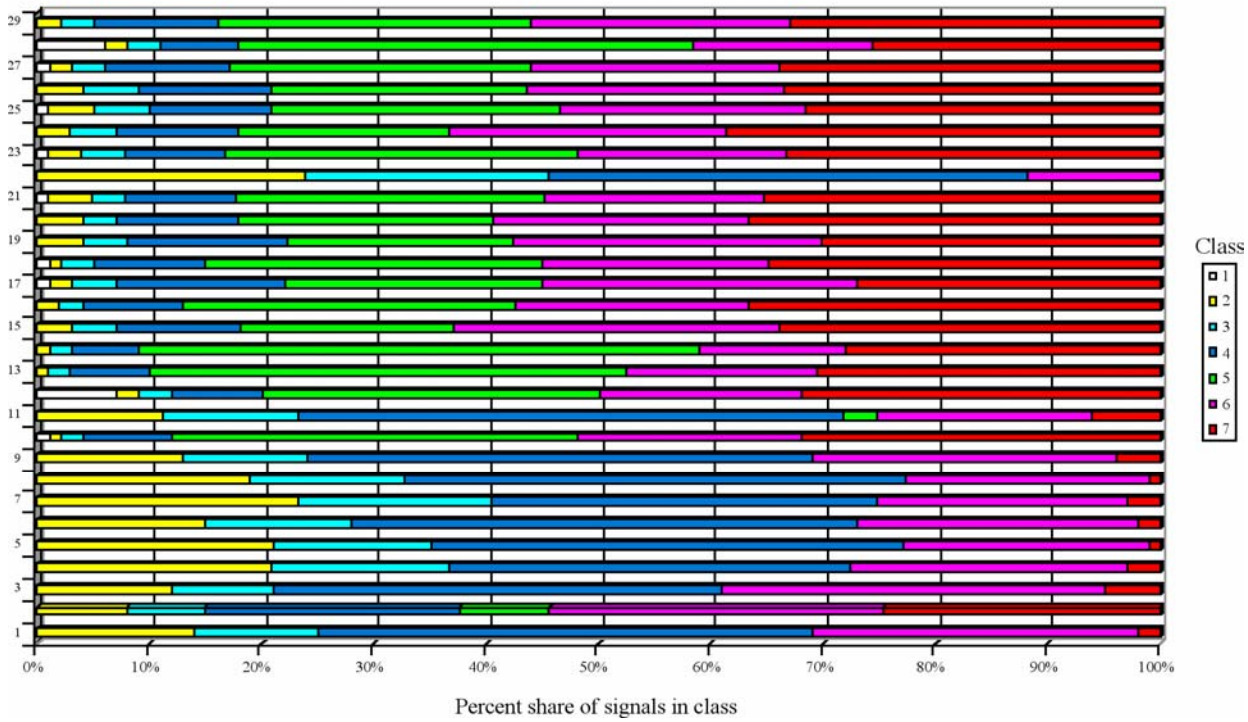

Fig. 7 Graphical results of classification, in the percentage of signals of different class by color.

All of Group **I** pipes and one from Group **IV** (#12) were sound. Among others, we rejected 3 pipes outright because they failed all the AE criteria. The results were confirmed by other NDT methods. These had cracks and local heterogeneity. The remaining 8 pipes failed some AE criteria and were subjected to other NDT methods. They were qualified for use after passing NDT criteria.

Conclusions

Based on the obtained results and on their analysis, the following conclusions can be drawn:

- The PR analysis with VisualClass software showed its utility in a field test application.
- Pipes in Group **I** category were sound after proper and stable over-straining process.
- Most of Groups **II**, **III** and **IV** were pipes with a risk due to incorrect over-straining process and with flaws present in material structure. Three of them were rejected while the rest were qualified for further use after passing other NDT criteria.
- It is advisable and recommended to continue developing the PR analysis, especially as regards the possibility of identifying mechanisms of individual classes of signals.

It should be stressed that this article demonstrates practical benefit of the application of pattern recognition analysis technique to an industrial problem of pipe over-straining.

References

1. M. Ohtsu and K. Ono, J. Acoustic Emission, **3**, (1984) 69-80.
2. R. W. Y. Chan, D. R. Hay, J. R. Hay and H. B. Patel, J. Acoustic Emission, **8** (1989) S12-15.
3. A. A. Anastassopoulos et al., J. Acoustic Emission, **20** (2002) 229-237.
4. A. A. Anastassopoulos, J. Acoustic Emission, **23** (2005) 318-330.
5. M. Nowak, I. Baran, J. Schmidt, Z. Plochocki: "Application of Acoustic Emission in control of high-pressure pipe overstraining," Advanced Materials Res. **13-14**, (2006) 153-158.

ACOUSTIC EMISSION EVALUATION SYSTEMS OF TOOL LIFE FOR SHEARING OF PIANO AND STAINLESS STEEL WIRES

MASANORI TAKUMA[1], NOBORU SHINKE[1], TAKAKO NISHIURA[2] and KENSUKE AKAMATU[3]

[1] Department of Mechanical Engineering, Kansai University, 3-35, Yamate, Suita, Osaka, 564-8680 Japan; [2] Aisin AW Co., Ltd., Fujii, Anjo, Aichi, 444-1192 Japan; [3] Sankyo Seiki Industry Co., Ltd., Higashiyodogawa, Osaka, 533-0006 Japan.

Abstract

Shearing is a machining operation that separates the workpiece material by the growth of a crack, which occurs in the narrow region around the tool tip. It is necessary to evaluate the tool life because the product quality is influenced by the wear conditions of the tool. However, the problems for evaluating the condition and the tool life have not been solved yet. In this study, chaos time series analysis, wavelet transform and waveform analysis are applied for recognizing the characteristics of the detected AE signals in the shearing of piano and stainless steel wires. The results are as follow: (1) AE signals have the chaotic property, and the wear condition and the tool life will be evaluated by the largest Liapunov exponent and the correlation dimension; (2) the RA (rise time/amplitude) value of the time fluctuation waveform of the wavelet coefficient is an effective parameter for tool life prediction; (3) the validity of this system for the tool life by the RA value was confirmed by the comparison with the experimental results.

Keywords: Tool life, evaluation system, chaos time series analysis, wavelet transform, shearing

Introduction

Shearing is one of the most important working methods in the manufacturing process. We need to evaluate tool wear conditions for the quality control of products and the improvement of the productivity. Such a system is yet unavailable [1]. In this study, chaos time series analysis, wavelet transform analysis and waveform analysis were applied for evaluating the tool wear conditions in shearing of piano and stainless steel wires, and the extraction of the parameters from detected AE signals for evaluating the tool life was investigated. From the study, it became clear that the RA (rise time/peak amplitude) value of the time fluctuation waveform of wavelet coefficient is an effective parameter. An evaluation system using the parameter was proposed, and its validity was confirmed by comparing with the experimental results.

Chaos Time Series Analysis and Wavelet Transform

Chaos time series analysis

Chaos time series analysis is one of the effective methods, when the cause of the complexity of the signal is the fluctuations of the nonlinear dynamical system or the internal factors. In the judgment of the chaos property, the recurrence plots that represent the distance $D_{i,j}$ between two points (*i.e.* X_i and X_j) in the phase-space on the two-dimensional coordinate plane (i, j) are used. The plots are evaluated by the texture of the gradation colors for $D_{i,j}$ and the

monochrome representation of the plotting density. It is judged that the time series signals are deterministic data, when the features of the recurrence and the iso-directional neighbors plots (*i.e.,* the common sets of the iso-directional recurrence plots and the recurrence plots) are similar [2-6]. The features of deterministic chaos are the self-similarity (*i.e.,* the geometric features which are evaluated by the structure of the attractor) and the orbit instability (*i.e.,* the dynamical features). In the analysis methods for evaluating the features, fractal analysis and Liapunov spectrum analysis are used. The instability of the signal is quantitatively evaluated by the fractal dimension and the Liapunov exponent. The instability becomes strong when the exponent is big, and becomes weak when the exponent is small. The Liapunov spectrum is the parameter that combined each exponent. It is decided that the time series signal has the chaotic property [2-6], when the following conditions are satisfied: (1) the x_1, x_2 and x_3 in the three-dimensional attractor that reconstituted the signal show plus, zero and minus, respectively; (2) the correlation exponents, which were obtained with the correlation integration method converge on the constant value (*i.e.,* the correlation dimension) with the increase of the embedded dimensions in the phase-space. The asymptotic value is judged by the correlation dimension (*i.e.,* the fractal dimension).

Wavelet Transform

AE signals in shearing arise from the deformation of the wire, the growth of the crack, the tool wear condition, etc. Various such factors may be elucidated by grasping the occurrence time of the frequency components corresponding to each factor. The frequency analysis results with FFT are effective for identification and discrimination of the microscopic fracture factor, and FFT contributes to the solution of the fracture mechanism. However, it is not suitable for the analysis of the signals, whose the statistical properties change with the time [7-11]. Therefore, another method that transforms a signal into a time-frequency domain is needed for analyzing non-stationary or transient signals such as AE. Wavelet transform (WT) is one of the methods for supplementing the shortcoming of FFT. The WT of the signal $f(x)$ is defined by:

$$[WT\,f](a,b) = \int_{-\infty}^{\infty} \Psi^*(x) f(x) dx [WT\,f](a,b) = \int_{-\infty}^{\infty} \Psi^*(x) f(x) dx \qquad (1)$$

where Ψ^* is the complex conjugate of the wavelet function $\Psi a,b(x)$. The function $\Psi a,b(x)$ is defined by $|a|^{-1/2}\,\Psi((x-b)/a)$. The function $\Psi(x)$ is the mother wavelet (e.g., Gabor wavelet) with the scale parameter a and the shift parameter b and provides a set of the localized functions in both frequency and time. The scale parameter a gives the width of window and consequently the frequency as the mother wavelet is expanded or compressed in time. The shift parameter b determines the position of the window in time and thus defines the analysis part of the signal $f(x)$. Therefore, it is possible to make the optional wavelet of the angular frequency ω_o/a in time b by changing both parameters, and the signal $f(x)$ is represented by putting the various optional wavelets together. The wavelet coefficient and its fluctuation enlarge respectively, if the wavelet $\Psi((x-b)/a)$ that was deformed by the parameter a and b resembles a part of the signal $f(x)$. The intensity of the coefficient is correspondent to the amplitude of the signal $f(x)$ [7-11]. Therefore, the fluctuation of the coefficient shows the activity of the component with the frequency ω_o/a in time b. WT becomes effective for the analysis of AE signals, in which sudden fluctuations and many phenomena are mixed, when the transform result was represented on the plane of b and $1/a$. Therefore, it is possible to contribute to the grasp of the fracture phenomena, if the features of the time fluctuation waveform of the wavelet coefficient in each frequency component are extracted. This feature of WT is very important for grasping each factor of fracture by the features of the analysis result.

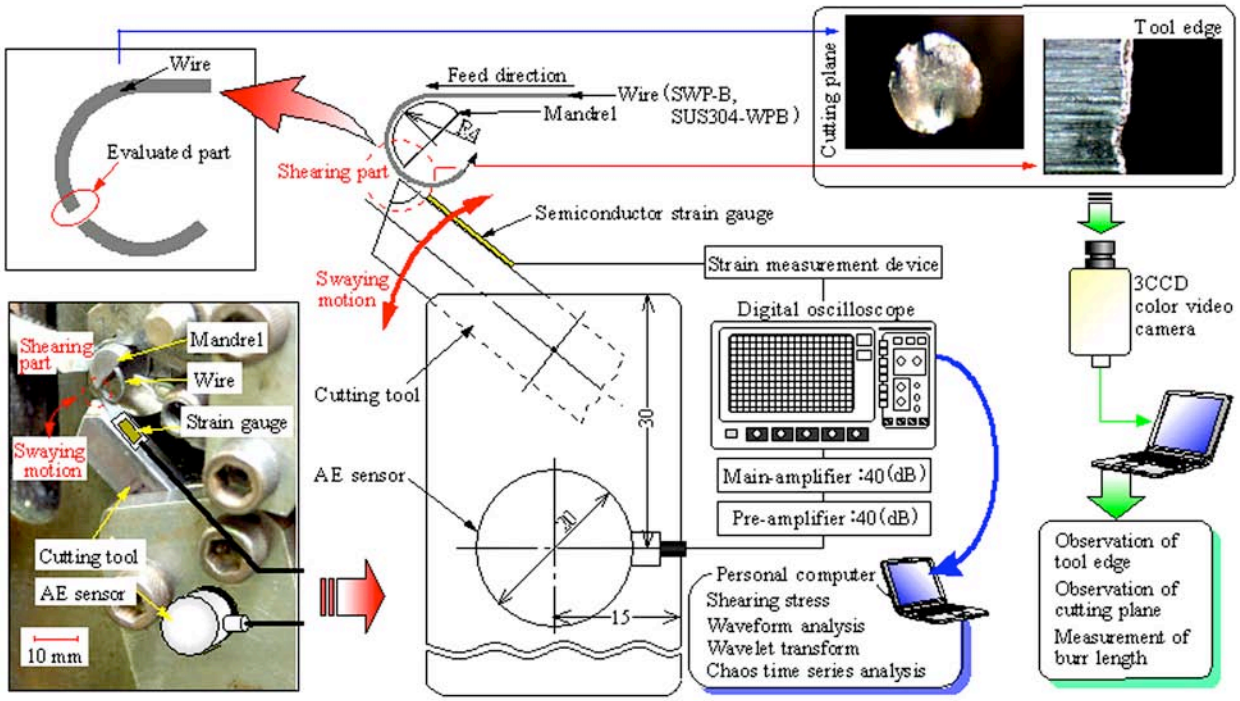

Fig. 1 Experimental device and conceptual scheme in this study.

Experimental Method

The piano wire SWP-B and stainless steel wire SUS304-WPB were used as the workpiece material. The tensile strength was 2.5 GPa for piano wire and 1.9 GPa for stainless steel wire, respectively, and the diameters of both wires are 0.7 mm. The high-speed tool steel SKH-51 was employed as the materials of a shearing tool and a mandrel.

Figure 1 is the schematic drawing that shows the experimental equipment and the processing order of the detected AE signals. The signals from shearing in a coiling machine are detected by an AE sensor of the wide-band type and are recorded in a digital oscilloscope. The distance to the center of an AE sensor from the AE source (*i.e.,* the tip of the cutting tool) is fixed at approximately 58 mm. The features of the signals for evaluating the wear condition and tool life are extracted by the chaos analysis, the wavelet transform and the waveform analysis. On the other hand, the shearing stress is calculated from the detected strain by the semiconductor strain gauge attached on the tool. Here, the initial clearance between a tool and a mandrel was set at 0 mm in order to give priority to the quality of the shear plane, and the burr length is measured every 100 shearing. In the criterion of the machining field, it is judged that the tool reached its life when the burr length became 10~15% of the diameter of the wire. Therefore, the limit was set at 70~100 μm.

In order to extract the features for evaluating the tool life, the following operations are done: (1) the wear conditions are decided by the features of the obtained information (*i.e.,* the behavior of the burr length and the shearing stress, and the conditions of the shear plane and the tool tip, *etc.*); (2) the property for the determinism of the detected signals is examined by observing the results of chaos time series analysis; (3) the frequency components, which characterize the tool life are specified by the wavelet transform results, and the features (*i.e.* the

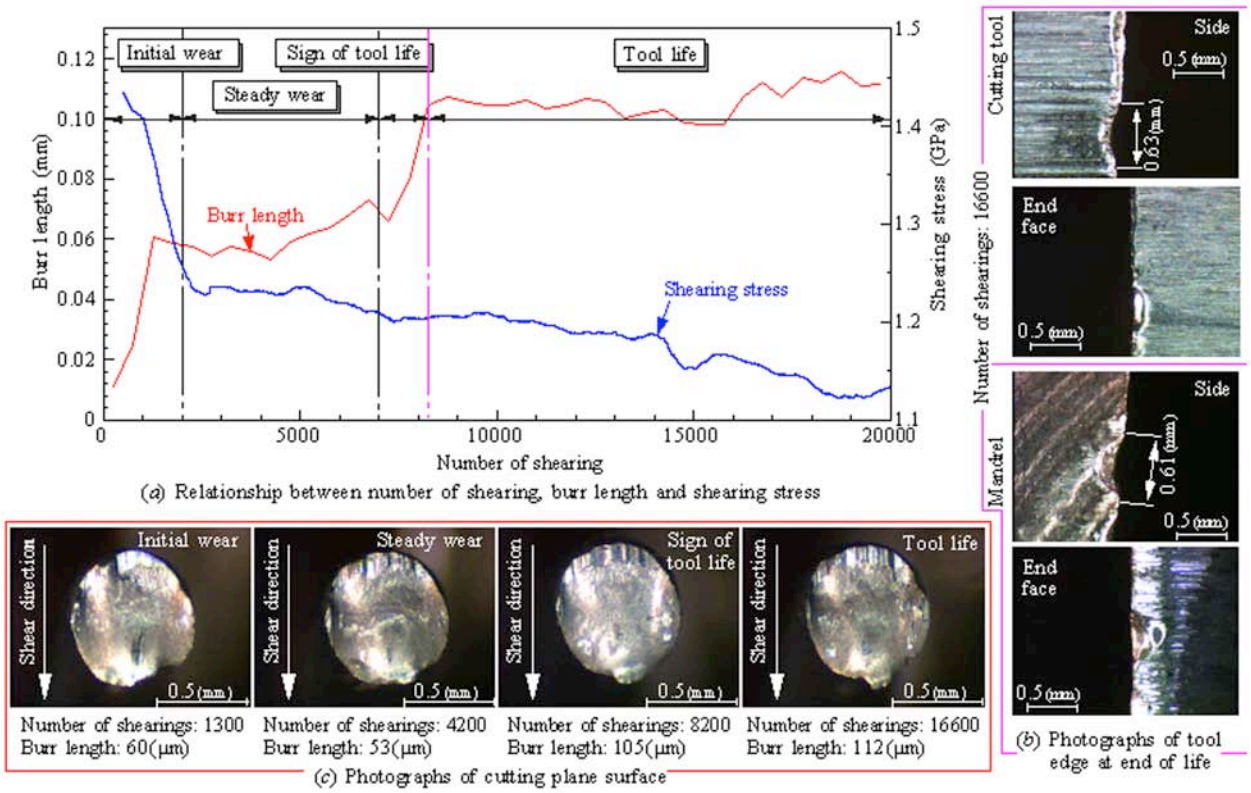

Fig. 2 Examples of experimental results for piano wire.

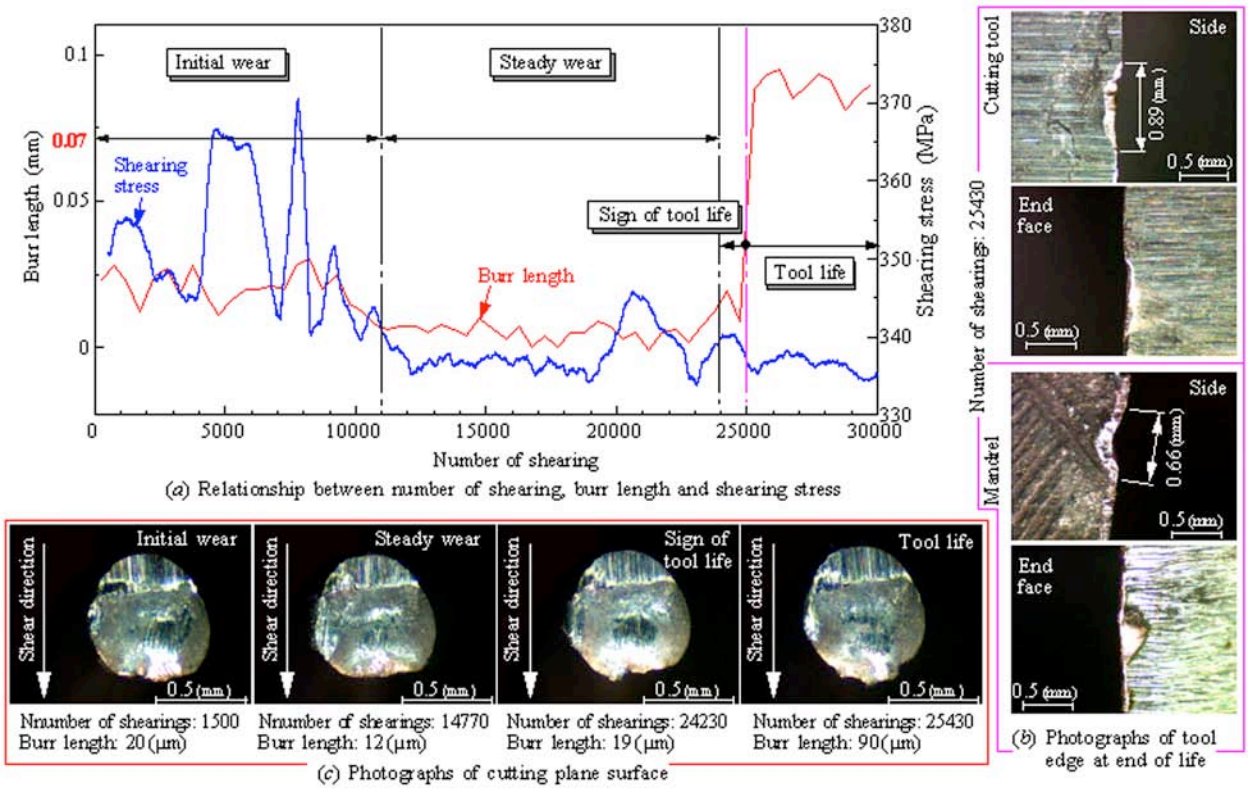

Fig. 3 Examples of experimental results for stainless steel wire.

maximum amplitude, the energy and the RA value, *etc.*) of the time fluctuation waveform of the wavelet coefficient in the components are extracted.

Experimental Results and Considerations

Shearing stress and burr length

Figures 2 and 3 show the experimental results of the piano and stainless steel wires against the number of shearing. In each, the burr length, the shearing stress, the photographs of the shear plane, the cutting tool and the mandrel are shown. From the results shown in the figures, the wear conditions of both wires were classified into the initial wear area, the steady wear area, the sign of tool life area and the tool life area. The features in each wear condition of the piano wire are as follows (*cf.* Fig. 2): the burr length rapidly increases and the shearing stress sharply decreases in the initial wear area; the length slowly increases and the stress slowly decreases in the steady wear area; the length rapidly increases and the stress very slowly decreases in the sign of tool life area; the length reaches at 100 μm in the tool life area. On the other hand, the features in each wear condition of the stainless steel wire are as follows (*cf.* Fig. 3): the fluctuations of the burr length and the shearing stress are extreme in the initial wear area; the fluctuations become moderate in the steady wear area; the length increases in the sign of tool life area; the length rapidly increases and reaches 70 μm in the tool life area. From these results, it is difficult to evaluate the tool wear conditions after the steady wear area by only observing the behavior of the shearing stress. Especially, in case of the stainless steel wire, which is more ductile than the piano wire, the evaluation of the condition is difficult because the fluctuation of the stress is extreme and the large burr easily occurs by the extrusion action that was caused by the wear of the tool tip. Therefore, it is important that the features capable of evaluating the conditions and the tool life are extracted from the AE signals. For extracting the features, it is necessary to grasp the relationships between the conditions and the crack initiation modes. Then, the relations between the RA value [12] and the average frequency [12] were examined for discriminating the modes. In the relationships, the signals of the tensile mode crack have the features, of which the RA value is small and the frequency is high, and the signals of the shear mode crack have the features, of which the RA value is large and the frequency is low [12]. Here, the discrimination criterion of each crack initiation mode is determined by considering the distribution conditions of the plots in the phase-space of the two-dimensional coordinate plane by both parameters.

Figure 4 shows the discrimination criteria of the crack initiation modes (*i.e.,* discriminated by the RA value and average frequency) and the distributions of each crack mode occurrence every 500 shearing. From the results, the AE signals of the composite mode crack that combined the features of the tensile and the shear mode crack were observed as follow.

Piano wire: The occurrence rates of the crack initiation modes before the tool life show large values in the order of the tensile, the composite and the shear mode crack. On the other hand, the rates after the tool life show large values in the order of the composite, the shear and the tensile mode crack. After the tool life, the occurrence conditions of the modes changed to the shear or the composite mode crack from the tensile mode crack. This means that worn tools resulted in the occurrences of the composite and the shear mode crack. Finally, the occurrence of the composite mode crack rapidly increases from the sign of tool life area.

Stainless steel wire: The shear mode crack is mainly detected right after the experiment start. After that, the occurrence of the tensile mode crack becomes predominant. The occurrence of the composite mode crack begins to increase from the sign of tool life area.

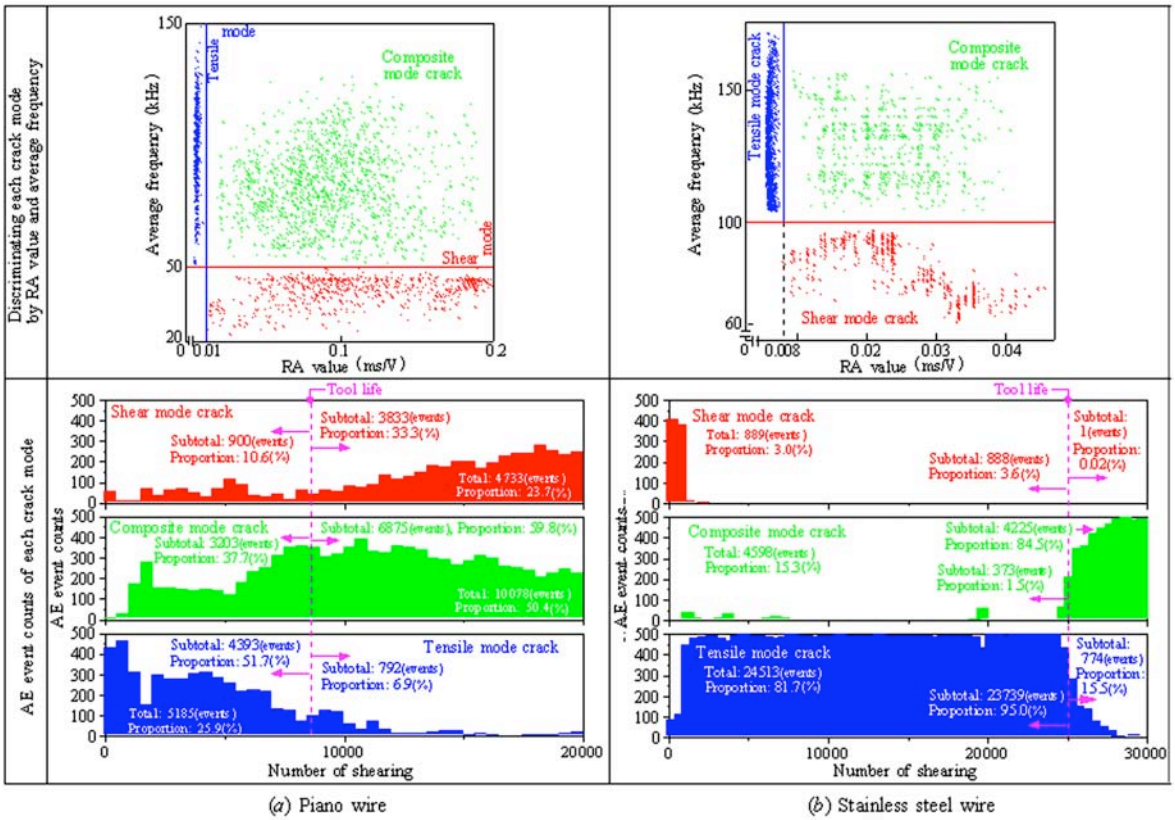

Fig. 4 Discrimination standard and event counts of each crack mode for piano and stainless steel wire.

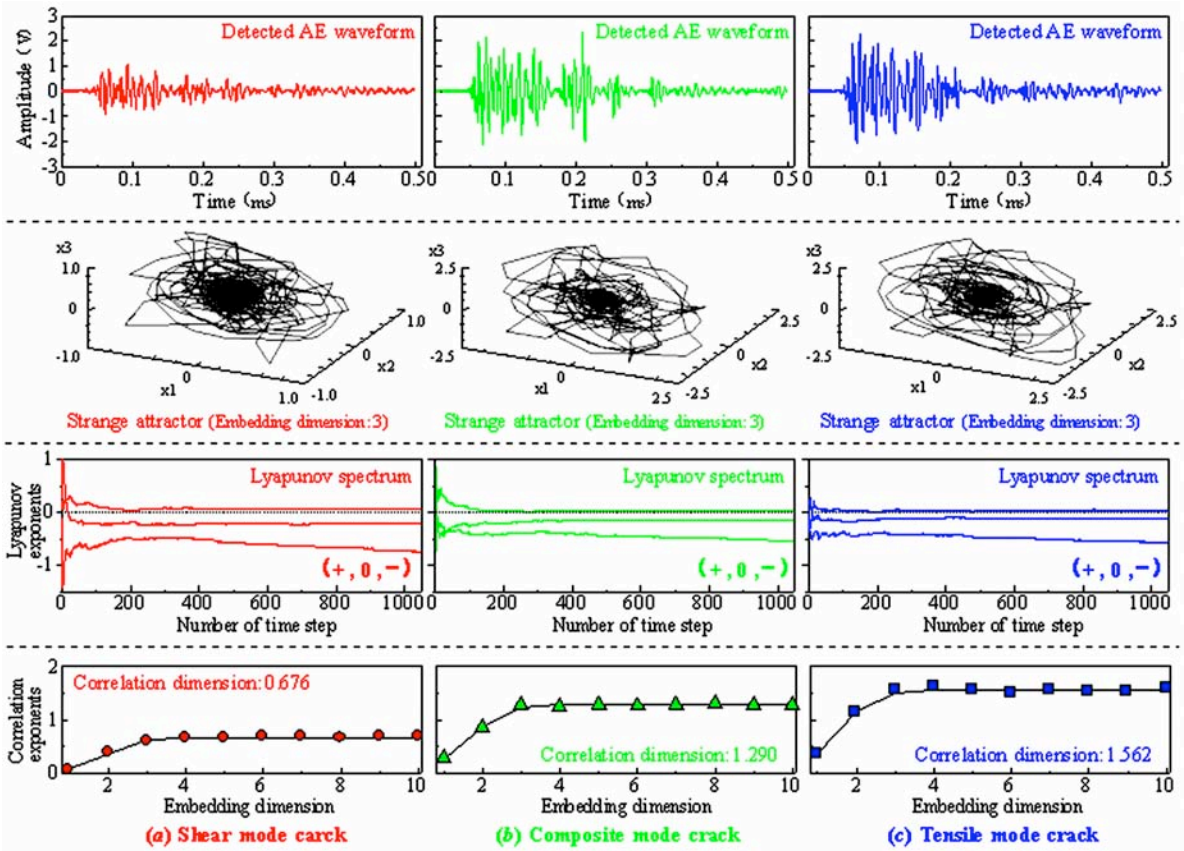

Fig. 5 Chaos time series analysis results of each crack mode for piano wire.

Therefore, the growth of the wear also affected the occurrence conditions of the crack initiation modes.

The above results indicate that the occurrence conditions of the crack initiation modes are influenced by the growth conditions of the tool wear caused by the difference of the mechanical properties of the work piece materials.

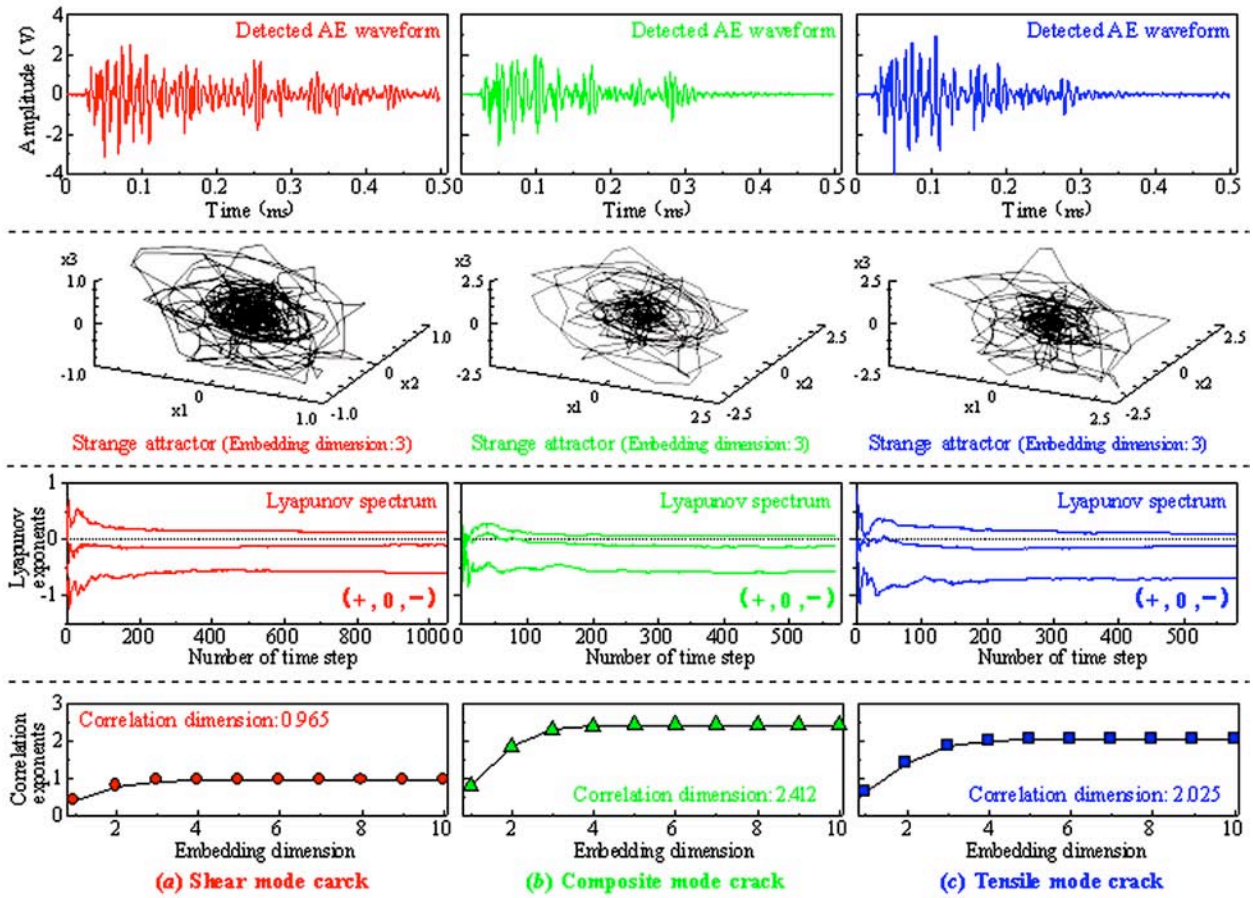

Fig. 6 Chaos time series analysis results of each crack mode for stainless steel wire.

Results of chaos time series analysis

Figures 5 and 6 show the results of the chaos time series analysis of each crack initiation mode. The signs of the exponents in the Liapunov spectrum of three dimensions to the modes show a plus, nearly zero and a minus, respectively. Also it is possible to obtain the correlation dimension because the dimension of each mode converges to a constant value. Therefore, it is judged that the detected AE signals have the chaotic property.

Figures 7 and 8 show examples of the recurrence plots of the crack initiation modes. In these figures, the recurrence plots that were represented by the gradation and the monochrome colors, the iso-direction recurrence and the iso-direction neighbors plots are shown. Here, the recurrence plot is evaluated by the texture of the gradation colors and the comparison of the plotting densities of the plot and the iso-directional neighbors plot. In Fig. 7(*a*) and Fig. 8(*a*), it is clear that the space patterns are aperiodic and the textures are non-uniform. These show that the signals have the property of the unsteady behavior. From the results of Fig. 7(*b*)(*d*) and Fig. 8(*b*)(*d*), one finds that the detected signals have the property of the deterministic chaos, because the densities of the recurrence and the iso-directional neighbors plot were similar.

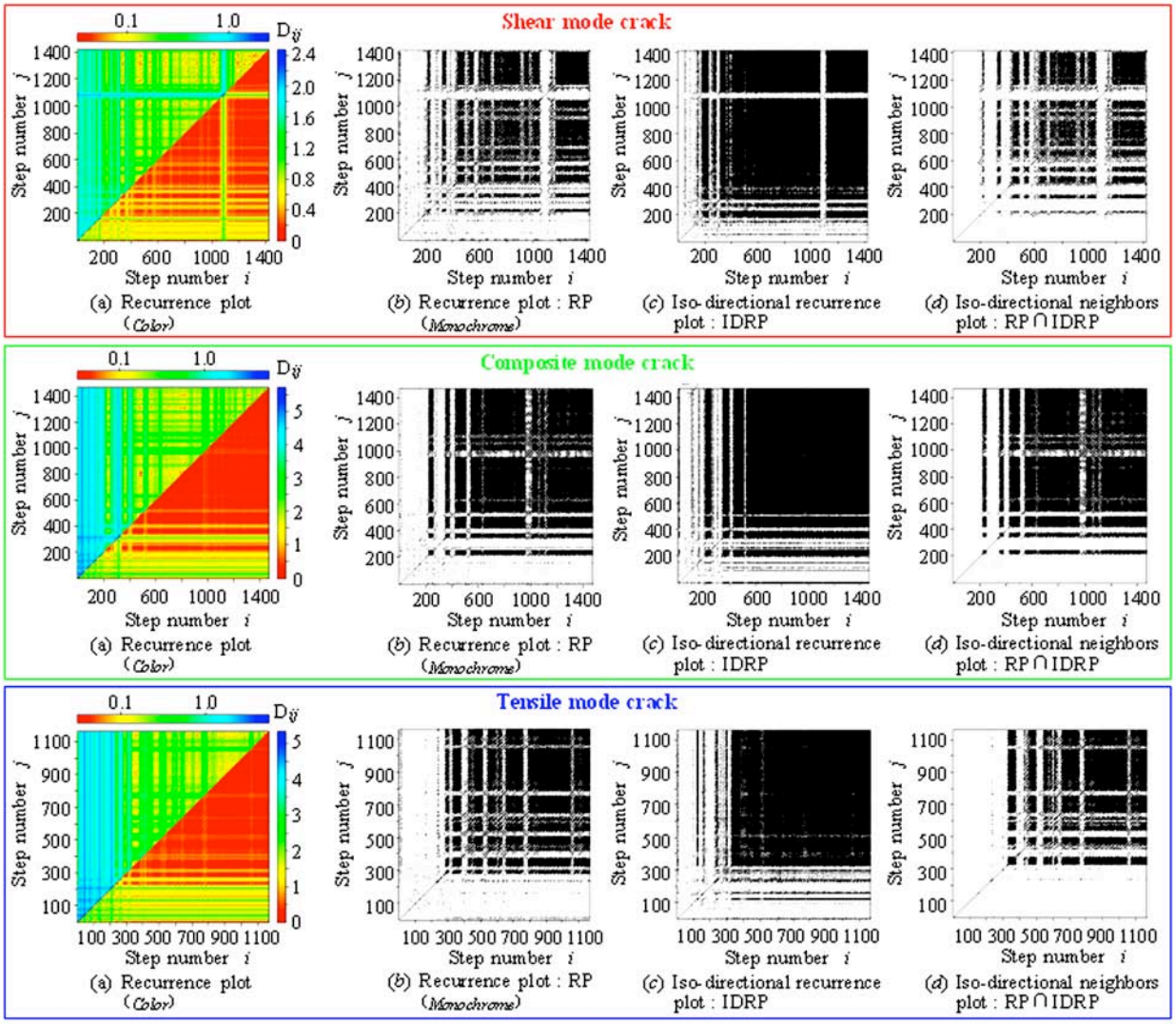

Fig. 7 Recurrence plots of AE signals on each crack mode for piano wire.

Therefore, it is concluded that the detected signals are not stochastically caused and are arising deterministically along some rules. From the above results, it was found that the extraction of the features of the signals and the observation of the behaviors of the features are effective.

Figure 9 shows the relationships between the largest Liapunov exponents and the correlation dimensions of both wires to the number of shearing. From the results, we find the following.

Piano wire: The largest Liapunov exponents of the crack initiation modes in the steady wear area show comparatively large values. However, the exponents decrease from the sign of tool life area and converge to constant values in the tool life area. This indicates that the chaotic property becomes strong in the first half of the steady wear where the multiple factors were mixed. Then, it becomes weak from the first half of the tool life area. The correlation dimensions of the crack initiation modes do not cross, and the dimensions show high values in the order of the tensile, the composite and the shear mode crack. Especially, the dimension of the shear mode crack reaches the maximum value near the tool life area. On the other hand, the dimensions of the tensile and the composite mode crack reach the maximum value in the steady wear area.

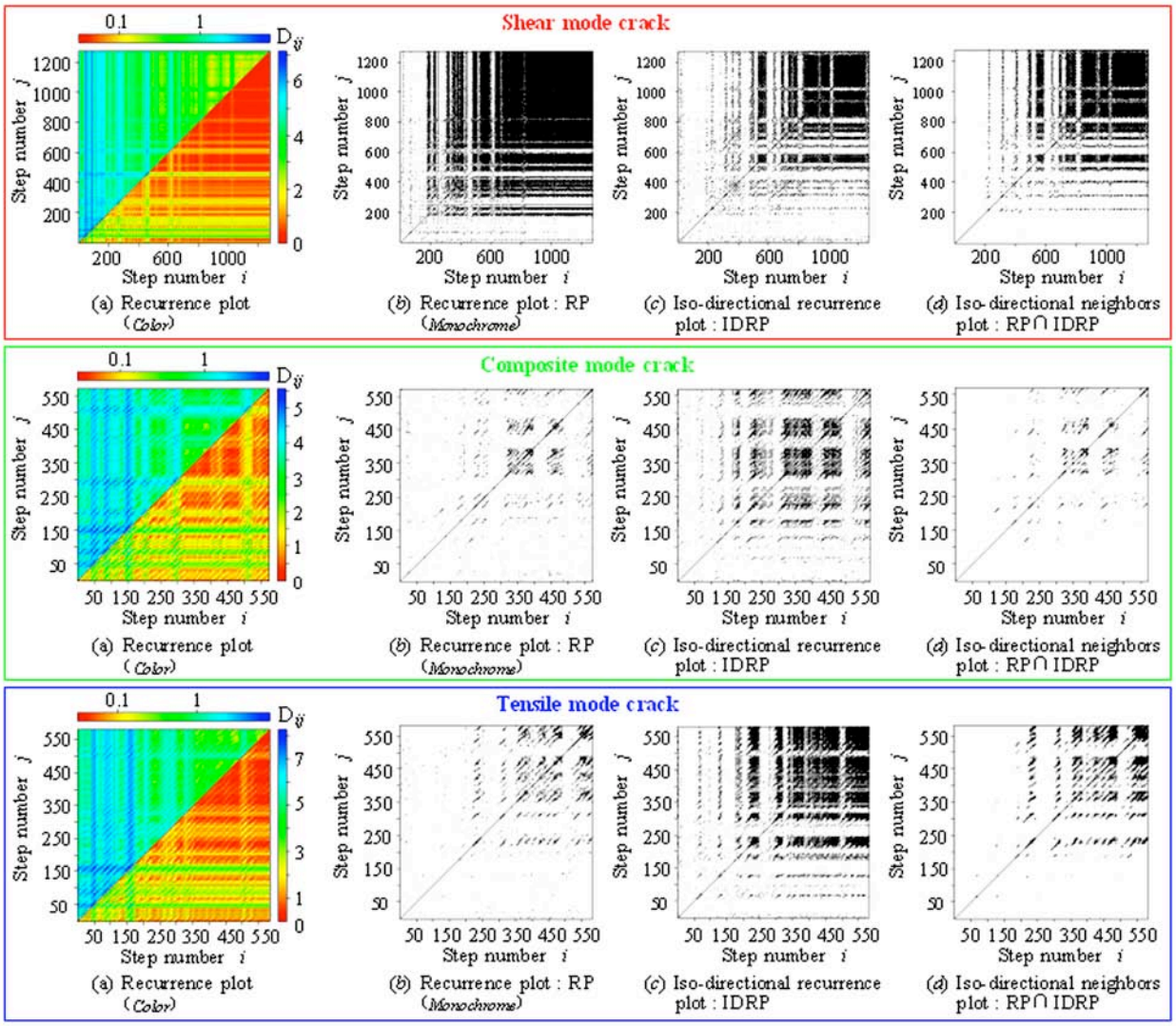

Fig. 8 Recurrence plots of AE signals on each crack mode for stainless steel wire.

Stainless steel wire: The largest Liapunov exponents of the crack initiation modes show relatively large values in the initial wear area. The exponents then converge to near 0.4 in the tool life area. Therefore, the chaotic property becomes weak when the wear grew and the tool was nearing its life. As in the piano wire, the correlation dimensions show high values in the order of the tensile, the composite and the shear mode crack. Therefore, it is possible to discriminate each mode by observing the dimensions. The dimensions of the tensile and the composite mode crack become the highest in the tool life area and exceed two. The dimensions are generally higher than the dimensions of the piano wire. It is believed that this phenomenon was caused by more ductile mechanical property of the stainless steel wire.

From the above results, it was proven that the chaotic property of the AE signals becomes weak regardless of the mechanical property of the workpiece materials when the tool is coming near a tool life.

Evaluation by wavelet transform and waveform analysis

It has been reported that a close relation exists between the fracture surface condition and the fracture energy. In short, the energy becomes smaller when the surface is smooth, and the

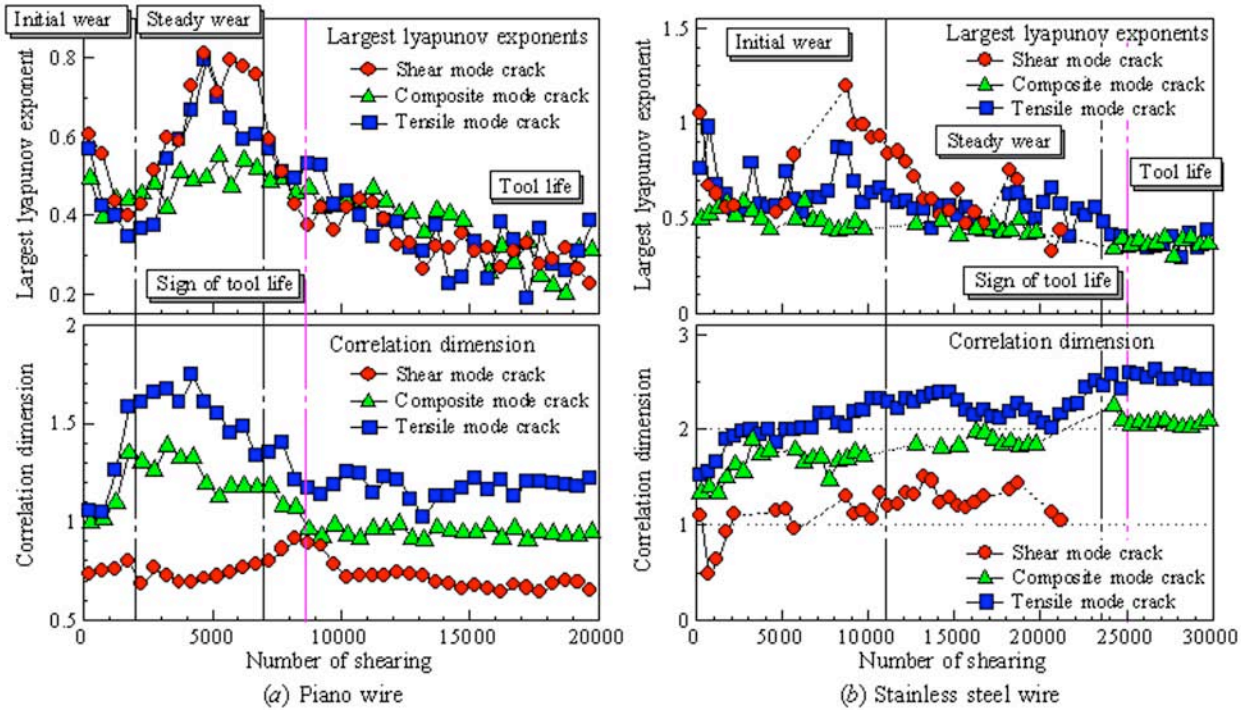

Fig. 9 Parameters of evaluating wear conditions with chaos time series analysis method.

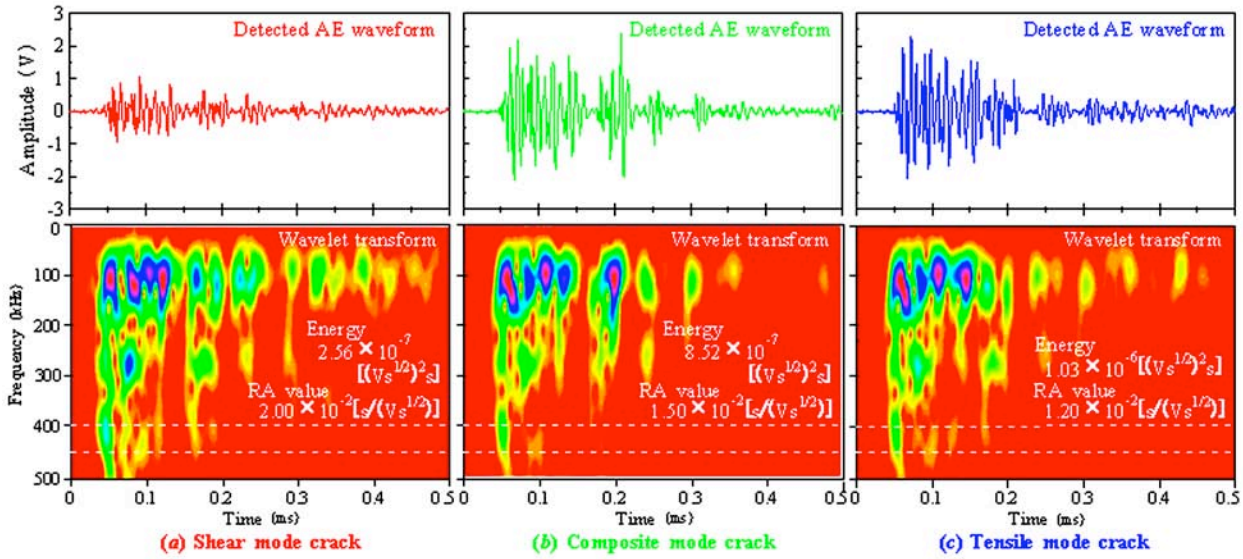

Fig. 10 Features of detected AE signals and wavelet transform results of each crack mode for piano wire.

energy becomes larger when the surface is rough [13]. The relationships between the crack initiation modes and the AE signals' features were investigated. As the features, the energy and the RA values for the time fluctuation waveforms of the wavelet coefficient from 50 to 500 kHz were employed. Figures 10 and 11 show the examples of the results, which show the following.

Piano wire: The energy of the time fluctuation waveforms of the wavelet coefficient of each crack initiation mode from 400 to 450 kHz shows large values in the order of the tensile, the composite and the shear mode crack. On the other hand, the RA values of the waveforms of each mode in the frequency range show large values in the order of the shear,

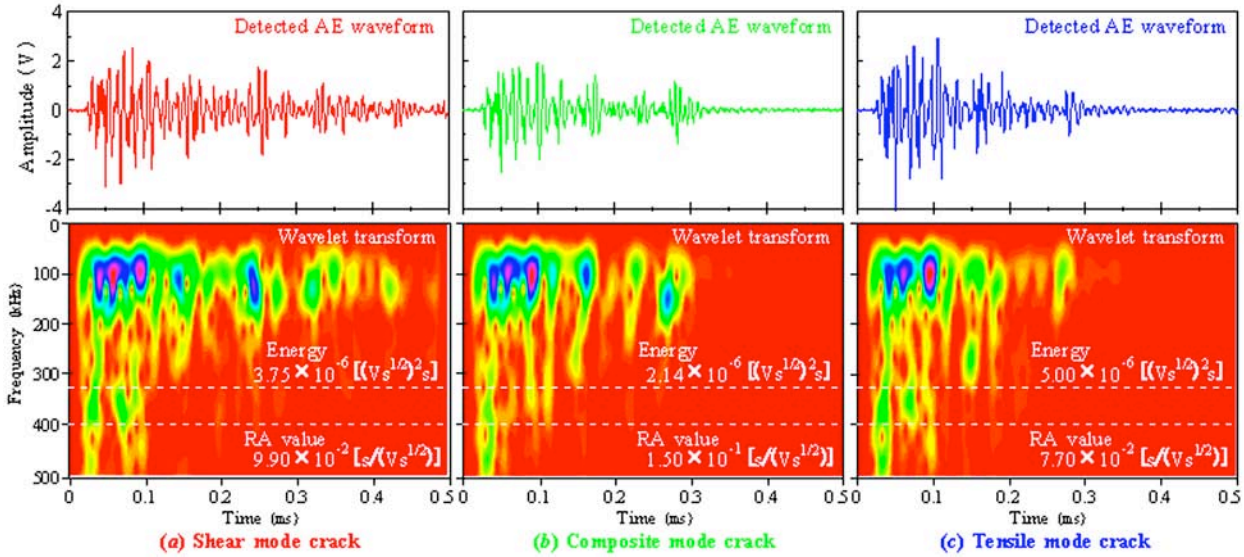

Fig. 11 Features of detected AE signals and wavelet transform results of each crack mode for stainless steel wire.

the composite and the tensile mode crack.

Stainless steel wire: The energy of the time fluctuation waveforms of the wavelet coefficient of each crack initiation mode from 350 to 400 kHz shows large values in the order of the tensile, the shear and the composite mode crack. On the other hand, the RA values of the waveforms of each mode in the frequency range show large values in the order of the composite, the shear and the tensile mode crack.

Figure 12 shows the relationships between the RA value and the energy to the number of the shearing. In this figure, the red circle shows a point, at which the RA value went beyond its maximum value (*cf.* white circle) in the initial wear area. The number of the shearing at the point belongs to the sign of tool life area.

Piano wire: The energy decreases with the growth of the tool wear. This is because the occurrence of the AE signal of the tensile mode crack that has the high energy decreased (*cf.* Fig. 4(*a*) and Fig. 10). Especially, the rapid decrease of the energy from the sign of tool life area is explained by the decrease of the tensile mode crack and the increases of the shear and the composite mode crack. The behaviors of the RA value and the burr length are similar (*cf.* Fig. 2). The RA value and the burr length rapidly increase in the two ranges. One of the ranges is from the initial wear area to the steady wear area and the other is from the sign of tool life area to the tool life area. The difference in both areas is that the former decreases after the increase while the latter converges on the maximum value after the increase. This is because the occurrence conditions of the crack initiation modes in both areas were different (*cf.* Fig. 4(*a*)). The wear of the side edge of the tool was the main cause on the increase of the clearance between the tool and the work piece in the initial wear area. This is because the wear of the tool tip greatly affects the burr length.

Stainless steel wire: The energy decreases with the growth of the tool wear. This is because the occurrence of the AE signal of the tensile mode crack that has the high energy decreased rapidly, and the occurrence of the signal of the composite mode crack that has the low energy increased rapidly (*cf.* Fig. 4(*b*) and Fig. 11). As in the piano wire, the behaviors of the RA value and the burr length are similar (*cf.* Fig. 3). In short, the

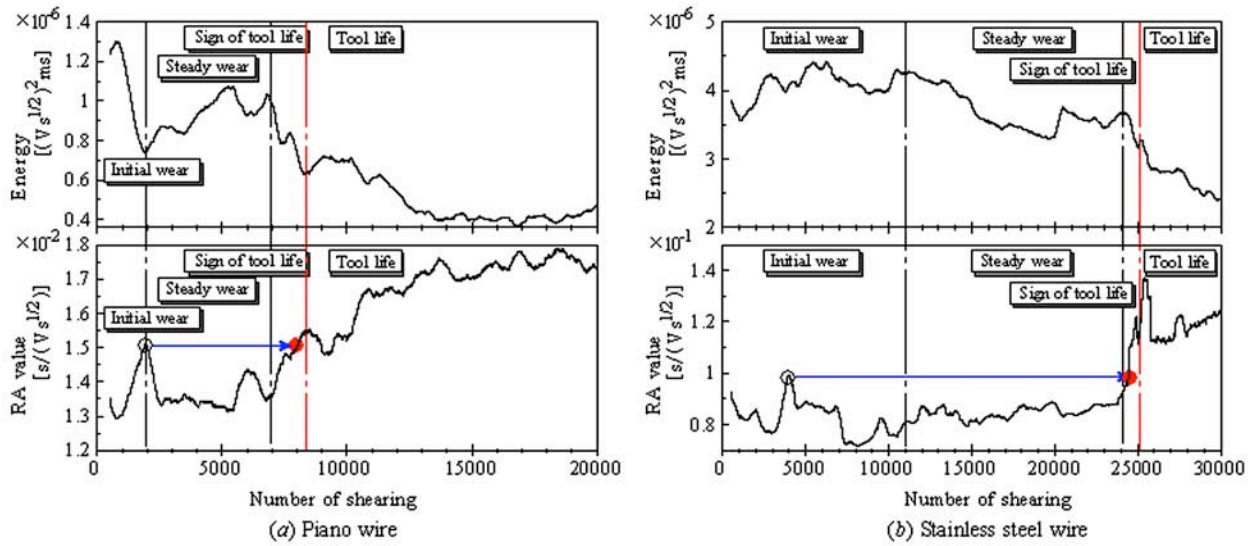

Fig. 12 Energy and RA value of time fluctuation waveform of wavelet coefficient for evaluating wear conditions of piano and stainless steel wire.

fluctuation of the RA value is severe in the initial wear area, becomes stable in the steady wear area and rapidly increases from the sign of tool life area to the tool life area. This is because more ductile wire is susceptible to extrusion.

From the above experimental results on the two kinds of the workpiece materials, we show the existence of a close relationship between the behavior of the RA value of the time fluctuation waveform of the wavelet coefficient and the growth of the tool wear.

Evaluation System for Tool Life

We constructed a tool life evaluation system, based on the RA value mentioned previously. Figure 13 shows the flow diagram of this system. Here, we propose to use the parameter L_{wear}.

$$L_{wear} = (RA_{MA} / RA_{max}) \times W \qquad (2)$$

Here, the RA_{MA} is the moving average of the RA value for a set of 500 shearing, the RA_{max} is a maximum value of the RA_{MA} in the last set, W is the coefficient for representing the degree of the cumulative wear and its initial value was set at 3.5. The following sequences are done when the RA_{max} was renewed: the cumulative index w is added to W and its initial value is 0.001; the increment value of 0.001 is added to w. The initial and increment values of w were determined by the experimental results, of which there was the change in the tool wear condition at a shearing number of 1000 or more. The parameter N in the execution part of the tool change shown in Fig. 13 is the number, of which the evaluation result was judged to be "Warning", and the tool is checked if the "Warning" continued 1000 times. The criteria shown in Table 1 were established so that several of the evaluations by L_{wear} in the initial wear range become "Warning", because the wear condition in this range gives a large influence in tool life.

Figure 14 shows the evaluation results of the tool life by this system. In this figure, the relationships between the RA value and L_{wear} to the number of the shearing are shown, and the wear conditions that were evaluated by the observation information (*i.e.,* the burr length, the shearing stress and the shear plane condition, *etc.*) are shown on the top of the figure. In the

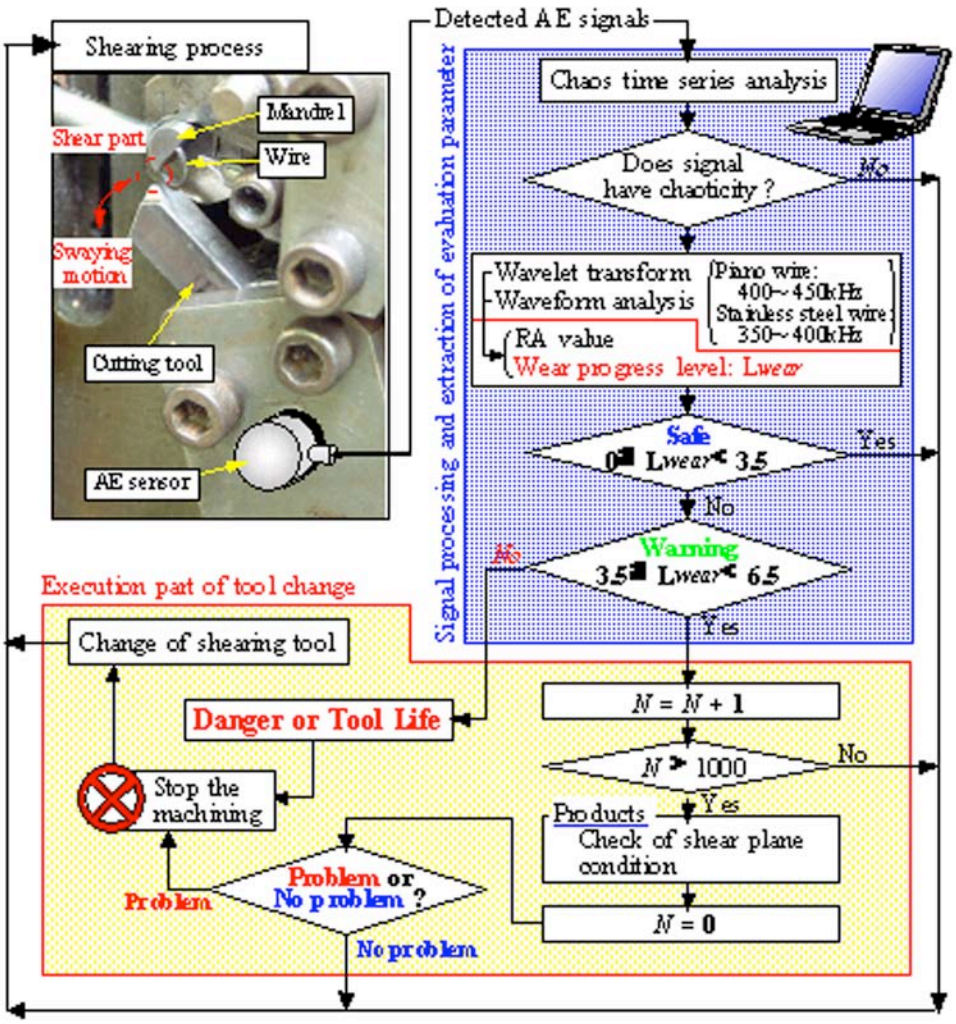

Fig. 13 Flowchart of AE signal processing in this study.

Table 1 Criterion by wear progress level L*wear*.

Safe	0 ≦ Lwear < 3.5
Warning	3.5 ≦ Lwear < 6.5
Danger	6.5 ≦ Lwear < 9.5
Tool life	9.5 ≦ Lwear

results, the execution part of the tool change shown in Fig. 13 was not carried out, and the shearing was continued until the tool life. The results indicate that the evaluation by L*wear* is appropriate, because the evaluation results are similar to the judgments of the wear conditions, for which we used the following in each wear region: the evaluations in the initial and the steady wear region are "Safety" and "Warning"; the evaluations from the sign of tool life change to “Danger” from the “Warning” and to the “Tool life” from the “Danger”. This system correctly evaluated the wear conditions for two kinds of wires having different mechanical properties.

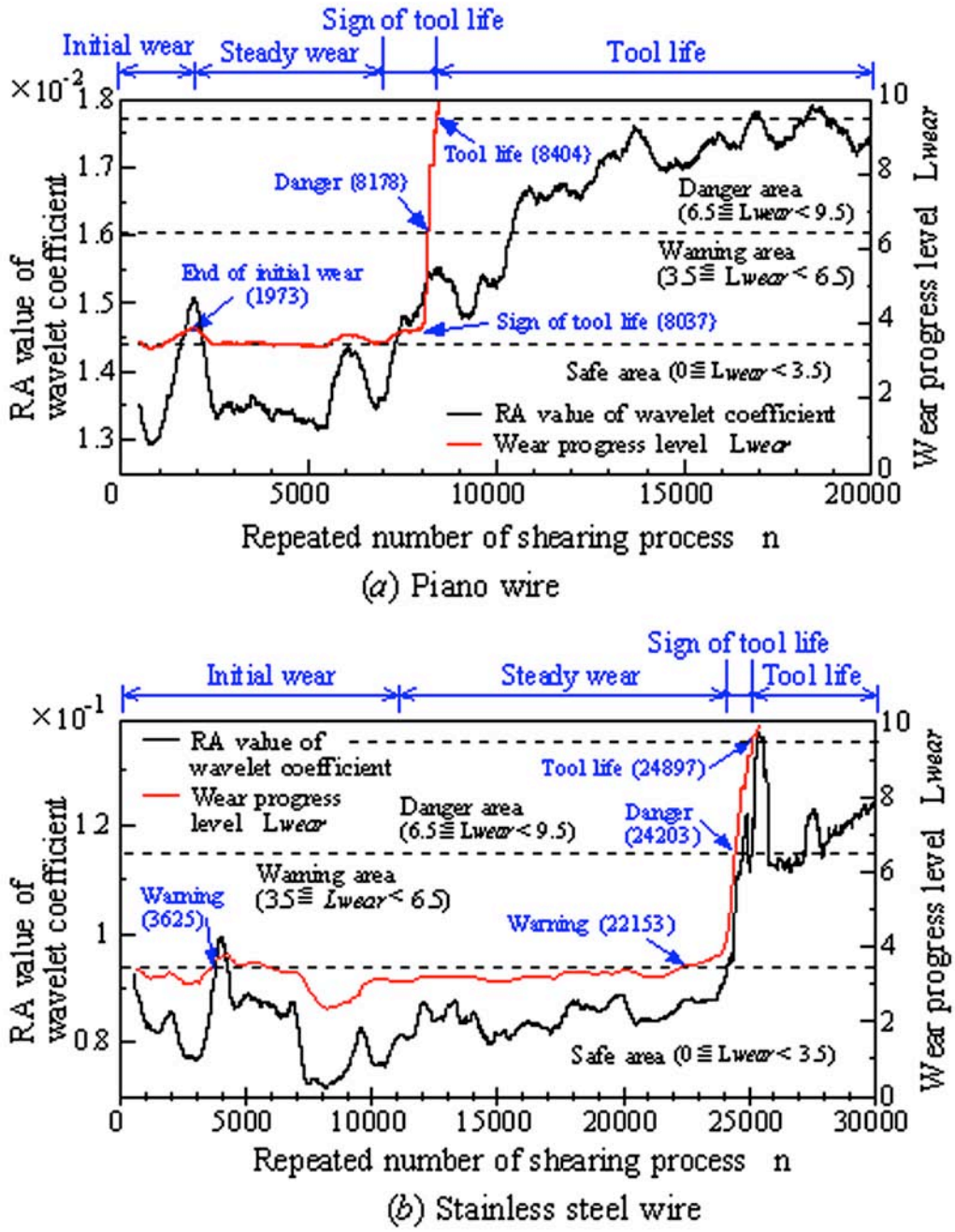

Fig. 14 Relationship between RA value of wavelet coefficient and wear progress level.

Conclusions

For evaluating the tool wear conditions and the tool life, the feature extraction of the detected AE signals in the shearing of two kinds of wires was examined. We constructed the system that evaluates the tool life by the features based on RA values.

(1) The detected AE signals have the chaotic property. The wear conditions and the tool life can be evaluated by the largest Liapunov exponent and the correlation dimension, because the behaviors of both parameters in each condition (*i.e.,* the initial wear, the steady wear, the

sign of tool life and the tool life area) have the expected features.

(2) The RA value of the time fluctuation waveform of the wavelet coefficient becomes larger in the range where the burr length rapidly increases. Therefore, RA value is one of the effective parameters for evaluating the tool wear conditions and the tool life. Here, the frequency ranges that should be used in the piano and the stainless steel wire are 400~450 kHz and 350~400 kHz, respectively.

(3) The system that evaluates the tool life by the RA value was constructed, and its validity was confirmed by the comparison with the experimental results.

References

[1] S. Koike, H. Shimizu, Y. Namiki, Y. Masuzawa, K. Kanno and K. Kato, The method of detecting the damage of a punch and die in blanking, Bulletin of Tokyo Metropolitan Industrial Technology Research Institute, (in Japanese), No. 17 (1988), pp. 1-6.

[2] K. Aihara, T. Ikeguchi, T. Yamada and M. Komuro, Basics and Applications of Chaos Time Series Analysis, (in Japanese), (2002), Sangyo-Tosho Co., Ltd.

[3] J.C. Schouten, F. Takens, Cor M. van den Bleek, Estimation of the dimension of a noisy attractor, Physical Review, **50**, (3), E (1994), 1851-1861.

[4] S.T.S. Bukkapatnam, A. Lakhtakia, and S.R.T. Kumara, Analysis of sensor signals shows turning on a lathe exhibits low-dimensional chaos, Physical Review, **52**, (3), E (1995), 2375-2387.

[5] F.M. Atay and Y. Altintas, Recovering smooth dynamics from time series with the aid of recurrence plots, Physical Review, **59**, (6), E (1999), 6593-6598.

[6] A. I. Mees, P. E. Rapp and L. S. Jennings, Singular-value decomposition and embedding dimension, Physical Review, **36**, (1), A (1987), 340-346.

[7] E. P. Serrano and M. A. Fabio, Application of the Wavelet Transform to Acoustic Emission Signals Processing, IEEE Transactions on Signal Processing, **44**, (5) (1996), 1270-1276.

[8] H. Suzuki, T. Kinjo, Y. Hayashi, M. Takemoto and K. Ono, Wavelet Transform of Acoustic Emission Signals, Journal of Acoustic Emission, **14**, (2) (1996), 69-84.

[9] Qing-Qing Ni and Y. Misada, Analysis of AE Signals by Wavelet Transform, Journal of the Society of Materials Science, (in Japanese), **47**, (3) (1998), 305-311.

[10] H. Inoue, Wavelets Extending the Frontiers of Ultrasonic Evaluation of Materials, Journal of the Society of Materials Science, (in Japanese), **45**, (12) (1996), 1353-1354.

[11] H. Inoue, K. Kishimoto, T. Nakanishi and T. Shibuya, Time-Frequency Analysis of Dispersive Stress Waves by Means of Wavelet Transform (Identification of Group Velocity and Application to Ultrasonic Materials Evaluation), Transactions of the Japan Society of Mechanical Engineers, (in Japanese), **61**, (581), A (1995), 153-160.

[12] N. Tsuji, M. Uchida, T. Okamoto and M. Ohtsu, Application of Acoustic Emission Technique to Evaluation of Cracking in Concrete Structures, Progress in Acoustic Emission X (2000), pp. 189-194.

[13] The Japanese Society for Non-Destructive Inspection, Acoustic Emission 1990, The Japanese Society for Non-Destructive Inspection, (in Japanese), (1990).

OPTICAL FIBER SYSTEM FOR AE MONITORING OF HIGH TEMPERATURE DAMAGE OF STAINLESS STEEL TUBING

TOMOHARU HAYANO, TAKUMA MATSUO, HIDEO CHO and MIKIO TAKEMOTO
College of Science and Engineering, Aoyama Gakuin University
5-10-1 Fuchinobe, Sagamihara, Kanagawa 229-8558, Japan.

Abstract

We utilized optical fibers as heat-resistant AE sensor elements, and monitored acoustic emission (AE) from molten salt (85 mol% V_2O_5 + Na_2SO_4) attack of 304 stainless steel tubing at elevated temperatures. AE signals were monitored by a homodyne Mach-Zender-type laser interferometer developed in our laboratory. Using optical fibers coated by UV-cured polymer or by copper, we monitored cylindrical-wave AE signals below 450ºC and 750ºC, respectively. Multiple winding of the sensing fiber on the tubing significantly improved the sensor sensitivity and allowed the detection of L- and F-mode cylindrical waves. Source location in the longitudinal direction of the tubing was obtained accurately utilizing the wavelet-based arrival-time difference of L(0,2)- and F(1,1)-mode waves at selected frequencies.

Keywords: Catastrophic oxidation, high temperature, heat resistant sensor, optical fiber sensor, metal coated fiber

Introduction

AE monitoring of hot structural members has been an important technical goal, but has been difficult to achieve success. AE monitoring by conventional AE systems inevitably needs a special waveguide and/or cooling system for protecting the sensing element. However, waveguides severely distort AE signals [1]. Heat resistant AE sensors utilizing $LiNbO_3$ element were developed but their use has been limited due to high cost and bulk. Our own heat resistant sensor with $LiNbO_3$ element had the temperature capability up to 600ºC, but was prone to noise and only for a relatively short time. The degradation of brazed joints in the sensor was the main problem and inflexible heat-resistant cable of ceramic insulator was difficult to handle [2].

Both the heat resistance and thermal stability of heat resistant AE sensors are important for long-term AE monitoring of creep damage and environmental degradation. Development of new heat resistant AE sensors that are flexible, non-water cooled and inexpensive has been desirable in laboratory tests as well as for field inspection. Non-contact sensors like laser interferometers cannot satisfy the sensitivity requirement and also is expensive. Such systems need a vibration-free optical table and cannot be used in dusty and noisy environment.

We have developed an optical fiber AE monitoring system [3], utilizing an optical fiber coated with polymer as a sensing fiber. Though the core of the fiber is made of silica, most commercial fibers have poor heat resistance due to polymer coating. Fiber development in the telecommunication industry is, however, remarkable, and has now resulted in various types of optical fibers. One is the fiber coated

with metal and another is an extremely small diameter fiber with small critical curvature. These new fibers can open a new way for developing the needed heat resistant sensor. In this study, we first utilized a polymer-coated optical fiber as a sensing fiber and monitored AE signals from the fracture of oxidation film produced by molten salt attack during cooling. Next, we studied the applicability of a copper-coated optical fiber as the heat resistant fiber. This fiber makes the AE monitoring at elevated temperatures possible. This paper shows that the optical fiber sensor is particularly useful for monitoring cylindrical-wave AE signals of hot tubes since the sensor sensitivity is significantly improved by multiple winding on the tube surface.

Sensitivity and Heat Resistance of Optical Fiber

AE system utilized in this research is identical to that utilized in another research of our group [3]. It is a homodyne Mach-Zender-type laser interferometer. Optical fiber used as the sensing and reference arms is the telecommunication-grade single-mode fiber for 1300 nm wavelength. Table 1 shows details of the polymer- and copper-coated fibers. Both the core and clad diameter are the same for the two fibers. Cost of the copper-coated fiber is about 100 times that of the polymer-coated fiber. The sensing fiber monitors the in-plane motion of AE signals in the fiber direction when it is glued on the medium. Thus, we can improve the sensors sensitivity to cylindrical waves by winding the sensing fiber on the tube surface multiple turns. The wound fiber monitors the change of circumferential length and is particularly sensitive to the longitudinal mode. In this study, we used a tubular specimen, which is commonly used in boilers, furnaces and reactors.

Table 1 Details of polymer- and copper-coated fibers.

	Core [um]	Clad [um]	Jacket [um]	Critical radius for bend [mm]	Cost [yen/m]
polymer fiber	9	125	250	30	25
Cu coated fiber	9	125	165	16	2,400

Figure 1 shows experimental setup for studying the sensitivity and heat resistance of sensing fiber. For the sensitivity measurement, we excited the cylindrical waves by a pulse laser (Nd:YAG; 20 mJ) and detected the propagated waves by the wound-fiber sensor and a laser interferometer, as shown in Fig. 1(a). For the heat resistance study, the fiber windings were heated by a tubular furnace and monitored the cylindrical waves excited by a compression-type PZT transmitter (PAC, R6) mounted on one end of the pipe, as shown in Fig. 1(b).

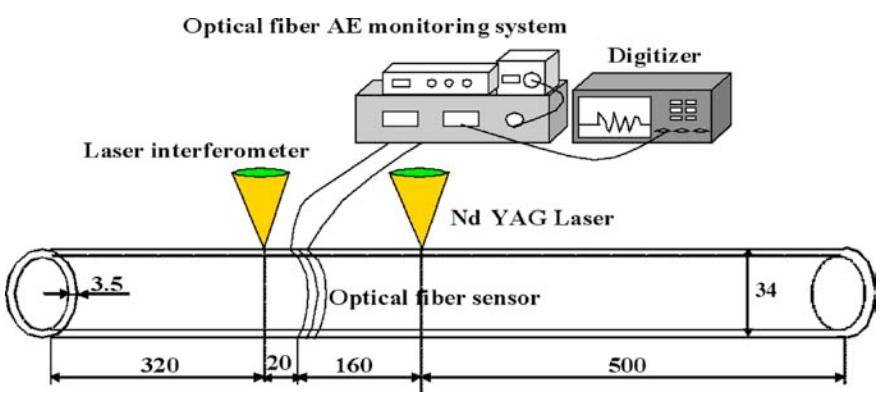

(a) Study for the sensitivity of sensing fiber.

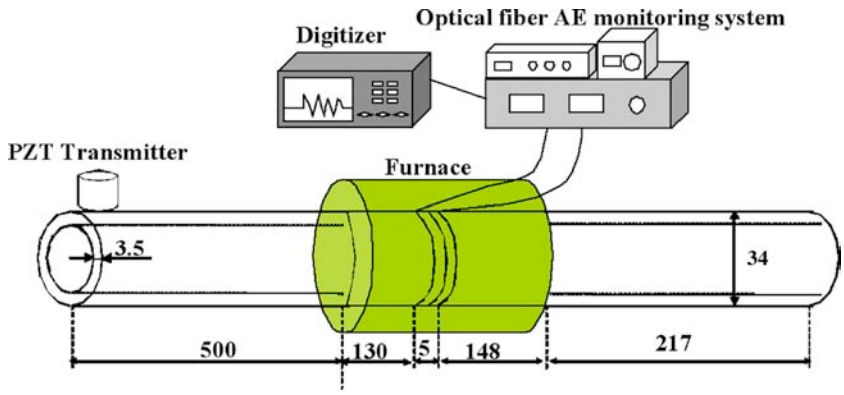

(b) Study for the heat resistance of sensing fiber.

Fig. 1 Experimental setup for studying the sensitivity and heat resistance of sensing fiber.

Figure 2 compares the waveforms of the cylindrical waves, excited by a pulse laser and detected by polymer-coated sensing fiber, as a function of the number of winding. First arriving weak signal is the L(0,2) mode. Amplitude of this mode remarkably increases with the number of the sensing fiber winding. Amplitude of the trailing F(1,1) mode also increases with the turn number. This effect is beneficial for AE monitoring of cylindrical-wave AE signals.

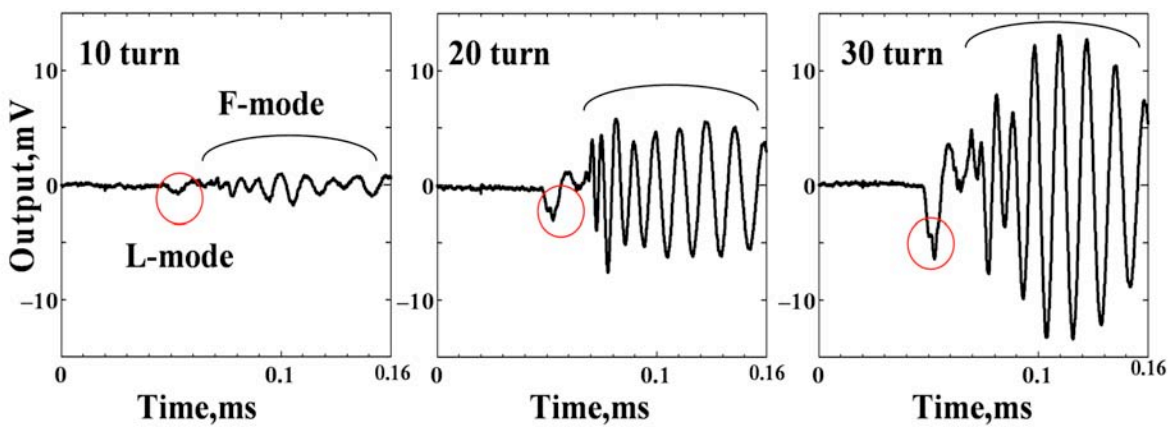

Fig. 2 Waveforms of cylinder waves excited by pulse laser and detected by polymer-coated sensing fiber.

Heat resistance of two types of optical fiber was studied next. Figure 3 shows the waveforms of cylindrical waves as a function of temperature. Here, temperature refers to the tube temperature where the sensing fiber was wound. The waves were monitored at 4 ks after the tube temperature reached the pre-determined value. The polymer-coated fiber broke at 521≈C and the copper-coated fiber at 753ºC. Figure 4 shows SEM of fractured fibers. Fracture of the polymer-coated fiber appears to be caused by the fused polymer, but that of copper-coated fiber was caused by the oxidation of the copper coating.

As shown in Fig. 5, the amplitude of the first L-mode peak and the maximum peak of F-mode wave slightly decreased with temperature for the copper-coated fiber until 700ºC, but the S/N ratios of the wave by two sensors were similar over the service temperatures. The S/N ratio for the polymer-coated fiber remained at ~28 dB and was slightly better than copper-coated fiber at 22-26 dB (also see Fig. 3).

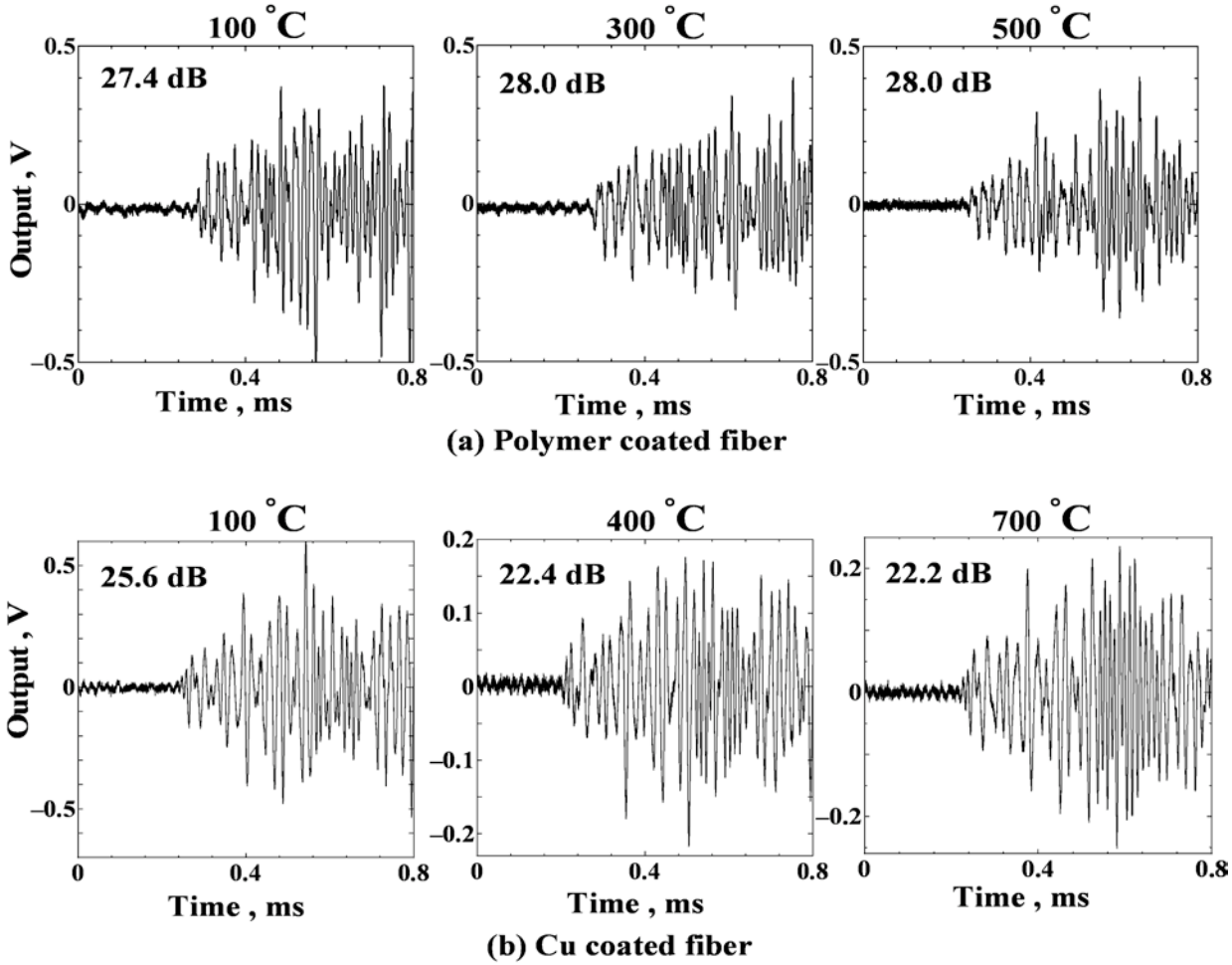

Fig. 3 Waveforms detected by optical fiber sensors as a function of temperature.

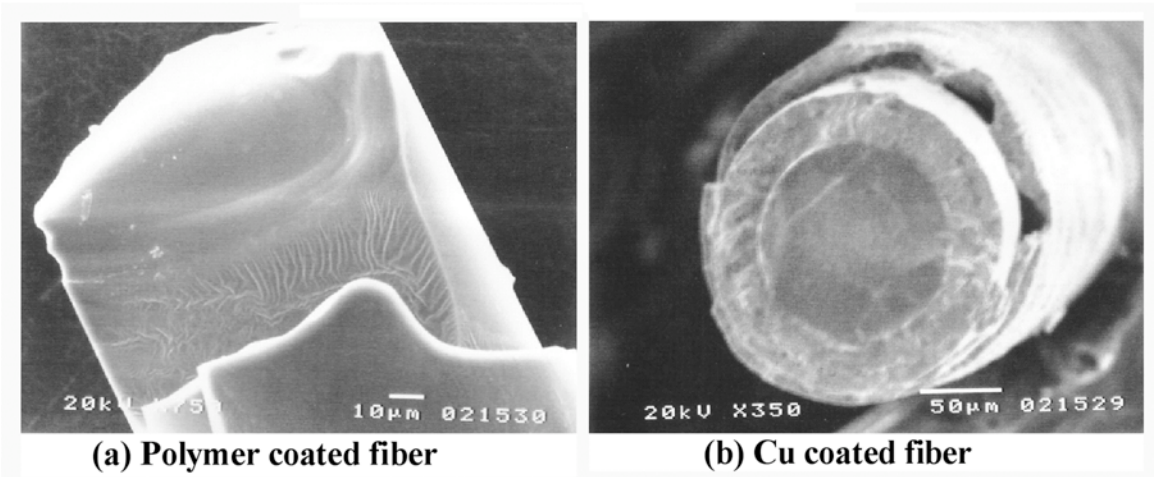

Fig. 4 SEM of the fractured part of (a) polymer-coated and (b) Cu-coated fiber.

Source Location of Cylindrical Wave Utilizing Single Waveform

It is often difficult to mount AE sensors on hot surfaces. We attempted to estimate the location of cylindrical-wave sources from a single waveform detected by the sensing fiber. We previously tried to

use this method for the cylindrical waves detected by a PZT sensor mounted on the surface of a pipe [4]. We could not estimate the source location correctly since the PZT sensor could not detect the L-mode waves with sufficient amplitude. In contrast, the wound optical fiber sensor can detect both the L- and F-mode waves, allowing source location as shown below.

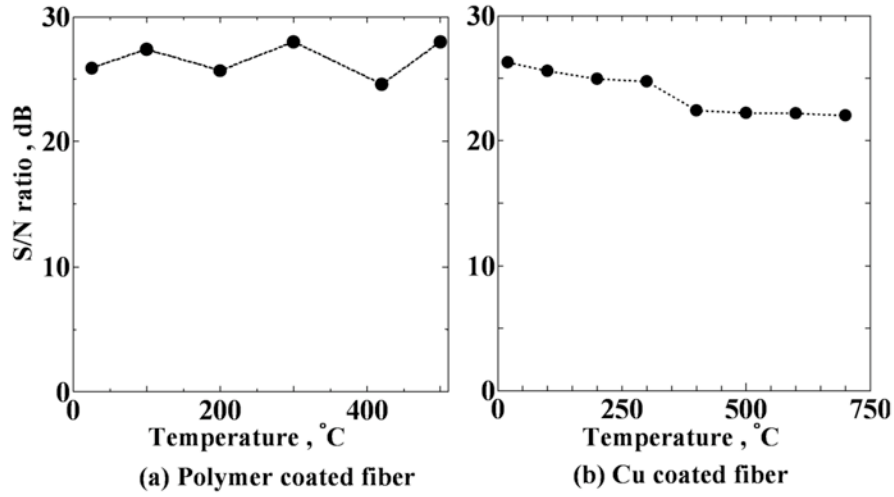

Fig. 5 S/N ratio of cylindrical wave AE signals detected by polymer- or copper-coated fibers as a function of temperature.

Estimation method is shown below for the case of Hsu-Nielsen sources on the tube [4]. Figure 6 shows the cylindrical waves excited by the Hsu-Nielsen source at 200 mm from the 30-turn optical fiber sensor on a 34-mm diameter steel tube (thickness of 2.8 mm). Time transient of wavelet coefficient at 80 kHz is shown at right. We observe two peaks at 1.6~0.2 ms, i.e., L(0,2) at t_L and F(1,1) at t_F. Wave velocities of L(0,2) and F(1,1) modes of this pipe at 80 kHz are calculated as V_L= 4950 m/s and V_F= 1952 m/s, respectively. Therefore, the distance Z of the source from the sensor is given by equation (1);

$$Z = \frac{V_L \times V_F}{V_L - V_F} \times (t_F - t_L) \tag{1}$$

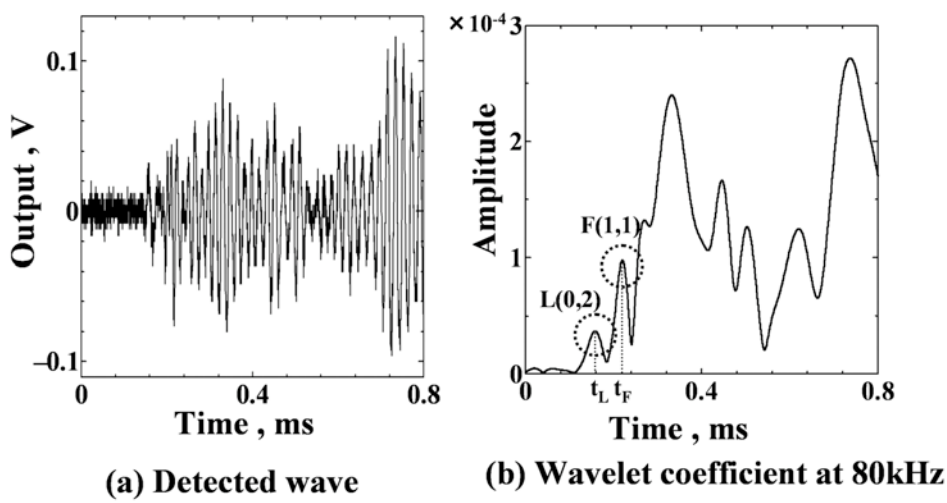

Fig. 6 Waveform excited by Hsu-Nielsen source and wavelet coefficient at 80 kHz.

Figure 7 shows the accuracy of estimated source distance. Here, the vertical axis designates the distance of the source from the sensor. Source locations of 10 trials at each distance are shown by ●.

Sources were located to better than 9.9 mm for 300-mm distance. This accuracy is adequate to estimate the damage location in the axial direction of the tube.

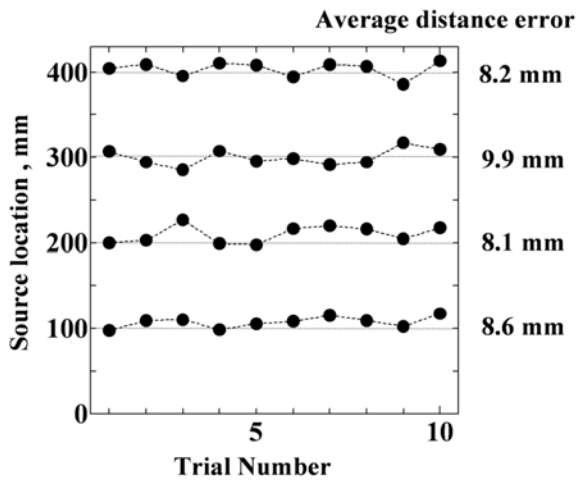

Fig. 7 Source location results estimated and average distance error.

AE Monitoring of Molten Salt Attack by Optical Fiber Sensors

Accelerated oxidation of heat resistant alloys by molten salt is well known as the most dangerous damage, and often called catastrophic oxidation. We measured AE signals from the fracture of non-protective oxide films produced by molten salt (85 mol% V_2O_5+Na_2SO_4) by using optical fiber sensors. Figure 8 shows experimental setup for molten salt test and AE monitoring method of a hot tube. The sensing fiber was wound on a 304-stainless steel tube of 35-mm diameter and 1000-mm length. The polymer-coated fiber was wound on the tube at 50 mm from the edge of the furnace to avoid the heat damage of the fiber, while the copper-coated fiber on the tube was in the hot zone of the furnace. Fiber was wound with heat-resistant couplant and over-wrapped by soft glass fiber mat to minimize thermal noise. We also monitored AE using a conventional monitoring system. Two PZT sensors (Pico, PAC) were mounted on the tube ends, where temperatures were lower than 40ºC. We placed 0.1 g of a salt mixture in a small crater on the upper portion of the tube at the center of the furnace and then heated the tube.

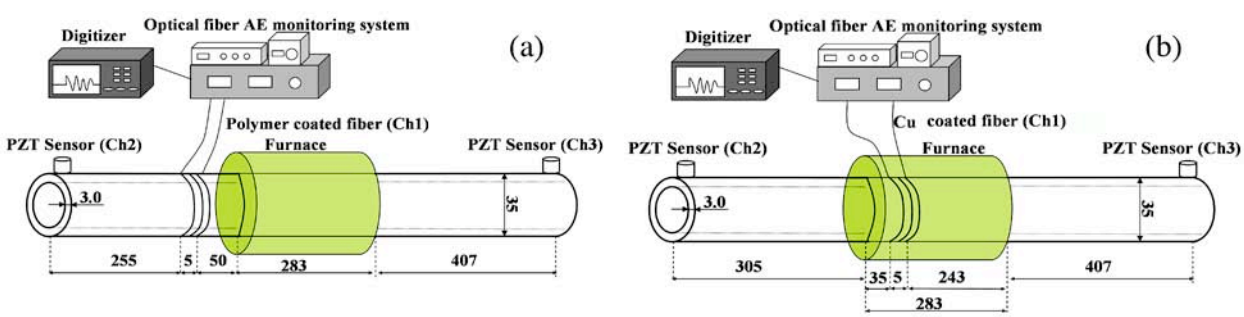

Fig. 8 Experimental setup for molten salt attack AE. (a) polymer-coated, (b) Cu-coated.

Figure 9 shows changes of cumulative AE counts and temperature history of furnace and tube with optical fiber (fiber temperature). For the right figure, fiber temperature is the same that of the furnace temperature. We did not detect AE during heating and holding, but detected frequent AE signals during

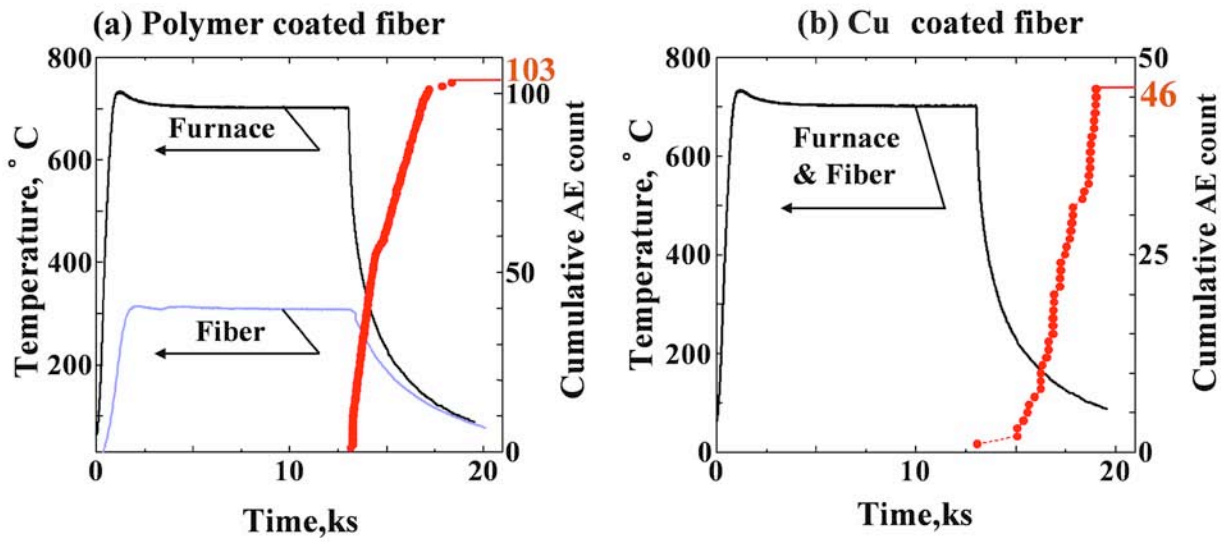

Fig. 9 Changes of cumulative AE counts detected by (a) polymer- and (b) copper-coated fiber sensors with temperature during molten salt attack.

cooling. Cumulative AE counts by the sensor with copper-coated fiber is approximately half that by polymer-coated fiber sensor. This is from the reduced sensitivity of the copper-fiber sensor exposed to high temperatures and partly due to less severe oxidation as shown later. The results, however, strongly demonstrate the heat resistance of the copper-coated fiber for monitoring the AE signals. The fiber was heated for 13 ks at above 700ºC and was still functional for AE detection.

Shown in Fig. 10 are the examples of AE signals detected by polymer- and copper-coated fiber sensors. Without using a preamplifier, we detected a number of strong cylindrical waves. Both L-mode and F-mode waves were present in the detected waves. We then estimated the location of AE sources. Location results are shown in Fig. 11. Here the symbol ● designates the source locations estimated by using the outputs of two PZT sensors and symbol ○ those by the mode-difference method proposed here. Here, the origin of Z-axis is set at the right end of the fiber windings. AE sources were located in wide range from z = 165 mm to 215 mm for AE signals detected by the polymer-coated fiber, and from z = 135 mm to 165 mm for AE signals detected by the copper-coated fiber. This is because the molten salt spread over the wide pipe surface and produced catastrophic oxidation as shown in Fig. 12. Non-protective oxide scale was observed in the region of $165 < z < 215$ mm for the test by polymer-coated fiber and the region of $135 < z < 165$ mm for the test by copper-coated fiber. These regions agree well with the source zones of Fig. 11. It should be noted that the distance error of ○ and ● is less than 20 mm, and the oxidation damage by the test with copper-coated fiber is lower compared to those by the test with polymer-coated fiber.

Conclusions

We used optical fibers as heat resistant AE sensor and monitored AE signals from molten salt attack of 304-stainless steel tube at elevated temperatures. Results are summarized below.

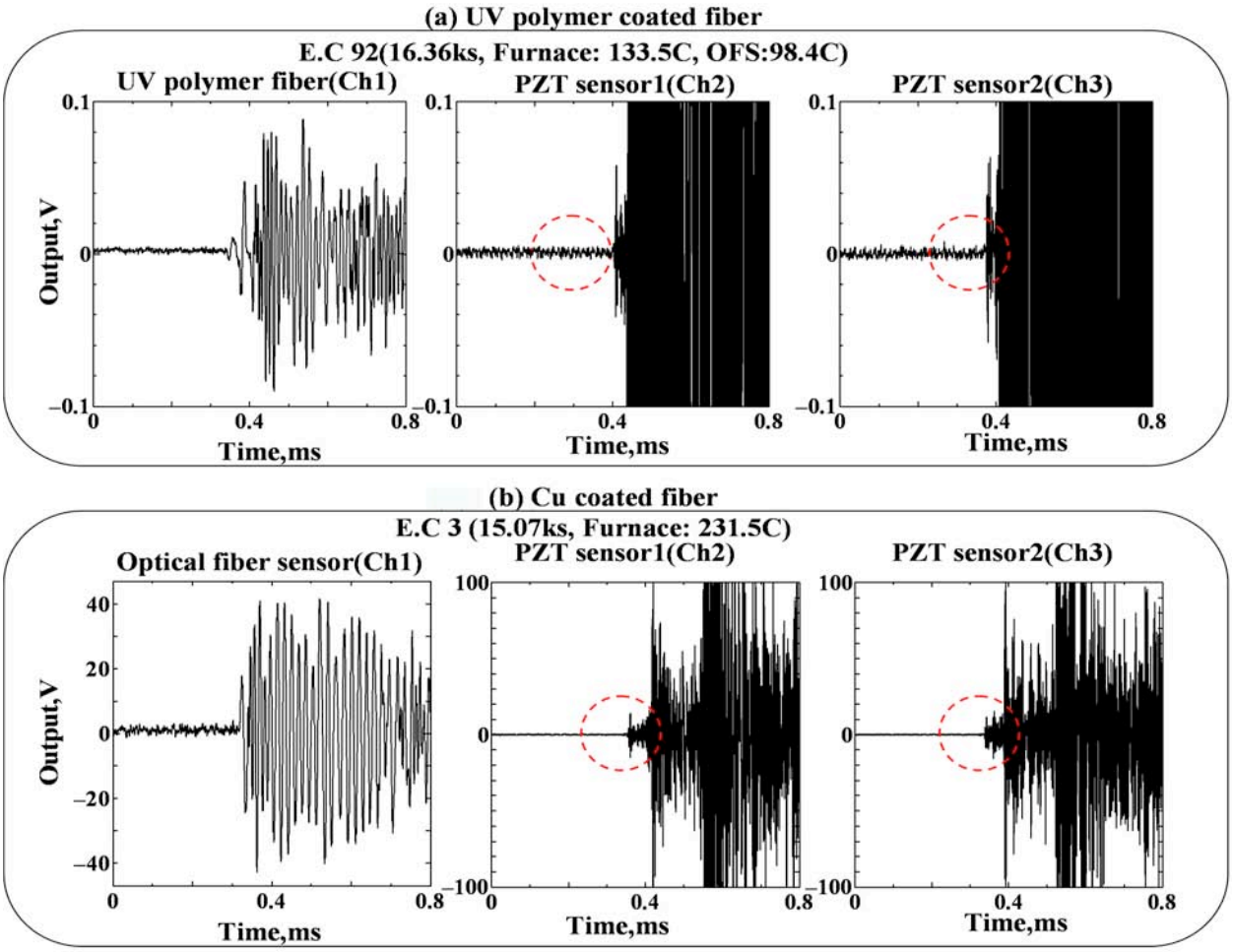

Fig. 10 AE waveforms detected by (a) polymer-coated fiber and by (b) copper-coated fiber.

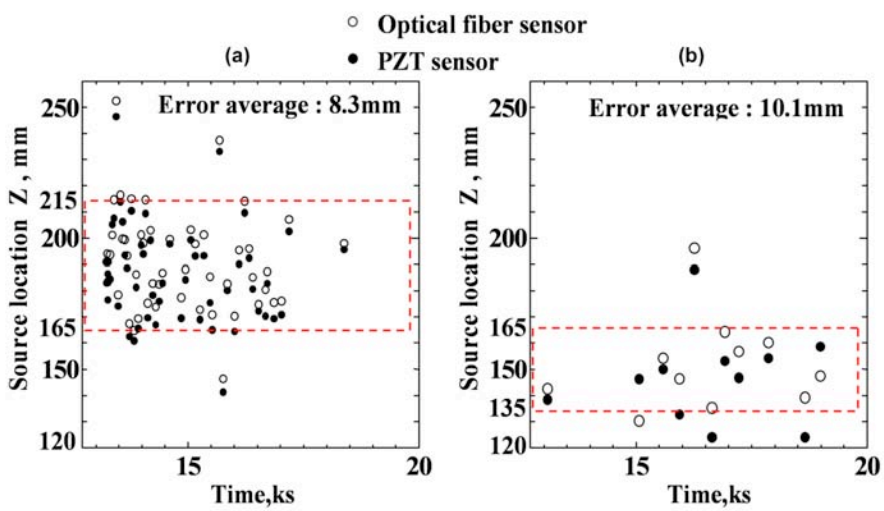

Fig. 11 Estimated source locations detected by polymer-coated fiber (a) and copper-coated fiber (b).

1) Sensitivity of the optical fiber sensor to cylindrical wave AE increases with the number of the wound fiber on the tube. Heat resistance of the polymer-coated fiber was below 500ºC while that of the copper-coated fiber was about 700ºC.

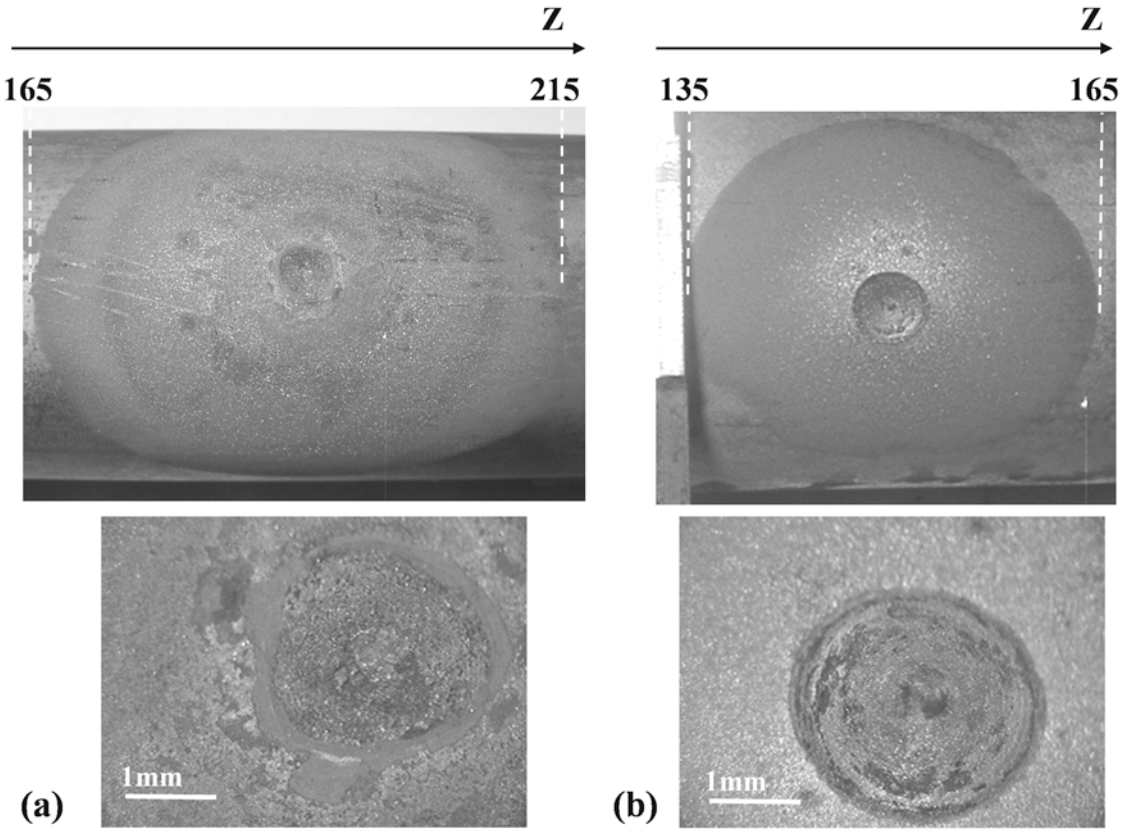

Fig. 12 Surface of oxidized specimens submitted for AE monitoring by (a) polymer-coated fiber and (b) copper-coated fiber. Craters in the mid portion of photos are reservoir for the mixed salt. Upper photos show the zone of spread molten salt, and lower photos the fractures of the scale in and along the periphery of the craters.

2) We proposed a new source location method of cylindrical wave AE with a single sensor. Accurate location is possible for the cylindrical waves with strong L- and F- modes. Developed fiber sensors detected the both wave modes and made the source location possible.
3) Developed system detected cylindrical wave AE signals from fracture of non-protective oxide film produced by molten salt attack. Frequent AE signals were emitted during cooling. Sources of AE signals ware located over the wide pipe surface attacked by spread molten salt.

References

[1] K. Ono and H. Cho: Rods and tubes as AE waveguides, J. of Acoustic Emission, **22**, 243-252 (2004).
[2] K. Hayashi, H. Suzuki and M. Takemoto: Intergranular brittle fracture of SUS 304 stainless steel with residual tensile stress during the molten chloride attack, Zairyo-to-Kankyo, **46**, 30-36 (1997). (in Japanese)
[3] H. Cho, R. Arai, H. Suzuki and M. Takemoto: Development of stabilized and highly sensitive optical fiber acoustic emission monitoring system and its application for leakage detection, J. JSNDI, **53** (11), 709-714 (2004). (in Japanese)
[4] H. Nishino, F. Uchida, S. Takashina, M. Takemoto and K. Ono: A new method of AE source location in pipes using cylindrical guided waves, J. of Acoustic Emission, **18**, 102-110 (2000).

DEVELOPMENT OF MEASUREMENT SYSTEM USING OPTICAL FIBER AE SENSORS FOR ACTUAL PIPING

SATOSHI NISHINOIRI, PORNTHEP CHIVAVIBUL, HIROYUKI FUKUTOMI and TAKASHI OGATA
Materials Science Research Laboratory, Central Research Institute of Electric Power Industry (CRIEPI), 2-11-1, Iwado Kita, Komae, Tokyo 201-8511, Japan.

Abstract

AE monitoring for high-temperature components such as high energy steam pipings necessitates the use of waveguides to protect the sensor. However, this causes distortion of propagating waveforms and it is very difficult to quantitatively analyze AE using such modulated waveforms. From these backgrounds, recently CRIEPI has developed the optical fiber sensor that can be applied up to 600˚C and the measurement system. The aims of this study are to develop practical sensor installation techniques of the optical fiber sensors for high-temperature pipings and to investigate the suitable waveform analysis technique of optically detected AE signals. (1) Direct attachment of the sensor on piping surface using couplant and (2) attachment of the sensor on the end of a stud-welded waveguide were proposed for suitable sensor installation techniques. The wavelet-based signal processing has been applied to the detected signal by the optical fiber sensors to improve the accuracy of source location on steel pipings. It was demonstrated that locational error of this technique was less than ±4% (direct attachment on the surface) or less than ±25% (attachment on the end of the waveguide).

Keywords: High-temperature components, pipings, damage monitoring, wavelet transformation

Introduction

Ultrasonic testing (UT) is the most popular nondestructive test for large-scale structures. However, it requires installation and removal of scaffolds and inspection of narrow portions is difficult due to limitation of instruments. By using acoustic emission (AE) testing in combination with UT, in particular inspecting only the concentrated parts of AE, reduction of inspection time and cost is expected. In the electric power industry, AE testing has been applied to location of the partial electric discharges in a transformer. It has been also applied to erosion monitoring of the steam turbine blades caused by collision of the oxide scales in steam flow [1]. However, since there are not sufficient references and sensor installation is difficult, there are a few reports about application of AE testing to monitor high-temperature components. In addition, since PZT elements generally used as an AE sensor lose the piezoelectricity at Curie temperature, it cannot be used at temperatures above 300˚C. Cooling of attachment area of a sensor or use of a waveguide is required to apply PZT sensors to high-temperature components. It causes modulation of waveforms and makes it difficult to analyze these waveforms.

In the U.S., AE monitoring for inspection of actual pipings in fossil power plants has been carried out since 1986. PZT sensors attached on the end of metal waveguides welded on piping surface have been used for these monitoring. Electric Power Research Institute (EPRI) has established guidelines for performing an AE inspection on seam-welded hot reheat pipings in 1995 [2]. In-service monitoring based on this guideline has been performed for 75 lines in the U.S. by

2002 and it has been reported that location of defects indicated by the other nondestructive inspections showed good agreement with the concentrated parts of AE signal [3].

Since an optical fiber has durability and corrosion resistance, some types of optical fiber-based AE sensor have been developed in recent years [4-7]. From these backgrounds, Central Research Institute of Electric Power Industry (CRIEPI) has developed the optical fiber sensor that can be applied up to 600˚C and the measurement system [8]. However, it is still difficult to apply these sensors to high-temperature pipings. The aims of this study are to develop practical sensor installation techniques of the optical fiber sensors for high-temperature pipings and to investigate suitable waveform analysis technique of optically detected AE signals.

Measuring System

CRIEPI and LAZOC Inc. have developed the optical fiber sensor that can be applied up to 600˚C and a Mach-Zehnder type optical fiber laser interferometer [9]. Figure 1 shows the optical system of the interferometer. The light source is a laser diode with a wavelength of 1550 nm. The light from the source is divided into the signal beam and the reference beam. When an optical fiber receives vibration by elastic waves, a frequency shift will arise in the passing signal beam. The reference beam is guided to the acousto-optic modulator (AOM) and the frequency is shifted by 80 MHz. These beams are combined and sent to a photo-diode (PD), and then frequency change is detected as voltage change in a frequency detection circuit (f-V circuit). Detectable frequency band of the interferometer is 0.1 Hz - 5 MHz, and the interferometer has high-pass filter (HPF) of 0.1 to 100 Hz, and low-pass filter (LPF) of 200 kHz to 1.5 MHz. The sensor used in this study consists of 50 loops of fiber entirely sandwiched between Kapton films (LAZOC, LAEDS505SB). The dimensions of the Kapton films, inner diameter and outer diameter of optical fiber sensor are 35 x 30 mm, 5 mmϕ and 21 mmϕ, respectively.

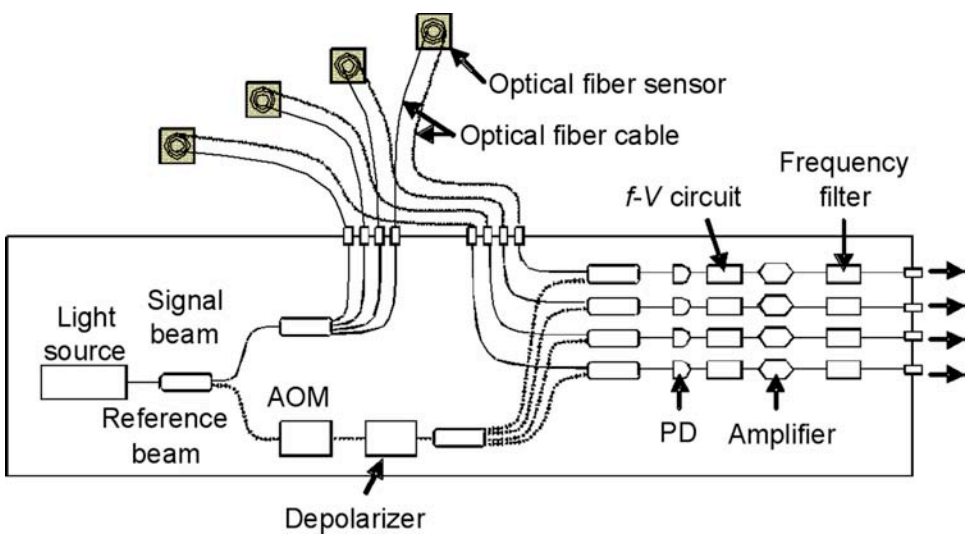

Fig. 1 Optical system of the interferometer.

Figure 2 shows the measuring system used in this study. Output signals from the interferometer were recorded by an AE analyzer (PAC, DiSP) or an oscilloscope (Yokogawa Electric, DL750) through a frequency filter (NF Corp., FV-628B). Recorded waveforms were analyzed by a program developed with LabVIEW and MATLAB to extract AE parameters and to carry out source location. A pulse generator (PAC, C-101-HV) and a PZT pulser (PAC, R15, resonance frequency of 150 kHz) were used for excitation of simulated AE signals. Resonance type AE

sensors (PAC, Nano30, resonance frequency of 300 kHz) and preamplifiers (PAC, 1220A) were used for comparison. Each sensor was attached to measuring plane with silicone grease (Shin-etsu Chemical, HIVAC-G).

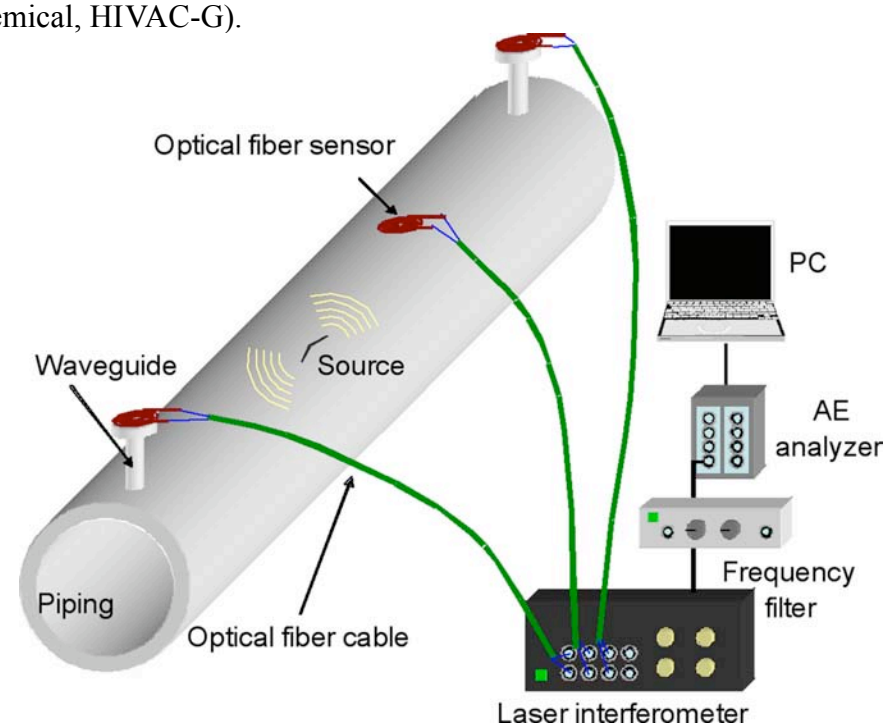

Fig. 2 Monitoring system for piping.

Sensor Installation Techniques for Piping

To apply sensors to high-temperature components, it is required that coupling between a sensor and a measuring plane is strong enough and stable at elevated temperatures during long-term monitoring as well as heat resistance of sensor itself. Furthermore if removing and recovery of insulation is not necessary for sensor installation, time and cost can be reduced. In this study, applicability of two installation techniques was investigated; (1) direct attachment of the sensor on pipe surface using couplant; (2) using waveguides as the U.S. electric utilities have already applied to AE monitoring of actual piping installations.

Firstly, the applicability of commercial high-temperature adhesives was investigated by a heat exposure test. The detailed descriptions of the test are as follows. An adhesive was applied to a stainless steel disc with dimensions of 30 mmϕ x 5 mm to fix it on a stainless steel block with dimensions of 60 x 40 x 20 mm or a steel plate with radius of curvature of 190 mm and thickness of 5 mm, and then cured according to the instruction. After that, the bonded stainless steel was heated to 600˚C and kept at this temperature for 6 hours and then cooled to room temperature. The PZT sensor and the pulser were adhered to the stainless steel surfaces at the opposite side. Simulated AE signals were excited by the pulse generator and the pulser, then detected by the PZT sensor and recorded by the oscilloscope. The reduction of acoustic transmission was evaluated by the maximum amplitude ratio normalized by the maximum amplitude at room temperature using the silicone grease as couplant. The heat exposure test was repeatedly carried out until the adhesive fractured. Figure 3 shows change of acoustic transmission with the number of heat exposure cycles. Adhesive (a) cracked within the first cycle and the signal could not be detected. Although adhesives (b) and (c) had no visible cracks, acoustic transmission decreased with number of cycles and it became impossible to detect the signal after 2 cycles. All tested

adhesives cracked within the first cycle in the case of the curved surface so that the signal could not be detected. It is considered that uneven adhesive thickness led to fracture due to the difference in the coefficients of thermal expansion. From these results, it can be concluded that commercial high-temperature adhesives are unsuitable for fixing the sensor to high-temperature pipings.

Secondly, the applicability of commercial high-temperature greases was investigated as above. High-temperature grease is useful because it requires no curing and no surface pretreatment to attach sensors. The change of acoustic transmission with the number of the heat exposure cycles was also shown in Fig. 3. It was observed that grease (a) cracked and flaked off due to evaporation of the water at elevated temperatures. On the other hand, grease (b) showed good performance. Simulated AE signals could be detected after 2 cycles and even detected after 2 cycles of 120 hours hold at 600˚C. Below the glass-transition temperature, the grease is hardened, and it becomes soft at elevated temperature and acts as an acoustic medium. Although acoustic transmission decreased due to reduction of the contact area because of flow of the grease in the case of the curved surface, the signal could be detected after 2 cycles. Since the grease itself lost adhesion at elevated temperatures, mechanical support of the sensor is required [10].

Since an actual piping is covered with insulation, removal and recovery of the insulation is required for sensor installation. In addition, maintenance of sensors is very difficult because we cannot observe sensor condition from outside and access to the sensor until next plant outage time. Use of a waveguide is a simple way to install sensors to an actual piping without complete removal of the insulation. Applicability of the short-cycle stud welding technique, which can attach a metal rod, called a stud, in a short time (less than 0.01 second) to a metal component, was investigated. The advantages of this technique are (1) firm joint is possible even if a surface oxidization films or contamination have not been removed. (2) Installation of sensors to narrow portions is possible. Figure 4 shows cross-section of a steel stud welded on a steel plate. The depth of weld penetration was less than 300 μm and the melted area was close to the diameter of the stud. The damage to the base metal was smaller than from other welding techniques such as the arc welding. Figure 5 shows schematic figure of the designed waveguide. As the result of detection of simulated AE signals on a steel plate with a thickness of 0.75 mm, the maximum amplitude of the signals detected by the sensor attached at the waveguide root was 12 dB smaller than that directly attached on the surface, in the range of 10-700 kHz.

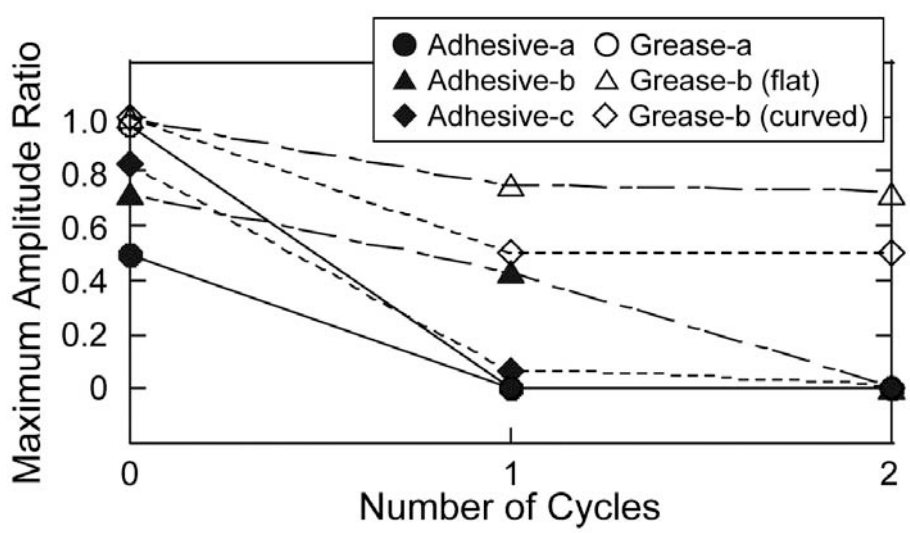

Fig. 3 Change of acoustic transmission with number of the heat exposure cycles.

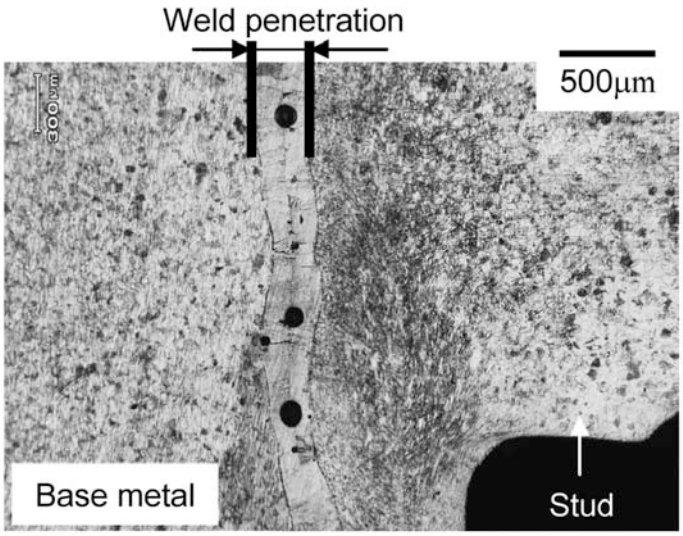

Fig. 4 Cross-section of a steel stud welded on a steel plate.

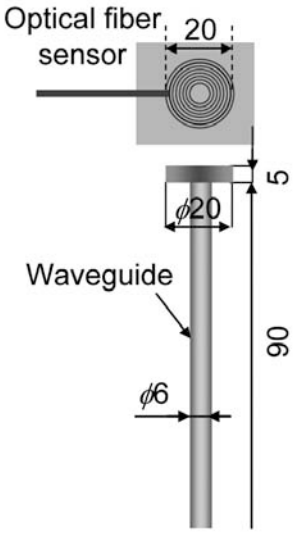

Fig. 5 Schematic drawing of the designed waveguide.

Accuracy of Source Location on Piping

Linear source location on a pipe using the arrival time interval of elastic waves becomes possible by attaching two or more sensors. However, the accuracy may be affected by the sensor spacing (position and distance between the sensors and the source), and by use of waveguides. In this study, the accuracy of linear source location on a pipe using the optical fiber sensors was investigated.

We have reported that the interval between the first peak times of the wavelet coefficients at specific frequency is suitable for determination of the arrival time interval of optically detected AE signals [7]. In order to automate this peak determination, (a) threshold crossing of the wavelet coefficients at specific frequency and (b) cross-correlation between the coefficients of each sensor were investigated. The wavelet coefficients at 150 kHz were chosen. Morlet was used as the mother wavelet. Figure 6 shows experimental setup of a location test using waveguides. Two optical fiber AE sensors were attached on a low alloy steel pipe with outer diameter of 400 mm and inner diameter of 380 mm. The sensors were attached directly on the pipe surface or on the end of the stud-welded waveguides with length of 90 mm. Simulated AE signals were excited by the PZT pulser attached on the pipe surface with varying distance and angle between the sensors and the source. The frequency filter was set as HPF of 10 kHz and LPF of 250 kHz. The arrival time interval between each sensor was determined by conventional threshold crossing technique, techniques (a) and (b) using the wavelet coefficients.

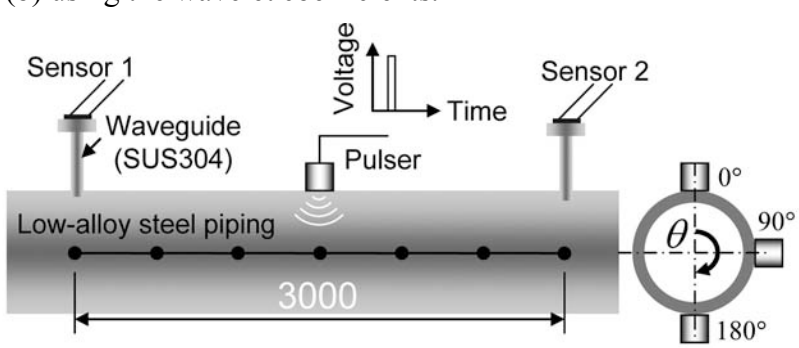

Fig. 6 Experimental setup of a location test using waveguides.

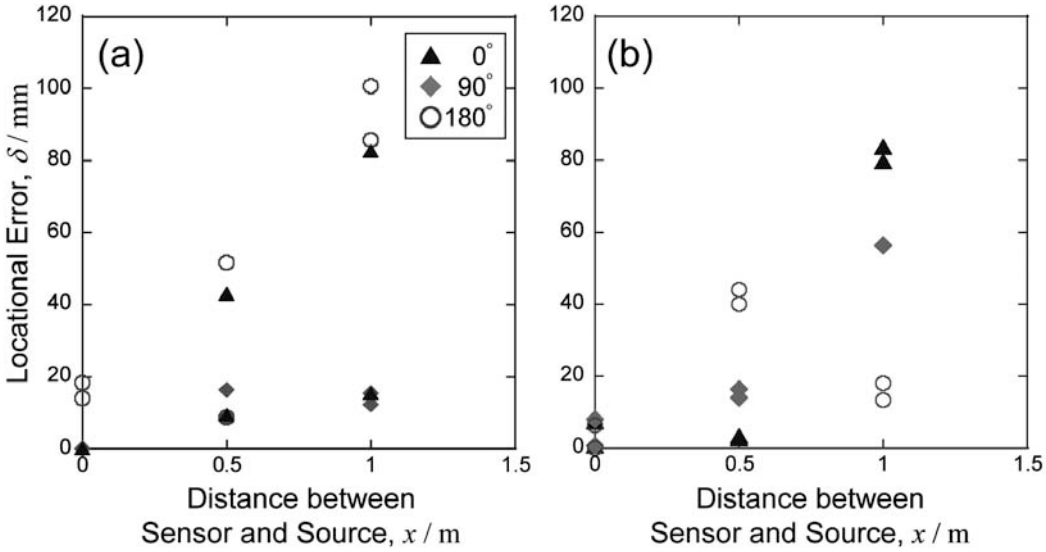

Fig. 7 Changes of locational errors with distance and angle between the trigger sensor and the source; (a) conventional threshold crossing technique; (b) threshold crossing of the wavelet coefficients at specific frequency.

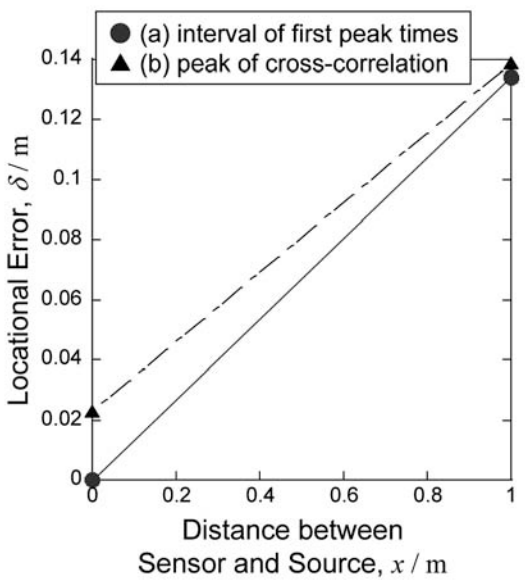

Fig. 8 Locational errors of each technique.

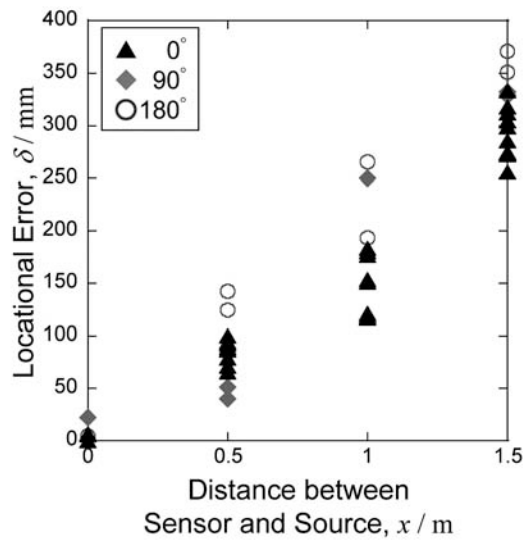

Fig. 9 Change of locational errors where the sensors were attached on the end of the waveguides.

The accuracy of location where the sensors were attached directly on the pipe surface was examined. Figure 7 shows changes of the locational errors with distance and angle between the trigger sensor and the source. Figure 7(a) and (b) show results by threshold crossing technique and technique (a) with wavelet, respectively. By conventional threshold crossing technique, the error became large with increase in distance and angle. The maximum error was approximately 100 mm. By technique (a) with wavelet, when the source was placed at center of sensor spacing, the maximum error was approximately 10 mm and significant increase in the error with increase in angle was not observed. Although the error became large with increase of distance between the trigger sensor and the source, the error was approximately ±4%.

The accuracy of location where the sensors attached on the end of the waveguides was examined. The time interval was determined by two techniques; (a) interval of the first peak times of the wavelet coefficients and (b) peak of cross-correlation between the coefficients of each sensor. Figure 8 shows locational errors of each technique. Although the error increased with distance between the trigger sensor and the source, it was demonstrated that (a) was better technique to determine the time interval. It was considered that correlation of the first peak including noise led to increase of the error in technique (b) using cross-correlation. Figure 9 shows change of the locational errors with distance and angle between the trigger sensor and the source. Here x = 1.5 m means that the source was placed near the waveguide root. The maximum error was approximately ±25% and the error became large with distance and angle between the trigger sensor and the source. The error was larger than that where the sensors attached directly on the surface. This seemed to be caused by modulation and attenuation of elastic waves during propagating the waveguides.

Figure 10 shows the accuracy of location by the optical fiber AE. The accuracy for the pipings that EPRI carried out was also shown in the figure, where PZT sensors were attached on the end of the waveguides approximately 4 m apart and conventional threshold crossing technique was applied [3]. Since the accuracy could not be compared simply due to difference in the sensor spacing, the accuracy of our technique seemed to be sufficient. Especially when the source was close to the center of the sensor spacing, very good accuracy was acquired. Therefore, appropriate sensor spacing can improve the accuracy of location.

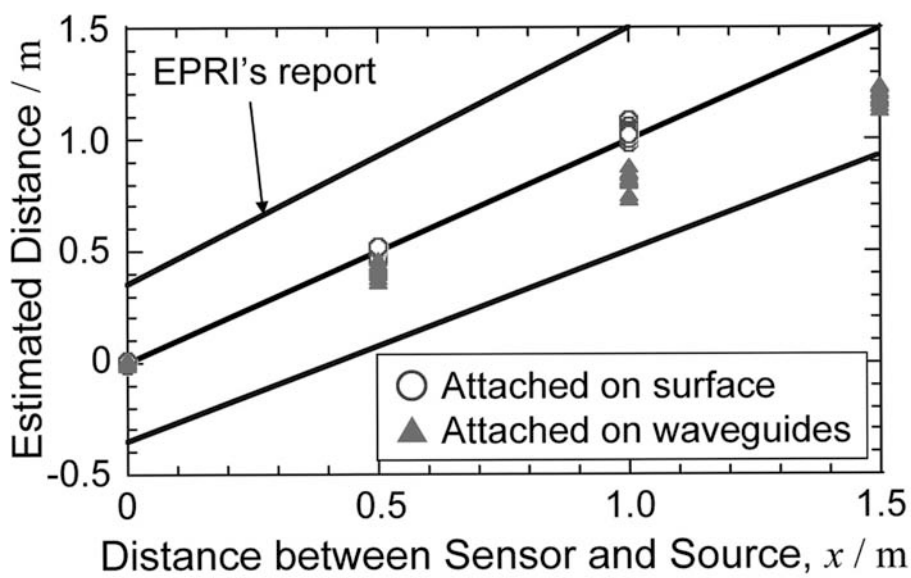

Fig. 10 Accuracy of location by the optical fiber AE in comparison with conventional technique.

Conclusions

In this study, the optical fiber AE system developed was applied to location on a piping, and suitable sensor installation techniques were investigated. The obtained results are as follows:

(1) Some installation techniques of the optical fiber AE sensor to a low alloy steel piping were investigated. As the result, combination of a high-temperature grease and mechanical fixing was proposed as the most suitable way to attach the sensor if welding was not permitted. Attachment on the end of a stud-welded waveguide was proposed as a suitable way to attach the sensor to narrow portions or insulated components.

(2) Accuracy of source location on a piping using the continuous wavelet transformation and the optical fiber AE sensors attached by each installation technique was examined. The error was less than ±4% where the sensors were attached directly on the piping surface and less than ±25% where the sensors were attached on the end of stud-welded waveguides.

References

1) A. Sato, E. Nakashima, M. Koike, M. Maeda, T. Yoshiara and S. Nishimoto: *Progress in Acoustic Emission X* (2000), JSNDI, p. 399.
2) Acoustic Emission Monitoring of High-Energy Piping, Volume 1: Acoustic Emission Monitoring Guidelines for Hot Reheat Piping, TR-105265-V1, EPRI (1995).
3) R. M. Tilley: *Proc. of Conference on Advances in Life Assessment and Optimization of Fossil Power Plants*, EPRI/DOE (2002).
4) I. Ohsawa, K. Kageyama, Y. Tsuchida and M. Kanai: *Progress in Acoustic Emission XI* (2002), JSNDI, p. 160.
5) T. Matsuo and M. Takemoto: *Progress in Acoustic Emission XI* (2002), JSNDI, p. 168.
6) J-R Lee and H. Tsuda: Scripta Materialia **53** (2005), 1181.
7) H. Yuki and Y. Mine: *Progress in Acoustic Emission XII* (2004), JSNDI, p. 35.
8) P. Chivavibul, H. Fukutomi, T. Ogata, S. Takahashi, F. Matsumura and Y. Machijima: CRIEPI Report Q04014 (2005) (In Japanese).
9) P. Chivavibul, H. Fukutomi, S. Takahashi and Y. Machijima: *Progress in Acoustic Emission XII* (2004), JSNDI, p. 29.
10) S. Nishinoiri, P. Chivavibul, H. Fukutomi and T. Ogata: CRIEPI Report Q05015 (2006) (in Japanese).

UTILIZATION OF CASCADE OPTICAL FIBER AE SYSTEM FOR SOURCE LOCATION OF LAMB WAVES THROUGH A CROSS-PLY CFRP PLATE

TAKUMA MATSUO, HIDEO CHO and MIKIO TAKEMOTO
Faculty of Science and Engineering, Aoyama Gakuin University,
5-10-1 Fuchinobe, Sagamihara, Kanagawa, 228-8558 JAPAN.

Abstract

We propose a new source location method of Lamb-wave AE signals detected by three optical fiber sensors in cascade mode. Three fiber sensors were mounted on a cross-ply CFRP plate and detected the Lamb waves over 50-130 kHz range with increased sensitivity at sensor resonances. Source locations were performed by 1) determining arrival sequence of Lamb waves to the three sensors using the resonance frequencies, 2) finding arrival time differences of A_0-mode at a selected frequency (120 kHz) and 3) scanning for a virtual source utilizing the constant group velocity of 1280 m/s for this frequency. Location accuracy of the Lamb waves produced by the Hsu-Nielsen sources and compression-type transmitter was evaluated. Next, we monitored the progression of internal damages of the CFRP plate subjected to indentation loading. AE analysis provided the location of internal damages and revealed four types of damage, including delamination and transverse cracking.

Keywords: Optical fiber AE sensor, Mach-Zender-type interferometer, multi-sensing function, resonant frequency, source location.

Introduction

Carbon fiber reinforced plastics (CFRP) possess high specific strength and have been widely utilized in aeronautical systems [1]. This material tends to suffer various types of internal damages such as transverse cracks, delamination and fiber fracture by impacts of flying objects and tool drops. Conventional AE system has been utilized to monitor these fracture. The current AE system needs one signal processor for each sensor. Thus, a multi-channel AE system inevitably becomes bulky and expensive. The system possesses another drawback of the sensitivity to electromagnetic noise. Some of the drawbacks of the current AE system can be eliminated by the AE system with a cascade multi-sensing optical fiber we have developed [2]. The sensing parts of this system are lightweight and immune from electromagnetic noise.

We studied the utility of the cascade multi-sensing optical fiber AE system for monitoring the damage progression in a cross-ply CFRP plate subjected to indentation loading. This paper reports the source location method of artificial sources on the CFRP plate. Locations of various sources were obtained successfully. Next, we report monitoring results of progressive internal damages in the loaded CFRP plate.

Specimen and Experimental Method

Specimen is a $(0^\circ_{10}/90^\circ_{10})_{sym.}$ cross-ply CFRP plate of 420 x 340 x 5 mm. AE signals from artificial sources and internal damages during local loading were monitored by the optical fiber AE system reported previously [2]. Figure 1 shows the monitoring method of Lamb-wave AE signals

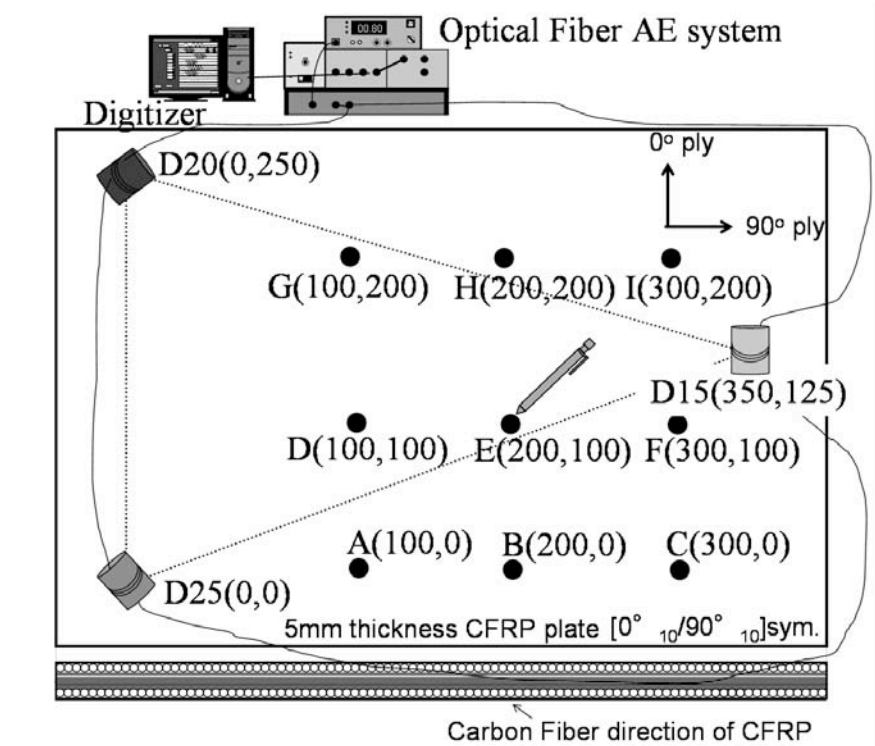

Fig. 1 Experimental setup for studying the source location accuracy using the cascade multi-sensors.

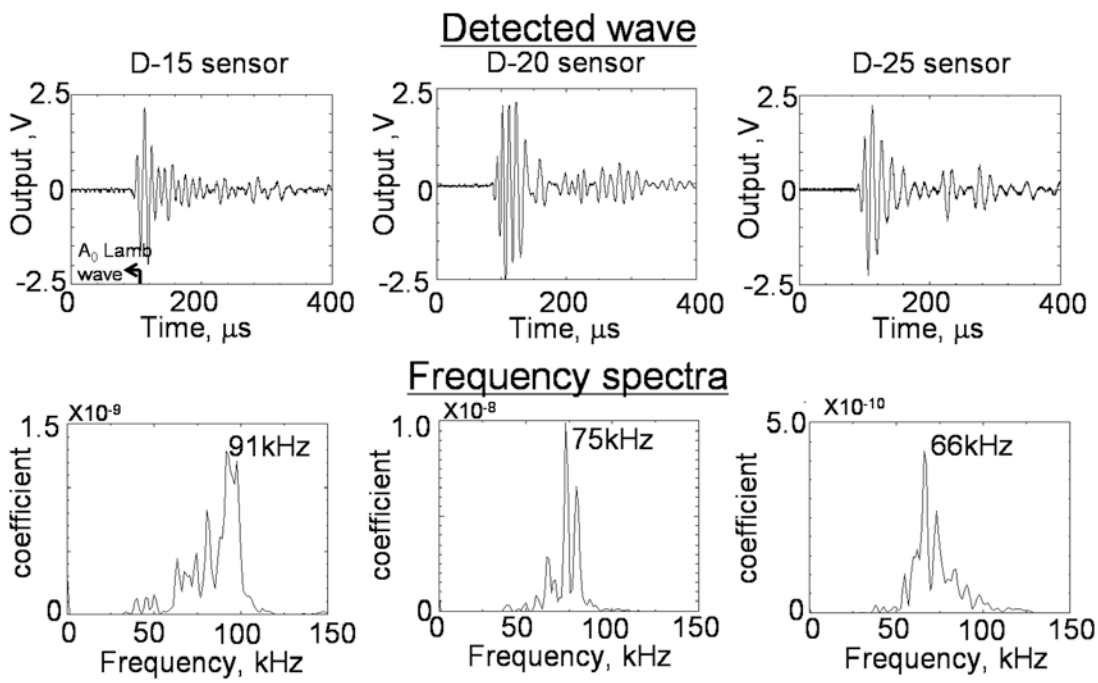

Fig. 2 Comparison of waveforms and power spectra of AE signals detected separately by the pipe shaped sensor holder as a function of diameter of the pipe

from nine artificial sources on the plate. Three sensors were mounted at the apexes of a triangle. These fiber sensors are connected in series by a single optical fiber. Each sensor consists of a horizontal hollow-cylindrical holder with the diameters of 15, 20 or 25 mm. The sensing part of the optical fiber was wound on the holder. The sensors detects the Lamb waves over 50-130 kHz

range with increased sensitivity at sensor resonances, which are basically the sensor holder resonance. These sensors are designated as D15, D20 and D30 sensor, hereafter. It is noted that five sources, A, B, C, F and I, are out of the sensing zone.

Resonance frequencies of the three sensors were first studied separately. Figure 2 shows waveforms and frequency spectra of the waves produced by the Hsu-Nielsen source on a steel plate at 200 mm from the sensor and detected by the optical fiber sensors. Resonance frequency of D15 sensor was measured as 91 kHz. These of D20 and D25 sensors are 75 and 66 kHz, respectively.

We estimated the source locations of four types of artificial sources. These are Hsu-Nielsen source, a small AE sensor (PAC-Pico, 450 kHz resonance), steel-ball drop and pull-off of glued sewing needle. The first two produce the Lamb waves with high frequency components, while the latter two the Lamb waves with lower frequency components.

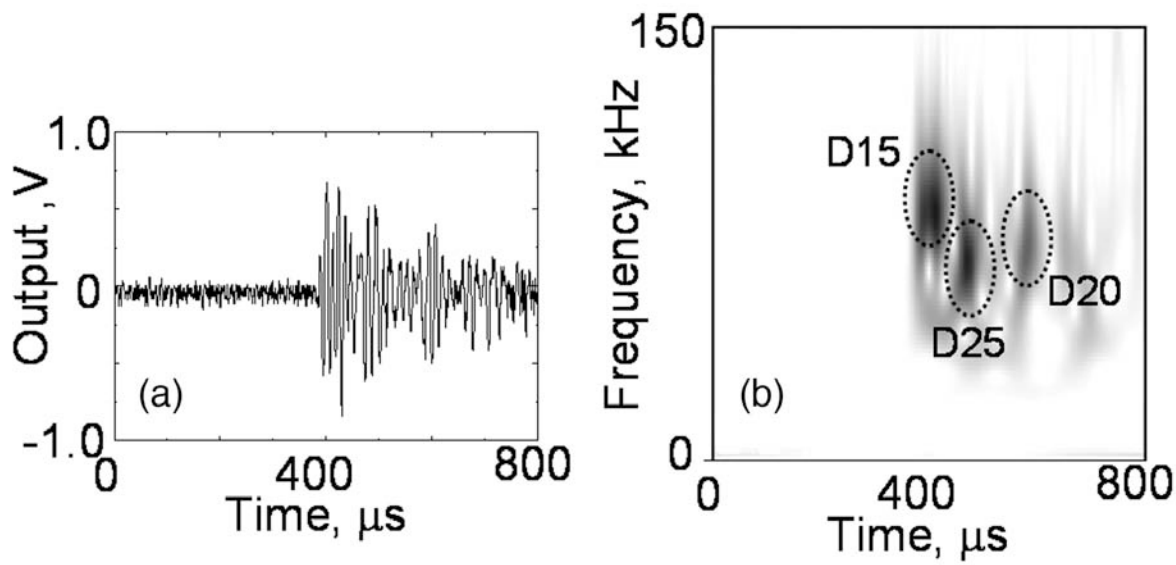

Fig. 3 Waveform (a) and its wavelet contour map (b) of AE detected by cascade optical fiber sensors. Source: Hsu-Nielsen source.

Source Location Accuracy

Location of Hsu-Nielsen sources

The source location procedure takes the following steps. Here, Hsu-Nielsen source at point E (200, 100) in Fig. 1 produced the waveform (Fig. 3(a)). This combines all the signals detected by the three sensors.

Step 1: Determination of the sensor sequence from the peak arrival times using the time transient data of wavelet coefficients at the resonance frequencies of the three sensors.
Step 2: Utilization of the group velocity of the A_0-Lamb waves at a selected frequency at which the group velocity is the same in all directions [3].
Step 3: Determination of three arrival times of the Lamb waves at the selected frequency and the time differences between two sensors.
Step 4: Virtual source scanning scheme assuming the CFRP is isotropic.

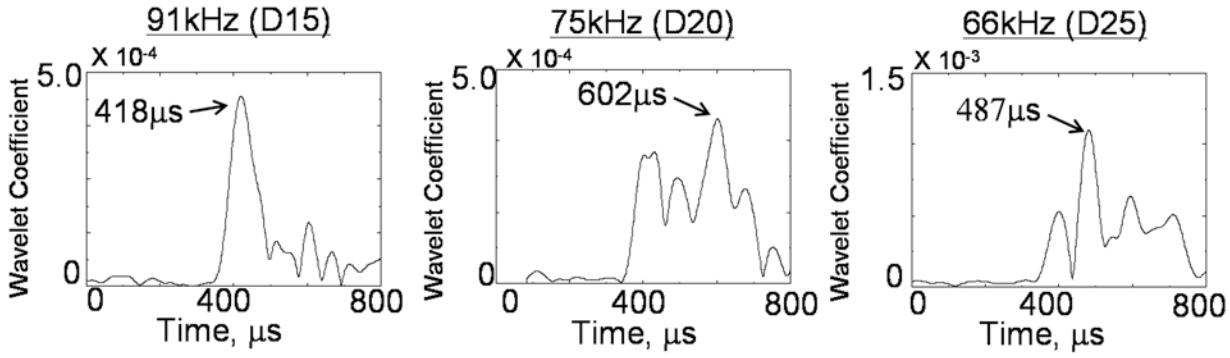

Fig. 4 Wavelet coefficients at 91, 75 and 66 kHz of AE detected by cascade optical fiber sensors. A Hsu-Nielsen source at point E (200, 100).

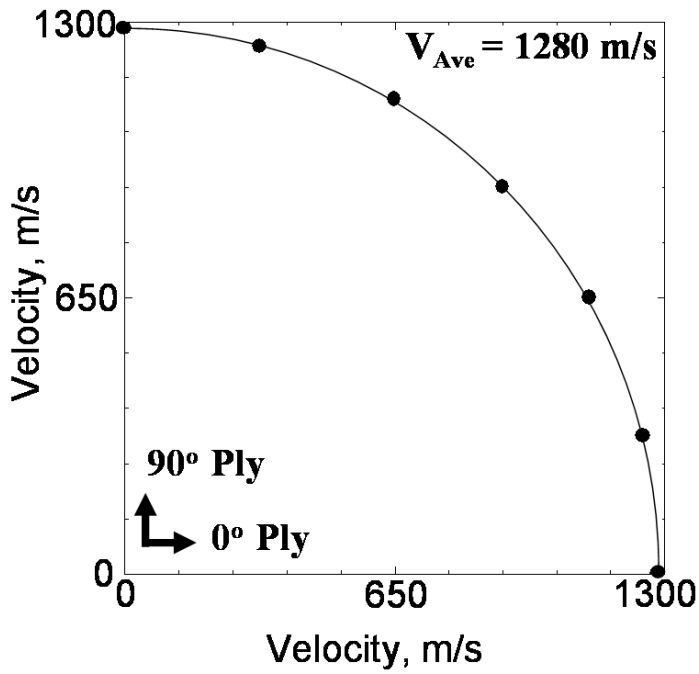

Fig. 5 Group velocity profile of the A_0 Lamb wave at 120 kHz for the cross-ply CFRP plate used.

Wavelet contour map of Fig. 3b indicates that the system detected three wave packets corresponding to the resonance frequencies of three cascade sensors. Step 1 begins with accurate determination of arrival times at the three sensors using the time transient of wavelet coefficients (Fig. 4) at the resonance frequency of 91 kHz (D15 sensor), 75 kHz (D20) and 66 kHz (D25). Arrival time of the maximum peak at three frequencies indicates that the sensor detected the AE in order of D15 (418 μs)>D25(487 μs)>D20(602 μs). Figure 5 shows the orientation dependence of the group velocities of the A_0-mode Lamb wave at 120 kHz for the CFRP plate tested. The velocity can be represented by a circle and is deemed as isotropic at 1280 m/s. This part is Step 2.

Figure 6 shows the time transient of wavelet coefficient at 120 kHz of the Lamb waves, which cannot be seen in Fig. 3a because of stronger signals at resonances. Three peaks from the left to right correspond to the arrival time of Lamb wave at 1280 m/s in the order of sensors, D15, D25, D20, as determined in Step 1. This completes Step 3. Using these data, the location of a given source at E (200, 100) was estimated as (188, 85) in Step 4. Distance error of this estimated location to the given source is 19 mm.

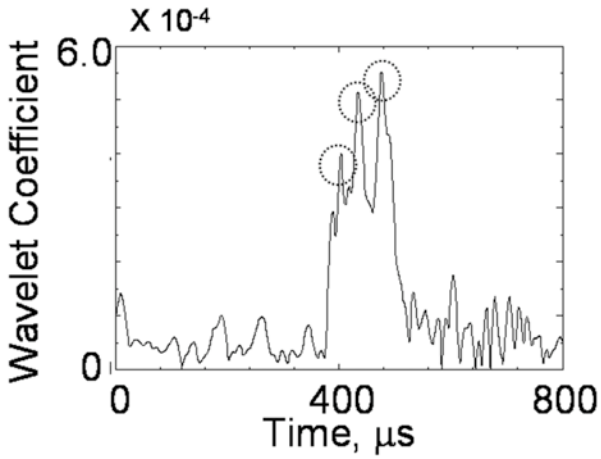

Fig. 6 Wavelet coefficients at 120 kHz of the A_0-Lamb waves detected by cascade optical fiber sensors.

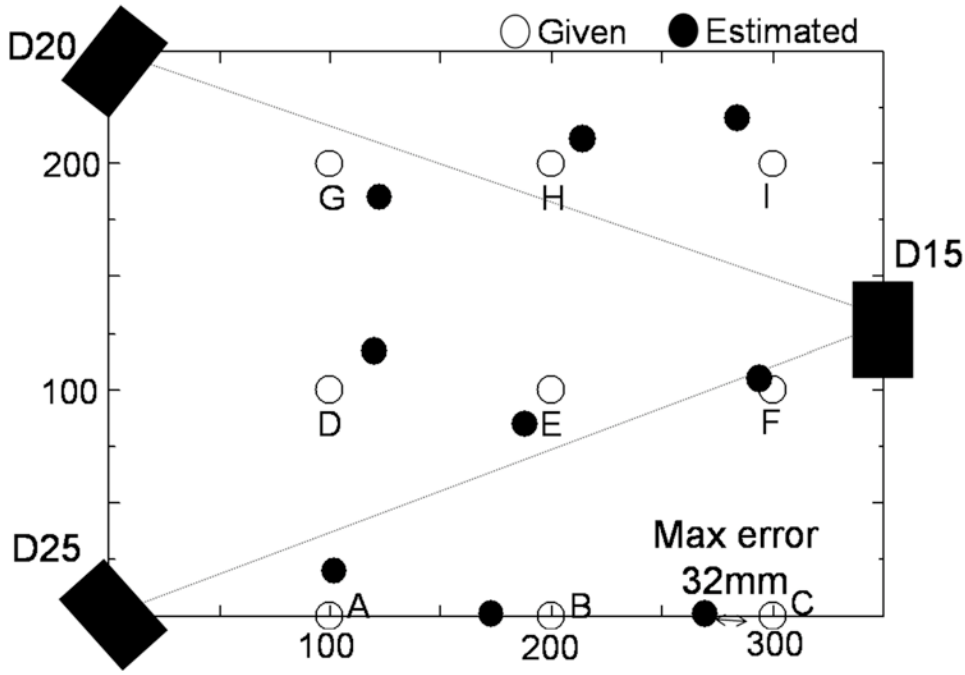

Fig. 7 Source location result of Hsu-Nielsen sources using cascade optical fiber sensors.

We estimated the source locations of nine Hsu-Nielsen sources. Results are shown in Fig. 7. The maximum and average distance errors were calculated as 32 mm and 21 mm, respectively. It is noteworthy that the maximum error occurred at source C, which is out of the sensing zone. Location accuracy by the proposed method is considered good for the Hsu-Nielsen sources.

Source Location of Pico-Sensor Sources

Figure 8 shows waveform and wavelet contour map of the AE produced by a Pico-sensor as the trasmitter at point E (200, 100) and detected by three cascade sensors. Three packets are difficult to see in the wavelet contour map. From the time transient of wavelet coefficients at 91 kHz (D15 sensor), 75 kHz (D20) and 66 kHz (D25), arrival times of the maximum peaks at the resonance frequencies were in the order of D15>D25>D20 (Fig. 9). This sequence is the same as that for the Hsu-Nielsen source at point E. Figure 10 shows the time transient of wavelet coefficient at 120 kHz. Three peaks were detected and the source was located at (185, 108). Distance

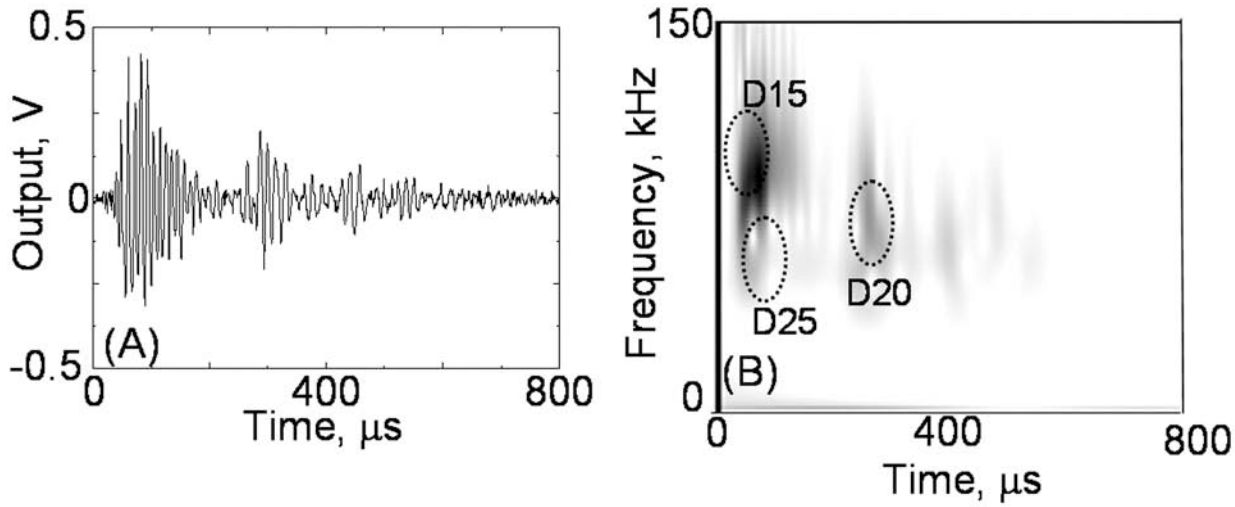

Fig. 8 Waveform (a) and its wavelet contour map (b) detected by cascade optical fiber sensors. Source: Pico sensor as transmitter.

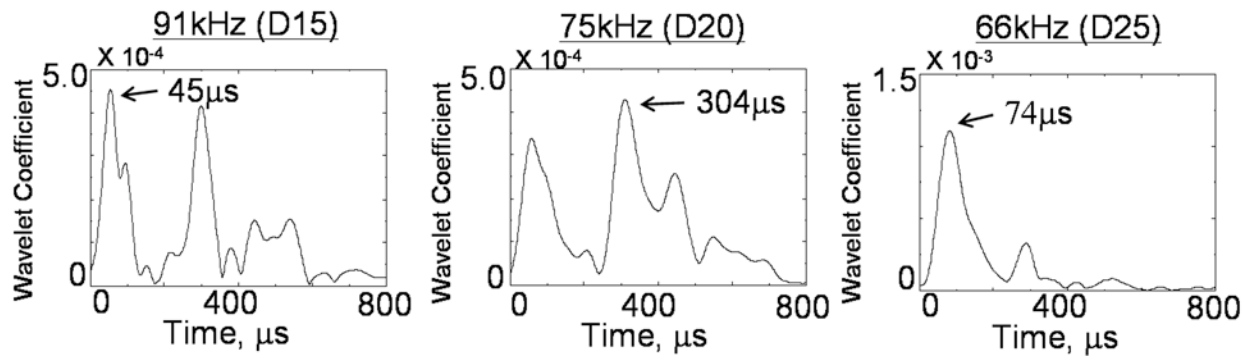

Fig. 9 Wavelet coefficients at 91, 75 and 66 kHz of AE produced by a Pico-sensor transmitter at point E (200, 100).

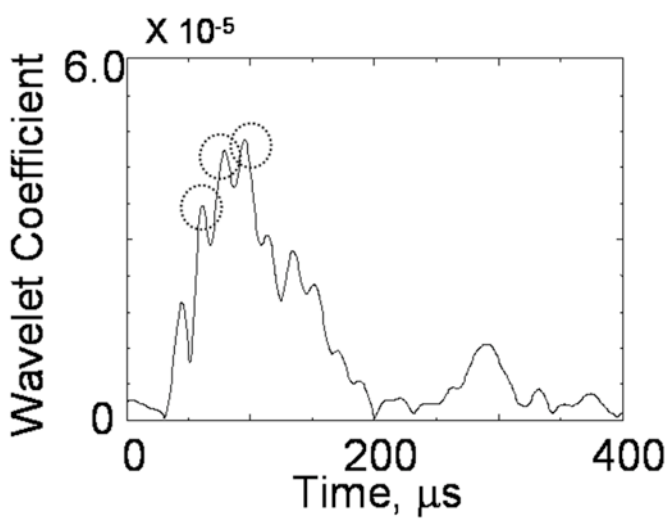

Fig. 10 Wavelet coefficients at 120 kHz of the A_0-Lamb waves produced by a Pico-sensor transmitter.

error to the given source E (200, 100) was 17 mm. This is comparable to that produced by Hsu-Nielsen source, although the amplitude of the waves below 75 kHz was low. Figure 11

shows the location results of nine source positions. Maximum and average errors were obtained as 33 and 17 mm, respectively. The maximum error was observed at source F, which is out of the sensing zone.

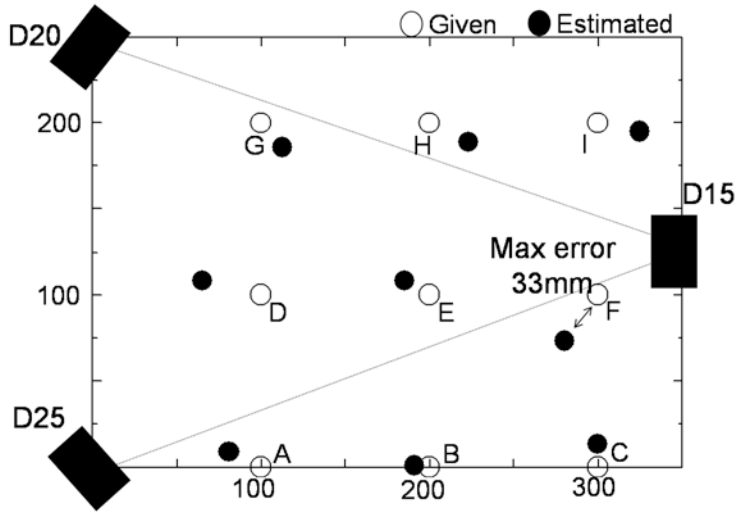

Fig. 11 Source location result of PZT transmitter using multi-channel optical fiber sensors.

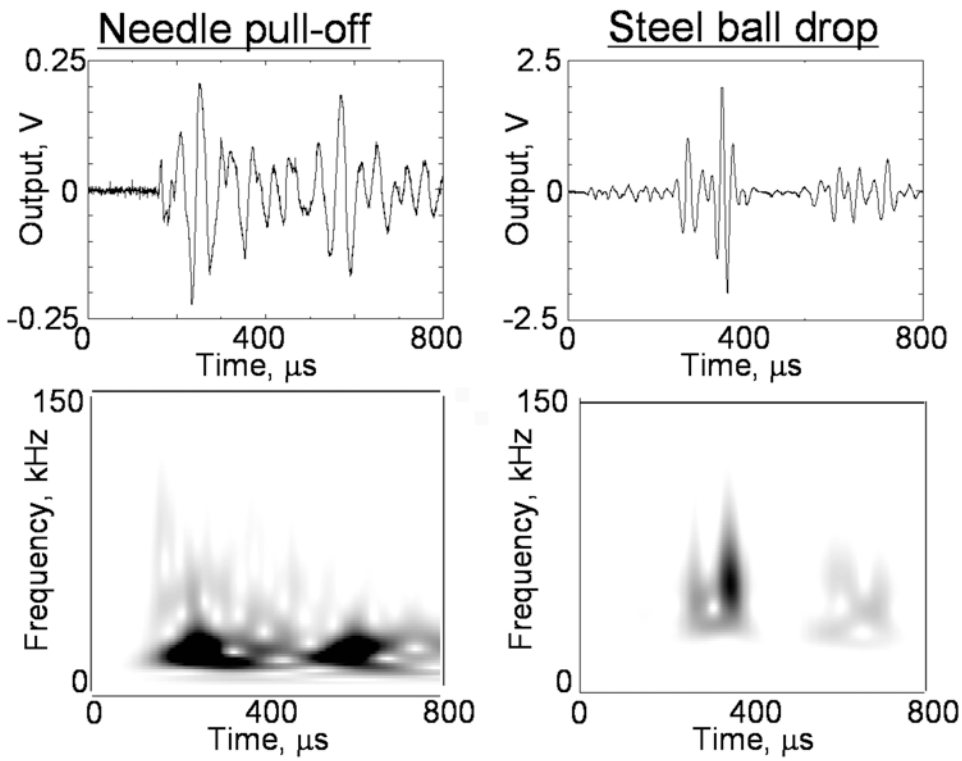

Fig. 12 Waveforms and their wavelet contour maps produced by a needle pull-off and a steel ball drop at E.

Source Location of Steel-Ball Drop and Needle Pull-Off

Next, we attempted to identify the source location of AE signals produced by a steel-ball drop and a pull-off of 1.5-mmϕ needle. We could not estimate the location of these sources, because these sources emitted weak AE signals in the sensing frequency range as shown in Fig. 12, and the time transient of wavelet coefficient at 120 kHz was too weak to determine the arri-

val times. Because we use both the resonance frequencies of the sensors and the uniform group velocity at 120 kHz, AE signals must contain the frequency components from 60 kHz (lowest resonance frequency of D25 sensor) to 130 kHz.

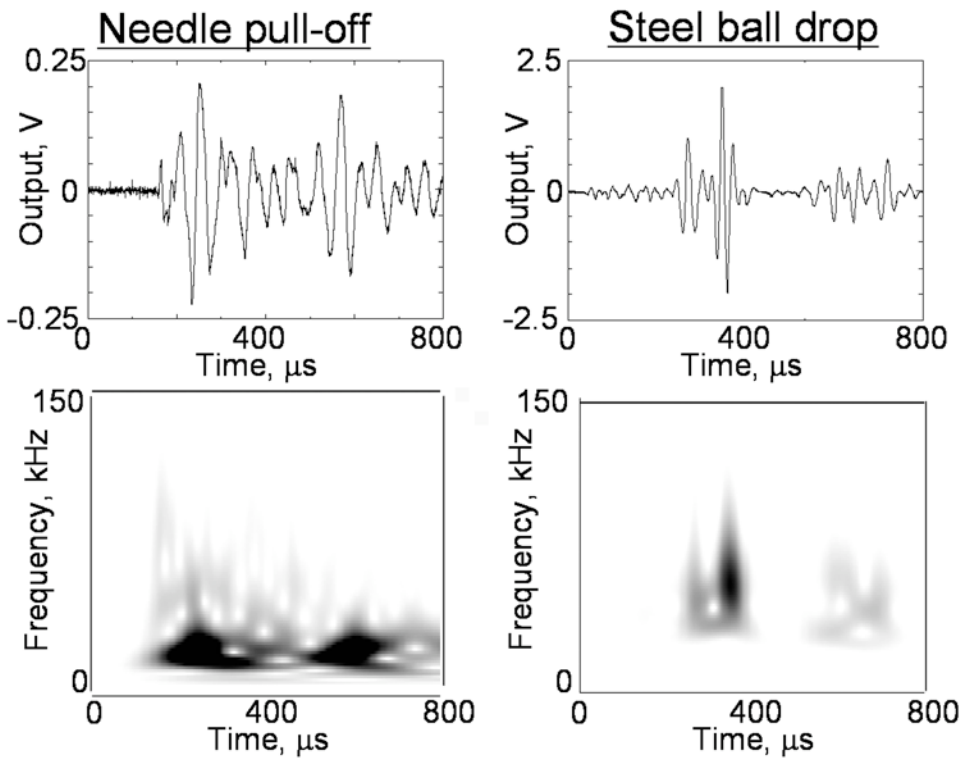

Fig. 12 Waveforms and their wavelet contour maps produced by Needle pull-off and steel ball drop at E.

Damage Monitoring of CFRP Plate during Indentation

We monitored AE signals from internal damages in the cross-ply CFRP plate during an indentation test using the experimental setup of Fig. 13. The CFRP plate was supported by a circular jig of 200-mm diameter and loaded on the opposite surface by a rod of 1.65-mm diameter with a spherical tip. Three optical fiber sensors and PZT sensors (PAC Pico) were mounted on the apexes of triangles as indicated. Outputs of the PZT sensors were amplified by 40-dB preamplifiers. Outputs of the optical fiber sensors were filtered by a band-pass filter of 50-300 kHz. In this test, we used two digitizers. Digitizer 1 is used for optical fiber sensor signals and Digitizer 2 with a multi-trigger function was used to monitor both signals from PZT and optical fiber sensors. AE event counts by the two systems were compared. Additionally, Digitizer 2 was used to classify the fracture types by waveform comparison.

Figure 14 shows the load vs. crosshead displacement curve with cumulative AE counts from the optical fiber sensor (Digitizer 1). First AE was detected at a large load drop at 4.3-mm deflection. After this, AE counts increased nearly linearly. When the displacement reached 9.4 mm, the loading rod penetrated through the plate and test was stopped. AE generation continued even after the test stop. The optical fiber sensor detected 902 events. These events were classified into four types based on the waveforms.

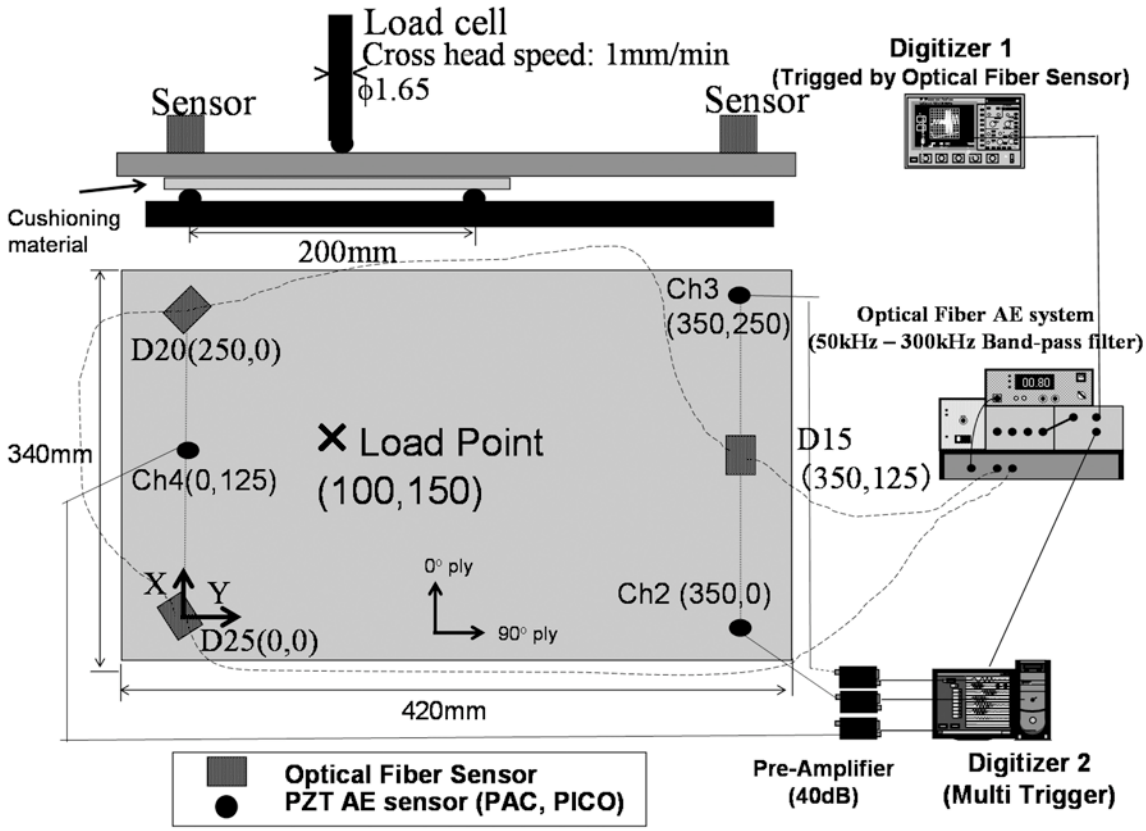

Fig. 13 Experimental setup for indentation test of a cross-ply CFRP plate and AE monitoring method.

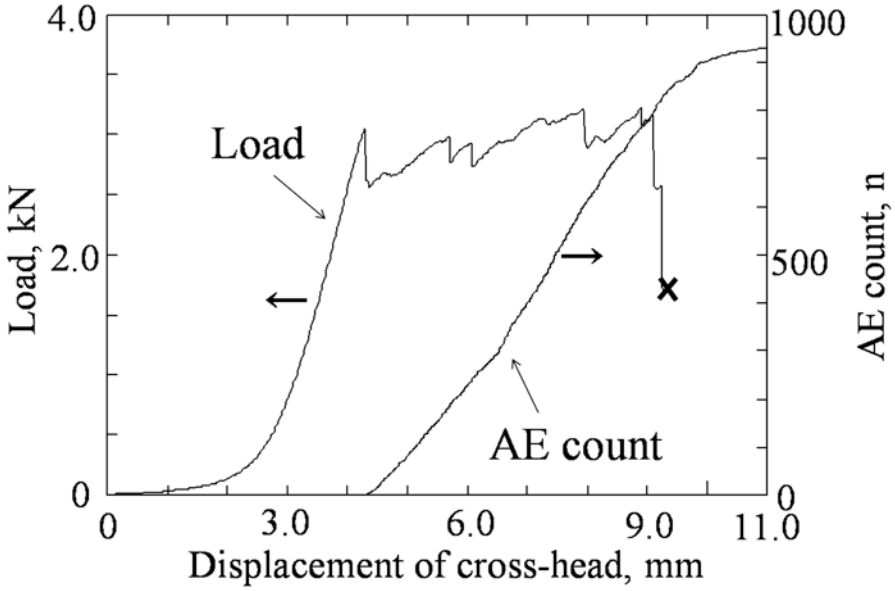

Fig. 14 Load vs. displacement curve during indentation of CFRP plate and cumulative event counts of AE signals detected by the optical fiber sensor.

Figure 15 shows typical examples of four types of AE signals detected by the optical fiber AE system. These signals were classified based on the waveform shape and the distribution of different frequency components in the wavelet coefficient diagrams. Types A and B signals initially shows higher frequency components (75~150 kHz) waves followed by strong low-frequency waves (~60 kHz, beyond 0.4 ms). The initial waves were weaker in Type A signal

than in Type B. Type-B signal has strong initial waves with comparable amplitude as the trailing low-frequency waves. Type-C signal possesses a single frequency component at ~75 kHz and it rises slowly to the peak value. Type D has initial 75-kHz components before the main waves (at 65 kHz, starting at 0.3 ms). Note that these waveforms contain signals received by all three fiber sensors. Figure 16 compares waveforms of the four-type AE signals detected by the optical fiber and PZT sensors using Digitizer 2. Since the PZT sensor responds well to 0.5 MHz, well beyond the fiber sensor range, discrimination of high frequency components can be expected and separation of Lamb-wave modes may be possible by careful comparison. This remains to be studied. In reference to the waveform characterization study by Mizutani et al. [4], we anticipate the source mechanisms of the AE signals to be from delamination, transverse crack, fiber fracture, matrix cracks and secondary frictional sources. However, signals have not been classified.

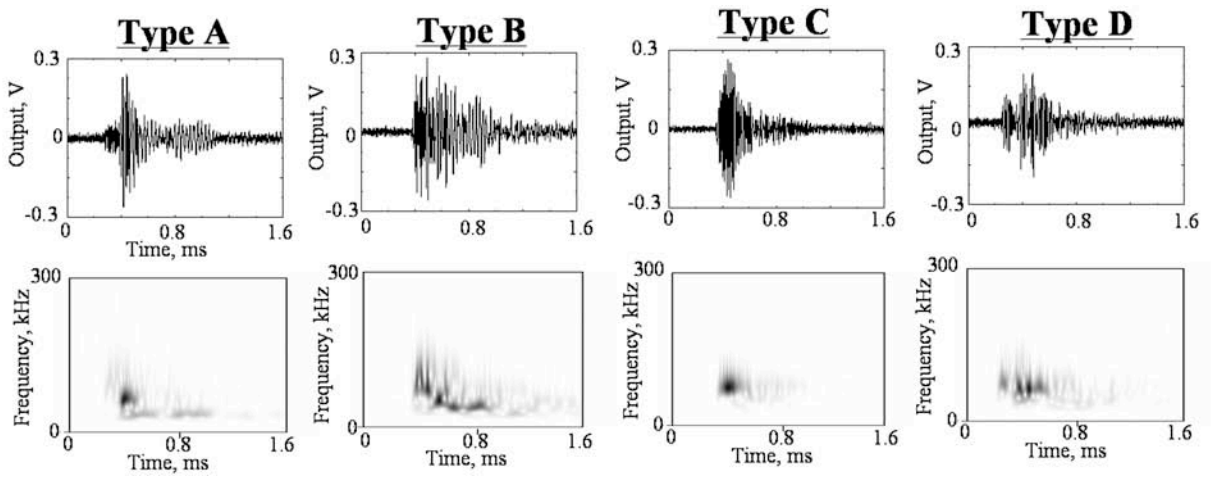

Fig. 15 Waveforms of four types of AE signals detected by cascade optical fiber sensors during indentation to a cross-ply CFRP plate. Wavelet coefficient diagrams are shown below.

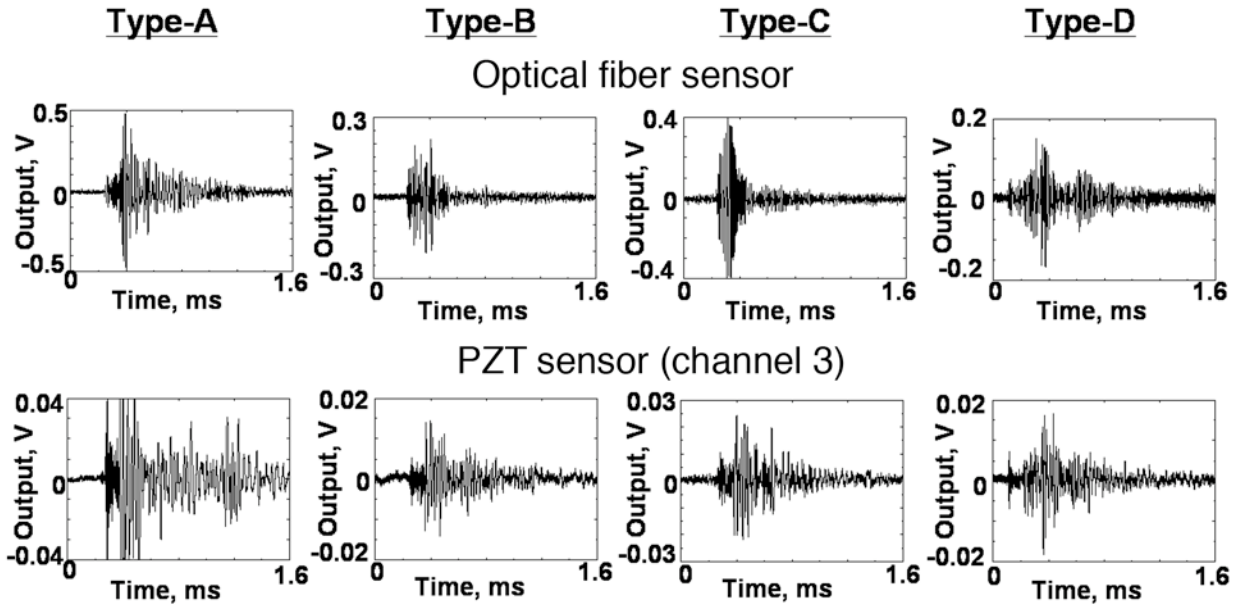

Fig. 16 Waveforms of four types of AEs detected by optical fiber sensor and PZT sensor during indentation of cross-ply CFRP plate.

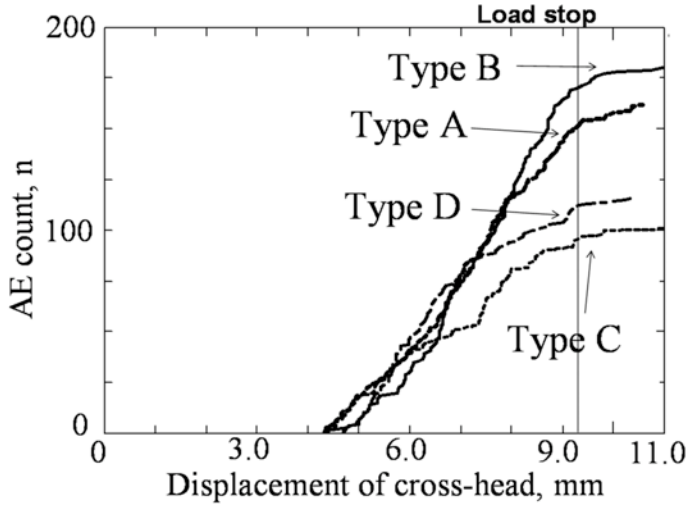

Fig. 17 Cumulative counts of AE signals vs. displacement of indenter-head.

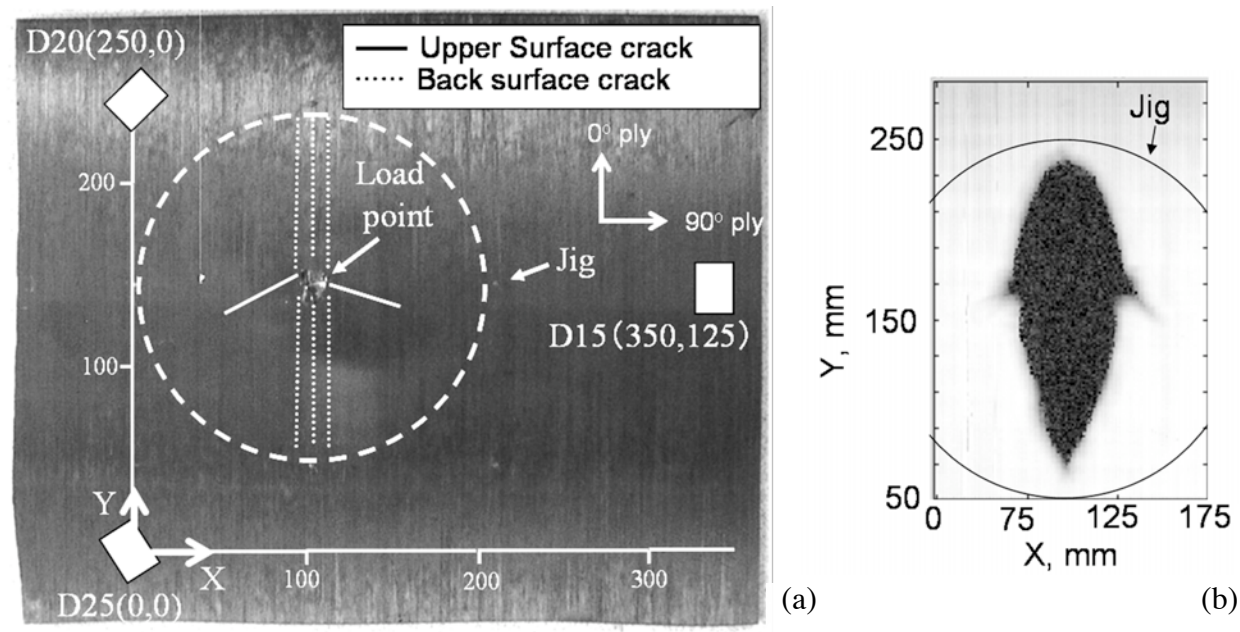

Fig. 18(a) Photograph of the upper surface of tested CFRP. Positions of upper and back surface cracks are shown. (b) Visualization of the damage distribution by using air-coupled ultrasonics.

Figure 17 shows the cumulative AE counts of four types of AE signals. It is noted that event counts of Types A and B increased almost linearly till the end of the test, but those of Types C and D signals increased linearly only for initial displacement and the rates of increase were lowered. Figure 18(a) shows the photo of upper (indentation side) surface of the CFRP plate after test. As the loading rod has a small diameter of 1.6 mm, it penetrated the CFRP and caused three types of visible damages. These are 1) fiber fracture in and near the through wall cavity, 2) fiber fracture of 50 mm length in the surface and 3) matrix crack of 100 mm length in the back surface. There are of course cracks inside. Air-coupled transmission ultrasonic image is shown in Fig. 18(b). It shows a large elliptical delamination having short axis of 50 mm and long axis of 180 mm.

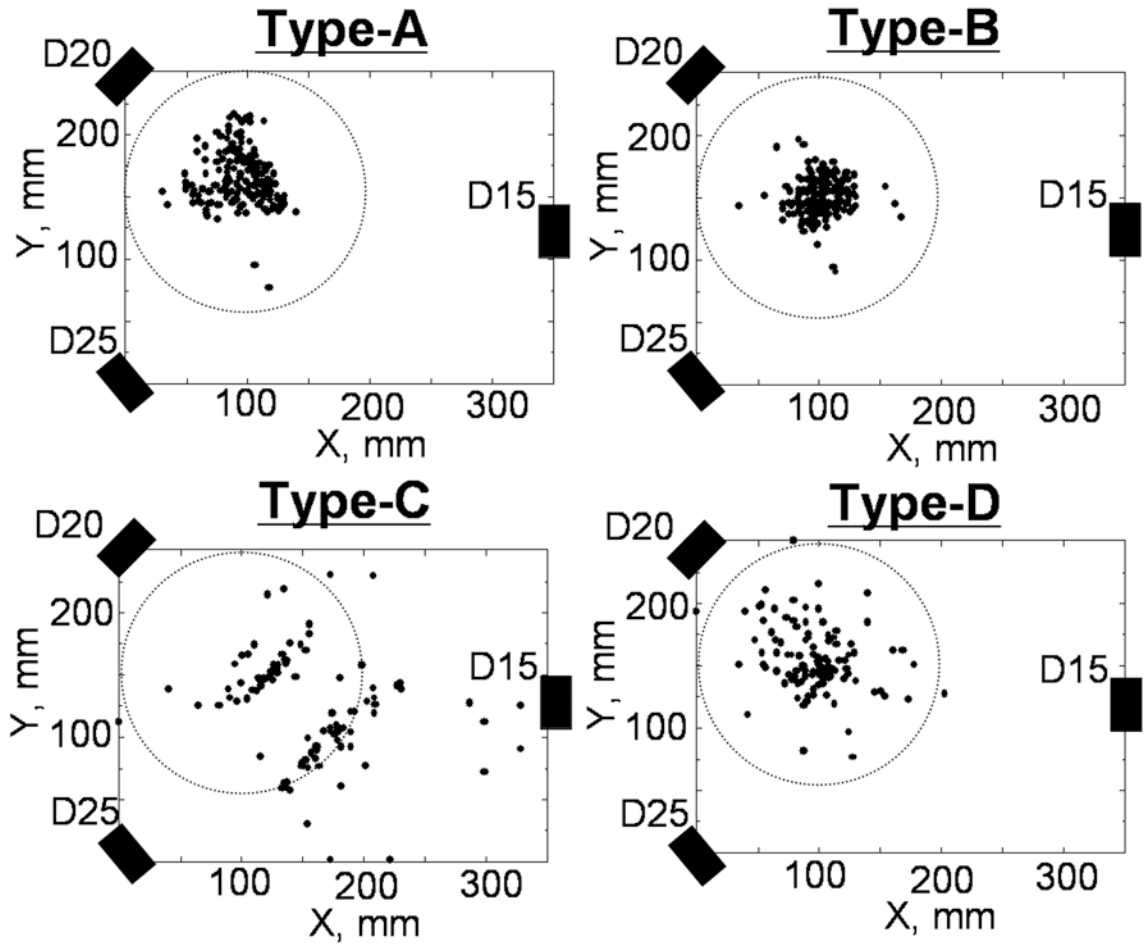

Fig. 19 Source location result of AE signals detected by cascade optical fiber sensors for cross-ply CFRP plate subjected to indentation.

Figure 19 shows source location results of four types of AE signals. Types A and B were located near the loading point. The scattering of Type-C sources may be due to their limited frequency component. Because Type-C AE signals were located along the circular jig, these are possibly from the friction of the jig and CFRP plate. In general, transverse cracks occurred around the loading point but Type-D AE signals were located over a wide zone. This demonstrates that source location is possible using a set of cascade optical fiber sensors, extracting the arrival time information. Because of the limited frequency ranges of the optical fiber sensors, however, source discrimination/identification requires further investigation.

Conclusions

We propose a new source location method of AE signals detected by cascade optical fiber sensors. Location accuracy of AE signals from artificial sources on cross-ply CFRP was studied first. We next classified AE signals from internal damages in a CFRP plate subjected to indentation. Sources of classified signals were located using the proposed method. Results are summarized below.

1) Cascade optical fiber sensors using horizontal sensor holders detect both the Lamb waves and resonance waves of the holders. Arrival time sequence of three sensors was successfully determined utilizing wavelet transform. AE sources of the Hsu-Nielsen and PZT transmitter

were accurately located, but those of ball drop and pull-off of a glued needle were not due to their limited frequency components.

2) We monitored AE signals from internal damages of a cross-ply CFRP plate during indentation. AE signals were classified into four types. Source mechanisms of these AE signals have not been identified yet, but their location can be estimated by extracting arrival times from cascade optical fiber sensor signals.

Acknowledgement

This research was conducted as a part of the High-Technology Research Center Program and the Center of Excellence (COE) Program, funded by the Ministry of Education, Culture, Sports, Science and Technology of Japan. We also thank for the research fund from the Japanese Federation of Private Universities.

References

[1] Y. Mizutani, Development of the Acoustic Emission Source Location Method for the Cryogenic FRP Tank, JAXA Research and Development Memorandum, RM-03-008, (2004).

[2] T. Matsuo, H. Cho and M. Takemoto, Development of a New Cascade Multi-Sensor Optical Fiber AE System, Progress in Acoustic Emission XIII, JSNDI, Tokyo, (2006), p.

[3] H. Yamada, Y. Mizutani, H. Nishino, M. Takemoto and K. Ono, Lamb wave source location of impact on anisotropic plates, J. Acoustic Emission, **18**, (2000), 51-60.

[4] Y. Mizutani, K. Nagashima, M. Takemoto, and K. Ono, Fracture mechanism characterization of cross-ply carbon-fiber composites using acoustic emission analysis, J. NDT&E International, **33**, (2000), 101-110.

ELASTIC WAVES FROM FAST HEAVY-ION IRRADIATION ON SOLIDS

TADASHI KAMBARA[1*], YASUYUKI KANAI[1], TAKAO M. KOJIMA[1], YOICHI NAKAI[1*], AKIRA YONEDA[2], YASUNORI YAMAZAKI[1], KENSUKE KAGEYAMA[3]

[1] Atomic Physics Laboratory, RIKEN, Wako, Saitama, 351-0198, Japan, [2] Nishina Center, RIKEN, Wako, Saitama, 351-0198, Japan, [3] Department of Mechanical Engineering, Saitama University, Sakura, Saitama, Saitama 338-8570, Japan.

Abstract

Fast heavy ions in GeV region penetrate in solids to mm of depth and can induce various radiation effects, which change the density and structure of the solids. The time-dependent stress and strain produced generate sound waves in ultrasonic frequencies. We have irradiated various solid samples; metals, alkali-halides and ceramics, with short-pulse heavy-ion beam of 3.8 GeV Ar and 3.54 GeV Xe from RIKEN ring cyclotron and detected elastic waves using piezoelectric sensors on the surface. Through the analyses of the observed waves we determine the position of the source and study the characteristics of the deformation processes in the medium.

Keywords: Heavy ion irradiation, radiation effects

Introduction

In the 1930's, invention of ion accelerators enabled artificial nuclear reactions with accelerated ions (charged atoms) for the first time. Since then, ion accelerators have developed to achieve higher energy and intensity as well as higher atomic number of the accelerated ions, which now covers nearly all elements up to uranium. Heavy-ion accelerators are now utilized in not only nuclear physics but also various applications. Radiation effects in materials induced by fast heavy-ions have also been studied and they were found to be diverse and complicated, depending on the accelerated ions, their speed and target materials.

The energy-loss processes of fast ions in matters are rather well understood. When a fast ion penetrates in matter, it loses its kinetic energy due to successive collisions with the atoms in the matter along its path, and finally stops. The decrease rate of the ion energy per its path length is called linear energy transfer (LET) and the total length of the ion path in the matter is called range. There are some common features of the energy-loss processes: When the ion is faster than the orbital electrons in the matter (around 10^{-2} of the speed of light), the collision processes are mainly electronic excitations and ionization of the atoms. This case is called "electronic stopping". When the ion is slower, the energy loss is mainly through direct collisions between the ion and whole atoms. This case is called as "nuclear stopping". The LET is higher for ions of heavier elements, and as a function of ion velocity it has a maximum at about 3-10% of the speed of light. Ziegler et al. developed a group of computer programs (SRIM) to estimate LET and range of various ions as functions of the ion velocity and the composition of the solid [1].

---

* Present address: Nishina Center, RIKEN, Wako, Saitama 351-0198 Japan

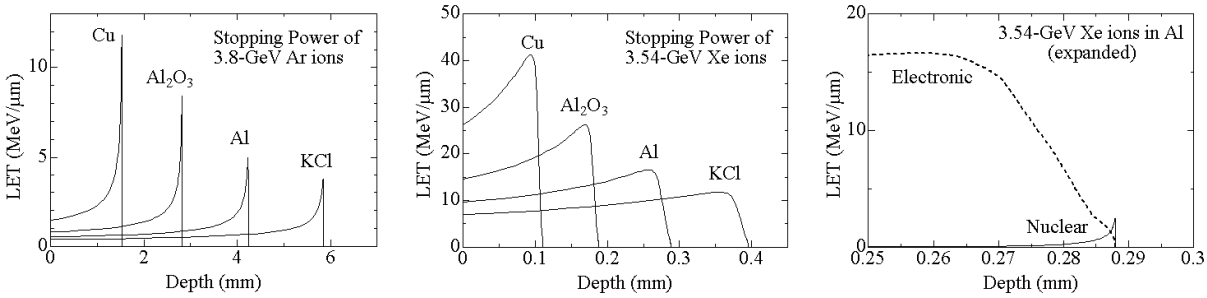

Fig. 1 Calculated LET of 3.8-GeV Ar ions (left) and 3.54 GeV Xe ions (middle) in copper, alumina, aluminum and KCl. Right figure shows the electronic and nuclear LETs of Xe ions in aluminum at the end of the range.

Figure 1 shows calculation results with SRIM of LETs due to electronic and nuclear stopping processes of 3.8-GeV argon ions (42% of the speed of light) and 3.54-GeV xenon ions (23% of the speed of light), which we have used for our experiments described later, in copper, alumina, aluminum and KCl as functions of the penetration depth. Slightly before the end of the range, the electronic LET has a maximum which is called a Bragg peak. The electronic LET dominates the nuclear one except at the very end of the range. For example, the 3.54-GeV xenon ion penetrates aluminum to 0.288 mm, and the nuclear stopping dominates only within 10 μm from the end of the range. The Bragg peak of the electronic stopping is at 0.26 mm.

A material under irradiation may change its structure and properties by the interactions with ions. In the nuclear stopping, the ion directly kicks the atoms in the material from the original position and produces lattice defects consisting of vacancies and interstitial atoms. In the electron stopping, the kinetic energy of the ion is first converted to the electrons in the matter and is then transferred to the lattice, and it may finally cause atomic displacements and produce defects. The interstitial atoms and vacancies thus produced may move in the material, recombine each other, be absorbed at grain boundary and surface, or accumulate. Since fast heavy ions have larger LET than other kinds of radiation, they deposit high density of energy in small region along the path. The radiation effects may leave permanent damages like destruction of lattice structure [2, 3], accumulation of interstitial atoms and vacancies and plastic flow of matter [4] and may change the mechanical, thermal and electromagnetic properties of the material.

Since the radiation effects of fast heavy ions are strongest near the end of the range where LET has maximum, the resultant radiation damage should reside deep in a bulk for very fast ions. Such radiation effects have been studied through microscopic observations [5], X-ray diffraction [6] or measurements of the electromagnetic characteristics [7] after the irradiations. On the other hand, real-time and on-line observation of the dynamical processes inside matter has been difficult and few experiments have been reported.

When irradiation changes the structure or density of matter or causes mechanical effects in a short time, it may generate stress and strain, which propagate as elastic waves and can be observed on the surface by ultrasonic sensors. Since many materials can transmit elastic waves effectively, acoustic emission (AE) technique can be a good tool for real-time and non-destructive study of the radiation-caused dynamical process. It can also be used to diagnose the radiation-caused damages in matter, especially at future high-energy and high-current ion accelerators.

We have studied the AE from fast heavy-ion irradiations in matters at RIKEN [8-11]. The propagation time of the AE waves was measured to determine the position of the wave source. The AE waveform was measured at different positions relative to the wave source and the kinematical characteristics of the stress at the wave source is discussed based on the onset height of the observed wave. Here we report on the experimental procedures and summarize the results we have obtained.

Experimental Procedures

The experiments have been performed at RIKEN accelerator facility with a beam of ^{40}Ar ions at energy of 3.8 GeV (0.61 nJ) and ^{136}Xe ions at 3.54 GeV (0.57 nJ). In order to determine the start time of elastic-wave propagation, the ion beam was bunched to pulses of 3 ns duration and a repetition frequency of 10-100 Hz. After acceleration by RIKEN Ring Cyclotron, the beam was introduced to an experimental setup shown in Fig. 2. Before the beam bunch reached a target, it passed through two aluminum foils and secondary electrons were collected for measurements of beam-bunch characteristics: 1) The time structure of the beam bunch was measured with a micro-channel plate (MCP) and 2) the number of ions in a beam bunch was measured with electron collectors. One ion bunch consisted of 10^2 to 10^4 ions, depending on the ion species and accelerator conditions.

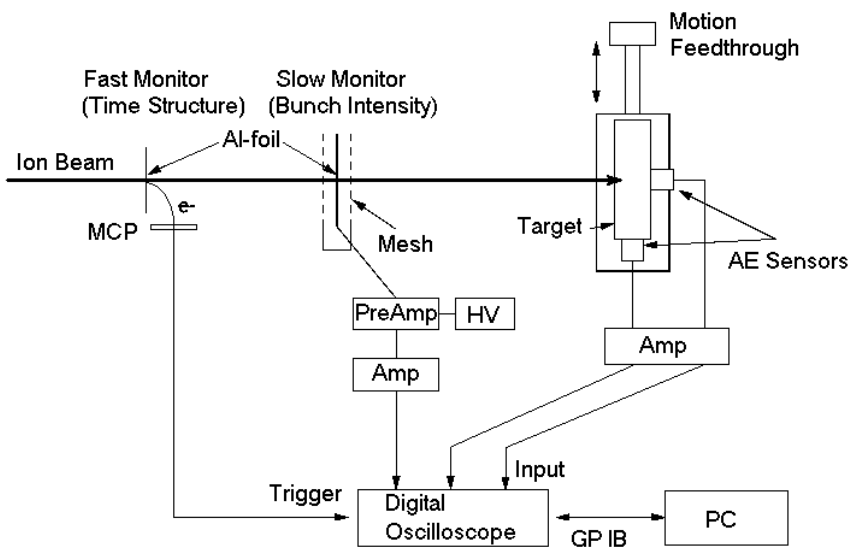

Fig. 2 Experimental setup.

The target materials were polycrystalline Al and Cu, Invar alloy, single crystals of LiF, KCl and BaF_2, fused silica and agate (SiO_2), and polycrystalline Al_2O_3. The target was square-shaped plate which was 40 mm × 40 mm or 35 mm × 35 mm in size and up to 10 mm in thickness. The ions were normally incident to the square-shaped surface of the target with a typical beam-spot size of 4 mm and all the ions were stopped in the target. The velocities of the elastic P and S waves were measured separately with a sing-around method.

The elastic waves were detected by two piezoelectric AE sensors (M304A, Fuji Ceramics) on the surface of the target: One, called hereafter as “back sensor”, was at the center of the surface opposite to the beam spot, and the other, called as “side sensor”, was on the side surface. The sensor was pressed to the target surface by a spring at 1 kg force and vacuum grease as couplant.

In order to measure the waveforms at different positions relative to the beam spot, the target and the sensors were fixed on a holder, which was movable perpendicularly relative to the beam. The signals from the AE sensors were amplified by preamplifiers A1002. A digital oscilloscope Tektronix TDS3054, which was triggered by the fast monitor, recorded the AE signals as well as the signals from the slow and fast monitors. About 50 sets of the waveforms were recorded at one beam-spot position, and the measurements were performed at different beam-spot positions within ±12 mm relative to the target center. The recorded waveforms were later sorted by the beam-bunch quality and averaged to reduce noise.

Results

In our experiments, acoustic emissions were observed for all target materials except for fused silica and Invar alloy, and the observed waveforms have some common features. Figure 3 shows examples of observed AE waveforms from a 10-mm-thick copper target irradiated with a 3.8-GeV Ar beam: Fig. 3(a) shows waveforms from the side sensor and Fig. 3(b) from the back sensor. The estimated range of the ion was about 1.54 mm and the velocities of the P wave and S wave in the target was 4711 m/s and 2275 m/s, respectively. At the top of each is shown the beam-bunch signal from the fast monitor and below are the AE sensor outputs obtained at different beam-spot positions aligned by 1-mm step. Each AE waveform is normalized to 1000 ions in a beam bunch. The numbers at the right-hand side of the graph indicate the sensor position relative to the epicenter. Zero of the time axis corresponds to the arrival time of the beam bunch to the target. Each waveform here is an average over up to 50 of beam bunches. Curves marked as P, PP, PPP and S show the expected arrival time of the P and S waves from a wave source presumed at the end of the ion range.

A. Propagation Time and Source Position

The start of the AE wave is later than the beam-bunch arrival and the delay depends on the position of the sensor relative to the epicenter. Since the ions stop in the target within picoseconds and the energy is transferred from the electrons to the lattice system within nanoseconds, we expect that the delay of the AE signal from the ion-beam arrival is due to the propagation of the elastic waves from the source to the sensors. As shown in Fig. 3(a), the delay time for the side sensor increases in proportion to the distance from the epicenter and is consistent with the P-wave propagation time. On the other hand, the delay time for the back sensor in Fig. 3(b) is shortest at the epicenter where the sensor is closest to the source, and is also consistent with the P-wave propagation time.

When the back sensor is at the epicenter and the delay is shortest, the depth R of the wave source from the beam spot surface is expressed as the following:

$$R = D - v_P t_d \tag{1}$$

where t_d is the time of delay, D is the thickness of the target plate, and v_p is the velocity of the elastic wave in the target. Using equation (1) the depth R was estimated for different target materials irradiated with the 3.8-GeV Ar ions [9]. For various target materials, the experimental results were in good agreement with the ranges calculated with SRIM within 11 %. It means that the source of the wave is close to the end of the ion range or the Bragg peak for any material. Solid lines in Fig. 3 show the expected arrival times of the P wave from a source assumed at the end of the calculated range: P is for the direct propagation, PP with one reflection and PPP with

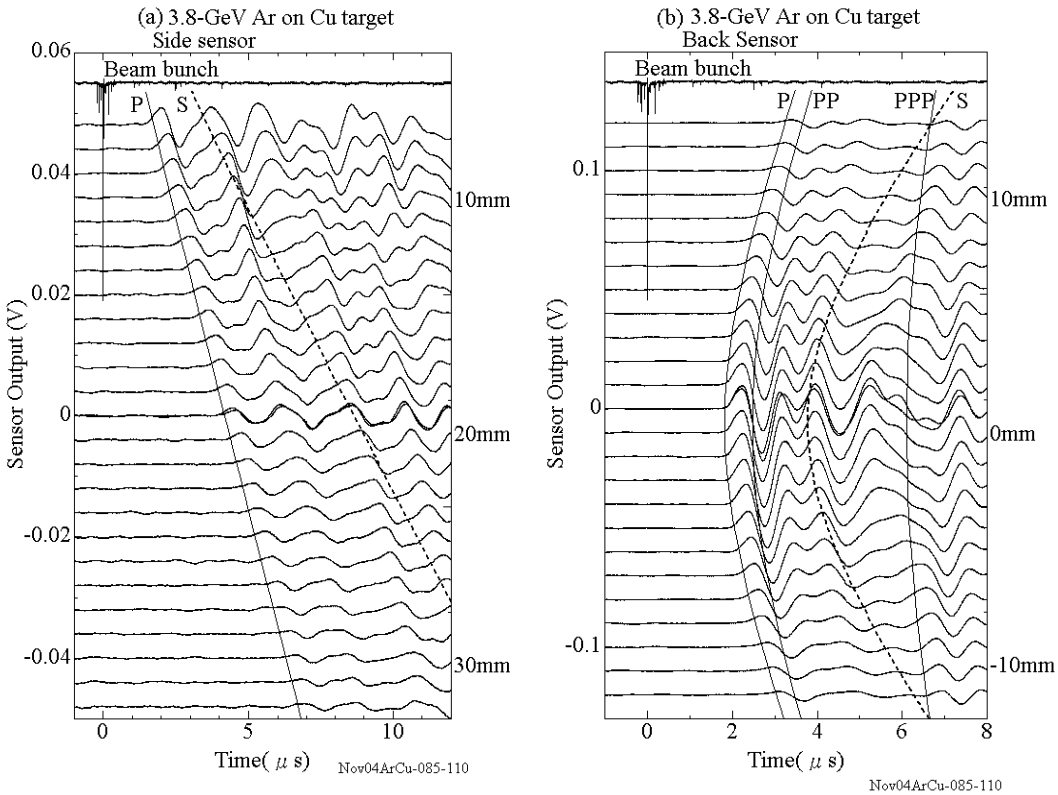

Fig. 3 Waveforms from AE sensors at (a) side and (b) back of a Cu target, irradiated with an Ar-beam bunch. Curves show the expected arrival times of the P and S waves.

two reflections at the surface. The onset time of the AE wave matches the expected P-wave arrival time, and there are also structures at expected arrival time of the twice-reflected P waves (PPP). On the other hand, no structure is observed along the S wave arrival time. The absence of the S-wave is common for the Ar-ion irradiation on different targets.

B. Position Dependence of Waveforms and Source Characteristics

The generation and the propagation of the elastic waves in the matter have been discussed on the basis of a kinematical model of seismology [10]. The dynamics of the source was replaced by a seismic moment tensor which represents a set of double force couple at the source. The displacement at any point in the matter can be expressed by the moment tensor and a Green function. To simplify the problem, we took the wave source as a point assuming that the source was small compared to the wavelength and adopted the Green function of an infinite homogeneous and isotropic medium. From the axial symmetry of the system about the incident beam, only diagonal components of the moment tensor remain to be non-zero and the source motion should be either an isotropic expansion or one-dimensional stretch motion in the beam direction. In the former case, an isotropic P wave is generated whereas in the latter case both P and S waves are generated and the S wave should have about 5 times higher amplitude than the P wave. The amplitudes of the far-field waves decrease as the inverse of the distance.

The experimental AE waveforms from the side sensor, as shown in Figure 3(a), are almost similar except for those at a few positions close to the epicenter, and the amplitude decreases with the distance from the source. The onset amplitude is nearly inversely proportional to the

distance to the wave source. These facts indicate that we observed far-field P wave and it propagated in the matter by several cm without much attenuation. The onset amplitude from the back sensor, as shown in Fig. 3(b), follows the prediction of vertical component of the P-wave amplitude from an isotropic expansion at the source. In our present experiments with the Ar beam, we have not observed an indication of S wave in the AE waves. From these findings we have concluded that the wave-source motion should be almost isotropic expansion in the matter, and the motion has little correlation with the beam direction.

C. Matter Dependence of Amplitude

In the experiments with 3.8-GeVAr-ions, no AE waves were observed from two of the target materials; Invar alloy and fused silica. A common feature of the two is low thermal expansion rates. This fact indicates that the expansion could be attributed to a thermo-elastic process as a thermal expansion.

D. Xe-ion Irradiations

Similar experiments were performed with 3.54-GeV Xe ions [11]. Several features of the observed waveforms are briefly listed:

1. Like in the Ar-ion irradiations, P wave is observed in the Xe-ion irradiations but the waveform is different. Especially those observed by the back sensor near the epicenter contain a high-frequency component.
2. In addition to P wave, S wave was observed for some materials.
3. For Al and Cu targets, the depth of the wave source was estimated from measurements of the propagation time of the P wave at the epicenter and it was consistent to the end of the range.

Although the Xe ion has almost same kinetic energy as the Ar ions, it has a larger LET, by a factor of 3-5, and therefore shorter range by more than 10 in the same matter, as shown in Fig. 1. The large LET and short range should be responsible for the waveform differences but details are not clear yet.

Summary

Acoustic emission has been observed from various materials irradiated by short bunches of fast heavy ions; 3.8-GeV Ar ions and 3.54-GeV Xe ions. The position of the wave source was estimated from the measured propagation time of the P wave and the result was consistent with calculated position of the end of the ion range for the both ions. Only P wave was observed in the Ar-ion irradiations. We have made seismological considerations on the position dependence of the wave, and revealed that the wave-source motion was mostly isotropic expansion at the end of the range or the Bragg peak. In addition, we observed no AE waves for fused silica and Invar alloy with low thermal expansion rates. These experimental results imply that the elastic waves were generated by thermo-elastic process in the matter. In the case of Xe-ion irradiations, on the other hand, S wave was observed in addition to P wave for some materials, and the waveform of the P wave at its onset looked different from that in the Ar-ion irradiations.

References

1) J.F. Ziegler, J.P. Biersack, U. Littmark: The Stopping and Range of Ions in Solids, Pergamon Press, New York, (1985).
2) N. Itoh and A. M. Stoneham: Nucl. Instr. and Meth. **B 146** (1998), 362.
3) M. Toulemonde, S. Bouffard, and F. Studer: Nucl. Instrum. and Meth. B **91** (1994), 108.
4) H. Trinkaus: Nucl. Instrum. and Meth. B **146** (1998), 204.
5) N. Kuroda, N. Ishikawa, Y. Chimi, A. Iwase, H. Ikeda, R. Yoshizaki and T. Kambara: Phys. Rev. **B63** (2001), 224502.
6) A. Iwase, N. Ishikawa, Y. Chimi, K. Tsuru, H. Wakana, O. Michikami and T. Kambara: Nucl. Instr. and Meth. **B 146** (1998), 557.
7) A. Iwase, Y. Hamatani, Y. Mukumoto, N. Ishikawa, Y. Chimi, T. Kambara, C. Müller, R. Neumann and F. Ono: Nucl. Instr. and Meth. **B 209** (2003), 323.
8) T. Kambara, Y. Kanai, T. M. Kojima, Y. Nakai, A. Yoneda, K. Kageyama, and Y. Yamazaki: Nucl. Instr. and Meth. **B 164-165** (2000), 415.
9) T. Kambara, K. Kageyama, Y. Kanai, T. M. Kojima, Y. Nakai, A. Yoneda and Y. Yamazaki: Nucl. Instr. and Meth. **B 193** (2002), 371.
10) T. Kambara: Nucl. Instr. and Meth. **B 230** (2005), 601.
11) T. Kambara: Nucl. Instr. and Meth. **B 245** (2006), 108.

ACOUSTIC EMISSION RATE BEHAVIOR OF LAMINATED WOOD SPECIMENS UNDER TENSILE LOADING

ANDREAS J. BRUNNER, MARTIN T. HOWALD* and PETER NIEMZ*
Empa – Swiss Federal Laboratories for Materials Testing and Research, Laboratory for Mechanical Systems Engineering, Überlandstrasse 129, CH-8600 Dübendorf, Switzerland.
*ETH Swiss Federal Institute of Technology, Institute for Building Materials, Schafmattstrasse 6, CH-8093 Zürich, Switzerland.

Abstract

Quasi-static tensile tests on two different types of laminated wood specimens are monitored with acoustic emission (AE). AE signal parameter data are analyzed with respect to AE rate behavior under quasi-static tensile loading to failure. For various AE signal parameters an exponential increase of the cumulative AE and of the AE rate curves is observed with time or load. The time-constant of this exponential increase is material-dependent. This is analogous to the AE rate behavior observed for various glass-fiber reinforced polymer-matrix composite specimens under similar tensile load conditions [1]. Implications of these results for damage accumulation in composites under tensile loading are discussed.

Keywords: Laminated wood, tensile test, damage accumulation, AE rate analysis

Introduction

Acoustic emission (AE) monitoring is an established technique for assessing the integrity of structures made from various materials (see, e.g., [2]). There are several standardized applications developed specifically for structures made from fiber-reinforced polymer-matrix composites (see, e.g., [3-5]). Typically, such structures are loaded by appropriate means and the resulting AE is analyzed with respect to AE activity and AE intensity, yielding an indication of the level of structural integrity. It is less common to apply AE monitoring to (standardized) materials tests in order to monitor damage accumulation. A series of such tests with different loading configurations, material and specimen types have been reported by Brunner et al. [1]. The main conclusion was that for quasi-static tests, a specific, exponential increase of the AE activity was observed with increasing load. The exponential increase (proportional to $\exp(\alpha t)$) could even be quantified by evaluating the exponential factor α. This factor was empirically shown to be independent of the AE signal parameter (AE hit, counts, energy) used to analyze the AE activity pattern, and also to be independent of the test temperature (within a specified range), but dependent on the strain rate.

Since wood can be interpreted as being a composite material also, it is of interest to see whether an analogous behavior is observed for the AE activity during quasi-static tests on wood specimens. The present paper reports on a first series of tensile tests with two different types of wood specimens.

Experimental Procedures

The specimens were of dog-bone shape, about 400 mm long, 20 mm wide gauge, 18 mm thick, and made of two different types of laminated wood (Fig. 1). The first type was medium density fiber-board (labeled Medium Density Fiberboard = MDF) with a density of 720 kg/m^3, the second particle board (labeled SP) with a density of about 650 kg/m^3. Three specimens per type were tested with quasi-static tensile crosshead displacements of either 1.7 mm/min or 2.5 mm/min.

AE was monitored with AE equipment (AMS-3, Vallen Systeme GmbH) with four resonant AE sensors (SE-150M, Dunegan Engineering Corp. Inc.). Two sensors each were mounted on either side of the specimens, at the top and bottom near the mechanical clamps, respectively (Fig. 1). The AE signal parameter set was recoded with a threshold of 31.2 dB_{AE}, a rearm-time of 1.382 ms, and with 100 kHz to 1,000 kHz band-pass frequency filters. Preamplifier gain was set at 34 dB. A silicone-free vacuum grease was used as coupling agent and the AE sensors were mounted with metal springs. AE source location was performed by linear interpolation between the two sensors (top and bottom) on either side of the specimens. An average signal speed was used, derived from Hsu-Nielsen sources applied on the surface of the specimens prior to the test.

Tensile loads were applied in a screw-driven test machine (Z100, Zwick) with a 50-kN load cell (HBM Z4). Strain was measured with a video extensometer (ME-46, Messphysik, Austria) between two marks (Fig. 1) applied within the gauge length of the specimens. Load and cross-head displacement were also recorded as analog external parameters with the AE equipment.

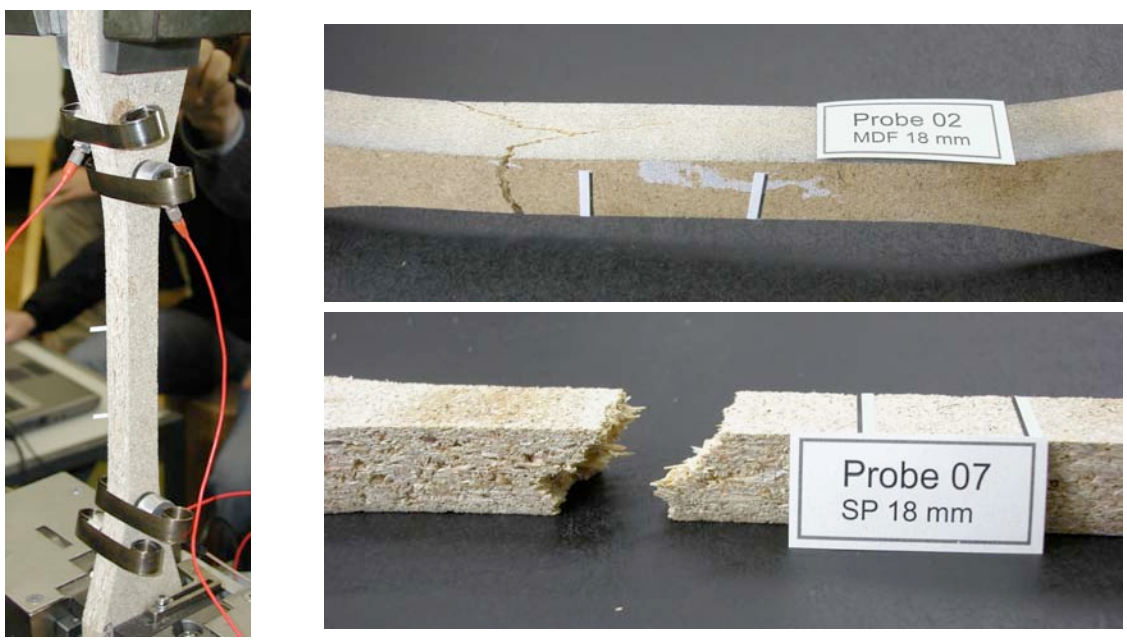

Fig. 1. (left) Experimental set-up with particle board specimen and AE sensors in test machine and (right) specimens after tensile failure (top) MDF-type, (bottom) SP-type. The white paper strips serve as reference marks for the video extensometer.

Results and Discussion

The tensile properties of the specimens are summarized in Table 1. Because of different strain-rates (crosshead speeds) used in the tests, no averages and standard deviations are quoted.

Table 1 Summary of mechanical properties from tensile tests on laminated wood specimens (σ_{max} = ultimate tensile strength, ε at F_{max} = failure strain, F_{max} = maximum load)

Specimen Type/label	E-modulus (tensile) [MPa]	σ_{max} [MPa]	ε at F_{max} [%]	F_{max} [N]	cross-section [mm^2]	crosshead speed [mm/min]
MDF / 1	3,100	18.7	0.87	7172	380.3	1.7
MDF / 2	2,620	18.9	1.02	7233	381.9	2.5
MDF / 3	4,240	18.6	0.65	6987	375.8	2.5
SP / 1	1,700	5.3	0.38	1951	368.4	2.5
SP / 2	1,350	4.8	0.45	1701	354.7	1.7
SP / 3	1,170	4.6	0.40	1634	357.7	1.7

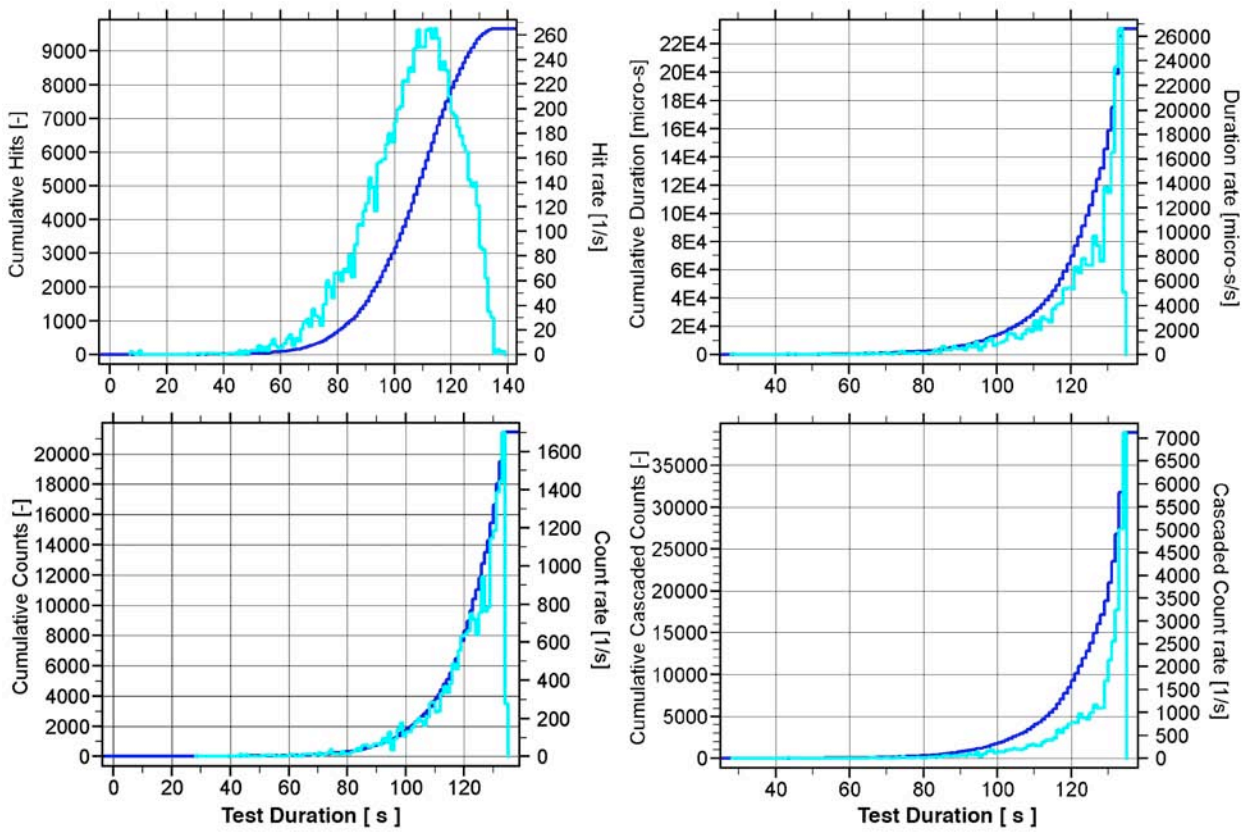

Fig. 2. Overlap of cumulative and rate-curves of selected AE signal parameters (indicated on the different graphs) from one test on one MDF specimen. The curves are shown as measured, covering the full test duration and AE signal parameter scale (dark curve = cumulative, light curve = rate). Horizontal axis is test duration, in sec.

The ultimate tensile strength in board plane of the two specimen types differs by about a factor of four, i.e., 18-19 MPa for MDF versus 4-5 MPa for particle board (SP), while the failure strains differ by about a factor of two, i.e. 0.7-1.0 % for MDF versus 0.4-0.5 % for particle board (SP). Typical macroscopic failure patterns are shown in Fig. 1. Strain rates are estimated from measured strains at maximum load and duration of the test (note that the specimens shown in Fig. 1 failed outside the measurement range).

An initial analysis checks whether an exponential behavior of AE rate and cumulative AE with time (and load in quasi-static tests) is observed. Selected examples of different AE signal parameters for one MDF specimen are shown in Fig. 2. If there is an overlap of the AE rate and the cumulative AE curves, this indicates an exponential behavior with time. The data as measured show some cases of overlap and others, where the two curves clearly deviate. If, however, the plot scales are adjusted, it can be seen that for the latter curves, an exponential behavior is observed at least for the initial part of the test, with a deviation of the two curves after a certain time (Fig. 3).

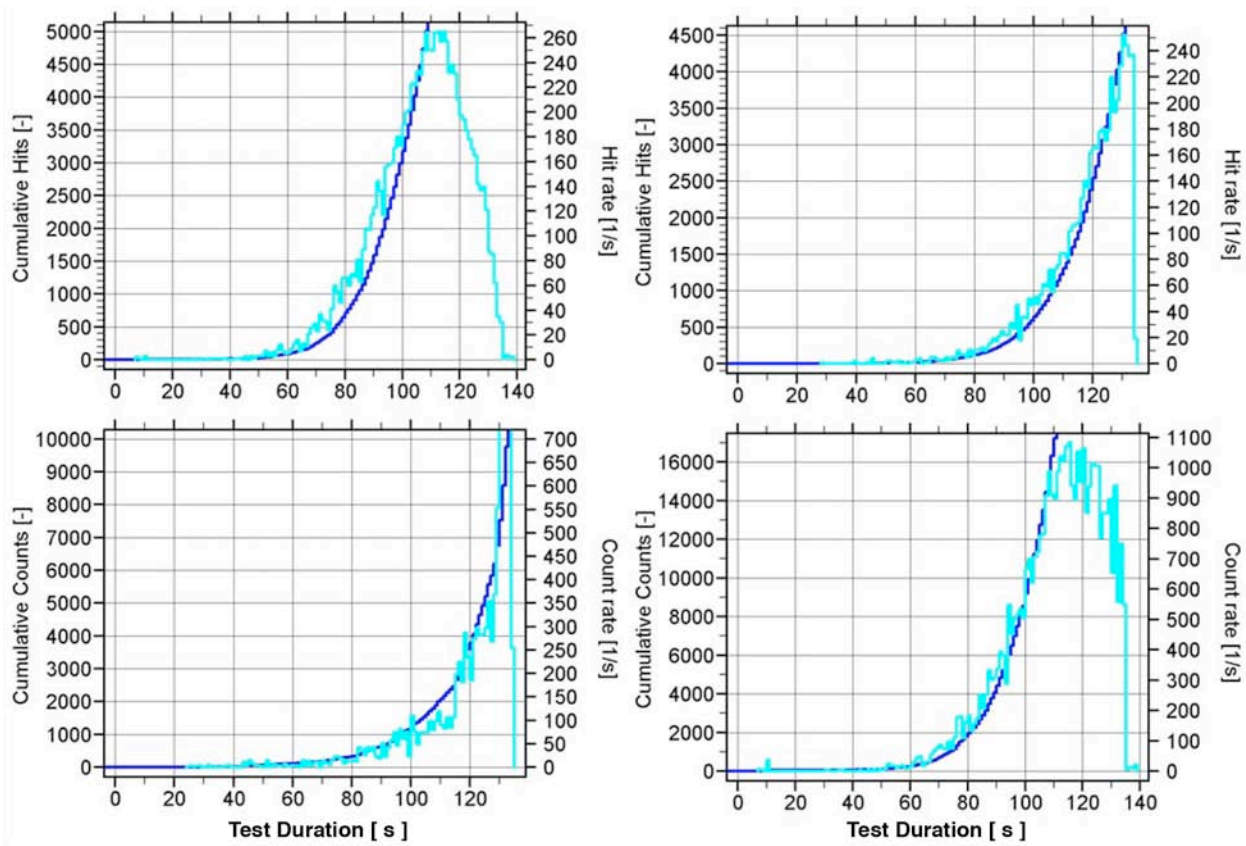

Fig. 3 Overlap of cumulative and rate-curves of AE hits (top) and AE counts (bottom) vs. test duration from tests on MDF specimens. The scale of the cumulative AE curves has partly been adjusted to emphasize the exponential behavior (dark curve = cumulative, light curve = rate).

From the ratios between the maximum scale values of the overlap plot of the cumulative and rate curves, the exponential factor α can be calculated. It is simply the ratio between the values of the AE rate curve and of the cumulative AE curve. This ratio has been calculated for all AE sensors on each specimen, using the ring-down count ("AE counts") as AE signal parameter. These values are listed in Table 2, together with the measured strain-rate. For selected specimens, the value of α has been calculated also based on the overlap plot of AE hits with time. The results (examples shown in Fig. 3) essentially yield the same values for the same value of strain rate. This confirms that as was the case for the GFRP specimens, the exponential behavior does not depend on the choice of the AE signal parameter for the analysis.

The values in Table 2 also show that for comparable crosshead speeds or strain-rates the MDF specimen type yields higher values of α than the SP type. This is similar to the situation observed for the GFRP materials, which yielded distinctly different values of α for a given strain-rate as well. Experiments varying the strain-rate over a fairly large interval indicated a linear increase of α with increasing strain-rate [1]. With the assumption that this linear behavior should include the origin (as it does seem to be the case for the GFRP), the dependence of α for the wood specimens can be plotted (Fig. 4). From that graph, a reference value for a fixed strain-rate (or crosshead speed) can be evaluated and compared with corresponding values for GFRP. Taking a crosshead speed of 1 mm/min, for example, yields values of a around 0.25 for MDF and around 0.35 for particle board (SP). This can be compared with values of 0.010, 0.020, and 0.014 s^{-1} for unidirectional glass-polyester, combined glass-mat polyester, and glass-roving epoxy (at 1 mm/min), respectively [1].

Table 2 AE rate behavior analysis: Determination of exponential coefficient α from hits and counts for the two types of specimens (strain-rate average, where applicable, average α calculated from all four sensors, stand. dev. = standard deviation)

Specimen Type	crosshead [mm/min]	strain-rate [%/min]	AE para-meter	average α [-]	stand. dev. [-]	stand. dev. [%]
MDF	1.7	0.31	hit	0.0432	0.0045	10.4
MDF	1.7	0.31	counts	0.0452	0.0068	15.1
MDF	2.5	0.40	hit	0.0561	0.0046	8.1
MDF	2.5	0.40	counts	0.0627	0.0097	15.5
SP / 2	1.7	0.41	hit	0.0614	0.0103	16.8
SP / 2	1.7	0.41	counts	0.0592	0.0090	15.2
SP / 3	2.5	0.56	hit	0.0796	0.0056	7.0
SP / 3	2.5	0.56	counts	0.0898	0.0112	12.5

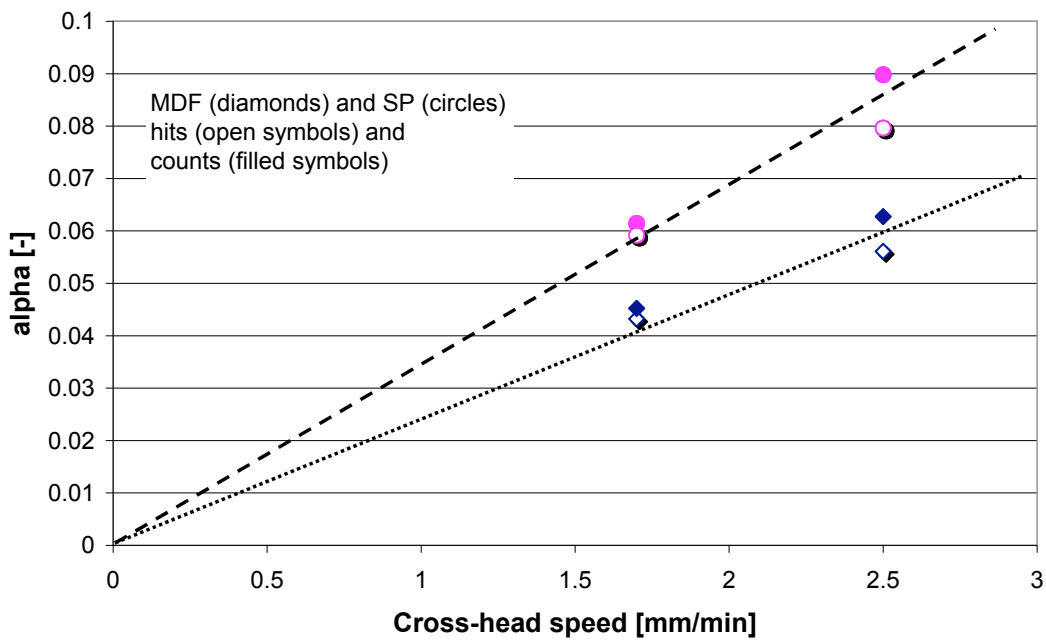

Fig. 4 Plot of average values of α for the two types of wood specimens (derived from AE count and AE hit rate behavior) as a function of crosshead speed.

The significance of the empirical analysis deriving the value of α from AE monitoring of simple, quasi-static tensile tests has not been discussed much in the original reference on the GFRP tensile specimens [1]. The exponential increase in AE rate and AE cumulative curves with time or load as shown by the analysis, however, differs qualitatively from previous models for composites, interpreting the steep increase in AE observed during the test as an "AE knee" [6]. Of course, drawing tangents on the initial and final part of the AE cumulative or rate curves will yield an apparent "knee" at the intersection of the two tangents. This intersection point, however, will not separate the curves into a "low" and "high" rate regime with a distinct transition of the activity, since the rate is following an exponential curve.

It is also important to note that not all quasi-static tensile tests on composites will yield the exponential AE rate behavior described above. Using a fiber-reinforced polymer-matrix specimen with a cross-ply lay-up (alternating 0°/90° plies, with uniaxial tensile loading along the 0°-fiber direction) yields an initial exponential increase, followed by a drop in activity and, later, the second increase in the AE rate (the second increase presumably again following an exponential behavior). This type of behavior can be explained in terms of distinctly differing dominant damage mechanisms [7] that occur sequentially. In the case of the cross-ply laminate, the first peak in the AE activity relates to transverse matrix cracking (up to saturation level), later followed by longitudinal matrix splitting upon increasing loading of the fibers along the loading direction. It is hypothesized that the exponential AE rate behavior indicates the action of one single dominant damage mechanism under the specified load type and load-rate. It is interesting that at least for the limited range of materials investigated in the two studies to date an analogous AE rate behavior is observed in spite of the apparently dissimilar nature of the test materials. The common link producing the analogous behavior does seem to be the composite nature of the materials, combining fibers inside a suitable matrix.

Summary

It has been shown that an AE rate behavior analysis applied to tensile tests on different types of glass fiber-reinforced polymer-matrix laminates is also applicable to different types of wood specimens. The AE rate determined from various AE signal parameters (e.g., hits, counts, duration, and energy) essentially indicates an exponential increase with time, or, equivalently with load in the quasi-static tests. The exponential factor α governing this AE rate increase scales linearly with crosshead speed (or strain-rate). A larger value of α for a given crosshead speed or strain-rate indicates higher AE rate increase, consistent with larger damage accumulation and lower ultimate tensile strength. Deviations from exponential AE rate behavior in quasi-static tensile tests on these materials are probably related to damage accumulation interfering with AE signal propagation, or a change in dominant damage mechanism.

References

1) A.J. Brunner, R. Nordstrom, P. Flüeler "A Study of Acoustic Emission-Rate Behavior in Glass Fiber-Reinforced Plastics", J. Acoust. Em., **13**, (3-4), (1995), 67.

2) R.K. Miller, E.v.K. Hill, P.O. Moore, *Nondestructive Testing Handbook*, Vol. 6 Acoustic Emission Testing, 3rd ed., American Society for Nondestructive Testing ASNT, Columbus, USA (2005), Chapters 8 and 11.
3) Standard Practice for Acoustic Emission Examination of Fiberglass Reinforced Plastic Resin (FRP) Tanks/Vessels, E 1067, *Annual Book of Standards*, Vol. 03.03, American Society for Testing and Materials, ASTM Intl., West Conshohocken, USA (2001).
4) Standard Test Method for Examination of Gas-Filled Filament-Wound Composite Pressure Vessels Using Acoustic Emission, E 2191, *Annual Book of Standards*, Vol. 03.03, American Society for Testing and Materials, ASTM Intl., West Conshohocken, USA (2002).
5) Standard Test Method for Acoustic Emission Examination of Pressurized Containers Made of Fiberglass Reinforced Plastic with Balsa Wood Cores, E 1888/1888M, *Annual Book of Standards*, Vol. 03.03, American Society for Testing and Materials, ASTM Intl., West Conshohocken, USA (2002).
6) J.R. Mitchell, "Standard Test to Quantify the Knee in the AE versus Load Curve as a Material Parameter for Composites", *Proceedings 3rd International Symposium on Acoustic Emission from Composites*, American Society for Nondestructive Testing ASNT, Columbus, USA (1989), pp. 207-219.
7) A.J. Brunner, R.A. Nordstrom, P. Flüeler, "Fracture Phenomena Characterization in FRP-Composites by Acoustic Emission", *Proceedings European Conference on Macromolecular Physics: Surfaces and Interfaces in Polymers and Composites* (ed. R. Pick), European Physical Society EPS, **21B** (1997), 83-84.

AE MEASUREMENTS FOR SUPERCONDUCTING DEVICES

KAZUAKI ARAI[1], KATSUYUKI KAIHO[1], HIROSHI YAMAGUCHI[1], HIROFUMI YAMASAKI[1], AKIRA NINOMIYA[2], TAKESHI ISHIGOHKA[2], KATSUTOSHI TAKANO[3], HIDEO NAKAJIMA[3] and KIYOSHI OKUNO[3]

[1] National Institute of Advanced industrial Science and Technology,
1-1-1 Umezono, Tsukuba, Ibaraki 305-8568, Japan.

[2] Seikei University, 3-3-1 Kichijoji-Kitamachi, Musashino, Tokyo 180-8633, Japan.

[3] Japan Atomic Energy Agency, 801-1 Mukouyama, Naka, Ibaraki 311-0193, Japan.

Abstract

This paper presents four topics about acoustic emission (AE) measurements for superconducting (SC) devices, which were conducted at National Institute of Advanced Industrial Science and Technology, Seikei University and Japan Atomic Energy Agency. (1) AE signals induced from typical phenomena of wire motion and friction in a high-temperature SC coil were demonstrated. AE signals of the repeated operation process by alternating current were also shown. (2) AE signals induced from a low-temperature SC coil were measured when quenching took place. AE signals have varied waveforms depending on quenching patterns, which included information of the instability and causes of quenching process. (3) AE method was applied to the International Thermonuclear Experimental Reactor (ITER) central solenoid model coil, the world's largest pulsed coil with a stored energy of 640 MJ. By measurement using multi-channel AE sensors and long duration data-acquisition, the rearrangement of the SC cables was clarified by combining AE signals and voltage signals. (4) A test result on the thin-film element for fault current limiters was shown. It is required that substrates of the elements are as thin as possible for the cost reduction. Too thin substrate is sometimes not tough for thermal stress, and time of breaking of substrate and thin-film layer was found using the AE signals and current information, respectively.

Keywords: Superconducting coil, ITER, fault current limiting element, quenching, NbTi, Nb_3Sn, $Bi_2Sr_2Ca_2Cu_3O_{10+x}$, $YBa_2Cu_3O_7$.

1. Introduction

There are many applications of SC devices for various areas including power, medical, traffic applications, fusion and high-energy physics. For those applications, SC coils (or SC magnets) play important roles because those coils can produce very high magnetic field without Joule-heating losses in superconductors.

AE measurement for SC devices was initially applied to a low-temperature SC coil and the AE signals were induced prior to the quenching of the coil [1]. Quenching means that SC state makes a drastic transition to normal state due to disturbances. That is, it was assumed that quenching can be avoided by monitoring AE signals. Since this initial research, AE measurement technique for SC coils has been studied in some institutes, and causes of AE induced from SC coils have been considered to be flux motion, strain effect and wire motion [1-4].

The AE monitoring technique has the advantage that it is not necessary to attach AE sensors directly onto the SC windings in SC devices, where SC windings should be electrically insulated from the sensors. Hence, the sensor does not disturb the SC windings. Another advantage is that one AE sensor can cover wide area of SC coil and can detect global information of SC coils.

2. Research on Superconducting Devices

A. AE signals induced from high-temperature SC winding (Motion of the coil winding)

High-temperature SC coils have high stability because their critical temperature is high compared with conventional low-temperature SC coils and their specific heat is high at its high operating temperature. Thus, the resistive transition of the high-temperature SC coil can be easily avoided.

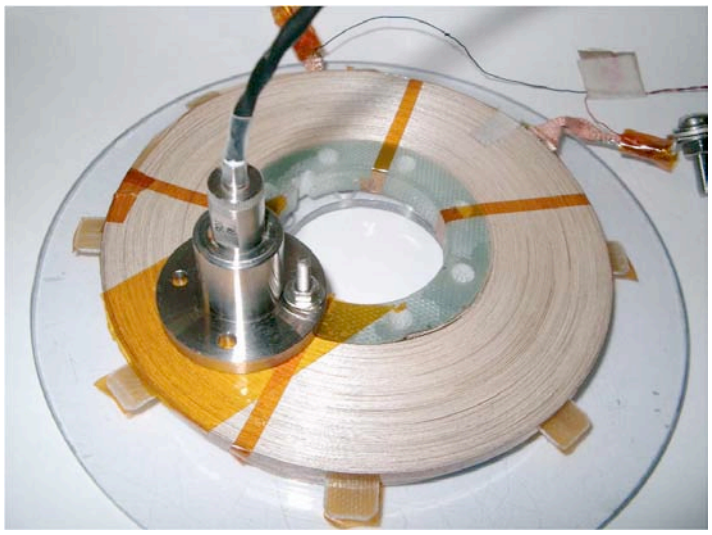

Fig. 1 The high-temperature SC coil and the AE sensor.

Figure 1 shows an SC coil using a Bi-2223 ($Bi_2Sr_2Ca_2Cu_3O_{10+x}$) high-temperature SC tape and an AE sensor, which was attached on the coil. The diameter of the sensor surface was 35 mm. Inner and outer diameters of the coil were 60 and 120 mm, respectively. There is a Kapton film between the coil and the AE sensor for insulation. The 50 Hz operating current was applied to the coil after the coil and the AE sensor were immersed in liquid nitrogen. The AE sensor has specifications for low temperature use at liquid nitrogen temperature, 77 K.

Here, in order to observe behavior of motion of SC winding, the coil was not epoxy-impregnated. The motion of the winding was induced by electromagnetic forces from the current in the winding. (Vibration of the winding of SC coils usually leads to mechanical losses. So the method such as epoxy-impregnation process may be applied to SC coils.)

Figure 2 shows 50 Hz alternating current (ac) applied to the coil and AE signals induced from the coil. Here, the envelopes of AE signals exhibit exponential decay. The current was applied five times. The AE signals drastically increased after a mechanical critical point. The source of the AE signals was mainly the friction and motion of coil winding. As the current application was repeated, the AE signals tended to decrease. The result shows the motion of the coil winding gradually settled when the ac operation was repeated, and it was demonstrated that AE measurement can detect those phenomena.

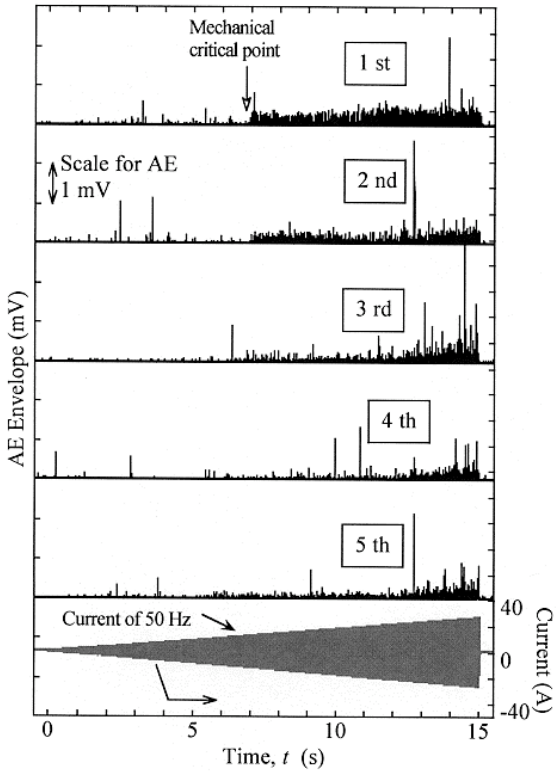

Fig. 2 AE envelopes and 50 Hz operating current when the same alternating current was applied to the coil five times.

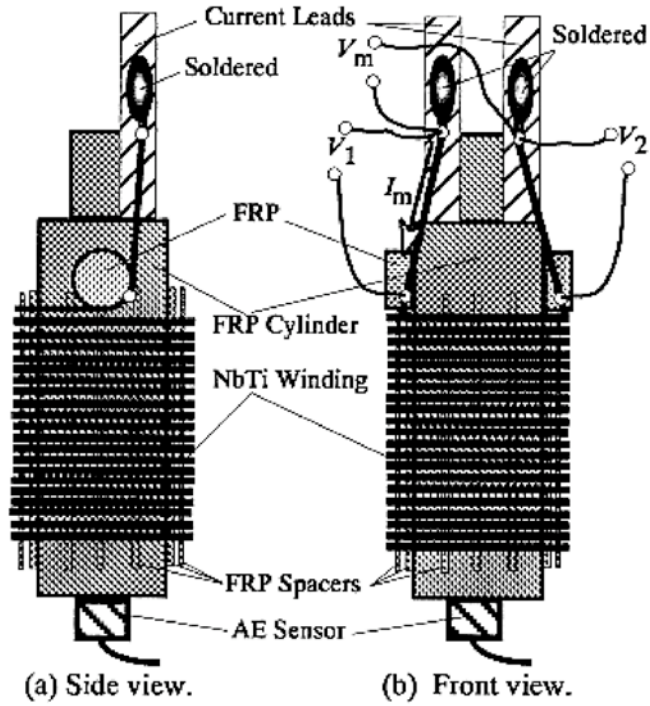

Fig. 3 Drawings of the NbTi alternating current SC coil tested at a commercial frequency of 50 Hz in liquid helium.

B. AE signals induced from low-temperature SC coil (Quenching) [5]

Figure 3 shows the drawings of a low-temperature alternating current SC coil of NbTi. The NbTi winding has specifications for an alternating current use. Inner and outer diameters of the coil winding were 30 and 33.6 mm, respectively, and height of the winding was 52.3 mm. The coil was epoxy-impregnated. Quenching tests were conducted in liquid helium at 4.2 K. In the tests, the operating alternating current was increased gradually and the quenching of the coil took place when the operating current exceeded a quenching current. The test result was shown in Fig. 4, where the vertical axis indicates the quenching current. In those tests, there are two patterns. One is the case that the quenching current was between two straight lines shown in the figure. The other is the case that the quenching current was out of this trend, which indicates the data of the 25th and 26th operation.

Figure 5(a) shows one example of AE and normal component that the quenching current was on the trend and Fig. 5(b) indicates the case of out of the trend. The normal component means the resistance values which appeared in the coil after quenching. In the case that the quenching current was on the trend as shown in Fig. 5(a), the AE signals increased with the normal component. This means that when quenching took place, the normal component grew and the normal component was a source to induce the AE signals. In the case of out of trend as shown in Fig. 5(b), the quenching took place by epoxy cracking, which induced AE signals. The epoxy cracking was a cause of local temperature rise of the coil winding, which led to quenching that increased the normal component. So the delay of the increase of the normal component can be seen compared with the rise of the AE signal in Fig. 5(b).

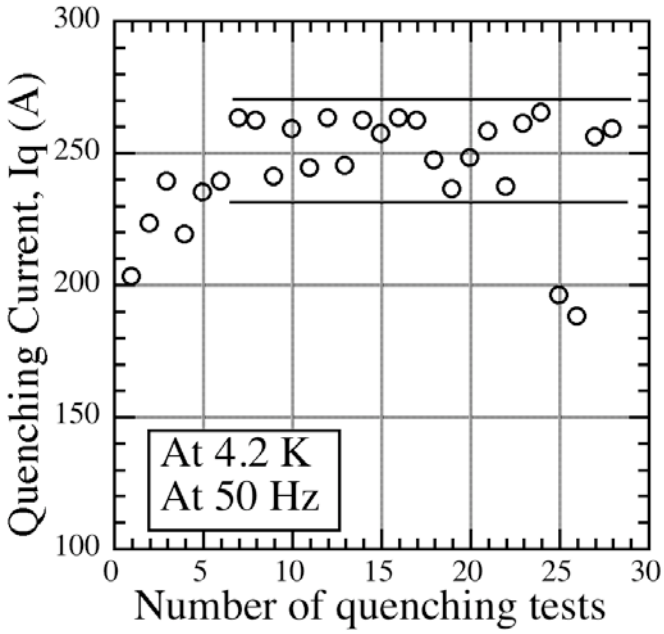

Fig. 4 Quenching current dependence on quenching test number at a commercial frequency of 50 Hz in liquid helium. Vertical axis indicates effective values of quenching currents.

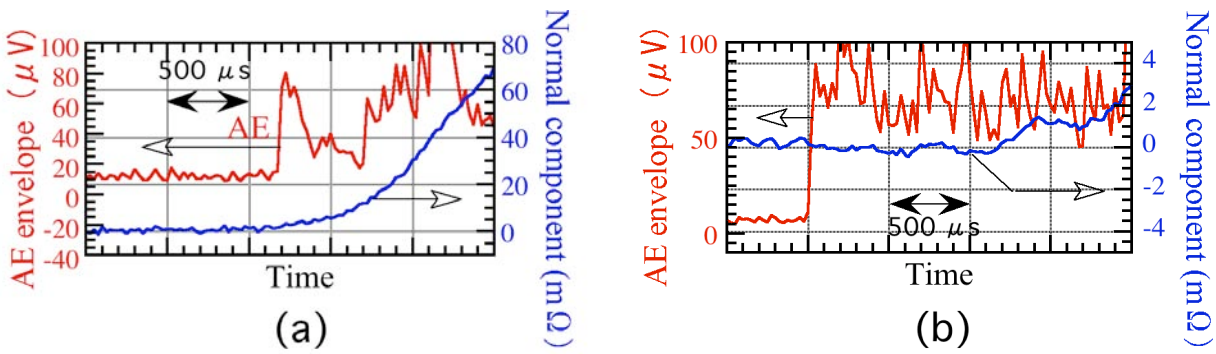

Fig. 5 Time profiles of data acquired in (a) the 24th and (b) 25th quenching test.

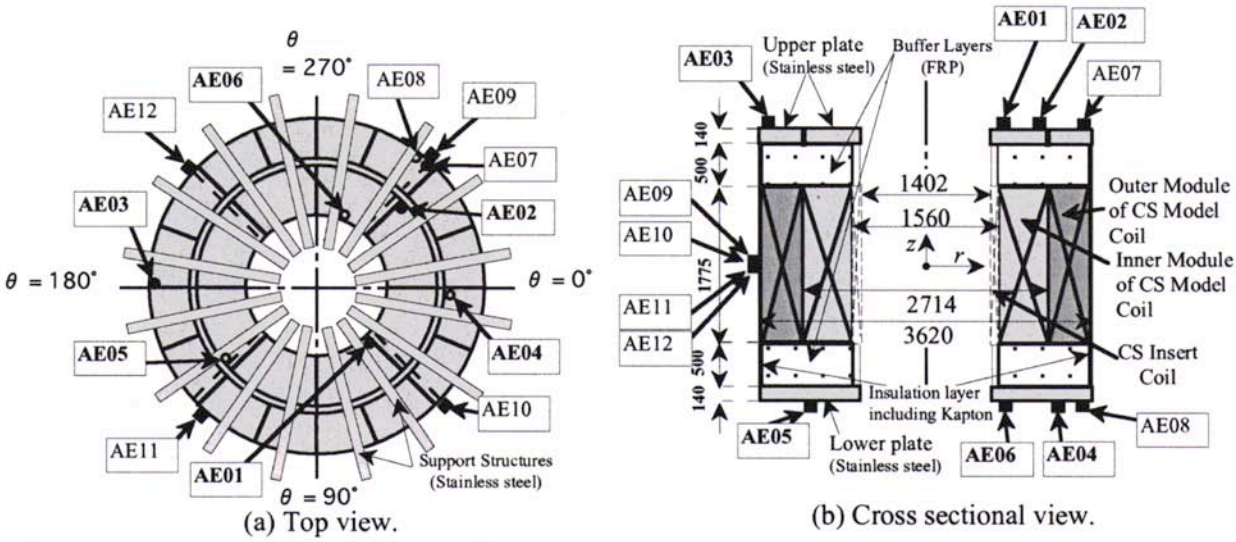

Fig. 6 ITER central solenoid model coil and AE sensors mounted on the coil.

C. AE signals induced from large-scale SC coil (Rearrangement of the SC cables) [6, 7]

As a part of the International Thermonuclear Experimental Reactor (ITER) program, a central solenoid (CS) model coil was developed in order to demonstrate the validity of the engineering design of the coil and to examine the actual performance of the CS model coil as the world's largest high-field pulsed SC coil. Figure 6 shows the drawings of the CS model coil with an inner diameter of 1.56 m and an outer diameter of 3.62 m. Twelve AE sensors were mounted on the CS model coil. The AE measurement was carried out quasi-stationary for a period; for example, 15 min. or one hour.

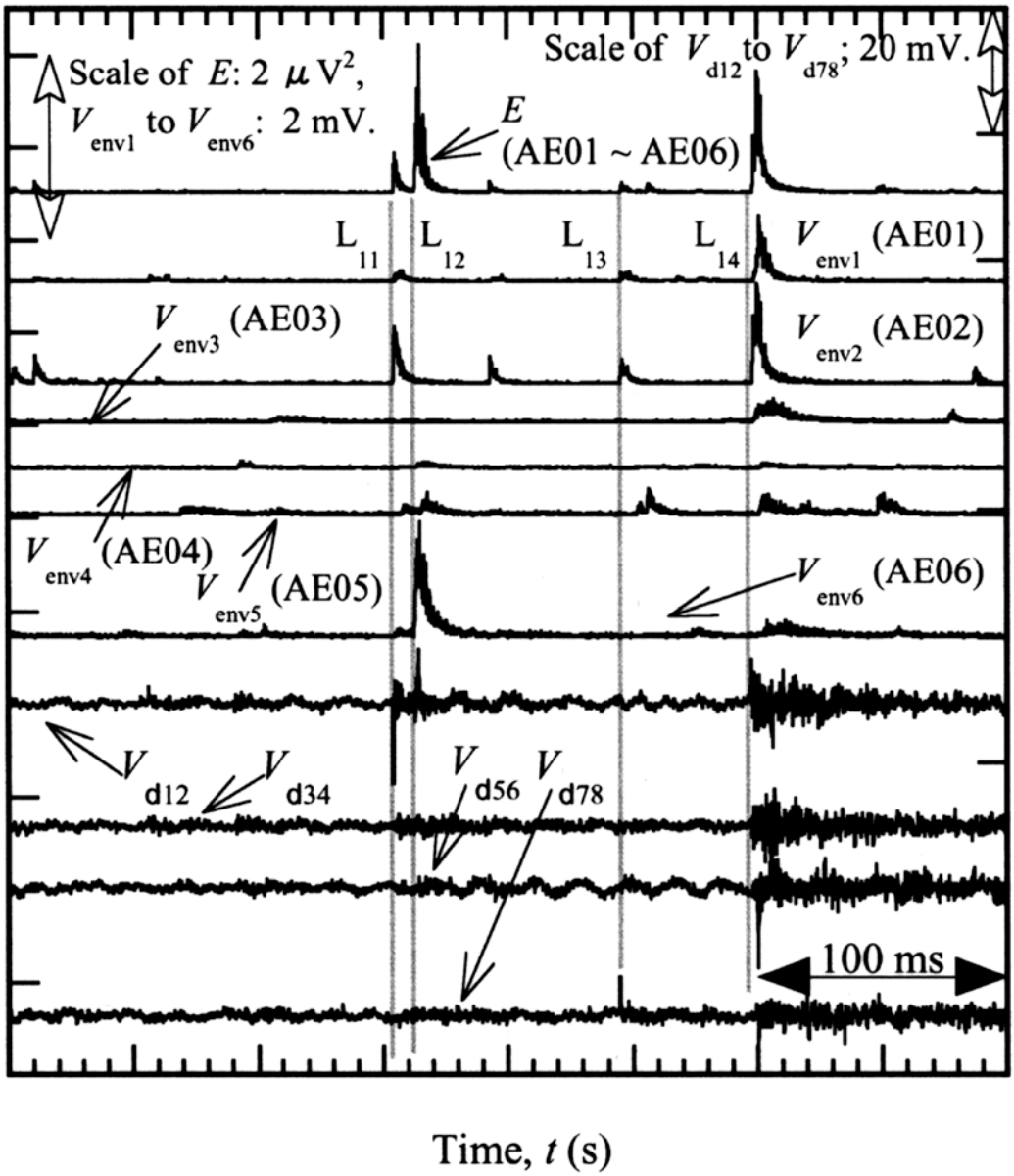

Fig. 7 AE signals and balance voltages in the virgin full-charging-up operation. The operating current was approximately 45 kA.

Figure 7 shows the data in the high current region at the operating current of approximately 45 kA. In this case, the data was obtained when the operating current increased from zero to the rated current of 46 kA. V_{env1} to V_{env6} indicate AE envelopes detected by AE sensors AE01 to AE06, respectively. V_{d12} to V_{d78} show balance voltages, where balance voltage $V_{\mathrm{d}jk}$ represents

a difference in voltages of the *j*th and *k*th layers of the CS model coil. A spike signal in V_{djk} means there was motion of the cables in the *j*th and/or *k*th layers. The 1st layer of the coil is the most inner layer having inner diameter of 1603 mm and the outer diameter of 1705 mm, and the 8th layer is placed between 2389 and 2480 mm in its diameter.

The lines L_{11} to L_{14} in Fig. 7 show clear correlations between the AE pulses and voltages, where the AE signals started to rise after voltage spikes. This implies the motion of the cables induced AE signals. In the case of L_{11}, the motion of the 1st and/or 2nd layers was induced judging from the spike in V_{d12}. The same motion induced the AE pulses in V_{env2} and V_{env1} with delays of approximately 300 and 700 μs after the rise of the voltage spike of V_{d12}. Therefore, the rearrangement of the SC cables apparently occurred near AE02 sensor and within 1st and 2nd layers at L_{11}.

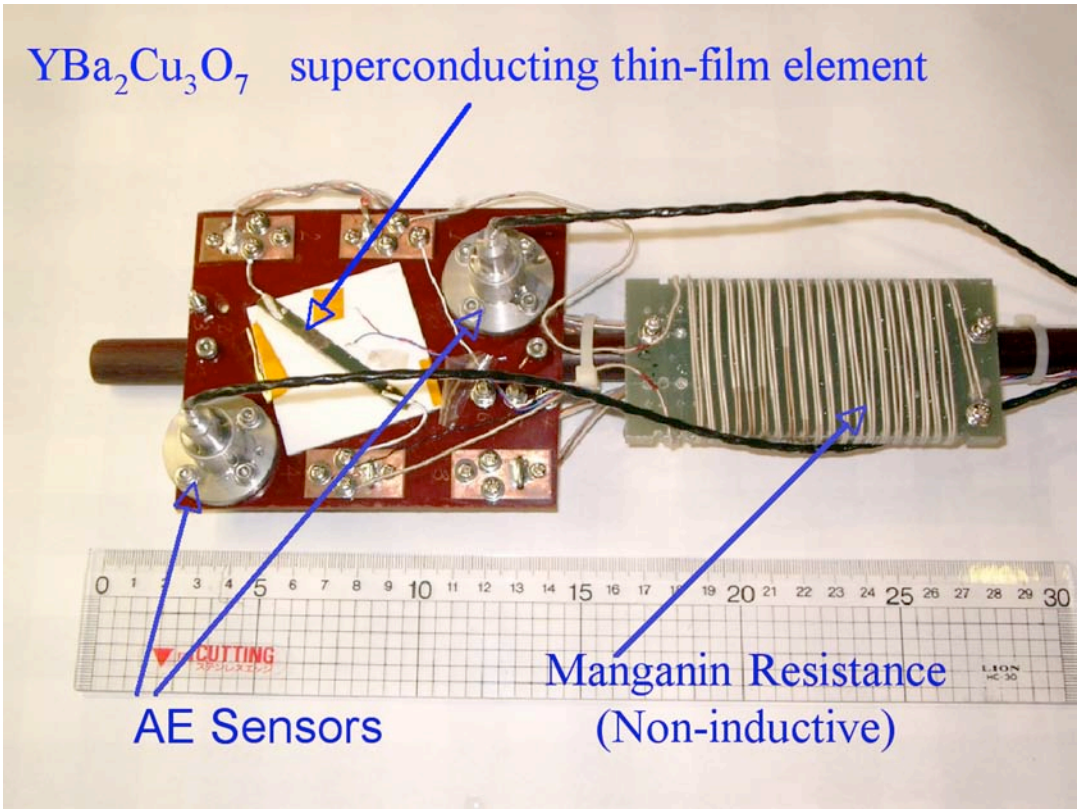

Fig. 8 Superconducting thin-film element and AE sensors.

D. AE signals induced from SC thin-film element for fault current limiter (Detection of breaking of the substrate)

Figure 8 shows an SC thin-film element and AE sensors. The thin-film element was used as a fault current limiter, which restricted fault current of the power lines when a short circuit occurred. The thin-film element was composed of a sapphire substrate and thin-film layers, where the film was composed of a $YBa_2Cu_3O_7$ SC layer and a stabilizer layer of Au-Ag.

The thin-film kept SC state while 50 or 60 Hz ac was below the rated current levels. When a fault occurred, the SC state of the thin-film element went into a resistive state. In that case, the thin-film element had high Joule heating and the substrate of the film was subjected to thermal stress.

Figure 9 shows time profiles of current I_{film}, voltage V_{film} in the thin-film element and an AE envelope when fault occurred. In this experiment, the thickness of the substrate was thinner than usual and was breakable. A large AE signal was observed as shown in Fig. 9 during the fault, where the element fractured at that instant. The reason of fracture is supposed to be thermal stress caused by a temperature difference between its center part and its gold electrode, coming from high Joule heating after the quenching took place. After the substrate fracture, the thin-film layer on the substrate fractured as indicated with the arrow in Fig. 9. These data indicate the processes of the damage to the thin-film element.

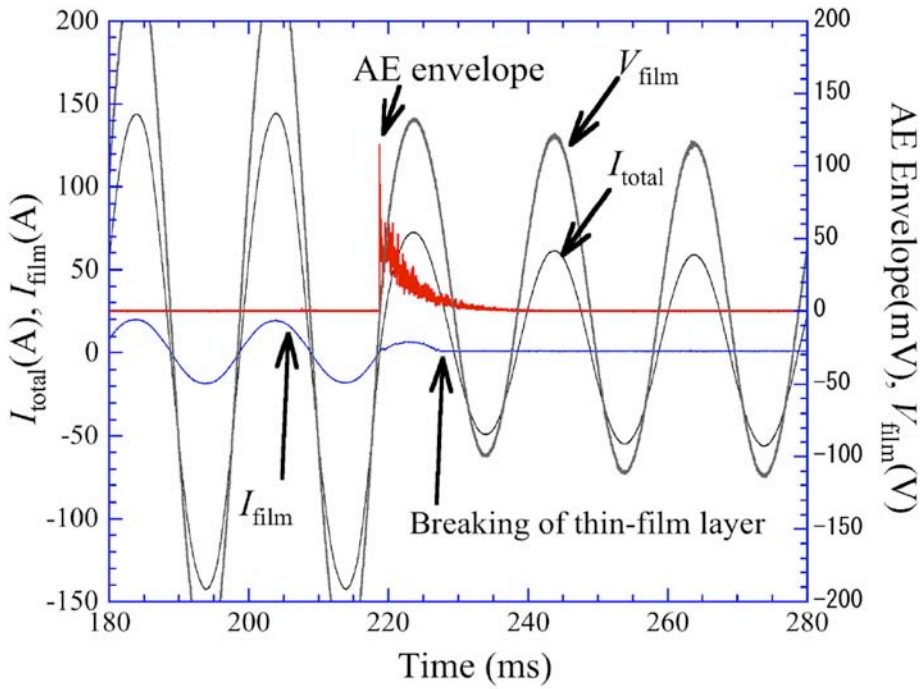

Fig. 9 AE signals induced by fracture of the substrate of the thin-film element.

3. Summary

The four topics about the AE measurements for monitoring SC devices were presented with some of the data, which were acquired at National Institute of Advanced Industrial Science and Technology, Seikei University and Japan Atomic Energy Agency. For the four cases, phenomena observed in SC devices were analyzed using AE signals along with voltage or current information. AE signals induced by mechanical phenomena provided additional information unavailable from voltage or current information.

References

1) H. Nomura, K. Takahisa, K. Koyama and T. Sakai: Acoustic emission from superconducting magnets, Cryogenics, **17** (8), 471-481 (1977).
2) C. Schmidt and G. Pasztor: Superconductors under dynamic mechanical stress, IEEE Transactions on Magnetics, **13** (1), 116-119 (1977).
3) G. Pasztor and C. Schmidt: Acoustic emission from NbTi superconductors during flux jump, Cryogenics, **19** (10), 608-610 (1979).
4) O. Tsukamoto and Y. Iwasa: Sources of acoustic emission in superconducting magnets, J. Applied Physics, **54** (2), 997-1007 (1983).

5) K. Arai, H. Yamaguchi, K. Kaiho, A. Ninomiya , T. Ishigohka, H. Fuji, N. Sadakata and T. Saitoh: Acoustic emission induced from an alternating current superconducting coil and quenching patterns, IEEE Transactions on Applied Superconductivity, **10** (1), 685-688 (2000).
6) K. Arai, A. Ninomiya, T. Ishigohka, K. Takano, K. Matsui, P. Michael, R. Vieira, N. Martovetsky K. Kaiho, H. Nakajima, Y. Takahashi, T. Kato, T. Ando, H. Tsuji and K. Okuno: Acoustic emission during DC operations of the ITER central solenoid model coil, IEEE Transactions on Applied Superconductivity, **12** (1), 504-507 (2002).
7) K. Arai, A. Ninomiya, T. Ishigohka, K. Takano, H. Nakajima, P. Michael, R. Vieira, N. Martovetsky, et al.: Acoustic emission and disturbances in central solenoid model coil for International Thermonuclear Experimental Reactor, Cryogenics, **44** (1), 15-27 (2004).

ACOUSTIC EMISSION OF SENSITIZED 304 STAINLESS STEEL WITH SIMULTANEOUS HYDROGEN CHARGING

S. H. CARPENTER, KANJI ONO* and D. ARMENTROUT
Department of Physics, University of Denver, Denver, CO 80208 USA.
*Department of Materials Science and Engineering, University of California,
Los Angeles, CA 90095 USA.

Abstract

The tensile deformation of as-received (non-heat treated) 304 stainless steel is known to produce low levels of measurable acoustic emission (AE), which only occur at failure. It is also known that cathodic charging of sensitized 304 stainless steel results in deleterious effects on the mechanical properties, and changes the AE behavior. Tensile deformation of the test sample with simultaneous charging decreases the maximum tensile load (MTL) and failure strain accompanied by a large increase in AE, observed only close to failure. Anomalous behavior occurs when the deformation is stopped after reaching the MTL and held at constant crosshead displacement. With charging maintained throughout the test, the load will decrease to zero with time, producing copious amounts of AE as failure is approached. Without charging until after the MTL is reached, the machine stoppage produces no anomalous behavior either in load or AE. These behaviors are rationalized in terms of grain boundary separation via hydrogen accumulation.

Keywords: Hydrogen charging, sensitized 304 stainless steel, stress relaxation, intergranular

Introduction

AISI 304 stainless steel (SS) containing chromium and nickel is an austenitic fcc alloy and it is widely used for its corrosion and heat-resisting properties. Stress-corrosion cracking (SCC), especially in sensitized conditions, has been studied extensively. Hydrogen also degrades the mechanical properties since the hydrogen solubility in austenitic alloys is many times higher than in bcc ferritic steels. With dissolved hydrogen, the resulting failure modes and fracture surfaces are altered as a function of heat and environmental treatments. Smith and Carpenter [1] reported that the type of failure (i.e., micro-void coalescence, transgranular and/or intergranular (IG) separations) is correlated with the measured acoustic emission (AE) generated during testing of DCB specimens, sensitized and cathodically charged with hydrogen.

Work has been continued on the tensile properties and generated AE from 304 SS varying heat treatment and cathodic charging. As-received 304 SS is known to produce very little AE when pulled to failure. If any AE is produced, it occurs just before failure. It has, however, been shown that the tensile testing of sensitized 304 SS, which has been cathodically charged during testing, will fail primarily by IG separation causing significant AE at failure. In the present investigation we have investigated the effects of current density on the tensile properties and resulting AE with simultaneous hydrogen charging. We also report results of stress relaxation experiments and their possible interpretation.

Experimental

The AE was measured using standard commercially available equipment. A resonant piezoelectric transducer with a resonant frequency of ~140 kHz (D-E S9204) was used with a Panametrics 5660B broadband (0.02–2 MHz) ac-coupled preamplifier (60 dB gain) and a bandpass filter of 100– 300 kHz for all AE experiments. The filtered and amplified AE output was then monitored by a series of HP 3400A RMS voltmeters, each with a different range. Tensile samples were machined from a rolled sheet of commercial grade 304 SS with a gage volume of 0.5 cm x 0.5 cm x 2.0 cm. The samples were sensitized before testing. The heat treatment was: 1) Solution treatment at 1373 K for 1 hour followed by water quenching. 2) Sensitization anneal at 923 K for 24 hours, furnace cooled. The sensitizing heat treatment produced an equiaxed microstructure with an average grain size of approximately 64 μm. The solution heat treatment dissolves all carbide particles and produces a uniform austenitic microstructure via quenching. The second step allows chromium carbides to form at grain boundaries. This depletes the grain boundary region of chromium. Since chromium is the main corrosion resisting element in 304 SS, the grain boundaries become more susceptible to IG corrosion and SCC as a result of the sensitizing heat treatment.

Background tensile tests were run on samples that were not charged at all and on samples that were cathodically charged in the laboratory for a predetermined time period (1 A/cm^2 for 6 hours) before testing. Most tests were run while the samples were deformed in tension (at a constant crosshead speed of 0.2 cm/min) and cathodically charged simultaneously with hydrogen [2]. In these experiments, the entire test specimen except the gage section was coated with silicone rubber. A solution cup was then glued to the sample to hold and maintain the charging solution of H_2SO_4 with traces of As_2O_3 and CS_3.

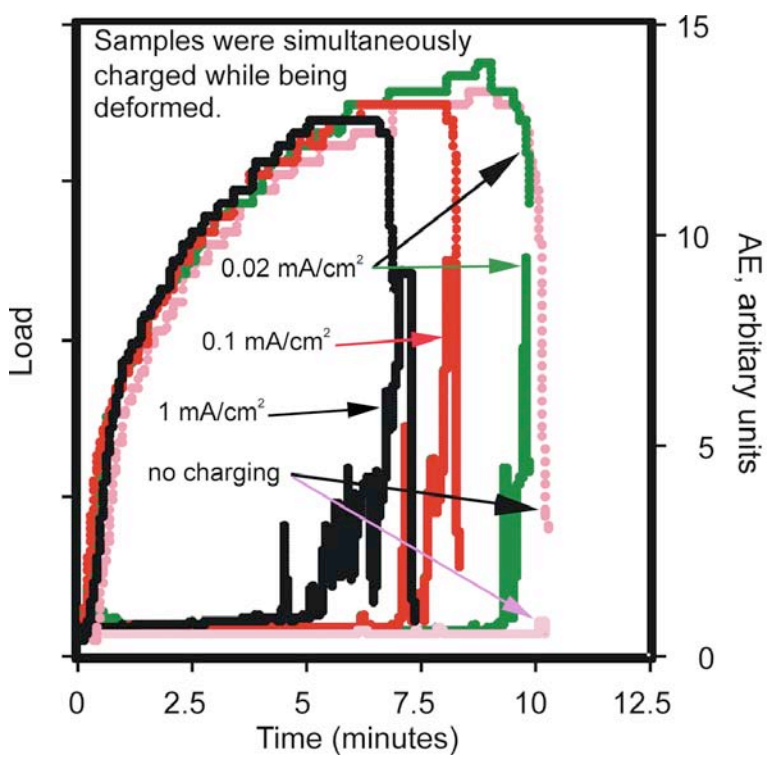

Fig. 1 Load and AE vs. time for three samples, simultaneously charged, and that for non-charged one with almost no AE.

Results

Tensile Deformation

Running tensile test and measuring the AE for two sensitized samples obtained background measurements for comparison. One was with no cathodic charging and the other sample had been cathodically pre-charged (1 A/cm^2, 6 hours) and then pulled to failure. The cathodic pre-charging significantly lowered both the MTL (–70%) and the failure strain (–15%). However, only very weak AE was detected at failure. As-sensitized sample failed mostly by micro-void coalescence together with transgranular quasi-cleavage along twins and martensite laths. Charged samples showed large areas of IG failure.

Figure 1 shows data for three samples, which were simultaneously charged during deformation (and non-charged one for comparison, shown in pink). Three different current densities (0.02, 0.1 and 1 mA/cm^2) were used, shown in green, red and black. The MTL is reduced only moderately, but the failure strain is lowered by nearly 30% with 1-mA/cm^2 charging. Notice however, that the charging lasted between 7 – 10 minutes at much lower current densities (cf. 1 A/cm^2 used on the pre-charged sample). The main difference is the amount of the AE. The AE measured from samples simultaneously being charged and deformed also occurs near the end of the test but is about 20-times higher. As the current density is increased, the AE occurred earlier in the test and was more than 20-times higher. The fracture surfaces of the failed deformed-while-charging samples are primarily IG, as shown in Fig. 2.

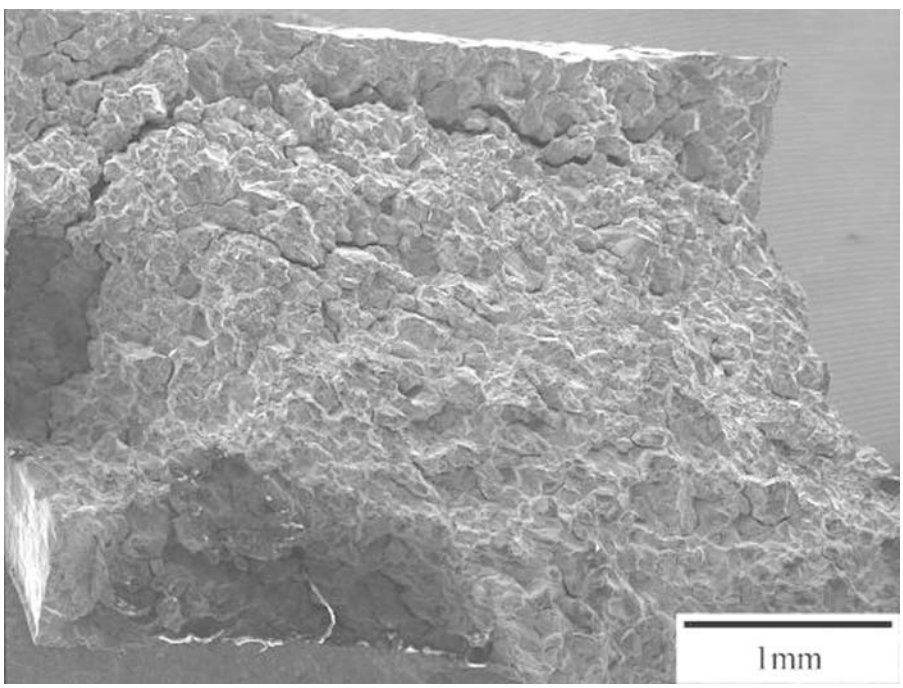

Fig. 2 Intergranular fracture surface of sensitized 304 SS, deformed to failure with charging.

Figure 3 provides a graphical compilation of the tensile properties of charged-and-deformed samples. The data has been normalized to values for the non-charged sample. The current density in mA/cm^2 used is indicated. Both the normalized MTL and the normalized failure strain decrease with increasing current density. A straight line represents the limited data obtained as shown. A limit of current density likely exists above which no further decrease in load is observed.

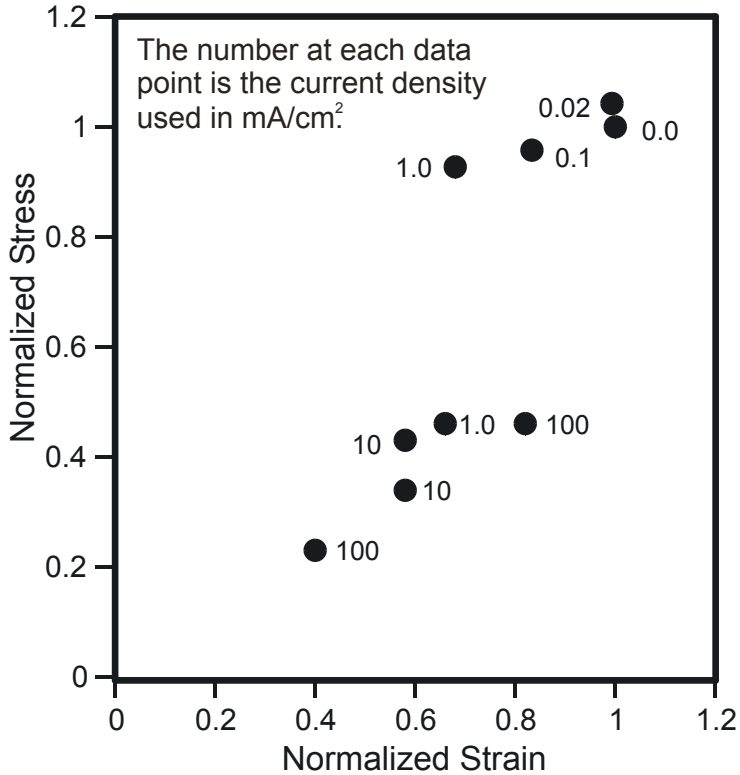

Fig. 3 MTL and failure strain data, normalized to data with no charging. Current density value is given for each point.

Stress Relaxation

In a stress relaxation experiment, the sensitized 304 SS specimen was pulled to a predetermined strain (or displacement), at which point the testing machine was stopped. Subsequent changes in load were measured while the sample was held at a constant strain. Here, the elastic strain is reduced while the sample undergoes further plastic deformation. Figure 4(a) shows the results for a tensile sample deformed just beyond the MTL at which point the machine was stopped, while cathodic charging at 100 mA/cm^2 was applied during the entire test through stress relaxation. After the deformation stoppage, the load begins to decrease almost immediately. The load decreased with time until it vanished. Notice that essentially no AE was detected until the load dropped about 20%. As the load decreased further, the AE increased to copious amounts as the sample approaches failure. Figure 4(b) shows the AE and load during the last minute of the test, when AE activities were the strongest. Figures 5 and 6 show the SEM fractographs showing IG cracking and the side surface of the sample near the failure site with numerous small cracks visible.

Whether or not a test sample is cathodically charged through the MTL has a strong effect on the load relaxation observed. Figure 7 demonstrates this effect. The upper curve is data for a sample deformed through the MTL with no cathodic charging. After passing the MTL the testing machine was stopped and charging at 100 mA/cm^2 was started and continued for the rest of the test. For this sample, relaxation of load was observed and continued indefinitely without much additional load change. No AE activities were observed throughout. Consider next the lower curve in Fig. 7. This sample was deformed and simultaneously charged at 100 mA/cm^2 from the beginning through the MTL. After passing through the MTL, the deformation stopped. Unlike the test in Fig. 4(a), the charging was discontinued. The sample again demonstrated load

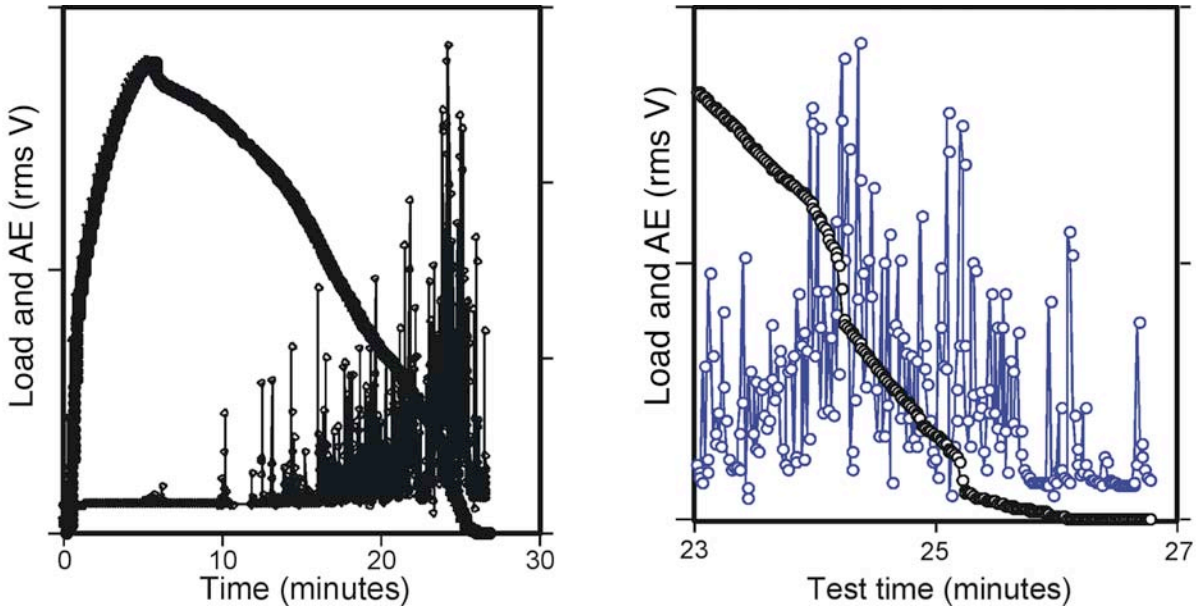

Fig. 4 (a) Stress relaxation experiment with continued charging. (b) Load and AE for the last part of the test shown in (a).

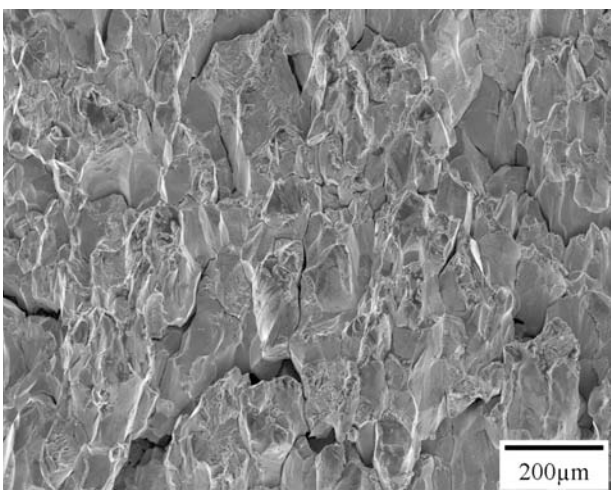

Fig. 5 Fracture surface of a sample after stress relaxation experiment.

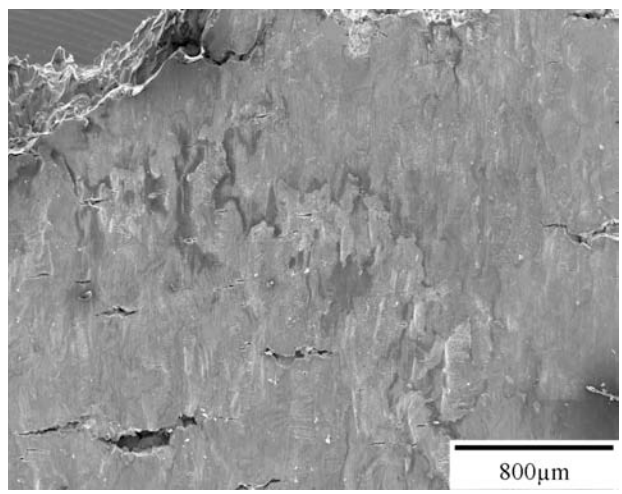

Fig. 6 Side surface of a failed sample near the fracture (cf. Fig. 5).

relaxation behavior as shown. The load decreased to zero but at a slower rate than observed with continuous charging (cf. Fig. 4(a)). In this sample, AE activities started after 20% load drop and increased to the levels similar to those in Fig. 4(a).

It has been found that one must cathodically charge the sample while it is deformed through the MTL to obtain complete load relaxation. Continual charging is not needed to achieve full relaxation. To date we have not had sufficient time to investigate the effect of using different charge densities on the load relaxation, however.

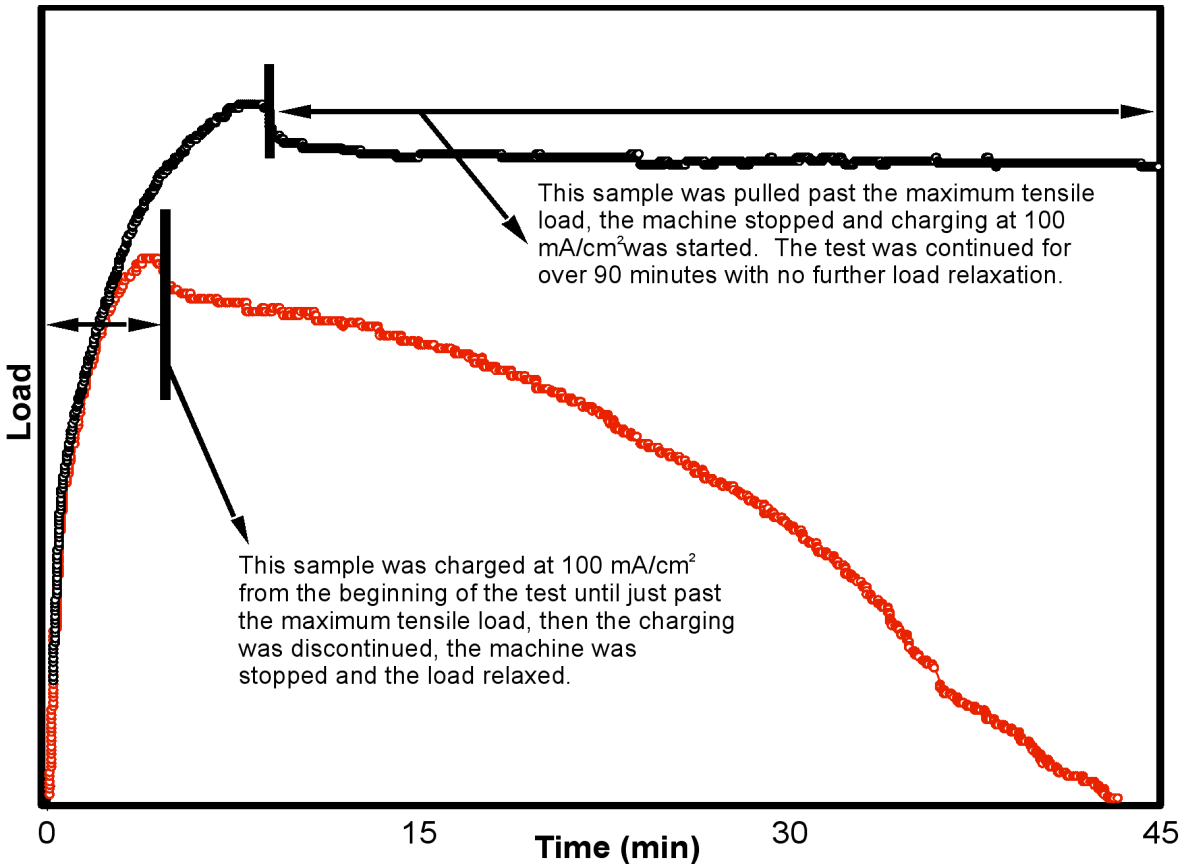

Fig. 7 Load relaxation tests of a sample charged only after passing MTL (upper curve) and that with charging till reaching MTL, then discontinuing hydrogen charging (lower curve).

Discussion

Hydrogen effects on SS continue to be investigated [3-7] in connection to hydrogen embrittlement. Thompson noted metastable austenitic stainless steels were embrittled by hydrogen charging even at room temperature [3]. The formation of hcp ε-martensite in 304 SS is reported both from cathodic hydrogen charging and from high pressure charging [4]. Existence of hydride phase is disputed and it appears hydrogen dissolves in SS without any miscibility gap, producing continuous expansion of austenite lattice. Typical cathodic charging provides 10 to 30 ppm H, whereas high pressure (3-7 GPa) charging can go as high as 100 ppm H. The amount of ε-martensite in cathodically charged 304 SS is much higher than in high pressure charged and this is attributed to the combined influence of intrinsic effects of hydrogen and the high local compressive stresses from a large hydrogen concentration gradient. This stress is estimated to be 5 GPa [6]. The maximum surface hydrogen concentration after cathodic charging was found as 10,000 ppm H [7].

Hydrogen effects on tensile properties of solution-treated 304L and 316L SS were minimal after high pressure charging to 10-30 ppm H. In all cases, reduction in area was 40%, showing ductile behavior [8]. However, high pressure charged 304L lost the fracture toughness with H addition, from 600 to 100 MPa$\sqrt{m}$ with 0 to 30 ppm H. No such effect was found on 316L SS [9]. In sharp contrast to solution-treated SS, sensitized austenitic stainless steels showed severe hydrogen embrittlement [10]. Two mechanisms have been proposed for this; the fracture of grain

boundary carbide and that of strain-induced α' martensite. A recent study shows α' martensite to be the cause [11].

Let us now consider our observations starting with the behavior of pre-charged sensitized 304 SS. The amount of cathodic hydrogen charging is estimated as 25 ppm H from comparable data, although the surface concentration is expected to be much higher as noted above. From the kinetic point of view, the diffusion coefficient of hydrogen in 304 SS at 300 K is 10^{-13} to 10^{-12} m^2/s [12]. Over 6 hours, the average hydrogen diffusion distance is 50-150 μm. For the mm-order sample dimensions, this implies the bulk diffusion is limited to the near-surface region. The fracture surfaces of samples pre-charged with hydrogen are covered with IG fracture. Since the grain boundary separation is caused by the presence of hydrogen, this observation indicates the hydrogen diffusion reaches the middle of the sample, 2.5 mm from the surface. This is feasible through grain boundary diffusion with surface compressive stress providing additional driving force. In parallel, high surface H-concentration can precipitate out as hydrogen gas at grain boundaries, thus shortening the diffusion path. Either effect can effectively produce 1000-times increase in H-diffusion coefficient. In the pre-charged sample, AE was as low as the as-sensitized SS. If the grain boundaries had been separated during the charging, no AE is expected and separated grain boundaries cannot support the load, reducing the MTL. Remaining ligaments produce little AE as is usual for SS materials.

When cathodic hydrogen charging was imposed during tensile testing (see Fig. 1), AE activity increased during loading, especially near fracture. These tests were short, all less than 10 minutes and did not provide enough time for H diffusion to the center of the sample. In these samples, IG fracture was found near surface. Some of the IG fracture must occur during deformation as AE activity accompanied later stages of plastic deformation. It has been observed that 304 SS under some SCC conditions produces AE from IG fracture, but transgranular SCC emits no AE [13]. The presence of IG fracture is expected to reduce the MTL. In addition, local residual stresses should change the MTL; when high surface compressive stress exists, complementary tensile stress must be present in the middle. This acts to reduce the MTL.

The stress relaxation experiments provide another insight to hydrogen effects observed. When samples were deformed and charged past the MTL, and the samples were held under elastic stress, the samples lost their load carrying capacity and failed in relatively short times of 20-45 min. The fracture surfaces are dominated by the IG fracture and it is clear that grain boundary separation due to hydrogen gas accumulation caused the failure. The charging did not have to continue during the load relaxation, indicating the amount of hydrogen that enters the sample till reaching the MTL was adequate. Because active AE was observed as load reduction progressed, IG fracture continued. Again, hydrogen path must have been reduced through the grain boundaries since bulk diffusion distance is around 30 μm or about one half of the average grain diameter.

When a sample deformed past MTL and then charged with hydrogen, no anomalous stress relaxation occurred. This indicates that hydrogen cannot diffuse in to interior grains even though the dislocation density is high due to heavy plastic deformation. On the other hand, hydrogen charging up to the MTL produced rapid stress relaxation. This suggests that the mere presence of dislocations and grain boundaries is inadequate to provide easy pathways for hydrogen diffusion. It is possible that a moving dislocation transport model in the SCC literature [14] is active here. We have not considered strain-induced martensite transformation in the hydrogen transport as no AE is emitted in the early stage of deformation (see Fig. 1 and Fig. 4(a)). However, this trans

formation is enhanced at higher hydrogen concentration and its contribution could be involved in the AE activity during stress relaxation.

We have attempted to rationalize anomalous stress relaxation behavior of sensitized 304 SS during hydrogen charging. Hydrogen induced grain separation is a natural mechanism deduced from our observations. Quantitative correlations of IG fracture areas to the loading capacity and finding the minimum hydrogen needed for anomalous behavior will further validate the concept given in this paper.

References

1. D.R. Smith, S.H. Carpenter, J. Acoustic Emission, **7**, (1988) 9-20; S.H. Carpenter, D.R. Smith, Met. Trans. A, **21A**, (1990) 1933-39.
2. S.H. Carpenter, W. Xu, D.R. Smith, *Progress In Acoustic Emission IV*, JSNDI, (1988) pp. 598-604.
3. A.W. Thompson, "*Hydrogen in Metals*", ASM International, Metals Park, (1974), p. 91.
4. M. Hoelzel et al., Materials Science and Engineering **A384** (2004) 255–261.
5. A. Inoue, Y. Hosoya, T. Masumoto, Trans. ISIJ **19** (1979) 170.
6. P. Rozenak, L. Zevin, D. Eliezer, J. Mater. Sci. Lett. **2** (1983) 63.
7. V.N. Bugaev et al., Int. J. Hydrogen Energy **22**(2/3) (1997) 213.
8. M. Saito et al., *Proceedings of the 11th World Hydrogen Energy Conference*, Stuttgart (Germany), 23-28 June, 1996. http://www.enaa.or.jp/WE-NET/ronbun/1996/e16/naga1996.html
9. S. Okaguchi et al., http://www.enaa.or.jp/WE-NET/ronbun/1996/e14/sumitomo1996.html
10. J.P. Fidelle et al., Hydrogen Embrittlement Testing, ASTM-STP 543, ASTM, (1974) p. 221.
11. G. Han et al., http://www.enaa.or.jp/WE-NET/ronbun/1998/08/0898.htm
12. M. Bernardini et al., J. Vac. Sci. Technol. **A16** (1) (1998) 188-193.
13. M. Takemoto, H. Cho, K. Ono, Proc. Eur. Conf. AE Testing, Berlin, (2004) pp. 617-629.
14. J.K. Tien, *Effect of Hydrogen on Behavior of Materials*, TMS-AIME, (1976) pp. 309-326.

AE AND CORROSION POTENTIAL FLUCTUATION (CPF) FOR ENVIRONMENTAL ASSISTED FRACTURE

KOJI KAGAYAMA, TAKESHI OGAWA, AKIO YONEZU, HIDEO CHO and MIKIO TAKEMOTO
College of Science and Engineering, Aoyama Gakuin University
5-10-1 Fuchinobe, Sagamihara, Kanagawa 229-8558, Japan.

Abstract

Dual phase stainless steel of austenite and ferrite possesses a susceptibility to both active-path-corrosion type SCC (APC-SCC) and delayed fracture (DF) when it is exposed to a concentrated chloride solution. We utilized acoustic emission (AE) and corrosion potential fluctuation (CPF) to study the fracture mechanism of a dual-phase stainless steel in 42 and 35 % $MgCl_2$ solution at 90 ˚C. We detected characteristic CPFs but no AE in the 42 % $MgCl_2$ solution, while we detected strong AE signals but no CPFs in the 35 % $MgCl_2$ solution. It was concluded that the environment assisted fracture in the 42 % $MgCl_2$ solution was caused by the APC-type SCC but that in the 35 % $MgCl_2$ was by the delayed fracture or hydrogen assisted cracking.

Keywords: Dual phase stainless steel, stress corrosion cracking, delayed fracture, corrosion potential fluctuation, chloride solution

Introduction

Mechanisms of environment-assisted fracture (EAF) have not been well understood in spite of a number of research studies. Here, the EAF includes both the stress-corrosion cracking (SCC) and delayed fracture (DF). The SCC occurs in a limited anodic potential range and can be prevented by the cathodic polarization. Japanese corrosion engineers consider SCC to be separate from the DF. The SCC is often called as the active-path corrosion (APC) type SCC. This means that SCC is caused by the anodic dissolution of metal along the active paths such as slip lines, grain boundaries and martensite laths, and not by the mechanical fracture. As long as the SCC is caused by anodic dissolution of metallic elements, it does not produce strong AE signals [1, 2]. Contrary to this, the DF of high strength ferritic steels is well known to produce strong AE signals [3, 4] and is accelerated by cathodic polarization where hydrogen cations can exist on the surface and in the crack.

Okada [5, 6] first studied the mechanism of APC-SCC by AE and concluded that APC-SCC did not produce strong AE signals, but the DF did produce strong AE signals. We also found that transgranular SCC (TG-SCC) of solution annealed type-304 in a 35 mass % $MgCl_2$ solution did not emit AE signals, but the intergranular SCC (IG-SCC) of sensitized 304 steel produced AE signals [7, 8]. This mechanism appears to be similar to the intergranular separation [9], observed for the sensitized type-304 stainless steel absorbing the hydrogen.

Duplex stainless steels show excellent resistance to chloride SCC. Kowaka et al. [10] studied in detail the SCC of 26Cr-Ni duplex stainless steel (DP-3 alloy by Sumimoto Metal Co.) in boiling 45 % $MgCl_2$ solution. They reported that the APC-SCC propagated through the ferrite phase (28Cr-4Ni) and stopped by austenite phase (21Cr-9Ni). Damage mechanism of the EAF is generally estimated from potential

range and fractographic (metallographic) studies, but such inverse estimation of the mechanism often leads to a wrong conclusion. Another powerful tool to study the mechanism of EAF is the corrosion potential fluctuations (CPF). Characteristic potential fluctuations were reported to occur in the APC-SCC [11, 12]. In this paper, we studied the EAF mechanism of DP-3 steel in 42 and 35 % $MgCl_2$ solution by simultaneous monitoring of AE and CPF.

Specimen and Experimental Setup

Plate shaped specimens of 20-mm width and 120-mm length and 2-mm thickness were prepared from a 20-mm thick, 100-mm wide, cold-rolled DP-3 (JIS SUS329J1L) steel plate (0.21C, 0.43Si, 0.85Mn, 0.024P, 0.001S, 25.43Cr, 7.23Ni, 3.11Mo, 0.15N) and submitted to three-point bend EAF test. The cold rolled plate shows a strong elongated texture, as shown in Fig. 1. In the figure, surface corrosion pits and fine cracks produced in 35% $MgCl_2$ solution is also shown. Specimens were sensitized by heat treatment of 923 K for 20 hours and air cooled. Vickers hardness of ferrite and austenite grains was measured as 280 and 190, respectively. Stress-strain curves of each phase were estimated by dual indentation method and shown in Fig. 2. A stress-strain curve obtained by a tensile test is also shown. It is noted that the yield strength of austenite phase (Δ) is 250 MPa but that of ferrite phase (○) is as high as 800 MPa. Fracture strain is measured as 18% by the tensile test. Sensitization treatment increased the hardness of ferrite phase significantly. This effect appears to be due to the precipitation of sigma phase.

Figure 3 shows test method of environment assisted fracture (EAF). A glass cell of 20-mm diameter was mounted on the tensile surface of a bent specimen, and filled with 42 or 35 mass% $MgCl_2$ solution. Both the cell and specimen were heated by band heater and plate-shaped ceramic heater, respectively, so that the solution and specimen temperature were at 90ºC and 80ºC, respectively. Corrosion potential was measured by a digital voltmeter using a platinum electrode immersed into the solution and fed to a personal computer. The measured potential was converted to the potential referred to an Ag/AgCl standard electrode. Vertical resolution of the potential is 0.1 μV, but the time resolution is 0.25 s.

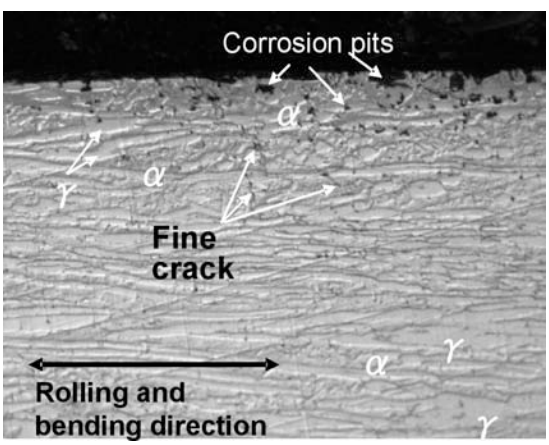

Fig. 1 Cross-sectional (transverse) microstructures of DP-3 steel, showing surface pitting corrosion and cracks after an EAF test in 35% $MgCl_2$ solution.

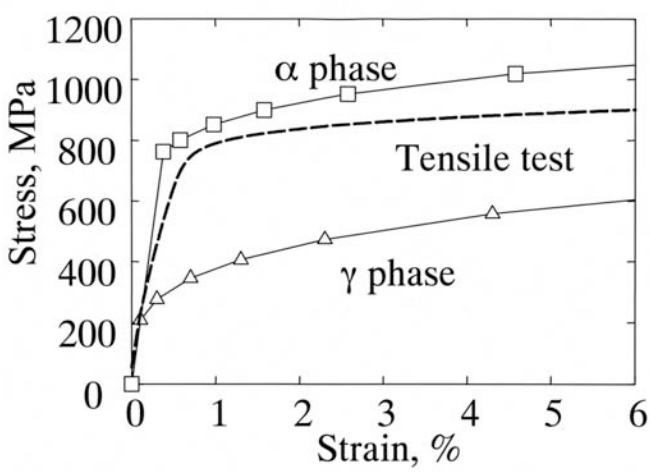

Fig. 2 Stress-strain curves of ferrite and austenite phases estimated by dual indentation test and that of DP-3 specimen by tensile test.

We monitored Lamb wave AE signals by two small resonant-type sensors (PAC, Type-Pico, resonant frequency of 0.45 MHz, sensing diameter of 3 mm) mounted on the tensile surface. Outputs of the sensors were amplified to 80 dB and digitized by an A/D converter and stored in a hard disk.

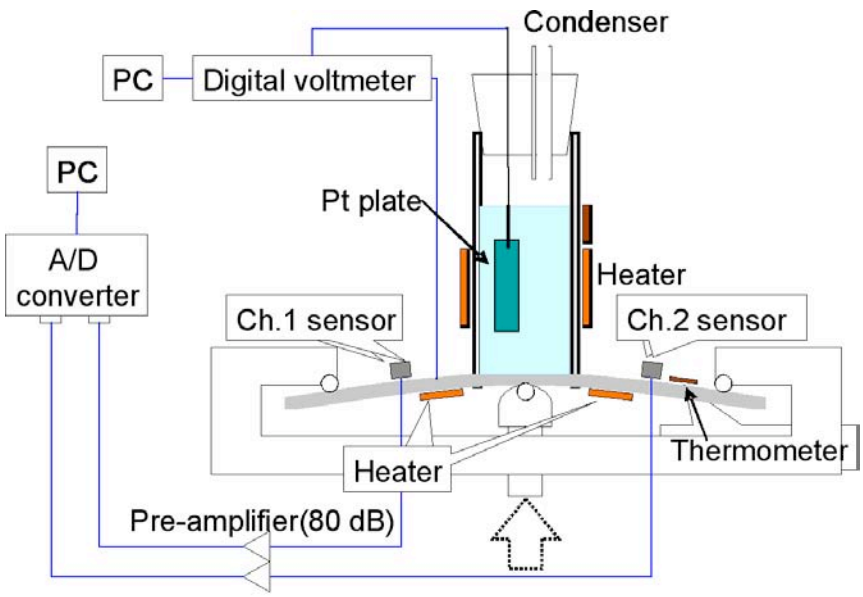

Fig. 3 Experimental setup for three point bending EAF test.

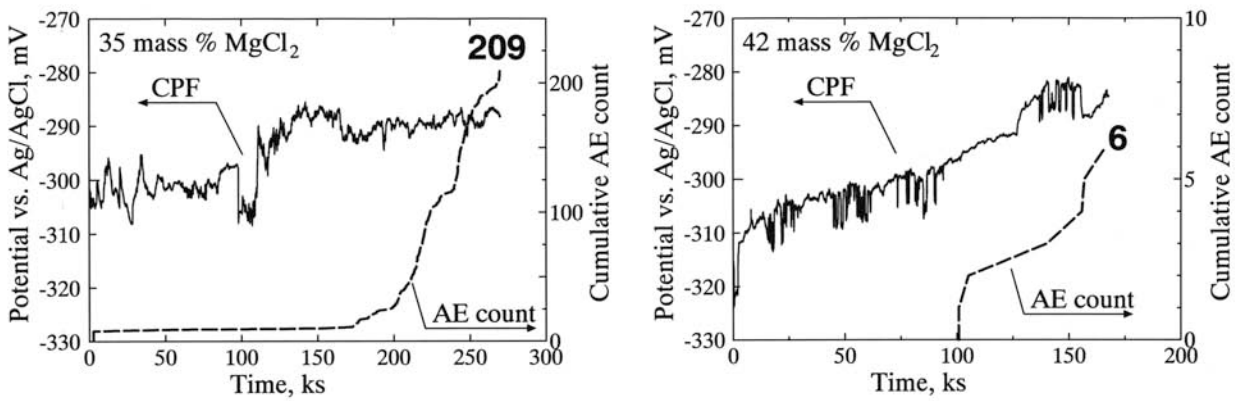

Fig. 4 Change of cumulative AE counts and corrosion potential with test time of DP-3 steel in 35 and 42 mass% $MgCl_2$ solution at 90ºC.

Results and Discussion

Figure 4 compares the change of corrosion potential and cumulative AE counts with test time in 35 and 42% $MgCl_2$ solutions. Frequent rapid-drop (RD)-type potential fluctuations were observed in the 42% $MgCl_2$ solution but no RD fluctuation in the 35% $MgCl_2$ solution. We detected a number of AE (209 events) in the 35% $MgCl_2$ solution, starting at ~170 ks, but only 6 AE events in the 42% $MgCl_2$ solution. Another experiment in the 42% $MgCl_2$ solution detected only five AE events with frequent RD-type potential fluctuations. Small, branched cracks were observed at around 100 ks in the 42% $MgCl_2$ solution, when the first AE was detected. AE counts in the 35% $MgCl_2$ solution increased rapidly at around 170 ks, or 50 ks after visible small corrosion pits appeared at 120 ks. Characterization of AE and CPF in the 42 and 35% solutions will be discussed separately in the next section.

Characterization of AE and CPF in 42% $MgCl_2$ Solution

In this solution, we detected 79 events of RD-type CPFs prior to the AE detection at 100 ks. Figure 5 shows the magnified potential fluctuation. Fluctuation magnitudes are of a few mV and weak, as shown

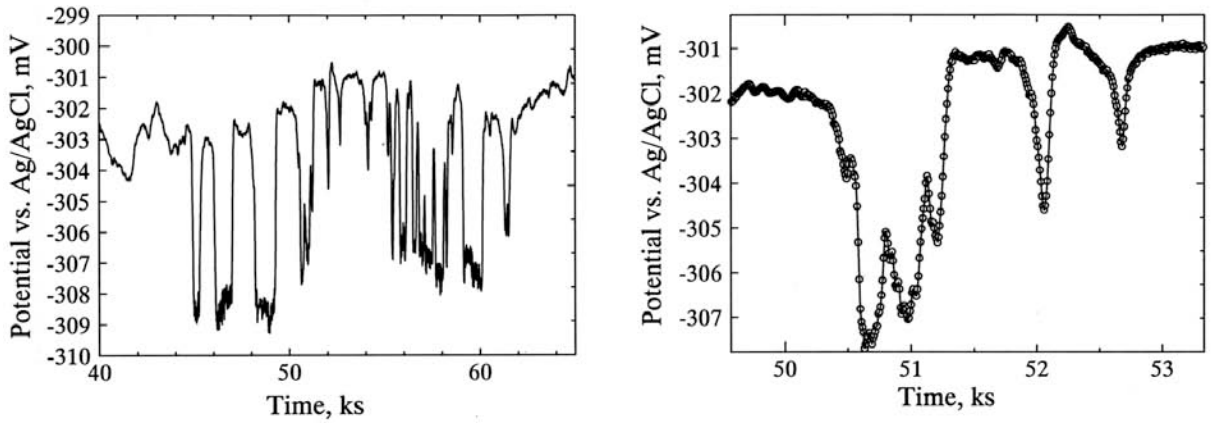

Fig. 5 Corrosion potential fluctuation detected for DP-3 steel in 42% $MgCl_2$ solution at 90ºC.

in the figure at right. The down-shooting velocity: *dE/dt*, which determines the anodic current: *I*, is low. We estimated *I* by using Eq. (1).

$$I = -C_d \times dE/dt \quad (1)$$

Here, C_d designates the capacitance of the electrochemical double layers and is taken as 20 μF/cm^2 [13]. Result is shown in Fig. 6. Current density is of order of 0.02 μA or less and is 200 times smaller than that previously estimated for the APC-SCC of Type-304 stainless steel in a 35% solution [13]. Such a small current of the DP-3 alloy is supposed to be due to the high resistance of this alloy to APC-SCC. It is noteworthy that both the anodic (+) and cathodic (–) currents were exhibited at certain periods, but they were not detected for AE generation period at around 100-130 ks. Figure 7 shows expanded sections of corrosion current vs. time. Except for E.C. 6, little corrosion current flows at the time of AE. Cathodic current suggests that the hydrogen reduction reaction is taking place in the crack and the competition of non-Faradic and Faradic reactions occurs. Hydrogen bubble formation requires prior accumulation of hydrogen reaction.

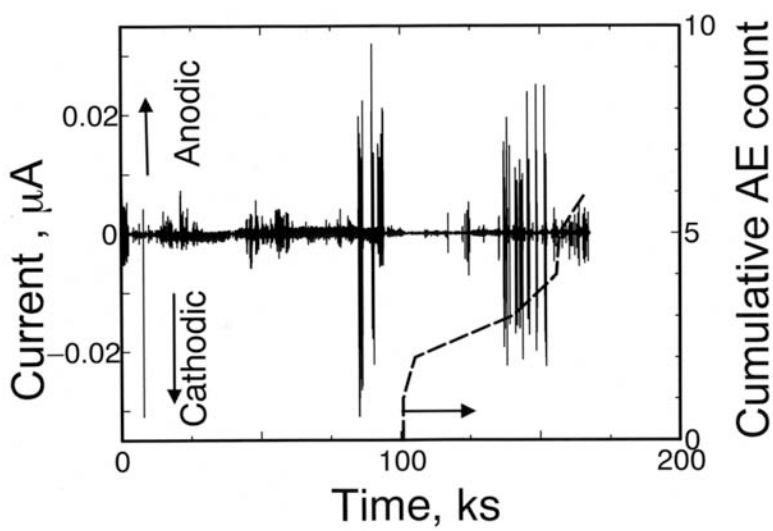

Fig. 6 Change of current estimated from the rate of RD-type corrosion fluctuation for DP-3 steel in 42 % $MgCl_2$ solution.

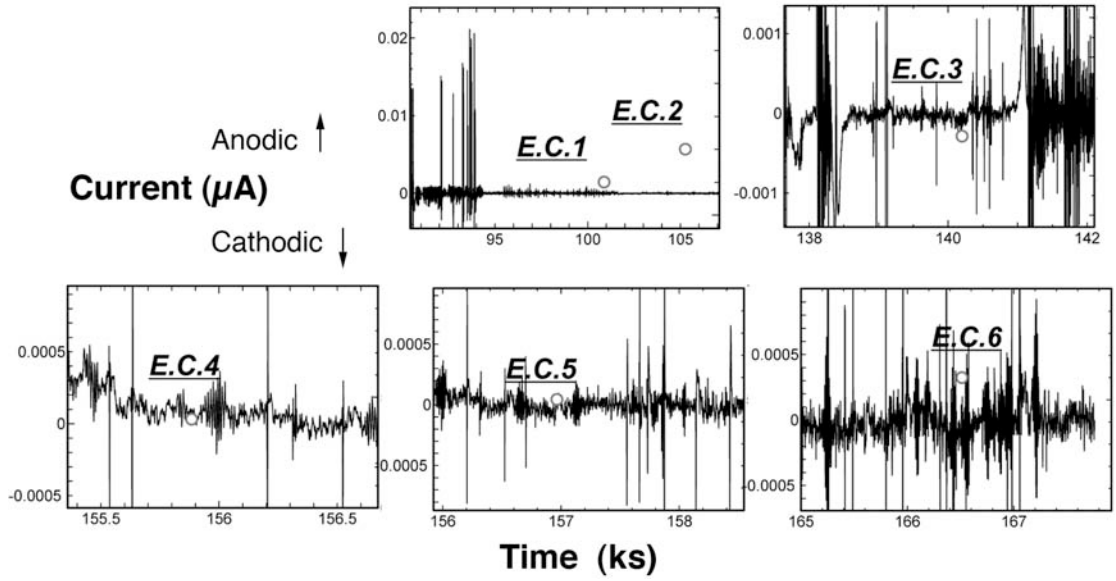

Fig. 7 Change of corrosion current corresponding to AE generation for DP-3 steel in 42 % $MgCl_2$ solution. Timing of AE events is given by circles.

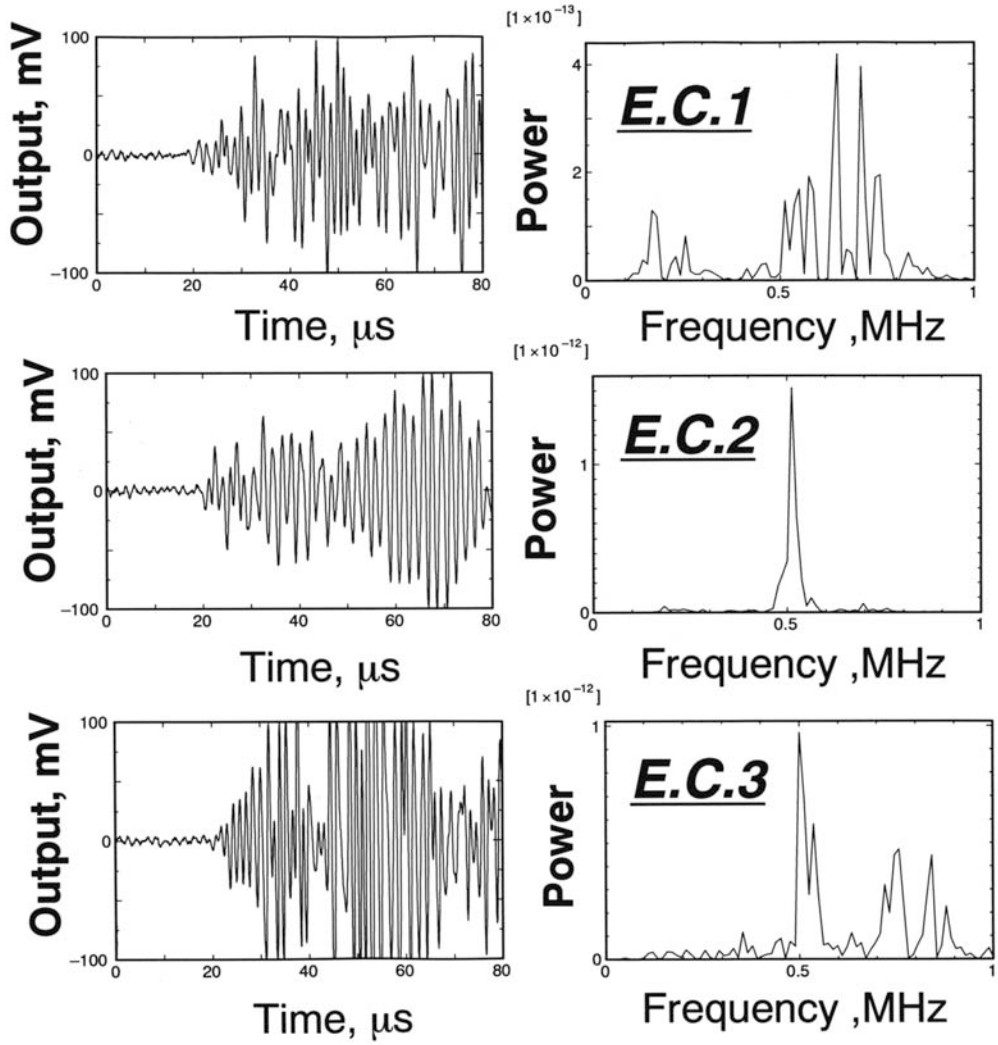

Fig. 8 Examples of waveforms and frequency spectra of AE signals detected by channel 1 sensor during EAF test of DP-3 steel in 42% $MgCl_2$ solution.

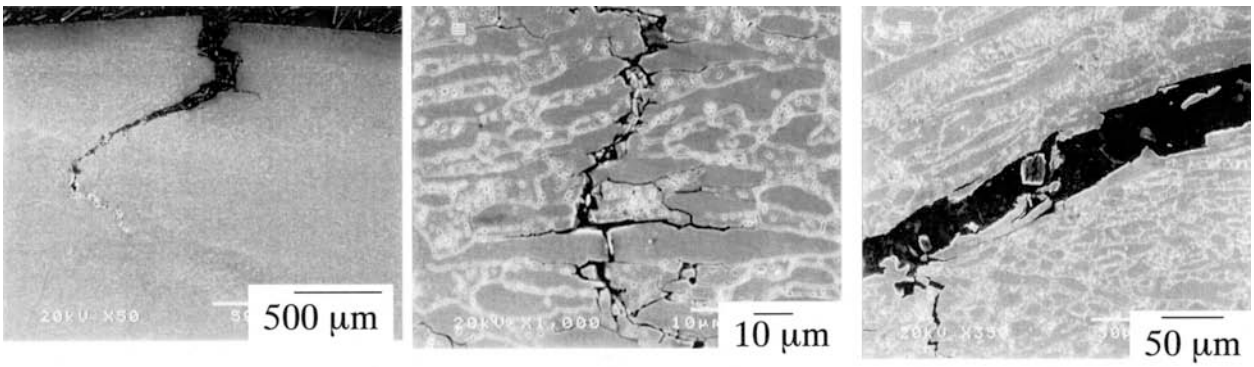

Fig. 9 Transverse cracks of DP-3 steel produced by EAF in 42% $MgCl_2$ solution.

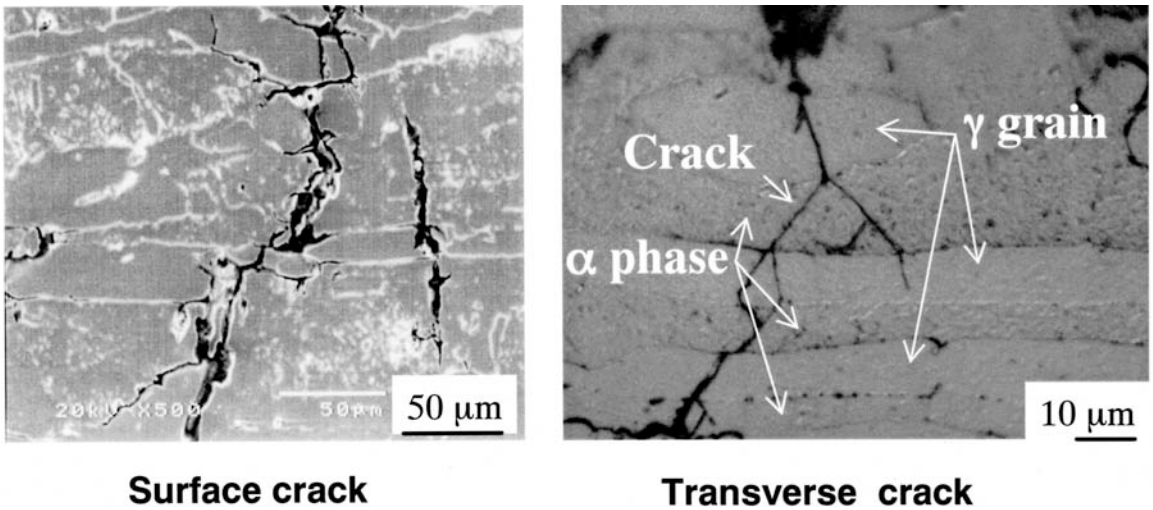

Fig. 10 Surface and transverse cracks observed for DP-3 steel in 42% $MgCl_2$ solution.

Figure 8 shows waveforms and frequency spectra of first three events of total six AE signals detected in the 42% solution. AE signals are typical Lamb waves with first arrival So-mode and late arrival Ao-modes. AE signal of event count 2 (E.C. 2) shows a strong, sharp peak at 0.5 MHz. Events 3-6 also had a similar peak at ~500 kHz. E.C. 4 had a strong peak at 190 kHz in addition. Another event, E.C. 1, had stronger peaks at 650 and 700 kHz, but there was a weak peak at ~500 kHz. This signal may be different from the rest and resembles Type-A signals found in the 35% solution. The Pico sensor used have a broad resonance centering at 450 kHz, but the observed peaks at ~500 kHz are much sharper than the sensor resonance. This is well-known characteristic of acoustic/AE signals produced by hydrogen gas evolution [13]. Morikawa and Ono [14] reported earlier that numerous hydrogen bubbles produced AE as "continuous wave" mode in contrast to cracking AE. AE signals due to gas bubbles have been reported to have a narrow spectrum and this was confirmed in our laboratory [15]. This resonance frequency approximately corresponds to 100 μm hydrogen bubbles [16]. Another support to the hydrogen bubble source was given in Fig. 7. Here, corrosion current curves for most events showed the absence of cathodic current. This implies that fresh cracking did not occur when AE signals were detected. Two events (E.C. 1 and 4) had additional peaks. These can be due to simultaneous evolution of bubbles, larger or smaller. The broader frequency components in E.C. 1 may also originate from other AE sources, such as the friction of crack faces or the fracture of rust, but further confirmation is needed. As shown in Fig. 9, we observe an S-shaped crack and fragmented particles of ferrite grains due to strong texture. This type of SCC tends to produce the friction induced AE.

Crack morphology is shown in Fig. 10. Cracks are observed in ferrite grains and along grain boundaries of ferrite grains. Interesting finding is that the cracks were observed even in the austenite grains. This is contrary to the perfect keying action of the austenite grains in the 35 % $MgCl_2$ solution as will be discussed later.

These data suggest that the EAF in the 42% solution is caused by the APC-SCC, which does not produce primary AE. When the APC-SCC progresses, solution in narrow grooves or cracks is changed to strong acidic solution due to hydrolysis reaction of chromium chloride with water, and then the hydrogen gas evolution takes place in the crack. Though we did not observed hydrogen gas evolution by visual inspection, this is consistent with the expected small size of hydrogen bubbles.

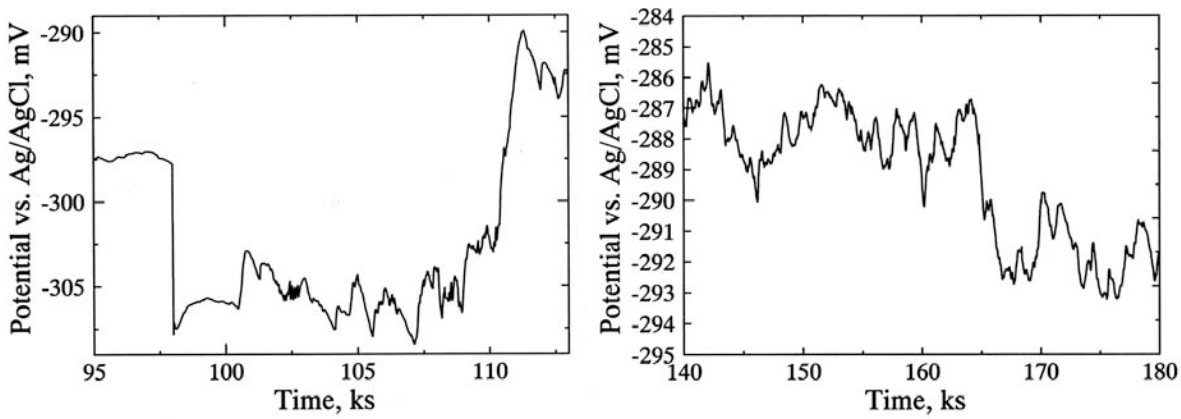

Fig. 11 Magnified corrosion potential fluctuation detected for DP-3 steel in 35 % $MgCl_2$ solution at 90ºC.

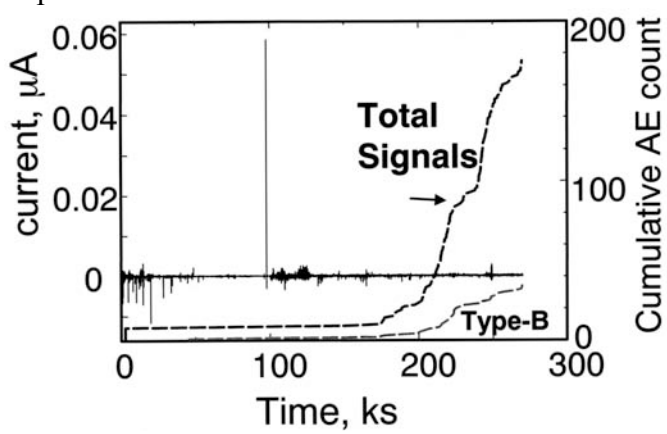

Fig. 12 AE counts and change of estimated current from RD-type corrosion fluctuation for DP-3 in 35% $MgCl_2$ solution.

Characterization of AE and CPF in 35% $MgCl_2$ Solution

We did not observe characteristic RD-type potential fluctuation (see Fig. 4). Figure 11 shows magnified potential changes before and during the AE generation. Current density estimated by Eq. (1) was very low, as shown in Fig. 12. We observed no coincidence of AE timing and CFP.

We detected two types of AE as shown in Fig. 13. These waveforms resemble those detected in the 42% solution, i.e., Type-A with broader frequency content and Type-B with a single frequency peak from hydrogen gas evolution. Here, Type-A signals appear to arise from fracture events, as will be shown below. In the previous section, only E.C. 1 fits Type-A behavior, while the rest were single or

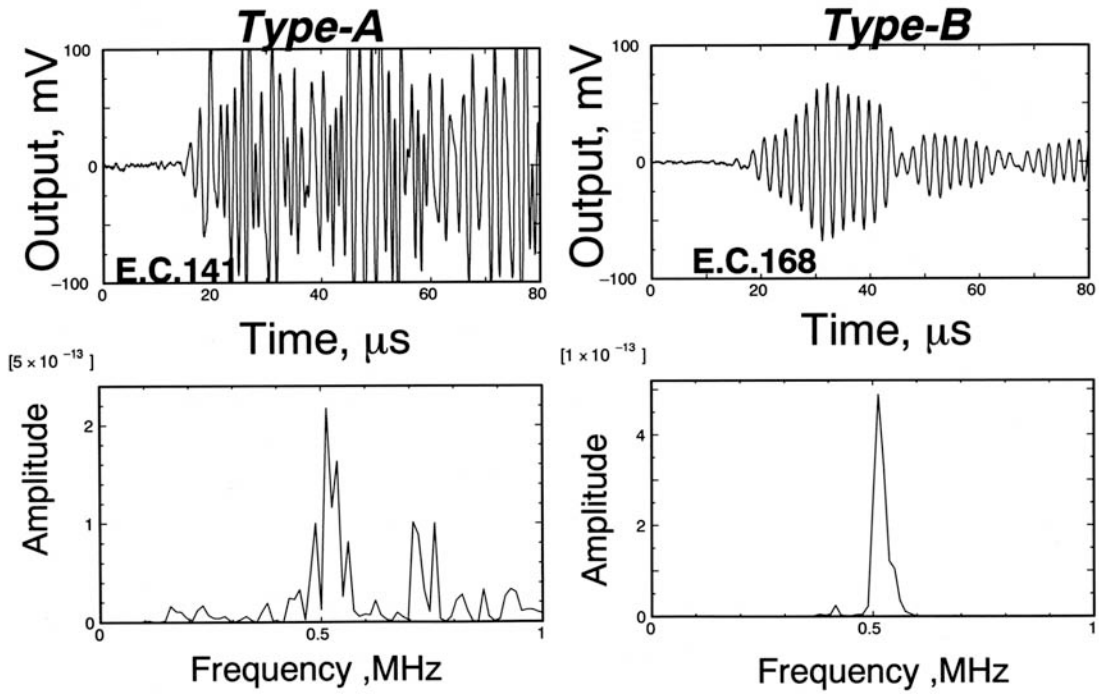

Fig. 13 Two types of AE signals detected for DP-3 steel in 35 % $MgCl_2$ solution.

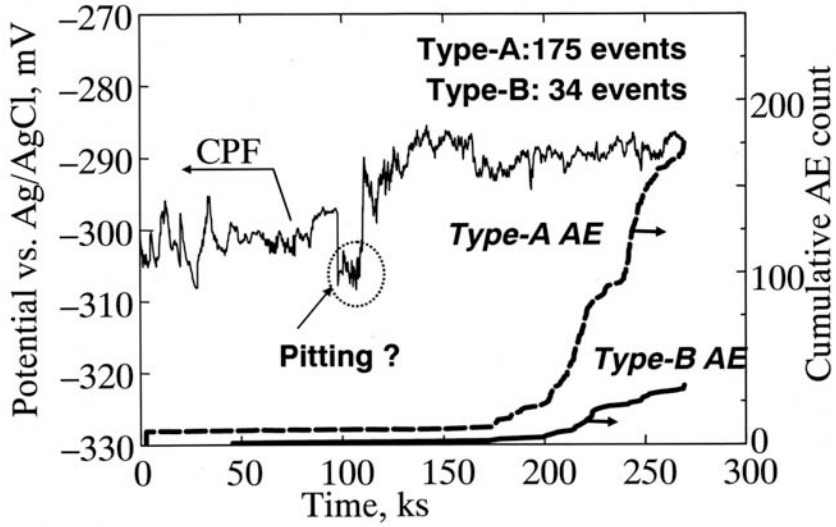

Fig. 14 Change of cumulative counts of Type-A and –B AE signals during EAF of DP-3 steel in 35% $MgCl_2$ solution. CPF at 100 ks may be due to pitting.

double peaks. Cumulative AE counts of Type-A and –B are shown in Fig. 14. Event counts (175) of Type-A signals is eight times large that (34) of Type-B. Shown in Fig. 15 are the waveform detected by two sensors. Waveforms of E.C. 60 with opposite polarity of first-arriving So-mode indicate a mixed mode fracture while the E.C. 67 with the same polarity the Mode-I (crack opening) fracture. Mode classification was possible for 39 events with strong amplitudes. Of these, 29 events were from the Mode-I fracture and this is three times large that ten events from the mixed mode fracture. The mixed mode fractures are probably due to zigzag-shaped cracks owing to the elongated grain texture. Short rise time of the first So-component strongly indicates the fast mechanical fracture by the delayed fracture. Fracture dynamics was estimated by waveform simulation of the first So-wave using the experimental transfer function. Detail of this method can be seen elsewhere [17].

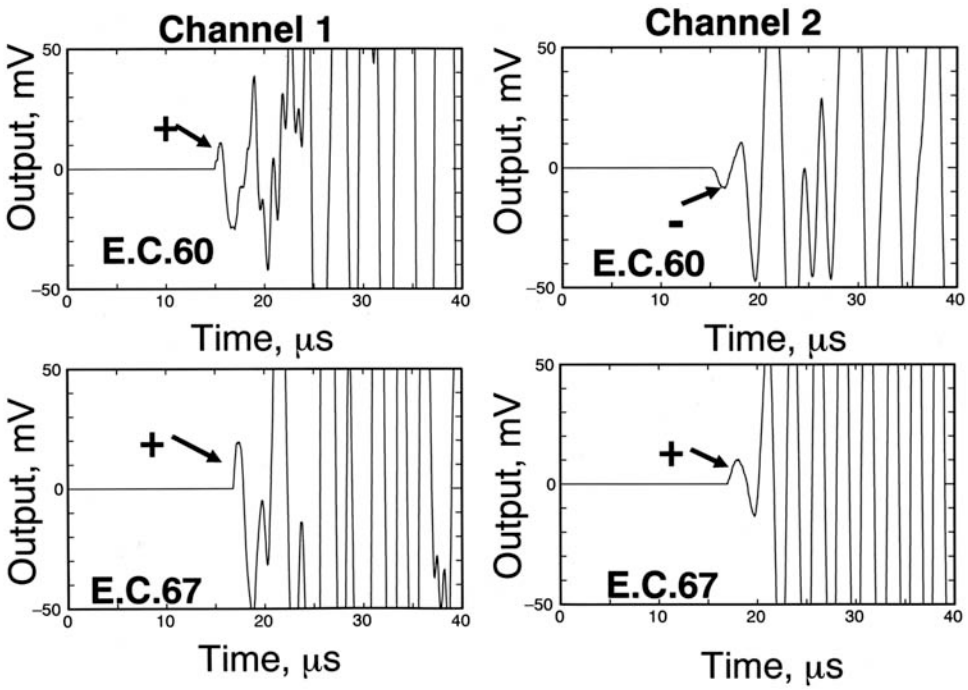

Fig. 15 AE waveforms indicating the mixed mode crack (E.C.60) and Mode-I crack (E.C. 67) for DP-3 steel in 35% $MgCl_2$ solution.

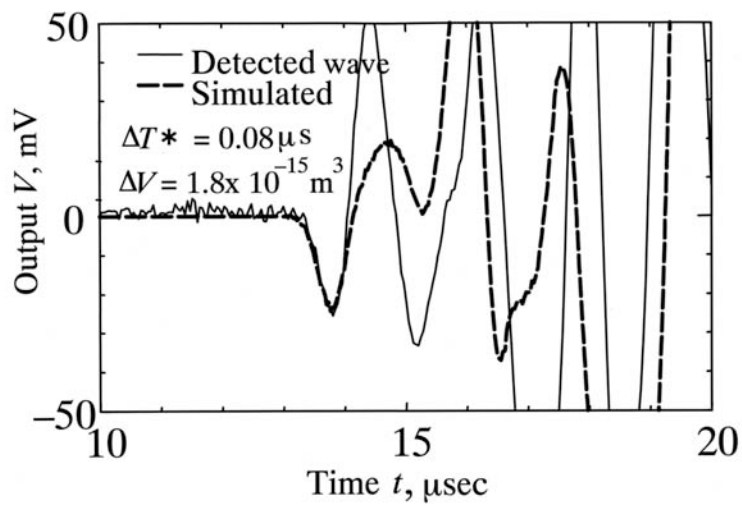

Fig. 16 Overlapping of simulated Lamb waveform on the detected wave.

Figure 16 shows the overlapping of simulated waveform and the detected one. The source parameters, crack volume ΔV and effective rise time ΔTr^*, are shown in the figure. Effective rise time is less than 0.1 μs. This short rise time is indicative of fast fracture due to hydrogen induced cracking. Our previous research on the delayed fracture of dual phase stainless steel R4 (Nippon Yakin Co. Ltd.) under hydrogen charging showed the effective rise times from 0.1 to 0.4 μs [18].

Figure 17(a, b) show macroscopic and microscopic surface crack geometry. On the surface, branched cracks along the axial direction of the specimen can be seen in addition to the normal (vertical in the photo) cracks. The driving force to the axial cracks is the tensile stress in the width direction of the bent specimen. This stress is calculated as half of the axial tensile stress under the plane strain and stress states. Attacks in the 35 % $MgCl_2$ solution begin with the localized corrosion of ferrite grains as shown in

Fig. 17(b). This process is needed to produce enough protons for subsequent delayed fracture and corresponds to the incubation period for the delayed fracture. Cross-sectional micrographs, Fig. 17(c, d), show the cracking to be mostly in the ferrite grains or grain/phase boundaries. In this solution, a crack occurs in the ferrite grains and along grain boundaries of ferrite grains, but it is completely stopped by the austenite grains as shown in Fig. 17(c) and (d). Such complicated cracks are likely to produce the mixed mode fracture, combining Modes I and II, and attendant AE signals.

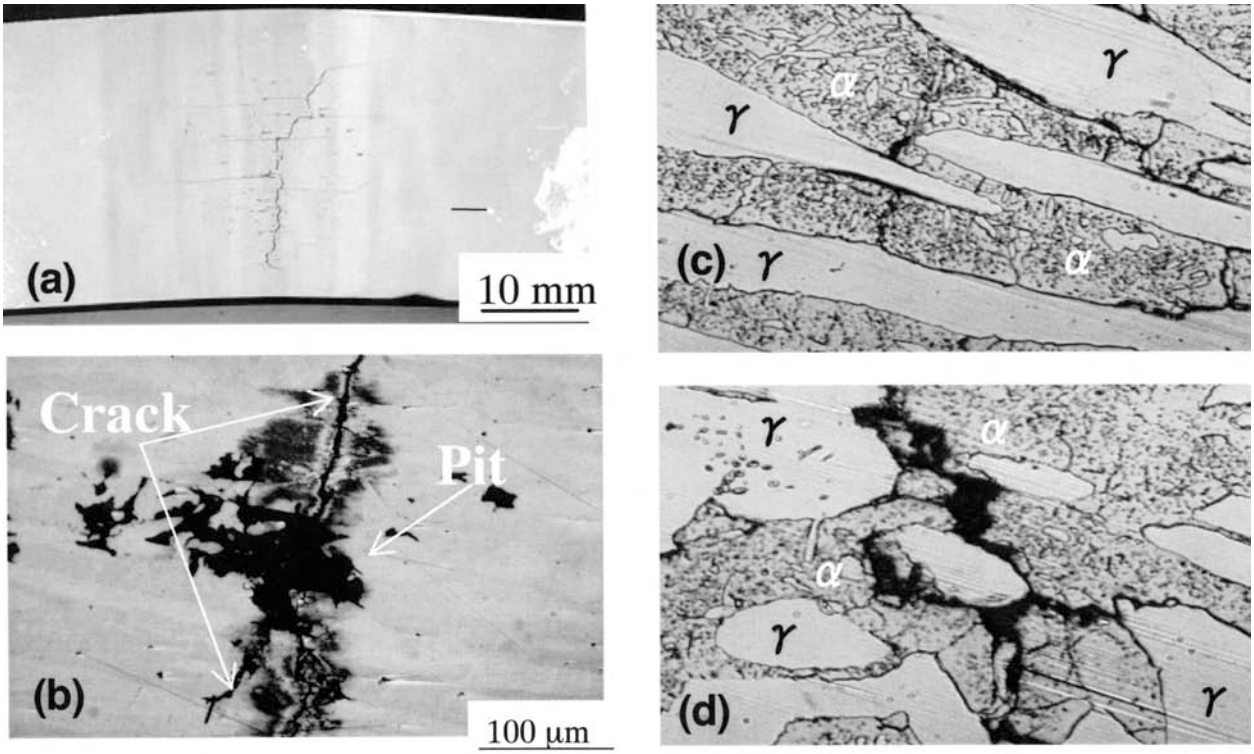

Fig. 17(a, b) Surface crack structures; (c, d) Cross-sectional microstructures of cracked DP-3 steel in 35% $MgCl_2$ solution.

Discussion

Results indicate that the EAF of sensitized DP-3 steel in the 42% $MgCl_2$ solution is the APC-SCC, but that in the 35% $MgCl_2$ solution is the delayed fracture. Regarding the APC-SCC in the 42% $MgCl_2$, we observed gradual shift of the corrosion potential to noble direction with frequent RD-type CPFs before 100 ks (Fig. 1(b)), but very few CPF from 100 ks to 130 ks during which AE signals were monitored. This period indicates the progression of APC-SCC into ferrite grains by anodic dissolution. The solution in the initial shallow APC-SCC was converted to acidic solution and reduction of hydrogen ions takes place. Progression of anodic dissolution due to a high concentration of chloride ions in the 42% $MgCl_2$ solution is apparently faster than the delayed fracture due to slow hydrogen diffusion rate.

Corrosion potential of –305 mV at around 100 ks in Fig. 1(a) in the 35% $MgCl_2$ solution corresponds to the anodic dissolution of ferrite grains. Acidity of the solution in corrosion pits becomes high and protons are adsorbed on the pits wall. These reactions do not cause RD-type CPF. Hydrogen ions are absorbed on the bottom and sidewalls of the pits and then diffuse into the ferrite grains faster than into the austenite grains, and finally causes delayed fracture of the ferrite grains. Frequent emissions of Type-A AE is produced by delayed fracture of ferrite grains.

Conclusions

Mechanisms of environmental assisted fracture (EAF) of sensitized dual-phase stainless steel, DP-3, in 42 and 35% $MgCl_2$ solutions were studied by simultaneous monitoring of acoustic emission (AE) and corrosion potential fluctuation (CPF). Results are summarized below.

1) For the tensile loaded DP-3 steel in 42 % $MgCl_2$ solution at 90˚C, we detected only limited AE events (6 events), but frequent RD-type CPFs (79 events). The CPFs were, however, not detected during the initiation and progression of crack. "Crack" propagated in both the ferrite and austenite grains. The EAF of DP-3 steel in 42% $MgCl_2$ solution was caused by the active-path-corrosion type SCC (APC-SCC). Observed AE signals were due to hydrogen gas bubbles.
2) For the tensile loaded DP-3 steel in 35% $MgCl_2$ solution at 90 ˚C, we detected frequent AE signals (209 events), but no characteristic CPF. Cracks propagated in the ferrite grains and stopped completely by the austenite grains. Waveform simulation suggested fast fractures with effective rise time of approximately 0.1 μs. The EAF of DP 3 in this solution was caused by the hydrogen-induced delayed fracture.

References

[1] S. Fujimoto, M. Takemoto and K. Ono, "AE Monitoring of Chloride Stress Corrosion Cracking of Austenitic Stainless Steel", Journal of Acoustic Emission, **19**, (2001) 63-72.

[2] M. Takemoto, H. Cho and K. Ono. "Acoustic Emission during Stress Corrosion Cracking Tests", *Proceeding of 26th European Conference on Acoustic Emission*, DGZIP, (2004), pp. 311-321.

[3] Y. Hayashi, M. Takemoto and M. Takemoto, "A Novel Acoustic Emission Monitoring and Signal Processing to Elucidate the Fracture Dynamics of Hydrogen Assisted Cracking", National Association of Corrosion Engineers, *CORROSION '94*, (1994) Paper No. 220.

[4] R. Masaki, M. Takemoto and K. Ono, "A Faster Fracture Source For Quantitative Acoustic Emission Simulation - Laser Break-down of Silicone in a Crack," *AIP Conference Proceeding 497*, ed. by R.E. Green, Jr. (1999) pp. 3-8.

[5] H. Okada, Y. Yukawa and H. Tamura, "Application of Acoustic Emission Technique to Study of Stress Corrosion Cracking in Distinguishing Between Active Path Corrosion and Hydrogen Embrittlement." Corrosion, **30**, (1974), 253-255.

[6] H. Okada, Y. Yukawa and H. Tamura, "Transition of cracking mechanisms from active path corrosion to hydrogen embitterment in high strength steels in a boiling nitrate solution." Corrosion, **32**, (1976) 201-213.

[7] M. Takemoto and T. Nakazawa, "Mechanism of the So-called Active Path Corrosion Type Stress Corrosion Cracking", Boshoku-Gijyutu (In Japanese), **44**, (1995) 166-173.

[8] A. Yonezu, H. Cho, T. Ogawa and M. Takemoto, "Simultaneous Monitoring of Acoustic Emission and Corrosion Potential Fluctuation for Mechanistic Study of Chloride Stress Corrosion Cracking", Key Engineering Materials, **321-323**, (2006) 254-259.

[9] S.H. Carpenter and D.R. Smith, Jr, "The Effect of Cathodic Charging on the Acoustic Emission Generated by Intergranular Cracking in Sensitized 304 Stainless Steel", Metallurgical Transaction A, **21A**, (1990) 1933-1939

[10] M. Kowaka, H. Nagano, T. Kudo and K. Yamanaka, "High Stress Corrosion Resistance of Duplex Stainless Steels in Boling $MgCl_2$ solution", Boshoku-Gijyutu (in Japanese), **30** (1981) 218-226

[11] H. Inoue, "A Grounding in Electrochemical Noise Measurement", Zairyo-to-Kankyo, **52**, (2003) 444-451 (in Japanese).

[12] A. Yonezu, H. Cho and M. Takemoto, “AE and Corrosion Potential Fluctuation From Chloride SCC of Weld AISI 304 Pipe under Heat Flux”, *Progress in Acoustic Emission XII*, JSNDI, (2004) pp. 473-480.
[13] A. Yonezu, H. Cho, T. Ogawa and M. Takemoto, “Monitoring of Stress Corrosion Cracking in Stainless Steel Weldments by Acoustic and Electrochemical Measurement”, *Proceedings of the 2006 SEM X Annual Congress and Exposition on Experimental and Applied Mechanics*, Society for Experimental Mechanics, S49P03.pdf, (2006-6), p. 127.
[14] T. Morikawa and K. Ono, "In Situ Acoustic Emission Detection of Cracks during Electroplating Process", *Progress in Acoustic Emission X*, JSNDI, (2000), pp. 345-350.
[15] A. Yonezu, K. Kagayama, H. Cho and M. Takemoto, “AE for Susceptibility Evaluation of Type-304 Steel to Polythionic Acid Stress Corrosion Cracking”, *Progress in Acoustic Emission XIII*, JSNDI, (2006), pp. 489-496.
[16] C.E. Brennen, “Cavitation and Bubble Dynamics”, Oxford Univ. Press, New York (1995) and Physics Today, February 2003, http:/www.aip.org/pt/vol-56/iss-2/p36.html.
[17] T. Matsuo, H. Cho and M. Takemoto, “Development of a New Cascade Multi-sensor Optical Fiber AE System”, and Y. Taniyama, T. Matsuo, H. Cho, M. Takemoto and G. Nakayama, “AEs from Titanium During Deformation and Hydrogen Charging”, *Progress in Acoustic Emission XIII*, JSNDI, (2006), pp. 19-26 and pp. 295-302.
[18] R. Masaki and M. Takemoto, “Fracture Dynamics of Delayed Fracture of Dual Phase Stainless Steel Plate by Wave-front Simulation of Lamb-Wave Acoustic Emissions”, Zairyo-to-Kankyo, **53**-1(2004), 662-668 (in Japanese).

DAMAGE EVALUATION BY FREQUENCY ANALYSIS OF CONTINUOUS RECORDED AE WAVEFORM

KAITA ITO and MANABU ENOKI
Department of Materials Engineering, The University of Tokyo,
7-3-1 Hongo, Bunkyo-ku, Tokyo 113-8656, Japan

Abstract

When AE activity is high, the waveforms of AE events overlap each other. Conventional AE measurement systems, which handle discrete AE events, are not suitable here because overflow and miss-detection occur frequently. A new AE measurement system was developed to solve this problem by recording AE waveforms continuously to hard disks for several hours throughout testing. This system gives new possibilities to AE signal analysis. The continuously recorded AE waveforms can be repeatedly replayed from hard disks and analyzed to obtain AE parameters. The continuous time-frequency data of the AE waveform can be calculated and gives effective information for the damage evaluation of materials. In this study, the degradation of ceramic fiber mat during cyclic compression test was evaluated by this new system. The time-frequency data of AE waveforms delineated the causes of degradation of the mat during the test. Breakage of fibers is the main cause in the initial 10 cycles and sporadic rearrangement of fibers becomes the main cause in the later cycles. The effect of organic binder to prevent the degradation of the mat was also estimated. In binder-added specimens, the fiber-breakage signals weakened and the rearrangement signal disappeared.

Keywords: Continuous waveform memory, short-time Fourier transform, alumina fiber mat, cyclic compression

Introduction

In catalytic converters of automotive exhaust, alumina fiber mat is employed as the sealing medium to affix the main body of converter inside the casing [1]. However, the gripping force of the mat degrades gradually during long-term use under varying pressure caused by runs and stops of engine. In our previous studies [2, 3], AE events of the mat were measured to estimate the degradation under cyclic compression test. However, conventional AE measurement systems often missed the events, especially under high compression state. It is because the conventional systems overflowed by high generation rates of AE events from the fibers inside mat. The conventional systems process the events one-by-one after triggering by pre-set threshold voltage, so miss-detections will occur if the next event arrives within the processing time (dead-time) of the last event. Conventional solution to this problem is to adjust frequency filter and threshold level to reduce the event rate. However, these restrictions tend to spoil the information from the AE signals.

The most fundamental way to solve this dead-time problem is continuous recording of AE waveform. Thompson et al. [4] developed a continuous recorder of AE waveform. However, they adopted solid-state random access memory (RAM) as the storage device, and the recording time was only a few minutes and the cost of a system became high. Kurz et al. [5] showed a system, which can record the transient AE waveforms (i.e., split AE waveform into one event length

in advance) continuously to hard disks. However, their system could not handle the continuous waveform directly. Additionally, the sampling frequency (2.5 MHz) was insufficient for general materials.

In this study, a new AE measurement and analysis system was developed to solve the dead-time problem and was applied to evaluate the degradation of the mat. The new system can record AE waveform to high-capacity hard disks continuously with 10-MHz sampling frequency throughout testing. This new system was named "Continuous Wave Memory" (CWM). Of course, there is no dead-time and no pre-set threshold voltage in CWM measurement. Therefore, this CWM enables successful evaluation of the damage of materials or structures with high AE activity.

Development of Continuous AE Waveform Analyzer

CWM is built using common PC and commercial hardware. No special hardware is needed. Figure 1 shows the block diagram of the hardware. CWM can convert 4-channel AE signals into digital waveform data continuously with 10-MHz sampling frequency and 12-bit resolution by high-speed analog-to-digital converter (PCI-3525, Interface Corp.). The digitized waveform data is recorded to hard disks, which are interfaced in parallel by RAID-0 technology. The data recording rate is 20 MB/s/ch. Therefore, the maximum recording time is about 1.7 hours for 4 channels, or 7 hours for 1 channel in the currently used disks of 500 GB.

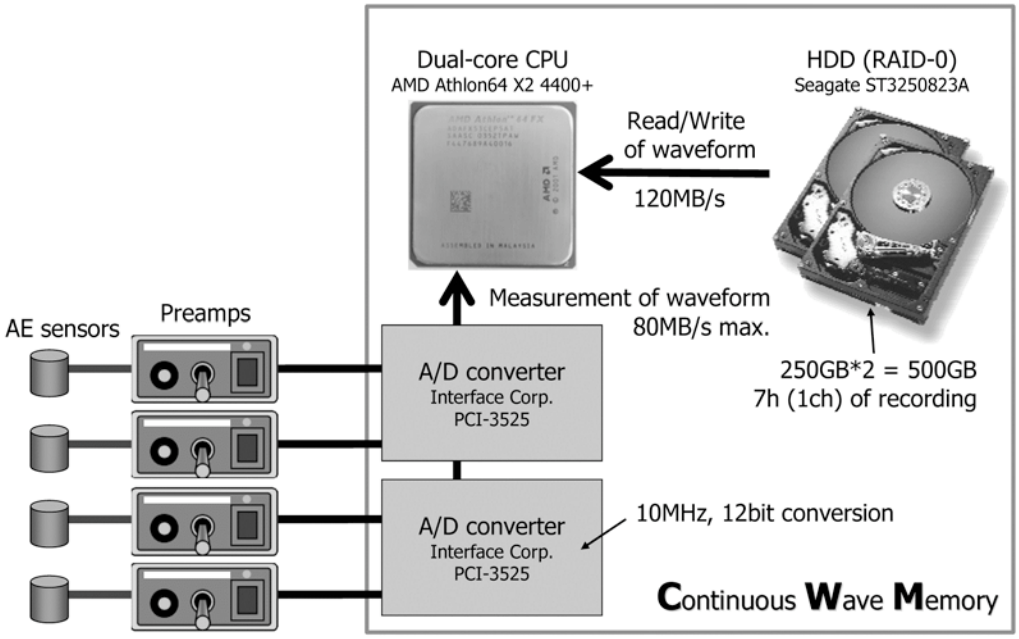

Fig. 1 Hardware block diagram of CWM.

A set of software to analyze the continuous waveform data was also developed. The functions are listed in Fig. 2. The frequency analyzer can also target continuous waveform data by short time Fourier transform (STFT) method. The software can handle two types of data. One is measured data, which is directly imported from the AD converter and analyzed in real-time. This procedure is compatible with conventional AE systems. The other is recorded data, which is read from hard disks as many times as needed and analyzed repeatedly. This "re-analysis" of AE signals newly becomes possible by CWM. The software is optimized for parallel operation by

using latest dual-core CPU (Athlon 64 X2 4400+, Advanced Micro Devices) to reduce analysis time.

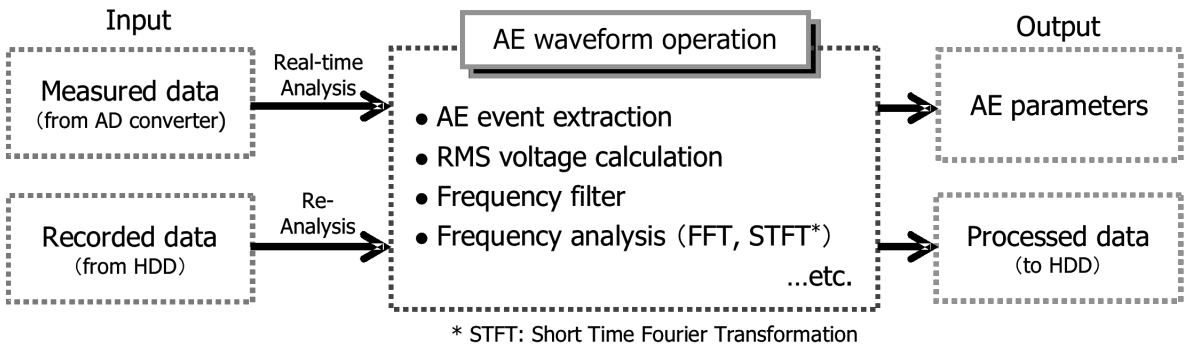

Fig. 2 Software block diagram of CWM.

Experimental Procedures

Ceramic fiber mat was compressed to evaluate the degradation of its resilience. Figure 3 shows the experimental equipment. The mat used for specimens is the same as a current commercial product, which consists of 72% alumina and 28% silica. The specimen was cut from this mat to a disk of 25.4 mm in diameter.

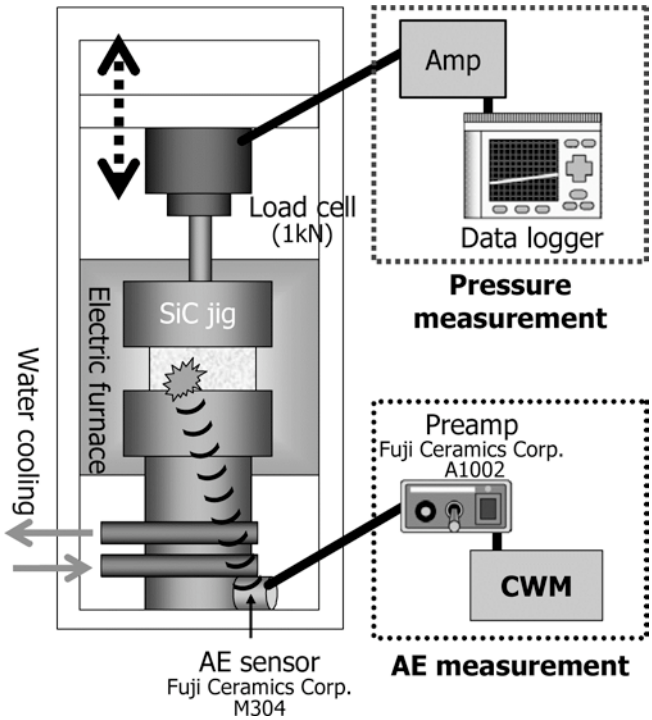

Fig. 3 Equipment for cyclic compression test.

Two conditions of compression were used. One is compression and decompression between 0.331 and 0.376 g/cm^3 at room temperature and 900°C. This experimental condition simulates the real in-service environment of automobile. The other is compression only once from the virgin state (= 0.150 g/cm^3) to 0.400 g/cm^3 at room temperature. This condition simulates the

assembling process of the catalytic converter. Specimens with 1, 5 and 10% of organic binder were also tested to evaluate the effect of the binder in this test. The binder tends to reduce the damage of fibers during the compression process by fixing the cross points of fibers.

The load and AE signals were monitored during the tests. A piezoelectric transducer (PZT) with built-in head-amplifier (Fuji Ceramics, M304) captured AE signals. The sensor was protected from the heat of electric furnace by water cooling. AE signals were amplified further by a preamplifier (Fuji Ceramics, A1002) and input to CWM.

Results and Discussion

Evaluation of Damage of the Mat

Two peak frequencies were found near 600 kHz and 220 kHz from the time-frequency data of the continuous AE waveform, which was calculated by short-time Fourier transform (STFT) method. Specifically, the continuous waveform was split into 4096-sample (i.e. 409.6-µs length) short windows and each window was processed by FFT method. Then, the frequency characteristics of each window was averaged over time and mapped in single graph. Figure 4 shows the results of the 1st, 10th and 70th compression of the mat. The horizontal axis is the density of the mat, the vertical axis is the frequency of AE signal and the gray scale reflects the magnitude. The magnitude is normalized by the maximum magnitude in each graph.

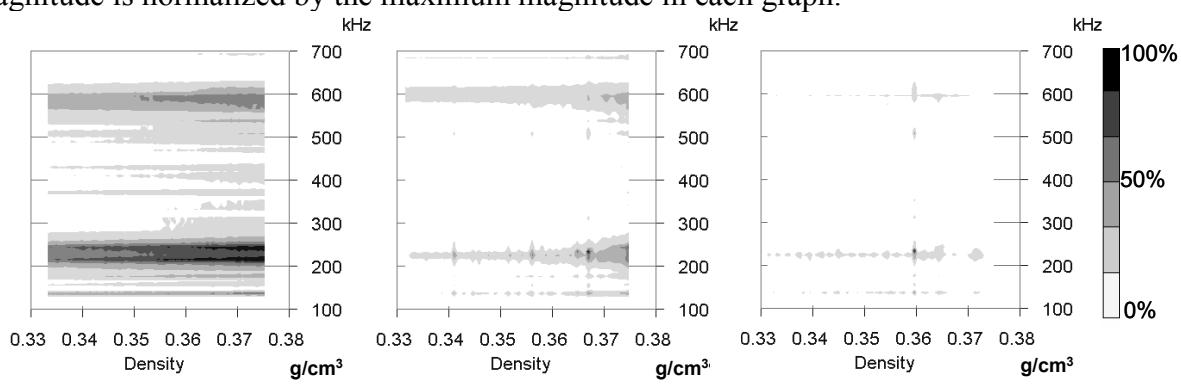

Fig. 4 Plot of mat density-frequency-magnitude of the 1st (left), 10th (middle), 70th (right) cycle.

The causes of these peaks are determined from the shape of waveform [3]. The 600-kHz peak originated from burst-type waveforms due to breakage of fibers, and the 220-kHz peak is from continuous-type waveforms, i.e., the friction of fibers. The intensity of these peaks increased with the progress of compression in each cycle during the first ten cycles, while the maximum intensity of peaks in each cycle was not always observed at the maximum compression stress in later cycles. Toward the end of cycling, only the 220-kHz peak appeared sporadically. The result of SEM observation showed that the fibers were gradually re-arranged to uneven distribution. Figure 5 shows the same place on a single specimen before and after the cyclic compression test. A large void developed in the photograph after 1000-cycle compression.

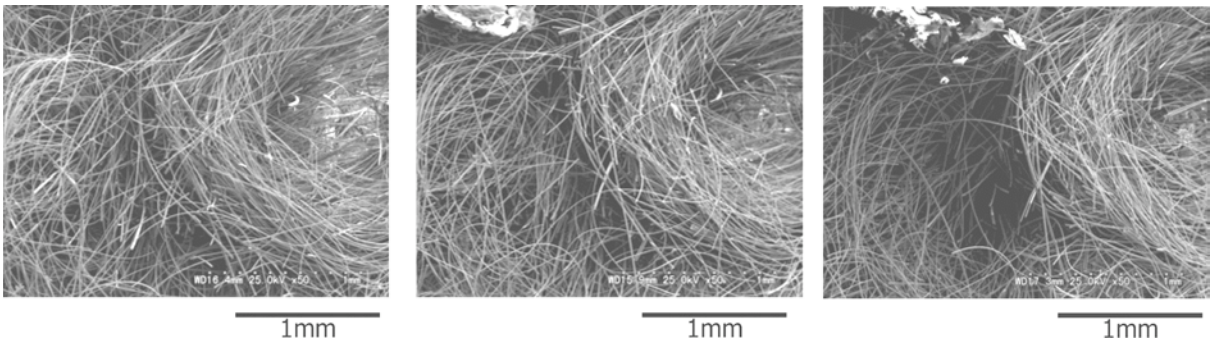

Fig. 5 SEM observation of the same location before (left), after 10 cycles (middle) and after 1000 cycles (right) of compression.

As described above, the cause of degradation of the gripping force seems to change during the cyclic compression test. Initially, the breakage of fibers during compression is the main cause of degradation. Gradually, this shifts to the re-arrangement of fibers, causing discontinuous AE signals from friction in later cycles.

Effect of Binder Addition

Figure 6 shows the result of STFT of specimens with 0, 1, 5 and 10 wt% binder addition. As these specimen was compressed only once from 0.15 to 0.40 g/cm^3, the magnitude is normalized by the maximum magnitude in each figure. Figure 7 shows the magnitude of friction peak (220 kHz) and breakage peak (600 kHz) of each specimen. The 220-kHz peak is observed in only binder-less specimen and the 600-kHz peak becomes weaker with increasing binder addition. Figure 8 shows SEM images at a single position on a specimen with 10% binder before and after the cyclic compression test. The rearrangement of fibers was absent. These results show the effect of organic binder, which fixes the cross points of fibers and reduces the damage of fibers during compression.

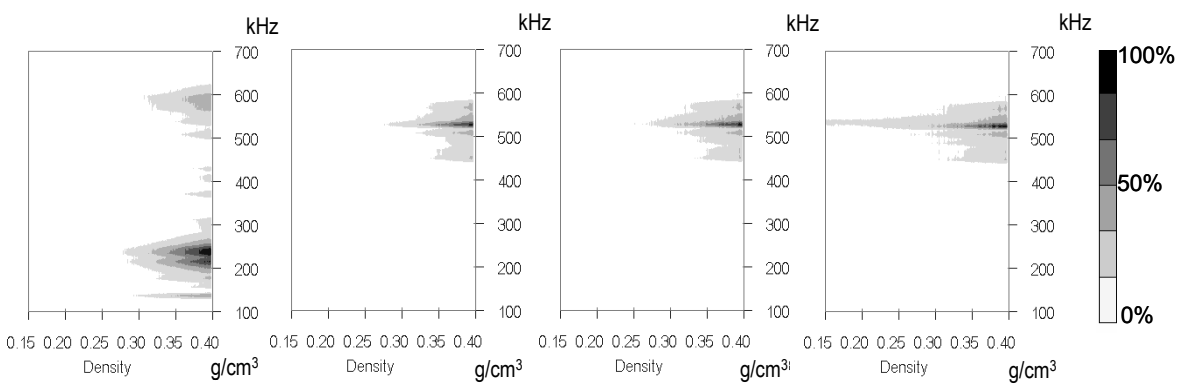

Fig. 6 Plot of mat density-frequency-magnitude of the specimen with 0, 1, 5, 10% binder addition (from left to right).

Conclusions

(i) The degradation of ceramic fiber mat during cyclic compression test was evaluated by a newly developed AE system, which continuously records AE waveforms to hard disk throughout a few hours of testing.

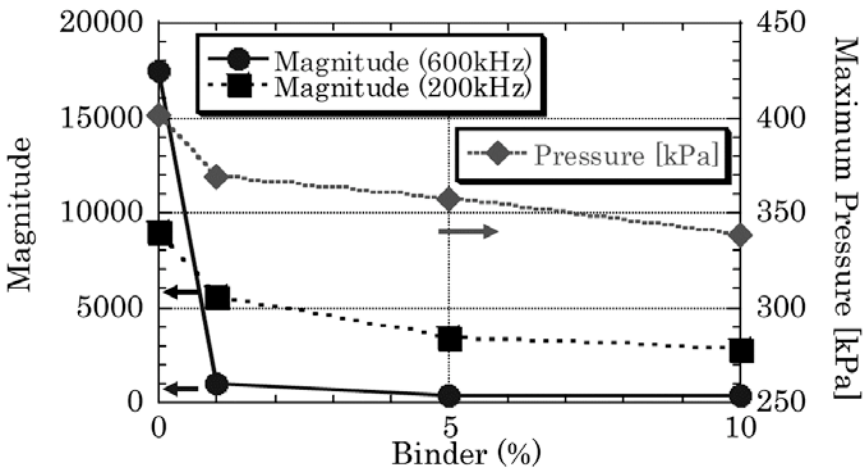

Fig. 7 Binder contents vs. the magnitude of AE signal and maximum pressure.

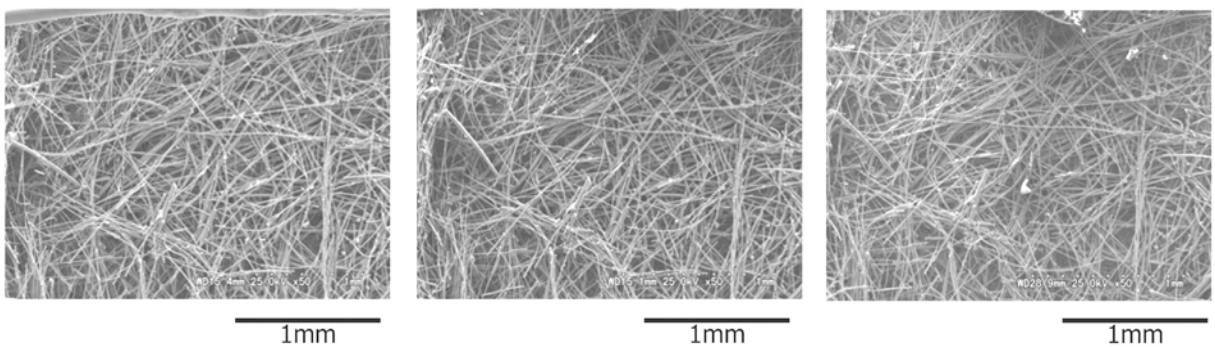

Fig. 8. SEM observation of the specimen with 10% binder before (left), after 10 cycles (middle) and after 1000 cycles (right) compression.

(ii) Two peaks were found near 600 kHz and 220 kHz in the AE waveform of the mat. They are caused by the breakage and friction of fibers, respectively.
(iii)The time-frequency data of the AE waveforms showed the cause of the gripping force degradation of the mat changes during the cyclic compression tests. In the initial 10 cycles, the breakage of fibers is the main cause. At later cycles, the gradual rearrangement of fibers becomes the main cause.
(iv)The AE behavior of specimens containing organic binder was also evaluated by CWM. In binder-added specimens, the breakage signals weakened and the rearrangement signal disappeared.

References

1) M. Chatterjee, M. K. Naksar, P. K. Chakrabarty and D. Ganduli: J. of Sol-Gel Science and Technology, **25** (2002), 169.
2) K. Ito, M. Enoki and H. Takahashi: Review of Quantitative Nondestructive Evaluation, **24** (2004), 1129.
3) K. Ito, M. Enoki and H. Takahashi: *Progress in Acoustic Emission, XII* (2004), 77.
4) R. P. Young and R. Bowes, http://www.liv.ac.uk/seismic/research/current/giga.html, (2003).
5) J. H. Kurz, V. Wolter, G. Bahr and M. Motz: Otto-Graf-Journal, **14** (2003), 115

FREQUENCY FILTERING ALGORITHMS OF PLATE WAVE AE FOR SOURCE LOCATION

YU KUROKAWA, YOSHIHIRO MIZUTANI and MASAMI MAYUZUMI
Department of Mechanical Science and Engineering, Tokyo Institute of Technology,
2-12-1-I1-70, O-okayama, Meguro, Tokyo 152-8552, Japan

Abstract

AE source location is widely conducted during fracture monitoring of industrial structures. However, special techniques are required for thin structures due to the dispersive nature of plate wave AE. We have suggested frequency filtering algorithm utilizing a fast continuous wavelet transform for the source location in thin structures. By utilizing this method, the source location of thin structures can be conducted with good location accuracy. The Gabor function had been used as a mother wavelet in the previous study, but the effectiveness of other mother wavelets or frequency filtering algorithms had not been examined. In this study, the usefulness of Mexican hat wavelet, French hat wavelet, Haar wavelet, Gabor function wavelet, Harmonic wavelet and Butterworth filter for source location on thin structures were investigated. The Gabor function wavelet produced the most accurate source location compared to the other frequency filtering algorithms.

Keywords: Source location, thin structures, Lamb wave, frequency filtering, Wavelet transform

Introduction

The fracture monitoring of CFRP (Carbon Fiber Reinforced Plastics) is important for ensuring structural reliability. AE testing is one of the most effective methods for monitoring fractures. Moreover, AE source location can be estimated by considering the arrival times and the velocity of the AE signals. However, special techniques are required for conducting the source location on thin structures [1-5]. The AE in thin structures, such as CFRP structures, propagates as plate waves and its velocity depends on the frequency. Due to its dispersive nature, it is difficult to determine the arrival time from AE signals. Further more, in anisotropic structures, the velocity of the AE depends on the orientation. The orientation dependence needs to be taken into account for precise source location.

In order to overcome these problems, we suggested two algorithms to realize the real-time executing source location [6]. One is the fast source location calculation algorithm utilizing affine transform for anisotropic structures. The other algorithm is the frequency filtering algorithm utilizing a fast continuous wavelet transform using Gabor function as the mother wavelet. By utilizing these methods, the source location of thin structures can be conducted with good location accuracy in real time. The Gabor function had been used as the mother wavelet in the previous study, but the effectiveness of other mother wavelet types or frequency filtering algorithms has not been explored. In this study, we investigated the usefulness of other wavelet transforms and other frequency filtering algorithms for source location in thin structures.

Frequency Filtering Algorithms

We investigated the usefulness of Mexican hat wavelet, French hat wavelet, Haar wavelet, Gabor function wavelet, Harmonic wavelet and Butterworth filter as a frequency filter for source location. These filtering algorithms are wavelet transform except the Butterworth filter. The general wavelet transform of real function *f(t)* is defined as

$$W(a,b)=\frac{1}{\sqrt{a}}\int_{-\infty}^{\infty} f(t)\psi^{*}\left(\frac{t-b}{a}\right)dt \tag{1}$$

where a>0 and the superscript * denotes a complex conjugate. The analysis function for the wavelet transform can be defined as in equation (2).

$$\psi_{a,b}(t)=\frac{1}{\sqrt{a}}\psi\left(\frac{t-b}{a}\right) \tag{2}$$

The analysis functions are generated by scaling and shifting a mother wavelet $\psi(t)$ by parameters *a* and *b*. The parameter "*a*" stand for the scale and the "*b*" stand for shift of the mother wavelet. In this study, we investigated five mother wavelets as follow.

(1) Mexican hat: Mexican hat mother wavelet is described as equation (3).

$$\psi(t)=\left(1-2t^{2}\right)e^{-t^{2}} \tag{3}$$

This function is the normalized second derivative of a Gaussian function. The time resolution is higher and the frequency resolution is lower than the Gabor function wavelet.

(2) French hat: French hat mother wavelet is described as equation (4).

$$\psi(t)=\begin{cases}1 & (-1\le t<1)\\ -0.5 & (-3\le t<1,\ 1\le t<3)\\ 0 & (elsewhere)\end{cases} \tag{4}$$

The shape of this function is similar to simplified Mexican hat by rectangle model.

(3) Haar: Haar mother wavelet is described as equation (5).

$$\psi(t)=\begin{cases}1 & (0\le t<1/2)\\ -1 & (1/2\le t<1)\\ 0 & (elsewhere)\end{cases} \tag{5}$$

This is the first known wavelet and the simplest possible wavelet.

(4) Gabor function: Gabor function mother wavelet is described as equation (6).

$$\psi(t)=\frac{1}{\sqrt[4]{\pi}}\sqrt{\frac{\omega_0}{\gamma}}\exp\left[-\frac{1}{2}\left(\frac{\omega_0 t}{\gamma}\right)^{2}+i\omega_0 t\right] \tag{6}$$

where γ and ω_0 are positive constants. This function is known to minimize time-frequency

uncertainty. The ω_0 is the center frequency of this function. In this study, we first set $\gamma = 5.336$ in order to satisfy the admissibility condition. If γ is set as 5.336, the time resolution is lower and the frequency resolution is higher than Mexican hat wavelet, French hat wavelet and Haar wavelet.

(5) Harmonic mother wavelet: Harmonic wavelet is described in frequency domain as equation (7).

$$\Psi(\omega) = \begin{cases} 1/2\pi\,(n-m) & (m2\pi \le \omega \le n2\pi) \\ 0 & (elsewhere) \end{cases} \tag{7}$$

The shape of this function is rectangle in frequency domain. The n and m determine the bandwidth of the function. In this study, the n and m were set that the bandwidth became 50 kHz bandwidth.

Figure 1 shows the shapes of these mother wavelets in both the time domain and the frequency domain. All mother wavelets is scaled to have same peak frequency.

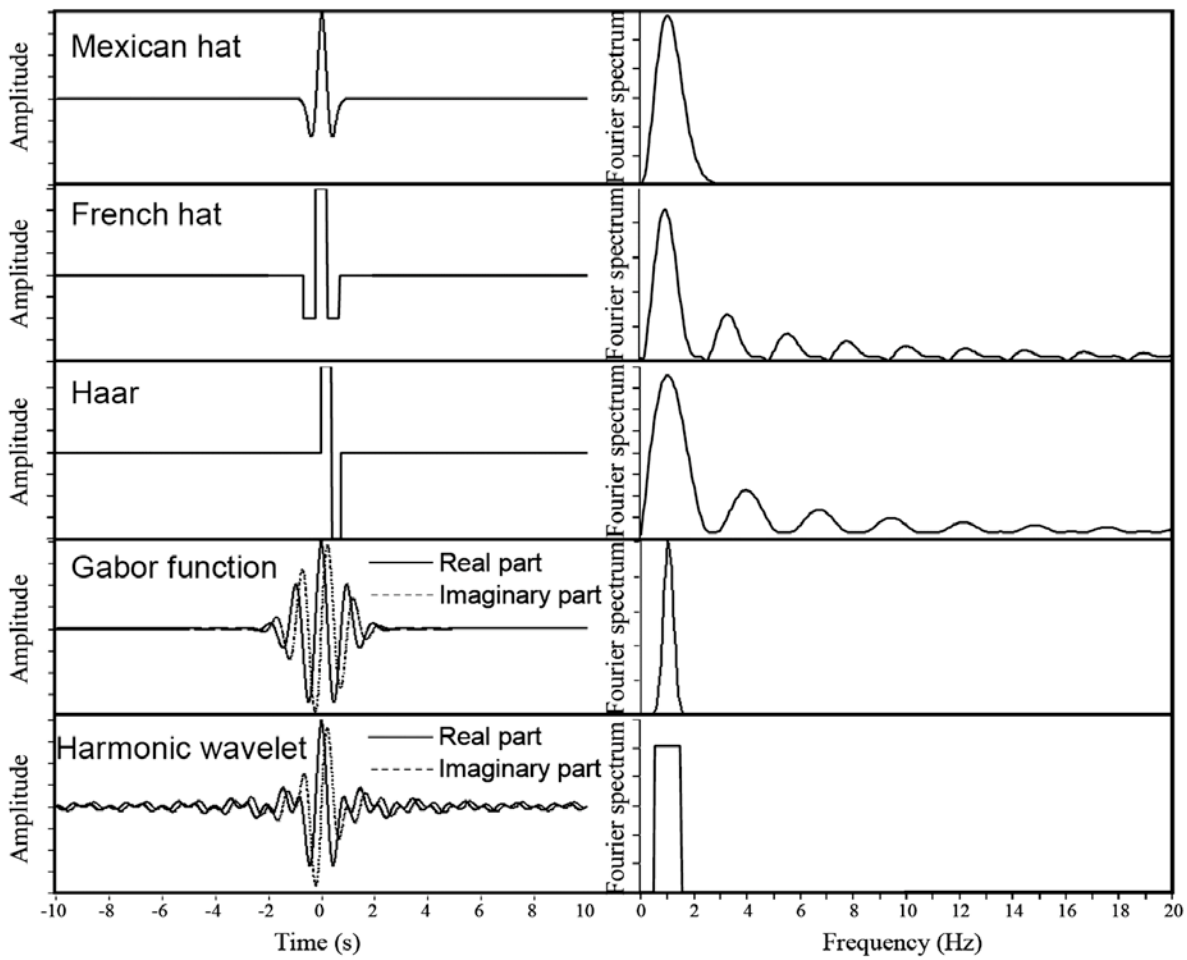

Fig. 1 Mother wavelets in time domain (left) and frequency domain (right)

In addition to these frequency filtering algorithms, the capability of the Butterworth (order 3) bandpass filter was investigated. The bandwidth was set as 50 kHz, which was same as Harmonic wavelet.

The result of Gabor function wavelet and Harmonic wavelet are complex number, so the absolute magnitude was calculated for detecting the peak arrival time. On the other hand, the result of Mexican hat, French hat, Haar wavelet and Butterworth filter are real number. Thus, we calculated their envelopes by utilizing Hilbert transform and compared them to those of Gabor function and Harmonic wavelet.

Specimen and Velocity Anisotropy

For this study, we prepared a $820^{L}\times300^{W}$ mm CFRP plate ($[90°]_7$) with a 1-mm thickness aluminum liner. A schematic drawing of the specimen is shown in Fig. 2. The total thickness of the composite plate is 2 mm. The Y-axis in Fig. 2 corresponds to the fiber direction of the front CFRP layer. This specimen simulates the propellant tank of a future rocket in Japan.

We first investigated the orientation dependence of the AE velocity using pulses produced by pencil-lead breaks on the front surface. We measured the velocity anisotropy every 10° angle (θ) at 300 kHz frequency component by each frequency filtering algorithms, and approximated by an elliptical function. The measured and approximated orientation dependence of the 300 kHz components is shown in Fig. 3.

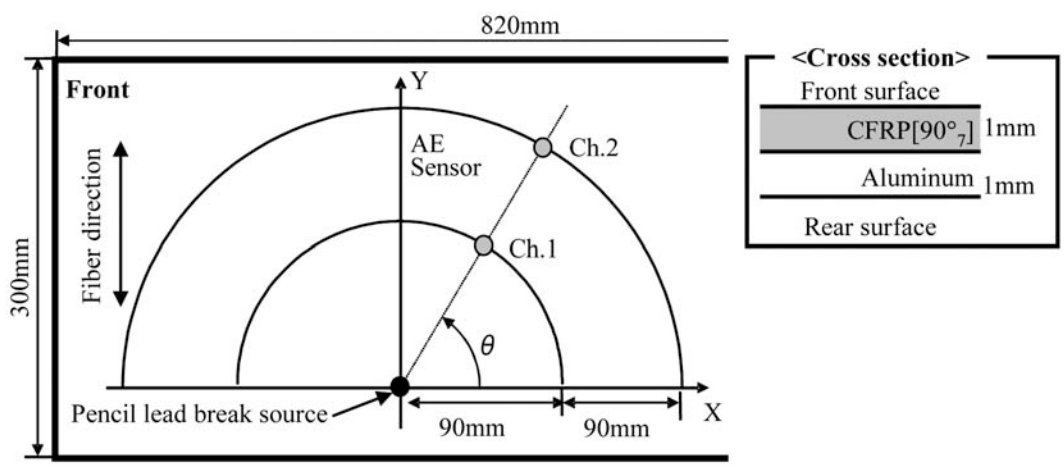

Fig. 2 Schematic illustration of the specimen and the AE velocity measurement.

Source Location System and Experimental Results

The source location experiment used three AE sensors (PAC, Pico; 4.0 mm diameter). The sensors were mounted on the front surface (CFRP side) on the apex of an equilateral triangle, 200 mm on a side. The AE signals were artificially produced using pencil-lead breaks and steel ball drops. Outputs of the AE sensors were digitized using an A/D converter on a PC (National Instruments, NI-5122; 14-bit resolution). The sampling frequency and points are 5 MHz and 4096 points, respectively.

An example of detected AE signal (at 0, 0; Ch.1) produced at (x, y) = (100, 80) and its 300 kHz component by various frequency filtering algorithms are shown in Fig. 5. Dispersive AE signal propagating as plate waves (primary A-mode) were observed in raw signal (upper left). In contrast, the peaks were obtained clearly for the all filtered signals, though their shapes are different from each other.

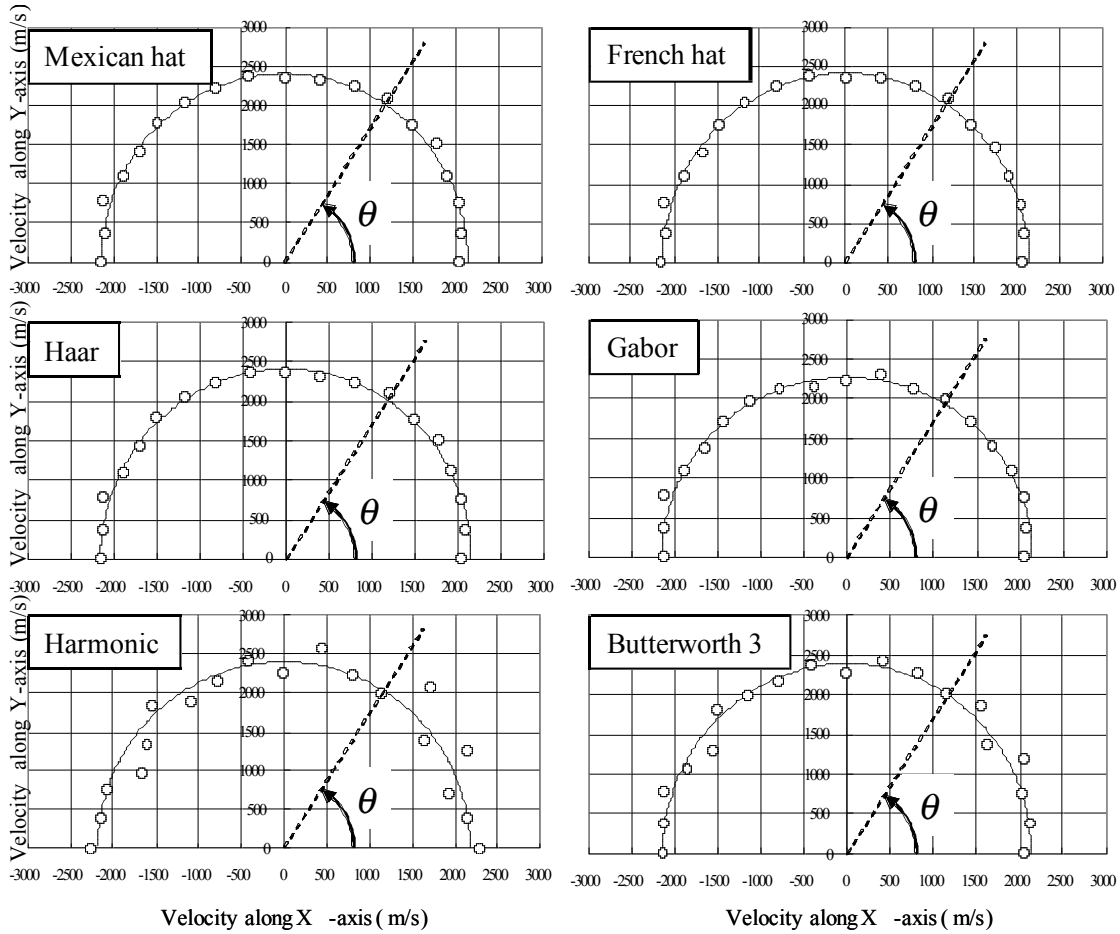

Fig. 3 Orientation dependence of the AE velocities at 300 kHz by six frequency filtering algorithms.

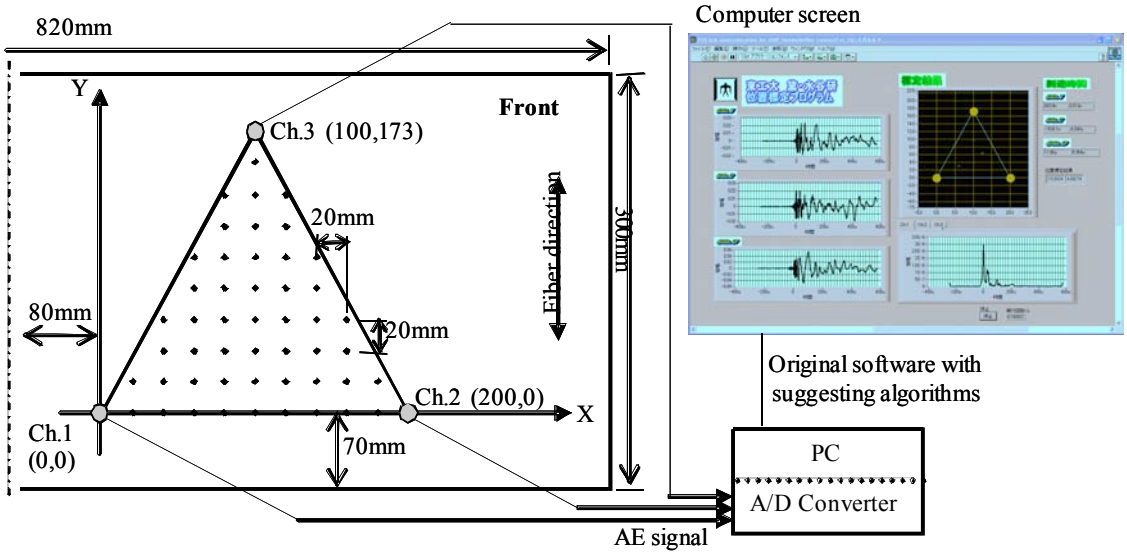

Fig. 4 Schematic illustration of the source location system.

Next, we conducted the source location by measuring peak arrival time differences between three sensors. Peak arrival time was determined using the following steps. Suitable parameters α and β for peak detection were determined for each filtering algorithms.

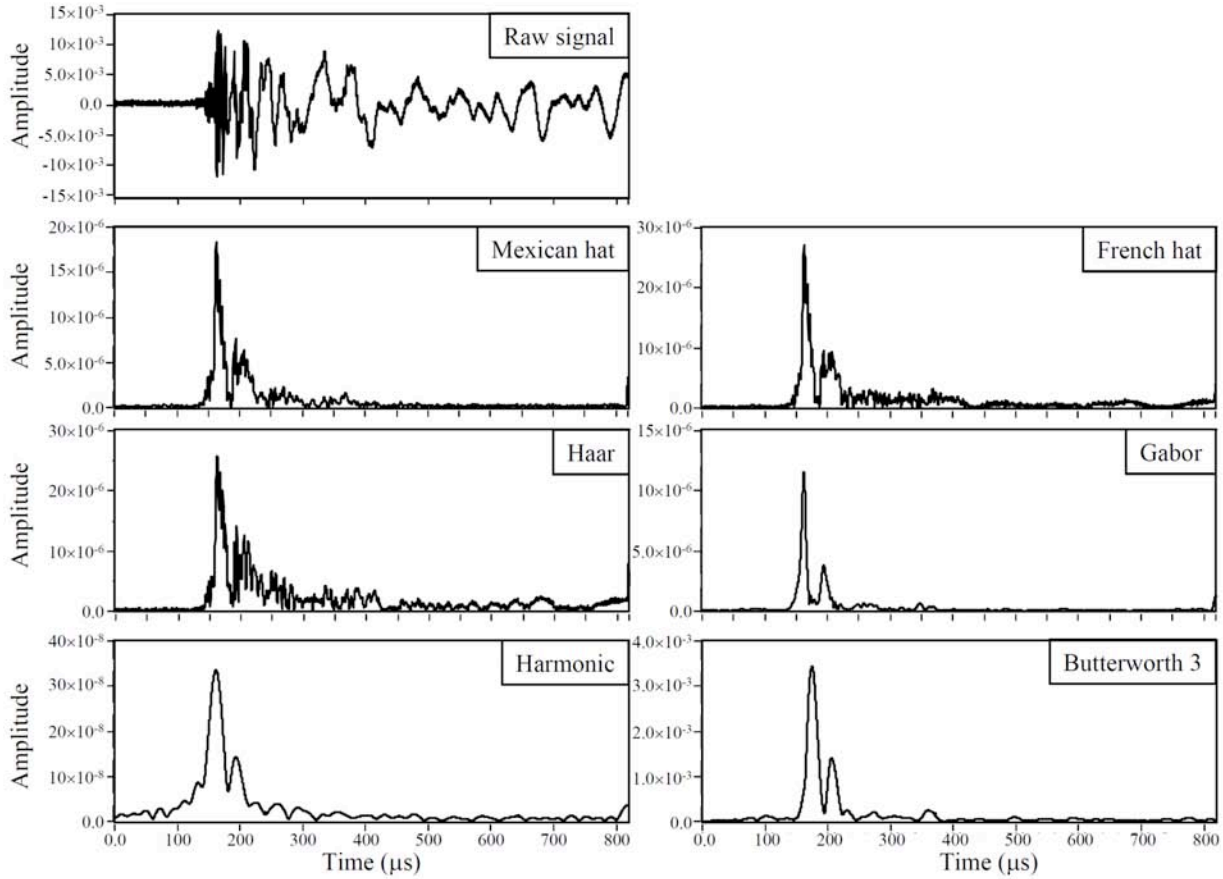

Fig. 5 A detected AE signal and its 300-kHz component by six frequency-filtering algorithms.

1) Set parameter α and β.
2) Search maximum value M of signal.
3) Search peak from $t = 0$.
4) If the peak value is larger than $\alpha \times M$, then go to the next step. If this condition is not satisfied, search next peak.
5) If the value remains lower for β points after the peak, the peak is taken as an arrival time of the signal. If this condition is not satisfied, search next peak.

We changed parameter α from 0.3 to 0.6 in steps of 0.1 and parameter β from 2 to 25 in steps of 1. Next, we conducted source location at 49 point (shown by black circle in Fig. 4) with all α and β pairs and investigated average error of the source location. Finally, optimum parameters of α and β for each frequency-filtering algorithm were determined and final source locations were conducted for each algorithm with optimum parameters.

The source location results for each algorithm are shown in Fig. 6. Average estimation error, maximum error and standard deviation are shown in Table 1. Comparing all result, the Gabor function wavelet produced the most accurate source location.

Since we found that the Gabor function (equation 6) is most suitable for the source location, the optimization of parameter γ in Gabor function was conducted. Usually, γ is set as 5.336 to satisfy the admissibility condition. Since the admissibility condition does not need to be satisfied for our purpose, parameter γ is changed from 1.336 to 9.836 at an increment of 0.5. Figure 7 shows the relationship between parameter γ and average source location error. When $\gamma = 5.336$,

the source location error became minimum (error = 1.9 mm). When the γ-value is lower than 2.336, the estimation error increased rapidly. In these cases, some source location results become infinity, and the average error becomes a very large value. When the γ-value is set between 4.836 to 9.836, the average estimation errors are lower than 3 mm. The error of 3 mm should not become a serious problem for practical use, so the choice of the gamma parameter is not critical.

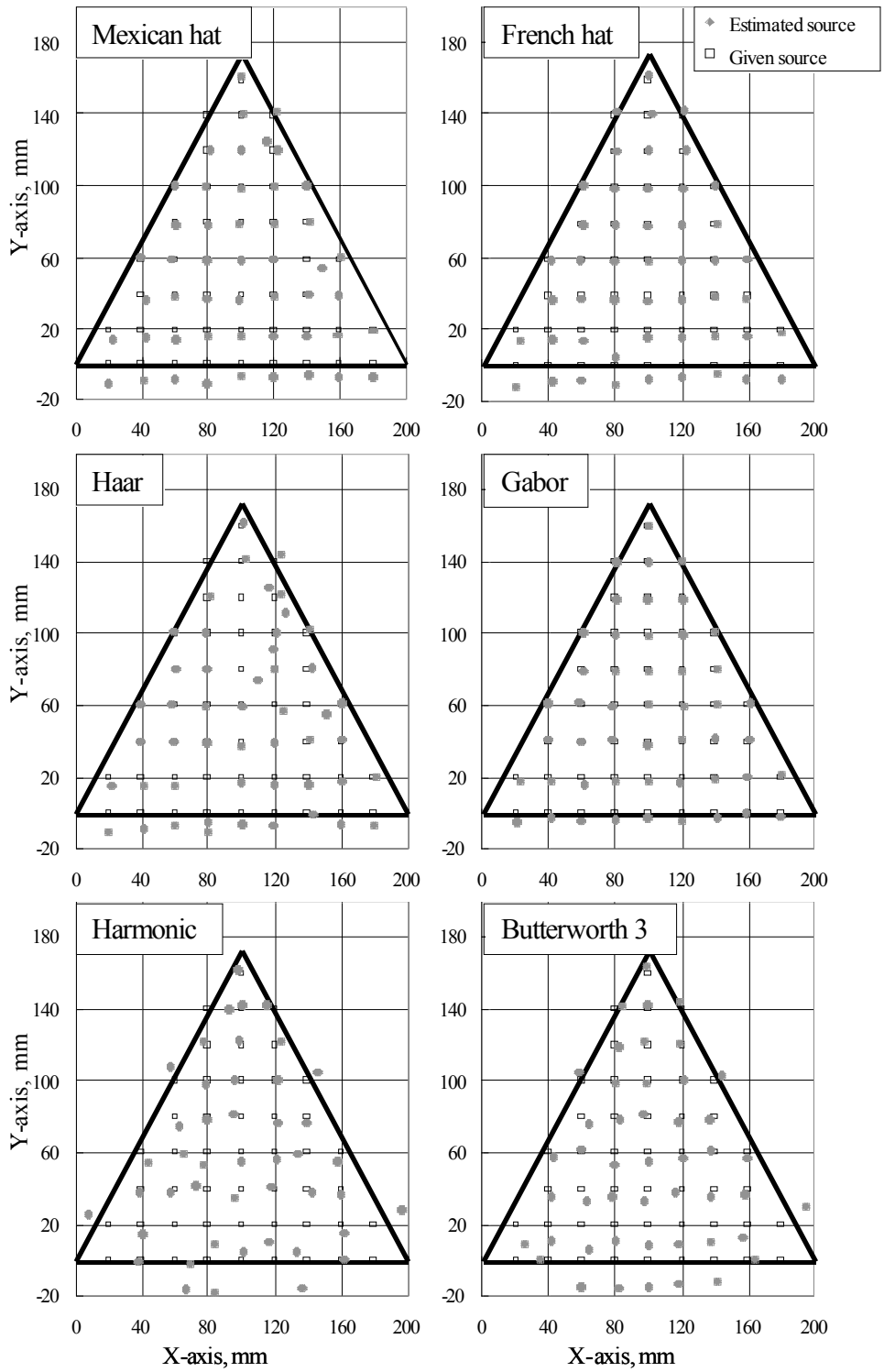

Fig. 6 Source location results by various frequency filtering algorithms.

Table 1 Estimation errors and standard deviations by various frequency algorithms.

	Mexican hat	French hat	Haar	Gabor	Harmonic	Butterworth
Average error	4.5	3.9	6.0	1.9	9.0	7.1
Maximum error	39	16	39	5.4	35	24
Standard deviation	6.0	3.6	7.8	1.2	8.2	5.5

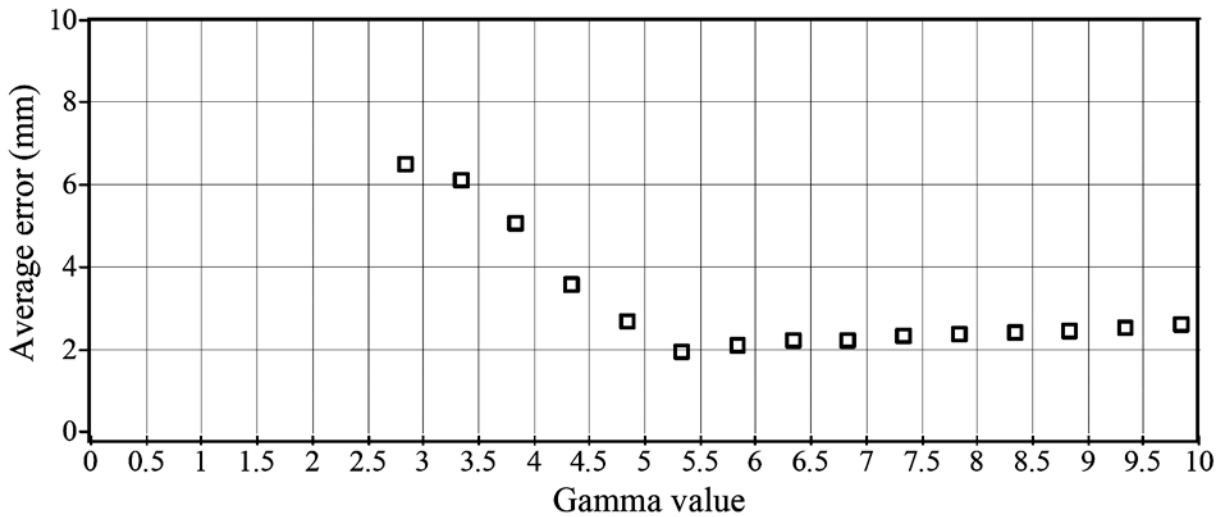

Fig. 7 Gamma parameter of Gabor function versus average source location error.

Conclusion

The frequency filtering algorithms for source location on thin structures were examined. The usefulness of Mexican hat wavelet, French hat wavelet, Haar wavelet, Gabor function wavelet, Harmonic wavelet and Butterworth (order 3) filter was examined. The Gabor function wavelet was found to provide the most accurate source location compared to the other frequency filtering algorithms. Next, the relationship between the gamma value of the Gabor function equation and source location error was investigated. The average estimation error was lower than 3 mm when γ-value was set to 4.5 to 10; i.e., the choice of the gamma parameter is not critical.

References

1) M.R. Gorman and W.H. Prosser, "AE Source Orientation by Plate Wave Analysis", J. Acoustic Emission, **9**, (1991), 283-288.
2) H. Yamada, Y. Mizutani, H. Nishino, M. Takemoto and K. Ono, "Lamb wave source location of impact on anisotropic plates", J. of Acoustic Emission, **18**, (2000), 51-60.
3) M. Blahacek and Z. Prevorovsky, "Probabilistic definition of AE events", *European Conference on Acoustic Emission Testing*, Prague, 2002, pp. I/63-I/68.
4) O.Y. Kwon and Y.C. Joo, *Progress in Acoustic Emission IX*, JSNDI, (1998), pp. 9-17.
5) S.M. Ziola and M.R. Gorman, "Source Location in Thin Plates Using Cross-Correlation", J. Acoustic Soc. Am., **90** (5), (1991) 2551-2556.
6) Yu Kurokawa, Yoshihiro Mizutani and Masami Mayuzumi, "Real-Time Executing Source Location System Applicable to Anisotropic Thin Structures", J. of Acoustic Emission, **23**, (2005), 225-232.

EVALUATION OF TWO TYPES OF MARTENSITIC TRANSFORMATION IN Cu-Al-Ni SHAPE MEMORY ALLOY SINGLE CRYSTAL BY ACOUSTIC EMISSION WAVEFORM ANALYSIS

TAKESHI YASUDA, DAIKI TANI, HIDEO NISHINO and KENICHI YOSHIDA
Faculty of Engineering, The University of Tokushima, 2-1 Minamijosanjima,
Tokushima, 770-8506 Japan

Abstract

Dynamic behavior of two types of martensitic transformation during tensile deformation of Cu-Al-Ni shape memory alloy single crystal has been investigated using acoustic emission (AE) waveform analysis. The martensitic transformation consisted of $\beta_1 \Leftrightarrow \beta_1$' (structural change of DO_3 to 18R) and $\beta_1 \Rightarrow \gamma_1$' (structural change of DO_3 to 2H), called super-elastic and thermo-elastic martensitic transformation, respectively. The martensitic transformation occurs during tensile deformation because of different heat treatment. The rise time at the source in finite elastic solid by a modified Takashima's method was analyzed using the AE waveform detected during the martensitic transformation. The mean rise time to the γ_1' phase was smaller than that to the β_1' phase before yielding and became the same after yielding. The former means that the nucleation of the γ_1' phase is faster than that of the β_1' phase because of different crystallographic structure. The latter result shows that the growth rate of the γ_1' phase is the same as that of the β_1' phase.

Keywords: Martensitic transformation, Source rise time, Cu-Al-Ni shape memory alloy.

Introduction

A peculiar character of the shape-memory alloy accompanies the martensitic transformation. The Cu-Al-Ni shape memory alloy causes two kinds of martensitic transformation such as stress induce martensitic transformation and thermoelastic martensitic transformation after different heat-treatment. It is thought that they have the same matrix phase (β_1 matrix phase) of the crystal structure (DO_3 structure), and it was transformed by shearing to parallel (110) directions of the β_1 structure [1]. However, the stress-induced martensitic transformation and the thermoelastic martensitic transformation have different structures when they undergo the martensitic transformation. In the case of the stress-induced martensitic transformation, the matrix phase was transformed to β_1' phase. On the other hand, it was transformed to γ_1' phase in the thermoelastic martensitic transformation. The accumulating stacking structures are of six kinds of martensitic plane generated in the (110) plane. The β_1' phase has 18R structure and the γ_1' phase has 2H structure [1]. When 2H structure is compared with 18R structure, 2H structure is simpler than the 18R structure, as shown in Fig. 1. When the martensitic transformation occurs, we can detect acoustic emission (AE) generated by the formation of these martensitic plates. AE is useful to monitor the dynamic behavior of the material during martensitic transformation. Source rise time is one of the AE source characteristics observed in this research. We use the AE parameter and investigate how the two different martensitic transformations affect the rise time of AE sources and how one transformation differs from the other transformation.

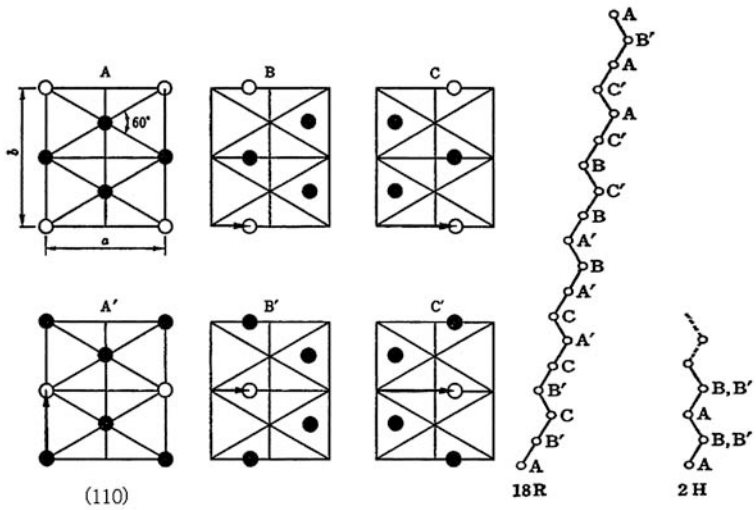

Fig. 1 (110) plane stacking figures of martensitic formations from β_1 phase, and 18R and 2H structures.

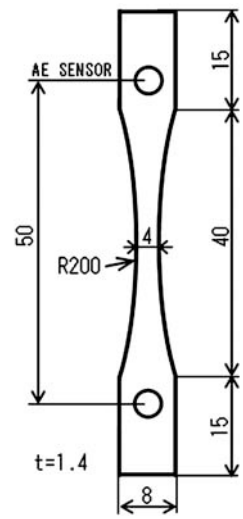

Fig. 2 Shape of specimen used.

Experimental Procedures

The material used is Cu-14.1wt%Al-4.1wt%Ni. It was melted in a high-frequency induction furnace under argon atmosphere and cast into a plate-shaped metal mold. The single crystal of the Cu-Al-Ni alloy was grown in a graphite mold using the Bridgman method at a pulling down rate of 32 mm/hr. All specimens had (001) surface and [110] tensile orientations. It was solution-treated at 1273K for 1 hr and then quenched into water at room temperature (RT) or water at 373K. In either case, β_1 matrix phase was retained. For RT quenched, M_s = 250K, A_f = 280K, and for 373K quench, M_s and A_f were higher room temperature. The RT-quenched specimen shows the martensitic transformation of β_1 to β_1'. The 373K-quenched specimen shows that of β_1 to γ_1'. Specimens had a reduced section with arcs having the radius of curvature of 200 mm, as shown in Fig. 2. These were machined with an electron discharge machine, polished mechanically and then electropolished in a solution of phosphoric acid supersaturated with chromium trioxide.

Tensile test of these single crystals was carried out with a screw-drive testing machine at a crosshead speed of 0.02 mm/min. Changes of the sequential morphology during the tensile test were observed and recorded microscopically by an optical microscope. We used the time sequence in order to let the morphology correlate with the detected AE events and waveforms.

AE measurements were made using a 2-channel AE monitoring system. The AE signals were detected by two AE transducers with the wideband frequency response (M5W), which were directly attached through rapid adhesive on the gripping parts of the specimen. Detected AE signals were amplified 60 dB through a band-pass filter of 100 kHz to 1.2 MHz. The signals generated between two transducers within a time lag of 2 μs were sent into the AE data memory. The threshold level was 45 dB or 50 dB. AE waveforms were sent to a microcomputer through a wave memory, in which the sampling time of 40 ns and the number of sampling points are 1024. AE waveform analysis was conducted by the off-line treatment using wavelet transform software by AGU-Vallen. Lamb waves mainly propagated through the specimen used in this research, because of a thin thickness (1.4 mm). Characteristics of Lamb waves are complex and the

waveform includes the velocity dispersion and mode change. Therefore, all Lamb waveform is unsuitable for AE waveform analysis. However, it is thought that this analysis is possible if it will be used for the first arrival waveform (S_0 mode) for AE waveform that consists of Lamb waveform [2]. The wavelet transform was given the detected. We calculate the rise time of the AE source using S_0 mode, in a finite elastic body and discuss the dynamics of the martensitic transformation.

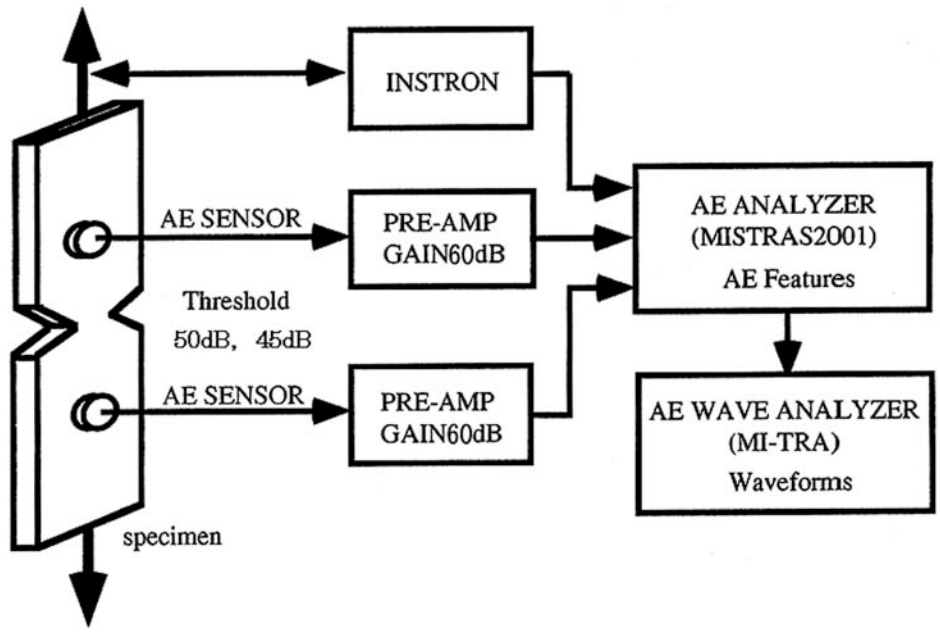

Fig. 3 AE measurement system.

Results and Discussion

Microscopic Observation and its Structural Verification

The nucleation and growth of martensites were observed using an optical microscope. In order to identity martensites β_1' or γ_1' phase, we used the surface trace analysis with the β_1' and γ_1' habit plane traces in the (100)[001] stereographic projection [1, 4]. The surface appearances of the specimens were correlated to load-elongation curves. The surface appearances and load-elongation curves of the stress-induced martensitic transformation ($\beta_1 \Rightarrow \beta_1$' phase) are shown in Fig. 4. Figure 5 shows those for the thermo-elastic martensitic transformation ($\beta_1 \Rightarrow \gamma_1$' phase). In the case of the stress-induced martensitic transformation, the acicular shapes are observed beyond yielding as shown in micrographs. The phase change progresses to a single crystal as the deformation after yielding continues. Upon unloading, the elongation is recovered perfectly. In the case of the thermo-elastic martensitic transformation, γ_1' martensite phase was nucleated at the center of the specimen and extended instantaneously. The interface between β_1' and γ_1' phases moved rapidly to the β_1 phase (bottom right) direction with each deformation step as shown in Fig. 5. The γ_1' martensite phase with the fine acicular shapes are observed in the upper-right insert of Fig. 5. The fine acicular phase is considered to be the twin-like variant of γ_1' phases. Because the elongation is hardly recovered upon unloading [3], the reverse transformation of γ_1' to β_1 phase is induced by heating in hot water of 373K.

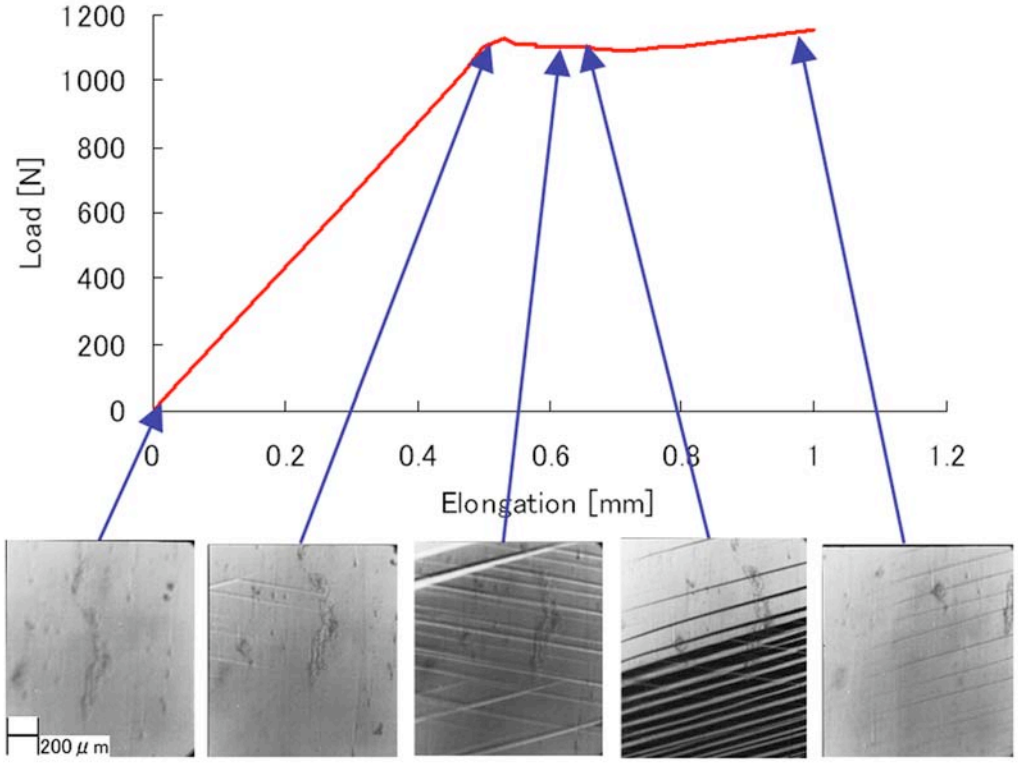

Fig. 4 The microphotograph and load-elongation curve of the stress-induced martensitic transformation ($\beta_1 \Rightarrow \beta_1$' phase)

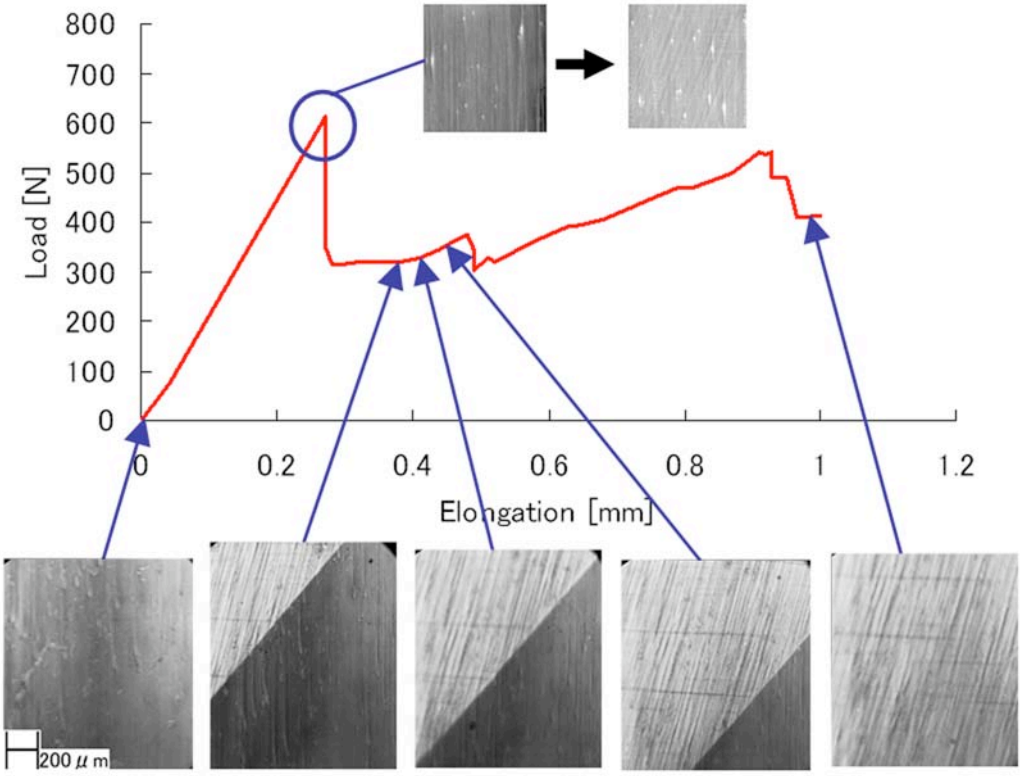

Fig. 5 The microphotograph and load-elongation curve of the thermoelastic martensitic transformation ($\beta_1 \Rightarrow \gamma_1$' phase)

Source Rise Time as AE Parameter

Takashima and co-workers [5] proposed a frequency spectral analysis to obtain AE source rise time. According to the theoretical analysis in infinite elastic body, the gradient of the log-log plot of Fourier spectrum, m, represents the source rise time, $\Delta\tau$, given by

$$m = \omega^2 \Delta\tau^2 / 8 \tag{1}$$

where ω is the center frequency used. In this research, AE waveform analysis was conducted using wavelet transform, because the first arrival waveform (S_0 mode) is suitable for this analysis. We calculated the wavelet spectrum and used it instead of the Fourier spectrum to calculate the source rise time by equation (1).

Results of Source Rise Time

AE waveform was detected during tensile test and the source rise time was calculated from the above-mentioned analysis. In each types of martensitic transformation, two experiments were conducted. First, AE threshold level was 50 dB until 1-mm elongation was reached during a tensile test. Second, the AE threshold level was lowered to 45 dB until yielding or during the elastic loading. The first experiment is to detect AE waveforms when the martensitic transformation is mainly in the growth stage, when the martensites become more complicated. The second experiment in to detect AE waveforms due to the nucleation of martensitic transformation at the early stage. The results obtained are described as follows.

The source rise times of stress-induced martensitic transformation ($\beta_1 \Rightarrow \beta_1$'phase) are shown in Fig. 6 along with load and elongation. The data for thermoelastic martensitic transformation ($\beta_1 \Rightarrow \gamma_1$'phase) is shown in Fig. 7.

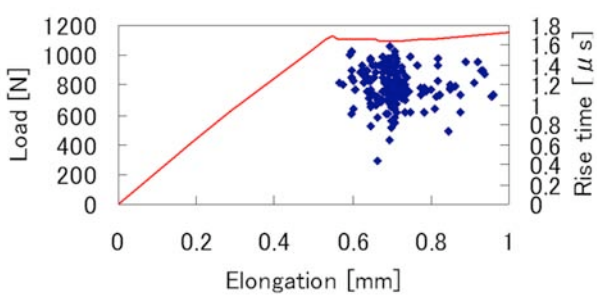

Fig. 6 Source rise time distribution during $\beta_1 \Rightarrow \beta_1$' transformation and load-elongation curve after yielding.

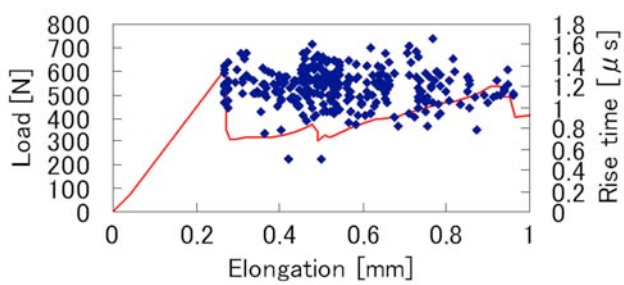

Fig. 7 Source rise time distribution during $\gamma_1 \Rightarrow \beta_1$' transformation and load-elongation curve after yielding

Table 1 Maximum, minimum values, average rise time and standard deviation of the source rise time obtained after yielding in two types of specimens.

Type of specimen	Maximum value[μs]	Minimum value[μs]	Average rise time[μs]	Standard deviation[μs]
$\beta_1 \rightarrow \beta_1$'	1.59	0.431	1.19	0.184
$\beta_1 \rightarrow \gamma_1$'	1.60	0.509	1.19	0.167
Difference	0.01	0.078	0.00	0.017

The source rise times for martensite growth in two types of specimens are given in Table 1. The average rise time was 1.19 μs for both $\beta_1 \Rightarrow \beta_1$' and $\beta_1 \Rightarrow \gamma_1$' transformation. The ranges of the values were between 0.4~1.6 μs and the standard deviation was 0.17-0.18 μs, indicating that there was no difference in the data. It appears that the same growth behavior of martensite plates is exhibited.

In the second experiment, AE waveforms are detected during tensile loading before yielding in both specimens, because AE threshold level was lowered to 45 dB. Previously, no AE events were detected in the elastic range. The data of stress-induced martensitic transformation ($\beta_1 \Rightarrow \beta_1$'phase) is given in Fig. 8 and that of thermo-elastic martensitic transformation ($\beta_1 \Rightarrow \gamma_1$'phase) in Fig. 9, respectively.

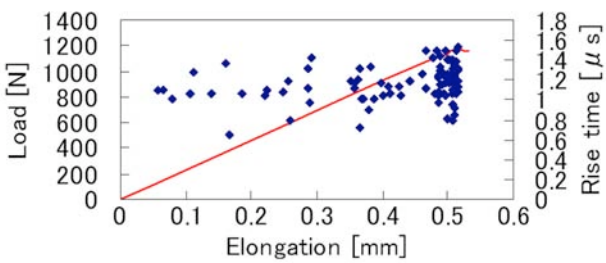

Fig. 8 Source rise time distribution during $\beta_1 \Rightarrow \beta_1$' transformation and load-elongation curve until yielding.

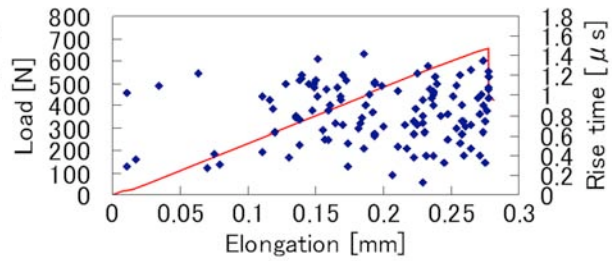

Fig. 9 Source rise time distribution during $\gamma_1 \Rightarrow \beta_1$' transformation and load-elongation curve until yielding.

Table 2 Maximum, minimum value, average rise time and standard deviation of the source rise time obtained until yielding in two types of specimens.

Type of specimen	Maximum value[μs]	Minimum value[μs]	Average rise time[μs]	Standard deviation[μs]
$\beta_1 \rightarrow \beta_1$'	1.54	0.646	1.17	0.173
$\beta_1 \rightarrow \gamma_1$'	1.43	0.130	0.818	0.296
Difference	0.11	0.516	0.352	0.123

Unlike in experiment 1, differences are found in the rise time results. The data are summarized in Table 2. The average rise time was 1.17 μs in the $\beta_1 \Rightarrow \beta_1$' phase transformation and was 0.818 μs in the $\beta_1 \Rightarrow \gamma_1$' phase transformation. The ranges were 1.54-0.646 and 1.43-0.13 μs, respectively. Considering the standard deviation of 0.173 and 0.296 μs, the source rise time of the $\beta_1 \Rightarrow \beta_1$' phase transformation is larger than that of the $\beta_1 \Rightarrow \gamma_1$' phase transformation. The minimum rise time (0.130 μs) in the $\beta_1 \Rightarrow \gamma_1$' phase is also much smaller than that (0.646 μs) in the $\beta_1 \Rightarrow \beta_1$' phase.

These two martensites come from the same matrix phase of the DO_3 structure, and it is transformed by shearing along parallel (110) plane of the β_1 structure as shown in Fig. 1. However, these have different structures when they undergo the transformation. In case of the stress-induced, it is transformed to β_1' plane with has 18R structure. When it is transformed to γ_1' phase in the thermo-elastic transformation, it has 2H structure. The 2H structure is simpler than the 18R structure and the nucleation of the γ_1' phase in considered to be easy to occur at shorter rise time that of β_1' phase.

AE Amplitude Distribution before Yielding

The AE amplitude distributions detected during the $\beta_1 \Rightarrow \beta_1$' and the $\beta_1 \Rightarrow \gamma_1$' transformation before yielding in the second experiment are shown in Fig. 10 and Fig. 11, respectively. The distribution in each transformation are almost identical, while the number of AE events in different. It appears that the AE sources in both transformation are almost same. Therefore, the AE sources are considered to be the nucleation of the transformation at the early stage. However, the growth of the martensite plates may also occur even in the elastic region. However, the more research is needed on this issue.

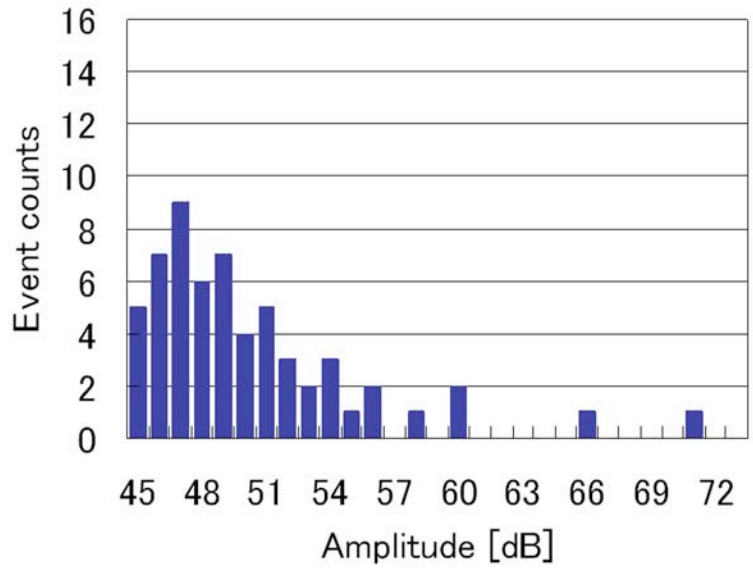

Fig. 10 AE amplitude distribution during $\beta_1 \Rightarrow \beta_1$' transformation before yielding.

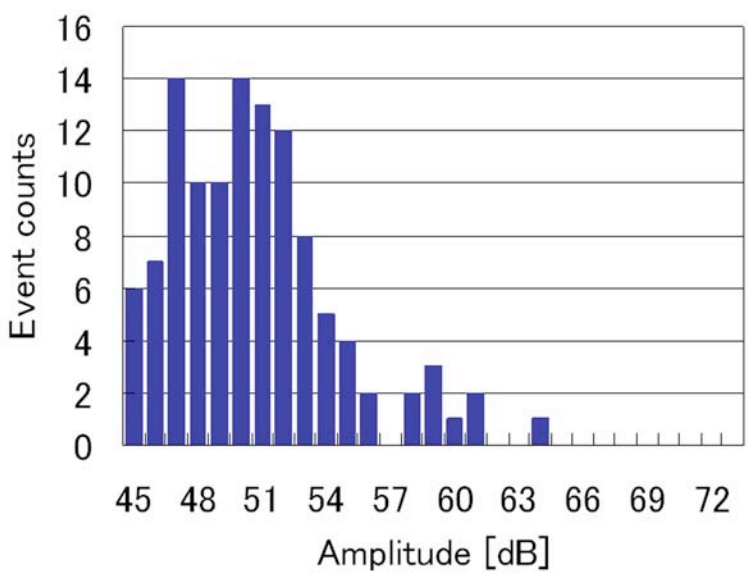

Fig. 11 AE amplitude distribution during $\beta_1 \Rightarrow \gamma_1$' transformation before yielding.

Conclusion

AE source rise times were examined using the wavelet transform of AE waveforms detected from martensitic transformation of $\beta_1 \Rightarrow \beta_1$' phase or $\beta_1 \Rightarrow \gamma_1$' phase in the Cu-Al-Ni shape memory alloy. The results obtained are as follows;

1) In the case of the specimens until yielding the average source rise time of the super-elastic martensitic transformation ($\beta_1 \Rightarrow \beta_1$' phase: $DO_3 \Rightarrow 18R$ structure) was larger than that of the thermoelastic martensitic transformation ($\beta_1 \Rightarrow \gamma_1$' phase: $DO_3 \Rightarrow 2H$ structure).
2) The differences of the source rise times until yielding between the super-elastic and the thermoelastic martensitic transformation was dependent on the crystallographic structure.
3) The average source rise time in all specimens after yielding was almost identical and had a value of 1.19 μs.

References

1) *Shape Memory Alloys* (in Japanese), Ed. T. Funakubo: Sangyou-tosyo (1984), pp. 12-17, 20-24.
2) M. Takemoto, H. Nishino, and K. Ono: Wavelet Transform - Applications to AE signal analysis, *Acoustic Emission-Beyond the Millennium* (2000), Elsevier, pp. 35-56.
3) Z. Nishiyama: *Martensitic Transformation -Basic Section* (in Japanese), Maruzen (1971), pp. 60-69.
4) X.Y. Zhang, L.C. Brinson and Q.P. Sun: The variant selection criterion in single crystal Cu-Al-Ni shape memory alloys, Smart Mater Struct., **9** (2000), 571-581.
5) K. Takashima, Y. Higo, and S. Nunomura: Determination of the duration of transient phenomena by frequency-domain analysis of acoustic emission, Philosophical Magazine, A**49-2** (1984), 221-229.

FATIGUE FRACTURE DYNAMICS OF HIGH STRENGTH STEEL STUDIED BY ACOUSTIC EMISSION TECHNIQUE

AKIO YONEZU, TAKESHI OGAWA and MIKIO TAKEMOTO
Faculty of Science and Engineering, Aoyama Gakuin University,
5-10-1, Fuchinobe, Sagamihara, Kanagawa 229-8558, Japan.

Abstract

This paper discusses the feasibility of AE technique for monitoring of fatigue damage of high strength bearing steel. We studied AE source mechanism in fatigue process using the waveform and source simulation analyses. The steel specimens, subjected to four-point cyclic bending, produced a few but strong AE signals just before the final fracture. Fractographic study showed a change of fracture type from transgranular (TG) to intergranular (IG). Crack volume was estimated by source simulation of AE as approximately 10^{-16} m^3. Another fatigue fracture test of a compact tension (CT) specimen also showed a change of fracture type from TG- to IG-fracture at around K_{max} of 8 MPa√m, above which both the fast crack propagation and high AE generation rates were detected. The source simulation analysis indicated simultaneous IG fracture of neighboring few grains as the source of AE for fatigue test of the CT specimen.

Keywords: High strength steel, fatigue fracture, source wave analysis, microcrack dynamics

Introduction

A consideration of ultra-high-cycle fatigue of more than 10^7 cycles is becoming important for maintenance of infrastructure [1]. This type of fatigue is called as giga-cycle fatigue, producing fatigue failure at stress lower than the fatigue limit determined by the conventional fatigue test up to 10^7 cycles. High-strength steels have been reported to exhibit a distinct knee point within a cycle range of $N = 10^5$-10^6 and the curve has another knee point in the long-life region of $N > 10^7$ [2, 3]. This "duplex *S-N* curve", consisting of two different curves, is observed for long-term cyclic loading, and suggests that the endurance limit by the conventional fatigue concept cannot provide the safety design data for mechanical structures. Many researchers [4] have studied the fracture mechanisms in high-cycle range. Although the monitoring technique of fatigue crack is urgent in infrastructure, it has not been performed well so far. Development of the monitoring method is also an important issue.

We studied feasibility of acoustic emission (AE) as a method of fatigue damage monitoring of a bearing steel (SUJ2). Both the smooth rectangular bend specimens and compact tension (1/2 CT) specimens were used for studying fatigue crack initiation and propagation. The mechanism of fatigue damage was also investigated by waveform and source simulation analyses of AE signals.

Test Specimen and Experimental Procedures

The specimen used is a high-carbon chromium bearing steel (JIS G4805), which is commonly used for bearing components. The steel grade is designated as SUJ2. Chemical composition and mechanical properties of the specimen were shown in Tables 1 and 2, respectively.

Table 1 Chemical composition of SUJ2 (mass%).

C	Si	Mn	P	S	Ni	Cr	Mo	Cu
0.99	0.27	0.41	0.011	0.007	0.07	1.41	0.03	0.02

Table 2 Mechanical properties of SUJ2.

Density ρ Kg/m^3	Young's modulus *E* GPa	Poisson's ratio ν	Bending strength MPa
7910	205	0.28	2000

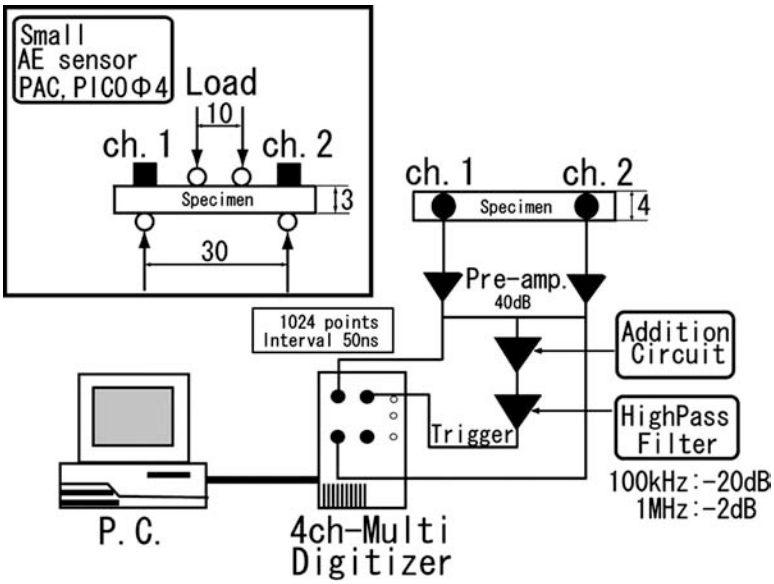

Fig. 1 AE monitoring system for four point cyclic bending test.

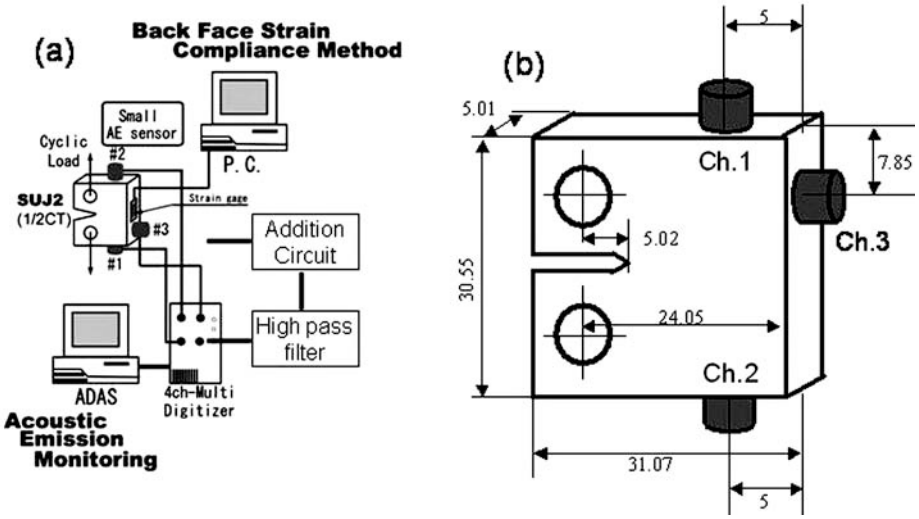

Fig. 2(a) Experimental setup for fracture mechanics test. (b) CT specimen with AE sensors.

Smooth rectangular bend specimens and compact tension (1/2 CT) specimens were prepared for studying the fatigue crack initiation and propagation. Figure 1 shows a monitoring system of AE from smooth rectangular specimens subjected to four-point cyclic bending test. AE signals are monitored by two small sensors (PAC, type Pico: resonant frequency of 450 kHz) mounted

on the compressive surface. Outputs of the sensors were amplified 40 dB by preamplifiers and fed to a personal computer via a high-speed A/D converter. In order to eliminate the low-frequency noise due to cyclic loading, the output signal via an adding-circuit and a high-pass filter was used as a trigger signal. Figure 2(a) shows an AE monitoring system for the CT specimen. The signal of channel 4 via the addition circuit and high-pass filter was used as trigger channel. Three sensors were used for monitoring the crack growth process as shown in Fig. 2(b). The length of fatigue crack was also monitored by the back-face strain compliance technique according to the ASTM standard.

Fatigue Fracture Mechanism of Smooth Specimen

Fatigue test at a constant load range (ΔP) was performed under the condition of maximum stress (σ_{max}) of 1000 MPa, stress ratio (R) of 0.1 and cyclic frequency (f) of 10 Hz. This specimen suffered fatigue failure at N_f of 4.9 x 10^4 cycles. We detected eight AE signals before the final fracture. Figure 3 shows typical AE waveforms detected. This specimen produces Lamb wave AE signals with symmetric (S-) and anti-symmetric (A-) modes. Weak first packet, indicated by arrows, was found to be the first component of the S_0-mode Lamb, traveled at sheet velocity of 5367 m/s. It is noted that the polarities of the first S_0 wave are the same (negative) for both sensors, indicating the Mode-I type fracture.

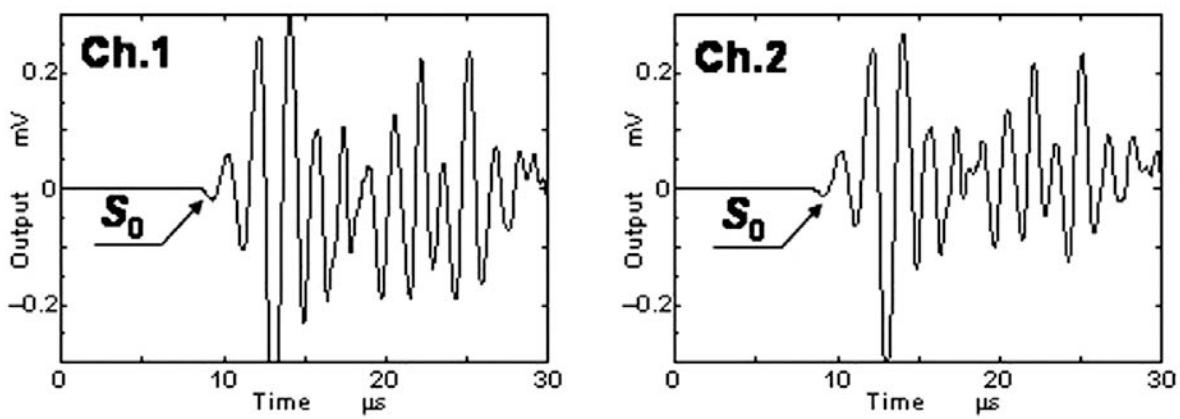

Fig. 3 Typical AE waveform detected during ΔP-constant test, Event count (E.C.7).

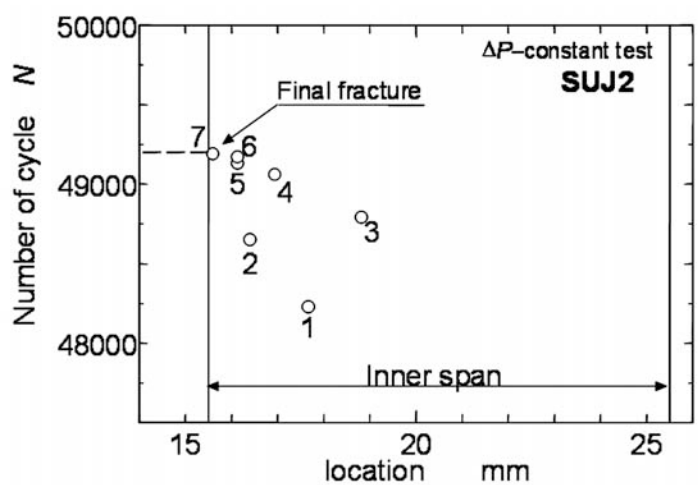

Fig. 4 Source location of AE detected during ΔP-constant test.

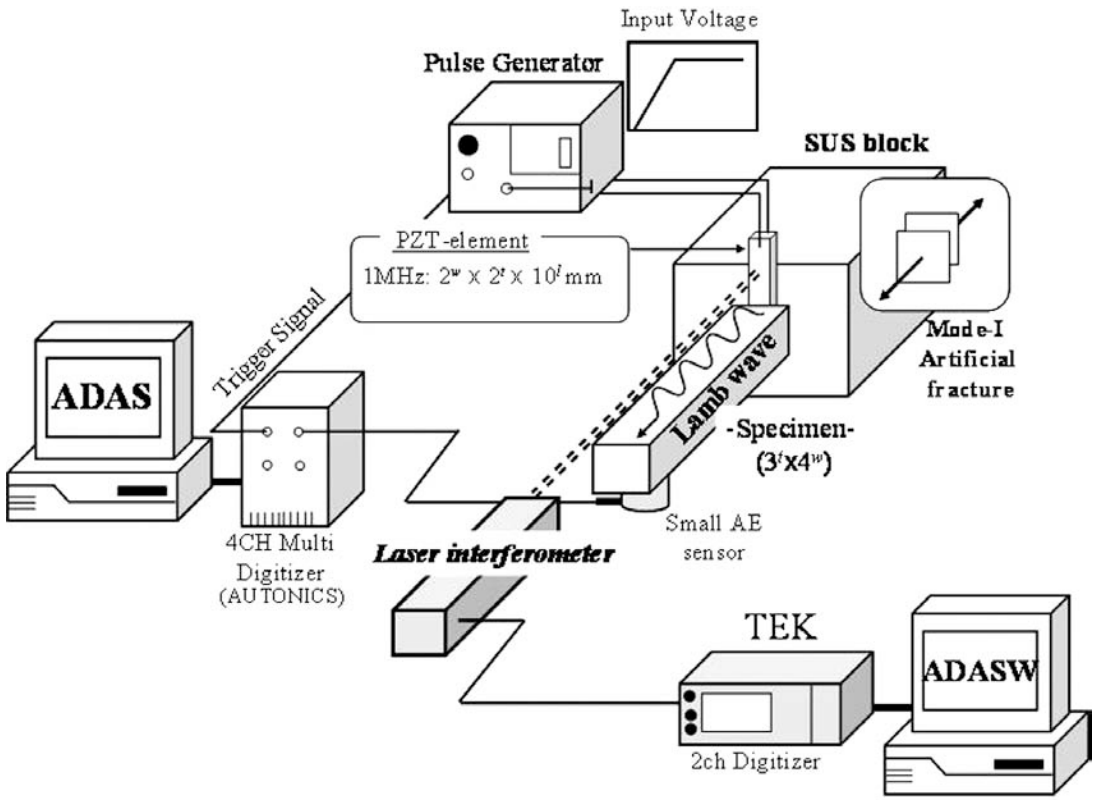

Fig. 5 Experimental setup to determine the experimental transfer function for source wave analysis of AE from smooth rectangular specimen subjected to four-point bend test.

Location of AE sources were estimated using the arrival time differences of the first S_0-waves between channels 1 and 2 and the sheet velocity. Figure 4 shows the source locations in the longitudinal direction of the specimen. The origin of abscissas (axial distance) is set at the left edge of the specimen. Both the inner span and final fracture location are indicated by vertical two lines. The vertical axis represents the number of cycle. Four AE signals (E.C. 2, 5-7) were located near the final fracture surface, and three AE signals (E.C. 1, 3, 4) were slightly far from the final failure.

In order to study the dynamics of micro-fractures, source wave analysis was attempted. Here, the fracture dynamics were estimated by waveform matching of the So-packet [5]. In order to estimate the source parameters (rise time ΔT_r and crack volume ΔV), the overall transfer function was first determined using the method shown in Fig. 5. We excited the Lamb wave AE by a thin compression-type PZT element glued to the end surface of a half-length specimen and a steel block. This simulates the Mode-I crack with Burgers (crack opening) vector in the direction of specimen axis. Figure 6(a) shows the waveform detected by AE sensor mounted on the same distance from the final fracture in the four-point cyclic bending. Out-of-plane vibration of the PZT element was separately measured by a laser interferometer and converted to a time transient function of crack volume: $Ab_j(t)$ in Fig. 6(b). Here, $b_j(t)$ designates the opening distance and A the contact area of the PZT element. A source wave of the Mode-I artificial fracture was given by a sinusoidal ramp function with rise time, ΔT_r, and crack volume, ΔV, as shown in Fig. 6(c). The overall transfer function to the Mode-I crack opening was obtained by the time-domain Gauss-Zeidel deconvolution of the detected waves (a) by the source wave (c), and is shown in Fig. 6(d).

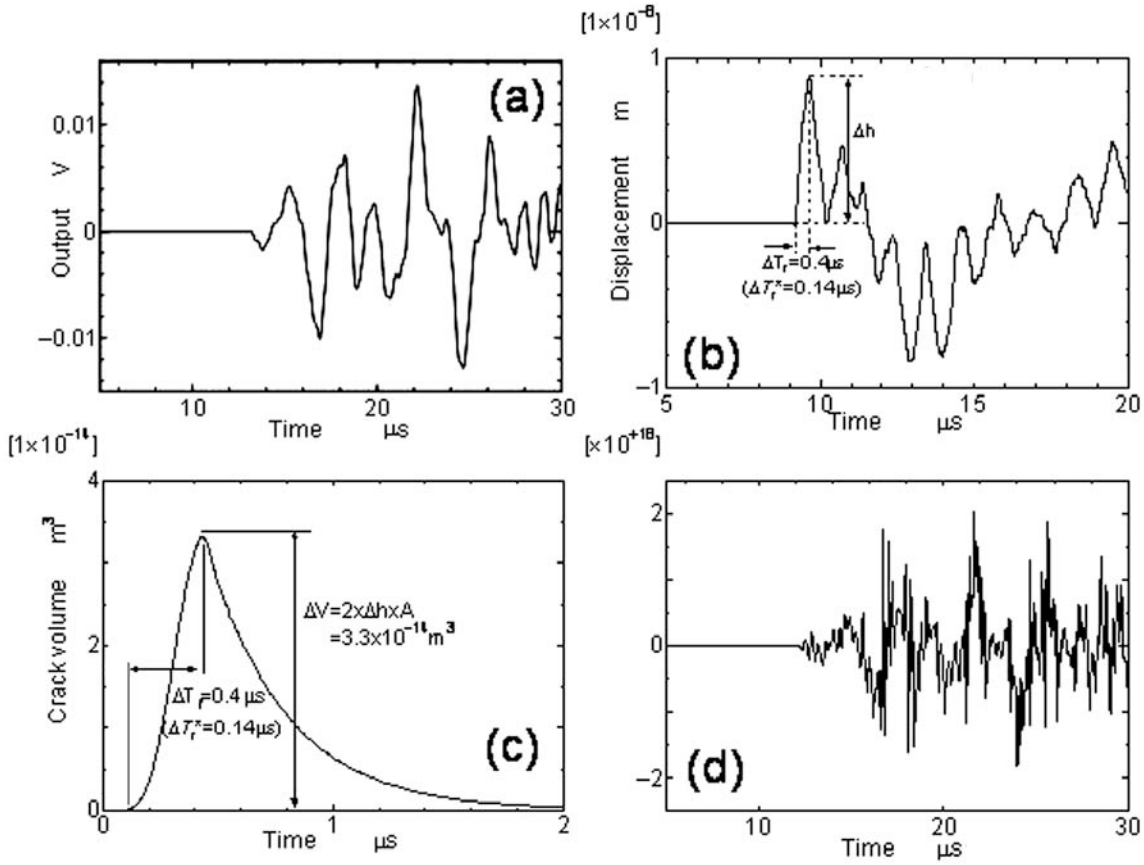

Fig. 6 Processing to determine the experimental transfer function. (a) Detected wave, (b) Out-of-displacement of PZT element, (c) Source wave of Mode-I artificial fracture, (d) Experimental transfer function for Mode-I fracture.

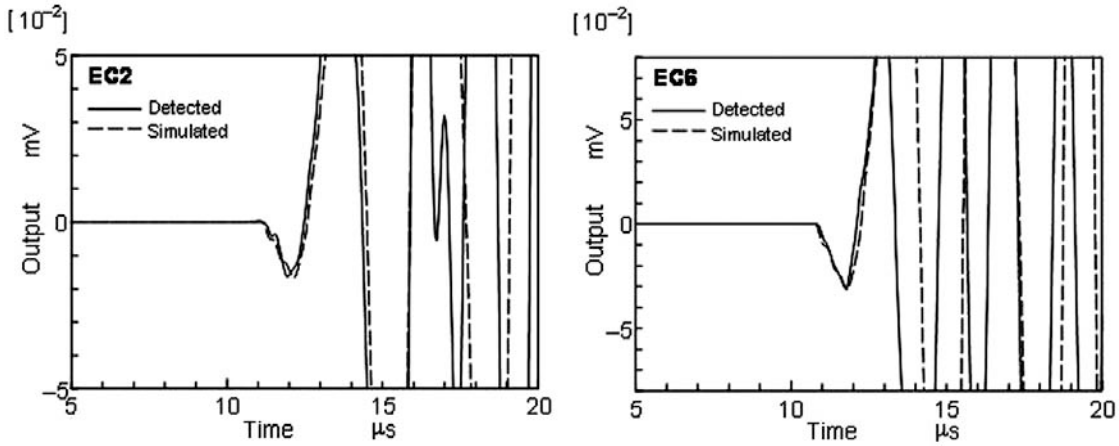

Fig. 7 Overlapping of simulated waveform on the detected Lamb wave under ΔP-constant test.

Figure 7 shows both a simulated wave (broken line) and a wave (solid line) detected during a fatigue test. The waveform was calculated repeatedly by changing the source parameters; ΔT_r and ΔV so that it matches the first wave of the S_0-mode. This simulation analysis was conducted for all the signals detected in a fatigue test. Figure 8 shows the ΔV distribution as a function of number of cycles. Crack volume (ΔV) appears to increase gradually with increasing the number of cycle (N). Figure 9(a) shows the fracture origin of the fractured specimen. We observed a semi-circular transgranular (TG) fracture and intergranular (IG) fracture further outside. Other specimens showed a similar surface morphology as schematically illustrated in Fig. 9(b). A mi-

cro crack was initiated at the origin near the tensile surface and propagated in TG and then IG manner. We, however, could not determine what is the AE source in this fatigue test. Therefore, we attempted another fatigue test to study quantitatively the relation of crack growth rate and AE behavior using a CT-specimen.

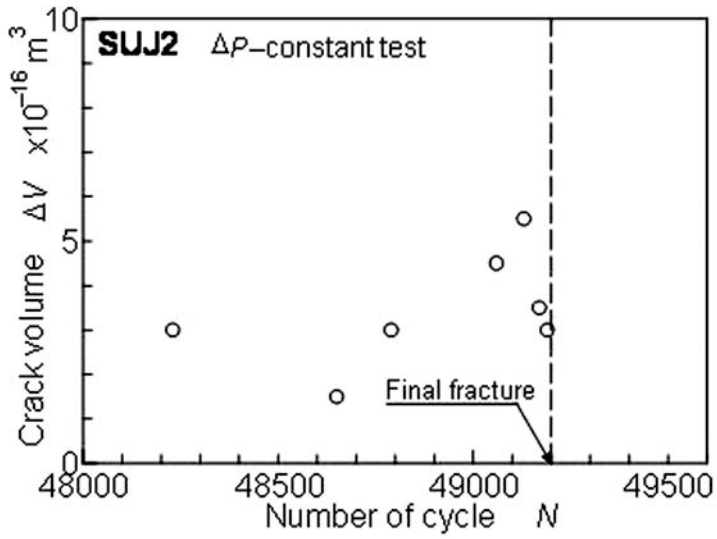

Fig. 8 Volume of micro cracks as a function of number of cycles during Δ*P*-constant test.

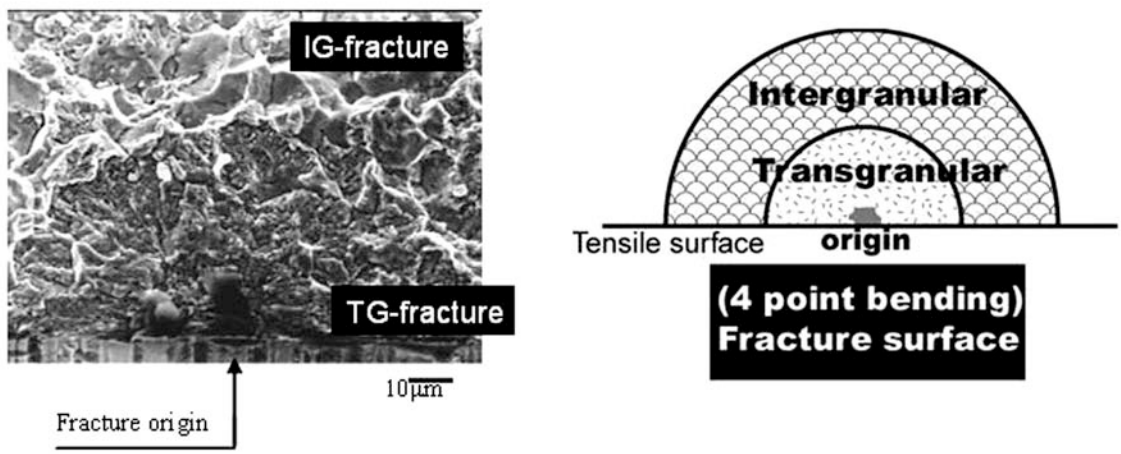

Fig. 9(a) SEM of fracture surface. (b) Schematic illustration.

AE Source Mechanism

Fatigue crack growth test was performed using the method shown in Fig. 2. We performed two common types of fatigue test. These are Δ*K*-increasing and Δ*K*-decreasing tests. Cyclic frequency (*f*) and stress ratio (*R*) were controlled at 20 and 0.1 Hz, respectively. Figure 10 shows the relationship between crack growth rate and maximum stress intensity factor (K_{max}). The solid line indicates the predicted crack growth rate for the high-strength steel proposed by Rolfe and Barsom [6]. Our data agreed well with the predicted rate in the second stage, but the crack growth rate increases at K_{max} larger than 8 MPa√m. Cumulative AE counts are also shown by dashed line in this figure, but the count data of Δ*K*-decreasing test was not shown, since only a few AE signals were detected. Total event counts reached 587 during Δ*K*-increasing test. The AE counts increased rapidly at *K* larger than K_{max} of 8 MPa√m, when the crack growth rate accelerated.

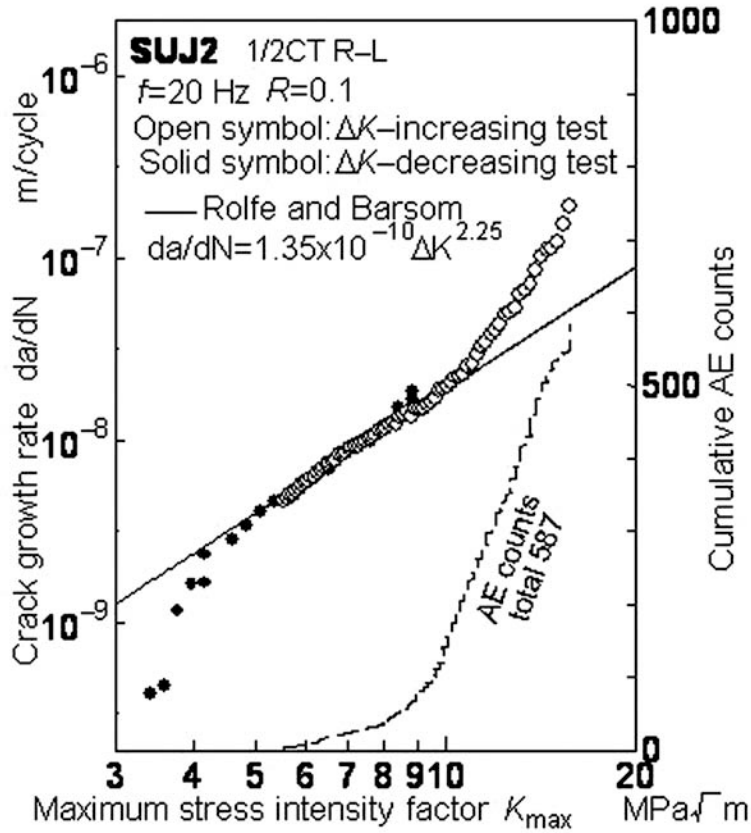

Fig. 10 Relationship between crack growth rate and maximum stress intensity factor with cumulative count of AE detected from a CT specimen.

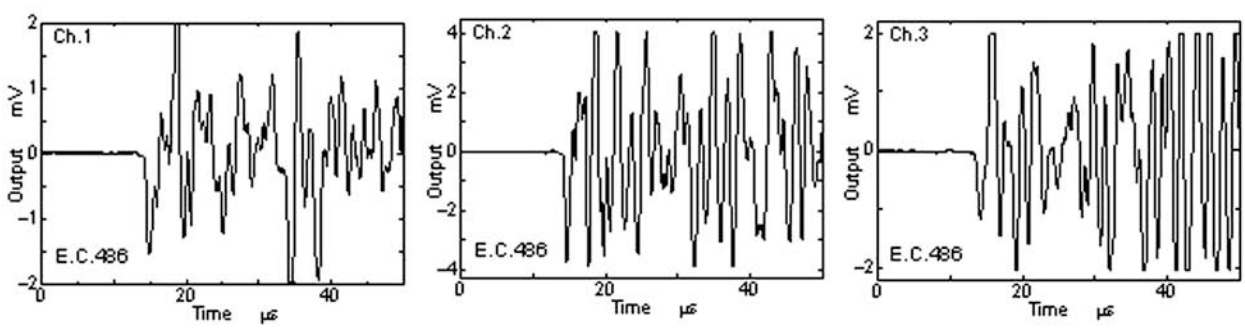

Fig. 11 Typical AE waveforms detected during fatigue crack growth of ΔK-increasing test.

Figure 11 shows typical waveforms of AE signals detected in the ΔK-increasing test. First sharp wave was found to be longitudinal wave traveling at 5657 m/s. Figure 12 shows two-dimensional AE source locations (x) during the fatigue test between K_{max} of 14.2 and 15.7 MPa√m. Sources were located near the fatigue crack. Location accuracy is relatively poor, since not all sensors detect AE with enough amplitude.

Figure 13(a) and (b) show the SEM photos of fracture surface during ΔK of 4 and 13 MPa√m. This shows a change of fracture mode from TG-fracture to IG-fracture with increasing the K_{max}. The ratio of IG-area was measured as shown in Fig. 14. Generation rate (counts/cycle) of AE was shown in the right vertical axis. The IG-fracture ratio increased rapidly after K_{max} of around

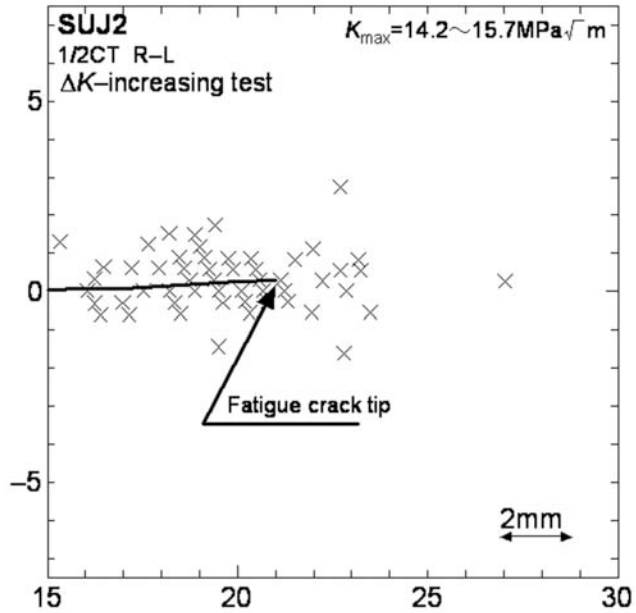

Fig. 12 Source location of AE signals detected in Δ*K*-increasing test.

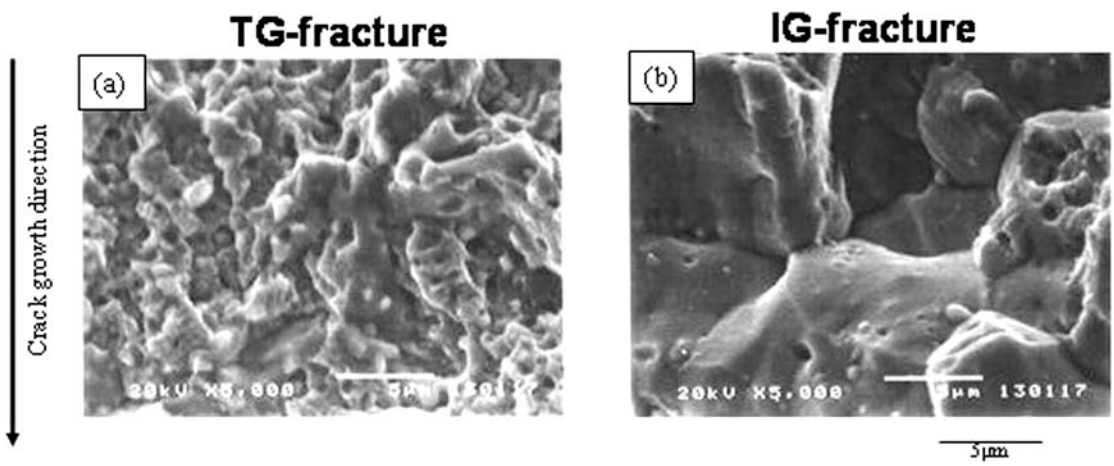

Fig. 13 SEM of fracture surface. (a) K_{max} of 4 MPa√m. (b) K_{max} of 13 MPa√m.

9 MPa√m, when the crack growth rate accelerated as shown in Fig. 10. These results revealed that AE signals were produced by IG-fatigue fracture.

Dynamics of Fatigue Fracture

Source wave analysis was conducted using the method of Fig. 5 in order to clarify the dynamics of IG cracking. Figure 15 shows an experimental setup for the determination of transfer function. We utilized a pulsed YAG laser [7] for this test. A pulse from the laser was focused into the slit filled with silicone grease to generate the breakdown of the grease. This can simulate the Mode I crack, since the expansion with opening vector in the loading direction occurs in a limited space. We detected the AE by a small PZT sensor and a laser interferometer. The latter measured the out-of-plane displacement of the P-wave and we utilized it to determine the source wave of the breakdown. Figure 16 shows a procedure for waveform simulation. First, we obtained the source wave of the laser breakdown by the deconvolution of detected out-of-plane displacement, Fig. 16(b), with the theoretical Green's function of the second kind, Fig. 16(a). The overall transfer function of the system was next obtained by the deconvolution of the PZT-

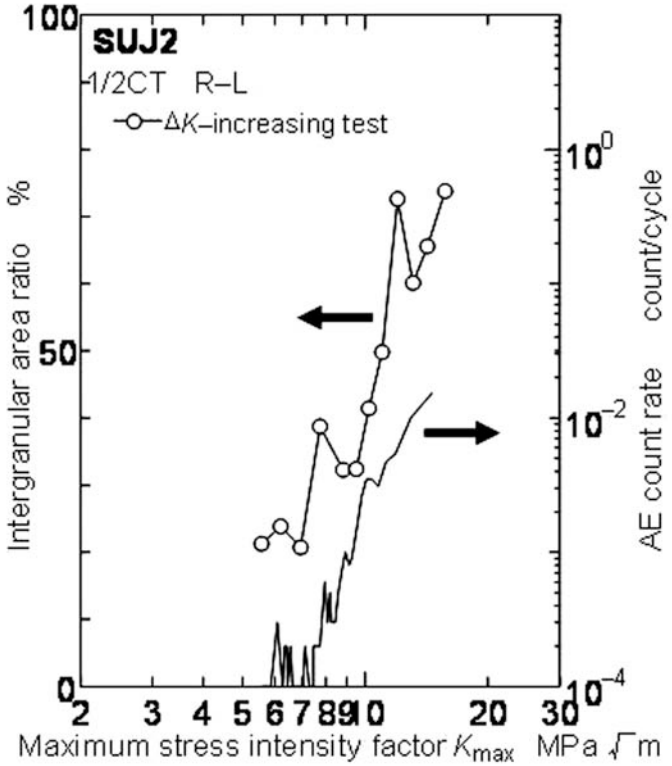

Fig. 14 Intergranular area ratio as a function of K_{max} with AE generation rate during ΔK-increasing test.

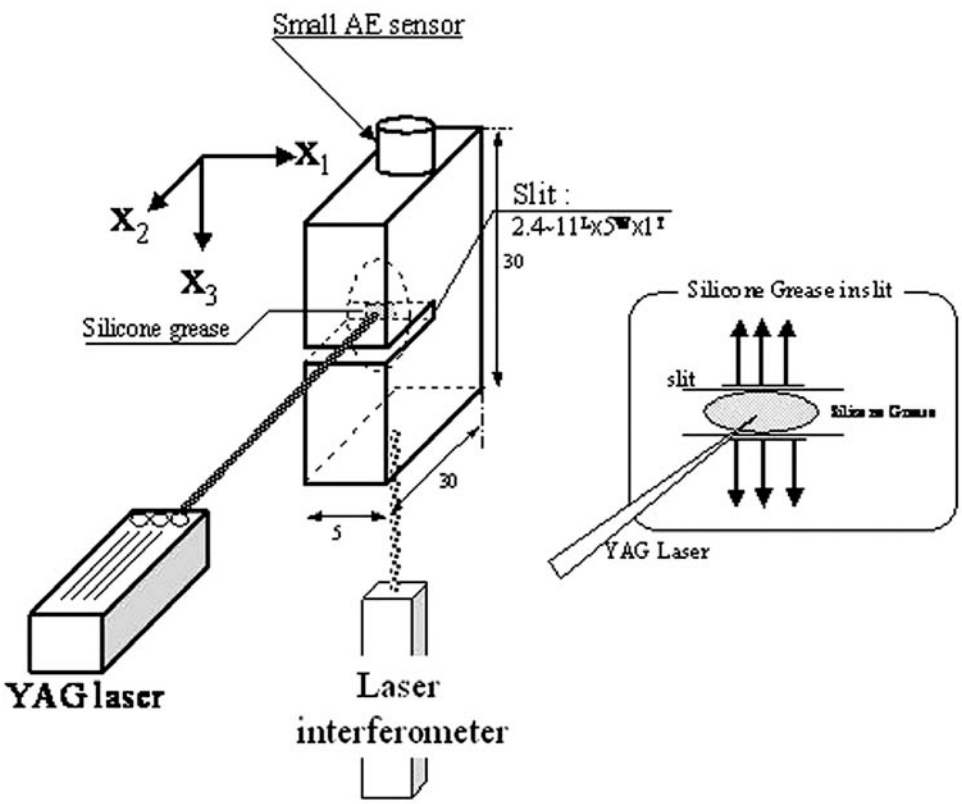

Fig. 15 Experimental setup to determine the experimental transfer function for source wave analysis of AE signals from a CT specimen during ΔK-increasing test.

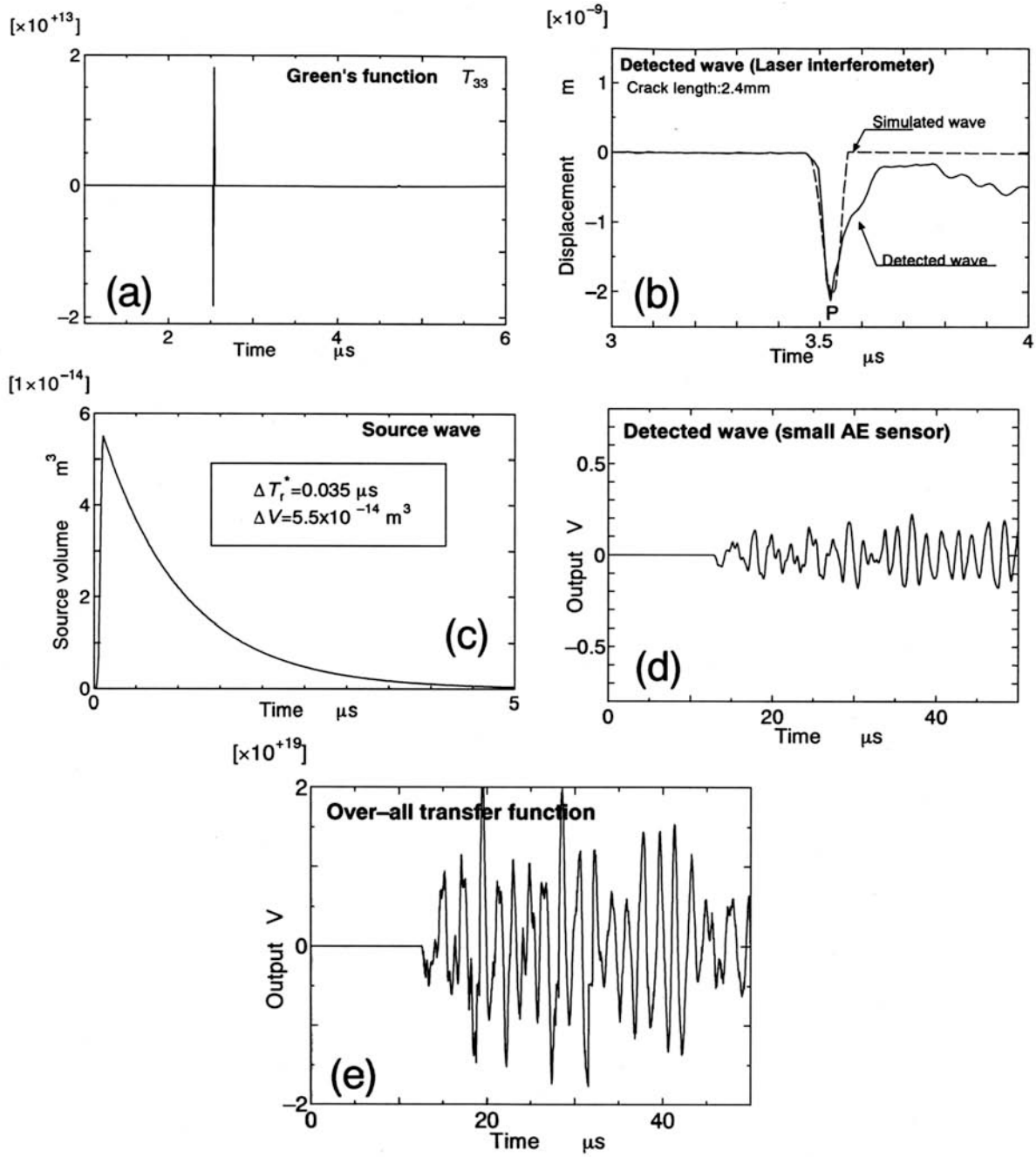

Fig. 16 Procedure to determine the overall experimental transfer function and crack volume ΔV. (a) Green's function, (b) Overlapping of out-of-displacement due to silicone grease breakdown and a simulated wave, (c) Source wave of Mode-I artificial fracture with selected values of ΔT_r and ΔV, (d) Detected wave of AE sensor, (e) Experimental transfer function for Mode-I fracture.

detected waves, Fig. 16(d), by the source wave Fig. 16(c), adjusting rise time and ΔV. The overall transfer function is obtained as Fig. 16(e). Finally, the source waves of AE signals produced by fatigue crack were estimated by the manner similar to that shown in Fig. 7.

Figure 17 shows the estimated crack volume as a function of K_{max}. Solid line indicates the IG-crack volume of a single grain. Here, the crack opening displacement (COD) was assumed to be 0.3 μm from the relationship of stress intensity factor and COD [8]. Crack volume: ΔV was found to increase with increasing K_{max}. These values correspond to the results of smooth rectan-

gular specimen as already shown in Fig. 8. Crack volume ΔV are mostly larger than those estimated for single grain fracture. Typically, two to three grains fracture, but at higher K_{max} values, ΔV was as high as 10-times the single grain ΔV. This suggests that fatigue crack propagates along some grains at one cycle and emits strong AE. Therefore, fatigue crack grows faster as shown in Fig. 10. AE sources were concluded to be IG-fracture. These results tell us that AE technique can be useful for the detection of IG cracks in the third-stage fatigue before the final fracture.

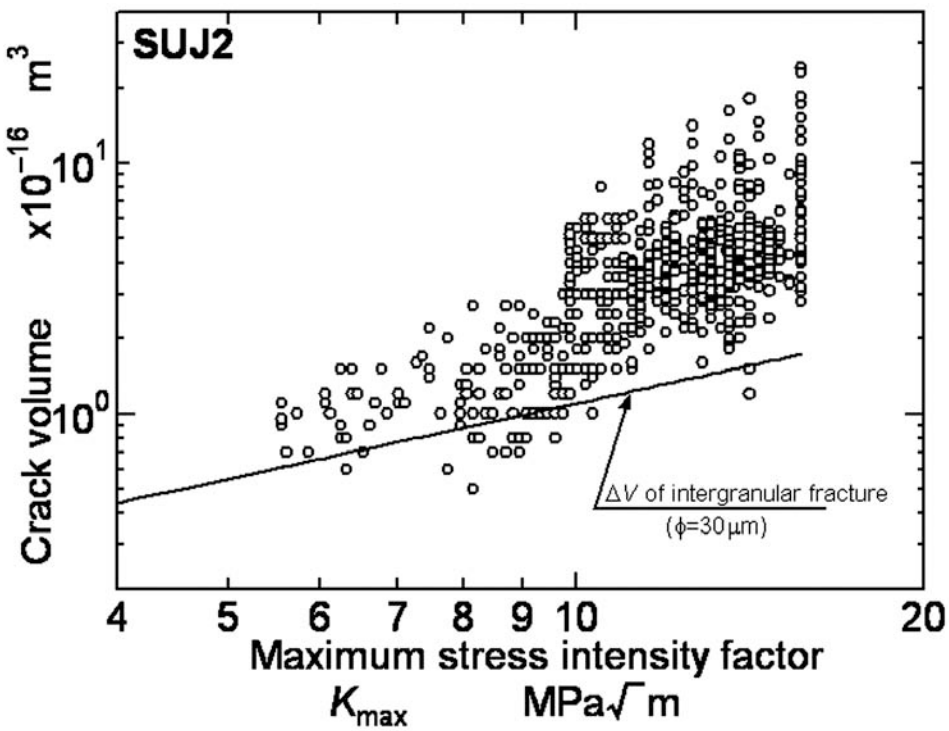

Fig. 17 Volume of micro cracks as a function of K_{max} under ΔK-increasing test.

Conclusion

We studied fatigue fracture behavior of a high-strength steel by AE technique. Source phenomena and source dynamics of AE signals were examined by fracture surface observation and waveform simulation analysis of AE signals . Results are summarized below.

1. High-strength steel subjected to four-point cyclic bending test suffered fatigue failure. The steel suffered the TG-fracture at the origin followed by the IG-fracture. A few strong AE signals were detected just before the final fracture. Source wave analysis estimated small fatigue crack of crack volume $\Delta V = 10^{-16}$ m^3.
2. The fracture mode of fatigue crack changes from TG-fracture to IG-fracture at K_{max} of 8 MPa√m. Fatigue test at higher K values produced faster crack propagation and higher AE generation. AE sources were located near the fatigue crack. IG fatigue fracture was found to produce strong AE.
3. Source wave analysis indicates that the fatigue crack progresses along a few grain boundaries during one cycle (IG-crack) and emitted strong AE. AE technique was found to be useful for the detection of IG crack before the final fracture.

Acknowledgement

This work was performed as a part of the Center of Excellence (COE) Program, funded by the Ministry of Education, Culture, Sports, Science and Technology.

References

1) E.g. H. Kobayashi, A. Todoroki, T. Oomura, T. Sano and T. Takehara, Elevated temperature ultra-high-cycle fatigue properties and fracture mechanism of modified 2.25Cr-1Mo steel, proc. 3rd conference on VHCF-**3**, pp. 536-541 (2004).
2) S. Masuda, S. Nishijima and Y. Tanaka, Relationship between fatigue strength and hardness for high strength steels, Trans. JSME, **52**A, 847-852 (1986). (in Japanese)
3) T. Sakai, M. Takeda, K. Shiozawa, Y. Ochi, M. Nakajima, T. Nakamura and N. Oguma, Experimental reconfirmation of characteristic *S-N* property for high carbon chromium bearing steel in wide life region in rotating bending, J. Soc. Mat. Sci, Japan **49**, 779-785 (2000). (in Japanese)
4) Y. Murakami, Metal Fatigue: Effects of small defects and nonmetallic inclusion, Yokendo Ltd (1993).
5) M. Takemoto, O. Tamura, and H. Suzuki, AE study of stress corrosion cracking mechanism of stainless steel foil using quantitative Lamb wave analysis and video images., J. Acoustic Emission, **16**, 177-204 (1998).
6) S.T. Rolfe and J. M. Barsom, Fracture mechanics properties of carbon and alloy steels, ASM **19**, p. 534 (1996).
7) K. Ono, Current understanding of mechanisms of acoustic emission, J. Strain Analysis, **40**-1, pp. 1-15 (2004).
8) H. Ishikawa, Finite element analysis of stress intensity factor by J-integral, Trans. JSME, **46**A, 67-76 (1979).

QUANTITATIVE DETECTION OF MICROCRACKS IN BIOCERAMICS BY ACOUSTIC EMISSION SOURCE CHARACTERIZATION

SHUICHI WAKAYAMA, TAKEHIKO JIBIKI and JUNJI IKEDA*
Department of Mechanical Engineering, Tokyo Metropolitan University, 1-1, Minami-Ohsawa, Hachioji, Tokyo 192-0397, Japan. * Department of Biomaterial Research Development, Japan Medical Materials Co., Miyahara, Yodogawa, Osaka 532-0003, Japan.

Abstract

Quantitative detection of microcracks generated in alumina bioceramics for artificial joints was carried out by AE source characterization. Fracture toughness tests using CT specimens were conducted in air and water. Stable crack propagation was observed with rapid increase in AE signals emitted from microcracking. The combined response function of the specimen and measurement system was determined using pencil-lead breaks as a simulated source. AE source functions were obtained by inverse calculation from detected AE signals. Size and nucleation velocity of microcracks were determined from the source function. From these results, it was found that both radial and nucleation velocity of microcracks in water is larger than those in air. They also show excellent agreement with the results of SEM fractography.

Keywords: Alumina, bioceramics, microcrack, AE source characterization

Introduction

The bioceramics are suited for medical use because of their high biocompatibility [1-3]. The femoral head in total hip replacement is the most representative application. The lifetime of the bioceramics was often designed as between 10 to 15 years. However, a number of ceramic femoral heads have failed in human body within several years after their installation. Thus, a technique to assure extended lifetimes of bioceramics is urgently needed.

Conventionally, the lifetime prediction based on the K-v curve was proposed considering the propagation of one maincrack [4]. However, the maincrack formation may result from the nucleation and coalescence of microcracks [5]. On the analogy of fatigue life in metals, the process to maincrack formation is considered to be dominant in the whole lifetime of ceramics. Therefore, it is important for the assessment of long-term reliability to understand the microfracture processes before the maincrack formation.

The purpose of the present study is to obtain the fundamental information for precise lifetime prediction of bioceramics. One of the authors has already quantitatively characterized microcracks of alumina ceramics in air by AE source characterization [6, 7]. In this study, the size and nucleation velocity of microcracks of bioceramics were characterized also in water simulating human body environment to evaluate the effect of environment on microcracking.

Theoretical Aspect

Figure 1 shows the model of a dislocation and displacement in an elastic solid. The displacement $u_i(\mathbf{x}, t)$ at the point $\mathbf{x} = (x_1, x_2, x_3)$ and time t due to the dislocation $\boldsymbol{\phi}(\mathbf{x'}, t')$ is

$$u_i(\mathbf{x},t) = \int_0^t dt' \int_A \nu_q \cdot \phi_p(\mathbf{x}',t) \cdot C_{pqjk}(\mathbf{x}) \cdot G_{ij'k'}(\mathbf{x},\mathbf{x}',t-t')dA \tag{1}$$

where ν_q is the q-component of the normal vector of the dislocation surface, ϕ_p is the p-component of the dislocation, C_{pqjk} is the elastic constant of the medium, A is the area of the dislocation surface, and G_{ij} is Green's function, which represents the displacement in the i-direction at $(\mathbf{x}, t)$ due to an instantaneous point force of unit impulse in the j-direction at $(\mathbf{x'}, t')$ [8]. $G_{ij,k'}$ is the derivative of G_{ij} in the k-direction (e.g. $\partial G_{ij}/\partial x_k$). As shown in Fig. 2, assuming the displacement in the x_3-direction at the epicenter of the microcrack opening in the same direction and is considered as a point source (e.g. i = j = k = 3, on ΔA), equation (1) becomes

$$u_3(\mathbf{x},t) = \int_0^t D(t) \cdot G_{33,3'}(\mathbf{x},\mathbf{x}',t-t')dt' = D(t) \otimes G_{33,3'}(t)$$

$$\text{with } D(t) = \phi_3(t) \cdot \Delta A \cdot (\lambda + 2\mu) \tag{2}$$

where $\phi_3(t)$ is opening displacement of the microcrack, ΔA is the area of the microcrack, and D(t) is an AE source function of the microcrack, and $\otimes$ represents time domain convolution. The AE source function is a step function with height of ΔD and rising time of Δt (shown in Figure 3). By using ΔD, radius of the microcrack, a, and nucleation velocity, V_c, could be determined as

$$a = \left(\frac{\Delta D}{3\pi^2 \sigma_c} \right)^{1/3} \tag{3}$$

$$V_c = 2\,a / \Delta t \tag{4}$$

where σ_c represents the critical stress for maincrack formation. However, when the displacement $u_3(\mathbf{x}, t)$ is detected by the AE sensor, its output V(t) is

$$V(t) = G(t) \otimes S(t) \otimes D(t) = R(t) \otimes D(t) \tag{5}$$

where S(t) is the response function of AE measurement system, R(t) is called combined response function. In order to calculate the AE source function, following time deconvolution is essential.

$$D(t) = V(t) \otimes R^{-1}(t) \tag{6}$$

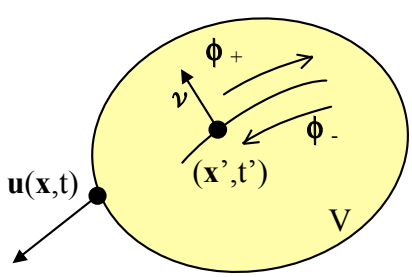

Fig. 1 Model of displacement dislocation in elastic medium.

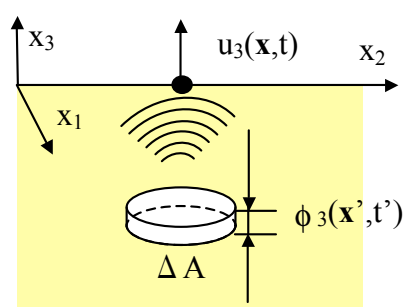

Fig. 2 Model of microcrack and epicenter displacement.

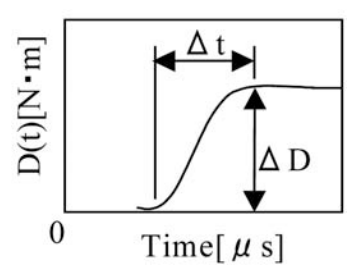

Fig. 3 Example of AE source function D(t).

The response function for monopole source, $R_m(t)$, could be determined by well-defined monopole source such as pencil-lead breaking. Conversion from monopole to dipole source such as crack opening can be accomplished by

$$R(t) = \frac{\partial}{\partial x_3} R_m(t) = \frac{\partial t}{\partial x_3}\frac{\partial}{\partial t} R_m(t) = \frac{1}{V_L}\frac{\partial}{\partial t} R_m(t) \tag{7}$$

where V_L is the longitudinal wave velocity.

Experimental Procedures

Specimens

High purity alumina ceramics (Japan Medical Materials Co.), the material for actual artificial joints, was used in this study. Mechanical properties are given in Table 1. The 0.5-inch CT specimens were used for fracture toughness tests. To avoid the influence of reflected waves, thickness of the specimen was selected as 1 inch. In order to minimize the effect of water content on fracture process especially at the tests in air, specimens were dried in a vacuum drying oven at 150 °C for 2h.

Table 1 Mechanical properties of alumina (Manufacturer's data)

Density [g/cm^3]	Purity [%]	Average Grain Size [μ m]	Elastic Modulus [GPa]
3.97	>99.9	1.4	400

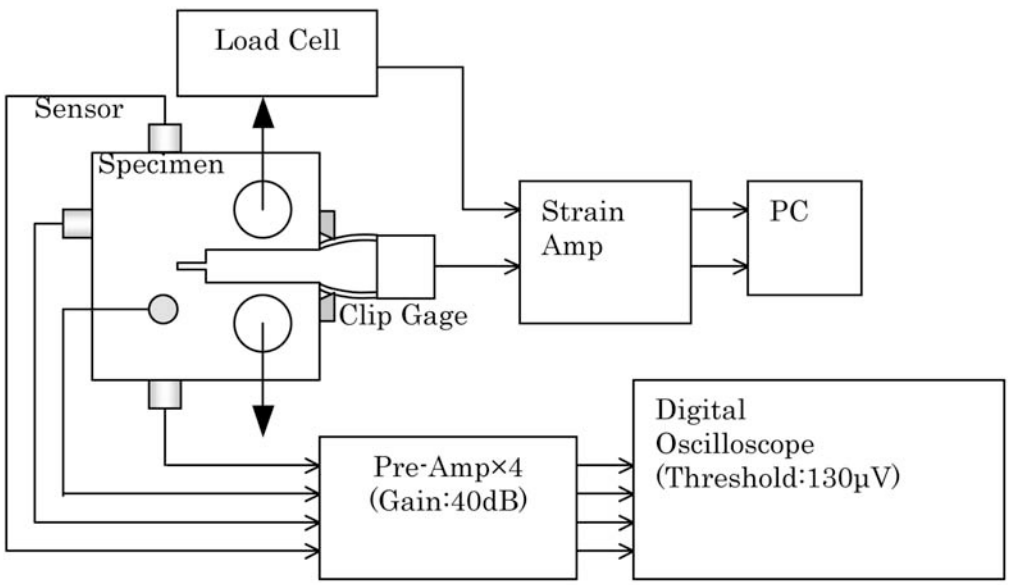

Fig. 4 Schematic diagram of the testing system.

Fracture Toughness Test using CT Specimens and AE Measurement

The testing system is described in Fig. 4. CT specimens were loaded at a crosshead speed of 0.01 mm/min in air and in water and the load was measured by load cell. The specimens used for the tests in water have been soaked in water with ultrasonic bath for 30 minutes before the tests.

During the tests in water, only the portion of notch tip has been filled with water. Crack opening displacement (COD) of specimens were also measured by clip gage. At the same time, the waveforms of AE signals emitted from microcracks were detected by four piezoelectric AE sensors (Pico, PAC). The AE signals were amplified by pre-amplifiers and sent to a digital oscilloscope, whose sampling interval was 10 ns. Preamplifier bandwidth was 100 kHz to 2 MHz. Total gain was 40 dB, and threshold level was 130 μV at the input of pre-amplifiers.

Results and Discussion

AE Source Chracterization

Figure 5 shows the typical result of AE behaviors during the fracture toughness test using CT specimen. In Figure 5, compliance of specimen has changed with rapid increase in AE event and energy. Figure 6 shows the typical waveforms. Figure 6(a) shows an example of AE signal emitted by a microcrack nucleation during the fracture toughness test. Figure 6(b) shows an example of combined response function of specimen and AE measurement system determined using pencil lead breaking. Figure 6(c) shows an example of AE source function of the microcrack nucleation. Using equations (3) and (4), it was estimated that the microcrack with radius of 9.6 μm and nucleation velocity of 37 m/s was nucleated.

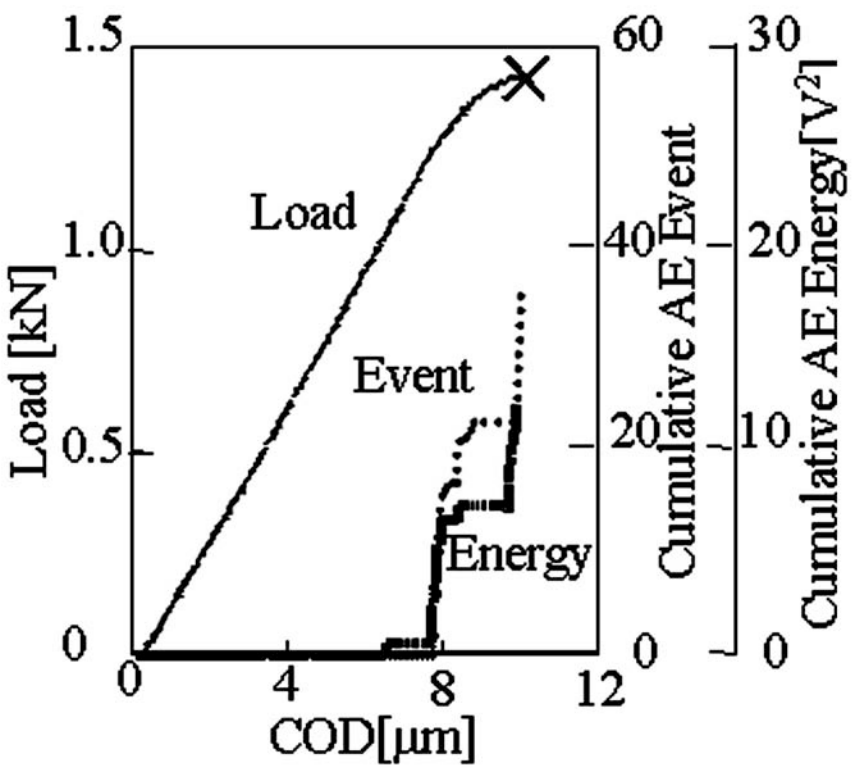

Fig. 5 Typical AE behavior during the test with notch in air.

Effect of Environment on the Microcracking

Figure 7 shows the result of the AE source characterization. Figure 7(a) shows the distribution of radius of microcracks generated during the fracture toughness tests. Figure 7(b) shows that of nucleation velocity. From the tests, microcracks with radius of 6.6~1 7μm and nucleation velocity of 9.5~47 m/s were detected. On the other hand, in water, the radius was 13~22 μm and

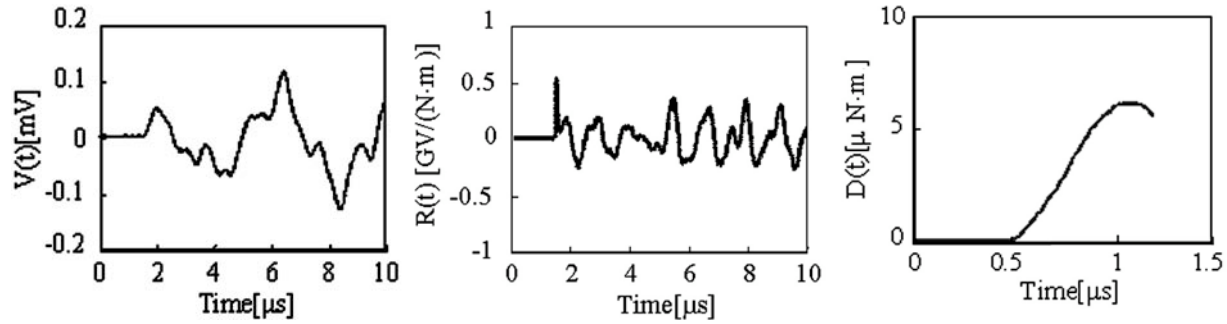

(a) AE signal, V(t). (b) Response function, R(t). (c) AE Source function, D(t).

Fig. 6 Typical waveform about microcrack nucleation.

the nucleation velocity was 26~86 m/s. Therefore, it is clear that both radius and nucleation velocity of microcracks formed in water are larger than those in air, which is likely due to the influence of stress corrosion cracking.

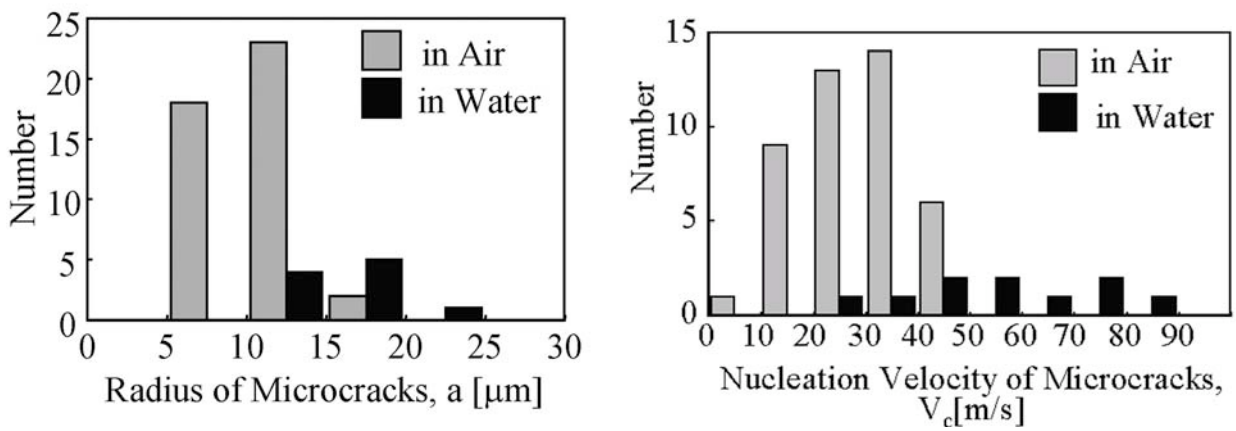

(a) Distribution of radius. (b) Distribution of nucleation velocity.

Fig. 7 The result of the AE Source characterization.

Average area of microcracks characterized by AE source characterization was 3.9 x 10^{-4} mm^2 in air and 8.9 x 10^{-4} mm^2 in water. On the other hand, coalescing intergranular cracks were observed on fracture surface by SEM and their average areas are 1.6 x 10^{-4} mm^2 in air and 7.9 x 10^{-4} mm^2 in water. Since they showed good agreement with each other, it was verified that the results of AE source characterization have reasonable accuracy.

Conclusions

Quantitative detection of microcracks in fracture process of bioceramics was conducted by AE source characterization, and the following conclusions can be drawn.

(1) By AE source characterization, it is understood that both radius and nucleation velocity of microcracks in water are larger than that in air, which might be the influence of stress corrosion cracking.
(2) The result of AE source characterization shows excellent quantitative agreement with that of observation by SEM, which verified that the results of AE source characterization have reasonable accuracy.

Although further investigation is needed for theoretical modeling of microfracture process, it should be emphasized that the indispensable knowledge for the reliability assessment of bioceramics was obtained in this study.

References

1) L. L. Hench: J. Am. Ceram. Soc., **81** (1998), 1705.
2) L. L. Hench, J. Wilson: *An Introduction to Bioceramics.* Advanced Series in Ceramics. World Scientific, **1** (1993), pp. 1-24.
3) H. Aoki and S. Tanba: *Bioceramics-Development and Clinical Applications, Quintessence* (1987), p. 26.
4) J. E. Ritter Jr, P. B. Oates, E. R. Fuller Jr and S. M. Wiederhorn: J. Mater. Sci., **15** (1980), 2275.
5) S. Wakayama, T. Koji and H. Nishimura: Trans. Jpn. Soc. Mech. Eng., **A57** (1991), 504.
6) S. Wakayama, T. Kishi, and S. Kohara: *Progress in AE, III, JSNDI,* (1986), p. 653.
7) S. Wakayama, T. Kishi, and S. Kohara: Frac. Mech. Ceram., **8** (1985), 85.
8) R. Burridge, L. Knopoff: Bul. Seis. Soc. Am. **54** (1964), 1875.

DETERMINATION OF WAVE ATTENUATION IN ROCK SALT IN THE FREQUENCY RANGE 1 - 100 kHz USING LOCATED ACOUSTIC EMISSION EVENTS

GERD MANTHEI, JÜRGEN EISENBLÄTTER and THOMAS SPIES*
Gesellschaft für Materialprüfung und Geophysik, Dieselstraße 9, D-61231 Bad Nauheim, Germany. *Federal Institute for Geosciences and Natural Resources (BGR), Stilleweg 2, D-30655 Hannover, Germany.

Abstract

Rock salt is a candidate material for construction of a telescope detecting ultrahigh-energy neutrinos by acoustic emission measurements. These ultrahigh-energy neutrinos are generated, for instance, by the collision of galaxies or supernova explosions. Interaction of these ultrahigh-energy neutrinos with matter is extremely seldom. Therefore, the telescopes have to have dimensions of kilometers in all directions and should be placed in the ocean, or in the polar ice, or in salt domes. The economical feasibility of an acoustic neutrino detector strongly depends on the spacing between the acoustic sensors. In this paper we will report on our experience of acoustic wave propagation and wave attenuation in rock salt in the frequency range of 1 to 100 kHz and some conclusions with respect to the usefulness of rock salt as a neutrino detector. The experience bases on long-term acoustic emission measurements in a salt mine.

Keywords: Acoustic emission, microcracking, rock salt, wave attenuation, neutrino detector

Introduction

Before we are going to present results of our acoustic emission (AE) measurements in salt rock, a brief introduction on neutrino detection is given. Neutrinos are particles which are emitted from most violent astrophysical sources like exploding stars (see http://icecube.wisc.edu). They are interacting extremely seldom with matter. The feeble interaction of neutrinos with matter makes them ideal astronomical messengers. Neutrinos can travel across the universe without hindrance and interference. However, this same attribute makes cosmic neutrinos difficult to detect. Most of the trillions of neutrinos that stream through a human body or a square meter of the Earth's surface every second do not leave any trace. But, on rare occasions, a passing neutrino crashes into a proton or neutron. This collision produces a particle called muon. The muon travels in the same direction as the parent neutrino hundreds of meters or even kilometres through a detector material like ice, water or salt rock. Muons from high-energy neutrinos (energy range between 10^{11} and 10^{16} eV) radiate blue light, which is the so-called Cherenkov radiation. In transparent ice or clear water this light can be detected by optical sensors like photomultiplier tubes. A neutrino telescope must be huge, transparent, dark, and below the earth surface to shield cosmic rays. Therefore, deep oceans or the 3000-m-thick Antarctic ice cap are used as a neutrino telescope. The so-called IceCube is the first kilometer-scale neutrino observatory, which is now under construction [1]. About 4800 photomultipliers will be installed 1500 m below the ice surface in a 1 km x 1 km x 1 km volume.

Ultrahigh-energy neutrinos (energy of $>10^{17}$ eV) have great cosmological significance and may reveal new physics beyond the standard models. Because of decreasing neutrino flux with

increasing energy an observatory far larger than one cubic kilometer will be required. An estimation shows that no more than one ultrahigh-energy neutrino per year can be detected with IceCube (see http://icecube.wisc.edu). For a few years, salt domes have been under consideration to detect the interactions of ultra-high energy neutrinos with rock salt. Salt domes are widely distributed and have a suitable size of typical dimensions 3 x 4 x 5 km. The disadvantage of salt relative to ice is due to the rapid decrease of Cherenkov light intensity. Ice is far more transparent than salt to light.

Besides the Cherenkov radiation, a part of the energy is converted into acoustic energy. The basis for the AE of ultrahigh-energy neutrinos is a thermo-acoustic effect, which was first proposed by Askariyan [2] and Learned [3]. Their model is based on the fact that in a condensed medium the energy of an electromagnetic cascade resulting from the neutrino interaction is concentrated in a roughly cylindrical volume of length $L \approx 5$ m and diameter $d \approx 5$ cm in a liquid or solid (see Fig. 1, left-hand side).

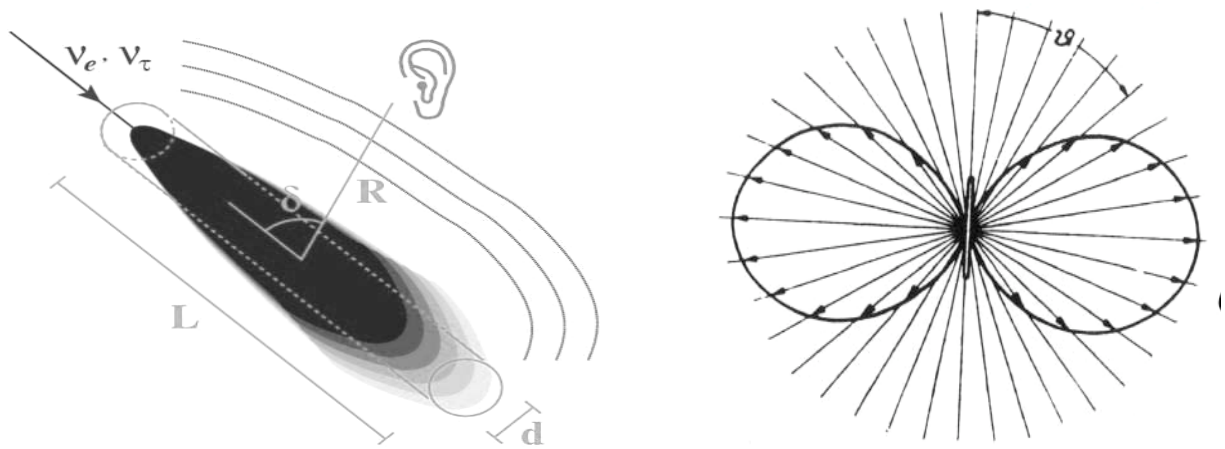

Fig. 1 Thermo-acoustic model of electromagnetic cascade resulting from the neutrino interaction (left-hand side) and radiation pattern of P wave with this model (right-hand side) [4].

Due to the rapid thermal expansion of the material in the cylindrical volume, compressional waves or so-called P waves are produced. The amplitude of the P wave is determined by the cascade energy, the thermal expansion coefficient, and the wave velocity in the medium. The maximal amplitude is in a direction orthogonal (incidence angle $\vartheta = 90°$) to the axis of the cylinder (right-hand side of Fig. 1). In axial direction ($\vartheta = 0°$) of the cylindrical volume only small signal amplitudes will be emitted. The expected frequency of the P wave is in the range between 10 to 60 kHz and lies exactly in the frequency range in which we are detecting microcracking in salt mines. Besides the primary effect of thermal expansion a secondary source of acoustic emission may be microcracking in the heated volume induced by the generated transient deviatoric stress field.

The idea of many researchers in this field is to investigate the feasibility of detecting high-energy neutrino interactions in underground rock salt domes using a network of many AE sensors. To determine the spacing between the sensors, attenuation of acoustic waves plays a major role for the use of salt domes as a neutrino detector. Price [5] calculated attenuation coefficients for grain diameters from 0.2 to 2 cm for rock salt as a function of frequency in a range from 1 to 100 kHz. He concluded that in pure and undisturbed rock salt, the scattering at grain boundaries is the limiting factor of the detection length and that absorption plays a minor role and can be

neglected. He compared the result of his calculations with ultrasonic measurements at 58 to 64 kHz in the Huckley Salt Mine, Texas [6] and with our AE measurements in the repository in Morsleben, Germany [7].

The present authors have already reported several times about AE measurements in rock salt at earlier conferences [8-11]. Their earlier contributions showed field studies from the central and southern sections of the underground repository of Morsleben in a salt mine in northern Germany. Originally, the central section of the repository was monitored by a network of 24 AE sensors since 1995. This network was recently enlarged to 48 channels and covers now a rock volume of about 250 m x 200 m x 120 m. The signals are recorded in the frequency range from 1 to 100 kHz. The sensors are distributed at three excavation levels installed in 3 to 20 m deep boreholes. The average depth of the monitored volume is about 400 m. Mining in this area continued until the 1960's, but most of the rooms in the rock salt were mined 60 to 70 years ago. The aim of these AE measurements is to investigate the micro- and macrocracking processes, which are important for the evaluation of the stability of cavities and the hydraulic integrity of the rock, which is of special interest in the case of an underground disposal of hazardous waste in salt rock.

To estimate the attenuation of ultrasonic signals during their propagation through the rock salt, we describe a method, which is successfully applied for many years during long-term AE measurements in salt mines. This method uses the maximum amplitudes of the signals and the location of the events to calculate an event magnitude analogous to the magnitude in seismology and the damping coefficient of AE signals in rock salt.

In general, the deformation of large rock salt formations occurs for the most part without the formation of macrocracking. Microcracking occurs, however, near cavities and at rock boundaries. The cavities are mined mostly in rock salt, which has a high tendency to creep. It is not always possible to avoid excavating cavities near anhydrite layers. The brittle anhydrite is much more rigid and has a higher strength than rock salt. The redistribution of stresses around cavities leads to deviatoric stresses near rock boundaries. If these stresses exceed a certain level, microcracks form.

For this study, we investigated wave attenuation in rock salt under high deviatoric stress conditions accompanied by high AE activity. For this purpose, AE events, which have been located in a time period of 9 months (November 15, 2004 to August 23, 2005), were considered in our analysis. Half a year before, in this mine segment, one cavity was backfilled. This mine segment showed persistent high AE activity because of stress redistribution and high humidity [11]. Previously, there was almost no activity before backfilling in this segment.

Location of AE Events

To determine the attenuation of acoustic waves the length of the travel paths from the AE source to the sensors and, therefore, source location is of upmost importance. During long-term AE measurements in salt mines, a huge number of events (up to 350 located events per hour) can be detected. Fast data-acquisition systems and in-situ location are essential to process all data. Therefore, in-situ location is a standard procedure during data acquisition [12]. The locations of AE events are determined by inversion of the travel times of P waves and S waves, which are extracted from the signals (see for example Fig. 2, where very clear P- and S-wave onsets are discernible at each channel).

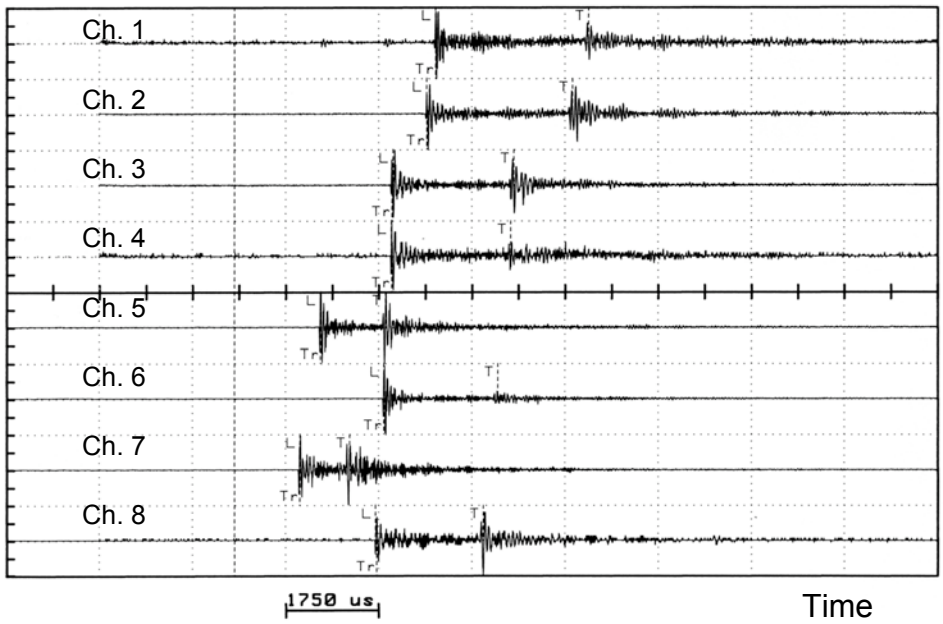

Fig. 2 Signals of a located AE event from the Asse salt mine, detected using 8 borehole sensors in rock salt [12]. This test site contains no larger cavities that could hinder wave propagation.

This is done in different steps. After pre-processing of the signals by filtering and smoothing operations, in a first step the P-wave onsets are automatically picked using high-quality signals only, i.e. signals with high signal-to-noise ratio. From these P-wave onsets a first estimation of the source coordinates is made using an iterative least-squares procedure. If the residual error is larger than 0.8 m, the onsets with the largest residues are stepwise eliminated and a new solution is calculated until the residual error drops below the 0.8-m limit.

In order to be able to locate sources outside of the sensor network, we also consider the S-wave onsets. Therefore, we automatically pick the S-wave onsets in a time interval around the S-wave onsets expected due to the result of the location using P-wave onsets only. In the second step of source location, we use the found S-wave onsets together with the remained P-wave onsets. P-wave and S-wave onsets with large residues are again eliminated until the residual error falls below 0.8 m. Locations are considered valid only if at least ten onsets (P wave or S wave) have remained. A by-product of such location procedure is that typical working noise without clearly discernible onsets and, therefore, wrong arrival times are eliminated due to large travel time residuals.

In spite of the complex geometric situation with AE sensors in the vicinity of closely spaced excavations and resultant masking of direct wave propagation paths, we obtain a location accuracy of about one meter in distance up to 50 m around the sensor network, using the described procedure.

Figure 2 shows the signals of a located event in salt rock. In this case, an array of eight AE transducers was used for source location. The onsets of the first signal peaks were automatically determined ("Tr"). In addition to the residual error, the agreement between calculated onsets of the P wave ("L") and the S wave ("T") with the observed onsets assesses the quality of location. In this example, the event is located within the sensor network in an undisturbed rock formation and, therefore, the location error is very small and amounts about 20 cm.

The sites of the AE activity from a time period of about 9 months between four excavation levels are shown in a top view in Fig. 3. The extension in vertical direction amounts to approximately 120 m. Each AE event is plotted as a point. Only strong events (696,278 events), which were precisely located using at least 16 P- and S-wave arrival times are included in this figure. The locations of the AE borehole sensors are plotted as open circles.

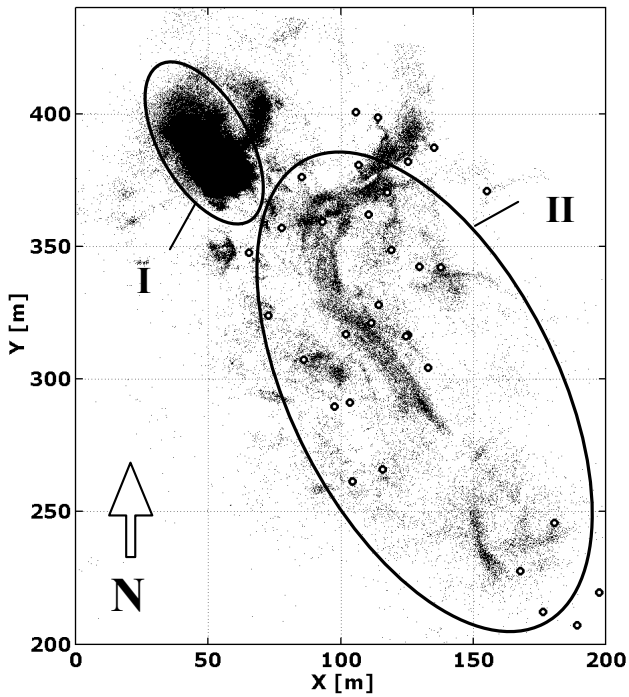

Fig. 3 Location of AE events between November 15, 2004 and August 23, 2005 (696,728 events) in top view.

The events can be roughly separated into two Regions I and II (marked by ovals). The highest density of AE events was observed in Region I outside the AE network above the backfilled cavity. The AE network is only able to monitor the roof of the cavity, not the floor and the walls, because all sensors are located at levels higher than the cavity. The events in Region II were preferably located along walls of open cavities, which will be backfilled in the future. Compared with Region I, most of the events of Region II occurred 50 m to 100 m higher than in Region I. The AE activity in this area is interpreted as ongoing damage in the immediate vicinity of mine cavities and rock boundaries due to dilatancy under deviatoric stress conditions.

Determination of AE Magnitude and Attenuation Length

The maximum amplitudes A of all sensors in a network and the distances r of an AE source to the sensors are used to determine a measure of signal strength in an analogous way as with magnitude determination in seismology using a relation, which considers geometric wave attenuation as well as attenuation by damping:

$$A(r) \propto \frac{1}{r} \cdot \exp(-\alpha \cdot r) \tag{1}$$

where α means the damping coefficient. The amplitudes are specified in the logarithmic decibel (dB) scale. In a semi-logarithmic plot (Fig. 4) of the product $A \cdot r$ versus r of all transducers a linear relationship is obtained by a straight-line fit to the data. The value of the straight line at the reference distance $r_0 = 50$ m is determined and regarded as the magnitude of the AE event.

The slope of the straight line corresponds to the damping coefficient. Generally, damping of high-frequency AE waves is caused by scattering and intrinsic absorption, which will mainly occur at grain boundaries or microcracks, by small inclusions of other rock materials, gas, or water, which are embedded in many rock formations, and by reflection, refraction, and mode conversion at boundaries between different rock materials.

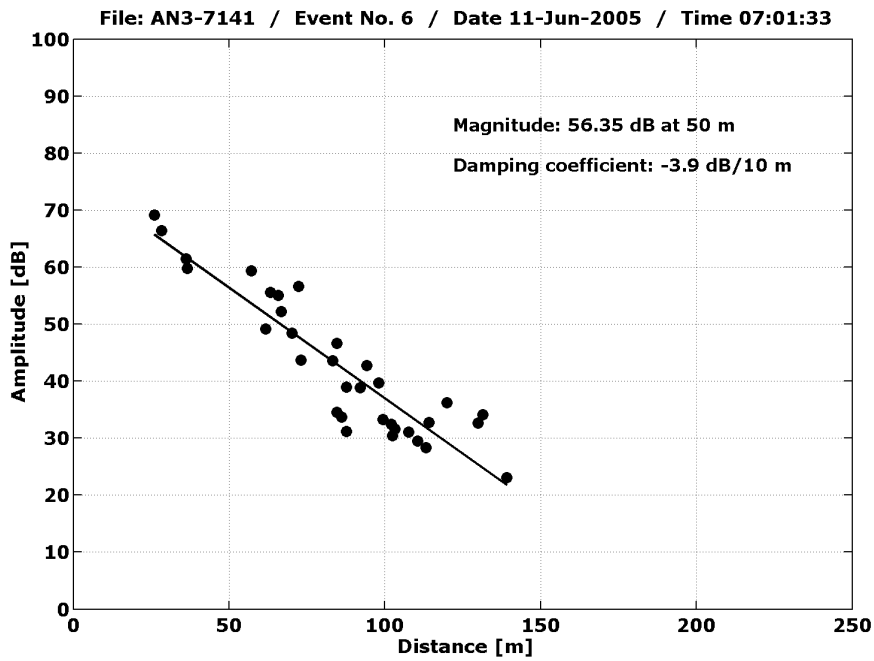

Fig. 4 AE amplitudes of one event measured with 28 sensors corrected for geometric wave dispersion versus distance.

It can be seen from Fig. 4 that travel paths of the signals range from 25 to 140 m. The slope of the line corresponds to a damping coefficient of 3.9 dB per 10 m which corresponds to an attenuation length of approximately 22 m. The attenuation length, in which the peak amplitude corrected for geometric wave dispersion, $A \cdot r/r_0$, is reduced to 37% (or 1/e), is a reciprocal measure of the damping coefficient. The value of this straight line corresponds to a magnitude of 56.35 dB at the reference distance r_0 = 50 m. It should be mentioned, that the damping coefficient and the magnitude are mean values which are determined at various travel paths from the source to the 28 sensors and in various directions.

Results

Figure 5 displays the distribution of the mean attenuation length of the events in a gray-scale density plot. The plot shows the attenuation length within horizontal cells of 5 x 5 m; cells containing less than 10 events are displayed as white areas. Again, as in Fig. 3, Regions I and II are marked by ovals.

The lowest mean attenuation length of about 25 m occurred in Region II in a small zone between y = 250 m and y = 290 m (light grey cells). In this area microcracking still takes place at the contours of closely spaced cavities even a long time after excavation. On the other hand, the highest attenuation length of about 510 m was obtained in Region I outside the sensor network (northwest direction). The highest and lowest attenuation lengths of 25 m and 510 m correspond to damping coefficients of 3.47 dB per 10 m and 0.17 dB per 10 m, respectively.

Scattering at microcracks occurs in regions of deviatoric stress, e.g. in the excavation disturbed zone (EDZ) with thickness of a few meters at the contour of underground cavities. That may be the reason for the high damping values found in regions of closely spaced cavities like Region II. On the other hand, in Region I with the lowest attenuation, the AE signals mainly propagate through undisturbed rock salt to the AE sensors. It should be mentioned, that this kind of analysis assumes implicitly no correlation between the radiation pattern and the orientation of the fracture plane of the source. However, this effect does not seem statistically important because of averaging over many events located in the whole monitored area.

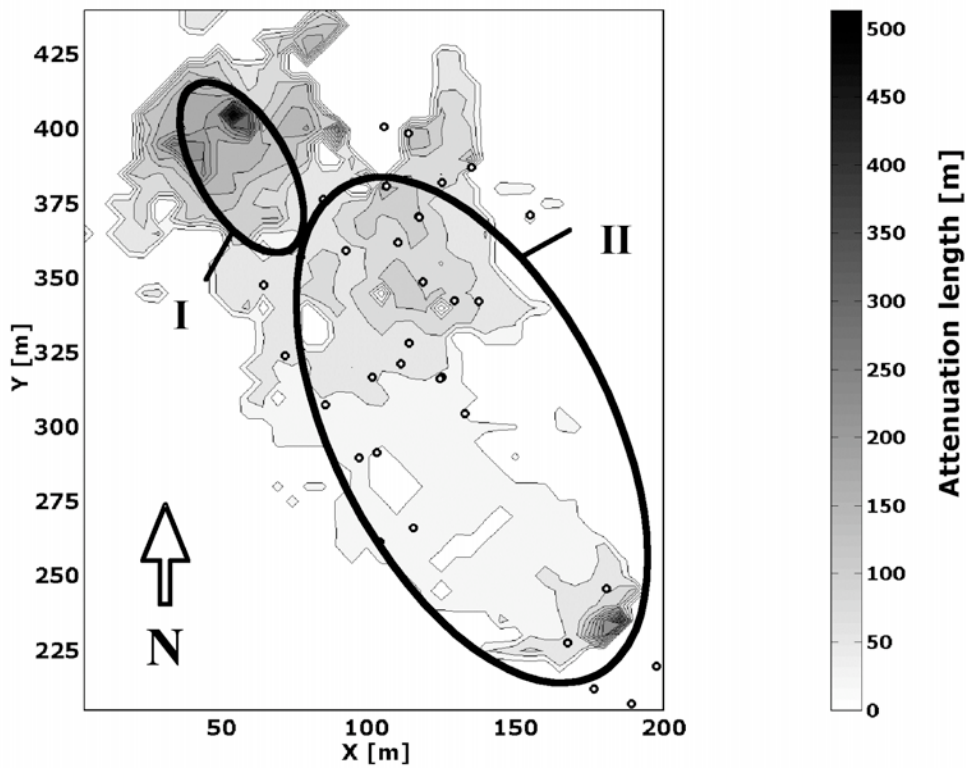

Fig. 5 Attenuation length obtained from AE events between November 15, 2004 and August 23, 2005 (696,278 events) in top view.

Conclusion

Apart from geometrical attenuation, intrinsic absorption, and shadowing effects by cavities and drifts, high-frequency acoustic waves are attenuated by scattering at small inclusions of anhydrite, clay, gas, or water, which are embedded in most salt rock formations. On the other hand, in regions of deviatoric stress, e.g., in the EDZ with thickness of a few meters at the contour of underground cavities, scattering at microcracks is the limiting factor of the attenuation length. Most of the AE signals partly travel through these zones because all sensors are installed in flat boreholes, which were drilled from the gallery walls. That may be the reason for the low attenuation lengths in regions of closely spaced cavities like Region II. A comparison of our estimated attenuation lengths with the calculated one, which Price published [4] seems doubtful. We assume that the main reason for scattering is microcracks in the EDZ. When measuring in very large volumes of homogeneous rock salt, the attenuation lengths should be even larger than 500 m. The critical point seems to be over which distances a salt dome is homogeneous enough.

Difficulties are to be presumed at boundaries between different rock materials like rock salt, anhydrite, or clay because of reflection, refraction, and mode conversion of acoustic waves.

Even under very slow creep conditions, microcracking and consequently AE activity may be induced at these geological boundaries. These interfering signals are to be possibly discriminated from neutrino generated events by careful source analysis.

References

1) J. Ahrens et al.: Astropart. Phys., **20**, (2004) 507.
2) G.A. Askariyan, B.A. Dolgoshein, A.N. Kalinovsky, N.V. Mokhov: Nucl. Instr. and Meth., **164** (1979) 267.
3) J.G. Learned: Phys. Rev., D**19** (1979), 3293.
4) R. Nahnhauer: Nuclear Physics B (Proc. Suppl.), **143** (2005), 387.
5) P.B. Price: J. Geophys. Res., **111**, (2006), B02201, 8.
6) N. Kirby: Senior thesis, Univ. of. Texas at Austin, Austin, (2004).
7) G. Manthei, J. Eisenblätter, T. Spies, *T. Experience on Acoustic Wave Propagation in Rock Salt in the Frequency Range 1-100 kHz and Conclusions with Respect to the Feasibility of a Rock Salt Dome as Neutrino Detector*, World Scientific Publishing Co. Pte. Ltd, 2006, p. 30.
8) T. Spies, J. Eisenblätter*, Progress in Acoustic Emission X*, JSNDI, Tokyo, (2000), p. 275.
9) G. Manthei, J. Eisenblätter, T. Spies: *Acoustic Emission – Beyond the Millennium*, eds. T. Kishi, M. Ohtsu, S. Yuyama, Elsevier, (2000), p. 127.
10) T. Spies, J. Eisenblätter: *Progress in Acoustic Emission XI*, JSNDI, Tokyo, (2002), p. 221.
11) T. Spies, J. Hesser, J. Eisenblätter: *Progress in Acoustic Emission XII*, JSNDI, Tokyo (2004), p. 361.
12) J. Eisenblätter, G. Manthei, D. Meister: *Proc. 6th Conf. Acoustic Emission/Microseismic Activity in Geologic Struc. and Mat*., Pennsylvania State Univ., Univ. Park, PA., USA, ed. H.R. Hardy Jr., Trans Tech Publications, Clausthal-Zellerfeld, (1998), p. 227.

ACOUSTIC EMISSION BEHAVIOR OF PRESTRESSED CONCRETE GIRDER DURING PROOF LOADING

LESZEK GOŁASKI, GRZEGORZ SWIT, MAŁGORZATA KALICKA and KANJI ONO*

Department of Civil Engineering, Kielce University of Technology, 25-314 Kielce, Poland.
*Department of Materials Sci. & Eng., University of California, Los Angeles, CA 90095, USA.

Abstract

A 26.5-meters long, prestressed concrete girder was loaded in 5 stages to failure in four-point bending to evaluate damage evolution. AE signals were recorded in 12 zones of the girder for zonal location. Using laboratory tests of reinforced concrete beams with known dominant deterioration mechanisms, seven classes of reference AE signals were identified. These signals were used for AE signal classifications in the monitoring of the girder, employing NOESIS supervised pattern recognition (SPR) procedure. AE activities generated by different types of sources characterized the deterioration evolution in girder. AE SPR analysis applications in civil engineering structures will need definitive correlation with failure progression.

Keywords: Prestressed concrete girder, pattern recognition analysis, deterioration mechanism

Introduction

Acoustic emission (AE) is suited for the health monitoring of concrete bridges and structures. A guideline for highway structures was developed following the conventional AE procedures [1 - 4]. For prestressed concrete (PC) bridges, which have been in use for a long time, we still lack adequate evaluation technology for damage development during service. Using current AE methods, we can estimate AE activities and their locations. The next objective is to assess the characteristics of the flaws and their severity. Moment tensor approach is a valuable method [5], but we rely on the evolution of AE parameters utilizing supervised pattern recognition (SPR) analysis techniques [6]. This requires a set of reference AE signals, which we have developed in laboratory. Here, we report the AE examination of a large PC girder during proof loading using SPR. With further work, AE monitoring in field tests of prestressed and post-tensioned concrete bridges will become a practical tool.

For wider acceptance of AE methodology by bridge inspection community, it is necessary to present the validity of AE tests effectively. We introduce the general approach used in that discipline [7 - 9], so that we can communicate the AE inspection results. General direction will be suggested, although we must continue to strive for satisfactory grading criteria based on AE and correlation work with fracture studies.

Bridge Inspection

Most bridges are primarily inspected visually. Assessment is made for all structural members. Inspected bridge members are rated from 0 (failed condition, closed for traffic) to 9 (excellent condition) in the US for overall characterization of the general condition of an entire component (see Table 1) [9]. Another approach is to give severity code for each structural

Table 1 Condition Rating

9. EXCELLENT CONDITION
8. VERY GOOD CONDITION - no problems noted.
7. GOOD CONDITION - some minor problems.
6. SATISFACTORY CONDITION - structural elements show some minor deterioration.
5. FAIR COldijITION - all primary structural elements are sound but may have minor section loss, cracking, spalling or scour.
4. POOR CONDITION - advanced section loss, deterioration, spalling or scour.
3. SERIOUS CONDITION - loss of section, deterioration, spalling or scour have seriously affected primary structural components. Local failures are possible. Fatigue cracks in steel or shear cracks in concrete may be present.
2. CRITICAL CONDITION - advanced deterioration of primary structural elements. Fatigue cracks in steel or shear cracks in concrete may be present or scour may have removed substructure support. Unless closely monitored it may be necessary to close the bridge until corrective action is taken.
1. "IMMINENT" FAILURE CONDITION - major deterioration or section loss present in critical structural components or obvious vertical or horizontal movement affecting structure stability. Bridge is closed to traffic but corrective action may put back in light service.
0. FAILED CONDITION - out of service - beyond corrective action.

Table 2 (a) Severity code and description

Code	Description
1	**As new condition or defect has no significant effect on the element (visually or functionally)**
2	**Early signs of deterioration, minor defect/damage, no reduction in functionality of element**
3	**Moderate defect/damage, some loss of functionality could be expected**
4	**Severe defect/damage, significant loss of functionality and/or element is close to failure/collapse**
5	**The element is non-functional/failed**

(b) Extent code and description

Code	Description
A	**No significant defect**
B	**Slight, not more than 5% of surface area/length/number**
C	**Moderate, 5%-20% of surface area/length/number**
D	**Wide, 20%-50% of surface area/length/number**
E	**Extensive, more than 50% of surface area/length/number**

element from 1 (no damage) to 5 (failed/non-functional) in Poland (see Table 2). For the latter, one also uses extent code from A (no significant defect) to E (extensive, more than 50% of surface area/length/number) to determine the surface area affected by the defects. Combinations of severity and extent codes are used to designate the state of a structure. Visual inspection, however, is unable to detect and evaluate internal deterioration, its localization and/or severity. Such characterization is feasible using AE testing, but we have to develop criteria to rate AE activity observed and to codify the extent of AE source distribution. These should correlate to the severity and extent codes or to the rating scale in the US. We believe the use of clustering of AE sources via SPR can rate AE activity, while zone location results can be converted to extent scale. Before reaching that stage, we need to identify deterioration mechanisms from the AE clustering and signal features through corroboration with the fracture study of beam elements.

Experimental Procedures and Results

We utilized standard AE instrumentation. A 12-channel MISTRAS system from PAC was used along with DECI 55-kHz sensors. For each signal, we recorded rise time (RISE), counts to peak (PCNT), counts (CNTS), energy (ENER), duration (DURA), peak amplitude (AMPL), average frequency (AFRQ), rms voltage (RMS16), reverberation frequency (RFRQ), initiation frequency (IFRQ), signal strength (SSTR), and absolute energy (ABEN). To locate AE sources, we localized them with zonal scheme only because of high inhomogenity of girder. The length of a zone depends on signal attenuation. We chose that the signal attenuation, when AE signal travels along the zone length, should be less than 10 dB. NOESIS Professional (ver. 4) pattern recognition software was used to group AE signals into clusters containing waves generated by a similar type of sources. For concrete engineering structures, most of the AE sources in a cluster can be referred to a specific deterioration mechanism. To identify this mechanism, experimentally determined reference signals by known failure mechanisms are necessary. Detailed examination of failure processes are also critically needed.

Reference AE signals

In our study, to create AE reference signal database, we recorded the AE events generated during laboratory tests on reinforced concrete (RC) beams of 1.15 x 0.15 x 0.15 m. Data from larger beams of 13 and 18 m in length was also considered. We utilized only AE signals recorded during the loading parts of experiment, when known failure mechanisms were dominant. Unsupervised pattern recognition analysis was applied to the AE signals produced by the deterioration processes during loading. We performed this classification based on twelve AE signal parameters. We assumed that each of failure events results in specific AE sources that produce characteristic signals, which belong to one of the clusters. From the AE data of RC beams, we obtained eight clusters.

AE Monitoring during the Loading of a Girder

A 26.5-m long and 1-m high prestressed-concrete (PC) girder was loaded in 4-point bending. Span length was 25.4 m and the center loading points were 5 m apart. The wire distribution in the girder was concentrated near the bottom to support tensile loads. Loading was applied in five cycles with unloading between them, as shown in Fig. 1. In each cycle or sequence, the applied load increased in multiple steps (usually the load increase for each step equals 60 kN). Maximum loads in the five sequences were 122; 232; 622; 996; and 1370 kN. The results presented below concern only the AE records collected during selected loading steps, represented by color bars in Fig. 2. That is, data presented will be from sequences III, IV and V. The crack distribution and crack opening were observed between loading steps. At the maximum applied load of 1.4 MN, a

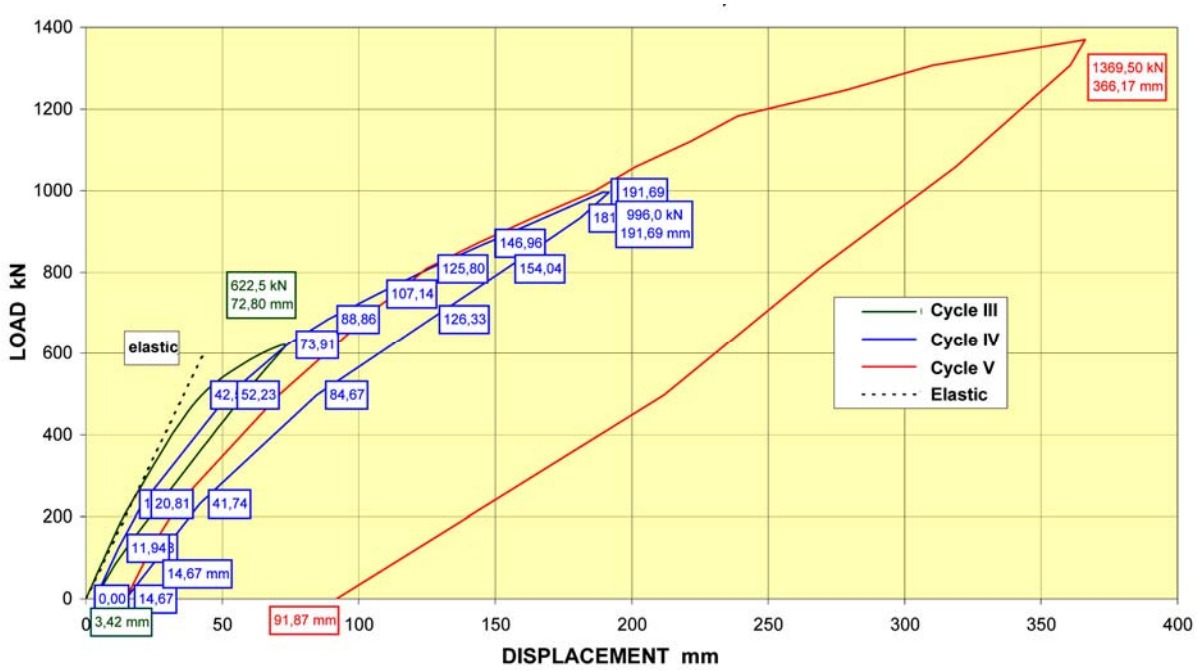

Fig. 1 Load-displacement curves of 26.5-m PC beam. Load was cycled 5 times.

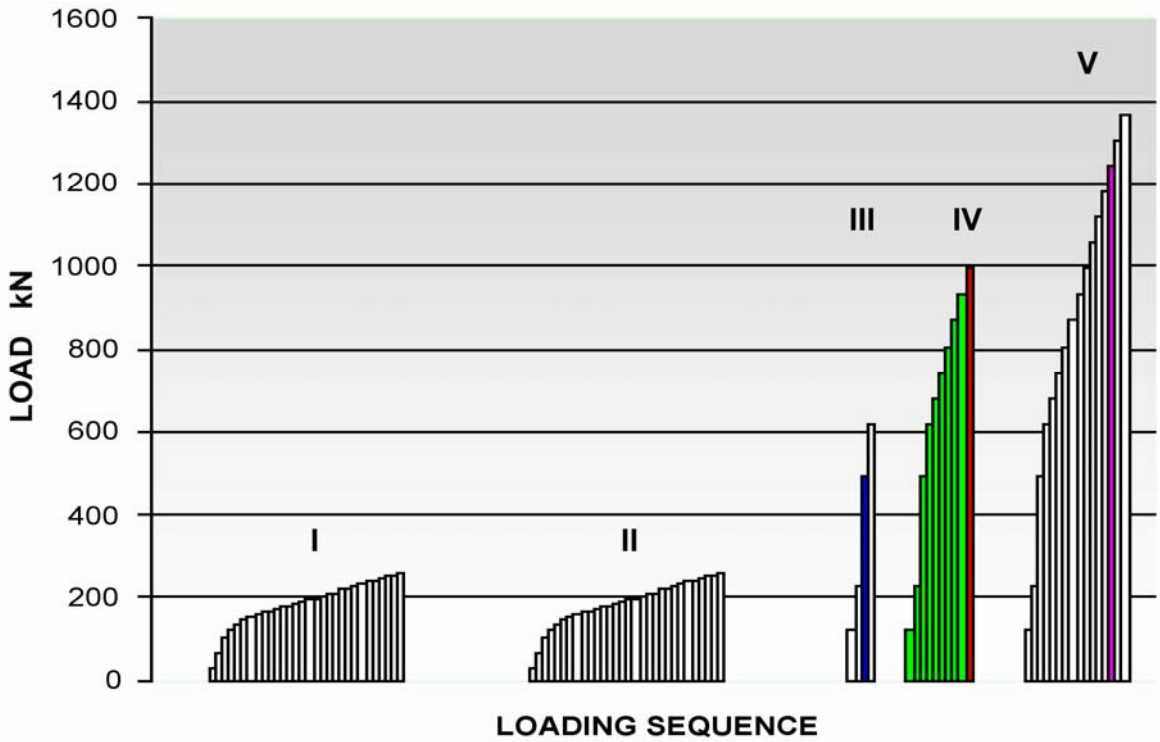

Fig. 2 Applied loading of 26.5-m PC girder in five sequences. Color bars show the periods of AE data analyzed.

significant deflection of the beam took place and made it impossible to continue loading, although the beam could bear higher loads. Twelve AE sensors were located at the bottom of the girder, and the AE activities recorded from only the high stress zones were analyzed using PAC MISTRAS 2001 processor for this paper. The sensor spacing was 1.72 m. The sensor positioning was asymmetrical and #1 sensor was at 2.70 m from one span support. Sensor pairs #5 and 6, 8

and 9 straddled the center loading points and are the closest to them. The strongest AE activities were usually found on these sensors, but the next strongest can be on other sensors, as shown in Fig. 3 (signal strength vs. time in sec). In zone 9, which showed the highest AE signal strength, AE signal strength reached a peak at 88 sec corresponding to a load of 956 kN. However, this sharp peak was not as prominent in the next zone (10), at which AE signal strength was the second highest. In zone 10, AE activities persisted ~10 sec longer, implying the AE source was propagating toward zone 10.

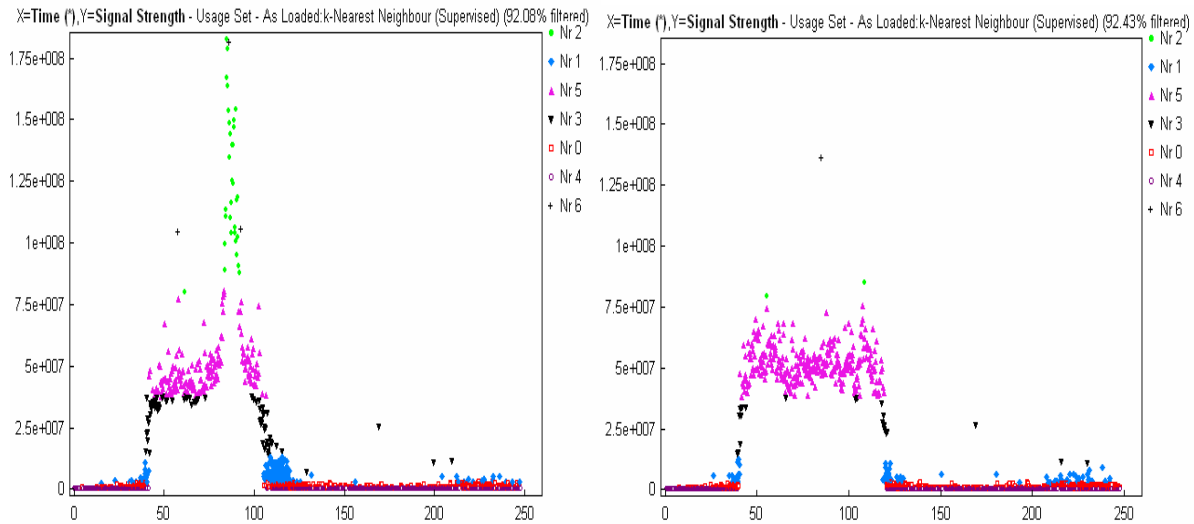

Fig. 3 AE activities in zones 9 and 10 during sequence IV, at the loading step 934 - 996 kN.

Table 3 The mean values of signal parameters in clusters.

Cluster No	C0	C1	C2	C3	C4	C5	C6
Color	□	◆	●	▼	○	▲	+
Mean rise time	254.48	276.75	287.18	258.18	121.80	294.49	256.50
Mean counts	192.40	947.57	8423.74	5300.82	16.31	7561.48	7961.00
Mean energy	171.5	887.0	19594	4260	11.07	7948	21116
Mean amplitude	63.15	72.76	87.85	77.21	46.65	83.01	99.25
Mean ave. frequency	18.46	20.01	33.71	23.70	87.91	30.40	32.00
Mean RMS (16)	0.22	0.33	1.55	0.42	0.13	0.71	2.86
Mean reverb. Freq.	18.18	19.93	33.71	71.57	11.32	30.39	32.00
Mean initiation freq.	118.71	101.30	46.62	71.57	273.29	47.29	35.00
Mean absolute energy	5.05e+4	5.50e+5	2.84e+7	1.96e+6	1.16e+3	6.70e+6	1.68e+8
Mean signal strength	1.07e+6	5.54e+6	1.22e+8	2.66e+7	7.18e+4	4.96e+7	1.32e+8
Mean duration	11124	47396	249991	220322	1164.1	248140	249981

AE Signals Analysis

With the help of Supervised Pattern Recognition (SPR), recorded AE signals during loading sequences III-V were grouped into clusters. This classification was performed for each loading

steps and each zone separately using NOESIS with the database of reference signals from laboratory RC beam tests. We found seven clusters containing AE signals from the 26.5-m beam test, but one cluster contained only a few signals and their origins were difficult to elucidate. Average values of AE parameters differed from cluster to cluster, as shown in Table 3.

In reporting AE analysis below, we suggest possible source mechanisms for some of the clusters. However, all such assignments are tentative and require further verification. Still, it is useful to point out likely origins where warranted. Among the clusters shown in Table 3, two clusters: C0 (represented in graphs by red squares) and C4 (pink circles), contain signals of low energy, signal strength, counts and duration. These appear to be from micro-cracking and from friction in concrete aggregates, respectively. In Fig. 3, red points constitute the background. Cluster C1 (with blue diamonds) are of AE signals of moderated duration and signal strength. They appeared when tiny cracks in the girder become visible. These signals precede the appearance of readily visible cracks. High-energy AE signals in clusters C2, C3 and C5, are much stronger than the three low energy clusters above (C0, C1 and C4). Long duration and high signal strength characterized them. We noticed that when these signals appear, signals in clusters C0 and C4 vanished. Signals of clusters C2, C3 and C5 were observed with the development of severe deterioration processes.

During loading sequences I and II, a few C1 signals were observed at these low load levels. Extensive cracking started during sequence III, at the load step marked by blue color in Fig. 2. AE activities during this loading step are shown in Fig. 4. The load increased linearly from 498 kN. After 50 sec or the load of 540 kN, stronger signals in clusters C3 and C5 were detected. This point diagram contains the AE data from the whole girder. Further load increases mainly resulted in crack opening and growth, and only a limited number of cracks were initiated. In the next load step, various types of sources produced the AE including cracks at the vicinity of prestressing wires.

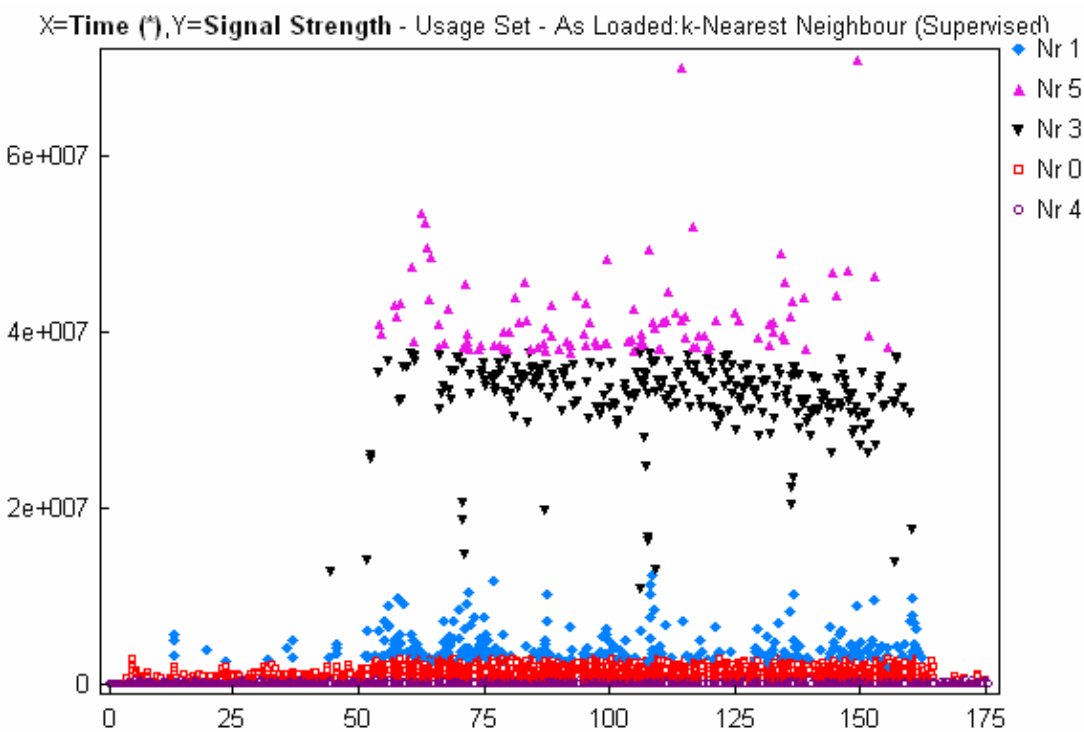

Fig. 4 AE activity of girder during the loading step 498 – 622 kN, sequence III.

From the beginning of loading sequence IV, the girder contained many defects of different severity. We expected that this would influence the AE activity during loading that started from zero level (cf. Fig. 2). During sequence IV loading, AE from load steps under 622 kN (prior maximum) produced weaker signal strength than in sequence III. In the next two higher steps to 685 kN and 747 kN, AE activities were comparable to those at sequence III. When the girder was loaded to 872 and 934 kN during subsequent load steps, however, AE activities were substantially lower. In the last step of sequence IV, AE activities returned to the previously observed level (similar to that shown in Fig. 4). Zone 9 AE behavior was similar, but the strong activities were found in load steps of 685, 747, 809 and 966 kN while weaker AE activities were again noted in steps of 872 and 934 kN. This is illustrated in Fig. 5. When we compare the data from sequence III and IV, it appears that previously introduced damages have no continual influence on AE during further loading where strong AE started at higher load levels. This is inferred from the near absence of AE activities in the step of 934 kN and from the strong emissions in the last load step of sequence IV. Some damages cease to develop, while other defects become active in enlarging damaged region.

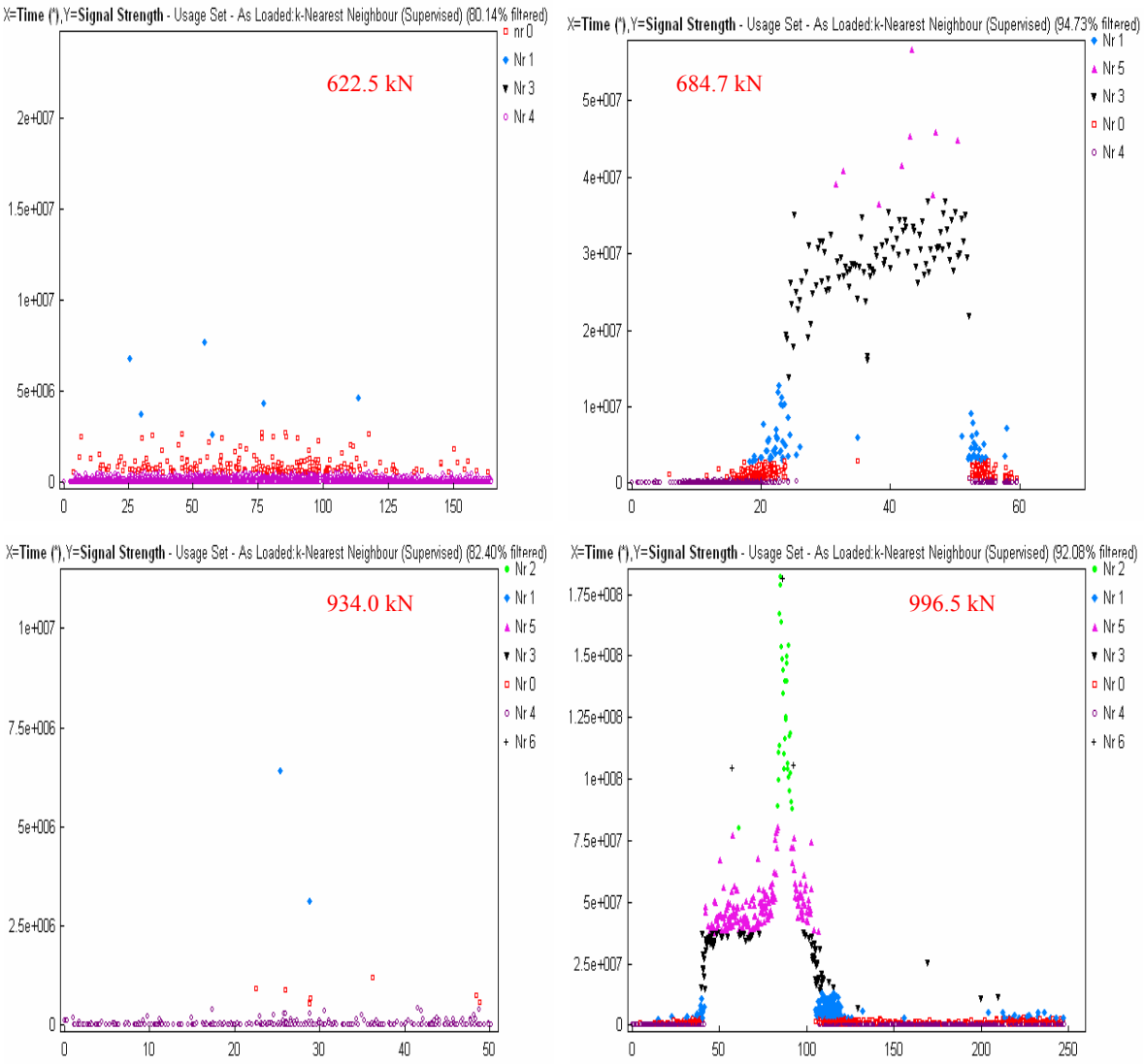

Fig. 5 AE activities of selected sequence IV load steps in zone 9. Prior load = 622 kN.

Figure 6 presents the amplitude data of classified signals; the data is from the last load step (996.5 kN) as shown in Fig. 5. The amplitude replaced signal strength in this plot. It is seen that C4 signals are mostly below 60 dB and at most 70 dB. C0 signals (red) range between 50 and 80 dB. In the other extreme, very strong C6 signals (numbering only 3) have 98-100 dB amplitude. High signal strength C2 signals have a range of 78 to 96 dB. It is interesting that signals from C1, C2, C3 and C5 clusters have amplitudes of overlapping values.

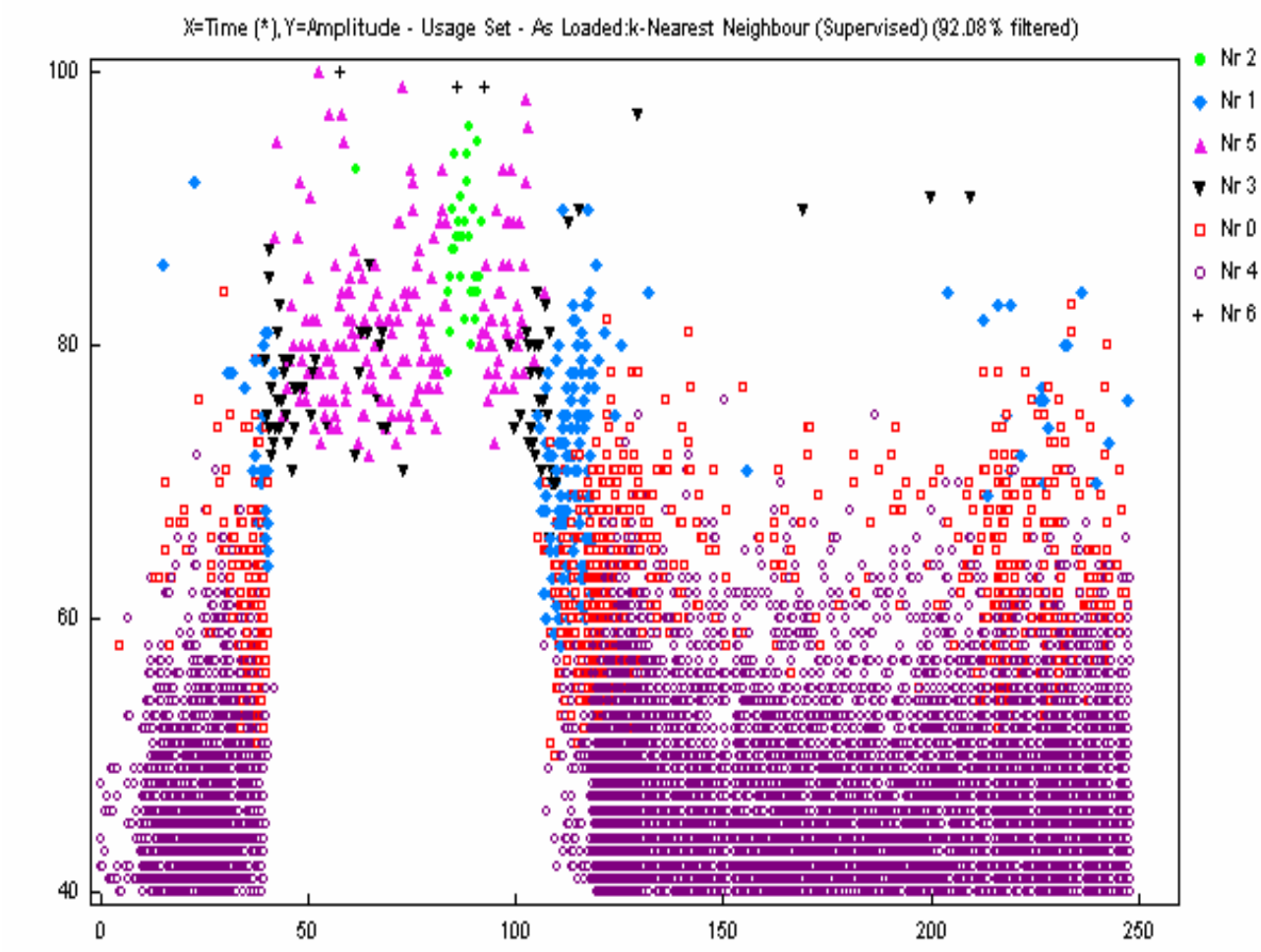

Fig. 6 Signal amplitude vs time of the last load step (996.5 kN); clusters shown by color.

When the girder was loaded in sequence V, the load exceeded the design capacity, although the girder was still supporting the applied load even at the maximum load applied. In spite of high load the recorded AE activity during the load step (1254 kN) was not much higher than those shown in Fig. 4 obtained at the load step of only 622 kN maximum. This is shown in Fig. 7. AE strength depends clearly on damage mechanisms rather than the applied load level.

Discussion and Concluding Remarks

AE signals recorded during the loading of a large girder are of two types: low-energy (LE) and high-energy (HE). LE activity (C0 and C4) took place from the beginning of the loading while the HE sources started at higher loads and exhibited intermittent nature. HE source initiation and activity depended on applied stress level and stress components (tension/shear), but low

activity periods were found even at very high loads. HE sources active in one zone may trigger AE activity in other zone far away.

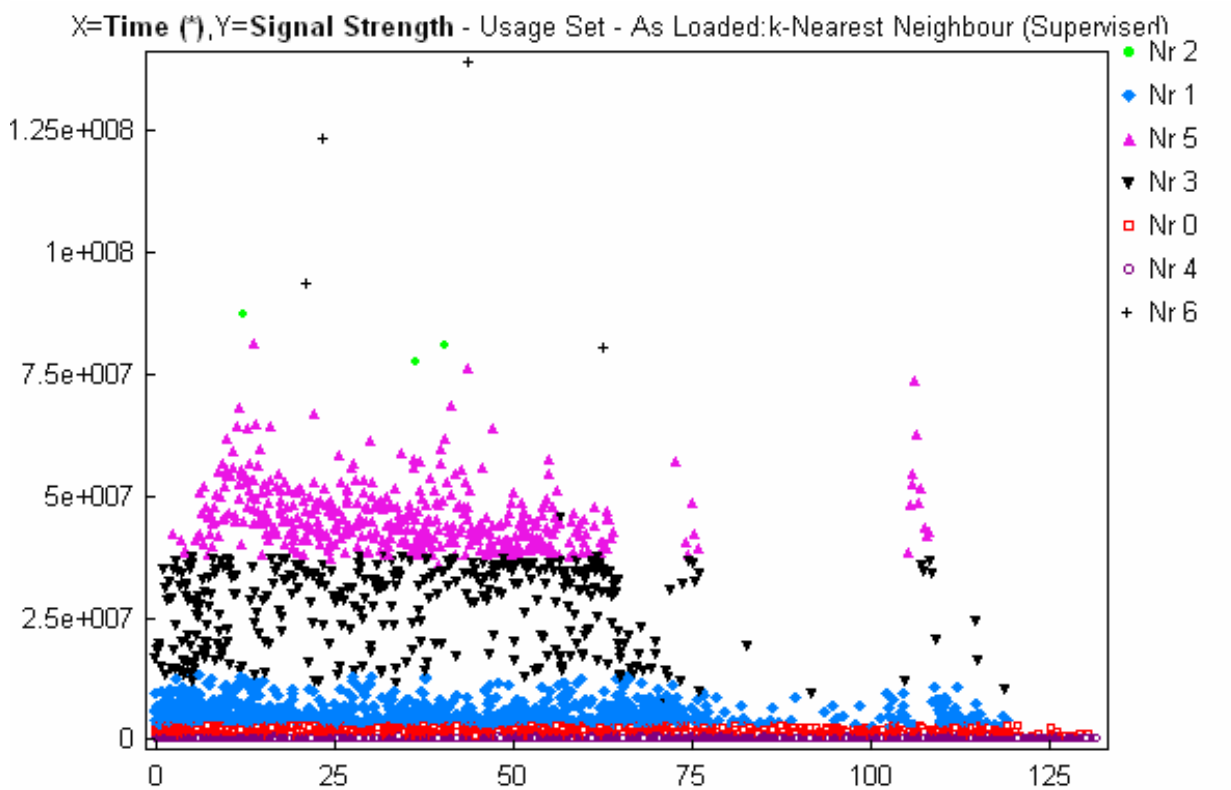

Fig. 7 AE activity in whole girder during sequence V, load step 1180 - 1254 kN.

AE of a girder was recorded and analyzed with the help of SPR and reference signal database. AE signals can be classified into clusters that can be referred to possible deterioration mechanisms and deterioration levels of structure. AE activity in clusters characterizes the level of deterioration better than empirically selected AE signal parameters. In the next step, we will try to develop from AE characteristics the scale that can be related to bridge inspection codes.

References

1. M. Ohtsu, (a) J. Acoustic Emission, **8**, 1989, 93-98. (b) Concrete Journal, **38**, 2000, 10-16.
2. C.A. Barnes and T.J. Fowler, *Proc. AECM-6*, ASNT, 1998, pp. 183-191.
3. *Recommended Practice for In-Situ Monitoring of Concrete Structures by Acoustic Emission*, NDIS 2421, Japanese Society for Non-Destructive Inspection, 2000.
4. B.V. Tinkey, T.J. Fowler, R.E. Klinger, *NDT of Prestressed Bridge Girders with Distributed Damages*, US Dept. Transportation Report FHWA/TX-03/1857-2, 2002, 106 p.
5. M. Ohtsu: *Acoustic Emission – Beyond the Millenium*, Elsevier, 2000, pp. 19-34.
6. A. Anastasopoulos, J. Acoustic Emission, **23**, 2005, 318-330.
7. P. Brinckerhoff, *Bridge Inspection and Rehabilitation: A Practical Guide*, Wiley, 1992, 304 p.
8. K. White (ed.), *Bridge Maintenance Inspection and Evaluation*, Marcel Dekker, 1992, 257 p.
9. R.A. Hartle, *Bridge Inspector's Reference Manual*, V. 1-2, US FHWA, 2006, 1760 p.

MULTIPLET ANALYSIS FOR ESTIMATION OF STRUCTURES INSIDE AN AE CLOUD ASSOCIATED WITH A COMPRESSION TEST OF A SALT ROCK SPECIMEN

HIROKAZU MORIYA, GERD MANTHEI*, HIROAKI NIITSUMA and JÜRGEN EISENBLÄTTER*
Graduate School of Environmental Studies, Tohoku University, Sendai 980-8579, Japan.
* Gesellschaft für Materialprüfung und Geophysik mbH, D-61231 Bad Nauheim, Germany.

Abstract

A multiplet analysis of acoustic emissions (AE) from a salt rock specimen was performed. A multiplet is a group of events with similar waveform considered to be generated on the same crack plane. We applied a multiplet analysis to determine the precise relative source locations of AE events and delineate the structures inside the rock specimen. The results were compared with the source locations determined by the joint hypocenter determination method. The crack planes were estimated from the source locations of multiplets, and the orientations of the planes were evaluated. No trend in the orientations of the crack planes defined by their source locations was found, and the multiplets did not occur on a single crack plane but on adjacent microcracks within a region. The feasibility of a multiplet analysis for finding microstructures and evaluating crack extension was demonstrated.

Keywords: Signal processing, microseismology, cross-spectrum analysis

Introduction

The determination of acoustic emission (AE) source locations is a key procedure for crack distribution evaluation and source mechanism analysis. Several precise mapping technologies have been developed in engineering seismology [1-4]. The application of precise mapping methods to phenomena such as earthquakes on natural faults, subduction zones, and geothermal or oil and gas reservoirs has revealed that such methods are feasible for the evaluation of fault/crack orientation and dynamics, such as the fault slip rate, as well as for determining the locations of the faults/cracks. The collapsing method is an advanced mapping technique for delineating structures. We previously applied this method to AE events from a salt rock specimen to identify the structure inside the specimen [5]. The collapsing method emphasizes structures by optimizing source locations, and it is a feasible means of quickly delineating structures from AE clouds of large numbers of events. However, with this method it is difficult to interpret directly the physical meaning of the delineated structures because the collapsing method is a relocation method, which moves the original source locations by taking into account the size and shape of the error distribution for each source location and then redetermines the source locations through mathematical optimization. On the other hand, a multiplet analysis is a precise mapping method for similar AE events and then determining their relative source locations by a cross-spectrum analysis. This method has been applied to AE events in geothermal fields to estimate the fractures activated by fluid injection to enhance the reservoir [6, 7]. Recently, multiplets were used to evaluate repeating earthquakes in a subduction zone in northeast Japan, and a multiplet analysis was found to be a feasible method for evaluating the slip rate and the relationships between slip behavior and earthquakes in the subduction zone [8]. However, a multiplet analy-

sis has not been applied to AE events from a rock specimen because the frequency component of AE events from the cracking of a rock specimen is several hundred kHz, which makes it difficult to obtain reliable full-waveform data, to which a cross-spectrum analysis can be applied, owing to the limitations of the digital data acquisition system. If a multiplet analysis could be applied to AE events associated with cracking in a rock specimen, then this technique would be feasible for measuring crack extension and investigating the dynamic behavior of cracks such as has been done in the case of natural earthquakes and AE events in geothermal fields. In this paper, we apply a multiplet analysis to AE events from a salt rock specimen to show the feasibility of a multiplet analysis for the evaluation of structures inside the specimen.

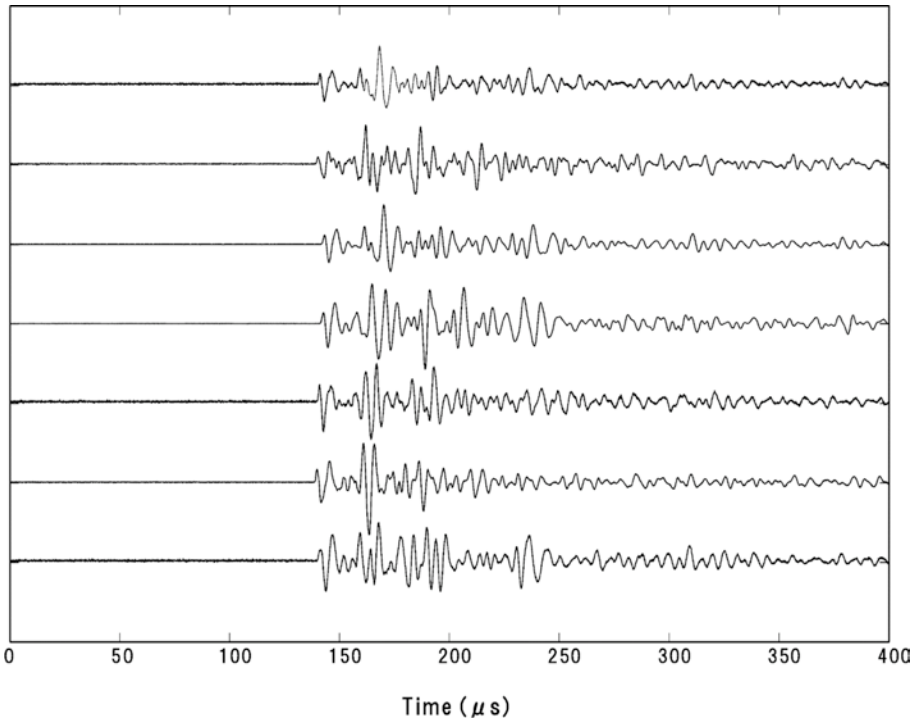

Fig. 1 Example of waveforms composing a multiplet.

Multiplet Analysis

Figure 1 shows waveforms of a multiplet detected during one axial compression test of a salt rock specimen. A group of similar microseismic events is called a multiplet [1]. A multiplet is most likely the expression of stress release on the same crack plane, with the same source mechanism. High-resolution mapping of multiplets by a cross-spectrum analysis makes detailed identification of small-scale fractures possible. A multiplet analysis is a method for determining relative source locations of similar AE events. AE events with similar waveforms are detected using a coherency function and visual observations. A cross-spectrum analysis is applied to similar AE events to detect differences in the relative arrival times of the waves. In general, source location errors are caused by picking errors in the detection of *P*- and *S*-wave onsets, because the precise detection of wave onsets is difficult. The introduction of a cross-spectrum analysis makes it possible to detect wave arrival times of slave events relative to the master event. In a multiplet analysis, the source locations are considered to be adjacent to one another; therefore, the wave propagation paths of similar events are almost the same, and the effect on the velocity structure along the ray paths can be cancelled. Thus, source locations determined by considering the origin of similar events can provide information on the spatial distribution and orientation of seismically activated cracks.

Experimental Procedures

The experiment was conducted on a cylindrical salt rock specimen (diameter, 150 mm; length, 300 mm) from the Asse salt mine in Germany, in the laboratory of the Department for Waste Disposal Technology and Geomechanics at the Technical University of Clausthal, Germany [5]. A triaxial hydraulic loading system, which contains a hydraulic cell where a cylindrical rock sample covered by a Viton sleeve is subjected to high hydraulic pressure, up to 75 MPa, and additional axial force up to 2.5 MN, was used for the test [9]. During the test, the axial displacement and axial force, the radial pressure, and the volume change (dilatancy) of the specimen were measured and displayed on the screen of a computer. The digitized data were recorded by means of a personal computer (PC) running Linux and stored every 5 s on the hard disk. The pore volume of the specimen, which corresponds to the change in the oil volume in the triaxial cell, was measured using a double-acting hydraulic cylinder. The accuracy of the dilatancy measurement was about 0.0025% of the total volume within the load cell. At the beginning of the test, the specimen was compacted overnight (16 h) under isotropic stress conditions at a pressure of 20 MPa to close open fractures at the surface of the specimen, which had been created during the forming of the sample. After the compaction phase, the test was performed by applying a constant strain rate of 0.05%/min and a constant radial pressure of 5 MPa. The strain rate corresponds to an axial displacement of 0.15 mm/min.

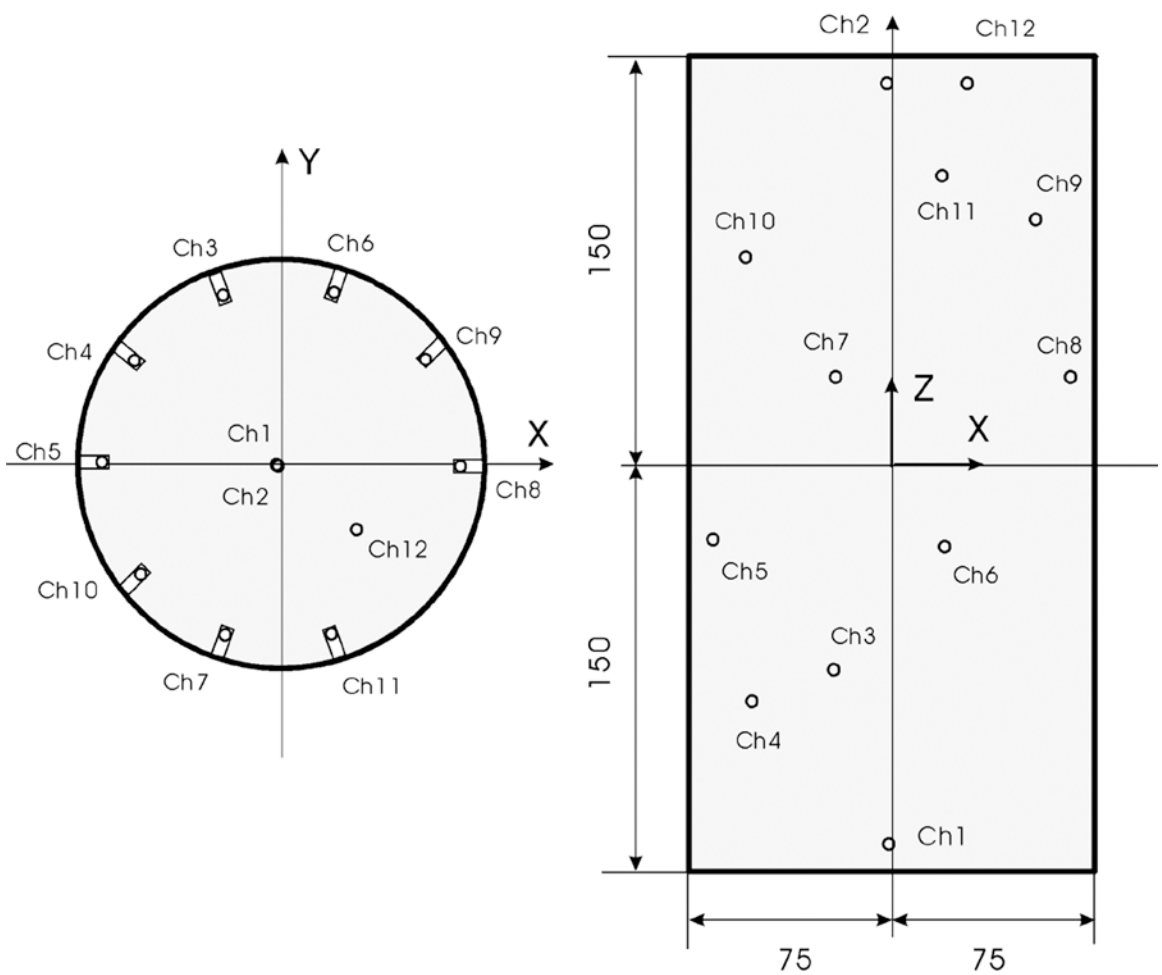

Fig. 2 Locations of sensors.

AE sensors were countersunk into the surface of the specimen in small milled holes (Fig. 2). A stiff strain gauge glue was used to affix the sensors within the holes. Each sensor was a piezoelectric disk made of lead metaniobate ceramic with an aperture of 7 mm and a thickness of 5 mm. Lead metaniobate ceramic has a low mechanical quality factor, a low dielectric constant, and no planar coupling factor. This material is used primarily when a clean impulse response is required. A brass casing protects the piezoelectric disk against damage from deformation of the specimen during compression. The AE measuring system includes three four-channel transient recorder cards in the PC. The transient recorder cards (sampling rate, 10 MHz; resolution, 14 bit; storage capacity, 512 kByte/channel) were read each time when at least two channels were hit. The digitized signals were stored on the hard disk of the PC.

Additionally, ultrasonic transmission measurements in the axial direction and at two high levels in the radial direction were performed using separate senders. A wide-band signal (like a step function) with a rise time of 1 μs was used. For the transmission measurements, which were repeated every 5 min, the axial compression and the AE measurements had to be interrupted. The overall duration of the test was about 4.3 h.

AE Source Location by Joint Hypocenter Determination

First, we determined the source location by using the travel-time inversion method, where *P*-wave arrival times were used to determine the source locations and the origin time. The velocity structure was assumed to be homogeneous (V_p = 4650 m/s). The RMS (Root Mean Square) of the residuals was 1.596 μs. Next, the joint hypocenter determination (JHD) method was applied to determine the source locations. The JHD method determines AE source locations jointing the whole events and picking values [10]. The source locations can be estimated by removing systematic errors through iterative compensation of the station correction. Figure 3(a) shows the source locations determined by the JHD method. The location accuracy was slightly improved and the RMS of residuals decreased from 1.596 μs to 1.549 μs (Table 1) when only the source locations of AE events identified as multiplets were plotted.

Application of A Multiplet Analysis

The best way to find similar waveforms is to identify them by eye. However, it is impossible to deal in this way with large numbers of events. To solve this problem, we previously introduced a coherence function, which calculates the correlation between two time series in the frequency domain [1]. A total of 10,000 events were searched for similar waveforms using the Ch. 1 signals, and the mean coherency values in the frequency range of 50–150 kHz were calculated. The time window used for the calculation was 400 μs, and the *P*- and *S*-wave codas were also included. AE events with a coherency of more than 0.68 were identified as a group of similar events. In all, 2856 events (approximately 29%) were classified into multiplet groups. Twenty-nine % is not a high value when compared with AE in, for example, a geothermal field. The waveform coherency when *P*- and *S*-waves are included is lower than that of AE events in a geothermal or other large field. In the case of AE in a small specimen, some of the events occur within the area regarded as the near field, because the distance from source to sensor is small compared with the wavelength. Therefore, the *P*- and *S*-waves cannot be distinguished, and the waveforms change dramatically depending on the apparent incident angle from source to sensor, which is the reason that the proportion of similar events is low.

Table 1 RMS of the residuals for different mapping methods.

	RMS of the residuals (μs)
Single Event Location	1.596
Joint Hypocenter Determination	1.549
Multiplet Analysis	0.317

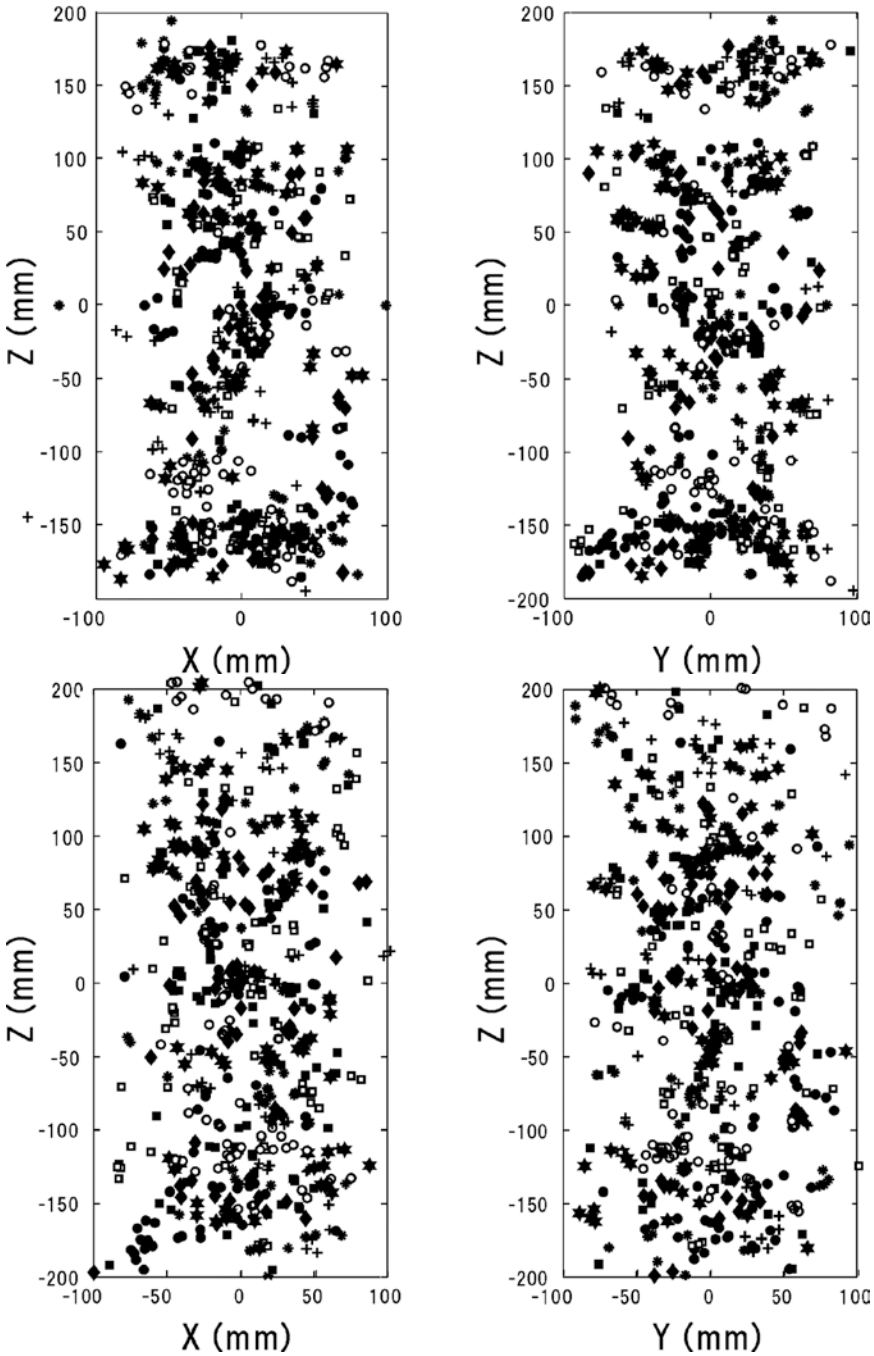

Fig. 3 Source locations by (a) JHD and (b) cross-spectrum analysis (multiplet analysis). The different symbols denote different groups (some of the groups have the same symbol due to the limitation of the number of symbols).

We selected those groups consisting of more than four similar events, and applied a cross-spectrum analysis to determine the relative travel time. A total of 199 groups were analyzed, and the relative source locations of 449 events were determined, where events were removed from the analysis if the RMS of the residuals exceeded 1 μs.

Figure 3(b) shows the source locations determined by the cross-spectrum analysis, and Fig. 4 shows source location projections for 20-mm-thick slices. AE clusters corresponding to each multiplet group are shown. The center of gravity of the multiplets is the same before and after the relocation of the AE clusters. A multiplet analysis can determine source locations only relative to a master event; and the absolute locations cannot be determined. Therefore, the relocated source locations for each group are shifted to the position, for which the center of gravity of source locations becomes the same before and after the relocation.

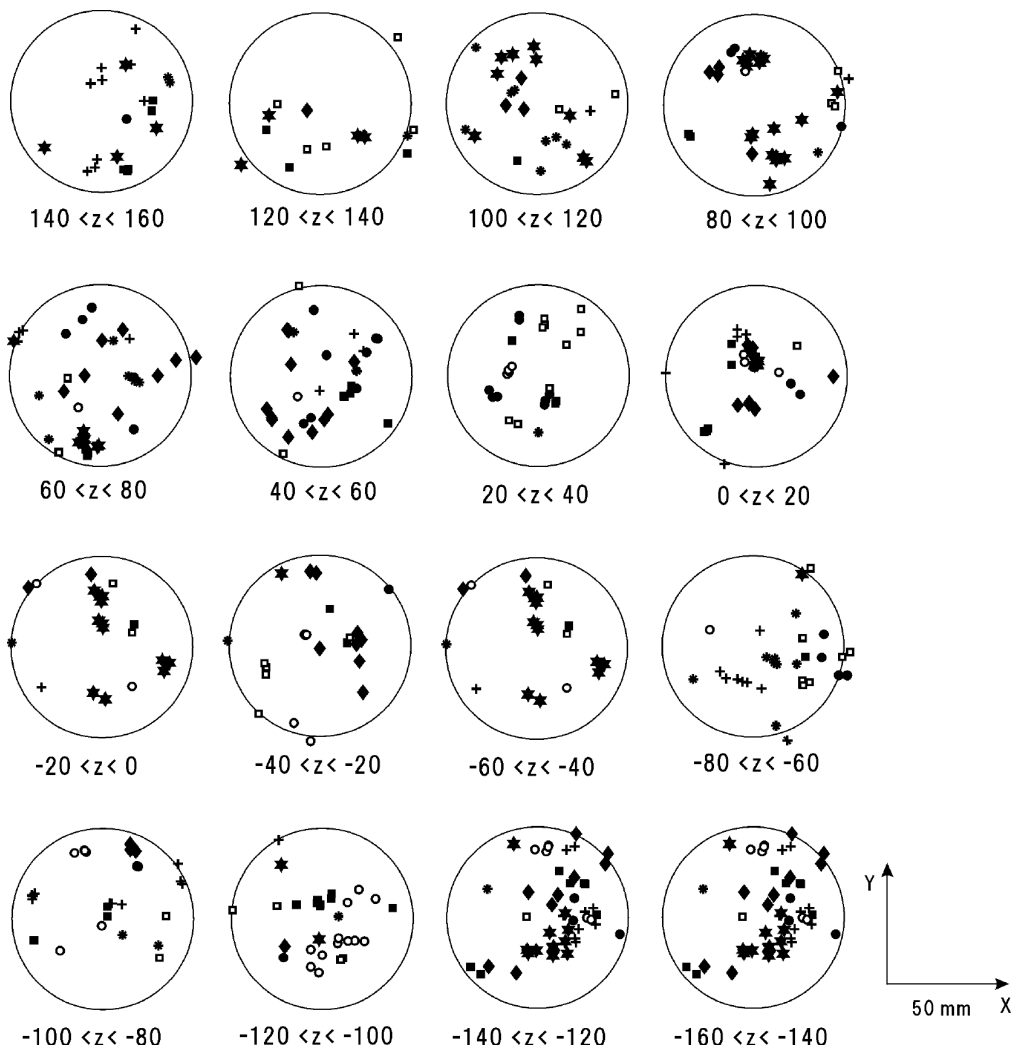

Fig. 4 Projections of source locations on 20-mm-thick slices.

Figures 5(a) and 5(b) show the source locations of a multiplet before and after relocation. The source distribution occupies a smaller area after the relocation because the error in the source locations was decreased by the cross-spectrum analysis. The RMS of the residuals for all of the estimated events was 0.317 μs in the multiplet analysis; therefore, the source location accuracy was improved.

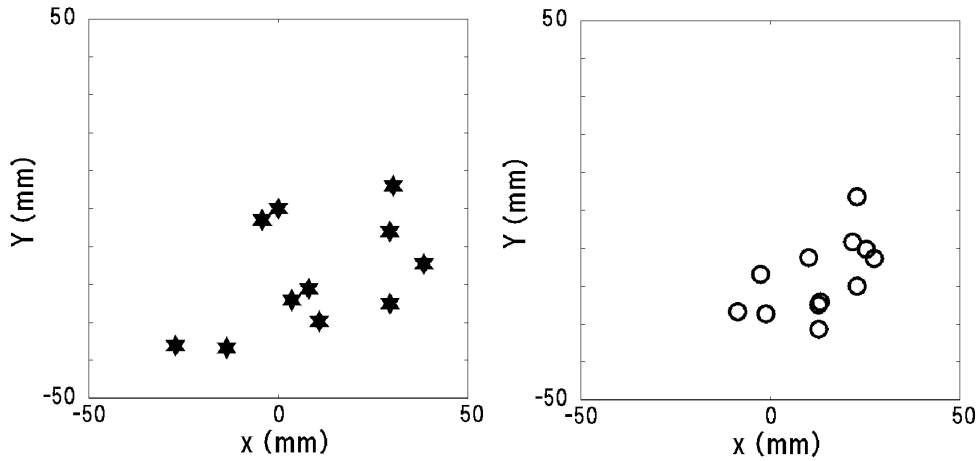

(a) JHD (b) multiplet analysis.

Fig. 5 Source locations before and after the multiplet analysis.

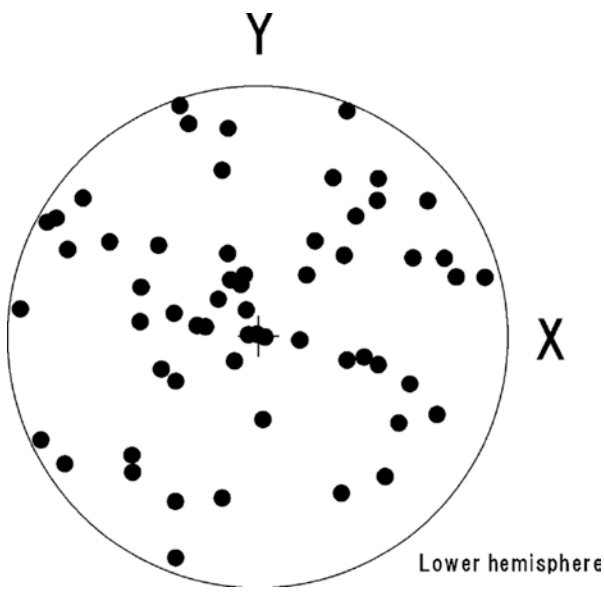

Fig. 6 Poles of calculated planes.

Discussion

The smaller RMS of the residuals suggests that the source location accuracy was improved by the multiplet analysis. On the other hand, because a multiplet can be considered to be the expression of stress release and destruction at the same crack with the same source mechanism, we might infer that the planes formed by each cluster represent the crack planes induced in the rock specimen. Therefore, we calculated the crack planes defined by the best-fitted plane for each source location. Figure 6 shows the poles of the calculated planes, where each pole represents a multiplet of at least five similar events. Although we expected the orientation of the planes to be vertical because the rock specimen was compressed in the vertical direction, thus inducing vertical cracks by tensile stress, no tendency was found in the orientations of the estimated planes. Figure 7 shows the contribution ratios calculated using the covariance matrix defined by the coordinate systems of the source locations and the eigenvalues of the matrix. This analysis is a part of the principal component analysis, and the contribution ratio is an indicator of the source distribution in space. For instance, if the first and second contribution ratio indicates 1.0, then the

source locations in the group lie on a plane. The population mode of the first contribution ratio was high, around 0.7, but the first and second contribution ratios ranged from 0.3 to 1.0 (Fig. 7). These contribution ratios indicate that the source locations were distributed within an elliptical region and not on a flat plane. This result implies that similar AE events did not occur in a simple crack plane; thus, AE behavior differed from that of AE in a subsurface field such as a geothermal field [6].

A moment tensor analysis suggested that crack formation was accompanied by a significant isotropic part and an increase in the specimen volume, and that the source mechanism was also a combination of tensile and shear modes. These analyses and observations suggest that the AE events did not occur along a crack plane caused by shear dislocation, such as with a fault in the Earth's crust, which is supported by the observation that a computed tomography image of the specimen embossed the visible open cracks associated with the compression test. On the other hand, the salt rock was composed of grains a few millimeters in diameter and exhibited a cellular structure. In such a case, the AE events would occur at the boundaries between grains, when grains become separated from each other or as a result of friction caused by the compression of the specimen, and the source locations would be dispersed around the grains.

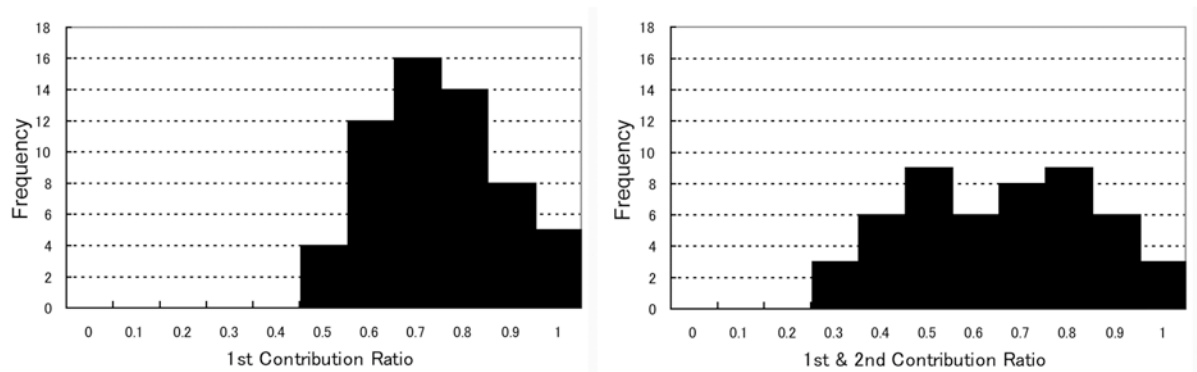

Fig. 7 Contribution ratios calculated using the coordinates of the source locations.

Therefore, we infer that the AE events with similar waveforms were induced by microcracks or by friction at the grain boundaries with the same source mechanism, and that the multiplet analysis of the rock specimen delineated the region where the AE events had the same source mechanism, which was not a planar structure like a fault in the Earth's crust. Clear planar structures could not be delineated because the AE mechanism in a rock specimen is different from that in the Earth's crust. AE events in the Earth's crust are generated along a fault by shear slip, and the source locations are distributed along the plane represented by the fault.

Conclusions

We used a multiplet analysis to determine relative source locations by a cross-spectrum analysis. The source locations were estimated by both the JHD method and the multiplet analysis. The RMS of the residuals revealed that the location accuracy in the multiplet analysis was better than that in JHD, and clusters could be identified after the relocation. The planes defined by the source locations of the multiplets were calculated to estimate the orientation of the crack planes in the specimen. No tendency was found in the orientations of the estimated planes, indicating that the source locations determined by the multiplet analysis depicted volume structures rather than planar structures. The explanation is that the AE events with similar waveforms were induced by microcracks or friction among the grains with the same source mechanism, and did

not occur along crack planes such as faults in the Earth's crust. Although crack plane-like structures were not clearly delineated, we confirmed that a multiplet analysis is a feasible method for estimating more precise source locations and for delineating structures within a rock specimen.

Acknowledgements

The authors thank Dr. U. Düsterloh and Mr. Niens from the Technical University of Clausthal for conducting the experiment. We are grateful to Dr. T. Spies and Dr. J. Hesser (Federal Institute for Geosciences and Natural Resources, Hannover) for providing us with the AE measuring system. This work was carried out as a part of MTC International Collaborative Projects.

References

1) G. Poupinet, W. L. Ellsworth and J. Fréchet: Monitoring velocity variations in crust using earthquake doublets: An application to the Calaveras fault, California, J. Geophys. Res., **89** (1984), 5719-5731.
2) H. Moriya, K. Nagano and H. Niitsuma: Precise source location of AE doublets by spectral matrix analysis of triaxial hodogram, Geophysics, **59** (1994), 36-45.
3) W. S. Phillips, L. House and M. Fehler: Detailed joint structure in a geothermal reservoir from studies of induced microearthquake clusters, J. Geophys. Res., **102** (1997), 11745-11763.
4) C. A. Rowe, R. C. Aster, W. S. Phillips, R. H. Jones, B. Borchers and M. C. Fehler: Using Automated high-precision repicking to improve delineation of microseismic structures at the Soultz geothermal reservoir, Pure Appl. Geophys. **159** (2002), 563-596.
5) H. Moriya, G. Manthei, S. Mochizuki, H. Asanuma, H. Niitsuma, R. H. Jones, and J. Eisenblätter: Collapsing method for delineation of structures inside AE cloud associated with compression test of salt rock specimen, *Progress in Acoustic Emission IX* (2002), 282-289.
6) H. Moriya, K. Nakazato, H. Niitsuma and R. Baria: Detailed fracture system of the Soultz-sous-Forets HDR field evaluated using microseismic multiplet analysis, Pure Appl. Geophys. **159** (2002), 517-541.
7) H. Moriya, H. Niitsuma and R. Baria: Multiplet-clustering analysis reveales structural details within the seismic cloud at the Soultz geothermal field, Bull. Seismol. Soc. Am., **93** (2003), 1606-1620.
8) T. Matsuzawa, N. Uchida, T. Igarashi, T. Okada and A. Hasegawa: Repeating earthquakes and quasi-static slip on the plate boundary east off northern Honshu, Japan Earth Planets Space, **56** (2004), 803-811.
9) K.-H. Lux, U. Düsterloh and Z. Hou: Increasing the Profitability of Storage Caverns by Means of a New Dimensioning Concept (I), Erdöl Erdgas Kohle, **118** (2000), 294-300 (in German).
10) A. Douglas: Joint epicentre determination, Nature, **215** (1967), 45-48.

DAMAGE DIAGNOSIS OF RAILWAY CONCRETE STRUCTURES BY MEANS OF ONE-DIMENSIONAL AE SOURCES

TOMOKI SHIOTANI, XIU LUO* and HIROSHI HAYA*
Research Inst. of Technology, Tobishima Corp., 5472 Kimagase, Noda, Chiba 270-0222, Japan.
* Railway Technical Research Institute, Kokubunji, Tokyo 185-0034, Japan.

Abstract

Damage of railway concrete structures has been evaluated using acoustic emission technique. In the technique quantitative assessments of damage can be conducted from three-dimensional (3D) AE activity induced by active live load with train passage. To obtain the 3D AE activity, however, it needs multiple AE sensors together with longer analysis time. In order to get the technique into widespread use, in this paper, linear AE source location, requiring two AE sensors, are applied for the damage evaluation. After comparison was made with 3D results it was concluded that the damage estimated by linear AE source location accorded well with those of 3D, and therefore the damage assessment of railway concrete structures can be reasonably evaluated using linear AE source location.

Keywords: Railway structures, damage assessment, Calm ratio, RTRI, linear source location

Introduction

Among modern infrastructures, railway structures have been constructed earlier than others, experiencing a variety of damage due to weathering, earthquakes and so forth. The upper part of railway structures can be investigated visually. It is difficult to conduct diagnosis for foundations like piers, except for general evaluation with natural frequency [1, 2]. In order to obtain the damage characteristics of lower parts, we have applied acoustic emission (AE) techniques, and showed that train-induced AE activity can be used to evaluate the damage of concrete structures. In this technique extant defects/damages contribute to the so-called secondary AE generation. Only identified AE sources with the source location algorithm are selected for a damage related AE activity. From the obtained AE sources such damage indices as Calm ratio, RTRI and *b*-value are obtained. Those damage indices show the degree of damage reasonably well when they are compared with actual damage conditions. The final goal of this study is to attain the state of widespread use of the AE technique and to establish reliable AE criteria for defining the degree of damage. In this paper, we report AE monitoring during the cyclic damaging of a full-scale railway concrete pier. To examine the potential of the simplest way of AE source identification, linear AE source location is used for determining the damage indices. The resultant damage is verified with 3D results. The applicability of linear AE source location for the damage evaluation of concrete is discussed.

Damage Evaluation with AE Activity

In concrete subjected to incremental cyclic loads, AE activity can be classified into four different levels with the progress of damage. The damage levels are: intact; almost intact; slight damage; and heavy damage. As shown in Fig. 1, during the second cyclic load, AE signals are

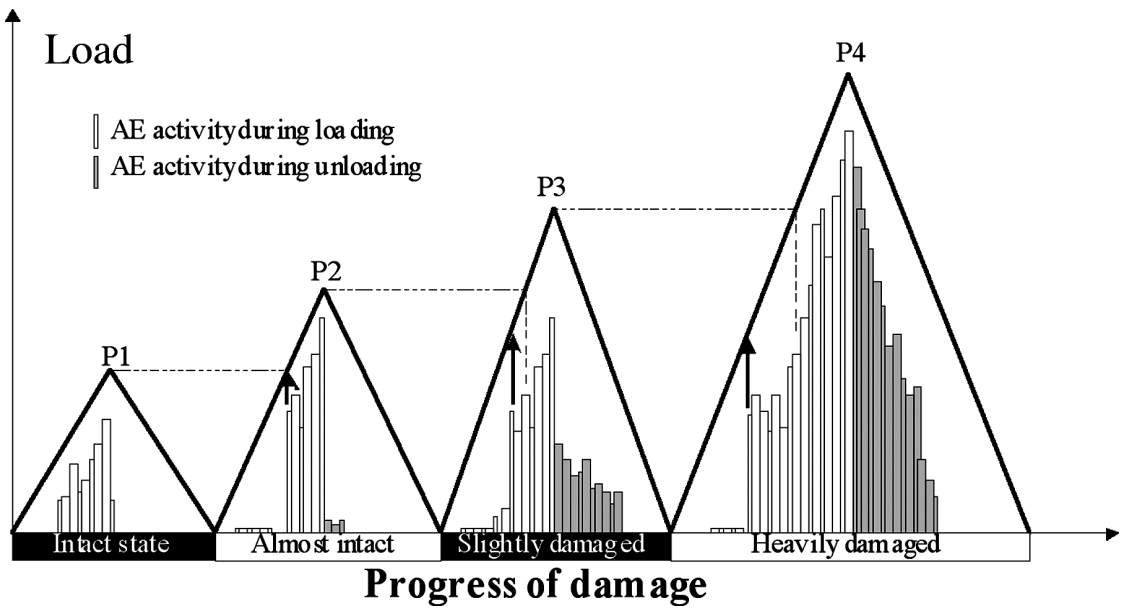

Fig. 1 A typical AE variation with damage progression.

generated at the load level of the maximum prior load. This is known as Kaiser effect. This material is intact or almost intact. In the third cyclic load, in which the material is slightly damaged,the onset of AE appearance is at a lower level than before. Decrease of effective areas against the external load or accumulation of microcracks within the material plays a significant role to show this behavior. Considering the AE activity to the stress level experienced, such damage indices as Felicity ratio [3], CBI ratio [4], and Load ratio [5] have been proposed. Also the AE activity during unloading processes is important for the damage characterization [6]. With damage evolution to heavy damage, not only the AE activity during uploading but that during unloading becomes more intense. Accumulation of shear-type cracks seems to induce this phenomenon. The ratio of the accumulated AE activity during unloading to that during the entire loading process, is referred to as Calm ratio [5]

The ratios mentioned previously may be difficult to apply for in-situ monitoring since the maximum stress that the materials have experienced is not readily estimated. Thus, we have proposed an RTRI ratio instead [7]. The RTRI ratio is defined by the following procedure: the onset of AE activity is estimated on the basis of whichever measured parameters, such as stress/load, strain/deformation and so forth, and the ratio is obtained as the ratio of the parameter's value corresponding to the onset of the AE activity to the maximum value (or peak value) during the whole inspection period. The latter is used instead of the maximum stress that the structure has experienced.

In addition to these indices, AE peak amplitudes are also known to be closely associated with the fracture scale, or the degree of damage. Accordingly, the peak amplitude might be larger with the progress of fracture. However, it was found that the damage evaluation was difficult from only the peak amplitude; i.e., as the fracture develops an apparent mechanical property of the structure decreases as well and this causes higher attenuation rates of the propagation medium resulting in smaller amplitude of AE signals at the sensor even while higher-energy AE signals were produced at the sources. Thus, in our study the peak amplitudes have been studied as their distributions, namely improved *b*-value (I*b*-value) [8, 9].

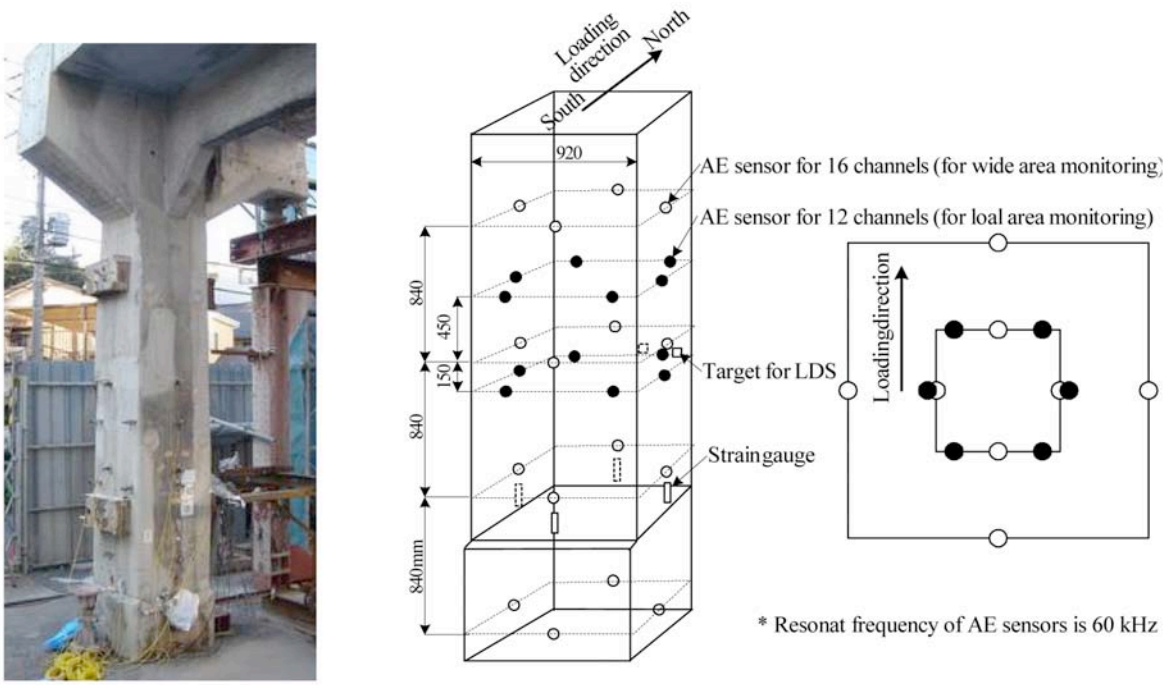

Fig. 2 Photo of tested railway RC pier (left) and sensor configuration (right).

Cyclic Fatigue Test of a Full-Scale Concrete Pier

Experimental Condition

To characterize the AE activity corresponding to damage evolution, a railway RC pier (5.87 m high) was subjected to incremental cyclic loads. This pier was demolished after the test to modify underground structures for subway construction. The cyclic test was controlled by the lateral displacement from the south-to-north direction with step-wise increments of 1, 2, 4, 8, 16, 32, 64, and 128 mm, where the load was applied by means of two hydraulic jacks (maximum capacity of 392 kN). The tested pier and the sensor configuration are shown in Fig. 2. 16 AE sensors (60-kHz resonance) covered the whole area of the pier, and additional 12 AE sensors (60-kHz resonance) were placed locally onto the area where stress concentration was expected. The former outputs were processed and recorded with a DiSP AE system and the latter with a

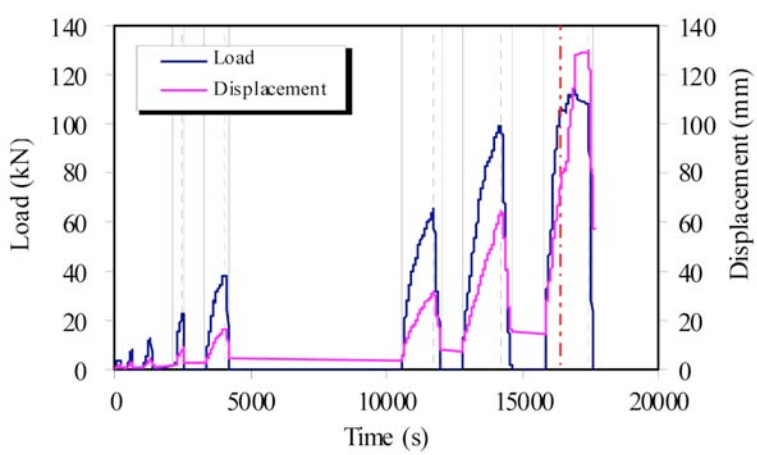

Fig. 3 Load applied and lateral displacement.

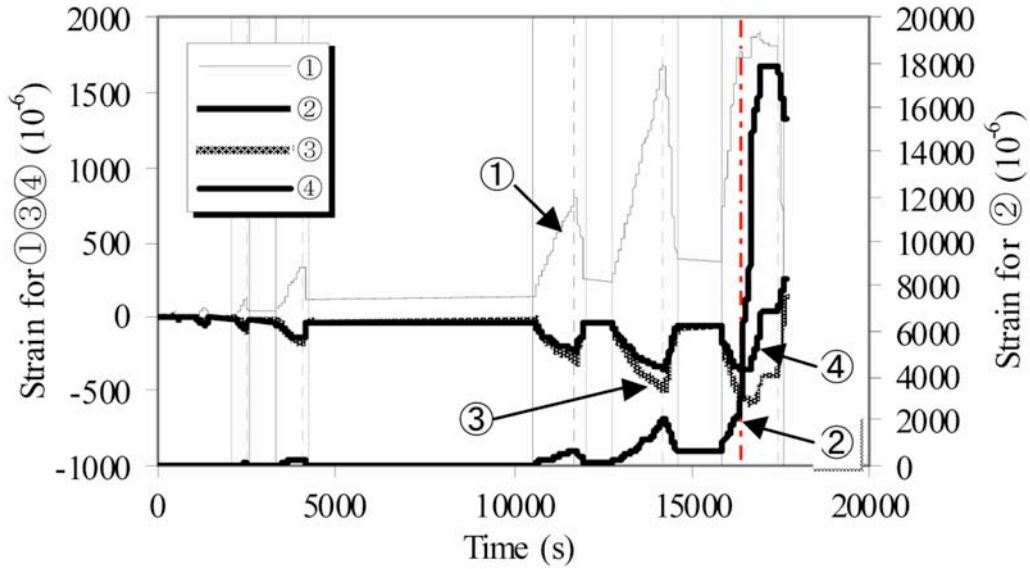

Fig. 4 Rebar strains at 400 mm high.

Mistras AE system (both by Physical Acoustics Corp.). Four strain gauges were attached to the lower four sides, and displacements on two sides, namely the north and the east side, were measured with laser displacement meters. To estimate the internal stress condition, strain gauges were also attached to rebars located at the four corners. A set of four strain gauges was each placed in three different heights: 400, 1800 and 3200 mm from the ground.

Results

Figure 3 shows the applied load and the lateral displacement as a function of elapsed time where the onset, peak, and termination of each step are indicated with solid lines, broken lines, and solid lines, in order. The load variation corresponds well to the response of the lateral displacement up to 15 ks; however, from 16 ks showing the step of 128 mm lateral displacement, the load decreased slightly whereas the displacement was constant. This implies fracture occurred either in the pier or in the ground support.

Figure 4 shows measured strains in the rebar at the height of 400 mm, where strain gages #1 and #2 were installed in the south and strain gages #3 and #4 in the north. Note the displacement was given by force from the north. Both strains of #3 and #4 gages showed negative values indicating compression, while the strains of #1 and #2 gages showed positive values or tensile state. These trends agreed with the expected stress conditions. Special note is given for strain gage #2 (showing the value in the right vertical axis), where a sudden jump is found at 16.35 ks denoted by a chain line. Tensile tests of rebar showed the yield point at 1500-1600 με and the tensile strength was reached at 2200-2300 με. The strain at 16.35 ks stood at 2274 με already, suggesting that the rebar with strain gage #2 had yielded during the previous step; namely, 64-mm displacement, and the sudden jump at 16.35 ks coincided the time when the stress had reached the tensile strength.

Figure 5 shows the cumulative AE events and the lateral displacement with respect to elapsed time. The AE events are defined as located AE sources in three dimensions with a source location algorithm. The AE events started to be active from 16-mm displacement (around 4 ks), and

intensive AE activities during unloading (or decrease of displacement) were observed from 32-mm displacement (11 ks). Using the onset of AE activity and the accumulated numbers of AE events during unloading to those during a whole loading process in every stage, RTRI and Calm ratios were calculated.

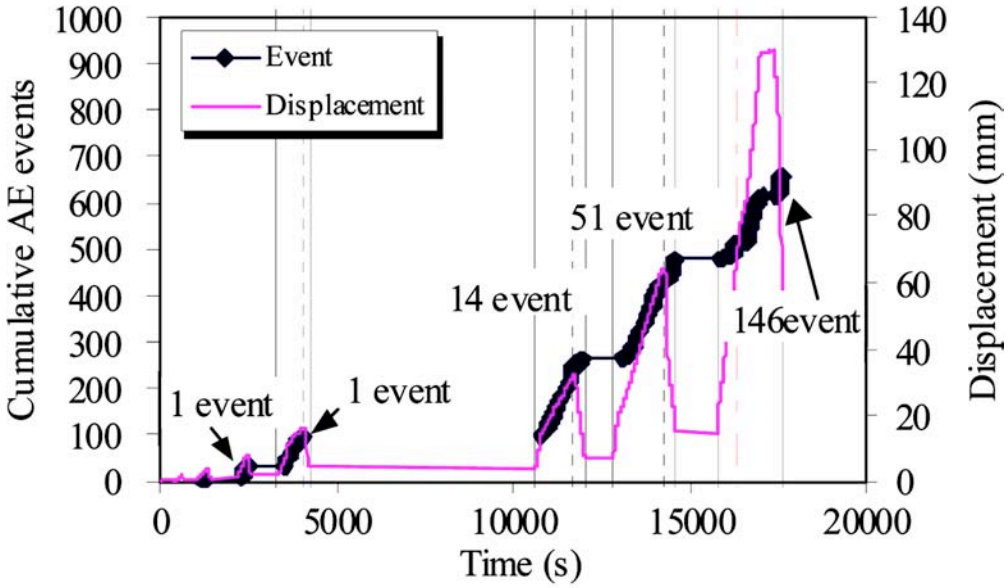

Fig. 5 Cumulative AE and lateral displacement. The number of unloading AE events at each stage is given in the figure, ranging from 1 to 146 events.

Figure 6 shows 3D AE source locations on the eastern surface for 32-mm (left) and 64-mm (right) displacements. The crack traces are also drawn in this figure and in Fig. 7. As shown the figure, AE sources at around 1.0 m height, corresponding to the observed vertical crack, were started to be active from 32-mm displacement. At this displacement, AE activity can be found in the foundation as well (see below 0.0 m). At 64-mm displacement, both AE sources at 1~1.5 m height and those at 2~2.3 m developed further and became more concentrated.

Figure 7 shows 1D AE sources on the same eastern surface. The 1D AE sources were obtained using the sensor array for wide area monitoring (see Fig. 2). In the figure, the crack trace and AE events are drawn at every step-wise lateral displacement with different colors. AE sources both in upper and intermediate areas started to appear from 8-mm displacement (see the red traces). Specifically numerous AE sources were observed during 64-mm displacement. AE sources under unloading are actively generated during 128-mm displacement and the locations of AE sources are almost identical to those of observed cracks.

Figure 8 shows RTRI on each surface obtained from 3D AE sources as well as 1D AE sources. It is noted that since the RTRI obtained in each step of displacement explained the damage condition in the previous stage, the horizontal axis can only show the damage up to 64 mm; i.e., the RTRI obtained based on 128-mm displacement shows the actual damage during 64-mm displacement. Except for the first drop from 2 mm to 4 mm since the values of more than 1.0 showing the intact state, the remarkable decrease can be found during 32-mm displacement. Regarding the trend of 3D and 1D, both showed the same variation as a function of lateral displacement, irrespective of the direction of surface. This suggests that one-dimensional sources can provide the same useful damage information as those of 3D.

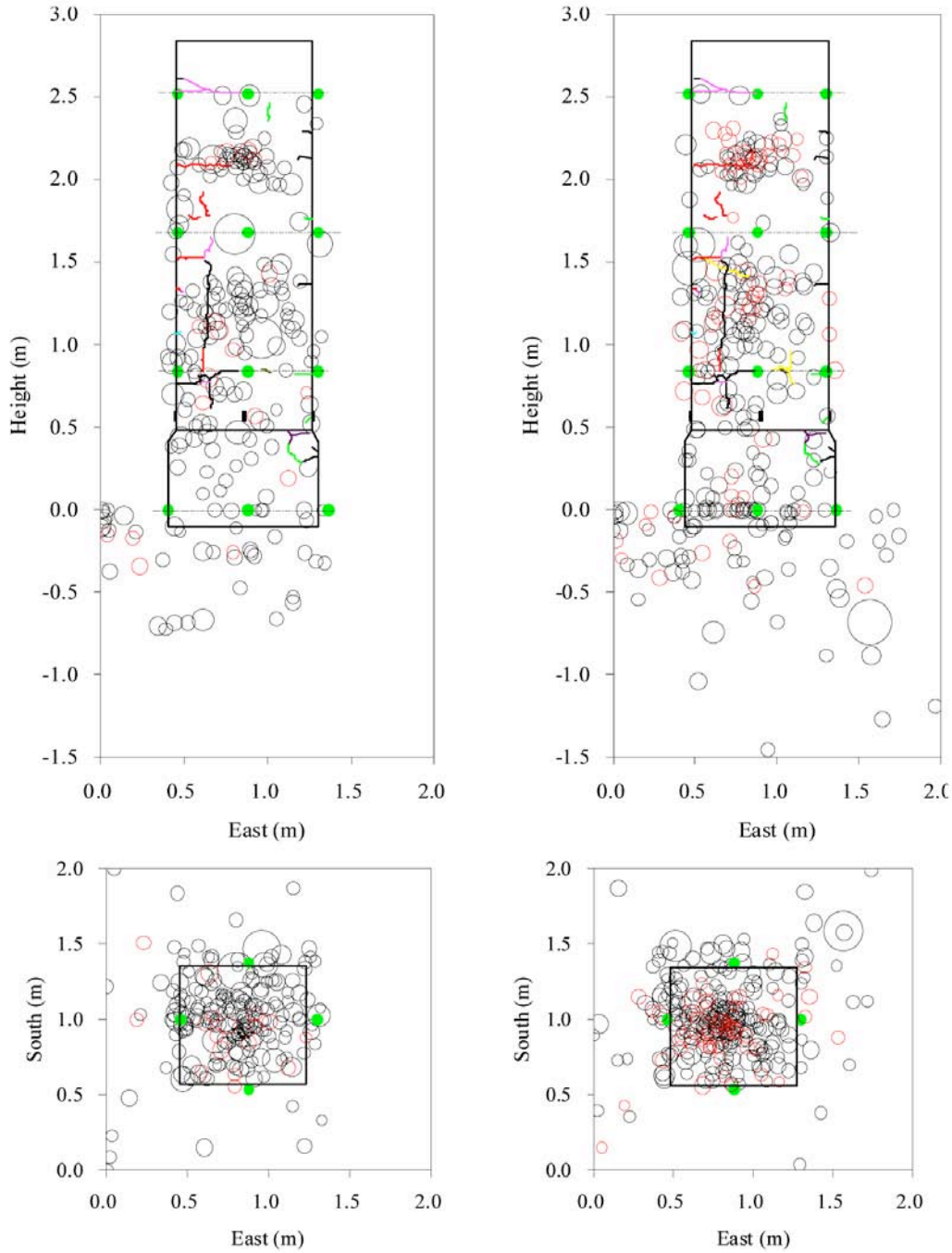

Fig. 6 Three-dimensional source locations.

Figure 9 shows similar results as Fig. 8 but for Calm ratio. Besides the RTRI, the Calm ratio can evaluate the damage up to 128-mm displacement. The Calm ratios in the chart obtained during 128-mm lateral displacement were calculated using three different parameters: lateral displacement; applied load; and rebar strain. The Calm ratio became active from 32-mm displacement and increased further at 64 mm. This trend agreed well to that of RTRI. However, at 128-mm displacement, the Calm ratio gives different values depending on the employed parameter; i.e,, considerable increase was found in rebar, a slight increase for load and remaining constant for displacement. The parameter, which can evaluate the damage condition properly, will be discussed next.

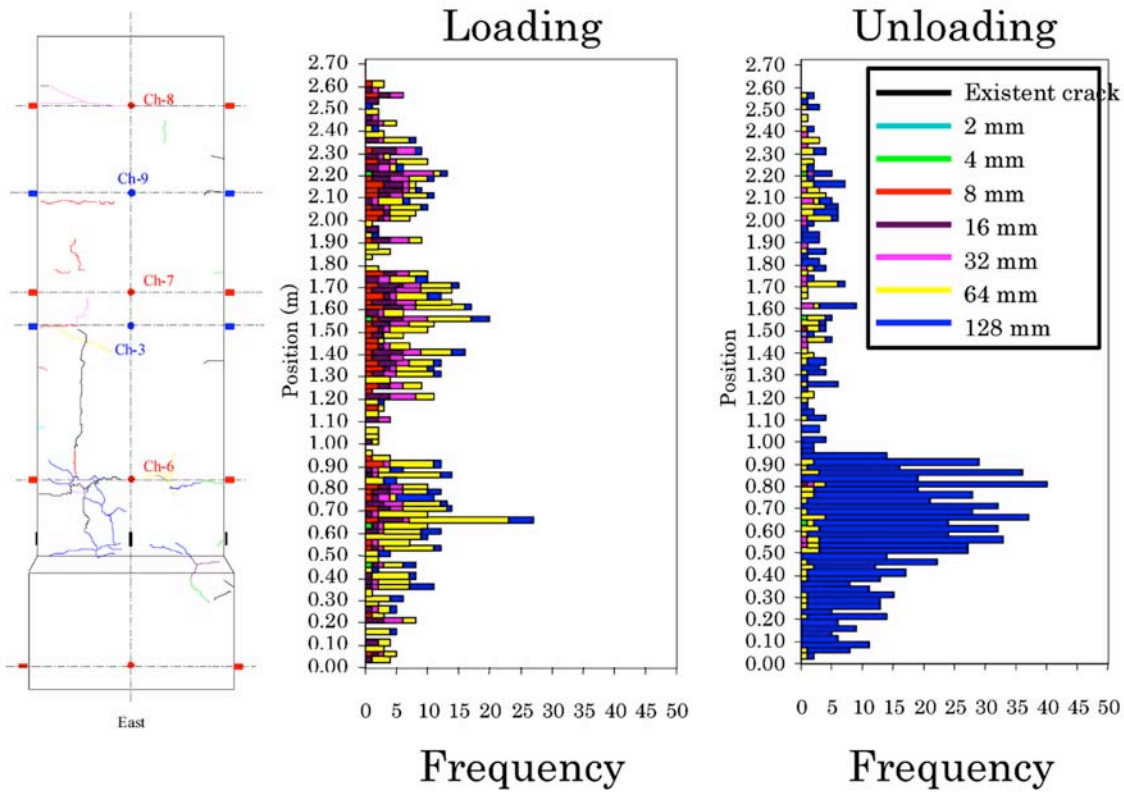

Fig. 7 One-dimensional source locations.

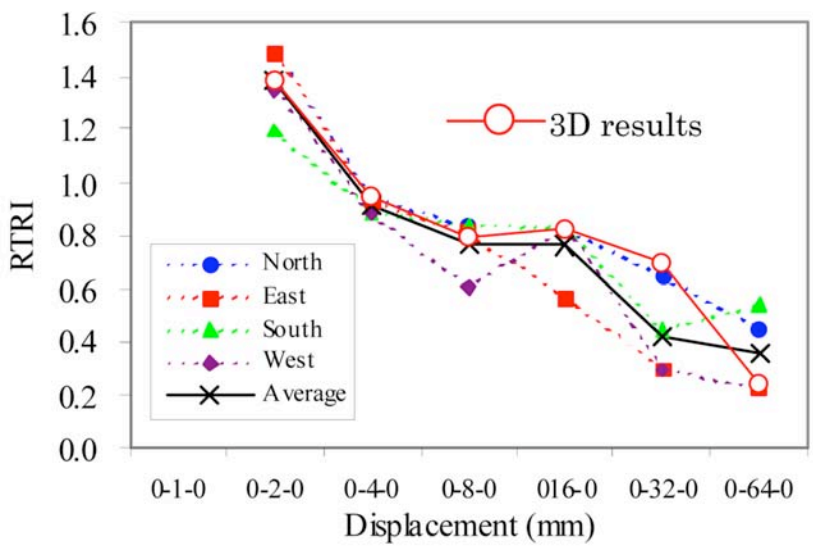

Fig. 8 RTRI obtained both from 1D and 3D AE.

Discussion

Effective Structural Behaviors in Association with AE Activity

As shown in Fig. 4, one of the rebars evidently yielded during 64-mm displacement stage and it reached the tensile strength during 128-mm displacement. Thus, the internal damage of the pier apparently developed intensively beyond the lateral displacement of 64 mm. Figure 10 shows the

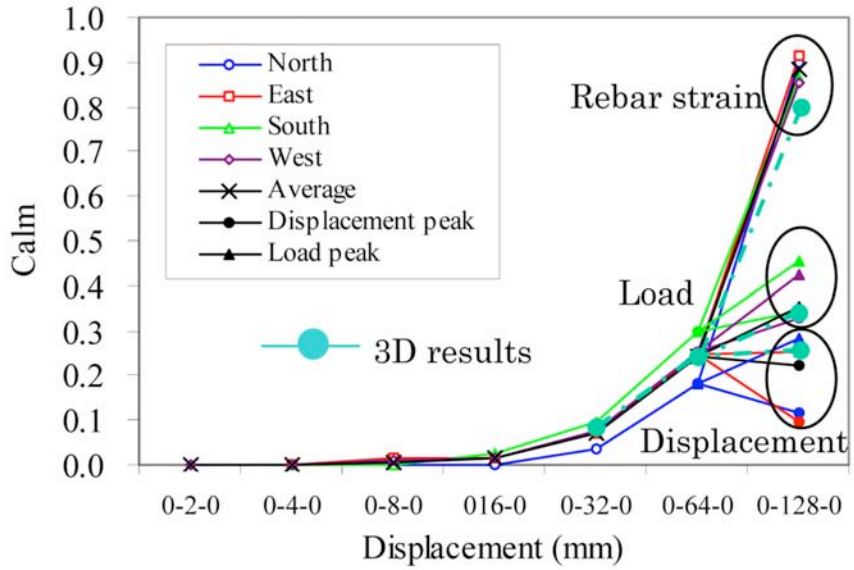

Fig. 9 Calm ratio obtained both from 1D and 3D AE.

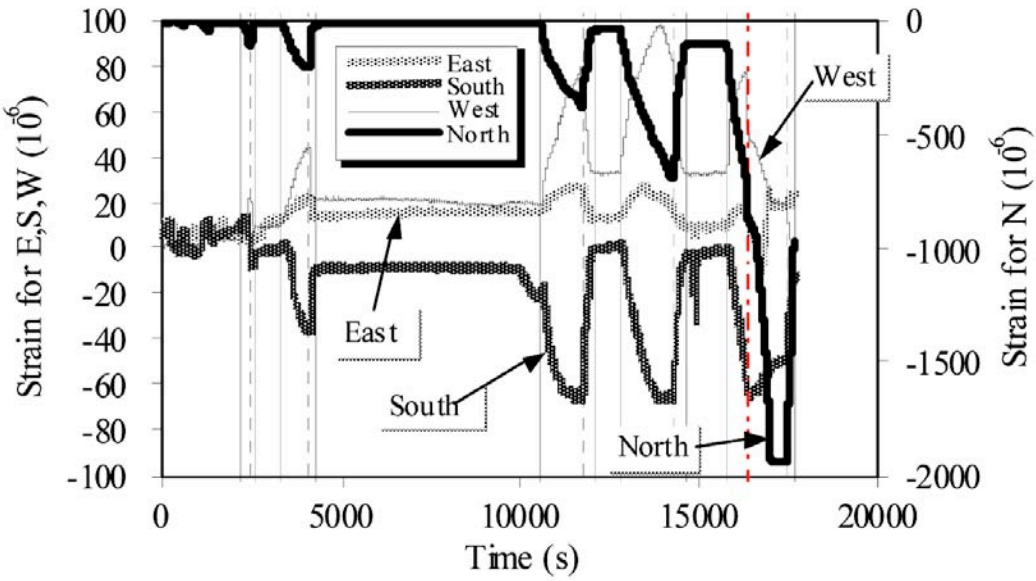

Fig. 10 Concrete strains on different surfaces.

surface concrete strains of the pier on all of directions. In sound or minor damage condition, the strain variation would follow that of applied deformation. However, both surface strains on the east and west walls decreased even during the up-deformation process (see 64 mm displacement or between 13 ks and 15 ks), implying that the pier had already lost the load bearing capacity. Furthermore, from the crack observation, distinct shear-type cracks could not be developed in the pier through the test. Accordingly, the damage evolution of the pier seemed to be terminated during 64-mm displacement and further development of the damage would not be introduced by the subsequent stage, namely 128-mm lateral displacement. Considering those findings, the Calm ratio on the basis of the rebar-strain overestimate the damage (see Fig. 9). Thus, the Calm ratio based on either the load or the displacement better evaluates the actual damage.

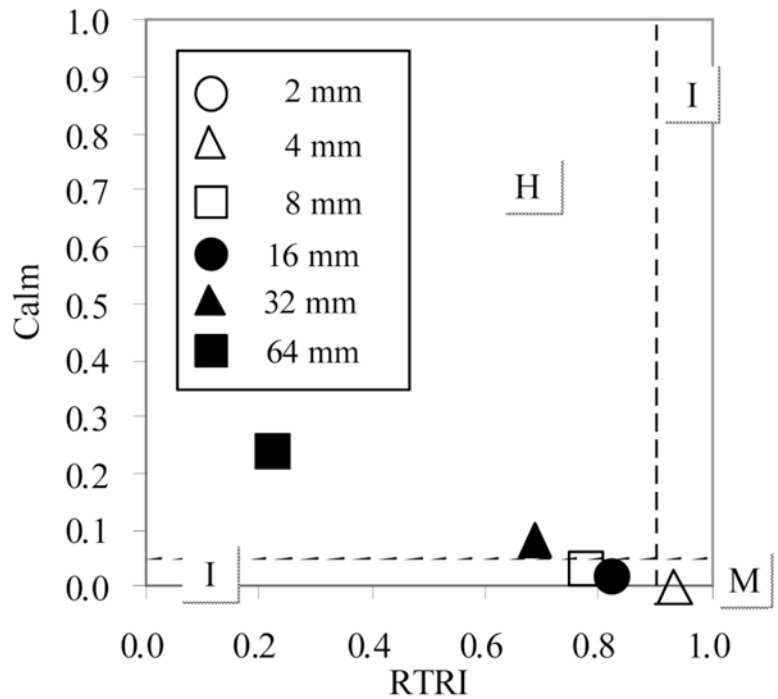

Fig. 11 Relations between Calm ratio and RTRI.

Damage Quantification of AE Damage Indices

Figure 11 shows a chart consisting of Calm ratio and RTRI. In the map, damage criteria reported [10] are overlaid with broken lines. H, I and M in the chart show the damage level: heavily, intermediate; and minor damage, respectively. Since the RTRI during 128-mm displacement could not be obtained, the plots up to 64-mm in the lateral displacement are shown. Using the reported criteria, the minor damage was estimated when 4-mm displacement was given. The intermediate damages were indicated both during 8- and 16-mm displacement, and from 32-mm displacement heavily damage in the pier was indicated. Conclusively, these evaluations were in good accordance with other findings as well as actual damage.

Conclusions

A full-scale railway concrete pier was cyclically loaded and damaged with AE monitoring. Main findings obtained through the test are as follows:

1) Damage indices obtained from AE activity in combination with structural behaviors showed a good agreement with actual damage. Among structural parameters used, internal strains measured on rebars showed overestimation for the actual damage. The applied load or the deformation is more appropriate parameter when evaluating the structural integrity quantitatively.
2) Since the aforementioned issue was both found in 3D and 1D AE sources, it can be concluded that structural integrity of railway concrete structures is potentially evaluated by using the simplest array of AE sensors, namely 1D AE sources.

References

1) Y. Kikuchi, A. Nishimura and M. Yamada: Investigation on the method of judging of integrity for the foundation of the bridge, *The Proceeding of the 43rd JSCE Annual Meeting*, Japan Society of Civil Engineering, pp. 250-251, 1988, in Japanese.
2) A. Nishimura and H. Haya: Assessment of the structural integrity of bridge foundation by the impact vibration test, *Proceedings of GEO-COAST '91*, pp. 719-724, 1991.
3) T. J. Fowler: Experience with acoustic emission monitoring of chemical process industry vessels, *Progress in Acoustic Emission III*, JSNDI, pp. 150-162, 1986.
4) S. Yuyama, T. Okamoto, M. Shigeishi, M. Ohtsu and T. Kishi: A proposed standard for evaluating structural integrity of reinforced concrete beams by AE, *Acoustic Emission: Standards and Technology Update*, ASTM STP1353, pp. 25-40, 1998.
5) The Japanese Society for Non-Destructive Inspection: Recommended practice for in situ monitoring of concrete structures by acoustic emission, NDIS2421, 24 p, 2000.
6) T. Shiotani, M. Shigeishi and M. Ohtsu: Acoustic emission characteristics of concrete-piles, Elsevier Science Ltd., Construction and Buildings Materials, **13**, 73-85, 1999.
7) X. Luo, H. Haya, T. Inaba, T. Shiotani and Y. Nakanishi: Experimental study on evaluation of breakage in foundations using train-induced acoustic emission, *Proc. Structural Engineering World Congress 2002*, Paper No. T9-1-e-3, 2002
8) T. Shiotani, K. Fujii, T. Aoki and K. Amou: Evaluation of progressive failure using AE sources and improved *b*-value on slope model test, *Progress in Acoustic Emission VII*, JSNDI: 529-534, 1994.
9) T. Shiotani and M. Ohtsu: Prediction of slope failure based on AE activity, *Acoustic Emission: Standards and Technology Update*, ASTM STP 1353: 156-172, 1999.
10) M. Ohtsu, M. Uchida, T. Okamoto and S. Yuyama: Damage assessment of reinforced concrete beams quantified by acoustic emission, ACI Structural Journal, **99**(4), 411-417, 2002.

CHARACTARISTICS OF DAMAGE AND FRACTURE PROCESS OF SOLID OXIDE FUEL CELLS UNDER SIMULATED OPERATING CONDITIONS BY USING AE METHOD

KAZUHISA SATO[1)], TOSHIYUKI HASHIDA[2)], HIROO YUGAMI[3)], KEIJI YASHIRO[1)], TATSUYA KAWADA[4)] and JUNICHIRO MIZUSAKI[1)]

[1)] Institute of Multidisciplinary Research for Advanced Materials, Tohoku University, 2-1-1 Katahira, Aoba, Sendai 980-8577, Japan, [2)] Fracture and Reliability Research Institute, Graduate School of Engineering, Tohoku University, Sendai 980-8579, Japan, [3)] Graduate School of Engineering, Tohoku University, Sendai 980-8579, Japan, [4)] Graduate School of Environmental Studies, Tohoku University, Sendai 980-8579, Japan.

Abstract

The purpose of present research is to estimate the damage of solid oxide fuel cell (SOFC) by using a new factor of acoustic emission (AE) during loading test. Acoustic emission signals and fracture processes were monitored by AE measurement system in real time during the test. In the investigation of fracture process with AE amplitude distributions, high-amplitude, middle-amplitude and low-amplitude signals correspond to vertical cracking, delamination in the cathode, and vertical cracking in the elctrolyte, respectively. It was demonstrated that the AE method enabled us to detect these fracture processes and to determine the condition for the onset of the damage in a single cell.

Keywords: Solid oxide fuel cells (SOFCs), Ceria-based single cell, Simulated operating condition, Fracture process

Introduction

Solid oxide fuel cells (SOFCs) have been regarded as a highly efficient power generation system (70 %) for future applications. Since SOFCs convert the chemical energy of the fuel directly to electrical energy without the intermediation of thermal energy, conversion efficiency is not subject to the Carnot limitation. Because of their high temperature of operation (600 ~ 1000°C), natural gas fuel can be re-formed within the cell stack, which eliminates the need for an expensive, external re-former system [1, 2]. Thus, SOFCs are expected to become a major electric power source in the future. In SOFCs, large oxygen potential gradients exist across the two ends of the electrolyte, with the fuel side exposed to highly reducing conditions and the air side to ambient conditions. Under air conditions, electronic charge compensation occurs in ceria-based electrolyte by the formation of Ce^{4+}. However, when sufficiently reducing conditions prevail, oxygen vacancies form and the Ce^{4+} reduces to Ce^{3+} in order to maintain electrical neutrality via ionic compensation. The net result is a lattice expansion due to the change in the ionic radii of Ce [3, 4]. Thus, when exposed to a reducing environment, the ceria-based electrolyte exhibits lattice expansion, also called chemical expansion, and is therefore subject to differential strain across its thickness that could cause fracture (Fig. 1) [3–6]. In general, electrochemical techniques have been used extensively to determine the electrical performance and electrochemical reliability of SOFCs. In addition to the electrical reliability, it is also important to ensure the mechanical reliability of SOFCs under operating conditions. Thus, the establishment of a suitable

mechanical testing method under the operating conditions is a prerequisite for the development of reliable SOFCs.

This paper presents the experimental results of the investigation of damage on the ceria-based single cells under testing conditions. In this study, a simulated environment testing method combined with acoustic emission (AE) monitoring was developed in order to investigate the fracture processes of SOFCs. It was demonstrated that the AE monitoring conducted in this study was useful to detect and analyze the fracture processes in a single cell.

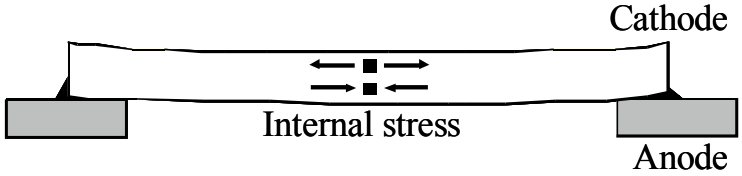

Fig. 1 Schematic diagram showing the electrolyte (fully relaxed case) [3].

Experimental Procedures

Sintered 20%-samarium-doped ceria, $(CeO_2)_{0.8}(SmO_{1.5})_{0.2}$, or 20SDC, disks were used as the electrolyte. The diameter and thickness of the 20SDC electrolyte were 16 mm and 1 mm, respectively. Cermets of NiO-$(CeO_2)_{0.8}(SmO_{1.5})_{0.2}$ (weight ratio of 60:40) and $La_{0.6}Sr_{0.4}Co_{0.2}$-$Fe_{0.8}O_3$ were used as the anode and cathode, respectively. The anode and cathode (10 mm diameter) were applied symmetrically on opposite sides of the $(CeO_2)_{0.8}(SmO_{1.5})_{0.2}$ electrolyte by a screen-printing method. The thicknesses of the anode and cathode were 30 μm, and 15 μm, respectively. Figure 2 shows a schematic of the test section of the apparatus used for evaluating the mechanical performance of a single cell under simulated operating conditions. The maximum temperature achievable with the apparatus is 1000°C. The single cell was placed between two concentric Al_2O_3 tubes. The internal diameters of the outer and inner tubes were 12 mm and 8 mm, respectively. H_2 and O_2 gases were supplied onto the anode and cathode surfaces of the cell through the inner tubes at a flow rate of 100 ml/min and were discharged through the annulus between the tubes. The sealing between the outer Al_2O_3 tubes and the cell was achieved by melting a soda-glass ring. The thickness of the soda-glass ring was 0.5 mm.

Prior to actual tests, the test section was initially heated to 800°C at a heating rate of 100°C/h and held at this temperature for 1 h in an atmospheric air environment in order to melt the soda-glass ring and form the glass seal. After melting the soda glass, it was then cooled to 550°C at 100°C/h and held at this temperature for 1 h.

Preliminary tests showed that the glass seal failed when the temperature was decreased below 450°C. Thus, the starting temperature was set as 550°C in this study. The temperature range for testing can be adjusted by selecting different types of glass. At this stage, H_2 and O_2 gases were introduced to the test section while the temperature was kept at 550°C. The temperature was then increased monotonically to 800°C and cooled to room temperature at 100°C/h in order to examine the fracture process under a heating cycle. To examine the effect of holding time, the temperature was held at 600°C, 700°C, and 800°C for 1 h during heating. Tests with different specimens were repeated three times to check the reproducibility.

In addition to the simulated operating environment tests, simple uniform heating tests under oxygen environment alone were conducted to examine the effect of the thermal stress on the

fracture processes of a single cell. For this purpose, only O_2 gas was supplied onto both the anode and cathode surfaces of the cell and the same heating experiment was undertaken using the same apparatus shown in Fig. 2. The temperature was raised up to 1000°C for the simple uniform heating tests. Three specimens were used for this series of experiments.

Acoustic emission (AE) signals were detected using a resonant piezoelectric transducer (PAC R15), concurrently with the simulated environment tests and simple uniform heating tests. The AE transducer was attached to the outer Al_2O_3 tube at room temperature away from the heated section. After the electronic signals from the transducer were preamplified (40 dB) and bandpass filtered between 20 kHz and 2 MHz, they were further amplified with a variable broadband amplifier that provided an additional gain of 45 dB. After measurement, in order to observe the fracture behavior of ceria-based single cells, cross sections were observed by scanning electron microscopy (SEM).

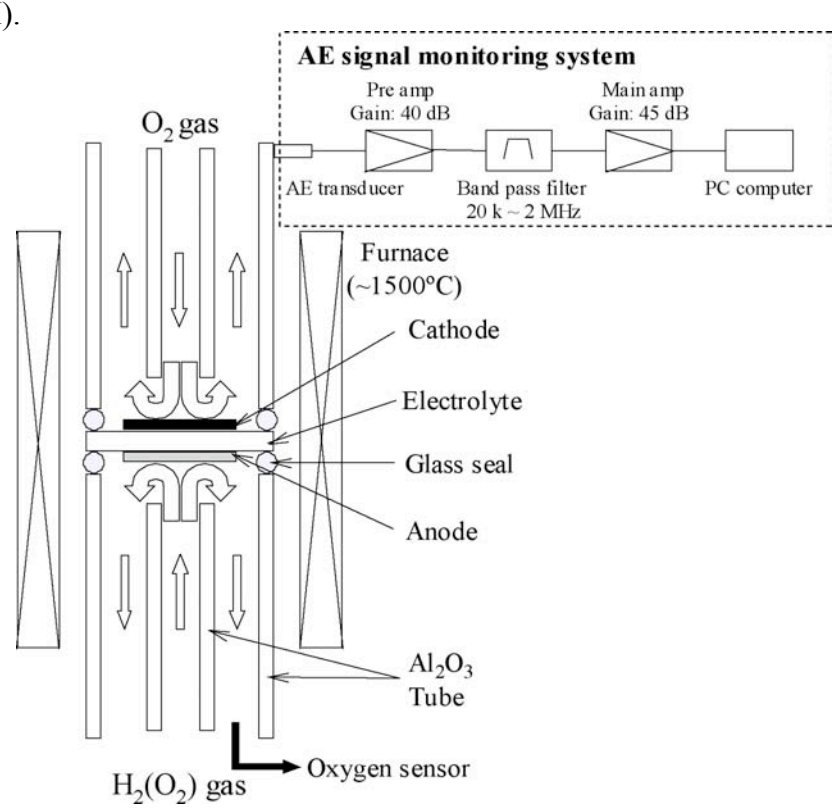

Fig. 2 Schematic layout of the SOFC performance test apparatus and AE monitoring system.

Results and Discussion

In the simple uniform heating tests, where both the cathode and anode were subjected to the oxygen environment, no AE signal was detected up to 1000°C. Furthermore, no damage was found by post-test observations using an SEM. The experimental results indicate that the thermal stresses due to the thermal expansion mismatch were insufficient to cause any damage in the single cell.

Next, the results obtained from the simulated environment tests are discussed. Three specimens used in this study produced almost identical results. The energy of the AE signal, E_{AE}, is plotted with the heating temperature in Fig. 3. This result was obtained from one of the three tests. The E_{AE} was determined by mean square amplitude of AE signals. The onset of AE activity occurred when the temperature reached 620°C. The AE activity increased with the increasing

temperature, and eventually ceased at 760°C with no AE activity in the temperature range between 760°C and 800°C. This may indicate that a complete fracture of the single cell had already occurred, approximately at 760°C. It is noticed that no AE activity is observed during the holding time at 600°C and 700°C, suggesting that the heating rate is sufficiently low with respect to the reaction rate responsible for this fracture process. Post-test observation showed that extensive through-thickness cracking took place in the specimens heated to 800°C, and the specimens were completely broken into a number of segmented pieces of several mm. Numerous vertical cracks were generated in the cathode and the crack spacing was typically in the range of 50 ~ 100 μm.

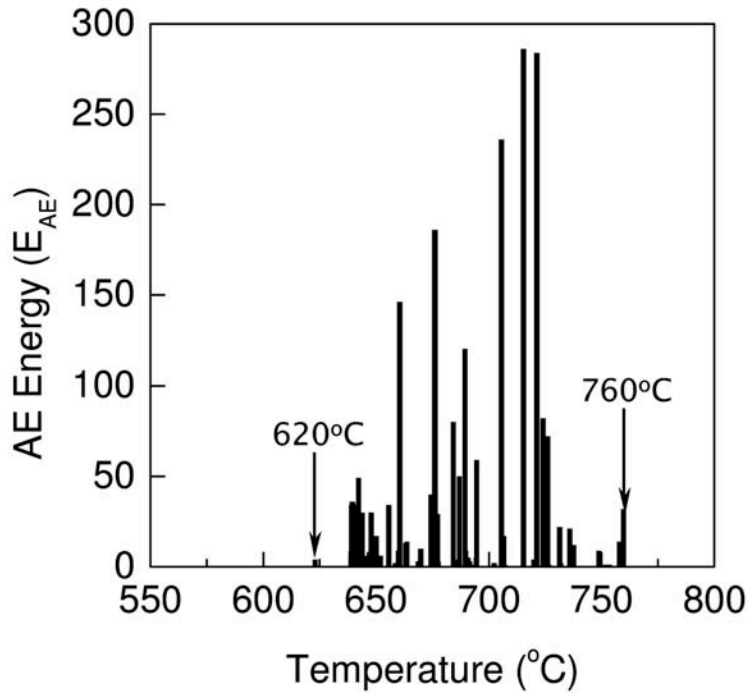

Fig. 3 Acoustic emission behavior under simulated operating condition.

A typical cross-section SEM image of the cathode/electrolyte interface is shown in Fig. 4. The SEM observations identified three types of damage: vertical cracking and delamination in the cathode, and vertical cracking in the electrolyte. Extensive propagation of delaminations was also observed in the cathode film close to the interface, and a limited portion of the cathode film was detached from the electrolyte. No such vertical cracking and delamination were observed in the anode film. The distance between individual vertical cracks was on the order of several mm.

The vertical cracking was observed to initiate from the location of the cathode/electrolyte interface and to frequently terminate inside the electrolyte. As shown in Fig. 4, it was often observed that there was a horizontal gap in the location between vertical cracks in the cathode and electrolyte. This observation suggests that the vertical cracking in the electrolyte was initiated only after the occurrence of the delamination in the cathode.

The salient difference in the damage between the simple uniform heating tests and the simulated environment tests suggests that the above-mentioned damages in the single cell may be primarily due to the chemical expansion in the anode side of the electrolyte and the anode itself. The chemical expansion in the anode side is expected to induce the tensile stress in the cathode side, which may cause the three types of damages. Thus, the vertical cracking in the

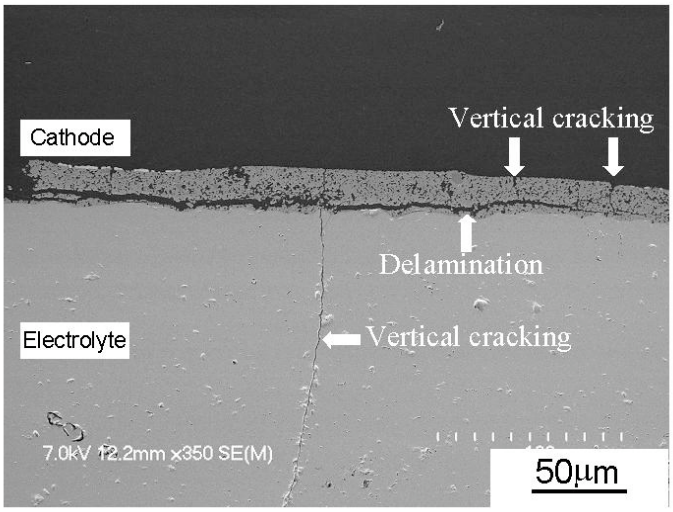

Fig. 4 SEM image of a cross section of a single cell after simulated environment test.

cathode and electrolyte is expected to occur in an opening mode, and the delamination growth in the cathode may be brought about by mixed mode cracking, including a shearing mode. Further investigation is needed to examine the contribution from the effect of the thermal expansion mismatch stresses. Figure 5 shows typical waveforms of AE signals. The results showed that AE signals observed during the tests can be classified into three groups, types A, B, and C. This classification is made on the basis of the difference in peak amplitude and wave shape of the AE signal. AE signals of type A have the peak amplitude smaller than 0.1 mV and is burst type. The peak amplitude of the type B signals was typically in the range of 0.1 ~ 0.2 mV and continuous type. Type C signals have the peak amplitude greater than 0.2 mV and burst type.

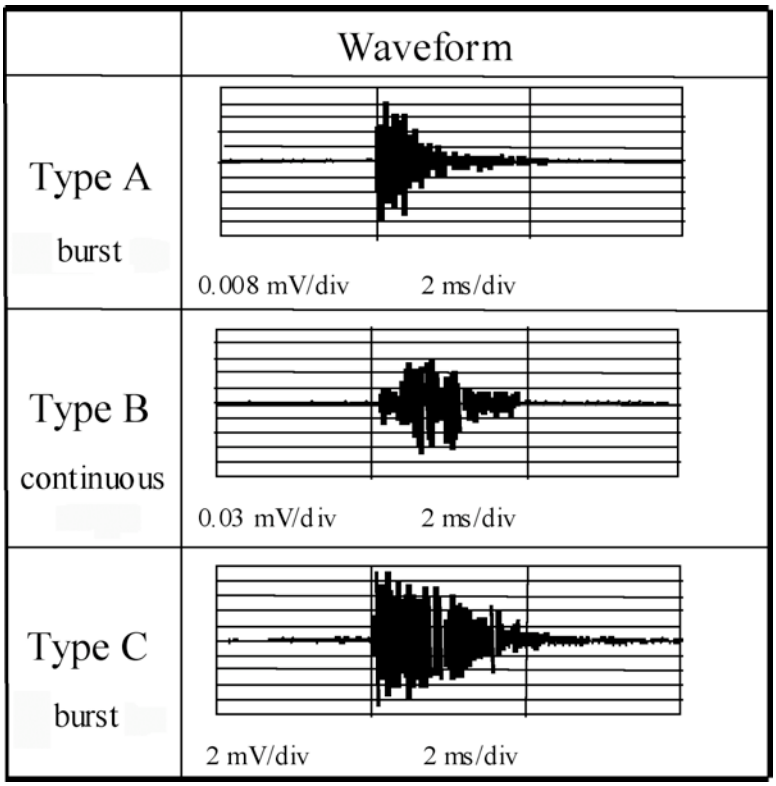

Fig. 5 Waveform patterns of the AE signals.

Figure 6 shows the fracture model of SDC20-based single cell under simulated operating conditions. The correspondence is based on the following observations and discussion. Our preliminary measurements showed that the cathode having a porous microstructure exhibited quasi-brittle fracture behavior with lower fracture energy than the electrolyte. In contrast, the fracture of the dense electrolyte was shown to take place in a catastrophic and brittle fashion. In view of its lower fracture energy and non-catastrophic fracture behavior, the cathode cracking is expected to emit an AE signal of smaller amplitude. In general, inclusion of a mixed mode in the crack propagation tends to increase the fracture energy compared with the crack-opening mode, producing a larger AE energy, and showing continuous-type AE. This suggests that type A may correspond to the vertical cracking and type B to the delamination in the cathode. Type C with larger amplitude and burst-type AE is expected to correspond to the vertical cracking in the electrolyte.

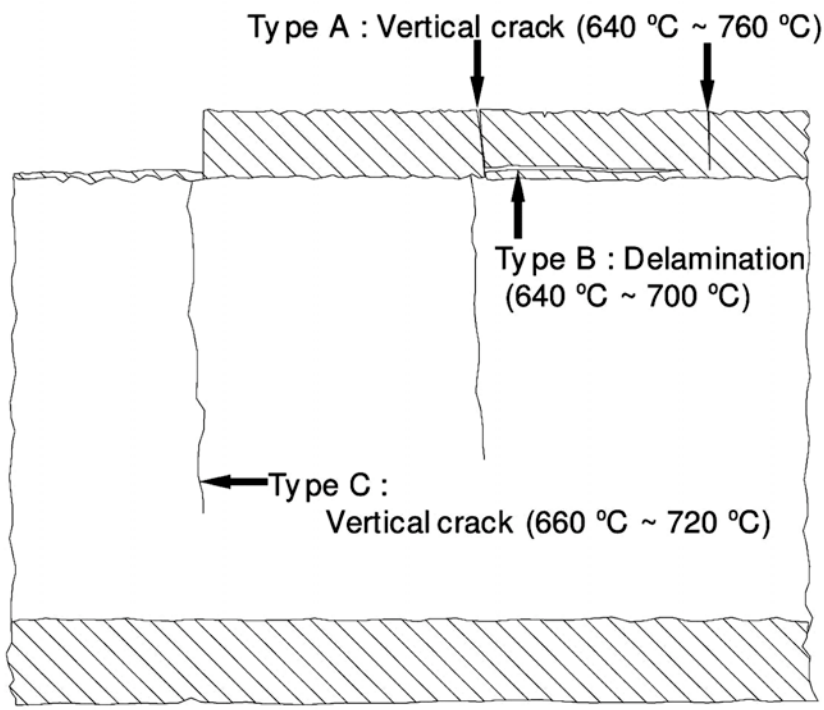

Fig. 6 Fracture process of SDC20-based single cell under simulated operating condition.

The sequence in occurrence of the three types of AE signals appears to correlate well with the fracture processes discussed above. Type A signals start to appear at 620°C, followed by the emission of type B signals. AE signals of types A and B are emitted constantly throughout the ranges of 620°C ~ 760°C and 640°C ~ 700°C, respectively. The first occurrence of type C signals takes place at 660°C. The type C activity increases with increasing temperature and eventually ends at 720°C.

The formation of vertical cracking in the electrolyte must be avoided, since it significantly degrades the electrical performance of the single cell and provides a direct path between the hydrogen and oxygen gases. It seems possible to detect the critical temperature condition of the SOFC by monitoring the AE activity. The present result shows that AE monitoring in the single cell experiment may provide useful information to examine the fracture processes and mechanisms under simulated operating conditions. More quantitative investigation of stress analyses is now underway, and the results will be combined with the present testing method to develop a design methodology for SOFCs.

Conclusions

The main results obtained in this study can be summarized as follow:

(1) A simple testing method was developed which enabled us to examine the fracture processes under the simulated operating environment. Monitoring AE activity was useful to detect and to identify the fracture processes.

(2) The fracture processes of the SOFC involved vertical cracking and delamination in the cathode, and vertical cracking in the electrolyte. The damages were attributable most likely to the stresses induced by chemical expansion.

(3) The AE activities correlated well with the fracture processes observed. The AE results showed that the cathode damage was initiated at 620˚C and the first occurrence of the electrolyte cracking took place at 660˚C.

Acknowledgements

This work was supported in part by the 21st Century COE Program Grants of "Exploration of the Frontiers of Mechanical Science Based on Nanotechnology" and "International COE of Flow Dynamics" and the Grant-in-Aid for Scientific Research on Priority Area, "Nanoionics (439)," all from the Ministry of Education, Culture, Sports, Science and Technology.

References

1) Minh, N.Q.: J. Am. Ceram. Soc., **76** (1993), 563.
2) Singhal, S.C.: Solid State Ionics, **135** (2000), 305.
3) Atkinson, A.: Solid State Ionics, **95** (1997), 249.
4) Yasuda, I., and Hishinuma, M.: Proc. Electrochem. Soc., **97,** No. 24 (1998), 178.
5) Atkinson, A., and Ramos, T.M.G.M.: Solid State Ionics, **129** (2000), 259.
6) Krishnamurthy, R., and Sheldon, B.W.: Acta Mater., **52** (2004) 1807.

ACOUSTIC EMISSION DETECTION OF DAMAGE EVOLUTION IN SHORT-FIBER COMPOSITES

JERZY SCHMIDT, IRENEUSZ BARAN, MAREK NOWAK and KANJI ONO*
Laboratory of Applied Research, Foundry Research Institute, ul. Zakopianska 73, Krakow 30-418, Poland. *Department of Materials Science and Engineering, University of California, Los Angeles, CA 90095, USA.

Abstract

Glass-fiber reinforced, polymer composites fabricated by pressure injection are characterized by acoustic emission (AE). Tested materials are composed of three layers with distinctly different orientation of the reinforcing phase, fabricated from 66 polyamide reinforced with 30% short fiber. The deformation processes in this type of laminate are difficult to identify because of the confined fiber orientation. Tests were made on specimens with three orientations relative to the direction of injection. By pattern recognition analysis of the AE signals recorded in monotonic tensile loading, five patterns typical of the material were identified. We used Vallen VisualClass program. The signal classes were considered in terms of various mechanisms of failure. In the analysis, the results of metallographic examinations of fiber orientation and of the condition of unloaded structure were used, as well as fracture surface examinations. The output of the analysis suggests correlations to possible failure mechanisms in the deformation process.

Keywords: Short-fiber composites, pattern recognition analysis, failure mechanisms

Introduction

Polymers reinforced with short fibers are materials often used for stressed components. These composites have a moderate strength with adequate elongation. The oft-used form of these materials is fabricated by injection molding. In these materials, layered structures characterized by different fiber orientation and content develop. In composites of semi-layered materials, the stress applied to individual layers is analyzed according to the theory of lamination. However, the results obtained by this method are poor due to the absence of a distinct border separating the individual layers. Additionally, the degree of homogeneity obtained in the layers or the transition zone between the layers depend on the parameters of the manufacturing process, on the properties of matrix, and on the geometry of the reinforcing phase. In evaluating the strength of such laminates, it is important to understand the phenomena, taking place during the deformation processes, especially micro-mechanisms of failure.

As in the case of continuous-fiber composites, the strength and fracture of short-fiber composites are dictated by the fiber fracture, by fiber-matrix interface failure via tension, shear or friction and by matrix fracture. Acoustic emission (AE) behavior of short-fiber composites has long been examined [1-3]. Amplitude, frequency, and other characteristics were evaluated in efforts to understand fracture mechanisms. Pattern recognition analysis was also used in composite study for some time [4-7].

In order to elucidate the damage evolution in short-fiber reinforced polymer laminates under the conditions of simple and complex states of loading, we attempted to correlate the failure

mechanisms to AE signals and to develop an effective method of the evaluation of the loading limit and of predicting the risk of damage in components made from these composites. The studies also covered the effect of the reinforcing phase distribution and an analysis of the damage development process. The studies were in most part financed by the Polish Ministry of Science and Higher Education.

Experiment and Analysis

The main goal of the studies was to identify the mechanisms responsible for composite damage under tensile loading. AE tests were performed on specimens made from 66 polyamide with 30% short-glass fiber (~0.7 mm long). The strength of such composites was examined for 0°, 90° and 45° orientations with respect of the direction of injection. They were cut to 25 mm width specimens from 120 x 120 x 5 mm test plates. Under uniaxial loading, three basic models at the fiber-matrix interface were distinguished and related to fiber and stress directions (Fig. 1). In real structures, the orientation of each fiber varies and the combination of these three cases needs to be considered. For each of the 0º, 90º and 45º orientations, the fiber distribution was evaluated by means of microscopic image analysis on specimen cross-sections [8]. Results are shown in Fig. 2 as LV parameter. This is the average length of fibers per volume obtained with statistical analysis from the observation of the polished cross-section. LV represents a characteristic feature of the volume fraction and orientation of the reinforcing phase in each layer of the composite. The LV values indicate that the alignment is far from complete as the LV values differ only by a factor of 2.5-3 between 0º and 90º specimens. The results further show that the near-surface layers and the middle behave in the opposite manner and the over-all composite behavior is always expected to show mixed characteristics. Unlike the usual expectation resulting from resin flow, the injection-molded specimens typify three-layer composites. This examination also revealed in unloaded cross-sections the occurrence of fiber damages in the form of cracks or fissures running along the fiber length. The damages were formed during composite fabrication.

Tensile properties of specimens are listed in Table 1. This reflects the microscopic observations and shows that 0º orientation samples have the lowest strength and 45º the highest. The knee stresses (from the first load drop or the deviation from linearity) are 50-60% of the tensile strength and correspond approximately to the beginning of AE detection.

The tensile tests were made on a Zwick 050 machine under the condition of controlled displacement. During the tests, AE signals were recorded using Dunegan SE25P miniature

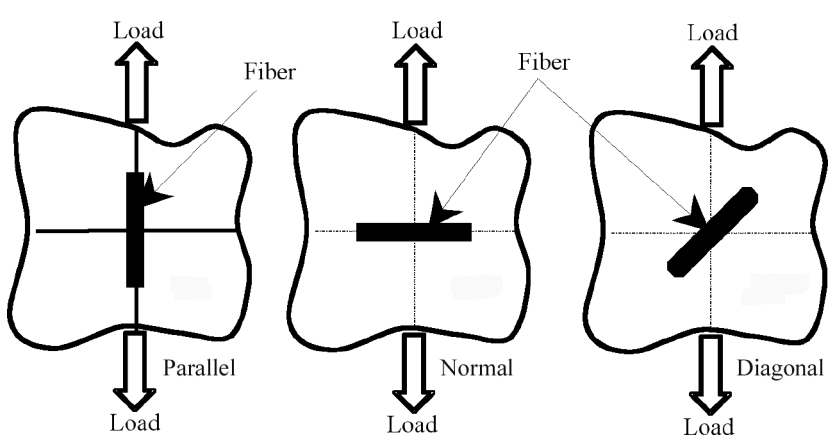

Fig. 1. Model of orientation of fiber according to direction of load.

sensors and Vallen AMSY5 system. Frequency range was 20-600 kHz. Pattern recognition analysis of the recorded AE signals for each specimen yielded typical patterns and by combining the results for three orientations a classifier common to all the examined specimens was designed. Vallen VisualClass program distinguished five classes present. The results of class distribution in percentages obtained for each of the examined orientations are shown in Fig. 3. Here, energy, amplitude, duration and other AE parameters were used as features in addition to frequency-based features.

Table 1 Tensile properties of specimens of three orientation.

Specimen	Knee stress	Tensile strength
0º	44.0 MPa	88.0 MPa
90º	61.6 MPa	100 MPa
45º	58.4 MPa	102 MPa

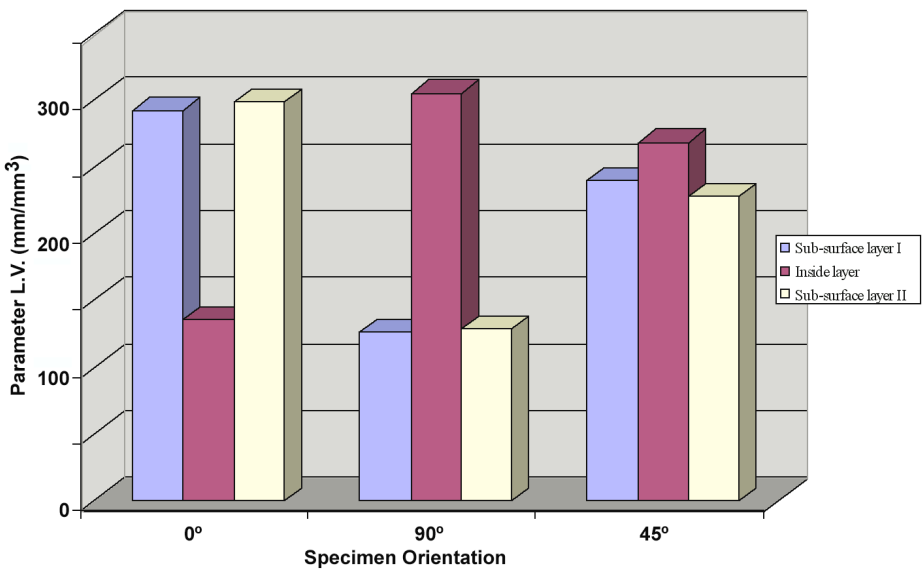

Fig. 2. Parameter LV according to the orientation of specimen.

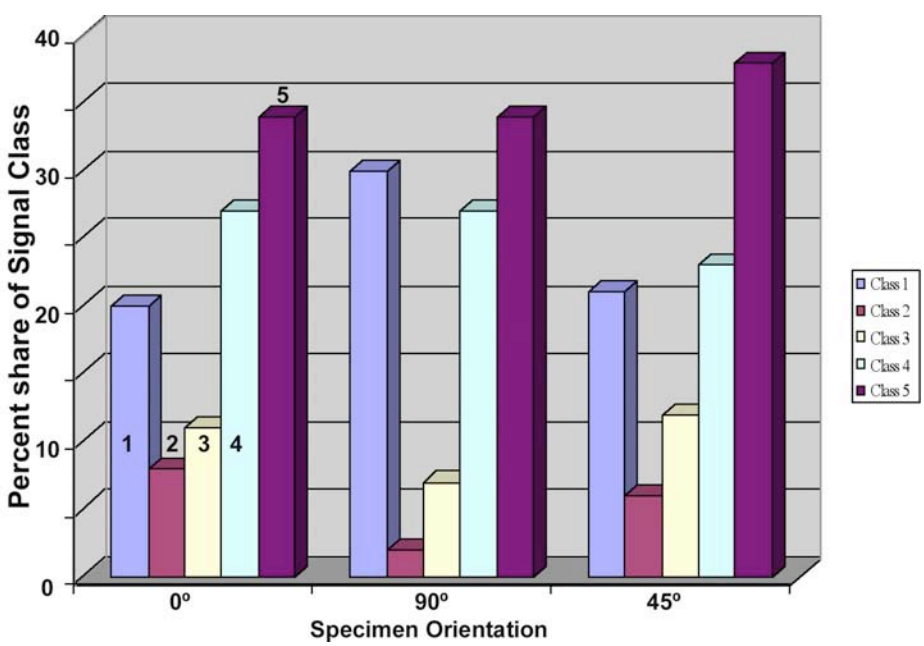

Fig. 3. Graphical results of classification, in the percentage of signal of class by color.

Figure 4 shows an example of the rate of occurrence of each of the classes during deformation for 0º-orientation specimen. The lower plot shows the hit rates of the signals. At the first load drop, AE starts and class II shows higher rates just prior to failure, though it is generally of low activity.

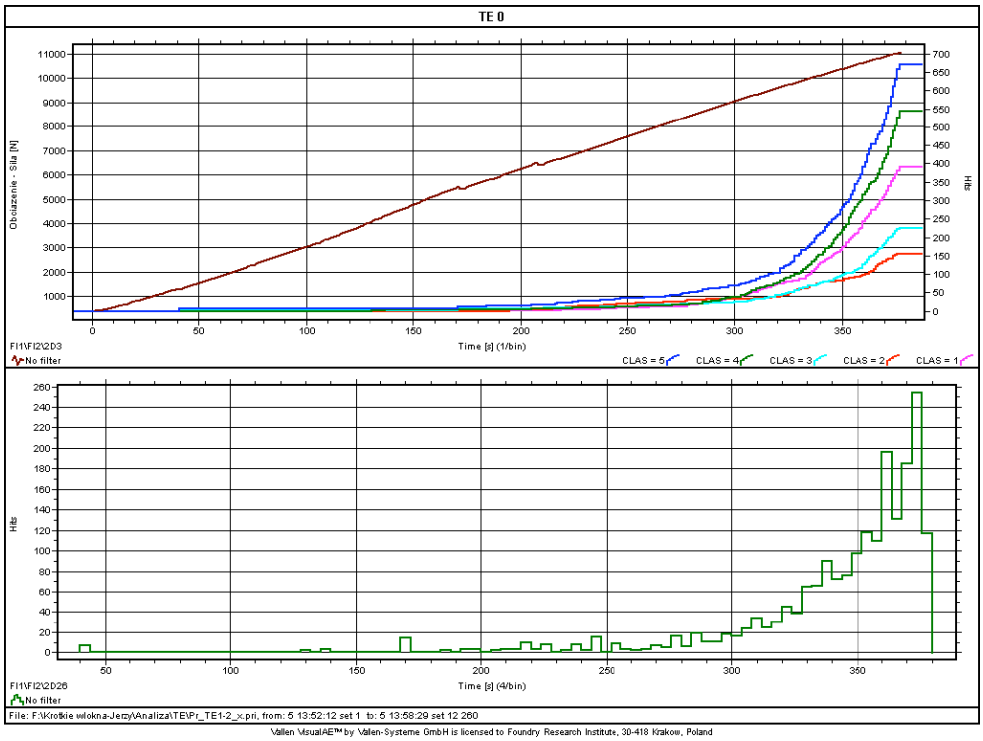

Fig. 4. Graphical presentation of classification for the AE data of 0º specimen.

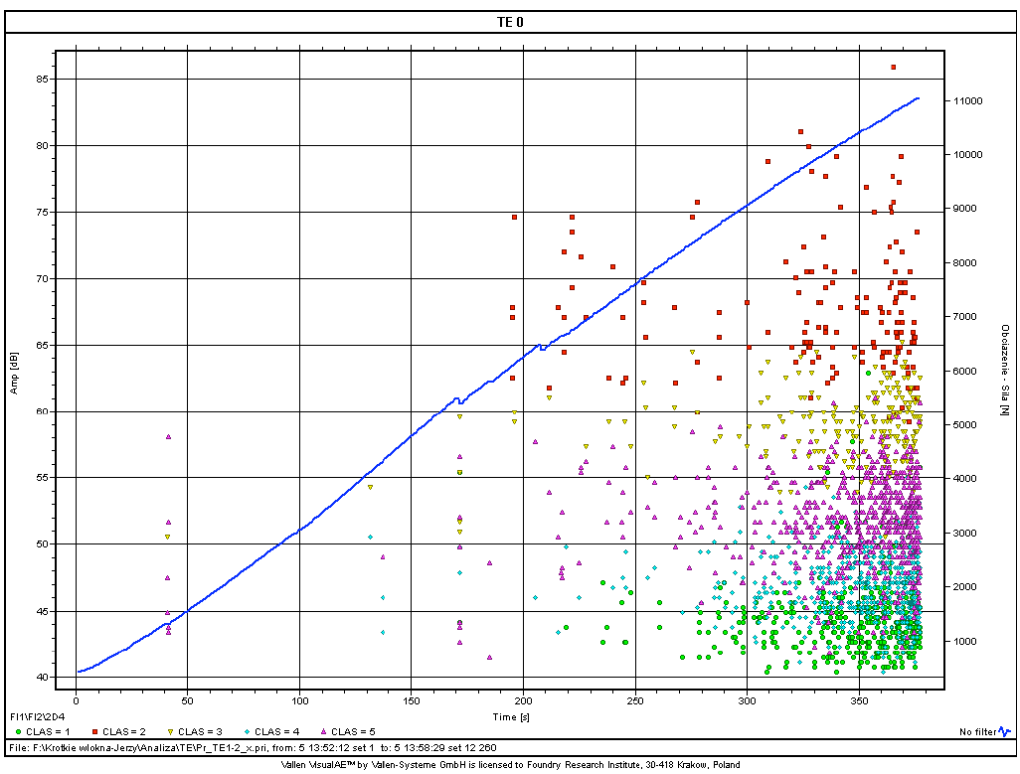

Fig. 5. Classified AE data of 0º specimen in load and amplitude plot. From low dB-levels, class I (40-47 dB), IV (45-55 dB), V (45-57 dB), III (55-65 dB) and II (59-86 dB), respectively.

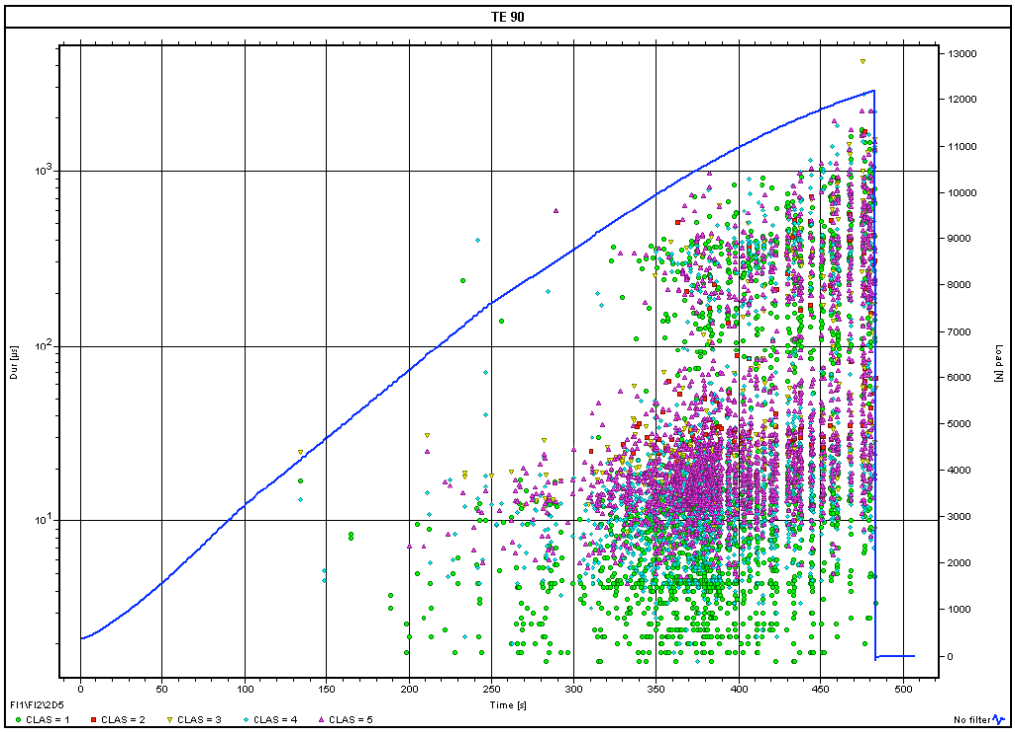

Fig. 6. Classified AE data of 90º specimen in load and duration plot.

In the 0º specimens it appears that the occurrence of classes I, IV and V is correlated, and these signals have low amplitudes, as seen in Fig. 5. Signals of classes II and III have higher amplitudes. The underlying causes of classes II and III signals are of higher energy variety. These trends appear to be common in other orientation samples examined. Figure 6 shows the load and duration plots for a 90º specimen. Most class II and III signals were in the range of 20-1000 µs, whereas the signals of the other 3 classes were either low (<30 µs) or high (<100 µs). The low group is probably from low signal levels relative to the threshold. The high group occurred later in the test and may arise from stress interaction between layers. This bimodal distribution could be the reflection of the three-layer microstructures and need further evaluation. To better characterize the operating failure mechanisms, additional loading tests were made on samples fabricated from 66 polyamide without the reinforcing fibers. Only class I, IV and V signals were detected in neat-resin specimens. It is noteworthy that 20-kHz frequency component was low in matrix-only samples.

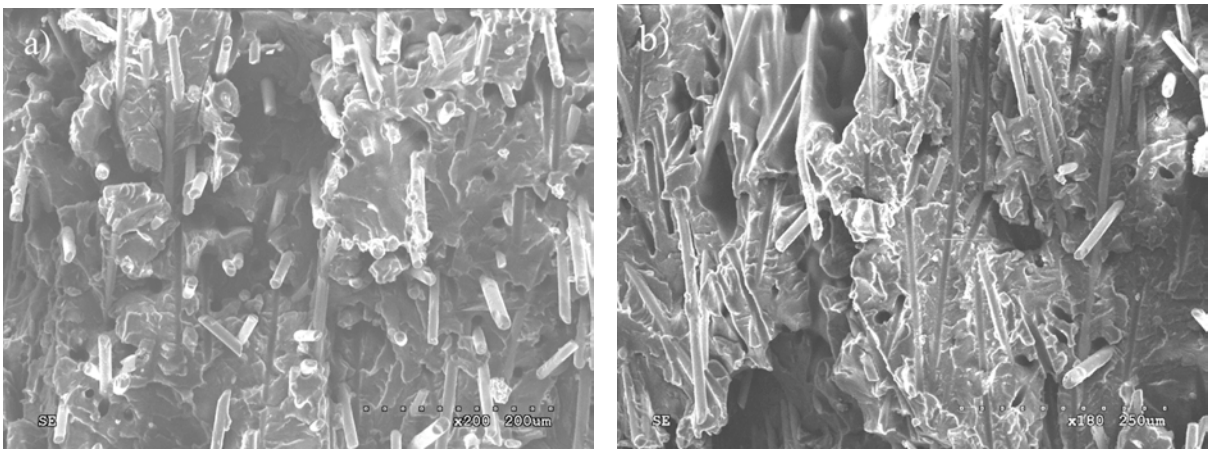

Fig. 7. Examples of fracture surfaces: Sub-surface layer (a) and inside layer (b). 0º specimen.

In order to distinguish the failure modes, extensive metallographic examinations were made. The studies also revealed three-layer structure of this composite. Figure 7 shows SEM images of fracture for the near-surface layer and for the center region. It is clear that numerous fibers broke, that fibers were pulled out of the matrix, that fibers separated from the matrix (some of these occurred in fabrication) and that the matrix showed many microcracks surrounding a fiber with clear sign of brittle matrix failure. These matrix cracks are typically in 30-100 μm diameter and all exhibit cleavage-like patterns. This is quite different from the fracture surfaces of neat resin of 66 polyamide that show smooth rounded surfaces [9].

At this stage of the study, we cannot assign the failure modes to individual signal classes. However, it is clear that classes II and III are associated with tensile and bending fiber fracture and possibly the separation of the fiber/matrix interface. Because of the highest amplitude and energy, class II is most likely due to tensile fiber fracture. The remaining classes, I, IV and V, are related to matrix microcracks at mid-fiber and at fiber ends, fiber disbonding from the matrix, and frictional fiber pull-out. Since class I has the lowest energy, and shortest duration, we suggest this is from matrix microcracks as the neat resin has a low strength level.

The present experiment and analysis will be continued to identify the operating failure mechanisms for each signal class with better characterized starting materials and comparative microscopic evaluation during deformation. It is our goal to extract the AE parameters that we can utilize to obtain individual modes of failure in components under complex stress states.

Conclusions

- The microstructures of short-fiber reinforced composites fabricated by injection molding feature the presence of three layers of different fiber orientation. This led to complex failure mechanisms, and affected the laminate strength.
- The application of AE technique and of the classification system has revealed five distinct signal classes arising from various failure mechanisms.
- The use of pattern recognition analysis and average signal parameters of classified signal groups enabled the discrimination of fiber- and matrix- originated signals.

References

[1] J. Wolters, J. Acoustic Emission, **3**, (1984) 51-58.
[2] H. Nakanishi et al., *Proc. 6-th ICCM*, vol. 1, Elsevier, 1987, pp. 1.395-404.
[3] N.S. Choi, K. Takahashi, *Progress in Acoustic Emission VII*, JSNDI, 1994, pp. 445-450.
[4] M. Ohtsu, K. Ono, J. Acoustic Emission, **6**, (1987) 61-72.
[5] K. Ono, Q. Huang, J-Y. Wu, *Proc. AECM-5*, ASNT, 1995, pp. 197-204.
[6] N. Ativitavas, T. Pothisiri, T. Fowler, J. Composite Materials, 3/2006; doi: 10.1177/ 0021998305053458.
[7] J. Schmidt, I. Baran, K. Ono, J. Acoustic Emission, **23**, (2005) 173-180.
[8] K. Hübner, unpublished, Foundry Research Institute, Krakow, Poland, 2006.
[9] W.L. Phillips, Jr., W.O. Statton, J. Materials Sci. Letters, **3**, (1968) 563-565.

AE MONITORING OF MICRODAMAGE DURING PROOF TEST OF BIOCERAMICS FOR ARTIFICIAL JOINTS

SHUICHI WAKAYAMA, CHIKAKO IKEDA and JUNJI IKEDA*
Department of Mechanical Engineering, Tokyo Metropolitan University
1-1, Minami-Ohsawa, Hachioji, Tokyo 192-0397, Japan.
* Japan Medical Materials Corp., Miyahara, Yodogawa, Osaka 532-0003, Japan

Abstract

AE monitoring was conducted during proof tests of high-purity alumina ceramics in order to detect microdamages, which might decrease the strength of surviving components. The ceramics tested is the bioceramics used in artificial joints for total hip replacement. Surviving specimens showed two types of AE behavior, with or without increasing point of AE energy. Specimens without increasing point of AE energy showed higher residual strength than specimens with the AE increasing point. In addition, the average strength of specimens without increasing point of AE energy was higher than specimens, which survived the conventional proof test. The AE source location during residual strength measurement demonstrated that the maincrack formed during proof tests were propagated to final unstable fracture during residual strength tests. Consequently, it was concluded that the proof test with AE monitoring of microdamage significantly enhances the reliability of bioceramics.

Keywords: Bioceramics, alumina, proof test, microfracture process, maincrack formation, residual strength

Introduction

Ceramics have been used for artificial joints because of the excellent biocompatibility [1-3]. The lifetime of artificial joints was often designed as 10 to 15 years. However, it was reported that a significant number of ceramic femoral heads have been broken in vivo within several years after operations [4]. Therefore, a technique for long-term reliability assessment is urgently needed. The proof testing has been used as one of such techniques. Loading the component before service, the reliability is ensured by removing the broken component. A maximum initial crack size in survivals can be estimated by fracture mechanical analysis, from which the minimum time-to-failure can be calculated [5, 6]. However, there may be still weak components in survivals, which had sustained damages during the proof test.

We have investigated the microfracture process during bending tests of ceramics using AE technique [7]. It was found that rapid increases in AE energy and events were observed before the final fracture. From the results of AE source locations and the observation of fracture process using fluorescent dye penetrant technique, it was demonstrated that these AE behaviors corresponded to the maincrack formation. It was shown that the microfracture process during bending test consists of the microdamage accumulation, the maincrack formation and its growth to the final fracture [8, 9]. The critical stress for maincrack formation, σ_c, was determined as the stress when the AE energy increased rapidly.

The objective of the present study is to develop the technique, which enables us to remove damaged specimens during the proof test. It is necessary to understand the microfracture process of the specimen during the proof test. In this study, AE monitoring during proof tests was carried out to detect the maincrack formation. After the proof testing, the residual strength was measured by four-point bending tests. The AE behavior and the residual strength were compared to investigate the effect of AE monitoring on the residual strength.

Experimental Procedures

Specimens

High purity alumina ceramics (Japan Medical Materials Co.) was used. Mechanical properties at room temperature are shown in Table 1. To eliminate surface defects, tensile surfaces and chamfered edges of specimens were polished using 3 and 1 μm diamond slurry. In order to minimize the effect of water content on the fracture strength, specimens were dried in a vacuum drying oven at 150 ºC for 2h. The size of specimen was 3 mm (height)×4 mm (width)×40 mm (length).

Table 1 Mechanical Properties of Alumina Ceramics (Manufacture's Data).

Density [g/cm^3]	Pulity [%]	Average Grain Size [μm]	Young's Modulus [GPa]	Poisson's Ratio [-]
3.97	>99.9	1.4	400	0.24

Four-point Bending Tests and AE Measurements

AE behaviors during the four-point bending test were measured in air and physiological saline (PS). Figure 1 shows the testing apparatus for PS condition schematically. The temperature of PS was kept at 36 ± 1ºC. Four-point bending tests were carried out according to JIS R 1601, with an inner span of 10 mm and an outer span of 30 mm. The crosshead speed was 0.1 mm/min. Two AE sensors were attached on both edges of the specimen and amplified by pre-amplifiers, then sent to an AE analyzer. Total gain was 80 dB, threshold level was 18 μV at the input terminal of pre-amplifiers, and the bandpass filter was used with a range of 100 to 500 kHz. Tests in air were performed at room temperature using a similar system without a liquid bath.

Four-point Bending Proof Tests

Four-point bending proof tests were conducted in a similar manner to four-point bending tests except for the loading history; the specimens were loaded to the proof stress with a crosshead speed of 0.2 mm/min, held for 10 minutes and unloaded with a crosshead speed of 0.1 mm/min.

Residual Strength Measurements

All samples which survived proof tests were classified into two groups; i.e. samples with or without the rapid increasing point of AE energy. The residual bending strengths in air and PS were measured for each group.

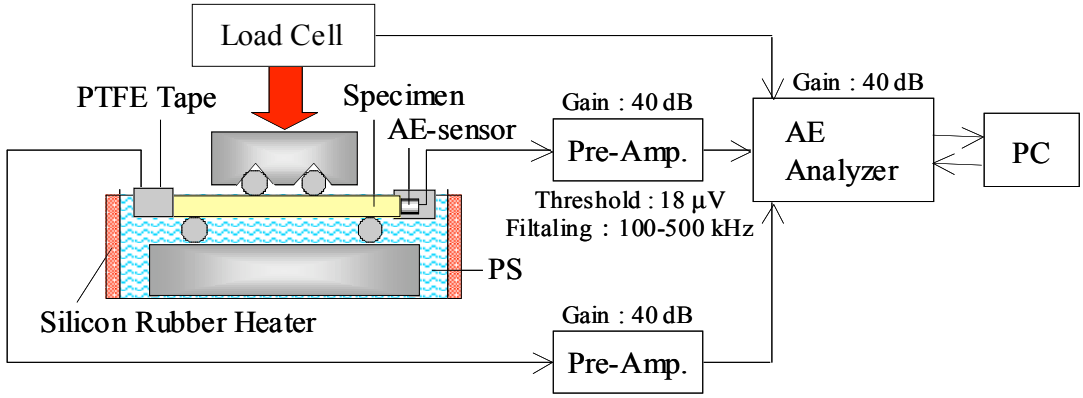

Fig. 1 Schematic diagram of the four-point bending test in PS.

Results and Discussion

AE Behaviors during Four-point Bending Tests

A typical result of the four-point bending test in air is shown in Fig. 2. The applied bending stress, AE cumulative energy, cumulative event and AE source location are plotted as a function of time. The size of the solid circles in the figure represents the amplitude of each AE signal. AE behavior indicated that the rapid increasing point of AE energy exists before the final fracture. As shown in the AE source location, before the rapid increasing point, small amplitude AE signals were detected over the whole range of the specimen. When the AE energy increased rapidly, the large amplitude AE signal was detected at -2 mm in the specimen. After that, large AE signals concentrated near the fracture point of the specimen. Similar to the previous study [7-9], it was concluded that the microfracture process during the bending test consists of the microcrack accumulation, the maincrack formation and its growth to the final fracture. Mean values of the fracture strength σ_B and the critical stress for maincrack formation σ_c are shown in Table 2. It was recognized that σ_B and σ_c in PS were lower than those in air.

Table 2 Average Values of σ_B and σ_C in each Test Environment.

Test Environment	Air	PS
Bending Strength σ_B [MPa]	501 (m=5.9)	371 (m=4.2)
Critical Stress for Maincrack Formation σ_C [MPa]	238 (m=2.8)	129 (m=1.5)

AE Behaviors during Proof Tests

Proof tests were conducted in air and PS, and microfracture processes during the test were monitored by AE technique. From the results of four-point bending tests, the proof stress, σ_P, in air and PS were determined as 200 and 100 MPa, respectively. These proof stresses are low enough to prevent fracture but high enough to induce the maincrack formation for approximately 50 % of specimens in each environment. Two types of AE behavior and AE source location during the proof test in air are shown in Fig. 3. In Fig. 3(a), the specimen had the rapid increasing point of AE energy. As mentioned in the previous section, the increasing point of AE energy corresponds to maincrack formation. On the other hand, in Fig. 3(b), there was no significant behavior in AE energy and events. It is considered that specimens with such behavior have little damage without the maincrack.

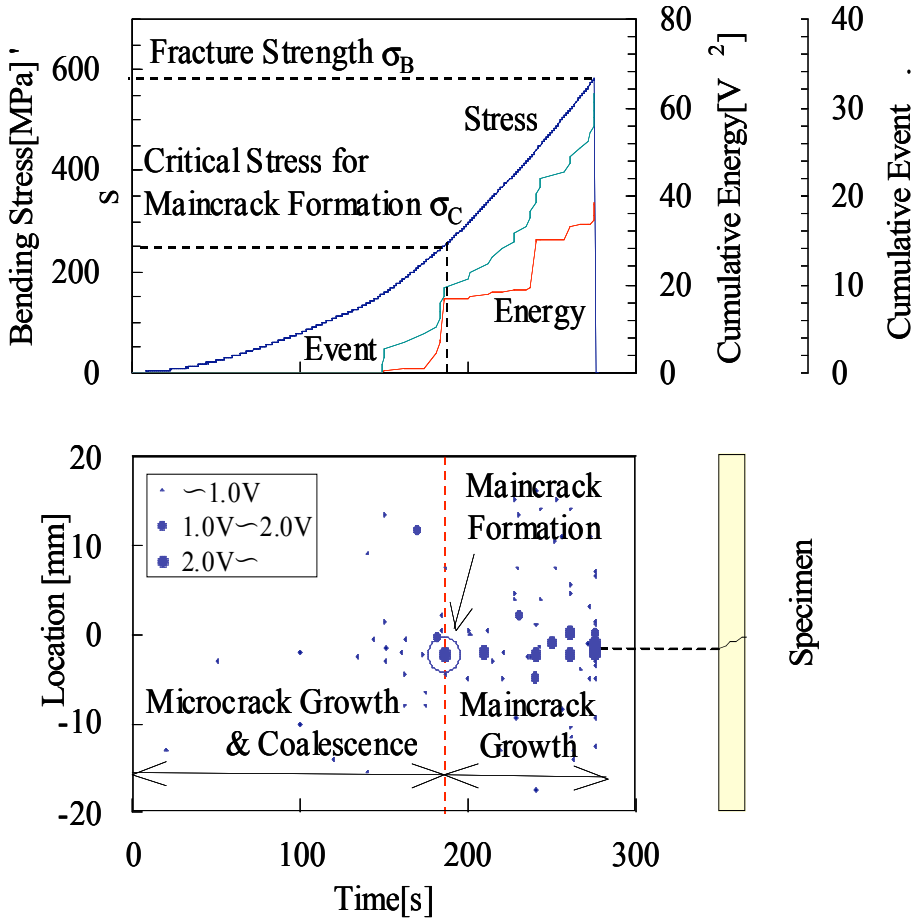

Fig. 2 Typical AE behavior during the bending test.

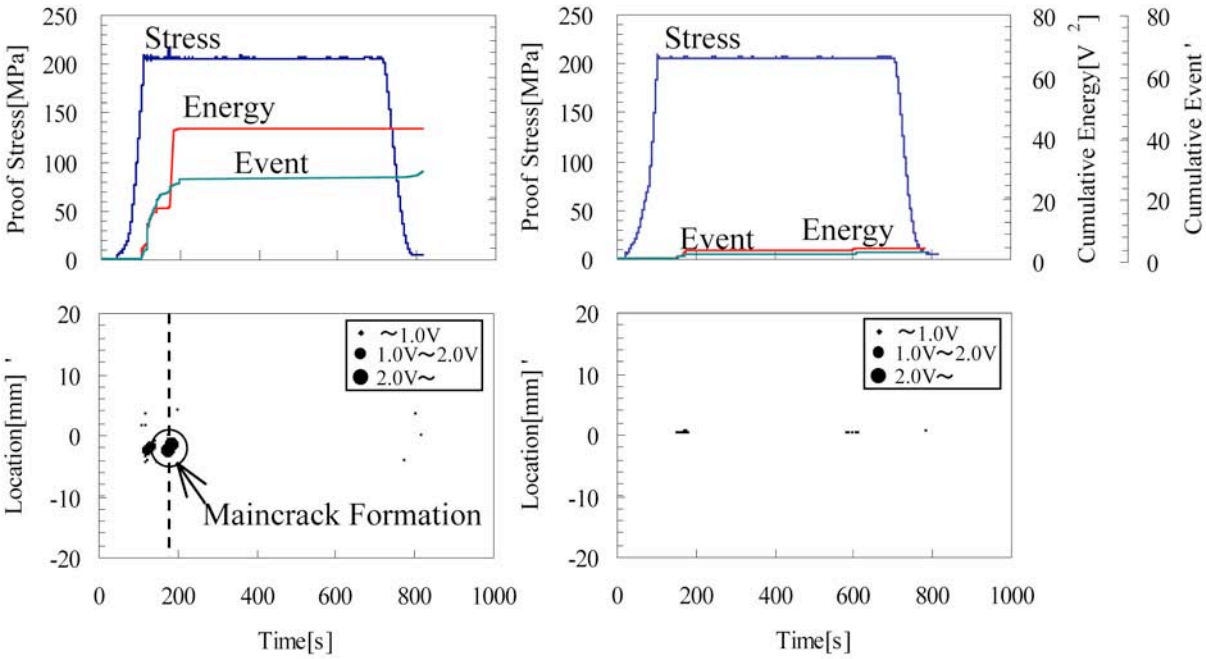

(a) Type A with increasing point of AE energy; (b) Type B without increasing point

Fig. 3 Typical AE behaviors during proof tests.

In this paper, it was found that the maincrack formation takes place only after AE signals with amplitude larger than 1 V were detected. Then, all specimen which survived at the proof test could be categorized into two groups: with increasing point of AE energy (Type A) and without increasing point of AE energy (Type B). From the results of the proof test, all specimens survived. There were 31 and 21 specimens with the increasing point in air and PS, respectively. On the other hand, 31 specimens were without the increasing point in air and 22 specimens in PS were without, respectively.

Residual Strength Measurements

Following proof tests, fracture processes during the residual strength measurement in air and PS were investigated. Figure 4 shows AE behaviors and AE source locations during the proof test (a) and the residual strength measurement after the proof test (b). In Fig. 4(a), the high AE energy event was observed at -2 mm in the specimen at about 180s. It was found that the maincrack was formed at this point. In Fig. 4(b), high AE energy events were observed, and source locations concentrated at near -2 mm in the same specimen. It appears that the maincrack, which initiated during the proof test started to propagate at this point.

Table 3 shows residual strengths in air and PS obtained by samples of Type A and Type B. This table shows the results of conventional proof tests, obtained from all the surviving specimens, in air and in PS. Residual strengths of Type B both in air and in PS were higher than Type A. This clearly demonstrates that that AE monitoring enables the removal of specimens damaged during the proof test. This was not possible for the conventional proof test.

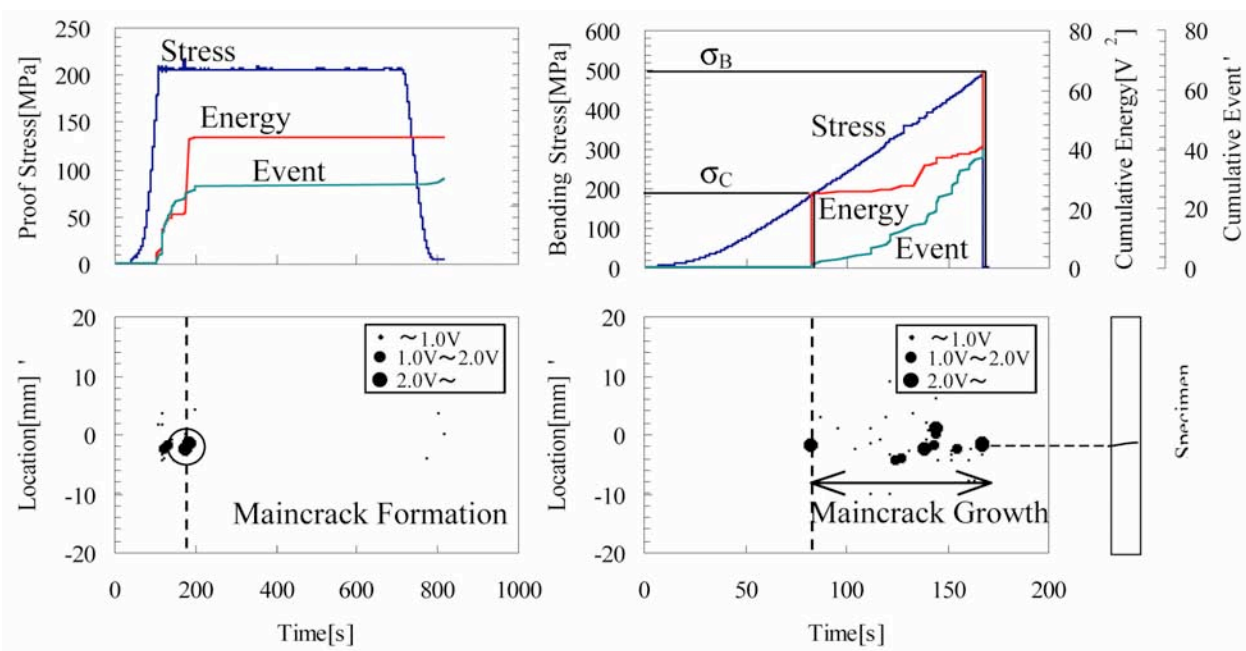

(a) Proof test (b) Residual strength measurement

Fig. 4 Typical AE behaviors during proof test and residual strength measurement.

Table 3 Comparison of the Residual Strength.

Residual Strength	in Air [MPa]		in PS [MPa]	
Proof Test Environment	Air	PS	Air	PS
With Increasing Point of AE Energy (Type A)	489 (n=22)	486 (n=11)	426 (n=9)	359 (n=10)
Without Increasing Point of AE Energy (Type B)	542 (n=13)	504 (n=13)	438 (n=18)	418 (n=9)
Conventional Proof Test (Type A + Type B)	532 (n=25)	496 (n=24)	433 (n=27)	390 (n=19)

Conclusion

In this study, the AE monitoring of microdamage during the four-point bending proof test was conducted for alumina bioceramics in air and in PS, and following conclusions can be drawn.

(1) AE behaviors during the proof test showed surviving samples could be classified as Type A and Type B. The increasing point of AE energy indicates the maincrack formation that degrades the strength of the specimen.
(2) The average strength of survivals showing no increasing point of the AE energy during the proof test was higher than that of specimens through the conventional proof test. Therefore, effectiveness of the proof test assisted with AE method was confirmed.

References

1) L.L. Hench: J. Am. Ceram. Soc., **81** (1998), 1705.
2) L.L. Hench and J. Wilson: *An Introduction to Bioceramics*. Advanced Series in Ceramics. World Scientific, **1** (1993), 1-24.
3) H. Aoki and S. Niwa: *Bioceramics-Development and Clinical Applications, Quintessence* (1987), 26.
4) Saint Gobain Advanced Ceramic Desmarquest, Prozyr®Zirconia Heads, URL; http://www.proyzer.com/PAGE_UK/Biomedical/brekages.htm
5) J.E. Ritter Jr, P.B. Oates, E.R. Fuller Jr and S.M. Wiederhorn: J. Mater. Sci., **15** (1980), 2275.
6) E.R. Fuller, Jr. and S.M. Wiederhorn: J. Mater. Sci., **15** (1980), 2282.
7) S. Wakayama, T. Koji and H. Nishimura: Trans. Jpn. Soc. Mech. Eng., **A57** (1991), 504.
8) T. Kawakami, S. Kobayashi and S. Wakayama: Trans. Jpn. Mech. Eng. Int. J., **A46** (2003), 348.
9) S. Wakayama, T. Kawakami, S. Kobayashi, M. Aizawa and A. Nozue: J. Acoustic Emission, **21** (2003), 149.

SMALL DIAMETER WAVEGUIDE FOR WIDEBAND ACOUSTIC EMISSION

M. A. HAMSTAD
National Institute of Standards and Technology, Materials Reliability Division (853), 325 Broadway, Boulder, CO 80305-3328 and University of Denver, School of Engineering and Computer Science, Department of Engineering, Denver, CO 80208.

Abstract

The signals obtained from two wideband conical sensors were compared in the time, frequency and time/frequency domains. The signals were generated by pencil-lead breaks on the surface (out-of-plane) or close to the midplane of the edge (in-plane) of a large (1220 mm by 1525 mm) aluminum alloy plate (thickness of 3.1 mm). One sensor was coupled to the plate surface by vacuum grease at a propagation distance of 254 mm, and the other sensor was coupled with vacuum grease to the end of a nominal 300 mm or 400 mm long small-diameter waveguide. The other end of the waveguide was coupled to the plate surface by vacuum grease at a 254-mm propagation distance. The waveguides were either aluminum alloy (1.59-mm or 3.18-mm diameter) or brass (1.59-mm diameter). The goal was to determine how closely the waveguide sensor signal duplicated the signal obtained from the plate-mounted sensor. Results were considered in the light of group velocity diagrams for the aluminum plate and the aluminum rods. The sensor mounted on the 1.59-mm diameter aluminum waveguide provided a signal that closely duplicated the signal from the plate-mounted sensor.

Keywords: Acoustic emission, waveguides, wideband sensors

Introduction

Waveguides are used in acoustic emission (AE) technology in several situations. Some of these are (i) a test sample at an elevated temperature above the maximum operating temperature of the AE sensor; (ii) a test item covered with insulation such that typical sensor mounting is inconvenient or precluded; and (iii) a test specimen that is either very small or sufficiently irregular that it does not allow mounting a sensor directly on the specimen. A recent publication [1] referenced several waveguide studies, and it studied waveguides for AE applications. This study did not include wideband small-aperture sensors nearly flat with frequency.

The purpose of the research reported here was to examine whether the combination of a wideband conical-type AE sensor with a waveguide of small diameter would result in the waveguide-mounted sensor signal closely duplicating the signal from a specimen-mounted sensor of the same design.

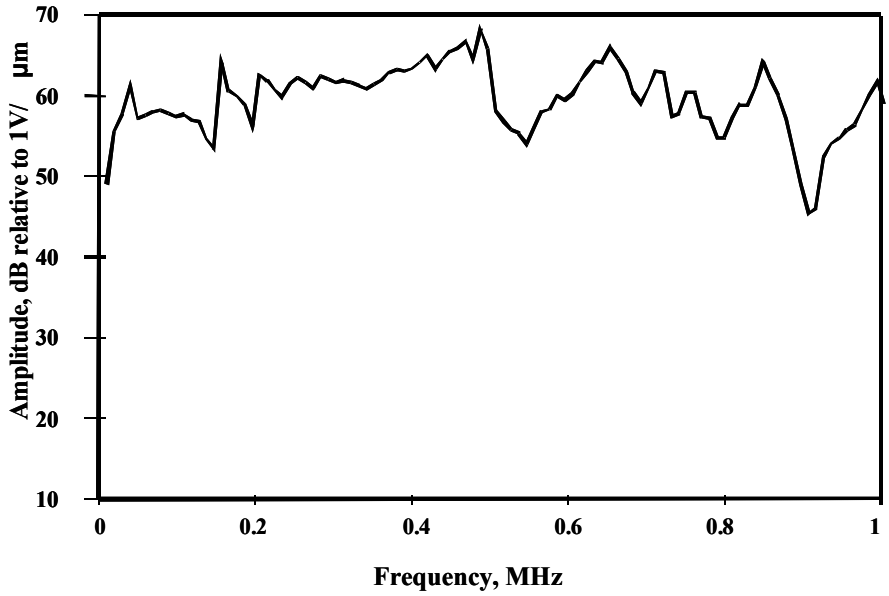

Fig. 1 NIST-based calibration of conical sensor at the preamplifier calibration gain (about 10 dB); out-of-plane displacement response.

Experiment

The conical sensors used in the research were manufactured at the National Institute of Standards and Technology (NIST) in Boulder, Colorado. This sensor design was fully described in two previous publications [2, 3]. Figure 1 shows the out-of-plane displacement-based frequency response of a sensor with this design when it was calibrated with its associated preamplifier at its "calibration" gain of about 10 dB (according to the manufacturer [4]). The results in this figure were generated at NIST in Gaithersburg, Maryland.

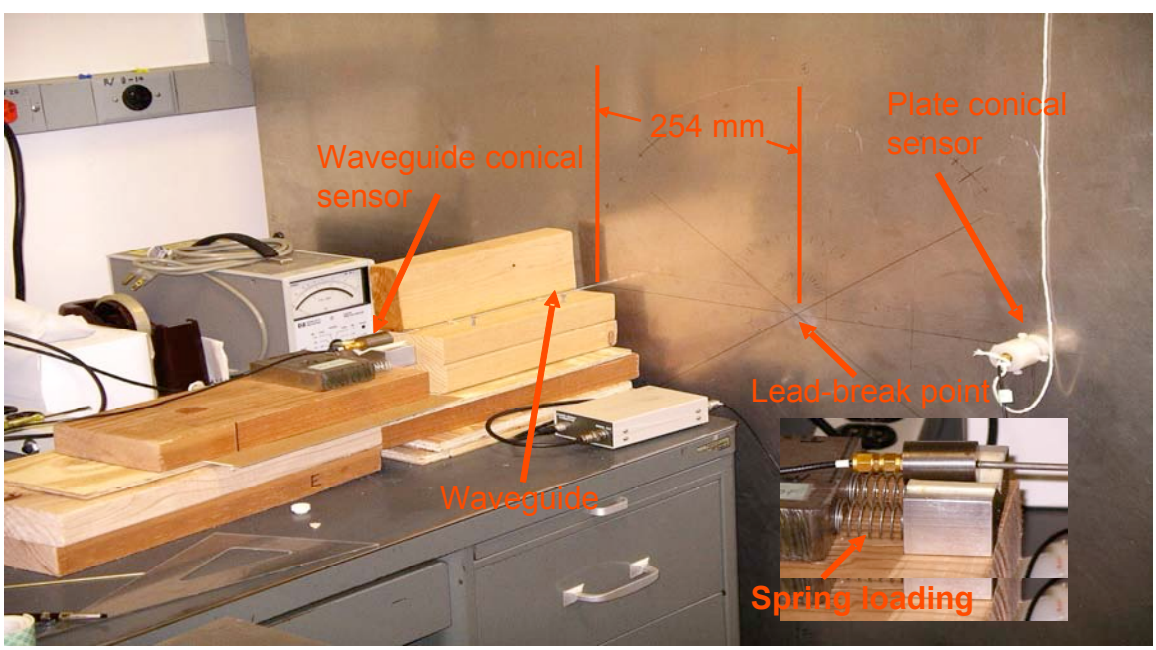

Fig. 2 Photograph of test setup for out-of-plane pencil-lead-break source with an insert of spring loading.

The sensor, which features a conical piezoelectric element with a 1.5-mm aperture, has internal electronics that are compatible with the preamplifier manufactured in Japan [4]. The internal electronics increase the sensitivity beyond that typical of a wideband sensor. In the experiments reported here, two such sensors were used. Each sensor was connected to a preamplifier using the "calibration" gain. Beyond the preamplifier, the signal was filtered by a high-pass, 50 kHz, four-pole Butterworth passive filter. The signal from the filter was recorded by a 12-bit digital recorder at a sample rate of 0.1 μs per point.

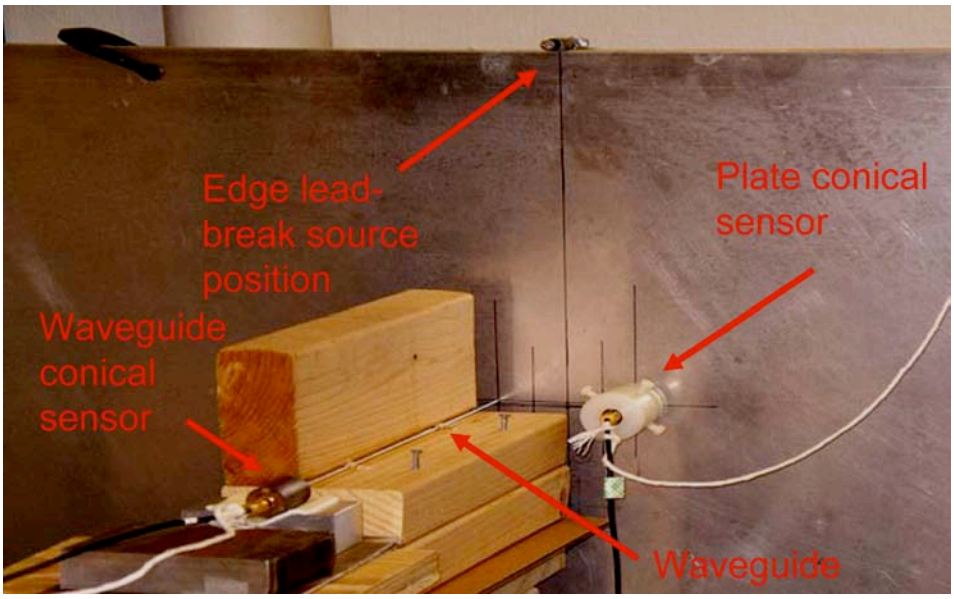

Fig. 3 Photograph of test setup for edge in-plane pencil-lead-break source.

The test setup is shown by photographs in Figs. 2 and 3. Pencil-lead breaks (0.3-mm diameter, 2H hardness and a length of about 2 mm) provided the source to generate the simulated AE signals. Both plate-top-surface out-of-plane (setup in Fig. 2) and plate-edge in-plane (setup in Fig. 3) pencil-lead breaks were applied on an aluminum alloy plate with a thickness of 3.1 mm. The transverse dimensions of the plate (1220 mm by 1525 mm) were large enough to preclude reflections from the plate edges arriving during the duration of the signals propagating directly from the pencil-lead break position to the plate-mounted sensor and the waveguide contact area. The waveguide (WG) as shown (see Figs. 2 and 3) was mounted perpendicular to the plate surface. The philosophy of the experimental approach was to have both the plate-mounted sensor and the WG contact area (with the plate) at 254 mm from the pencil-lead break point. Thus the differences in the signals from the two sensors can be attributed to the waveguide. This distance was sufficient to allow full development of Lamb waves.

Two WG materials were used: aluminum alloy rods with a diameter of either 1.59 mm or 3.18 mm, and brass rods with a diameter of 1.59 mm. No details on the exact alloys and their history were available. Prior to their use in the experiment, the ends of the rods were milled to provide a relatively smooth surface that was perpendicular to the axial direction of the rods. The nominal length of the WGs was 305 mm. Vacuum grease was used as a couplant for the two sensors and the WG-to-plate interface. In this initial study with wideband sensors and small diameter waveguides, no attempt was made to deal with the issues of coupling at other than room temperature. The two sensors and the WG were spring loaded (see the insert in Fig. 2) against their contact surfaces with a force of about 5 N.

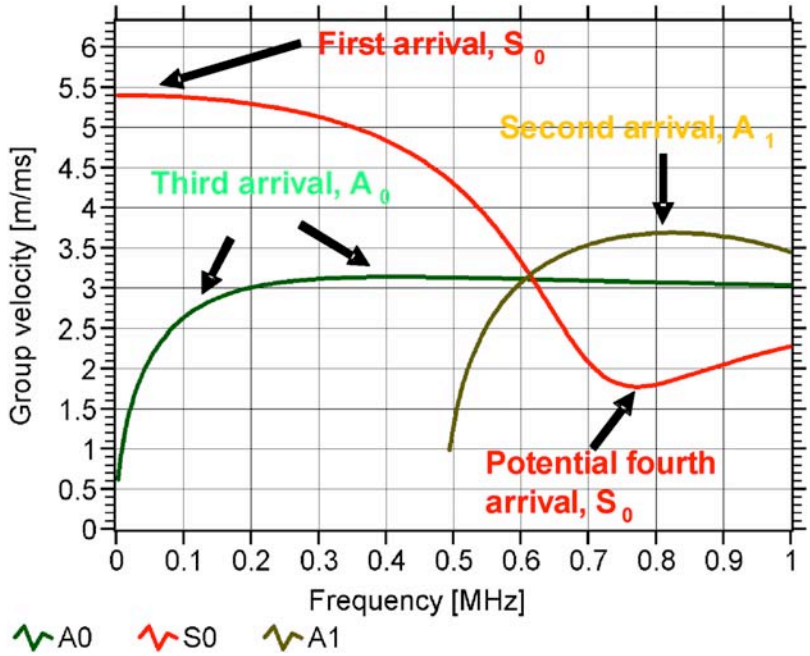

Fig. 4 Group velocity versus frequency for 3.1-mm thick aluminum plate showing A_0, A_1 and S_0 modes.

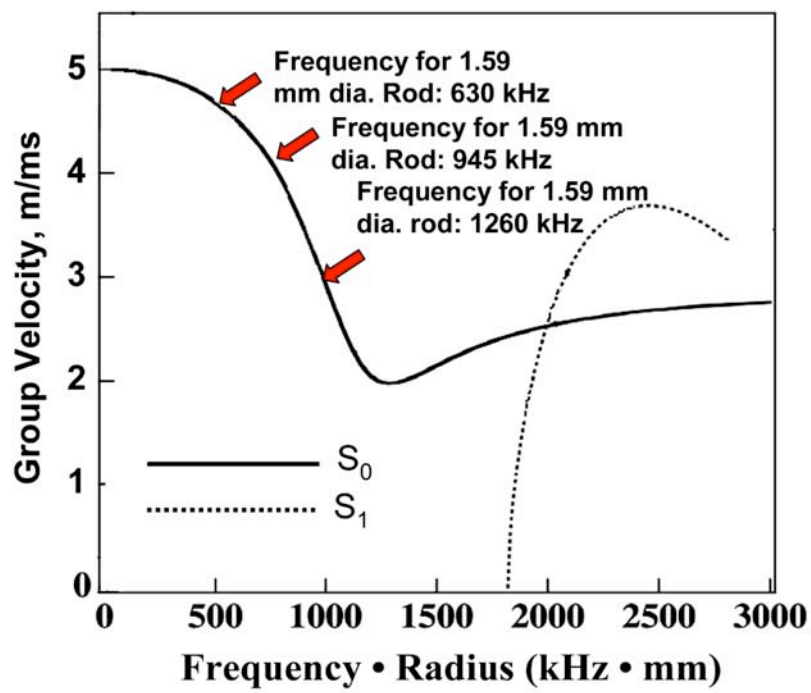

Fig. 5 Group velocity versus frequency•radius for aluminum rod showing S_0 and S_1 longitudinal modes (Adapted from Ono and Cho [1]).

Discussion of Expected Waves in the Plate and Waveguides

Due to the relatively small thickness of the plate, only lower Lamb modes were expected to be generated in the plate over the frequency range of interest. Figure 4 shows a plot of group velocity versus frequency of the lowest symmetric mode (S_0) and the two lowest anti-symmetric modes (A_0 and A_1) for the 3.1-mm thick plate. These curves were calculated (software reference

[5]) using Kolsky's [6] bulk velocities for aluminum. The frequency range in Fig. 4 was terminated at 1 MHz to correspond to the frequency range in Fig. 1.

Based upon the regions of the curves that are nearly stationary, as pointed out by Weaver and Pao [7], and the author's experience, the potential distinguishable sequence of arrivals in the pencil-lead-break-generated waves is pointed out in Fig. 4. Since the WG was oriented perpendicular to the plate surface and coupled by a viscous couplant, it was expected that the plate-end of the WG is significantly excited only by the out-of-plane displacement of the plate surface. Thus, only longitudinal waves were expected to be generated in the WGs. Figure 5 shows the group velocity versus frequency·radius of the two lowest longitudinal modes for the aluminum WGs. This figure was obtained by modifying a figure published by Ono and Cho [1].

For the signal from the WG-mounted sensor to closely duplicate the signal from the plate-mounted sensor, we assume that the input displacements from the plate to the end of the WG must be transmitted at the rod velocity (i.e., the velocity of the rod S_0 mode at near zero frequency). Such a transmission would mean the out-of-plane displacements from the sensor end of the rod into the WG-mounted sensor would be the same as if that sensor were mounted directly on the plate. Based on the S_0 group velocity curve shown in Fig. 5, this ideal situation would occur only for relatively low frequencies. But since the initial portion of the S_0 curve is relatively flat as the frequency • radius increases from zero for this range of frequencies in a small diameter WG, all these frequencies would be transmitted at about the same velocity. Thus, potentially the out-of-plane plate surface displacement might be preserved in the WG-mounted sensor signal.

To provide some perspective of how much the longitudinal-mode velocity might vary, the points that show the velocity at certain frequencies are shown in Fig. 5 for a 1.59-mm aluminum rod. Clearly up to about 630 kHz, the velocity is relatively constant, and the displacement as a function of frequency might be nearly preserved. Further, from examining Fig. 4 (plate group-velocity curves), we might expect that the first and third arrival regions would potentially be preserved. Contributing to this "preservation" would be the use of WGs that are not too long, since a very long WG would cause small velocity differences (for different frequencies) in the rod to produce significant propagation time differences. With WGs of larger diameter, the highest frequency that could be expected to travel at a velocity that would mostly preserve the signal would be lower.

Experimental Results and Discussion

An example of a typical set of experimental waveforms is shown in Fig. 6. In this case, the source was an out-of-plane pencil-lead break. A pre-trigger (based on the signal from the conical sensor mounted on the plate) was used to simultaneously trigger both recorder channels. The delay shown in the arrival of the signal from the 1.59-mm diameter aluminum WG sensor (Fig. 6(b)) was due to the propagation time along the length of the WG. In Fig. 6(b), the arrivals of the initial portion of the plate S_o and A_o modes are indicated for the WG-mounted sensor signal. These two arrivals are also obvious (see Fig. 6(a)) in the signal from the conical sensor coupled to the plate. In addition, based on the exact WG length (306.4 mm) and the aluminum rod velocity (5.09 mm/μs, [6]), an initial reflection in the WG of the plate A_0 mode was identified. This reflection is also indicated in Fig. 6(b). This reflection occurs after the signal in the WG has traversed its length three times after initially entering it. Due to its small amplitude, the plate S_0 mode reflection is not readily identified in this case.

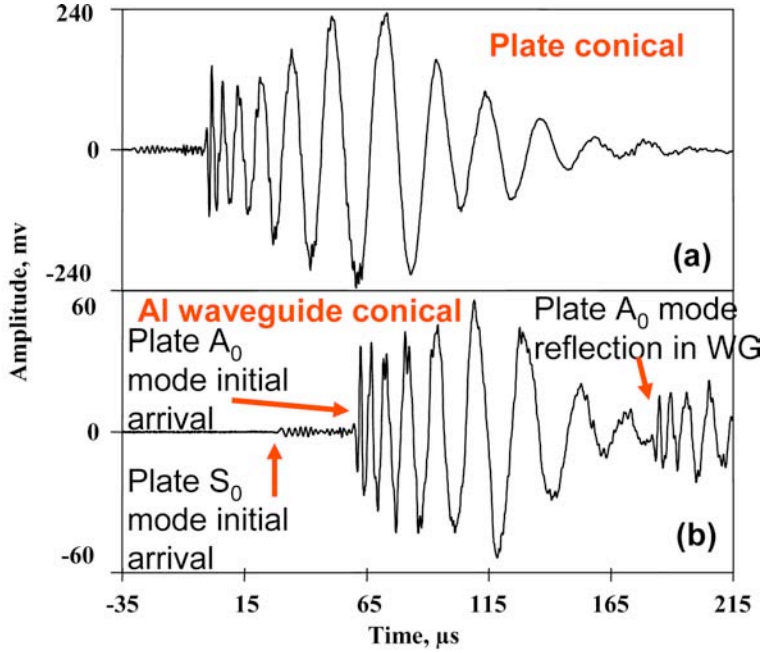

Fig. 6 Waveforms of signals from out-of-plane source with a 1.59-mm diameter by 306.4-mm long aluminum waveguide. Part (a) from plate conical sensor and part (b) from a conical sensor coupled to the end of the waveguide.

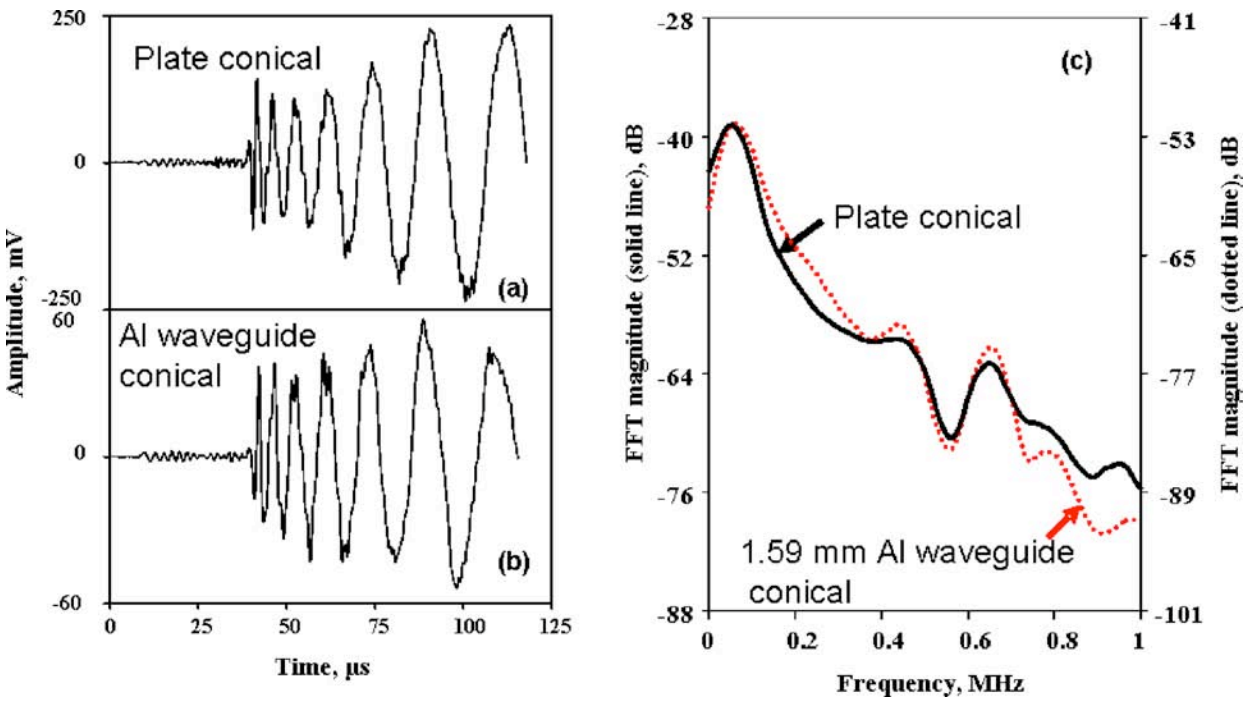

Fig. 7 Parts (a) and (b) are the same as those in Fig. 6, except that the offset in the waveguide sensor signal has been removed using the rod velocity and rod length. Also, the signals have been terminated at a zero prior to the reflection in the rod of the plate S_0 mode. Part (c) provides the FFT spectra of the two signals shown in parts (a) and (b).

Based upon the rod velocity and the WG length, the WG signal was offset forward by 60.2 µs to allow easier comparison of the signals from the two sensors. Figure 7 shows these signals from the plate and WG conical sensors terminated at a convenient zero prior to the expected reflection of the plate S_0 mode in the WG. The signals were terminated at zeros in preparation for

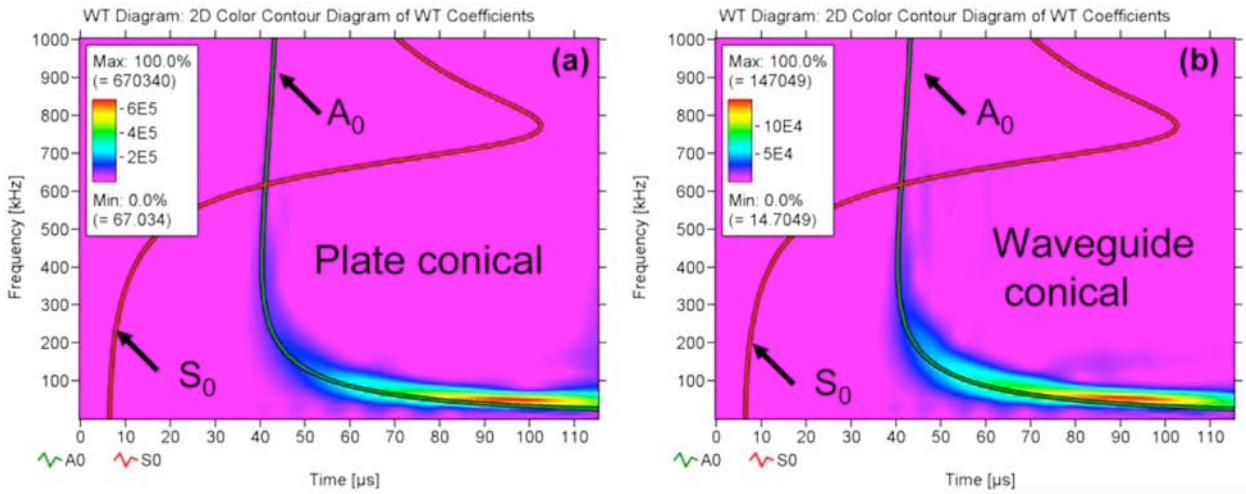

Fig. 8 WTs of the signals shown in Figs. 7(a) and (b) with the superimposed frequency versus propagation time (for 254-mm propagation distance) curves (based on group velocity curves) for the two lowest plate modes.

the calculation of the fast Fourier transform (FFT). The FFTs are shown in Fig. 7(c) over a frequency range from 0 to 1 MHz. The FFTs were calculated with a square window with the signals extended by zeros to a total length of 2048 points. For clarity, the resulting FFTs were smoothed over 30 points.

Examination of Fig. 7 shows that the signals from the plate and WG conical sensor are qualitatively very similar in both the time and frequency domains. In Fig. 7(c), the amplitude scales of the FFT results were adjusted to superimpose the results from zero to about 100 kHz (this procedure was used for all such FFT comparisons in this paper). As expected, the WG signal was reduced in amplitude. The reduction is about 13 dB, based on the offset of the magnitude scales to superimpose the FFT results.

At frequencies above about 700 kHz, the WG signal experienced a further reduction in the response level compared to the plate sensor response. The wavelet transforms (WTs) [8] of the two signals in Figs. 7(a) and (b) were calculated, and they are shown in Fig. 8 with superimposed S_0 and A_0 plate modes. These modes were superimposed by visually adjusting their time offset after the 254-mm propagation distance had been accounted for in the calculation of the propagation time. The key parameters chosen for the WT calculation were a frequency resolution of 3 kHz and a wavelet size of 600 samples. Clearly, the WT results also demonstrate the strong similarity of the signal from the WG sensor to that from the plate sensor.

In order to compare the WG sensor signal with the plate sensor signal when the signal in the plate was not as strongly dominated by the flexural, A_0, mode, an edge pencil-lead break was used. For this case, the configuration already shown in Fig. 3 was used with the contact point of the pencil lead being near the mid-plane of the edge of the plate. Figure 9 shows the two simultaneously recorded signals when the 1.59-mm diameter aluminum WG was used. As before, the initial regions of the S_0 and A_0 modes are indicated in Fig. 9. In addition, the plate S_0-mode reflection in the WG signal is pointed out in Fig. 9(b). As before, this reflection arrival was identified based on the calculated propagation time at the aluminum rod velocity for two additional WG lengths after its original arrival at the WG sensor.

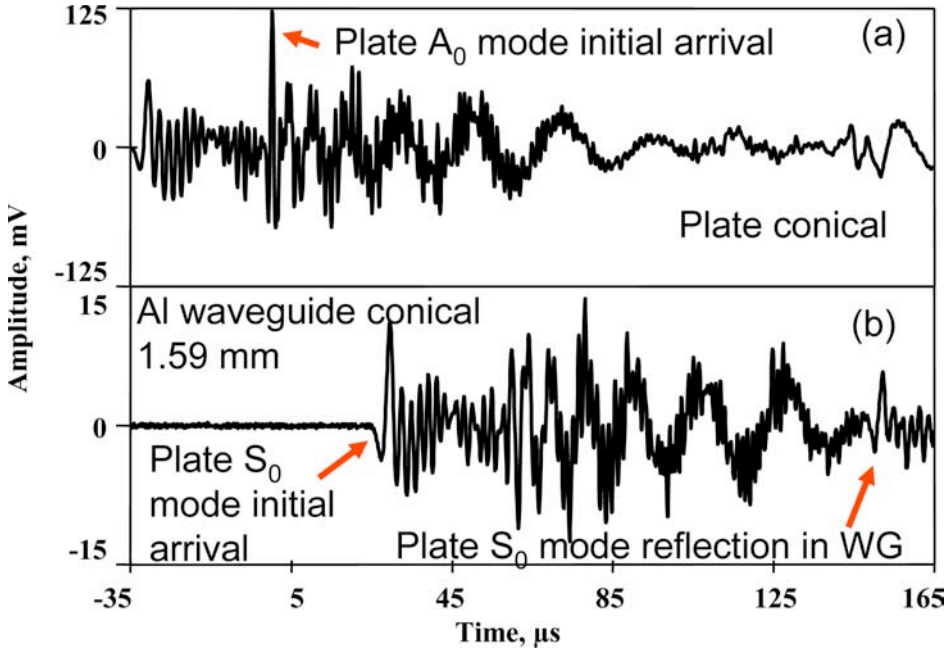

Fig. 9 Waveforms of signals from an edge, near-midplane pencil-lead break source with a 1.59 mm diameter by 306.4 mm long aluminum waveguide. Part (a) from the plate conical sensor and part (b) from the conical sensor coupled to the end of the waveguide.

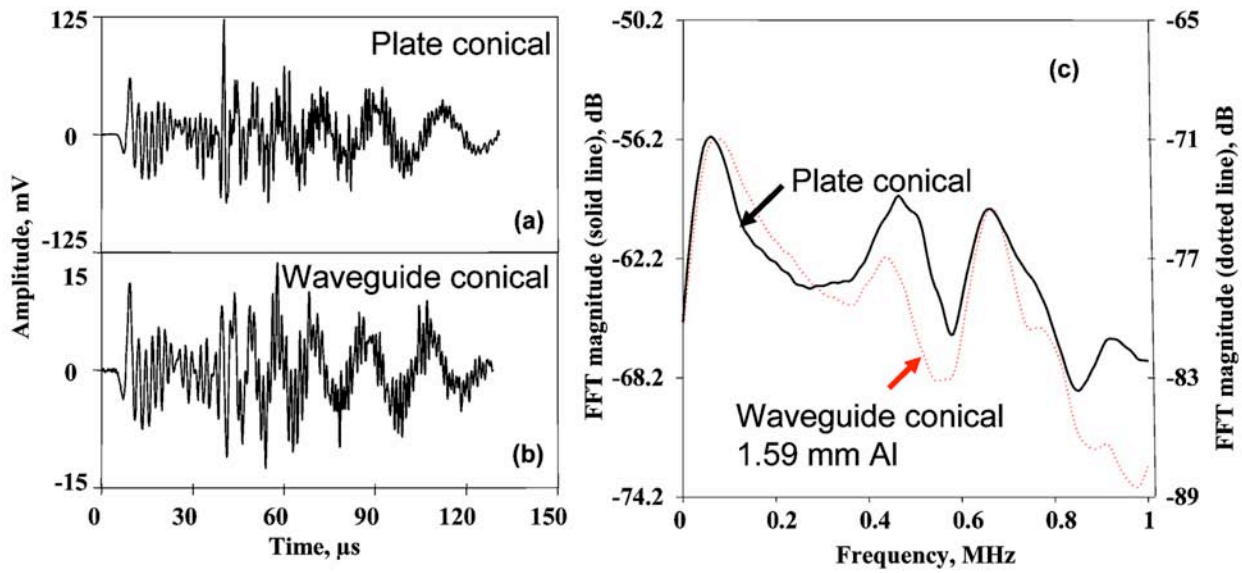

Fig. 10 Parts (a) and (b) are the same as those in Fig. 9, except for the conditions described in the caption of Fig. 7. Part (c) shows the FFT spectra of the two signals shown in parts (a) and (b).

To continue the comparison, the WG signal was offset as before by the rod-length transit time at the rod velocity. Figures 10(a) and (b) show both signals with a termination at a convenient zero before the plate S_0-mode reflection in the rod. In the same way as described earlier, the FFTs and the WTs were calculated, and the results are displayed in Figs. 10(c) and 11, respectively. In this case the amplitude of the WG sensor signal is down about 17 dB from the plate sensor signal as can be seen from the offset used in the FFT results. It should be noted that these comparisons should be viewed as a general trend since the "convenient" zero does not lead to the same signal length for the various cases in this paper and the variations in signal length occur in the region of the signal dominated by lower frequencies. Again the out-of-plane displacement

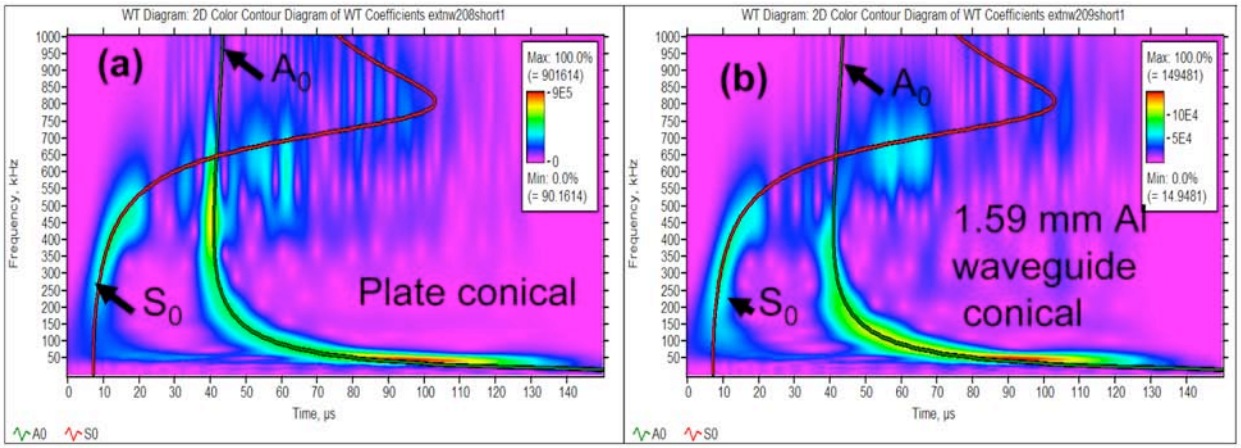

Fig. 11 WTs of the two signals shown in Figs. 10(a) and (b) with superimposed results from the A_0 and S_0 plate modes for a 254-mm propagation distance in the plate.

signals, FFTs and WTs are qualitatively quite similar. There is again a further reduction in the WG sensor signal at higher frequencies when compared to the plate sensor. This reduction is somewhat more than that seen with the out-of-plane pencil-lead break case (compare Figs. 7(c) and 10(c)). There is also some deviation between 400 kHz to 600 kHz in these FFT results.

It is possible that a part of the deviation of the WG sensor signal compared to the plate sensor signal is due to the fact that the edge of the aluminum plate had been sheared rather than machined. This may have resulted in a slightly different signal arriving at the plate sensor compared to that arriving at the point where the WG was coupled to the plate. It should also be noted that the WTs of both signals clearly show that both the A_0 and S_0 modes are present in both the plate and WG sensor signals. As described before, the plate group velocity curves for the A_0 and S_0 modes were superimposed on the WT results visually.

Larger Diameter Aluminum WG

Based on Fig. 5 and the accompanying discussion, a larger diameter WG was expected to result in a poorer duplication by the WG sensor signal of the signal from a plate-mounted sensor. Nevertheless a 3.18-mm diameter aluminum WG was tested with an out-of-plane pencil-lead break source on the plate. The results are shown in Figs. 12 and 13. Figures 12(a) and (b) demonstrate that the displacement signals from both sensors (after the WG sensor signal had been shifted forward by 80.5 µs, based on its exact rod length of 409.6 mm and the rod velocity) terminated at a zero before the plate A_0 mode reflection. The overall view seems to lead to the conclusion that the WG sensor signal is quite similar to the plate sensor signal, but a later closer examination will show some distinct differences.

The FFT and WT results in Figs. 12(c) and 13 respectively show fairly similar results between the signals from the two sensors. Based on the FFTs for this larger diameter case, the additional reduction of the WG sensor signal compared to the plate sensor signal begins at a lower frequency of about 300 kHz compared to that seen in the case of the 1.59 mm WG. In contrast to the smaller diameter WG, the signal amplitude decrease of about 5 dB with the 3.18 mm WG (based on the FFT offset used) was considerably less than the decrease of about 13 dB with the 1.59 mm diameter WG. For the same reasons noted before, these amplitude differences should be viewed as a trend indicator.

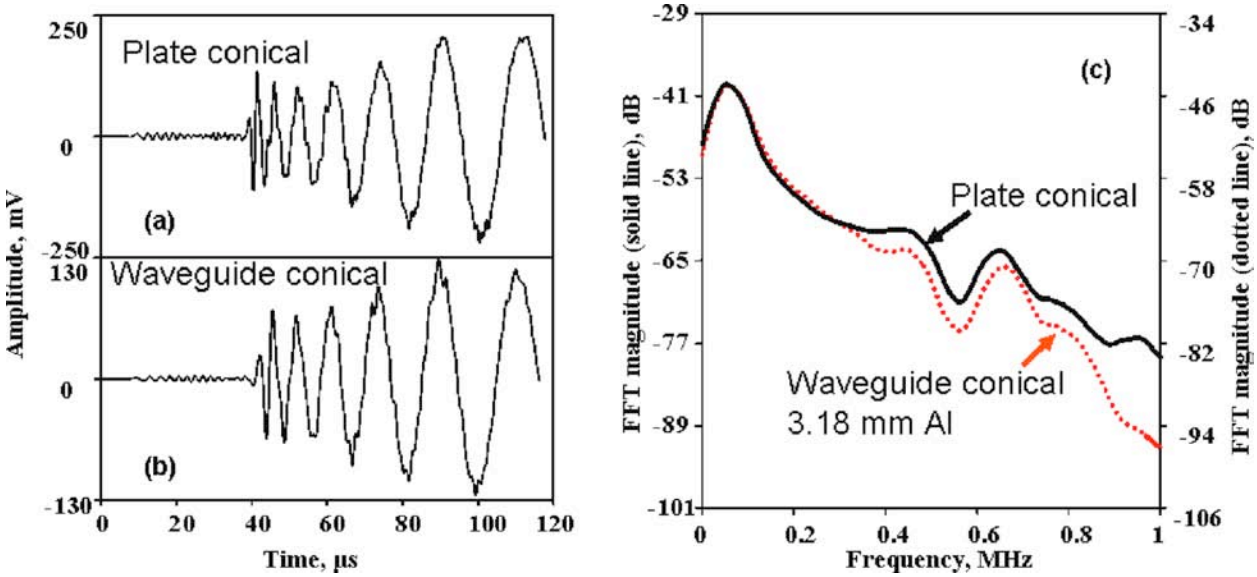

Fig. 12 Waveforms of signals from an out-of-plane pencil-lead break source with a 3.18-mm diameter aluminum waveguide of 409.6 mm length. Results are shown after the process described in the caption of Fig. 7. Part (c) provides the FFT spectra of the two signals shown in parts (a) and (b).

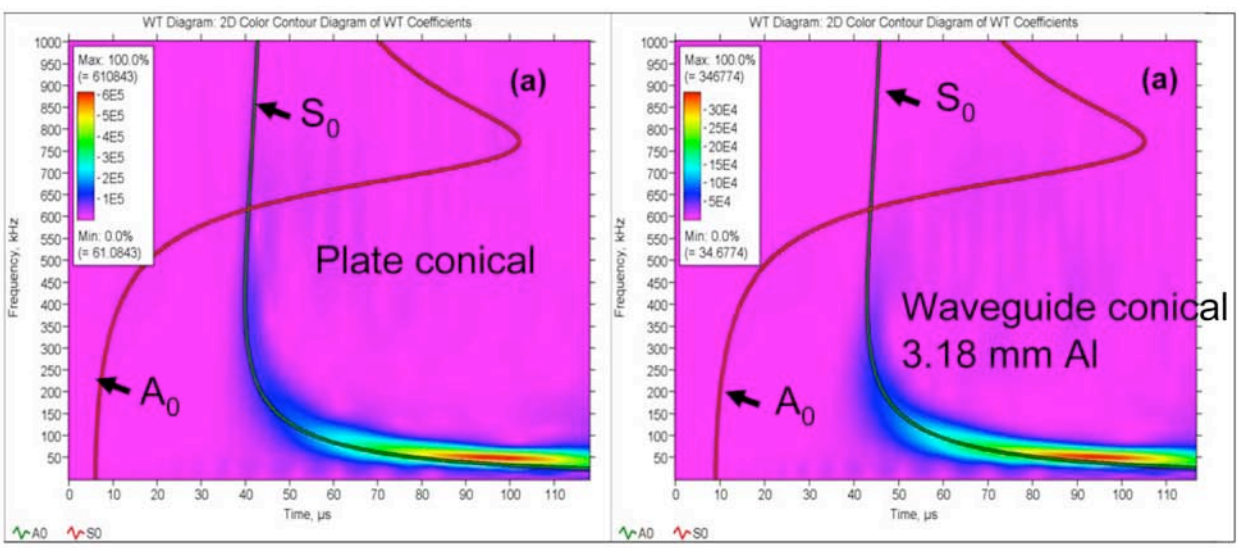

Fig. 13 WTs of the two signals shown in parts (a) and (b) of Fig. 12 with superimposed result from the two lowest plate group-velocity modes.

To examine more closely differences between the two diameters of the aluminum WGs, the signals were compared more directly in Figs. 14(a) and (b). In these figures, the time scale was changed so that the initial portion of the S_0 mode and the first few cycles of the plate flexural A_0 mode are shown, and the amplitude scales for the two curves were adjusted to enhance the comparisons. These results show (comparing Figs. 14(a) and (b)) for the larger diameter WG that there is a loss of duplication in the WG sensor signal of the S_0 mode just a few cycles after it arrives, and there is a more serious loss of duplication in the first two cycles of the arrival of the A_0 mode.

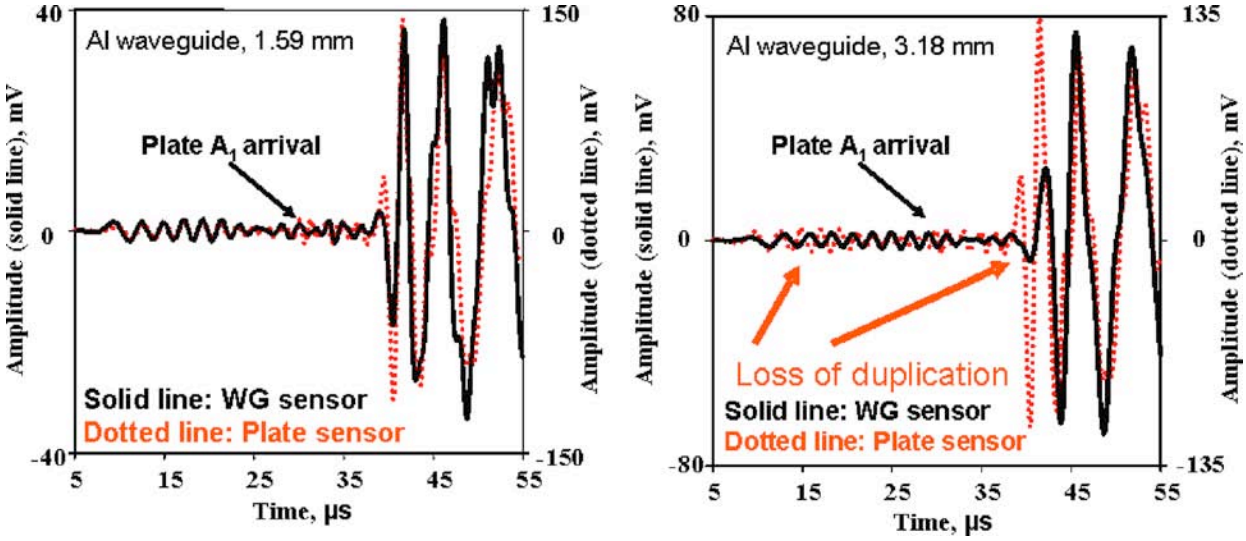

Fig. 14 Initial portions of the two sensor signals (after removal of the off-set due to the propagation time at the rod velocity) for the two aluminum waveguide cases with an out-of-plane pencil-lead break. Part (a) for the 1.59-mm diameter waveguide and part (b) for the 3.18-mm diameter waveguide.

It is relevant to point out that this latter deviation is in the high frequency region of that plate mode. It is not surprising that the duplication results are better for the smaller diameter WG (see Fig. 14(a)), where a larger portion of the frequencies of interest travel at or near the rod velocity. In the case of the larger diameter WG, the higher frequencies of the plate S_0 and A_0 modes that are transferred to the WG travel over a wider range of velocities in the rod S_0 mode, and thus those parts of the plate signal are dispersed and have less amplitude in the WG sensor signal. It is also relevant to point out that the larger diameter WG is longer, so small variations in the velocities in the rod would have a larger effect.

As a final observation from Fig. 14, the arrival of the beginning of the plate A_1 mode is indicated in the plate sensor signal. Since the plate group velocity diagram (shown in Fig. 4) indicates that the A_1 mode arrives with frequencies from about 800 kHz to 1000 kHz, it is not surprising that it is difficult to detect this arrival in the WG sensor signal in either diameter case.

Small Diameter Brass WG

To examine a case where the acoustic impedance of the WG does not match that of the plate, a small diameter (1.59 mm) brass rod was used with an out-of-plane pencil-lead break. As before, the simultaneously gathered signals were offset in time due to the added propagation time along the WG length of 300.4 mm. Since the exact rod velocity was unknown, the value (3.67 mm/µs) given by Kolsky [6] for copper was used with the rod length to correct for the offset in time between the two signals. Figures 15(a) and (b) show the resulting signals. In this figure both sensor signals were terminated at a zero prior to the plate A_o mode reflection in the brass WG. Figure 15(c) shows the FFT of the two time-domain signals. As before, the FFTs were calculated with a square window after they were extended to 2048 points from their zero-terminated length.

Qualitatively, in Figs. 15(a) and (b), the time domain signals are quite similar. The FFT result (after again changing the vertical scale to superimpose the results in the low frequency

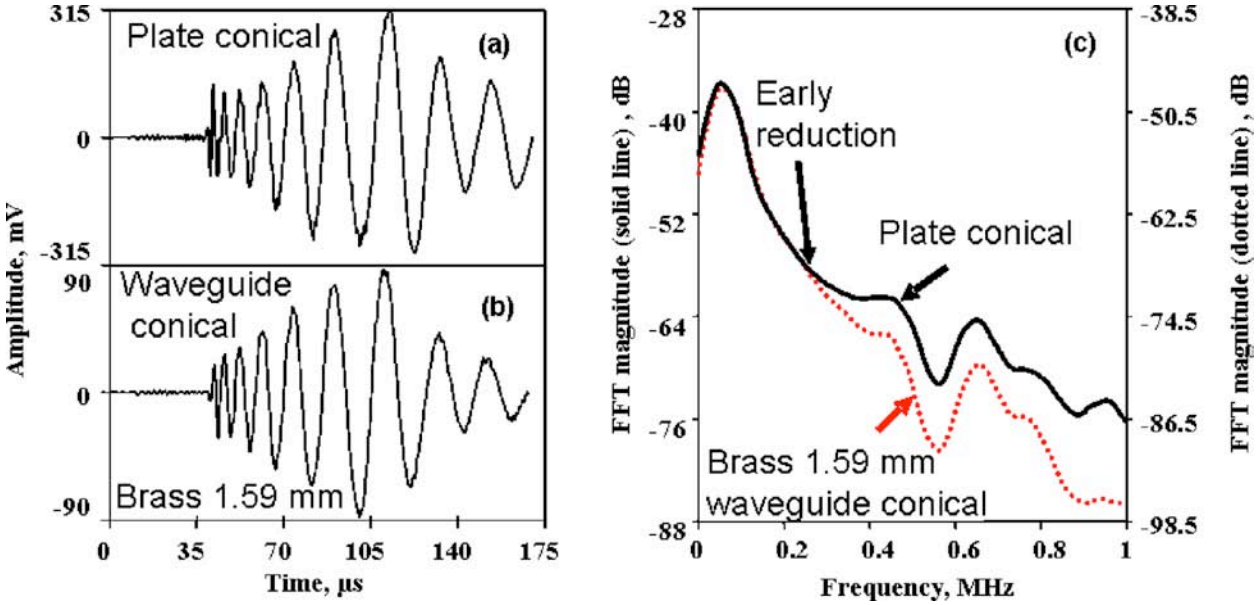

Fig. 15 Waveforms of signals from an out-of-plane pencil-lead break source with a 1.59 mm diameter by 300.4 mm long brass waveguide. Part (a) from the plate conical sensor signal and part (b) from the sensor coupled to the end of the brass waveguide. Signals are shown after the removal of the time offset as described in the caption of Fig. 7. Part (c) shows the FFT spectra of the signals shown in parts (a) and (b).

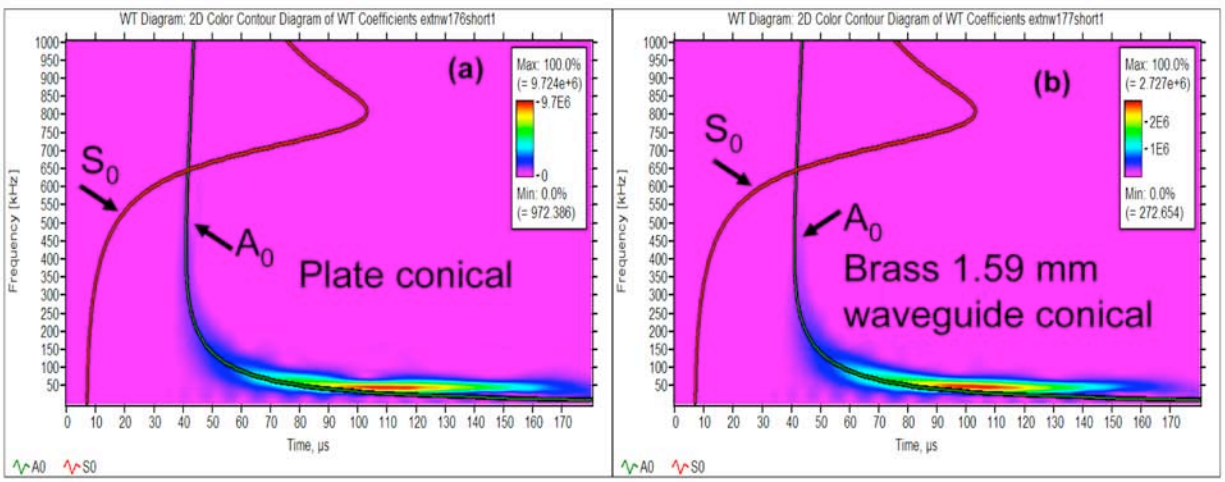

Fig. 16 WTs of the two signals shown in parts (a) and (b) of Fig. 15 with superimposed results from the two lowest plate modes group-velocity curves.

region) shows that the WG sensor signal starts to fall off at about 300 kHz relative to the plate sensor signal. As before, to help clarify the FFT results, the curves were smoothed over 30 points. With the limitations already pointed out, the FFT results indicate an amplitude decrease of about 11 dB of the WG sensor signal as compared to the plate sensor signal. This result compares with the approximately 13-dB loss for the same source with the aluminum rod WG (see Fig. 7(c)). As shown in Fig. 16, the WT results (calculated as described earlier) are very similar for the plate and WG sensors, and this figure shows the dominance of the low-frequency portion of the A_0 mode.

To show more closely the differences between the WGs of the two different materials of the same diameter (1.59 mm), the initial arrivals of the signals through the first few cycles of the A_0

mode are compared in parts (a) and (b) of Fig. 17. For the aluminum and brass WGs, each part of the figure shows the WG sensor signal stacked (by adjusting the vertical scales) with the plate sensor signal. The arrows in part (b) show the regions of poor duplication of the brass WG sensor signal compared to the plate sensor signal. Part (a) clearly shows that in these regions the duplication of the aluminum WG signal is much closer to that of the plate sensor signal.

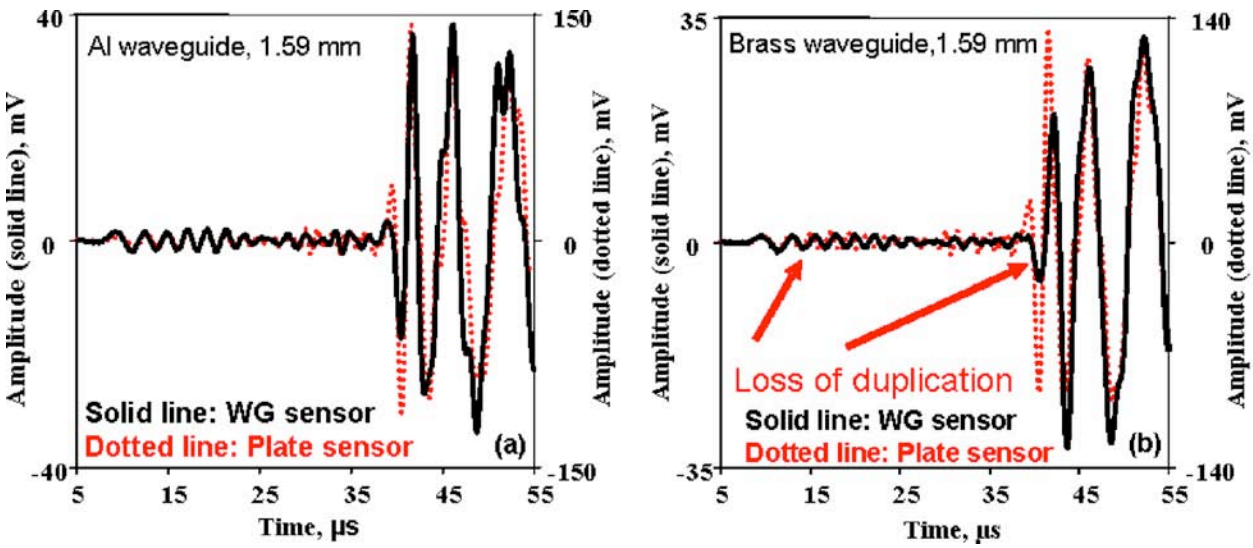

Fig. 17 Initial portions of the plate and waveguide sensor signals after the offset in time has been removed for the out-of-plane pencil-lead-break source and a waveguide diameter of 1.59 mm. Part (a) is for the aluminum waveguide and part (b) is for the brass waveguide.

Conclusions

The experiments presented here demonstrated that when a small 1.59-mm diameter waveguide was used with a wideband conical, nearly-flat-with-frequency sensor, the waveguide sensor can provide a wideband high-fidelity signal over the range of frequencies and Lamb modes generated by pencil-lead breaks in a thin aluminum plate. Specifically, one can conclude:

- A 1.59-mm diameter aluminum WG transmits a reasonable copy of the out-of-plane displacement that passes under the end of the waveguide coupled to the plate.
- The 1.59-mm diameter aluminum waveguide provides a better duplicate of the plate sensor signal than a 3.18-mm diameter rod of the same material.
- The superiority of the 1.59-mm diameter aluminum rod waveguide is particularly apparent at the beginning of the signal from the plate A_0 mode and part way through the initial portion of the signal from the plate S_0 mode.
- The signal regions where the larger diameter aluminum rod waveguide sensor does the poorest job of duplicating the plate sensor signal are those where higher frequencies are present. These frequency regions of the rod S_0 mode are those where the displacement waves are traveling at slower velocities than the rod velocity.
- The experimental results with the 1.59-mm brass rod mirror those of the 3.18-mm aluminum rod in the degradation of certain frequency regions in the waveguide sensor signal.
- In all cases, the signal level out of the waveguide end-mounted sensor is reduced in comparison to that for the plate-mounted sensor.

- The WG signal reduction trends in signal level for the out-of-plane pencil-lead break source are about 13 dB for the 1.59-mm aluminum waveguide, 5 dB for the 3.18-mm aluminum waveguide, and 11 dB for the 1.59-mm brass waveguide.

Acknowledgement

The efforts of Mr. David McColskey and Mr. Raymond Santoyo of NIST Boulder, Colorado in assisting with the experimental setup are acknowledged.

References

1. K. Ono, and H. Cho, "Rods and Tubes as AE Waveguides", J. of Acoustic Emission, **22**, 243-252 (2004). See also *Proceedings 26th European Conference on Acoustic Emission Testing*, Vol. 2, pp. 593-597, 2004.
2. M.A. Hamstad and C.M. Fortunko, "Development of Practical Wideband High Fidelity Acoustic Emission Sensors", *Nondestructive Evaluation of Aging Bridges and Highways*, Steve Chase, Editor, Proc. SPIE 2456, pp. 281-288, 1995.
3. M.A. Hamstad, "Improved Signal-to-Noise Wideband Acoustic/Ultrasonic Contact Displacement Sensors for Wood and Polymers", Wood and Fiber Science, **29** (3), 239-248, 1997.
4. Fuji Ceramics Corporation, Japan, Model A1002.
5. J. Vallen, "Vallen Dispersion Software, Version R2005.1121", Vallen-Systeme GmbH, Munich, Germany. Available as http://www.valleh.de/wavelet/index.html, 2005.
6. H. Kolsky, *Stress Waves in Solids*, Dover Publications Inc., New York, 1953.
7. R. L. Weaver and Y.-H. Pao, "Axisymmetric Elastic Waves Excited by a Point Source in a Plate," J. of Appl. Mech., Col. **49**, 821-836, 1982.
8. J. Vallen, "AGU-Vallen Wavelet Transform Software, Version R2005.1121", Vallen-Systeme GmbH, Munich, Germany. Available at http://www.vallen.de/wavelet/index.html, 2005.